BEILSTEIN JOURNAL OF ORGANIC CHEMISTRY

New reactive intermediates in organic chemistry

Edited by Götz Bucher

Imprint

Beilstein Journal of Organic Chemistry
www.bjoc.org
ISSN 1860-5397
Email: journals-support@beilstein-institut.de

The *Beilstein Journal of Organic Chemistry* is published by the Beilstein-Institut zur Förderung der Chemischen Wissenschaften.

Beilstein-Institut zur Förderung der Chemischen Wissenschaften
Trakehner Straße 7–9
60487 Frankfurt am Main
Germany
www.beilstein-institut.de

Beilstein Journal of Organic Chemistry

New reactive intermediates in organic chemistry

Götz Bucher

Editorial

Open Access

Address:
WestCHEM, School of Chemistry, University of Glasgow, Joseph-Black-Building, University Avenue, Glasgow G12 8QQ, United Kingdom

Email:
Götz Bucher - goebu@chem.gla.ac.uk

Keywords:
reactive intermediates

Beilstein J. Org. Chem. **2013,** *9,* 613–614.
doi:10.3762/bjoc.9.67

Received: 05 March 2013
Accepted: 11 March 2013
Published: 26 March 2013

This article is part of the Thematic Series "New reactive intermediates in organic chemistry".

Guest Editor: G. Bucher

Physical organic chemistry (POC) and reactive intermediate chemistry (RIC) belong to the core subjects of organic chemistry. During the 1990s and 2000s both had become increasingly less fashionable, and in many countries, the mass of active researchers working in POC and RIC was in danger of becoming subcritical. Consequently, in 2003, the Whitesides-Report on the status of chemistry in Great Britain pointed out shortcomings in POC. These shortcomings bore implications reaching beyond academia: in chemical industry, chemists with excellent skills in mechanistic organic chemistry are needed for many tasks, but an insufficient number were being educated. As a consequence of the Whitesides-Report, the Engineering and Physical Sciences Research Council of the UK (EPSRC) funded two Centres for Physical Organic Chemistry, one in Cardiff, and one in Glasgow, and launched two calls for research proposals in POC.

Research into reactive intermediates has historically been part of the work involved in product studies. In order to characterise a reactive intermediate, it had to be trapped. Thus, in order to characterise a carbene, for example, one would intercept it with an alkene and isolate the resulting cyclopropane. Using internal quenchers (molecular clocks) providing well-defined competing reactions, product studies can even yield accurate values for the kinetics of intermolecular quenching reactions of reactive intermediates. More recent techniques to characterise reactive intermediates include matrix isolation spectroscopy, where a reactive intermediate is generated in a cryogenic noble-gas matrix and hence can be studied for an extended period of time; or laser flash photolysis, where the reactive intermediate is generated by a very short pulse of laser light, and can be investigated in real time; or specialised mass-spectrometric techniques such as ion cyclotron resonance MS. Due to the exponential increase in computing power available to researchers, much of the mechanistic work nowadays is done using the tools of quantum chemistry. In particular, the various flavours of density functional theory have proven valuable in this respect, but high-level correlated methods such as CCSD(T) also have their place.

This Thematic Series of the *Beilstein Journal of Organic Chemistry* is meant to highlight recent developments in the chemistry of reactive intermediates, and to illustrate the current state of the art in a number of very varied research fields.

Götz Bucher

Glasgow, March 2013

Beilstein Journal of Organic Chemistry

Presence or absence of a novel charge-transfer complex in the base-catalyzed hydrolysis of *N*-ethylbenzamide or ethyl benzoate

Shinichi Yamabe*, Wei Guan and Shigeyoshi Sakaki

Full Research Paper

Open Access

Address:
Fukui Institute for Fundamental Chemistry, Kyoto University, Takano-Nishihiraki-cho 34-4, Sakyo-ku, Kyoto 606-8103, Japan, phone: +81-075-711-7907

Email:
Shinichi Yamabe* - yamabes@fukui.kyoto-u.ac.jp

* Corresponding author

Keywords:
basic hydrolyses; DFT calculations; ethyl benzoate; *N*-ethylbenzamide; reactive intermediates; transition states

Beilstein J. Org. Chem. **2013,** *9,* 185–196.
doi:10.3762/bjoc.9.22

Received: 06 November 2012
Accepted: 04 January 2013
Published: 29 January 2013

This article is part of the Thematic Series "New reactive intermediates in organic chemistry".

Guest Editor: G. Bucher

Abstract

Reaction paths of base-catalyzed hydrolyses of isoelectronic substrates, Ph–C(=O)–X–Et [X = O (ethyl benzoate) and X = NH (*N*-ethylbenzamide)], were traced by DFT calculations. To simulate bond interchanges accompanied by proton transfers, a cluster model of Ph–C(=O)–X–Et + $OH^-(H_2O)_{16}$ was employed. For X = O, three elementary processes and for X = NH four ones were obtained. The rate-determining step of X = O is the first TS (TS1, the OH^- addition step), while that of X = NH is TS2. TS2 of X = NH leads to a novel Mulliken charge-transfer complex, Ph–(OH)(O=)C···N(H_2)–Et. The superiority or inferiority between the direct nucleophilic process or the general base-catalyzed process for TS1 was examined with the model Ph–C(=O)–X–Et + $OH^-(H_2O)_n$, n = 3, 5, 8, 12, 16, 24 and 32. The latter process was calculated to be more favorable regardless of the number (n, except n = 3) of water molecules. The counter ion Na^+ works unfavorably on the ester hydrolysis, particularly on TS1. A minimal model of TS1 was proposed and was found to be insensitive to n.

Introduction

Basic hydrolyses of esters and amides have been extensively studied experimentally [1]. Use of dilute alkali is the usual way of hydrolyzing esters, and the reaction is called saponification. The base-catalyzed hydrolysis of amides is an important model for the enzymatic cleavage of peptide bonds [2,3]. The base-promoted hydrolyses of carboxylic esters and amides accompanying the ^{18}O exchange have been investigated to characterize reversibly formed intermediates [4-16].

Through the analysis of heavy-atom isotope effects, the rate-determining step of the alkaline hydrolysis of methyl benzoate (Ph–C(=O)–OMe) was shown to be the formation of the anionic tetrahedral intermediate by O'Leary and Marlier [17]. Marlier suggested that the attacking nucleophile in aqueous solution is water with OH^- assistance in the hydrolysis of methyl formate ($HCOOCH_3$) [18]. This suggestion is in sharp contrast to the traditional $B_{ac}2$ mechanism [19]. In this mechanism, the tetra-

hedral intermediate is formed by direct nucleophilic collisions between hydroxide ions and ester molecules. Marlier's suggestion was supported by a kinetic study of the saponification of ethyl acetate ($CH_3COOC_2H_5$) [20].

For the base-catalyzed amide hydrolysis, Brown and co-workers made extensive studies of the carbonyl ^{18}O exchange and D_2O solvent kinetic isotope effects [21-25]. They suggested intervention of a pair of a zwitterion and OH^- as well as that of the anionic tetrahedral intermediate (Scheme 1).

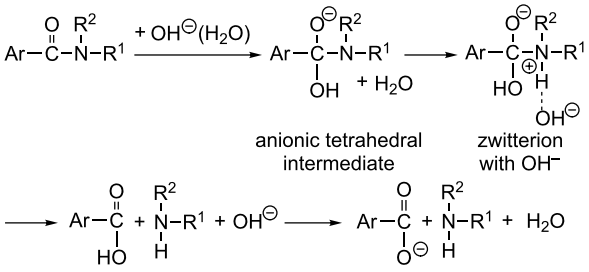

Scheme 1: A scheme of the base-catalyzed amide hydrolysis involving a zwitterion suggested by analyses of solvent kinetic isotope effects [22].

Although many theoretical studies of the basic amide hydrolysis have been reported so far [26-37], the presence or absence of the zwitterion has not been scrutinized.

As for zwitterions of amino acids and peptides, the effect of the solvent on the structure and various spectra has been examined carefully [38-46]. Explicit solvent models were reported to be necessary, and it was shown that the use of continuum solvent models is not adequate. For instance, Degtyarenko and co-workers demonstrated that 20 water molecules are needed to completely solvate the L-alanine zwitterion [46]. The average number of water molecules in the first hydration shell of an alanine molecule was found to be seven [44]. Thus, more than seven water molecules would be required to examine the reaction paths of hydrolyses reliably. However, less than six water molecules are included in the precedent computational studies [26-37]. As stated in [20], "an appropriate mechanistic picture for the system (saponification) must take into account the solvent molecules that should be included in the minimal TS structure".

The mechanisms of the well-known two base-catalyzed hydrolyses are still unclear in the following points:

1. The rate-determining step of the ester hydrolysis was suggested to be the nucleophilic OH^- addition to the carbonyl carbon according to the kinetic result of the heavy-atom isotope effect [17]. On the other hand, in the hydrolyses of a series of toluamides ($Me–C_6H_4–C(=O)–N(R^1)(R^2)$), the rate-determining steps were reported to vary from the OH^- attack to breakdown of the anionic tetrahedral intermediate [22]. It seems that the rate-determining step of the amide reaction is not as definite as that of the ester one.

2. The number of elementary processes in both hydrolyses is yet unknown. Is the zwitterion shown in Scheme 1 also present in the ester reaction?

3. In [25], the direct nucleophilic process was suggested to be more favorable than the general base-catalyzed process for the hydrolysis of formamide (Scheme 2). This suggestion is in contrast to Marlier's one mentioned above for the hydrolysis of methyl formate [18]. Does the amide take a different OH^- addition process from that of the ester? Is the controversial OH^- ad-

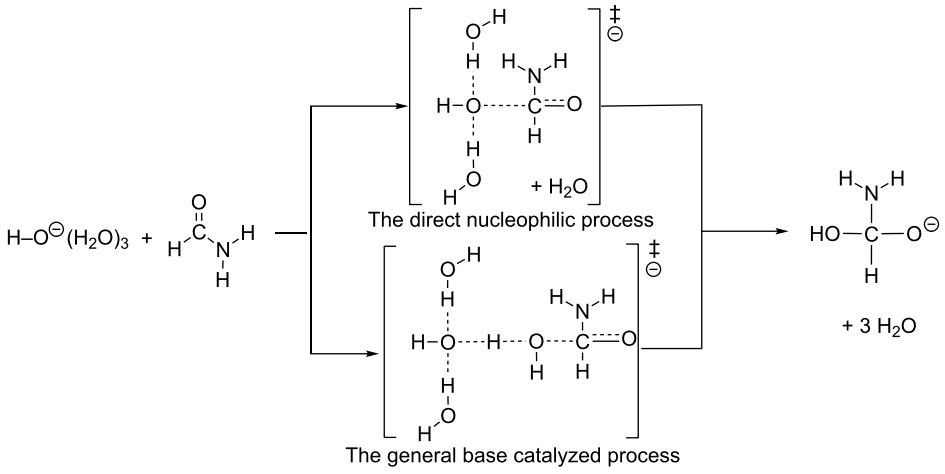

Scheme 2: Two processes suggested by a proton-inventory NMR study [25].

dition transition state affected by the number of water molecules adopted in calculations?

4. The base-catalyzed hydrolysis is conducted usually by the use of the NaOH (i.e., 0.01 to 1.0 mol/L aqueous) solution. Then, the role of the counter ion Na^+ on the reaction paths and energies needs to be investigated.

5. Is "the minimal TS structure" [20] predictable in the framework of the molecular model prior to any calculations?

In this work, DFT calculations were carried out to shed light on the five points above, 1–5. As isoelectronic substrates, ethyl benzoate and *N*-ethylbenzamide were employed, of which the reactions are shown in Scheme 3.

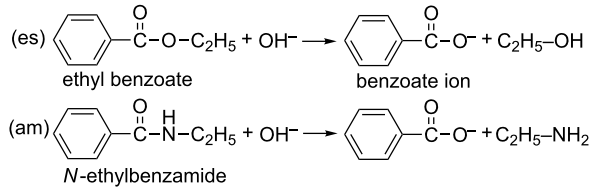

Scheme 3: Hydrolysis of the ester (saponification) and the amide adopted in this work. These are assigned as (es) and (am), respectively.

The former (ester) reaction has been studied well and its activation energy was reported to be 14.6 kcal/mol [47]. The latter (amide) analogous one (*N*,*N*-dimethyltoluamide, $Me–C_6H_4–C(C=O)–NMe_2$) was investigated and the experimental activation free energy was reported to be 27.1 kcal/mol [22]. The hydrolysis of the phenyl-group-containing substrate was studied computationally in a reaction between *N*-methylbenzamide and OH^- [37]. However, only one water molecule was contained in the reaction system.

In the present study, the number of water molecules (n) is changed systematically in Scheme 4 to address the latter part of point 3.

Method of calculations

The reacting systems were investigated by density functional theory calculations. The B3LYP [48,49] method was used to trace the reaction path. B3LYP seems to be a suitable method, which includes the electron correlation effect to some extent. The basis set employed was 6-31(+)G(d), where diffuse functions are added to oxygen and nitrogen atoms. Since the present systems are large (for the largest stoichiometry $C_9H_{76}NO_{34}{}^{(-1)}$ of n = 32 (amide), 952 basis functions of 6-31(+)G(d) in the geometry optimizations), calculations with higher-level basis sets than 6-31(+)G(d) are too difficult.

As for the key step, i.e., the OH^- addition process, TS geometries of n = 16 were re-optimized with B3LYP/6-311+G(d,p), B3PW91 [50]/6-31(+)G(d), B3PW91/6-31(+)G(d) SCRF (self-consistent reaction field) = PCM [51-53], B3PW91/6-311+G(d,p) and M06-2X [54]/6-31(+)G(d). These re-optimizations are needed to check whether the obtained TS structures are insensitive to the adopted method or not in relation to the former part of point 3.

Transition states (TSs) were sought first by partial optimizations at bond-interchange regions. Second, by the use of Hessian matrices, TS geometries were optimized. They were characterized by vibrational analyses, which checked whether the obtained geometries have single imaginary frequencies ($\nu^{\neq}$s). From TSs, reaction paths were traced by the intrinsic reaction coordinate (IRC) method [55,56] to obtain the energy-minimum geometries. In order to check the character of the HO^- addition TS, classical trajectory calculations using the atom-centered density-matrix-propagation molecular dynamics (ADMP) model [57-59] were also conducted.

Relative energies (ΔEs) and Gibbs free ones (ΔGs) were obtained by single-point calculations of RB3LYP/6-311++G(d,p) {SCRF = PCM, solvent = water} on the RB3LYP/6-31(+)G(d) geometries and their ZPVE and thermal corrections, respectively.

All the calculations were carried out by using the GAUSSIAN 09 [60] program package. The computations were performed at the Research Center for Computational Science, Okazaki, Japan.

Results and Discussion

Consideration of minimal and extended TS structures

According to the requirement of "an appropriate mechanistic picture of the minimal TS structure" [20], a model of the OH^- addition to the carbonyl carbon was made and is shown in

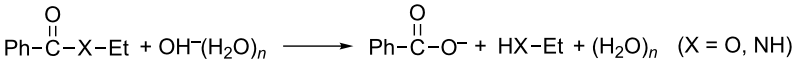

Scheme 4: A reaction model including the water cluster.

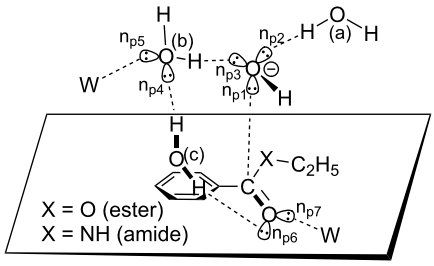

Figure 1: A minimal model of the OH^- nucleophilic addition to the substrate, Ph–C(=O)–X–Et. Three ((a), (b) and (c), n = 3) water molecules participate in the main hydrogen bonds to stabilize the TS structure. W stands for the water molecule as an outer catalyst. n_p denotes the lone-pair orbitals on the oxygen atom.

Figure 1. At the OH^- addition, one lone-pair orbital (n_{p1}) of OH^- is directed to the carbonyl carbon. The other two ones (n_{p2} and n_{p3}) should be linked to two water molecules, (a) and (b). n_{p4} and n_{p5} of the water (b) become anionic through the $OH^- \rightarrow H_2O$(b) charge transfer (CT). Then, a water (c) may be linked to n_{p4} of H_2O(b) and n_{p6} of the carbonyl oxygen in the bridged form. n_{p6} and n_{p7} of the carbonyl oxygen becomes anionic as the OH^- addition proceeds. Two anionic n_{p5} and n_{p7} are linked with the outer two water molecules (W's). The assumed picture in Figure 1 is in line with the experimental suggestion that five water molecules participate in the reaction center [25].

The assumption in Figure 1 was examined by varying the number of water molecules in Scheme 4 at the OH^- addition transition state (TS1). Figure 2 shows geometries of TS1(es) for

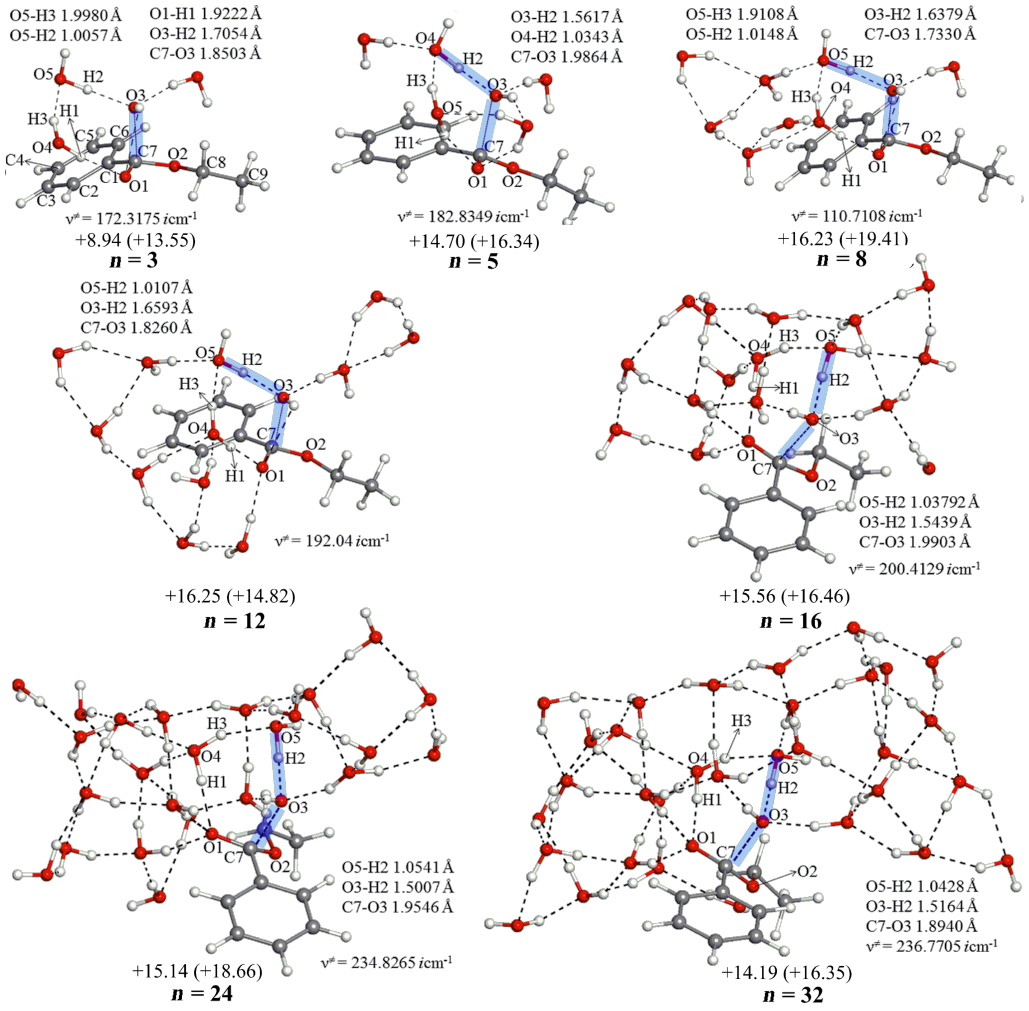

Figure 2: Geometries and B3LYP/6-31(+)G(d) activation energies of TS1(es) in the reaction between ethyl benzoate and $OH^-(H_2O)_n$. Activation and activation free energies in kilocalories per mole (1 kcal = 4.184 kJ) are shown without and with parentheses, respectively. For instance, E_a = + 8.94 kcal/mol and $\Delta G^{\neq}$ = + 13.55 kcal/mol for n = 3. Cartesian coordinates of all the TS geometries are shown in VII.a (Supporting Information File 1).

n = 3, 5, 8, 12, 16, 24 and 32 in the ester hydrolysis. Hereafter, the ester reaction is shown by (es) and the amide one is by (am). They exhibit that the skeletal part of n = 3 (without two W's in Figure 1) is retained in all the TS1(es) geometries. In addition, the n = 5 geometry is close to that drawn qualitatively in Figure 1. Here, H3–O5–H1 is the bridged H_2O (c) in Figure 1. Figure 3 shows those in the amide hydrolysis. Again, the n = 3 central parts are retained in TS1(am) geometries of n = 5, 8, 12, 16, 24 and 32.

From all TS1 geometries (except that of n = 3), IRC calculations were carried out to judge which is more likely, the direct

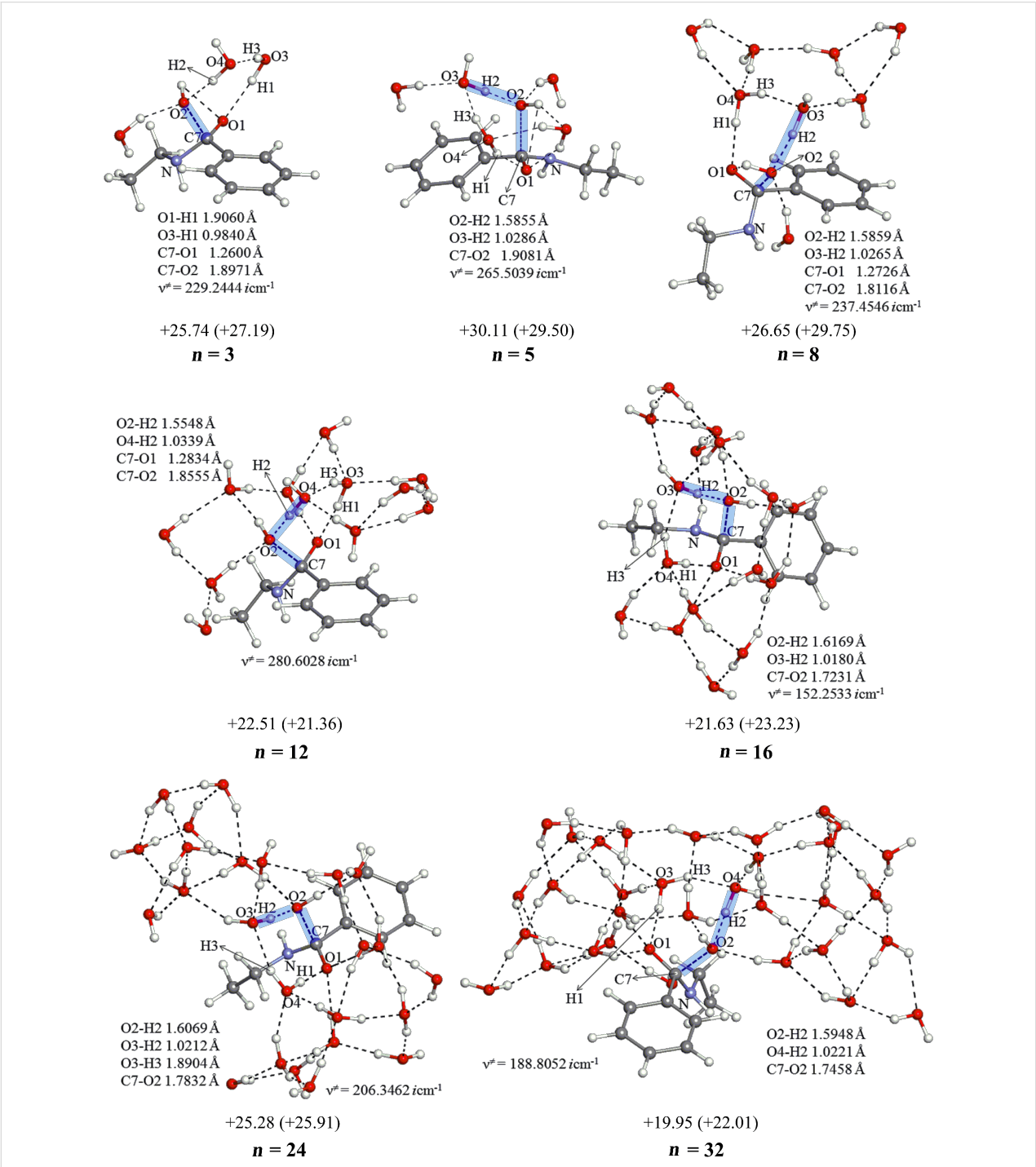

Figure 3: Geometries and activation energies of TS1(am) in the reaction between *N*-ethylbenzamide and $OH^-(H_2O)_n$. XYZ coordinates in VII.b (Supporting Information File 1).

nucleophilic process or the general base-catalyzed one in Scheme 2. All the "reverse" geometries (i.e., those of the reactant-like complex) are found to have the OH^- at the H_2O(b) position (see Figure 1). Thus, the general base-catalyzed process was calculated to be more likely regardless of the number of water molecules. The judgment is also checked by the other methods than B3LYP/6-31(+)G(d). They are B3LYP/6-311+G(d,p), B3PW91/6-31(+)G(d), B3PW91/6-31(+)G(d) SCRF = PCM, B3PW91/6-311+G(d,p) and M06-2X/6-31(+)G(d). By their TS and IRC calculations of the n = 16 system, the general base-catalyzed process was confirmed. Key distances in TS1(es) and TS1(am) are shown in Tables S1 and S2 (Supporting Information File 1), respectively.

The trajectory calculation may give a different result, if the potential surface at the OH^- addition step is shallow. In order to check this point, the ADMP molecular dynamics calculation was made starting from TS1(es) of the ester n = 16. After 800 femtoseconds, the resultant geometry is shown in the right of Figure S1. The geometry is similar to that of the reactant-like complex obtained in the IRC calculation. Again, the general base-catalyzed process was confirmed.

In view of geometries and the calculated activation energies, the n = 16 model was selected to trace elementary processes, in a balance between reliability and computational difficulty.

Reaction paths in the ester hydrolysis

Figure 4 exhibits geometric changes in the n = 16 ester hydrolysis. Starting from the reactant-like complex, OH^- adds to the carbonyl carbon at TS1(es). After TS1(es), the expected anionic tetrahedral intermediate, Int1(es), is formed. At the intermediate, the alkoxide oxygen O(3) is the most anionic.

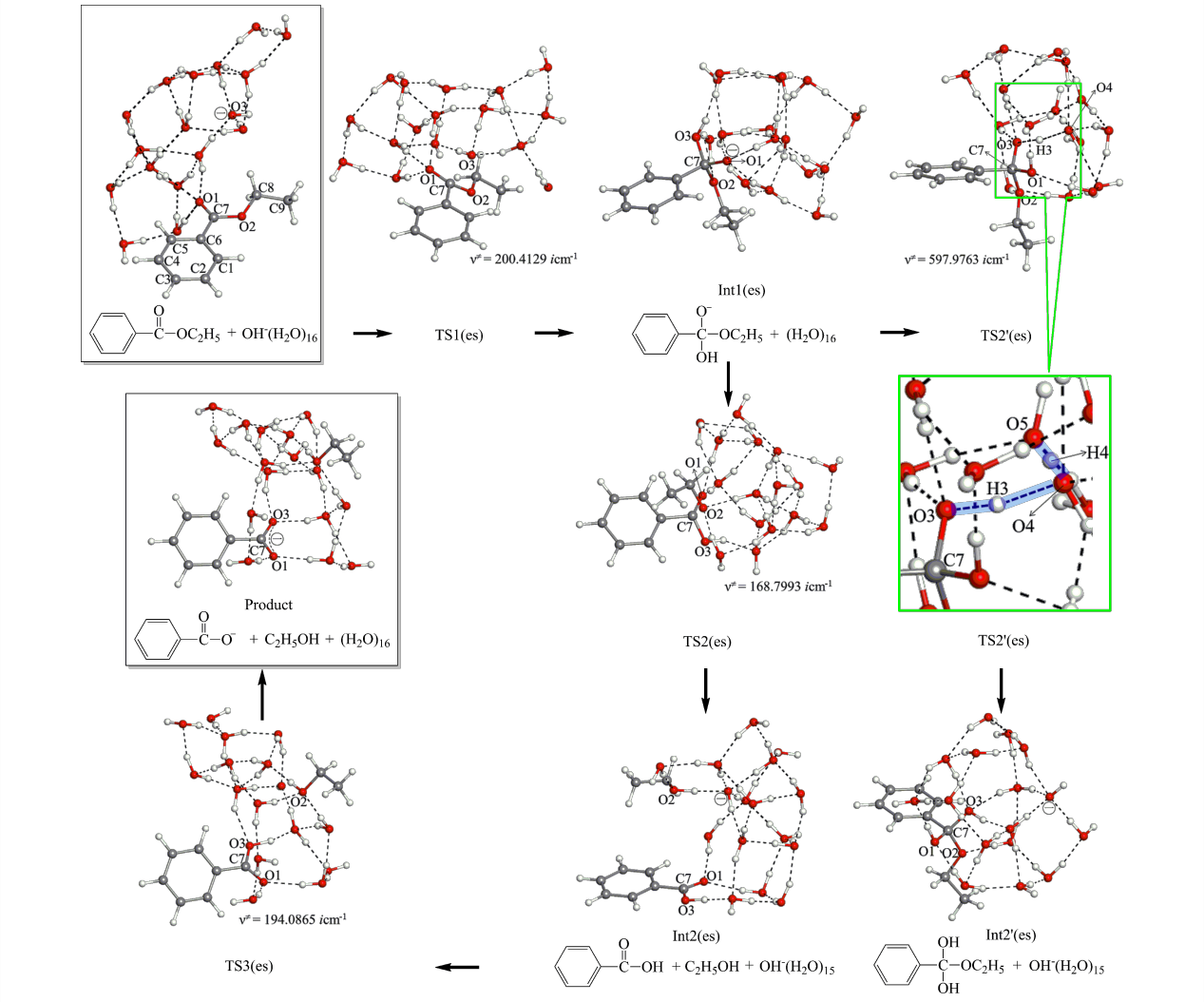

Figure 4: Reaction paths of the ester n = 16 hydrolysis, starting from the boxed reactant-like complex toward the boxed product. To TS2'(es), the magnified cut figure is attached. XYZ coordinates in VII.c (Supporting Information File 1).

A proton-attach TS, TS2'(es), was obtained. After TS2'(es), a neutral tetrahedral intermediate Int2'(es), is formed. If this intermediate is very stable, it should be in equilibrium with the reactant-like complex. Then, the hydrolysis occurs as a nonequilibrium route according to Le Chatelier's principle (Scheme 5).

The scheme will be evaluated by comparing the calculated energies. As the alternative route to Int1(es), TS2(es) was obtained. At TS2(es), C···O cleavage and the proton transfer occur simultaneously. This process is different to that thought so far (C···O scission only forming $C_2H_5O^-$). Formation of the unstable ethoxide ion is avoided by the concomitant proton transfer. After TS2(es), the {Ph–COOH + Et–OH + $OH^-(H_2O)_{15}$} intermediate (Int2(es)) is afforded. The combination of Ph–COOH and OH^- leads to TS3(es), where the double proton transfer is involved. After TS3(es), the product of {$Ph–COO^-$ + Et–OH + $(H_2O)_{16}$} is generated.

Figure 4 demonstrates that the hydrolysis of ethyl benzoate has three elementary processes (except TS2'(es)). The ethoxide-ion intermediate and the zwitterion shown in Scheme 1 were not found during the reaction. It is noteworthy that four TSs (TS1(es), TS2'(es), TS2(es) and TS3(es)) contain proton transfers. For instance, the reaction center of TS2'(es) may be described as O5----H4----O4----H3----O3. Lines ---- indicate the intermediate character of O–H covalent and O···H hydrogen bonds. Thus, proton transfers were found to regulate, significantly, the reaction paths of the ester hydrolysis.

Reaction paths in the amide hydrolysis

Figure 5 exhibits geometric changes in the n = 16 amide hydrolysis. The first step is the OH^- addition (TS1(am)) leading to the anionic tetrahedral intermediate, Int1(am). From the anion, a path similar to TS2(es) in Figure 4 was sought. However, a different TS, namely TS2(am), was obtained. At TS2(am), only the double proton transfer takes place, where the C(7)–N bond is retained. A "zwitterion ion" intermediate Int2(am) suggested in Scheme 1 was derived. This is the first case where the intermediate is calculated. However, the geometry is regarded as a Mulliken CT complex rather than a zwitterion, Et–(H_2)N → C(OH)(=O)–Ph. In fact, the C(7)–N distance, 1.659 Å, is appreciably larger than the 1.494 one of N–C(5). The CT complex may intervene only when it is surrounded by the water cluster. Hydrogen bonds to two amino hydrogens enhance the nucleophilicity of the nitrogen n_p. Those to the carbonyl oxygen enhance the electrophilicity of the carbonyl carbon. When the geometry of the CT complex moiety [Et–(H_2)N----C(OH)(=O)–Ph] is taken up and is re-optimized by B3LYP/6-31(+)G(d) SCRF = PCM, Et–NH_2 is completely separated from Ph–C(=O)–OH (infinite separation). On the other hand, when a geometry composed of Et(H_2)N----C(=O)(OH)Ph and five H_2O molecules is optimized by B3LYP/6-31(+)G(d) SCRF = PCM and B3PW91/6-311+G(d,p) SCRF = PCM, the CT-complex geometry is obtained (Figure S2). Thus, intervention of zwitter-ions and CT complexes should be described by cluster geometries with water molecules explicitly contained. This result is consistent with the proposal for the L-alanine zwitterion [38-46]. From the CT complex, the C(7)···N bond scission occurs at TS3(am). After TS3(am), the {Ph–COOH + Et–NH_2 + $OH^-(H_2O)_{15}$} intermediate, Int3(am), is generated. The generation is followed by TS4(am), which leads to the product {$Ph–COO^-$ + Et–NH_2 + $(H_2O)_{16}$}.

Figure 5 demonstrates that the hydrolysis of *N*-ethylbenzamide has four elementary processes. A crucial difference between the ester and amide hydrolyses is found in TS2; TS2(es) leads to the separated Ph–COOH and EtOH, while TS2(am) to the CT complex, Et–(H_2)N → C(OH)(=O)–Ph. The difference may be represented by that between the hard-base oxygen and soft-base nitrogen according to Pearson's HSAB concept [61].

Energy changes along the reaction paths

Figure 6 shows energy changes for the ester hydrolysis of Figure 4. Those of Na^+-containing paths in the system, Ph–C(=O)–OEt + $NaOH(H_2O)_{16}$, are also shown in green. Geometric changes in the Na^+-containing system are exhibited

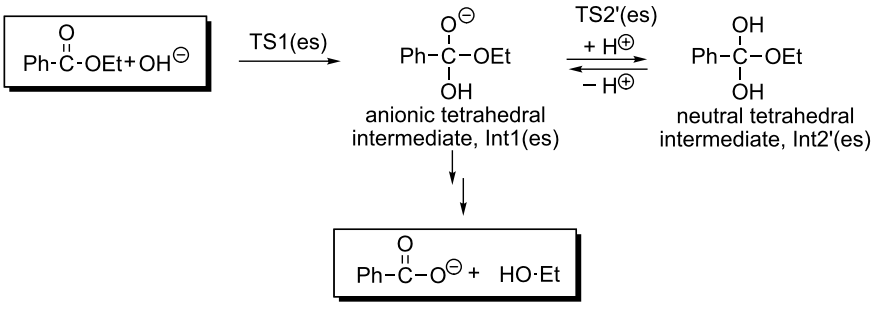

Scheme 5: A possibility that the neutral tetrahedral intermediate is the stock of concentrations for the irreversible hydrolysis route.

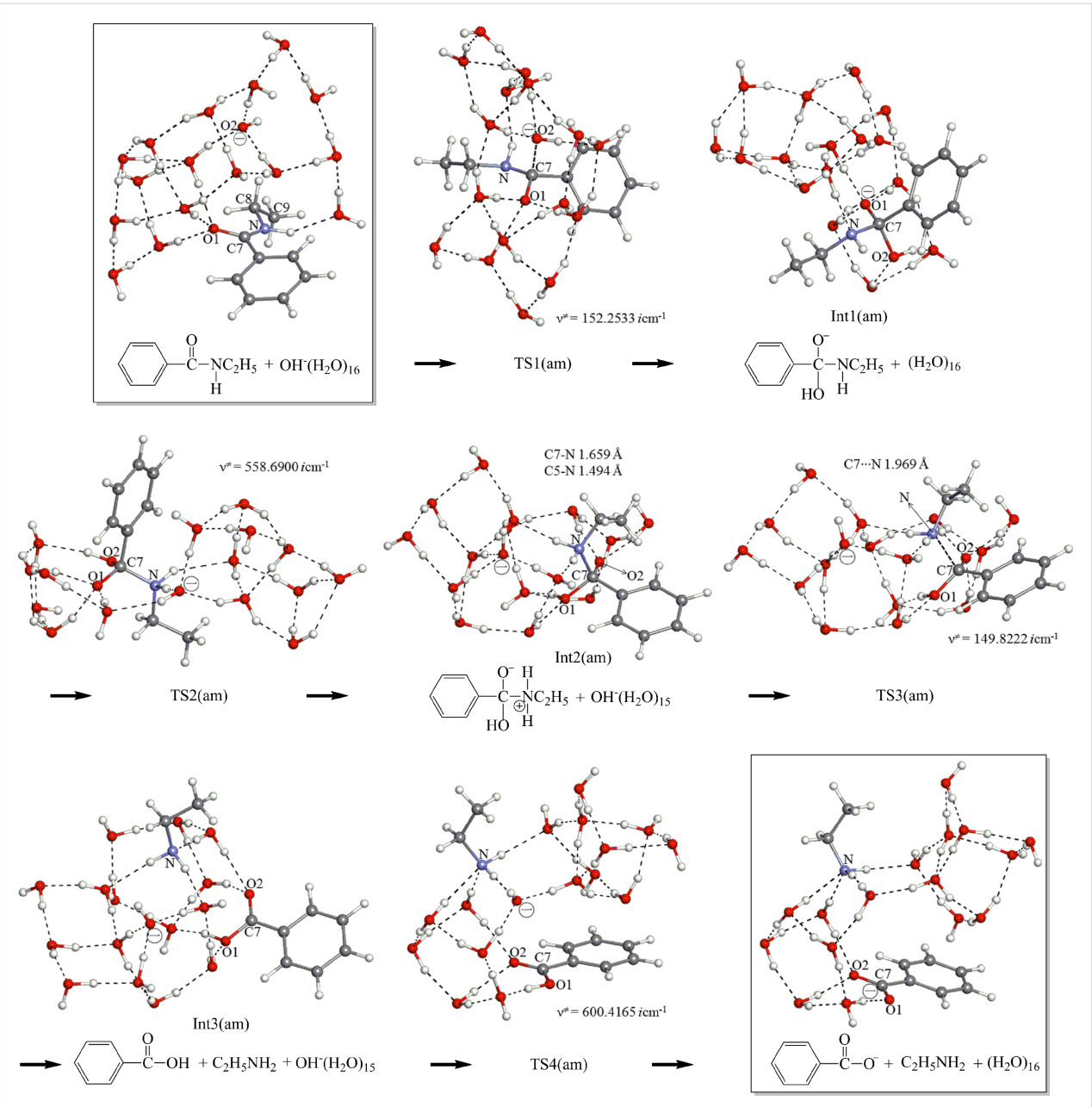

Figure 5: Reaction paths of the amide *n* = 16 hydrolysis. XYZ coordinates in VII.d (Supporting Information File 1).

in Figure S3 (Supporting Information File 1). For the geometry optimization, the position of Na^+ was assumed such that the reaction is promoted (i.e., (ii) in Figure 7).

In the changes of the Na^+-free system (Figure 4), the rate-determining step was confirmed to be TS1(es), with the calculated activation energy +14.45 kcal/mol (exp., +14.6 kcal/mol [47]). While TS2'(es) has a slightly lower energy (= +10.03 kcal/mol) than that (= +10.49 kcal/mol) of TS2(es), the former leads to an unstable intermediate, Ph–$C(OH)_2$–OEt, with the energy +8.86 kcal/mol. Therefore, the possibility {Ph–$C(OH)_2$–OEt as the concentration stock} raised in Scheme 5 has been ruled out. The energy changes of Figure 6 (without Na^+) demonstrate that the hydrolysis proceeds smoothly and suggest that intermediates may not be detected experimentally. When the Na^+ ion is included in the system, the activation energy of TS1(es) is enlarged appreciably (= +17.87 kcal/mol) in spite of the positional assumption (ii) in Figure 7. Thus, the counter ion works unfavorably on the rate-determining step TS1(es). The Na^+ ion has a very large hydration energy (= −97 kcal/mol), and the cation needs to be surrounded by many water molecules in the hydration shell far from the reaction region.

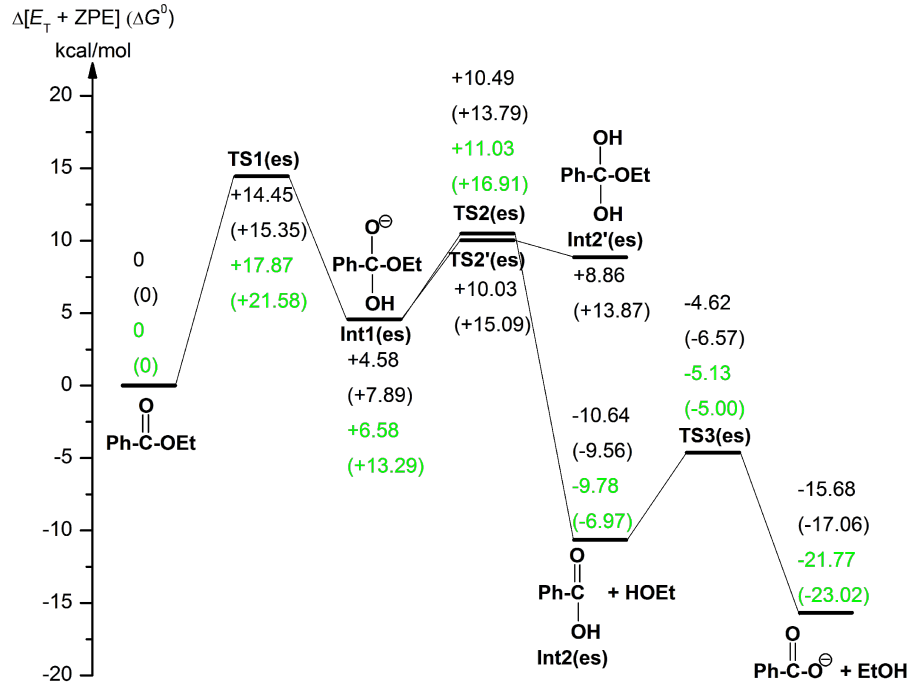

Figure 6: Changes of B3LYP/6-311++G(d,p) SCRF = PCM//B3LYP/6-31(+)G(d) Et + ZPE and (Gibbs free energies) of the ester hydrolysis in Figure 4 and Figure S3 (Supporting Information File 1). Energies given in green are for the Na^+-containing reaction in Figure S3.

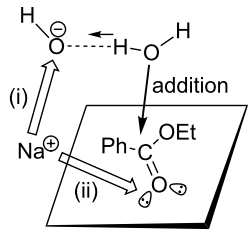

Figure 7: The effect of the counter ion Na^+ on TS1(es). When the position of Na^+ is near the nucleophile OH^- in (i), its addition is decelerated. On the contrary, when it is near the carbonyl oxygen in (ii), the addition is accelerated owing to the enhancement of the electrophilicity of the carbonyl carbon.

Figure 8 shows energy changes for the amide hydrolysis of Figure 5. Those of Na^+-containing paths in the system, Ph–C(=O)–NH–Et + $NaOH(H_2O)_{16}$ in Figure S4 (Supporting Information File 1), are also shown in green. In energies of the Na^+-free system, the rate-determining step was calculated to be TS2(am) with the activation energy 27.31 kcal/mol. This value is comparable to the experimental one 27.1 kcal/mol [22] in the basic hydrolysis of *N*,*N*-dimethyltoluamide (*para*-Me–C_6H_4–C(=O–NMe_2)). This result is consistent with the experimental suggestion that the second TS may be rate-determining as shown in Figure 5 of [22]. However, it is in contrast with the general scheme that the first OH^- addition step is rate-determining [36]. The result of Ea{TS1(am)} < Ea{TS2(am)} was checked by re-optimizing their geometries with B3LYP/6-311+G(d,p). Activation (free) energies were calculated to be 23.29 (25.74) kcal/mol for TS1(am) and 25.69 (28.68) for TS2(am) (detailed data in VII.i, Supporting Information File 1).

In the B3LYP/6-31(+)G(d) Et + ZPE (without B3LYP/6-311++G(d,p) SCRF = PCM single-point calculations), +21.63 kcal/mol of TS1(am) is similar to +21.92 kcal/mol of TS2(am). This ambiguity at the computational level was removed in the $(H_2O)_{16}$-using hydrolyses of two para-substituted aromatic amides, Y–C_6H_4–C(=O)–NH–Et Y = MeO and O_2N. For Y = MeO, +23.64 (+26.45) kcal/mol of TS2(am) is larger than +19.80 (+22.93) kcal/mol of TS1(am). For Y = O_2N, also, +22.99 (+24.86) kcal/mol of TS2(am) is larger than +18.80 (+20.56) kcal/mol of TS1(am) (detailed data in VII.j, Supporting Information File 1). Thus, as far as the aromatic amide is concerned, TS2(am) is thought to be rate-determining.

The effect of the counter ion Na^+ on activation energies was examined. The effect on free-energy changes of TS2(am), (+28.15 kcal/mol) and (+28.05 kcal/mol) was found to be small. Thus, in the amide hydrolysis of n = 16, the Na^+ cation is separated well from the reaction center.

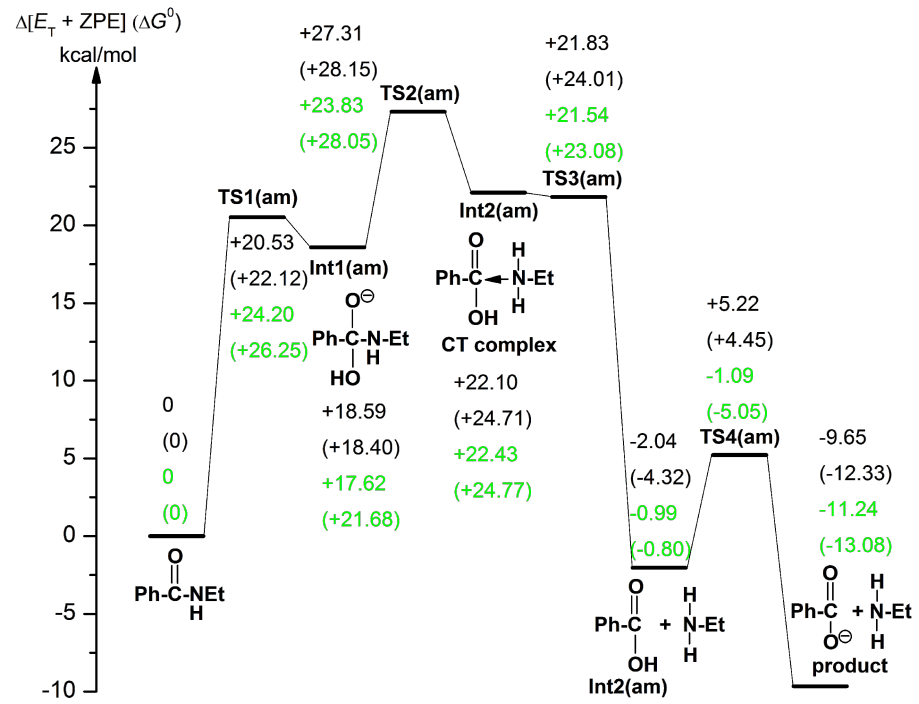

Figure 8: Changes of Et + ZPE and (Gibbs free energies) of the amide hydrolysis in Figure 5 and Figure S4 (Supporting Information File 1). Energies in green are for the Na^+-containing reaction in Figure S4.

Conclusion

In this work, reaction paths of base-catalyzed hydrolyses of isoelectronic substrates (ethyl benzoate and *N*-ethylbenzamide) were traced by DFT calculations. In Scheme 6, the obtained result is summarized.

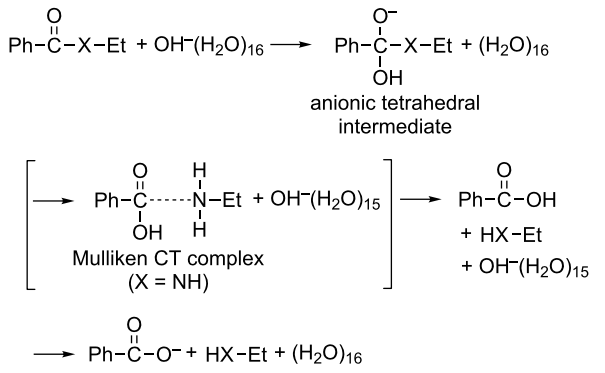

Scheme 6: Summary of the present calculations.

The five points 1–5 raised in the Introduction may be addressed on the basis of computational results:

1. The rate-determining step of the ester hydrolysis is the OH^- addition step, TS1(es). The energy change demonstrates that the reaction occurs spontaneously toward the product. On the other hand, that of the amide hydrolysis is TS2(am). TS2(am) is not at the "breakdown of the anionic tetrahedral intermediate" [21-25] but at the formation of the Mulliken CT complex.

2. The number of elementary processes is either three for the ester hydrolysis or four for the amide hydrolysis. The zwitter-ion suggested experimentally [25] is rather a Mulliken CT complex involved only in the amide hydrolysis. The intermediate is obtainable only in the H_2O-containing cluster system.

3. At both TS1(es) and TS1(am), the general base mechanism is more likely than the direct nucleophilic process regardless of the number of water molecules ($n > 3$).

4. The counter ion Na^+ works unfavorably on the hydrolysis, particularly on TS1(es). The ion should be separated from the reaction region in the hydration shell.

5. A minimal TS1 model composed of the substrate Ph–CO–X–Et, $OH^-(H_2O)_3$ and W_2 (W: catalytic water molecule) has been constructed in Figure 1. The model has been examined in Figure 2 and Figure 3 with the number (n) of water molecules, n = 3, 5, 8, 12, 16, 24 and 32. The model has been retained in all TS geometries, as exemplified in the n = 32 TS1(es) and TS1(am) (Figure 9).

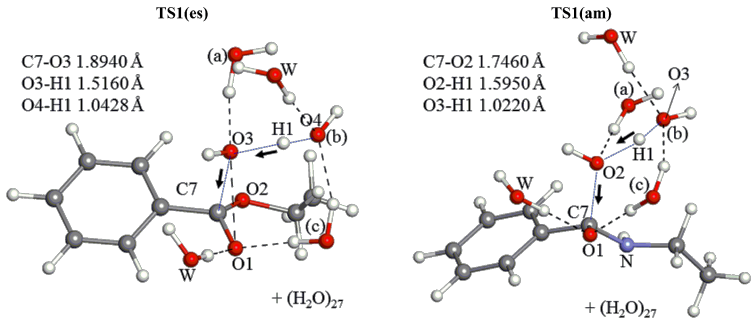

Figure 9: Central parts of the geometries of TS1(es) and TS1(am) of n = 32, which are taken from Figure 2 and Figure 3, respectively. Notations, (a), (b), (c) and W, are defined in Figure 1.

This work has demonstrated that proton transfers along hydrogen bonds have a significant role on the progress of the hydrolysis.

Supporting Information

Detailed geometric data along with those of complementary calculations. Figure S1 (geometry changes by the ADMP dynamical calculation), Figure S2 (the CT complex geometry), Figures S3 and S4 (reaction paths), Tables S1 and S2 (method dependence of TS1 geometries), and Cartesian coordinates of the optimized geometries.

Supporting Information File 1

Detailed geometric data along with those of complementary calculations.
[http://www.beilstein-journals.org/bjoc/content/supplementary/1860-5397-9-22-S1.pdf]

Acknowledgements

This work is financially supported by the Grants-in-Aid from the Ministry of Education, Culture, Science, Sport, and Technology through Grants-in-Aid of Specially Promoted Science and Technology (No. 22000009) and Grand Challenge Project (IMS, 90 Okazaki, Japan). We are also thankful to the computational facility at the Institute of Molecular Science, Okazaki, Japan.

References

1. Carey, F. A.; Sundberg, R. J. Chapter 8. *Advanced organic chemistry Part A: Structure and mechanisms,* 2nd ed.; Plenum Press: New York, NY, 1994.
2. Bender, M. L. *Chem. Rev.* **1960,** *60,* 53–113. doi:10.1021/cr60203a005
3. Štrajbl, M.; Florián, J.; Warshel, A. *J. Am. Chem. Soc.* **2000,** *122,* 5354–5366. doi:10.1021/ja992441s
4. Bender, M. L. *J. Am. Chem. Soc.* **1951,** *73,* 1626–1629. doi:10.1021/ja01148a063
5. Bender, M. L.; Ginger, R. D.; Kemp, K. C. *J. Am. Chem. Soc.* **1954,** *76,* 3350–3351. doi:10.1021/ja01641a084
6. Bender, M. L.; Ginger, R. D. *J. Am. Chem. Soc.* **1955,** *77,* 348–351. doi:10.1021/ja01607a032
7. Bender, M. L.; Ginger, R. D.; Unik, J. P. *J. Am. Chem. Soc.* **1958,** *80,* 1044–1048. doi:10.1021/ja01538a006
8. Bender, M. L.; Thomas, R. J. *J. Am. Chem. Soc.* **1961,** *83,* 4183–4189. doi:10.1021/ja01481a021
9. Bunton, C. A.; Nayak, B.; O'Connor, C. J. *J. Org. Chem.* **1968,** *33,* 572–575. doi:10.1021/jo01266a021
10. Bunton, C. A.; Lewis, T. A.; Llewellyn, D. R. *Chem. Ind. (London)* **1954,** 1154–1155.
11. DeWolfe, R. H.; Newcombe, R. C. *J. Org. Chem.* **1971,** *36,* 3870–3878. doi:10.1021/jo00824a005
12. Deslongchamps, P.; Cheriyan, U. O.; Guida, A.; Taillefer, R. J. *Nouv. J. Chim.* **1977,** *1,* 235–241.
13. Deslongchamps, P.; Gerval, P.; Cheriyan, U. O.; Guida, A.; Taillefer, R. J. *Nouv. J. Chim.* **1978,** *2,* 631–636.
14. Deslongchamps, P.; Bartlett, R.; Taillefer, R. J. *Can. J. Chem.* **1980,** *58,* 2167–2172. doi:10.1139/v80-347
15. Slebocka-Tilk, H.; Brown, R. S. *J. Org. Chem.* **1988,** *53,* 1153–1156. doi:10.1021/jo00241a006
16. Slebocka-Tilk, H.; Brown, R. S. *J. Org. Chem.* **1987,** *52,* 805–808. doi:10.1021/jo00381a019
17. O'Leary, M. H.; Marlier, J. F. *J. Am. Chem. Soc.* **1979,** *101,* 3300–3306. doi:10.1021/ja00506a027
18. Marlier, J. F. *J. Am. Chem. Soc.* **1993,** *115,* 5953–5956. doi:10.1021/ja00067a008
19. Kirby, A. J. Hydrolysis and Formation of Esters in Organic Acids. In *Comprehensive Chemical Kinetics;* Bamford, C. H.; Tipper, C. F. H., Eds.; Elsevier: Amsterdam, 1972; Vol. 10, pp 57–207.
20. Mata-Segreda, J. F. *J. Am. Chem. Soc.* **2002,** *124,* 2259–2262. doi:10.1021/ja011931t
21. Slebocka-Tilk, H.; Bennet, A. J.; Keillor, J. W.; Brown, R. S.; Guthrie, J. P.; Jodhan, A. *J. Am. Chem. Soc.* **1990,** *112,* 8507–8514. doi:10.1021/ja00179a040
22. Slebocka-Tilk, H.; Bennet, A. J.; Hogg, H. J.; Brown, R. S. *J. Am. Chem. Soc.* **1991,** *113,* 1288–1294. doi:10.1021/ja00004a032
23. Brown, R. S.; Bennet, A. J.; Slebocka-Tilk, H.; Jodhan, A. *J. Am. Chem. Soc.* **1992,** *114,* 3092–3098. doi:10.1021/ja00034a051

24. Brown, R. S.; Bennet, A. J.; Slebocka-Tilk, H. *Acc. Chem. Res.* **1992,** *25,* 481–488. doi:10.1021/ar00023a001
25. Slebocka-Tilk, H.; Neverov, A. A.; Brown, R. S. *J. Am. Chem. Soc.* **2003,** *125,* 1851–1858. doi:10.1021/ja021055z
26. Krug, J. P.; Popelier, P. L. A.; Bader, R. F. W. *J. Phys. Chem.* **1992,** *96,* 7604–7616. doi:10.1021/j100198a022
27. Stanton, R. V.; Perakyla, M.; Bakowies, D.; Kollman, P. A. *J. Am. Chem. Soc.* **1998,** *120,* 3448–3457. doi:10.1021/ja972723x
28. Zahn, D. *Chem. Phys. Lett.* **2004,** *383,* 134–137. doi:10.1016/j.cplett.2003.11.015
29. Zahn, D. *Eur. J. Org. Chem.* **2004,** *19,* 4020–4023. doi:10.1002/ejoc.200400316
30. Pliego, J. R., Jr. *Chem. Phys.* **2004,** *306,* 273–280. doi:10.1016/j.chemphys.2004.07.041
31. Hori, K.; Kamimura, A.; Ando, K.; Mizumura, M.; Ihara, Y. *Tetrahedron* **1997,** *53,* 4317–4330. doi:10.1016/S0040-4020(97)00158-0
32. Weiner, S. J.; Singh, U. C.; Kollman, P. A. *J. Am. Chem. Soc.* **1985,** *107,* 2219–2229. doi:10.1021/ja00294a003
33. Cascella, M.; Raugei, S.; Carloni, P. *J. Phys. Chem. B* **2004,** *108,* 369–375. doi:10.1021/jp035458c
34. Blumberger, J.; Ensing, B.; Klein, M. L. *Angew. Chem., Int. Ed.* **2006,** *45,* 2893–2897. doi:10.1002/anie.200600283
35. Blumberger, J.; Klein, M. L. *Chem. Phys. Lett.* **2006,** *422,* 210–217. doi:10.1016/j.cplett.2006.02.035
36. Xiong, Y.; Zhan, C.-G. *J. Phys. Chem. A* **2006,** *110,* 12644–12652. doi:10.1021/jp063140p
37. Cheshmedzhieva, D.; Ilieva, S.; Hadjieva, B.; Galabov, B. *J. Phys. Org. Chem.* **2009,** *22,* 619–631. doi:10.1002/poc.1492
38. Jalkanen, K. J.; Suhai, S. *Chem. Phys.* **1996,** *208,* 81–116. doi:10.1016/0301-0104(96)00042-0
39. Han, W. G.; Jalkanen, K. J.; Elstner, M.; Suhai, S. *J. Phys. Chem. B* **1998,** *102,* 2587–2602. doi:10.1021/jp972299m
40. Jalkanen, K. J.; Elstner, M.; Suhai, S. *J. Mol. Struct.: THEOCHEM* **2004,** *675,* 61–77. doi:10.1016/j.theochem.2003.12.045
41. Tajkhorshid, E.; Jalkanen, K. J.; Suhai, S. *J. Phys. Chem. B* **1998,** *102,* 5899–5913. doi:10.1021/jp9803135
42. Frimand, K.; Bohr, H.; Jalkanen, K. J.; Suhai, S. *Chem. Phys.* **2000,** *255,* 165–194. doi:10.1016/S0301-0104(00)00069-0
43. Jalkanen, K. J.; Nieminen, R. M.; Frimand, K.; Bohr, J.; Bohr, H.; Wade, R. C.; Tajkhorshid, E.; Suhai, S. *Chem. Phys.* **2001,** *265,* 125–151. doi:10.1016/S0301-0104(01)00267-1
44. Degtyarenko, I. M.; Jalkanen, K. J.; Gurtovenko, A. A.; Nieminen, R. M. *J. Phys. Chem. B* **2007,** *111,* 4227–4234. doi:10.1021/jp0676991
45. Jalkanen, K. J.; Degtyarenko, I. M.; Nieminen, R. M.; Cao, X.; Nafie, L. A.; Zhu, F.; Barron, L. D. *Theor. Chem. Acc.* **2008,** *119,* 191–210. doi:10.1007/s00214-007-0361-z
46. Degtyarenko, I.; Jalkanen, K. J.; Gurtovenko, A. A.; Nieminen, R. M. *J. Comput. Theor. Nanosci.* **2008,** *5,* 277–285.
47. Tommila, E.; Hinshelwood, C. N. *J. Chem. Soc.* **1938,** 1801–1810. doi:10.1039/jr9380001801
48. Becke, A. D. *J. Chem. Phys.* **1993,** *98,* 5648–5652. doi:10.1063/1.464913
49. Lee, C.; Yang, W.; Parr, R. G. *Phys. Rev. B* **1988,** *37,* 785–789. doi:10.1103/PhysRevB.37.785
50. Perdew, J. P.; Wang, Y. *Phys. Rev. B* **1992,** *45,* 13244–13249. doi:10.1103/PhysRevB.45.13244
51. Cancès, E.; Mennucci, B.; Tomasi, J. *J. Chem. Phys.* **1997,** *107,* 3032–3041. doi:10.1063/1.474659
52. Cossi, M.; Barone, V.; Mennucci, B.; Tomasi, J. *Chem. Phys. Lett.* **1998,** *286,* 253–260. doi:10.1016/S0009-2614(98)00106-7
53. Mennucci, B.; Tomasi, J. *J. Chem. Phys.* **1997,** *106,* 5151–5158. doi:10.1063/1.473558
54. Zhao, Y.; Truhlar, D. G. *Theor. Chem. Acc.* **2008,** *120,* 215–241. doi:10.1007/s00214-007-0310-x
55. Fukui, K. *J. Phys. Chem.* **1970,** *74,* 4161–4163. doi:10.1021/j100717a029
56. Gonzalez, C.; Schlegel, H. B. *J. Chem. Phys.* **1989,** *90,* 2154–2161. doi:10.1063/1.456010
57. Iyengar, S. S.; Schlegel, H. B.; Millam, J. M.; Voth, G. A.; Scuseria, G. E.; Frisch, M. J. *J. Chem. Phys.* **2001,** *115,* 10291–10302. doi:10.1063/1.1416876
58. Schlegel, H. B.; Millam, J. M.; Iyengar, S. S.; Voth, G. A.; Scuseria, G. E.; Daniels, A. D.; Frisch, M. J. *J. Chem. Phys.* **2001,** *114,* 9758–9763. doi:10.1063/1.1372182
59. Schlegel, H. B.; Iyengar, S. S.; Li, X.; Millam, J. M.; Voth, G. A.; Scuseria, G. E.; Frisch, M. J. *J. Chem. Phys.* **2002,** *117,* 8694–8704. doi:10.1063/1.1514582
60. *Gaussian 09,* Revision B.01; Gaussian, Inc: Wallingford, CT, 2009.
61. Pearson, R. G. *J. Chem. Educ.* **1968,** *45,* 643–648. doi:10.1021/ed045p643

License and Terms

Beilstein Journal of Organic Chemistry

Caryolene-forming carbocation rearrangements

Quynh Nhu N. Nguyen and Dean J. Tantillo*

Full Research Paper

Open Access

Address:
Department of Chemistry, University of California–Davis, 1 Shields Avenue, Davis, CA 95616, USA

Email:
Dean J. Tantillo* - djtantillo@chem.ucdavis.edu

* Corresponding author

Keywords:
carbocation; cycloaddition; density functional theory; mechanism; reactive intermediates; terpene

Beilstein J. Org. Chem. **2013,** *9,* 323–331.
doi:10.3762/bjoc.9.37

Received: 05 November 2012
Accepted: 21 January 2013
Published: 13 February 2013

This article is part of the Thematic Series "New reactive intermediates in organic chemistry". This is part 10 of our series on sesquiterpene-related calculations. For part 9 see [1].

Guest Editor: G. Bucher

Abstract

Density functional theory calculations on mechanisms of the formation of caryolene, a putative biosynthetic precursor to caryol-1(11)-en-10-ol, reveal two mechanisms for caryolene formation: one involves a base-catalyzed deprotonation/reprotonation sequence and tertiary carbocation minimum, whereas the other (with a higher energy barrier) involves intramolecular proton transfer and the generation of a secondary carbocation minimum and a hydrogen-bridged minimum. Both mechanisms are predicted to involve concerted suprafacial/suprafacial [2 + 2] cycloadditions, whose asynchronicity allows them to avoid the constraints of orbital symmetry.

Introduction

The cytotoxic sesquiterpenol caryol-1(11)-en-10-ol (**1**, Figure 1) was isolated by Barrow et al. in 1988 during an investigation of antiviral/antitumor compounds from New Zealand marine invertebrates [2]. Similar sesquiterpenoids were also found in *Campanella* fungi, *Streptomyces* bacteria, *Sinacalia tangutica* plants, and *Eurypon* sponges (Figure 1) [3-6]. The carbon skeleton of **1** is unusual, not only because it contains concatenated 4-, 6-, and 7-membered rings, but also in that it bears a bridgehead double bond. As noted in the original isolation report [2], this type of bridgehead C=C bond is rare for naturally occurring compounds, since it is expected to be associated with significant strain (although it is not technically in violation of Bredt's Rule) [7]. Intrigued by this structure, we proposed a biosynthetic mechanism for its formation (Scheme 1) and set about putting this proposal to the test using quantum chemical calculations [8].

Results and Discussion

Structure validation: We first computed ^{1}H and ^{13}C chemical shifts for **1** to assure ourselves that the assigned structure was reasonable [9,10]. Our calculated chemical shifts and the reported data matched well (Figure 2). The mean absolute deviations between computed and experimental chemical shifts were 0.10 ppm for ^{1}H and 1.96 ppm for ^{13}C, and the largest deviations were 0.31 ppm and 4.40 ppm for ^{1}H and ^{13}C, respectively. These values are typical for structures known to be

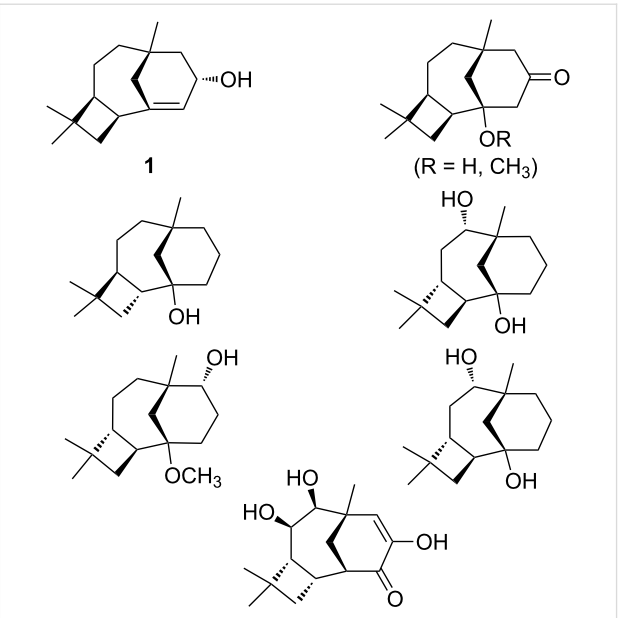

Figure 1: Caryol-1(11)-en-10-ol (**1**) and similar sesquiterpenoids. Note that a different atom numbering was used in the paper describing the isolation of **1** [2].

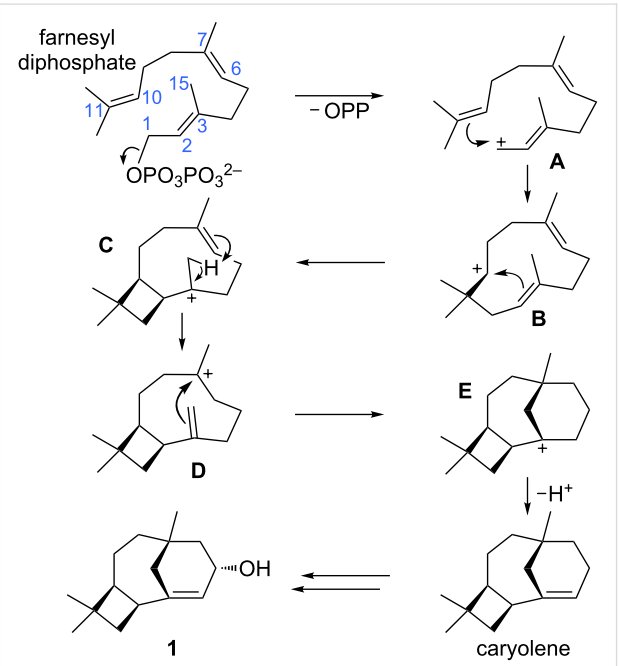

Scheme 1: Initially proposed mechanism for caryolene (caryol-1(11)-en-10-ol, **1**) formation. Atom numbers for farnesyl diphosphate are shown. These are used in the mechanistic discussions herein; note that this numbering system differs from that generally used for caryolene and caryolenol.

correct [11-16], giving us confidence in the original structural assignment. Interestingly, our calculations also indicate that the bridgehead C=C unit of **1** is not actually associated with much geometric strain [17].

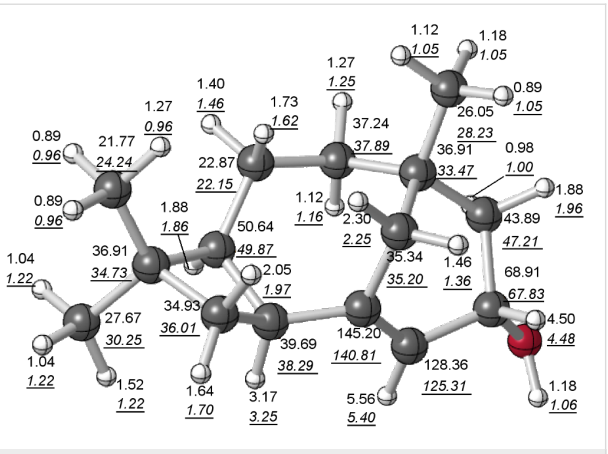

Figure 2: Computed (top) and experimental (bottom, underlined italics) [2] ^{1}H and ^{13}C chemical shifts for **1** (lowest-energy conformer found); see Experimental for details.

Proposed mechanism: Initially, we proposed the pathway shown in Scheme 1 for caryolene formation, applying the principles derived from previous theoretical studies on terpene-forming carbocation rearrangements [8]. In this mechanism, formation of the C1–C11 bond was expected to result in secondary carbocation **B**, in analogy to previously characterized pathways to sesquiterpenes containing 11-membered rings [1,8,18-22]. The C2=C3 π-bond was then expected to attack C10 to form the 4-membered ring (see **C**), in analogy to previously proposed mechanisms for caryophyllene formation [21,23]. An intramolecular proton transfer from the C15 methyl group to the nearby C6=C7 π-bond could then generate **D**. Related intramolecular proton transfers have been described [24-33]. Attack of the resulting C3=C15 π-bond onto C7 would complete the carbon skeleton of **1**, leaving a bridgehead carbocation [34], whose deprotonation would lead to caryolene, the putative biosynthetic precursor to **1**. Despite the apparent reasonability of this proposed mechanism, our quantum chemical calculations indicated that the pathway as formulated in Scheme 1 is not energetically viable (see below).

Computed mechanism: The first deviation from the proposed mechanism in Scheme 1 was encountered in the very first step involving carbocations. We were unable to locate a minimum for **B** in a productive conformation, despite the fact that alternative conformers of this secondary carbocation had been found to be involved in pathways to pentalenene and presilphiperfolanol [18-22]. Instead, a transition-state structure connected directly (by an IRC; see Experimental for details) to farnesyl cation **A** and cyclobutylcarbinyl cation **C** was located: **TS-AC** (Figure 3 and Figure 4). This process bypasses the generation of a secondary carbocation as a minimum [22], and overall corresponds to a formally orbital-symmetry-forbidden $[\pi 2_S + \pi 2_S]$ cycloaddition [35,36]. Although this process is predicted to be

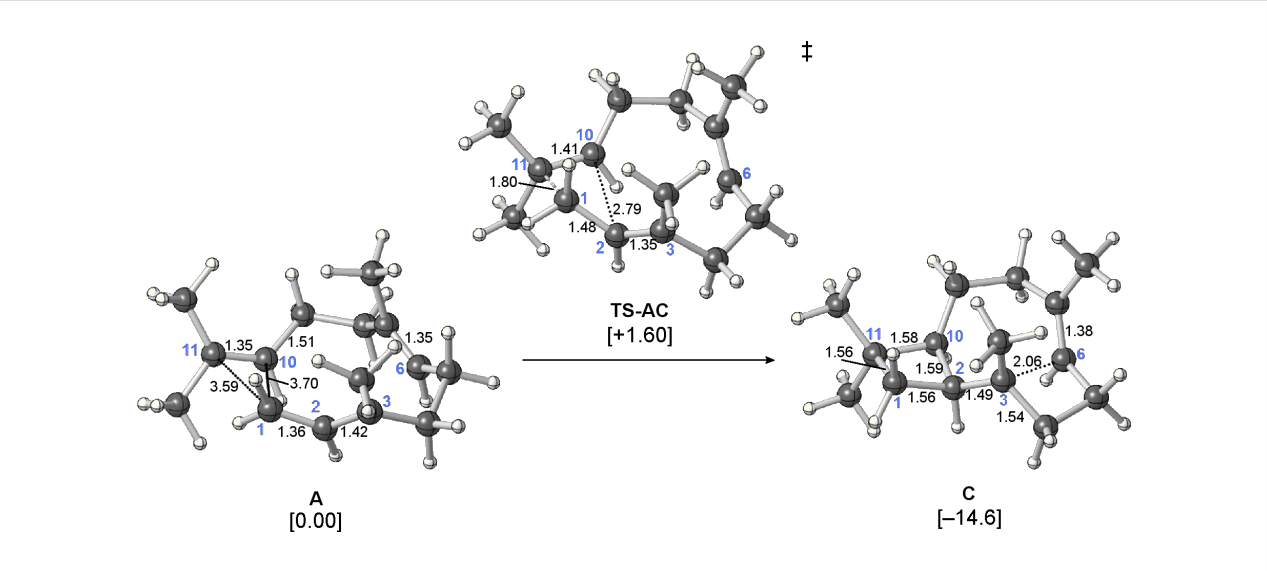

Figure 3: Computed minima and transition-state structure involved in the single-step conversion of **A** to **C**. Relative energies shown (kcal/mol) were calculated at the mPW1PW91/6-31+G(d,p)//B3LYP/6-31+G(d,p) level.

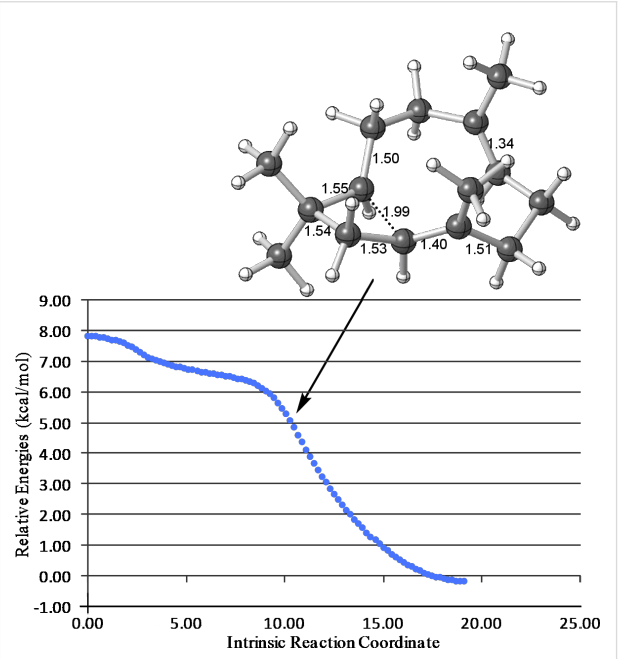

Figure 4: IRC from **TS-AC** toward **C**. Relative energies were calculated at the B3LYP/6-31+G(d,p) level.

concerted, the bond-forming events occur asynchronously [21,37,38] (note that the C1–C11 distance in **TS-AC** is approximately 1 Å shorter than the C2–C10 distance, indicating that C1–C11 bond formation leads C2–C10 bond formation) and at no point along the reaction coordinate is there significant cyclic delocalization of the sort that would be associated with a forbidden reaction. As described for other carbocation reactions [39,40], the constraints of orbital symmetry appear to have been circumvented. Interestingly, there is a shoulder (i.e., a sharp downturn) on the reaction coordinate in the vicinity of structures resembling **B** (Figure 4).

In the structure of **C** (Figure 3), C3 is quite close to C6 (only 2.06 Å away), indicating that this structure is perhaps best described as a hybrid of the tertiary cation **C** and a resonance structure with two 4-membered rings [22]. We performed a conformational search for **C** to assess whether other conformers lacking this close contact were possible, but all starting geometries examined in which the two methyl groups pointed to the same side of the ring as the first-formed cyclobutane, converged to the structure of **C** shown in Figure 3 [41].

Locating a pathway for the conversion of **C** to **D** (Scheme 1) also proved difficult. We expected proton transfer from the C15 methyl group to C6 of the C6=C7 π-bond to result in tertiary carbocation **D**. Surprisingly, only a transition-state structure for migration of the proton to C7 instead of C6, generating the secondary cation **F** (Scheme 2, left and Figure 5), was found. Attempts to independently locate **D** led instead to **G** (Figure 5), a nonclassical carbocation [42-46], or back to **C** [47]. Carbocation **G** contains a hydrogen bridge between C6 and C7, which also appears to interact with the nearby C3=C15 π-bond. If the interaction with the C3=C15 π-bond were stronger, this structure could be regarded as a "proton sandwich" [20,22,48]. An interesting question thus emerges about the nature of this structure: does the bridging hydrogen have hydride character (as expected for a structure resembling a transition-state structure for a 1,2-hydrogen shift) or proton character (as expected for a "proton sandwich")? This issue was addressed through calcula-

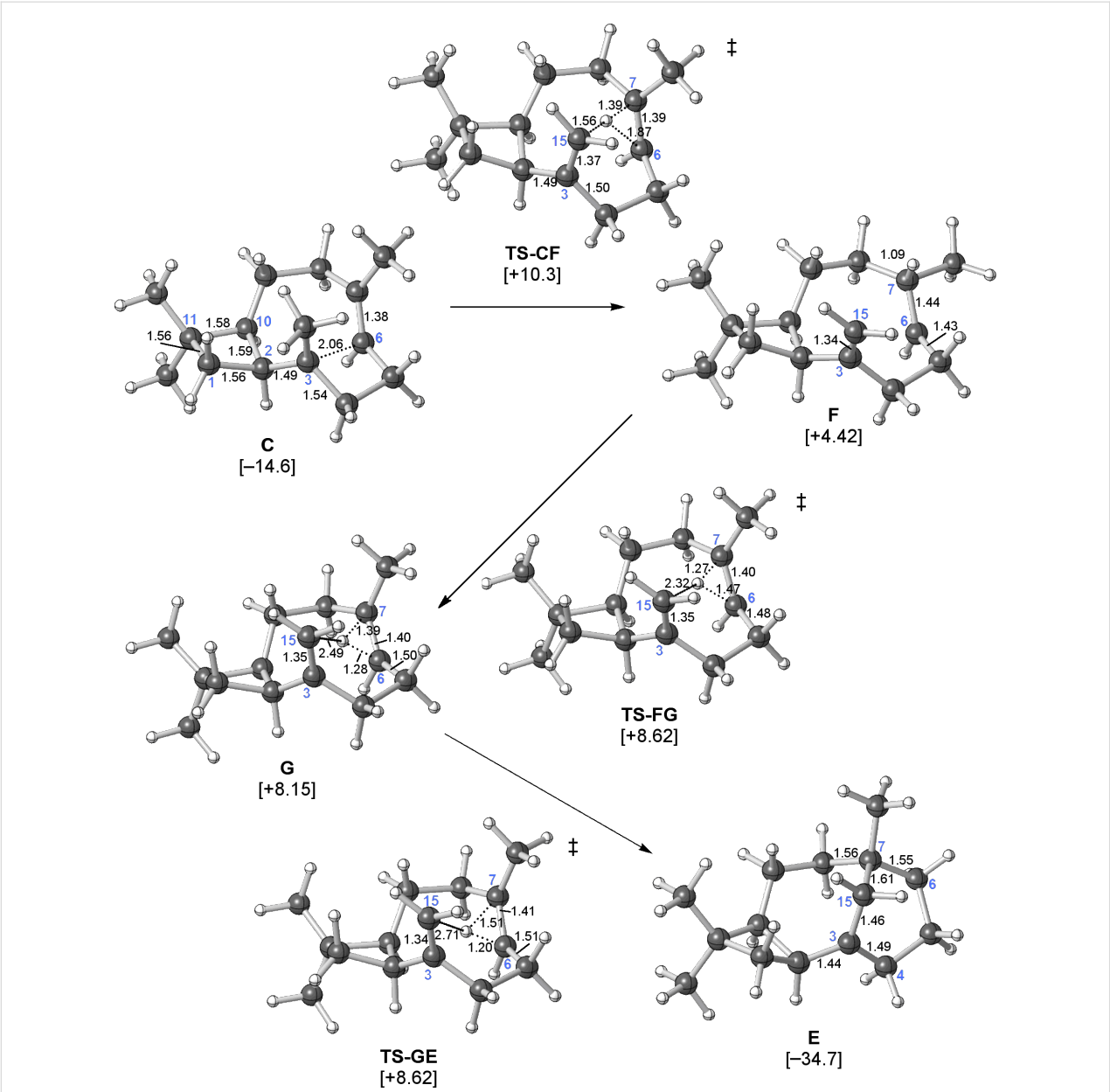

Figure 5: Computed pathway for the conversion of **C** to **E**. Relative energies shown (kcal/mol) were calculated at the mPW1PW91/6-31+G(d,p)//B3LYP/6-31+G(d,p) level.

tions of ^{1}H chemical shifts, which predicted a chemical shift of +4.0 ppm for the bridging hydrogen in **G**. Although this shift is not as far downfield as that predicted for structures with bridging protons (e.g., the predicted shift for the migrating proton in **TS-CF** is +9.1 ppm and the predicted shifts for symmetric "proton sandwiches" are around +13 ppm) [20], it is well downfield of shifts predicted for hydrides involved in three-center two-electron bonding arrays (e.g., see Supporting Information File 1 for a model transition-state structure for a 1,2-hydride shift with a predicted chemical shift of +1.9 ppm) [49-51] and approximately 2 ppm downfield of its value when merely hyperconjugated in **C** (+2.6 ppm; computed partial charges paint a similar, but less clear-cut picture; see Supporting Information File 1 for details).

Transition-state structures for the formation of **G** from **F** and **E** from **G** were also found (Scheme 2 and Figure 5). The former, **TS-FG**, resembles a transition-state structure for a typical 1,2-hydride shift, but the predicted chemical shift of the bridging hydrogen in this structure is +4.7 ppm. The developing close contact with the C3=C15 π-bond (the H---C15 distance is only 2.32 Å in **TS-FG**) also brings this transition-state structure

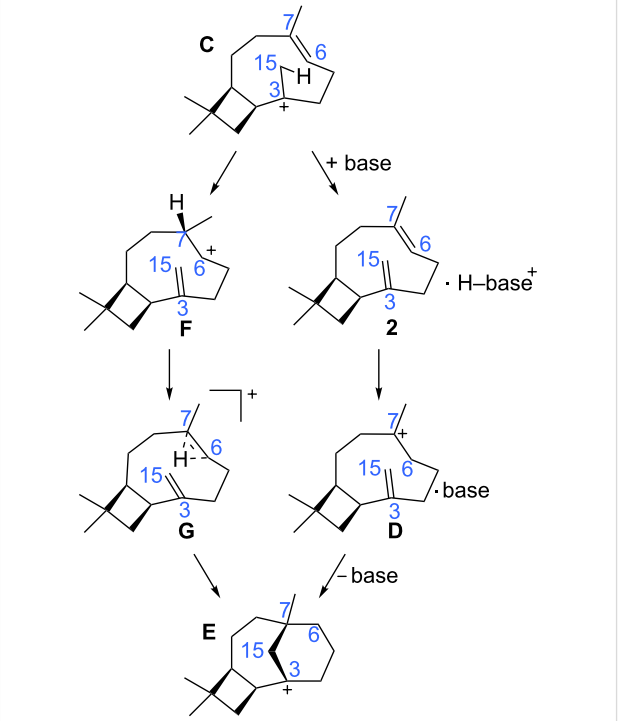

Scheme 2: Alternative mechanisms for caryolene formation.

closer to the realm of proton sandwiches. **TS-GE** looks very similar, but with different longer and shorter H---C partial bonds and a longer H---C15 distance (2.71 Å, consistent with its lower predicted chemical shift, +3.8 ppm). The **TS-FG**/**G**/**TS-GE** energy surface is rather flat (all three structures are predicted to be within 0.5 kcal/mol of each other; Figure 5). The **G**-to-**E** reaction involves concerted but asynchronous shifting of the bridging hydrogen toward C6 and subsequent ring closure (C7–C15 bond formation). As illustrated in the IRC plot shown in Figure 6, these two events are essentially separate, with structures part way along the pathway to resembling **D**. The two events are separated by a conformational reorganization in which some C–C bonds twist and release some strain (e.g., along the C5–C6 bond) while orienting the formally empty p-orbital on C7 toward the C3=C15 π-bond. Although the IRC calculation stopped while C15 and C7 were still 3.12 Å away, optimization of the final point led to **E**. Thus, a complete pathway to **E** was found, but this pathway differs in several ways from the pathway we expected to find.

Alternative mechanism: The pathway just described represents the inherent reactivity of the carbocations involved in the formation of **E**, but how might the mechanism change if we allowed for an enzymatic base to be involved? Would the same unusual sequence of events associated with the intramolecular proton transfer persist? Would a lower energetic pathway present itself? No changes to the formation of **C** were predicted in the presence of an ammonia molecule (a simple model base [52-55]), but a stepwise proton-transfer process was found in which the C15 methyl group was first deprotonated to form an

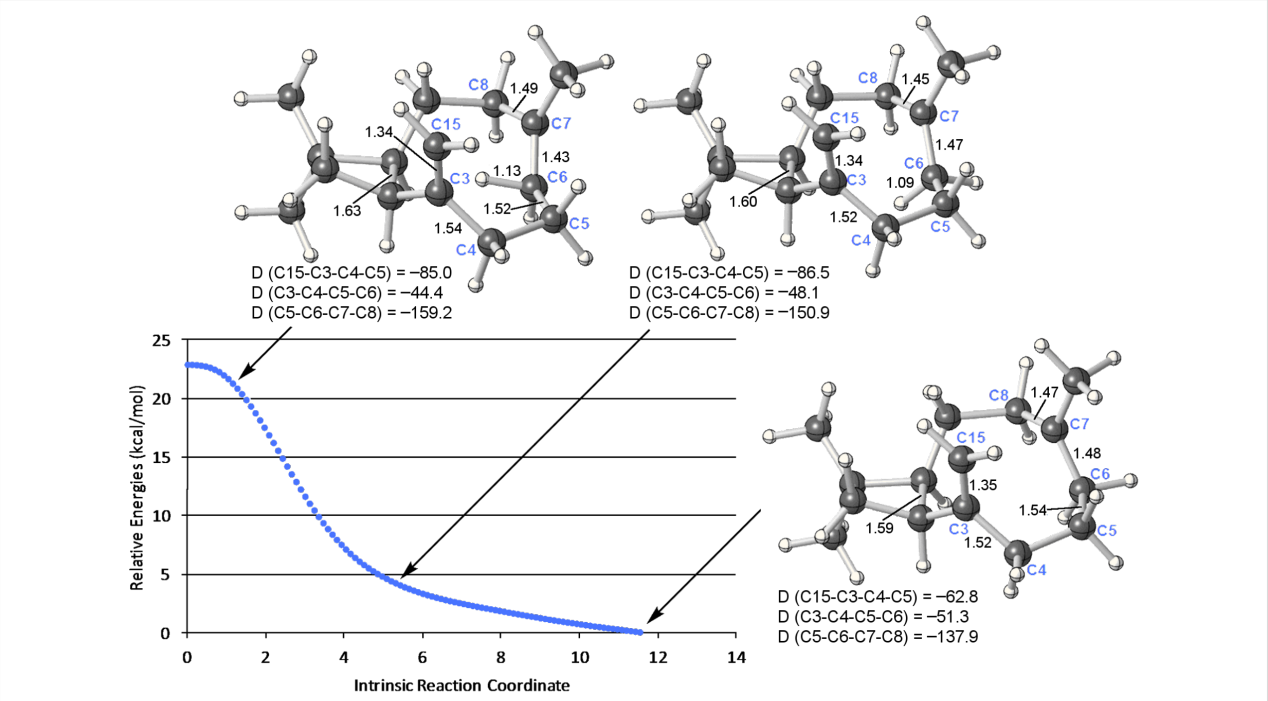

Figure 6: IRC from **TS-GE** toward **E**. Relative energies were calculated at the B3LYP/6-31+G(d,p) level. Selected dihedral angles are shown in degrees.

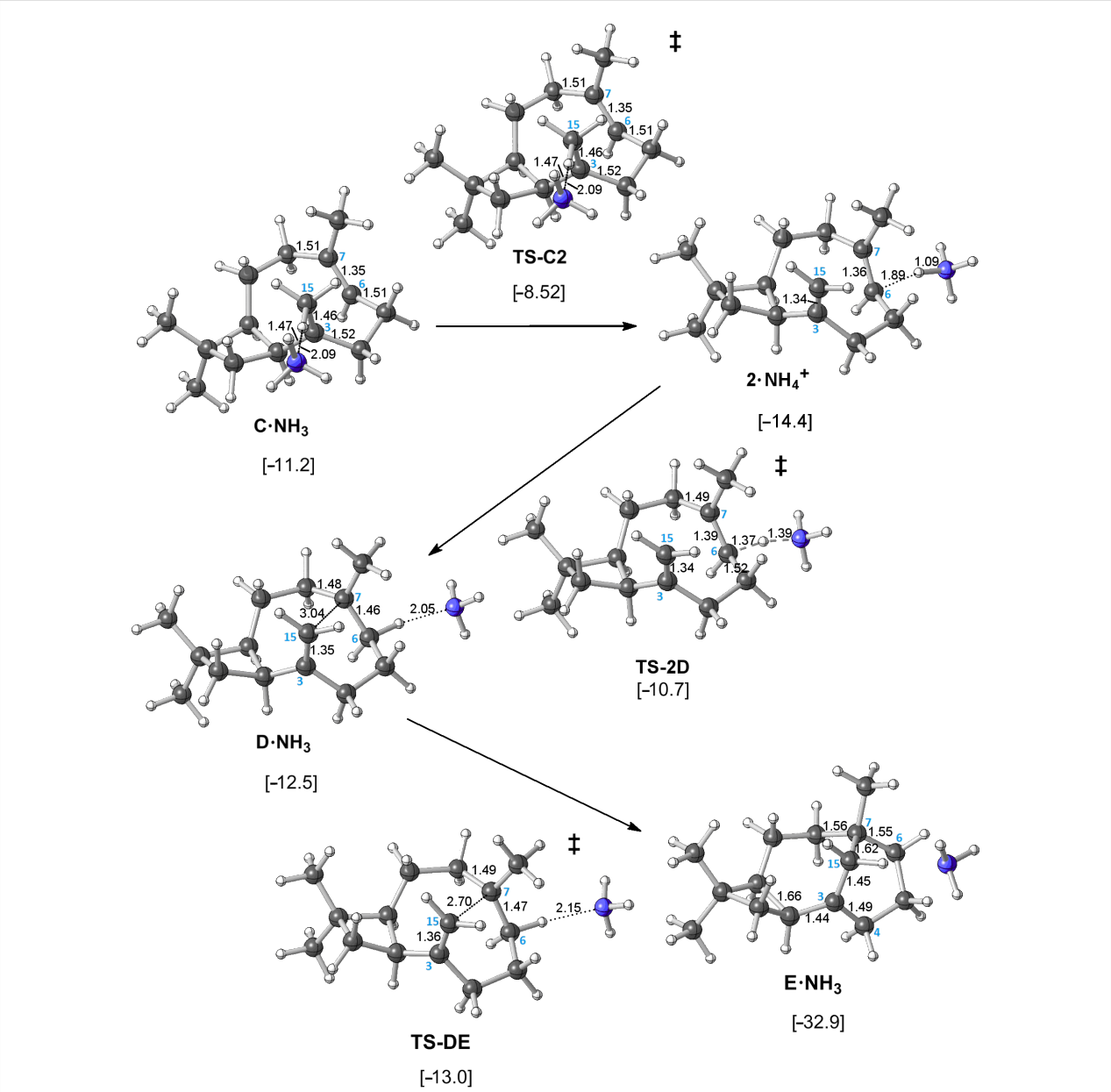

Figure 7: Computed pathway for the conversion of **C** to **E** in the presence of ammonia. Relative energies shown (kcal/mol) were calculated at the mPW1PW91/6-31+G(d,p)//B3LYP/6-31+G(d,p) level. Here energies are relative to that for a complex of **A** and NH_3.

ion·molecule complex (**2**·NH_4^+ in Figure 7; **2** is a caryophyllene) and then C6 was protonated to form **D** (Scheme 2, right). This surprisingly elusive tertiary carbocation appears to be stabilized in the presence of a C–H hydrogen-bond acceptor that interacts with its hyperconjugated hydrogen [52-56]. Here a tertiary carbocation requires selective stabilization in order to exist as a minimum; although it is inherently lower in energy than the secondary cation **F** (on the basis of single-point calculations without ammonia present), without the intermolecular C–H···X interaction described, there is no barrier for its conversion to **E** (removal of the ammonia molecule from **D**·NH_3 and reoptimization led to structure **E**) [57]. Still, even though tertiary carbocation **D** is predicted to exist as a minimum in the presence of a suitable base at the B3LYP/6-31+G(d,p) level, its conversion to **E** is predicted to be barrierless at the mPW1PW91/6-31+G(d,p)//B3LYP/6-31+G(d,p) level (Figure 7 and Figure 8). Thus, this ostensibly normal tertiary carbocation lacks the kinetic stability generally associated with the presence of three alkyl groups. Although cation **D** can be formed by protonation of an alkene as shown, such a scenario would likely require a separate base and acid positioned on opposite sides of the hydrocarbon substrate due to the steric congestion at its core

(note the position of NH_3 throughout Figure 7), a scenario that could be probed by deuterium labeling of farnesyl diphosphate if a suitable caryolene synthase were isolated.

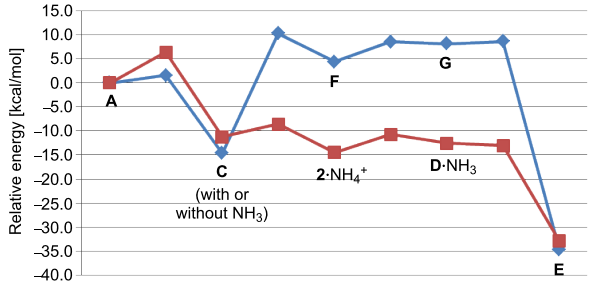

Figure 8: Predicted energetics for the conversion of **A** to **E** in the absence (blue) and presence (auburn) of ammonia. Relative energies shown (kcal/mol) were calculated at the mPW1PW91/6-31+G(d,p)// B3LYP/6-31+G(d,p) level. Energies for the pathway with ammonia are relative to those for an **A**·NH_3 complex.

The energetics for both pathways shown in Scheme 2 are summarized in Figure 8. The ammonia-free pathway has a substantial barrier, approximately 25 kcal/mol, after formation of **C**, but the ammonia-assisted pathway does not. In fact, after a small barrier for the formation of **C**, the potential energy surface for the deprotonation/reprotonation pathway is rather flat, indicating that once **C** is formed, transformation to **E** should be facile, provided that the architecture of the active site supports deprotonation/reprotonation.

Conclusion

Which pathway to caryolene is more likely? On the basis of our computed energetics (Figure 8), we favor a mechanism for caryolene formation that involves a concerted but asynchronous [2 + 2] cycloaddition, deprotonation by an enzyme active-site base (as yet, with identity unknown [55,58-64]), and concerted but asynchronous reprotonation/cyclization (Scheme 2, right). However, several interesting structures with unusual bonding arrays are encountered along the base-free pathway.

Experimental

All calculations were carried out with Gaussian 09 [65]. Geometry optimizations, frequency calculations and intrinsic reaction coordinate (IRC) [66,67] calculations were first carried out with B3LYP/6-31G(d) [68-72]. For IRC calculations, force constants were recalculated after every three points or at every point in the event of prematurely terminated jobs. All molecules were then subjected to optimization and frequency calculations at the B3LYP/6-31+G(d,p) level of theory [8,68-72]. Single-point energies were also calculated at the mPW1PW91/6-31+G(d,p) level [73,74] for comparison, since B3LYP energies are generally unreliable when comparing cyclic and acyclic isomers that differ in the number of σ- and π-bonds [8,74,75]. Chemical shifts (^1H and ^{13}C) in chloroform (treated with the SMD solvation model [76]) for selected structures were calculated by using mPW1PW91/6-311+G(2d,p) [11-13,73,74]. Computed scaling factors (slope = −1.0823 for ^1H and −1.0448 for ^{13}C; intercept = 31.8486 for ^1H and 186.0596 for ^{13}C) were used to convert computed isotropic values into chemical shifts [11-13].

Supporting Information

Supporting Information File 1

Coordinates and energies for all computed structures, IRC plots, additional computational details and full Gaussian citation.
[http://www.beilstein-journals.org/bjoc/content/supplementary/1860-5397-9-37-S1.pdf]

Acknowledgements

We gratefully acknowledge the National Science Foundation and the Pittsburgh Supercomputer Center for support, Phillip Painter for help and advice, and Young Hong and Ryan Pemberton for useful suggestions.

References

1. Zu, L.; Xu, M.; Lodewyk, M. W.; Cane, D. E.; Peters, R. J.; Tantillo, D. J. *J. Am. Chem. Soc.* **2012,** *134,* 11369–11371. doi:10.1021/ja3043245
2. Barrow, C. J.; Blunt, J. W.; Munro, M. H. G. *Aust. J. Chem.* **1988,** *41,* 1755–1761. doi:10.1071/CH9881755
3. Fraga, B. M. *Nat. Prod. Rep.* **2012,** *29,* 1334–1366. doi:10.1039/c2np20074k
4. Zhu, Y.; Zhao, Y.; Huang, G.-D.; Wu, W.-S. *Helv. Chim. Acta* **2008,** *91,* 1894–1901. doi:10.1002/hlca.200890203
5. Yang, Z.; Yang, Y.; Yang, X.; Zhang, Y.; Zhao, L.; Xu, L.; Ding, Z. *Chem. Pharm. Bull.* **2011,** *59,* 1430–1433. doi:10.1248/cpb.59.1430
6. Liu, R.; Zhou, Z.-Y.; Xu, D.; Wang, F.; Liu, J.-K. *Helv. Chim. Acta* **2009,** *92,* 375–378. doi:10.1002/hlca.200800298
7. Bredt, J. *Justus Liebigs Ann. Chem.* **1924,** *437,* 1–13. doi:10.1002/jlac.19244370102
8. Tantillo, D. J. *Nat. Prod. Rep.* **2011,** *28,* 1035–1053. doi:10.1039/c1np00006c
   See for leading references on quantum chemical calculations on terpene-forming carbocation rearrangements.
9. Suyama, T. L.; Gerwick, W. H.; McPhail, K. L. *Bioorg. Med. Chem.* **2011,** *19,* 6675–6701. doi:10.1016/j.bmc.2011.06.011
   Leading references on misassigned natural product structures.
10. Nicolaou, K. C.; Snyder, S. A. *Angew. Chem., Int. Ed.* **2005,** *44,* 1012–1044. doi:10.1002/anie.200460864
    Leading references on misassigned natural product structures.
11. Lodewyk, M. W.; Siebert, M. R.; Tantillo, D. J. *Chem. Rev.* **2012,** *112,* 1839–1862. doi:10.1021/cr200106v
    And references therein.
12. Jain, R.; Bally, T.; Rablen, P. R. *J. Org. Chem.* **2009,** *74,* 4017–4023. doi:10.1021/jo900482q

13. CHESHIRE, Chemical Shift Repository with Coupling Constants Added Too. http://cheshirenmr.info.
14. Lodewyk, M. W.; Tantillo, D. J. *J. Nat. Prod.* **2011,** *74,* 1339–1343. doi:10.1021/np2000446
15. Quasdorf, K. W.; Huters, A. D.; Lodewyk, M. W.; Tantillo, D. J.; Garg, N. K. *J. Am. Chem. Soc.* **2012,** *134,* 1396–1399. doi:10.1021/ja210837b
16. Lodewyk, M. W.; Soldi, C.; Jones, P. B.; Olmstead, M. M.; Rita, J.; Shaw, J. T.; Tantillo, D. J. *J. Am. Chem. Soc.* **2012,** *134,* 18550–18553. doi:10.1021/ja3089394
17. We computed the geometry of hydrogenated **1**, and the carbon skeleton did not relax much upon hydrogenation (see Supporting Information File 1).
18. Gutta, P.; Tantillo, D. J. *J. Am. Chem. Soc.* **2006,** *128,* 6172–6179. doi:10.1021/ja058031n
19. Wang, S. C.; Tantillo, D. J. *Org. Lett.* **2008,** *10,* 4827–4830. doi:10.1021/ol801898v
20. Gutta, P.; Tantillo, D. J. *Angew. Chem., Int. Ed.* **2005,** *44,* 2719–2723. doi:10.1002/anie.200461915
21. Tantillo, D. J. *J. Phys. Org. Chem.* **2008,** *21,* 561–570. doi:10.1002/poc.1320
22. Tantillo, D. J. *Chem. Soc. Rev.* **2010,** *39,* 2847–2854. doi:10.1039/b917107j
23. Croteau, R.; Gundy, A. *Arch. Biochem. Biophys.* **1984,** *233,* 838–841. doi:10.1016/0003-9861(84)90513-7
24. Hong, Y. J.; Tantillo, D. J. *J. Am. Chem. Soc.* **2011,** *133,* 18249–18256. doi:10.1021/ja2055929
25. Hong, Y. J.; Tantillo, D. J. *Nat. Chem.* **2009,** *1,* 384–389. doi:10.1038/nchem.287
26. Hong, Y. J.; Tantillo, D. J. *Org. Lett.* **2006,** *8,* 4601–4604. doi:10.1021/ol061884f
27. Hong, Y. J.; Tantillo, D. J. *Org. Biomol. Chem.* **2009,** *7,* 4101–4109. doi:10.1039/b908738a
28. Williams, C. D.; Carroll, B. J.; Jin, Q.; Rithner, C. D.; Lenger, S. R.; Floss, G. H.; Coates, R. M.; Williams, R. M.; Croteau, R. *Chem. Biol.* **2000,** *7,* 969–977. doi:10.1016/S1074-5521(00)00046-6
29. Allemann, R. K.; Young, N. J.; Ma, S.; Truhlar, D. G.; Gao, J. *J. Am. Chem. Soc.* **2007,** *129,* 13008–13013. doi:10.1021/ja0722067
30. Deligeorgopoulou, A.; Taylor, S. E.; Forcat, S.; Allemann, R. K. *Chem. Commun.* **2003,** 2162–2163. doi:10.1039/b306867f
31. Cane, D. E.; Prabhakaran, P. C.; Oliver, J. S.; McIlwaine, D. B. *J. Am. Chem. Soc.* **1990,** *112,* 3209–3210. doi:10.1021/ja00164a051
32. Miller, D. J.; Gao, J.; Truhlar, D. G.; Young, N. J.; Gonzalez, V.; Allemann, R. K. *Org. Biomol. Chem.* **2008,** *6,* 2346–2354. doi:10.1039/b804198a
33. Surendra, K.; Corey, E. J. *J. Am. Chem. Soc.* **2008,** *130,* 8865–8869. doi:10.1021/ja802730a
34. Abboud, J.-L. M.; Herreros, M.; Notario, R.; Lomas, J. S.; Mareda, J.; Müller, P.; Rossier, J.-C. *J. Org. Chem.* **1999,** *64,* 6401–6410. doi:10.1021/jo990724x
    Leading references on bridgehead carbocations.
35. Hoffmann, R.; Woodward, R. B. *Acc. Chem. Res.* **1968,** *1,* 17–22. doi:10.1021/ar50001a003
36. Woodward, R. B.; Hoffmann, R. *Angew. Chem., Int. Ed. Engl.* **1969,** *8,* 781–853. doi:10.1002/anie.196907811
37. Williams, A. *Concerted Organic and Bio-Organic Mechanisms;* CRC Press: Boca Raton, FL, USA, 2000.
38. Dewar, M. J. S. *J. Am. Chem. Soc.* **1984,** *106,* 209–219. doi:10.1021/ja00313a042
39. Nouri, D. H.; Tantillo, D. J. *Tetrahedron* **2008,** *64,* 5672–5679. doi:10.1016/j.tet.2008.04.028
40. Sio, V.; Harrison, J. G.; Tantillo, D. J. *Tetrahedron* **2012,** *53,* 6919–6922. doi:10.1016/j.tetlet.2012.10.019
41. Geometries in which the two methyl groups pointed in opposite directions were also examined, but the resulting structures were not productive for caryolene formation; see Supporting Information File 1 for details.
42. Grob, C. A. *Acc. Chem. Res.* **1983,** *16,* 426–431. doi:10.1021/ar00096a001
43. Brown, H. C. *Acc. Chem. Res.* **1983,** *16,* 432–440. doi:10.1021/ar00096a002
44. Olah, G. A.; Prakash, G. K. S.; Saunders, M. *Acc. Chem. Res.* **1983,** *16,* 440–448. doi:10.1021/ar00096a003
45. Walling, C. *Acc. Chem. Res.* **1983,** *16,* 448–454. doi:10.1021/ar00096a004
46. Brown, H. C. *The Nonclassical Ion Problem;* Plenum Press: New York, NY, 1977.
    With comments by P. v. R. Schleyer.
47. **D**-type structures arising from alternative conformers of **C** were examined, but these correspond to nonproductive stereoisomers; see Supporting Information File 1 for details.
48. Ponec, R.; Bultinck, P.; Gutta, P.; Tantillo, D. J. *J. Phys. Chem. A* **2006,** *110,* 3785–3789. doi:10.1021/jp0568430
49. McMurry, J. E.; Lectka, T. *Acc. Chem. Res.* **1992,** *25,* 47–53. doi:10.1021/ar00013a007
50. Ponec, R.; Yuzhakov, G.; Tantillo, D. J. *J. Org. Chem.* **2004,** *69,* 2992–2996. doi:10.1021/jo035506p
51. Tantillo, D. J.; Hoffmann, R. *J. Am. Chem. Soc.* **2003,** *125,* 4042–4043. doi:10.1021/ja021394s
52. Hong, Y. J.; Tantillo, D. J. *J. Org. Chem.* **2007,** *72,* 8877–8881. doi:10.1021/jo701526x
53. Lodewyk, M. W.; Gutta, P.; Tantillo, D. J. *J. Org. Chem.* **2008,** *73,* 6570–6579. doi:10.1021/jo800868r
54. Hong, Y. J.; Tantillo, D. J. *J. Am. Chem. Soc.* **2010,** *132,* 5375–5386. doi:10.1021/ja9084786
55. Hong, Y. J.; Tantillo, D. J. *Org. Biomol. Chem.* **2010,** *8,* 4589–4600. doi:10.1039/c0ob00167h
56. Nishio, M. *J. Mol. Struct.* **2012,** *1018,* 2–7. doi:10.1016/j.molstruc.2012.03.012
    See for leading references on C-H···X interactions.
57. Hong, Y. J.; Tantillo, D. J. *J. Am. Chem. Soc.* **2009,** *131,* 7999–8015. doi:10.1021/ja9005332
    See for the description of a related scenario.
58. Roy, A.; Roberts, F. G.; Wilderman, P. R.; Zhou, K.; Peters, R. J.; Coates, R. M. *J. Am. Chem. Soc.* **2007,** *129,* 12453–12460. doi:10.1021/ja072447e
    Discussions of pyrophosphate as a possible active site base in terpene synthases.
59. Greenhagen, B. T.; O'Maille, P. E.; Noel, J. P.; Chappell, J. *Proc. Natl. Acad. Sci. U. S. A.* **2006,** *103,* 9826–9831. doi:10.1073/pnas.0601605103
60. Shishova, E. Y.; Di Costanzo, L.; Cane, D. E.; Christianson, D. W. *Biochemistry* **2007,** *46,* 1941–1951. doi:10.1021/bi0622524
61. Peters, R. J.; Croteau, R. B. *Arch. Biochem. Biophys.* **2003,** *417,* 203–211. doi:10.1016/S0003-9861(03)00347-3
62. Garms, S.; Chen, F.; Boland, W.; Gershenzon, J.; Köllner, T. G. *Phytochemistry* **2012,** *75,* 6–13. doi:10.1016/j.phytochem.2011.12.009
63. Zhou, K.; Peters, R. J. *Chem. Commun.* **2011,** *47,* 4074–4080. doi:10.1039/c0cc02960b

64. Miller, D. J.; Allemann, R. K. *Nat. Prod. Rep.* **2012,** *29,* 60–71. doi:10.1039/c1np00060h
65. *Gaussian 09,* Revision B.01; Gaussian, Inc.: Wallingford, CT, 2004.
66. Gonzalez, C.; Schlegel, H. B. *J. Phys. Chem.* **1990,** *94,* 5523–5527. doi:10.1021/j100377a021
67. Fukui, K. *Acc. Chem. Res.* **1981,** *14,* 363–368. doi:10.1021/ar00072a001
68. Becke, A. D. *J. Chem. Phys.* **1993,** *98,* 1372–1377. doi:10.1063/1.464304
69. Becke, A. D. *J. Chem. Phys.* **1993,** *98,* 5648–5652. doi:10.1063/1.464913
70. Lee, C.; Yang, W.; Parr, R. G. *Phys. Rev. B* **1988,** *37,* 785–789. doi:10.1103/PhysRevB.37.785
71. Stephens, P. J.; Devlin, F. J.; Chabalowski, C. F.; Frisch, M. J. *J. Phys. Chem.* **1994,** *98,* 11623–11627. doi:10.1021/j100096a001
72. Tirado-Rives, J.; Jorgensen, W. L. *J. Chem. Theory Comput.* **2008,** *4,* 297–306. doi:10.1021/ct700248k
73. Adamo, C.; Barone, V. *J. Chem. Phys.* **1998,** *108,* 664–675. doi:10.1063/1.475428
74. Matsuda, S. P. T.; Wilson, W. K.; Xiong, Q. *Org. Biomol. Chem.* **2006,** *4,* 530–543. doi:10.1039/b513599k
75. Pieniazek, S. N.; Clemente, F. R.; Houk, K. N. *Angew. Chem., Int. Ed.* **2008,** *47,* 7746–7749. doi:10.1002/anie.200801843
76. Marenich, A. V.; Cramer, C. J.; Truhlar, D. G. *J. Phys. Chem. B* **2009,** *113,* 6378–6396. doi:10.1021/jp810292n

License and Terms

Beilstein Journal of Organic Chemistry

Electron and hydrogen self-exchange of free radicals of sterically hindered tertiary aliphatic amines investigated by photo-CIDNP

Martin Goez*, Isabell Frisch and Ingo Sartorius

Full Research Paper

Open Access

Address:
Institut für Chemie, Martin–Luther-Universität Halle–Wittenberg, Kurt–Mothes-Str. 2, 06120 Halle/Saale, Germany

Email:
Martin Goez* - martin.goez@chemie.uni-halle.de

* Corresponding author

Keywords:
amines; CIDNP; electron transfer; free radicals; hydrogen transfer; ketones; kinetics; photochemistry; self-exchange

Beilstein J. Org. Chem. **2013,** *9,* 437–446.
doi:10.3762/bjoc.9.46

Received: 19 December 2012
Accepted: 06 February 2013
Published: 26 February 2013

This article is part of the Thematic Series "New reactive intermediates in organic chemistry".

Guest Editor: G. Bucher

Abstract

The photoreactions of diazabicyclo[2,2,2]octane (DABCO) and triisopropylamine (TIPA) with the sensitizers anthraquinone (AQ) and xanthone (XA) or benzophenone (BP) were investigated by time-resolved photo-CIDNP (photochemically induced dynamic nuclear polarization) experiments. By varying the radical-pair concentration, it was ensured that these measurements respond only to self-exchange reactions of the free amine-derived radicals (radical cations $\mathbf{DH}^{\bullet+}$ or α-amino alkyl radicals $\mathbf{D}^{\bullet}$) with the parent amine **DH**; the acid–base equilibrium between $\mathbf{DH}^{\bullet+}$ and $\mathbf{D}^{\bullet}$ also plays no role. Although the sensitizer does not at all participate in the observed processes, it has a pronounced influence on the CIDNP kinetics because the reaction occurs through successive radical pairs. With AQ, the polarizations stem from the initially formed radical-ion pairs, and escaping $\mathbf{DH}^{\bullet+}$ then undergoes electron self-exchange with **DH**. In the reaction sensitized with XA (or BP), the polarizations arise in a secondary pair of neutral radicals that is rapidly produced by in-cage proton transfer, and the CIDNP kinetics are due to hydrogen self-exchange between escaping $\mathbf{D}^{\bullet}$ and **DH**. For TIPA, the activation parameters of both self-exchange reactions were determined. Outer-sphere reorganization energies obtained with the Marcus theory gave very good agreement between experimental and calculated values of $\Delta G^{\ddagger}_{298}$.

Introduction

Sensitized hydrogen abstractions from tertiary aliphatic amines present a mechanistic spectrum with a varying involvement of polar intermediates. Often, they are true two-step processes with an initial full charge transfer to give a radical ion pair, which then undergoes a proton transfer [1-7]; partial charge transfer (i.e., formation of an exciplex) as the first step has also been observed [8,9].

One of the most versatile methods to elucidate complex reaction mechanisms that occur via paramagnetic intermediates is

provided by measurements of chemically induced dynamic nuclear polarization (CIDNP) [10-15]. CIDNP arises from a spin-sorting process in radical pairs, which leads to opposite polarizations in the products of the two radicals of a pair with each other (geminate products) and the products of subsequent free radicals (escape products), and thus yields information about the entry and exit channels of the radical pairs. The spin sorting is driven by magnetic (i.e., Zeeman and hyperfine) interactions, completed during the pair life (i.e., on a subnanosecond timescale), and detected by NMR in the diamagnetic reaction products, where it persists for a time on the order of the nuclear T_1 (i.e., a few seconds for protons). In consequence, the CIDNP effect encodes the individual hyperfine coupling constants of the nuclei in a paramagnetic intermediate as individual polarization intensities of those nuclei in a product, the so-called polarization pattern [16]; not only is this obviously useful for the identification and characterization of the intermediate but it also establishes the chemical pathways between that intermediate and the resulting products. The disparity of timescales between CIDNP generation, subsequent chemical processes, and detection opens up the possibility of time-resolved photo-CIDNP experiments [17-20]: The flash of a pulsed laser triggers a photoreaction; after a short delay, the polarizations of the products are probed with an NMR pulse; variation of the delay yields the kinetics. The method is very well suited to study bimolecular reactions of the free radicals, because typical NMR pulses are of microsecond duration and, thus, fall within the relevant kinetic range.

In a series of previous CIDNP studies on triethylamine with different aromatic carbonyl compounds as sensitizers [5-7], we have used the dependence of the polarization pattern on the sensitizer and the solvent to show that these reactions are always two-step hydrogen abstractions according to Scheme 1. The source of the polarizations can be either the initially formed radical-ion pair $\overline{\mathbf{A}^{\bullet-}\,\mathbf{DH}^{\bullet+}}$ where $\mathbf{A}^{\bullet-}$ and $\mathbf{DH}^{\bullet+}$ are the radical anion of the sensitizer **A** and the radical cation of the amine **DH**, or a secondary pair of neutral radicals $\overline{\mathbf{AH}^{\bullet}\,\mathbf{D}^{\bullet}}$, where $\mathbf{AH}^{\bullet}$ and $\mathbf{D}^{\bullet}$ denote the sensitizer ketyl radical and the α-amino alkyl radical. The reason why some sensitizers yield polarizations that stem from the radical ion pair, even though the precursor to the products must be the neutral radical $\mathbf{D}^{\bullet}$, is the existence of two deprotonation pathways of $\mathbf{DH}^{\bullet+}$: The proton can be taken up by the sensitizer radical anion in a direct reaction within the cage, or in a relayed reaction outside the cage, with surplus amine and its protonated form $\mathbf{DH}_2^+$ functioning as mediators. The competition between in-cage deprotonation and escape from the radical-ion pair determines the source of the polariza-

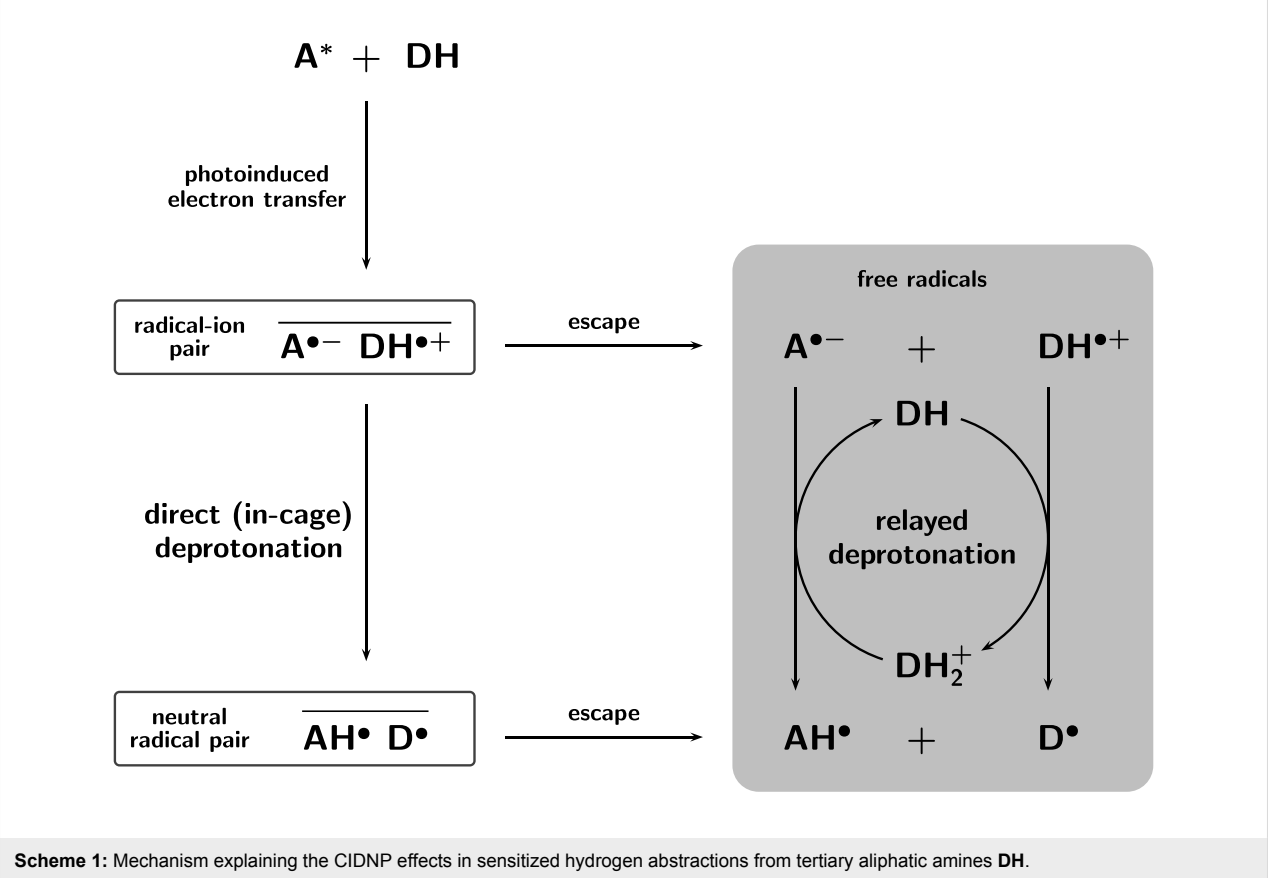

Scheme 1: Mechanism explaining the CIDNP effects in sensitized hydrogen abstractions from tertiary aliphatic amines **DH**.

tions. When escape predominates, all polarizations originate from the radical-ion pairs, when the in-cage deprotonation prevails, from the pairs of neutral radicals. Because the rate of in-cage deprotonation depends on the free energy of that reaction ΔG_{dep}, a threshold behaviour is observed: For triethylamine, a complete changeover of the polarization source occurs within a narrow (<20 kJ/mol) window of ΔG_{dep} far in the exergonic range (at around −100 kJ/mol).

In this work, we employ time-resolved CIDNP experiments to study two amines with hindered deprotonation of $\mathbf{DH}^{\bullet+}$, 1,4-diazabicyclo[2.2.2]octane (DABCO) and triisopropylamine (TIPA). The hindrance is due to a stereoelectronic effect with DABCO [21], and due to overcrowding with TIPA [22]. As sensitizers, we have chosen 9,10-anthraquinone (AQ) on one hand and xanthone (XA) or benzophenone (BP) on the other; with triethylamine, these are typical representatives that yield CIDNP from the radical-ion pairs and from the pairs of neutral radicals, respectively. Owing to competing side-reactions, kinetic studies were not feasible with triethylamine, but for the two amines of this work, they are. As we will show, depending on the sensitizer, different spin-polarized free radicals ($\mathbf{D}^{\bullet+}$ or $\mathbf{D}^{\bullet}$) escape from the pairs, and then undergo self-exchange with **DH** with different rates, which can be measured by the CIDNP decay kinetics. To the best of our knowledge, this is the first comparison of the electron and hydrogen self-exchange of the same substrates.

Results and Discussion

The relevant thermodynamic parameters of the sensitized hydrogen abstractions have been compiled in Table 1. As is evident from these values, the primary electron transfer is always so exergonic as to make it diffusion-controlled. In-cage deprotonation is also strongly exergonic, with the higher steric hindrance of TIPA being compensated by a more negative (by about 50 kJ/mol) ΔG_{dep}; for the two classes of sensitizers, the differences of ΔG_{dep} even amount to as much as 60…70 kJ/mol.

Table 1: Triplet energies E_T of the sensitizers, energies of the radical-ion pairs E_{RIP}, and energies of the pairs of neutral radicals E_{NRP} for the sensitizer/amine combinations used in this work. All energies are in kJ/mol and relative to the ground-state energies of the sensitizer plus the amine.

sensitizer/amine	E_T	E_{RIP}[a]	E_{NRP}[b]
AQ/DABCO	247[c]	146	79
AQ/TIPA	247[c]	156	36
XA/DABCO	310[d]	225	97
XA/TIPA	310[d]	235	53
BP/DABCO	287[e]	232	91

[a]Calculated from the reduction potentials Φ_{red} vs SCE in acetonitrile or DMF; Φ_{red} (AQ) = −0.94 V [23], Φ_{red} (XA) = −1.76 V [24], Φ_{red} (BP) = −1.83 V [24], Φ_{red} ($DABCO^{\bullet+}$) = −0.57 V [25], Φ_{red} ($TIPA^{\bullet+}$) = −0.68 V [8]. [b]From the differences of the heats of formation of the neutral radicals and their parent compounds, as calculated by Gaussian 09 [26] with the AM1 Hamiltonian. [c]See [27]. [d]See [28]. [e]See [29].

In experiments with continuous illumination, these systems exhibit practically no CIDNP; in time-resolved experiments, however, they yield strong CIDNP signals, which decay to zero, or to a small fraction of their initial value, on a microsecond timescale. This situation is typical for an exchange cancellation [30]: Geminate recombination of radical pairs $\overline{\mathbf{X}^{\bullet}\mathbf{Y}^{\bullet}}$ regenerates the starting materials **X** and **Y** with their respective polarizations, and escape affords free radicals $\mathbf{X}^{\bullet}$ and $\mathbf{Y}^{\bullet}$ bearing polarizations of exactly the same magnitudes but opposite signs to the geminate ones, owing to the spin-sorting nature of the CIDNP effect. By an exchange reaction of the free radicals with surplus reactants, e.g., $\mathbf{X}^{\bullet} + \mathbf{X} \rightleftharpoons \mathbf{X} + \mathbf{X}^{\bullet}$, the escape polarizations are then also transferred to the diamagnetic species **X** observable by NMR, and compensate the geminate polarizations already present in them. Hence, no CIDNP persists in **X** on long time scales, but the polarizations of **X** can be detected as transient phenomena because of the disparity of the timescales involved (geminate reactions are completed within nanoseconds, whereas the exchange reactions typically occur on a microsecond timescale for millimolar substrate concentrations). Residual signals remain only when the perfect neutralization of geminate and escape polarizations is disturbed by nuclear-spin relaxation in the free radicals or by secondary reactions of them.

Figure 1 shows such decay curves for the photoreactions of DABCO with different sensitizers. We stress that in all experiments of this work, the NMR signals of unreacted starting materials were eliminated by presaturation [31], thus the displayed signal intensities correspond to the pure polarizations. Furthermore, NMR spectra taken after a full series of time-resolved CIDNP measurements gave no indication of product formation; the remarkable photostability of the BP/DABCO system has already been reported in the literature [32]. The fast initial rise of the polarizations caused by radical-pair formation was suppressed by the use of a relatively long observation pulse, which acts as a low-pass filter and leaves unchanged the much slower subsequent CIDNP decay [33].

As follows from the described mechanism, the decay rate of the polarizations of DABCO should be completely independent of the sensitizer, because the latter is not at all involved in the exchange. For the two sensitizers BP and XA this is indeed the case, as Figure 1 shows, but in the AQ-sensitized reaction the decay is considerably faster, by a factor of more than 2.

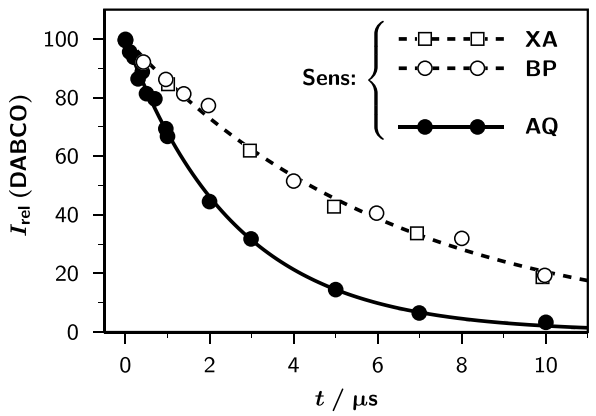

Figure 1: Time-resolved CIDNP in sensitized (sensitizers xanthone (XA), benzophenone (BP), or anthraquinone (AQ)) photoreactions of 1,4-diazabicyclo[2.2.2]octane (DABCO). Shown are the relative CIDNP intensities (integrals) I_{rel} (DABCO) of the 12 equivalent amine protons (s, 2.64 ppm) as functions of the delay t between the laser flash (80…90 mJ) and the sampling NMR pulse (duration, 1.0 μs). Temperature, 298 K; amine concentration c_0, 2.77 × 10^{-3} M; sensitizer concentrations, 1 × 10^{-3} M (AQ, XA) and 6 × 10^{-3} M (BP). The fit functions are first-order rate laws, 100exp [−$k_{ex}c_0t$]; they also include data points at longer times, which are not shown in the graph. Best-fit exchange-rate constants k_{ex}, 5.7 × 10^7 $M^{-1}s^{-1}$ (XA, BP) and 1.39 × 10^8 $M^{-1}s^{-1}$ (AQ). For further explanation, see text.

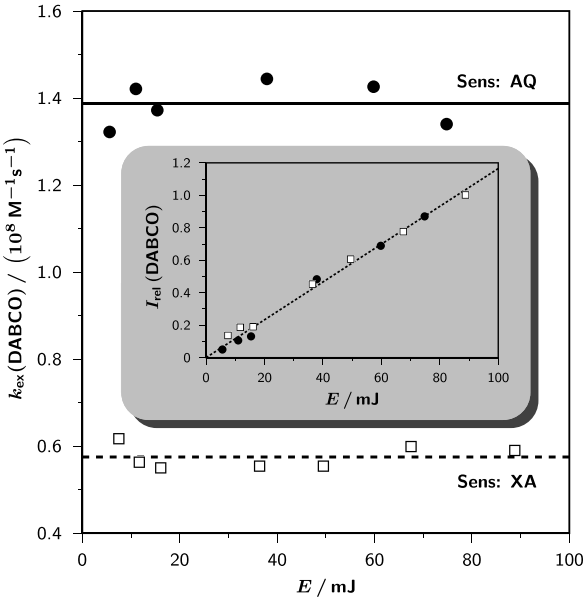

Figure 2: Influence of the laser intensity E on the observed exchange-rate constant k_{ex} (DABCO) (main plot) and on the relative CIDNP intensity I_{rel} (DABCO) of the amine protons, i.e., on the radical concentration, (inset) for the two sensitizers anthraquinone (AQ) and xanthone (XA). All other experimental parameters as in Figure 1. For further explanation, see text.

Nuclear-spin relaxation in the free radicals would increase the apparent exchange rates [34], but is ruled out by the absence of residual polarizations with AQ. This is consistent with our earlier observation of relaxation times well in excess of 100 μs for the aliphatic protons in the radical cations of methoxybenzenes [35]. The only additional pathway besides self-exchange that is capable of transferring the escape polarizations to the regenerated starting materials would be a recombination of the sensitizer-derived and amine-derived free radicals. This process is a bimolecular reaction; as a control experiment we, therefore, varied the concentrations of free radicals by varying the laser energy. The results are displayed in Figure 2. As is clearly discernible, the measured exchange rates remained constant over a concentration range spanning a factor of about 20. Because the ground states of our sensitizers can neither function as electron donors nor as hydrogen donors, exchange reactions involving different amine-derived radicals, meaning the intermediacy of different types of radical pairs, are the only remaining explanation for the different exchange rate constants for AQ as opposed to those for XA and BP. Our earlier results for triethylamine [5-7], in which time-resolved experiments are precluded by a high chemical turnover but the intermediates are identifiable through their polarization patterns, would suggest that in the present system AQ again yields CIDNP from the radical-ion pair, and the other two sensitizers produce CIDNP from the pair of neutral radicals, which is consistent with the much higher (compare, Table 1) driving force of in-cage deprotonation in the second case.

The polarization phase Γ_i of nucleus i in a product (Γ_i = +1, absorption; Γ_i = −1, emission) is connected to details of the reaction mechanism and to the magnetic properties of the intermediates through Kaptein's rule for a CIDNP net effect [36],

$$\Gamma_i = \mu \times \varepsilon \times \mathrm{sign}(\Delta g) \times \mathrm{sign}(a_i) \quad (1)$$

where μ and ε symbolize the multiplicities of the radical-pair precursors and the radical pairs affording the product in question (μ = +1, triplet; μ = −1, singlet; ε = +1, singlet; ε = −1, triplet), Δg is the g-value difference of the two radicals, with the one containing nucleus i taken first, and a_i is the hyperfine coupling constant of that nucleus in the radical. Together with the fact that the absolute CIDNP intensity of nucleus i is approximately proportional to a_i [12], this sign rule forms the basis for identifying a paramagnetic intermediate through the resulting polarization pattern.

All three sensitizers are typical triplet sensitizers (μ = +1). From Table 1 it is evident that the energies of the resulting radical pairs lie well below those of the sensitizer triplets. The saturated amine DABCO possesses an even higher triplet energy (about 360 kJ/mol, as estimated from the phosphorescence in frozen matrices [37]) than the sensitizers, so the radical pairs can only react back to the starting materials via the singlet exit channel (ε = +1).

The DABCO signal appearing in absorption (Γ = +1) thus means that the *g*-value difference and the hyperfine coupling constant must have the same sign. For a radical ion pair, this certainly holds because the reported very high *g* value of the DABCO radical cation (2.0048 [38]) clearly exceeds the *g* values of all the sensitizer radical anions (between 2.0036 for XA [39] and 2.00443 for AQ [40]) and the proton hyperfine coupling constant in the DABCO radical cation must be positive. For a pair of neutral radicals, the situation is equally predictable although the magnetic parameters of the α-amino alkyl radical of DABCO are not known precisely: A negative hyperfine coupling constant of about −14 G is to be expected for the single proton attached to its radical center, a noticeably larger positive one of about +19 G for the two protons at the adjacent carbon, and a smaller positive one of about +4 G for the four *γ* protons on the other two bridges [21]; in the regenerated DABCO, all protons are magnetically equivalent, so the observed polarization phase is governed by the balance between these hyperfine coupling constants, where the positive ones clearly dominate. To account for the absorptive polarization, the *g* value of the α-amino alkyl radical must thus be larger than that of the sensitizer ketyl radical, which is corroborated by the polarizations of the regenerated sensitizer. Whereas these are undetectably small in the case of AQ and BP, XA exhibits weak polarizations of $H^{1,8}$ and $H^{3,6}$ (8.25 ppm, d of d; and 7.82 ppm, d of t; for the assignment, compare the literature [41]), both in absorption. $H^{1,8}$ and $H^{3,6}$ possess the largest hyperfine coupling constants both in the xanthone radical anion (−3.9 G for both protons [38]) and in the xanthone ketyl radical (−4.1 G for $H^{1,8}$, −3.8 G for $H^{3,6}$ [42]). Because of their negative signs, the *g* value of the xanthone-derived radical is thus indeed lower than that of the DABCO-derived radical.

While the polarization phases can thus be reconciled with both types of radical pairs, the different decay rates are clear evidence for different free radicals with XA as opposed to AQ. It is natural to assign hydrogen transfer to the slower of the two exchanges and electron transfer to the faster one. This is corroborated by the absolute strengths of the CIDNP effects with these two sensitizers. There is an approximate proportionality between the magnitude of CIDNP and the inverse square root of Δ*g* [11]. For the pair of radical ions, Δ*g* is about three times larger with XA than with AQ (see above). This would predict correspondingly smaller polarizations, yet quite the opposite is observed: CIDNP is more than an order of magnitude larger in the case of XA (in fact so unusually strong that for aligning the optical path of the excitation laser we found XA/DABCO to be the best system, other points in its favour being that it is extremely photostable and that its NMR signal is a singlet). This remarkable signal strength must reflect an extremely small Δ*g*, which is consistent with a pair of neutral radicals because the unknown *g* value of the α-amino alkyl radical is expected to lie only very slightly above the *g* value of the sensitizer ketyl radical (2.00345 [5]).

To analyze the kinetics, we use Scheme 2. Polarized free radicals can escape either from the radical-ion pairs or from the pairs of neutral radicals. Each type of radical can undergo self-exchange with ground-state molecules **DH** (by electron transfer, with rate constant k_{ET}; by hydrogen transfer, with rate constant k_{HT}), which does not affect the chemical composition of the sample but transfers the polarizations from the radicals to **DH**, where they can be detected by NMR. We stress that there is no such thing as a polarized molecule, but that polarization is a property of the ensemble. However, because the polarizations are very small deviations of the populations of the nuclear spin states from the Boltzmann distribution (they are only noticeable compared to the tiny population differences caused by the field of the NMR magnet), the kinetics can be accurately described by a "polarized radical" $\mathbf{DH}^{\bullet+}_{\text{polarized}}$ or $\mathbf{D}^{\bullet}_{\text{polarized}}$ undergoing an exchange with an "unpolarized substrate molecule" **DH** to give an "unpolarized radical" and a "polarized substrate molecule" $\mathbf{DH}_{\text{polarized}}$, the concentration of which is monitored. Additionally, the relayed deprotonation (rate constant k_{dep}) transfers polarizations from the radical cation to the α-amino alkyl radical in the same way, but also involves macroscopic chemical turnover. All three processes can be formulated as pseudo first-order ones because the concentration of **DH** is much higher than the concentrations of "polarized molecules".

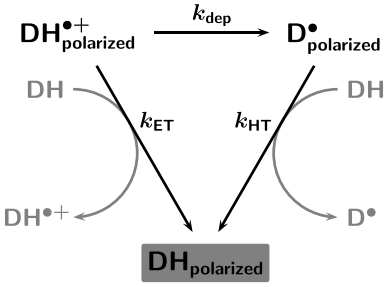

Scheme 2: Pathways from the free radicals to the product.

Starting with neutral radicals (i.e., for the sensitizer XA), the observable must follow a simple first-order rate law. However, starting with radical cations (i.e., in the case of AQ), Scheme 2 predicts more complex kinetics comprising two exponential terms, with rate constants k_{HT} and (k_{ET} + k_{dep}) and positive signs of both pre-exponential factors. Because the experimental results are evidently very well represented by a monoexponential decay (Figure 1), the data can only be accommodated by the intermediacy of radical-ion pairs in two limiting situations,

where one of the exponential terms dominates. The first is that relayed deprotonation is slower than electron self-exchange, in which case k_{ET} becomes the observed rate constant; the second is that relayed deprotonation is slower than hydrogen self-exchange, in which case it limits the rate for the right-hand-side pathway from $\mathbf{D}^{\bullet+}_{polarized}$ to $\mathbf{DH}_{polarized}$, and the observed rate constant is given by $k_{ET} + k_{dep}$.

The absence of a residual polarization with AQ, which is clearly perceived in Figure 1, allows a decision between these two alternatives. When the free radicals $\mathbf{DH}^{\bullet+}_{polarized}$ do not undergo relayed deprotonation, all protons remain in place throughout the reaction sequence; furthermore, none of them are directly bound to centers bearing the unpaired electron, so relaxation losses will be extremely small. In this situation, one therefore expects complete cancellation of cage and escape polarizations, and no signal should remain on long time scales. Relayed deprotonation, however, removes one of the 12 polarized protons, which the subsequent hydrogen exchange replaces by an unpolarized one. Hence the escape polarization can only compensate 11/12 of the cage polarization, and a residual signal of a little more than 8 percent is expected. The fact that no such residual signal is observed militates for the unimportance of relayed deprotonation for the CIDNP kinetics.

With Equation 2, the free energy of the relayed deprotonation $\Delta G'_{dep}$ can be estimated from the reduction potential Φ_{red} ($\mathbf{DH}^{\bullet+}$) of the radical cation (see, Table 1, but taken relative to NHE instead of SCE), the pK_a of the protonated amine $\mathbf{DH}_2^+$ (8.9 [43]), and the calculated heats of formation ΔH_f of $\mathbf{D}^{\bullet}$ (+208 kJ/mol) and **DH** (+87 kJ/mol):

$$\Delta G_{dep} = -F\left[\Phi_{red}\left(\mathbf{DH}^{\bullet+}\right) + 0.24\mathrm{V}\right] - 2.303RT\mathrm{p}K_a\left(\mathbf{DH}_2^+\right) + \Delta H_f\left(\mathbf{DH}\right) - \Delta H_f\left(\mathbf{D}^{\bullet}\right) \quad (2)$$

The obtained result, −8 kJ/mol, shows that, for this amine, relayed deprotonation is almost thermodynamically neutral. Newman projections further indicate relayed deprotonation to be sterically more demanding than hydrogen self-exchange, because two of the gauche interactions in the transition state are between larger groups in the former reaction compared to the latter. In combination with the lower rate in the XA-sensitized experiments, this lends further support to the presumption that k_{dep} is smaller than k_{ET}.

The low value of $\Delta G'_{dep}$ raises the possibility that, for DABCO, relayed deprotonation of $\mathbf{DH}^{\bullet+}$ may be reversible. Starting with neutral radicals, the kinetic analysis would then be completely analogous to the above one, but with the roles of k_{ET} and k_{HT} interchanged. Because the preceding discussion has shown that relayed deprotonation should definitely be slower than electron self-exchange, the condition for a monoexponential decay is very likely to be fulfilled. Hence, the observed decay rate constant in the photoreaction with XA may well be a compound quantity, ($k_{HT} + k_{dep}$). In that case, no residual CIDNP signal is expected because the α hydrogen of the amine is already removed in the cage, and the ketyl hydrogen, which re-enters the amine in the cage recombination, is easily exchangeable, so will not develop an appreciable polarization during the life of the radical pairs.

Nelsen et al. measured electron transfer rates for different redox couples and used the Marcus cross-rate theory to calculate self-exchange rate constants from these data; for DABCO, for which only one such couple was available, they reported a value of $7.3 \times 10^3\ \mathrm{M^{-1}s^{-1}}$ [44]. This indirectly obtained electron-self-exchange rate constant is four orders of magnitude lower than even the smaller of our two directly observed rate constants, and under no circumstances could the curves of Figure 1 be reconciled with such a slow process. We have no explanation for that discrepancy but point out that it would be very surprising if an electron self-exchange (which is accompanied by comparatively small geometry changes and is less influenced by sterical constraints than bond-forming reactions, because it can occur over longer distances than the contact distance [45]) should be so strongly decelerated in relation to the other chemical processes taking place in that sterically hindered system, namely, hydrogen self-exchange and almost energetically neutral proton transfer.

Figure 3 displays the outcome of a time-dependent CIDNP experiment on TIPA sensitized by XA. This amine exhibits the peculiarity that its CIDNP spectra are completely dominated by the emissive doublet of the β protons at 0.98 ppm; in the example, the α protons (septet at 3.13 ppm) bear no discernible polarization whatsoever, and with the sensitizer AQ, their CIDNP signals are so tiny as to prohibit any interpretation. In contrast to DABCO, the CIDNP phases with TIPA are emissive regardless of the sensitizer, and there is a much more noticeable initial increase of the magnitude of the polarizations.

However, the striking influence of the sensitizer is observed also for this amine, and is even stronger than for DABCO: With AQ as compared to XA, the polarizations of TIPA decrease faster by a factor of five at room temperature. The intermediacy of different radical pairs, and thus of different initial free radicals again provides a natural explanation.

The β protons must have a positive hyperfine coupling constant both in the radical cation and in the α-amino alkyl radical of

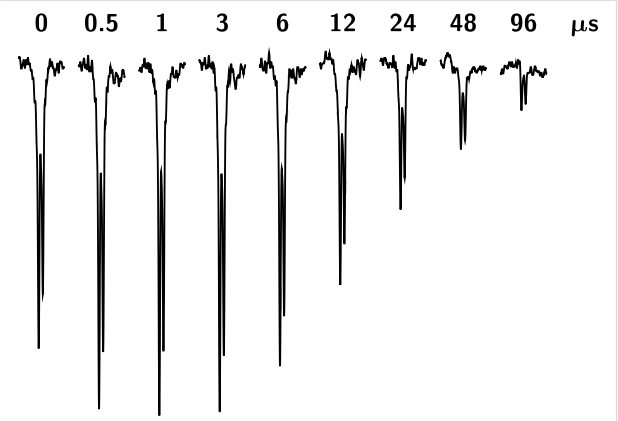

Figure 3: Time-resolved CIDNP signals of the 18 equivalent β protons (d, 0.98 ppm) of triisopropylamine (TIPA) in the photoreaction with xanthone (XA) as functions of the delay (given at the respective trace) between the laser flash and the sampling NMR pulse. Note the exponential increase of the delay with the spectrum number. Excitation intensity, ca. 80 mJ per flash; NMR pulse width, 1.0 μs; temperature, 279 K; amine concentration, 5.0×10^{-4} M; sensitizer concentration, 1×10^{-3} M. Further explanation, see text.

TIPA. The observed emissive polarization thus constrains the amine-derived radical to have a lower *g* value than the sensitizer-derived radical. For the sensitizer XA this in only possible in the case of the neutral radical pairs because the *g* value of the amine radical cation (2.0037 [46]) is higher than the *g* values of the sensitizer radical anion and ketyl radical (2.0036 and 2.00345 [5]), while for the α-amino alkyl radical of a saturated monoamine a *g* value of 2.0030 is typically expected [16]. The polarization phases of this substrate thus further support the intermediacy of a radical ion pair with AQ and of a pair of neutral radicals with XA.

For a pair of neutral radicals, the absence of CIDNP of the α protons can be understood because in the radical pair this proton is attached to the oxygen of the sensitizer ketyl radical and is, therefore, exchangeable, so cannot pick up a noticeable polarization during the pair life. For a radical ion pair, the α protons should exhibit only small polarizations, because the ratio of the hyperfine coupling constants of the α and β protons in the radical cation of TIPA is much smaller (about 2:1 [46]) than in a less strained amine, such as triethylamine, the number of α protons is six times smaller, and the signal splitting into a septet causes the individual lines to be concomitantly lower in intensity.

Because the observed β protons remain in place during all transformations from the radical pairs over the free radicals to the diamagnetic product **DH**, a residual polarization on long time scales is neither expected nor found. The initial signal growth in Figure 3 is due to radical-pair formation, i.e., to the quenching of the sensitizer triplet by the amine. We emphasize that the resulting biexponential rate law is characterized by opposite signs of the two pre-exponential factors as opposed to the equal signs that result from the decay kinetics of Scheme 2. In principle, the quenching rates could be extracted from the signal rise, but that determination is not very accurate under conditions best suited for investigating the self-exchange [34]. The decay of the signal is once more excellently described by a single exponential, with the same implications for the mechanism as in the case of DABCO.

The free energy for the deprotonation of the radical cation by the amine itself can again be calculated with Equation 2. The pK_a value of $\mathbf{DH_2^+}$ is only known in aqueous diglyme, where it is between 6.9 and 9.2, depending on the water content [47]. Even with the smaller of these values, using the reduction potential of Table 1 and the calculated heats of formation (ΔH_f ($\mathbf{D^\bullet}$), −33 kJ/mol; ΔH_f (**DH**), −111 kJ/mol) we arrive at an exergonicity of at least −50 kJ/mol, which means that a reversibility of that deprotonation can be discounted. Sterically, that deprotonation is much more demanding than the hydrogen self-exchange, as Newman projections of the expected transition states show. With both reactions, there are four gauche interactions between methyl and a large group (iPr or $N(iPr)_2$), whereas the other two gauche interactions are between the two large groups iPr and $N(iPr)_2$ in the former reaction, but only between two methyl groups in the latter. On these grounds, we assume that, notwithstanding the substantial driving force, k_{dep} is smaller than k_{PT} for this amine. That assumption immediately leads to the consequence that the rate constant in the reaction with AQ, i.e., the compound quantity ($k_{ET} + k_{dep}$), should again be dominated by k_{ET} because the rate constant k_{PT}, which is measured in the XA-sensitized reaction, is five times smaller than the observed rate constant in the AQ-sensitized reaction.

Experimental activation parameters should thus be meaningful for the presumed single reaction in each of these cases (sensitizer AQ, pure electron self-exchange; sensitizer XA, pure hydrogen self-exchange). Eyring plots are displayed in Figure 4. Their good linearity also in the AQ-sensitized reaction lends a posteriori support to our above reasoning.

From the regression lines in Figure 4, one calculates the activation parameters given in Table 2. The much more negative activation entropy in the XA-sensitized reaction is clearly consistent with our preceding explanation of the different reaction rates, because a hydrogen self-exchange must involve a more ordered transition state than an electron self-exchange; the small positive activation entropy in the AQ-sensitized reaction also supports our interpretation, because this is a well-known fact for outer-sphere electron transfer reactions of organic compounds in polar solvents [48].

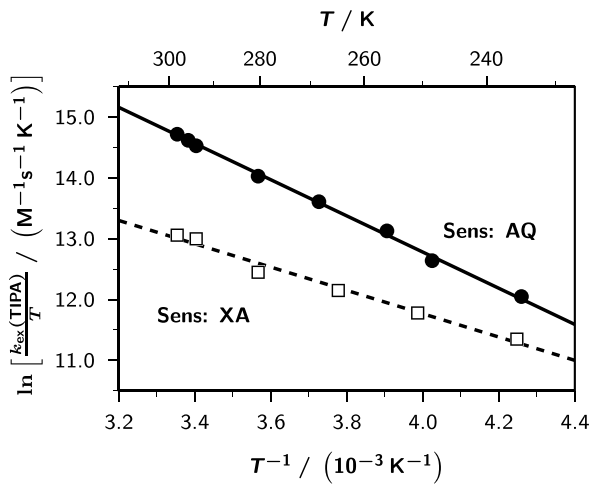

Figure 4: Eyring plots for the self-exchange rate constants k_{ex} (TIPA) of triisopropylamine (TIPA) sensitized by anthraquinone (AQ) (full circles and solid line; linear regression, 24.68 − 2975/T) and xanthone (XA) (open circles and broken line; linear regression, 19.43 − 1917/T). All experimental parameters, expect for the temperature T, as in Figure 3. Further explanation, see text.

Table 2: Activation parameters for the self-exchange reactions of TIPA, as obtained from the Eyring plots of Figure 4.

Reaction	$\Delta H^{\ddagger}$ (kJ/mol)	$\Delta S^{\ddagger}$ (J K^{-1} mol^{-1})	$\Delta G^{\ddagger}_{298}$ (kJ/mol)
DH$^{\bullet+}$ + **DH**	24.7	+7.6	22.4
D$^{\bullet}$ + **DH**	15.9	−36.0	26.6

According to the Marcus theory [49], the free energy of activation of an electron-self-exchange reaction equals one quarter of the reorganization energy λ, which is the energy needed to distort the geometries of the reactants (inner reorganization energy λ_i) and of the surrounding solvent shell (outer reorganization energy λ_o) to the geometries of the products including their solvent shell, but without transferring the electron. For organic compounds, λ_o typically dominates, with λ_i rarely accounting for more than 15% of the total reorganization energy [50]. For an estimate of λ, we therefore neglect λ_i.

Using a continuum model, Marcus [49] has derived the following expression for λ_o for a self-exchange of a singly charged ion with its neutral parent compound,

$$\lambda_o = \frac{N_A e^2}{4\pi\varepsilon_0} \times \left(\frac{1}{n^2} - \frac{1}{\varepsilon}\right) \times \left(\frac{1}{d_1} + \frac{1}{d_2} - \frac{1}{d}\right) \qquad (3)$$

where N_A, e, and ε_0 are Avogadro's number, the electron charge, and the vacuum permittivity, n and ε are the index of refraction and the relative permittivity of the solvent, d_1 and d_2 are the molecular diameters of the two reactants, and d is their encounter distance. For acetonitrile, the polarity parameter ($1/n^2 - 1/\varepsilon$) amounts to 0.527 at room temperature. The calculated shapes of **DH** and **DH**$^{\bullet+}$ are practically identical for our amines, and the geometries of both TIPA and DABCO deviate only slightly from spherical; they are are oblate spheroids with the shorter semi-axis orientated perpendicular to the plane of the three methine protons in the former case and along the N–N axis in the latter. To get the molecular dimensions, we added the van-der-Waals radii of the respective outermost atoms along each semi-axis (N, 1.55 Å [51] for the shorter semi-axis of DABCO; H, 1.1 Å [52] for all other semi-axes) and averaged the three diameters. Identifying the shorter diameter with the encounter distance, we arrive at an outer-sphere reorganization energy of 82.6 kJ/mol for TIPA ($d_1 = d_2 = 7.5$ Å; $d = 6.5$ Å), i.e., a value of 20.6 kJ/mol for $\Delta G^{\ddagger}_{298}$; if the encounter distance, which is not precisely known, were identical to the average molecular diameter $\Delta G^{\ddagger}_{298}$ would increase to 24.4 kJ/mol. In view of this uncertainty, an elaborate computation of λ_i is not justified, but the calculated activation parameter is seen to be in very good agreement with the experimental result of Table 2. Finally, the slightly smaller molecular size of DABCO ($d_1 = d_2 = 6.2$ Å; $d = 5.7$ Å) leads to a computed increase of $\Delta G^{\ddagger}_{298}$, relative to TIPA, by 6.3 kJ/mol, corresponding to a decrease of the self-exchange rate constant by a factor of 12.7, which at first glance does not seem to compare very favourably with the experimental ratio (5.3) observed in this work; however, DABCO has two nitrogen sites that can participate in the exchange, and taking this into account by multiplying the experimental ratio by 2 reduces the discrepancy to less than 20 percent.

Conclusion

The described direct measurements of self-exchange rate constants by time-resolved photo-CIDNP experiments have made it possible to distinguish between the different types of free radicals occurring in these systems, and have corroborated and complemented our previous [5-7] mechanistic findings on sensitized photoreactions of tertiary aliphatic amines. It would have been difficult or impossible to obtain these results by other techniques because no other kind of spectroscopy attaches labels (the polarizations) at the stage of the intermediates and observes them in the products, thus highlighting the interconnections of species along the reaction coordinate. The present study thus again demonstrates the power of CIDNP to provide detailed insights into complex reaction mechanisms.

Experimental

TIPA was synthesized and purified according to a literature procedure [47]; DABCO and all the sensitizers were commer-

cially obtained and purified by double sublimation. The purchased solvent acetonitrile-d_3 was carefully dried to a water content of less than 5×10^{-4} M in a specially designed apparatus [53]. Sensitizer concentrations were chosen to give an extinction of about 1 in a 5 mm NMR tube. ^{1}H CIDNP experiments were carried out on a Bruker WM 250 NMR spectrometer with a special probe [34] allowing side-on illumination of the samples. The temperature in the probe was controlled to ±0.3 K. Presaturation sequences [31] were used to remove unchanging background magnetization. The light source was a Lambda Physik EMG 101 laser (XeCl, 308 nm, 15 ns pulse width, ±5 ns jitter, ±3% energy fluctuations), which was triggered by the acquisition system of the spectrometer.

References

1. Schaefer, C. G.; Peters, K. S. *J. Am. Chem. Soc.* **1980,** *102,* 7566–7567. doi:10.1021/ja00545a030
2. Simon, J. D.; Peters, K. S. *J. Am. Chem. Soc.* **1981,** *103,* 6403–6406. doi:10.1021/ja00411a023
3. Inbar, S.; Linschitz, H.; Cohen, S. G. *J. Am. Chem. Soc.* **1981,** *103,* 1048–1054. doi:10.1021/ja00395a009
4. Miyasaka, H.; Morita, K.; Kamada, K.; Mataga, N. *Bull. Chem. Soc. Jpn.* **1990,** *63,* 3385–3397. doi:10.1246/bcsj.63.3385
5. Goez, M.; Sartorius, I. *J. Am. Chem. Soc.* **1993,** *115,* 11123–11133. doi:10.1021/ja00077a009
6. Goez, M.; Sartorius, I. *Chem. Ber.* **1994,** *127,* 2273–2276. doi:10.1002/cber.1491271128
7. Goez, M.; Sartorius, I. *J. Phys. Chem. A* **2003,** *107,* 8539–8546. doi:10.1021/jp030244g
8. Pischel, U.; Zhang, X.; Hellrung, B.; Haselbach, E.; Muller, P.-A.; Nau, W. M. *J. Am. Chem. Soc.* **2000,** *122,* 2027–2034. doi:10.1021/ja992508b
9. Pischel, U.; Nau, W. M. *J. Am. Chem. Soc.* **2001,** *123,* 9727–9737. doi:10.1021/ja011212e
10. Steiner, U. E.; Ulrich, T. *Chem. Rev.* **1989,** *89,* 51–147. doi:10.1021/cr00091a003
11. Goez, M. Photochemically Induced Dynamic Nuclear Polarization. In *Advances in Photochemistry;* Neckers, D. C.; Volman, D. H.; von Bünau, G., Eds.; John Wiley & Sons, Inc.: Hoboken, NJ, 1997; Vol. 23, pp 63–163. doi:10.1002/9780470133545.ch2
12. Goez, M. *Annu. Rep. NMR Spectrosc.* **2009,** *66,* 77–147. doi:10.1016/S0066-4103(08)00403-1
13. Goez, M. In *Carbon-Centered Free Radicals and Radical Cations: Structure, Reactivity, and Dynamics;* Forbes, M. D., Ed.; Wiley Series on Reactive Intermediates in Chemistry and Biology, Vol. 3; Wiley: Hoboken, NJ, 2010; pp 185–204.
14. Berliner, L. J.; Bagryanskaya, E. In *Multifrequency Electron Paramagnetic Resonance;* Misra, S. K., Ed.; Wiley-VCH: Weinheim, Germany, 2011; pp 947–992.
15. Goez, M. *Top. Curr. Chem.* **2012**. doi:10.1007/128_2012_348
16. Roth, H. D.; Manion, M. L. *J. Am. Chem. Soc.* **1975,** *97,* 6886–6888. doi:10.1021/ja00856a060
17. Schäublin, S.; Wokaun, A.; Ernst, R. R. *J. Magn. Reson.* **1977,** *27,* 273–302. doi:10.1016/0022-2364(77)90077-4
18. Closs, G. L.; Miller, R. J. *J. Am. Chem. Soc.* **1979,** *101,* 1639–1641. doi:10.1021/ja00500a068
19. Goez, M.; Kuprov, I.; Hore, P. J. *J. Magn. Reson.* **2005,** *177,* 139–145. doi:10.1016/j.jmr.2005.06.017
20. Goez, M.; Kuprov, I.; Mok, K. H.; Hore, P. J. *Mol. Phys.* **2006,** *104,* 1675–1686. doi:10.1080/00268970600634431
21. Griller, D.; Howard, J. A.; Marriott, P. R.; Scaiano, J. C. *J. Am. Chem. Soc.* **1981,** *103,* 619–623. doi:10.1021/ja00393a020
22. Bock, H.; Göbel, I.; Havlas, Z.; Liedle, S.; Oberhammer, H. *Angew. Chem., Int. Ed. Engl.* **1991,** *30,* 187–190. doi:10.1002/anie.199101871
23. Fickling, M. M.; Fischer, A.; Mann, B. R.; Packer, J.; Vaughan, J. *J. Am. Chem. Soc.* **1959,** *81,* 4226–4230. doi:10.1021/ja01525a027
24. Given, P. H.; Peover, M. E.; Schoen, J. *J. Chem. Soc.* **1958,** 2674–2679. doi:10.1039/JR9580002674
25. Hub, W.; Schneider, S.; Dörr, F.; Oxman, J. D.; Lewis, F. D. *J. Am. Chem. Soc.* **1984,** *106,* 701–708. doi:10.1021/ja00315a040
26. *Gaussian 09,* Revision A.1; Gaussian, Inc.: Wallingford, CT, 2009.
27. Herkstroeter, W. G.; Lamola, A. A.; Hammond, G. S. *J. Am. Chem. Soc.* **1964,** *86,* 4537–7540. doi:10.1021/ja01075a005
28. Scaiano, J. C. *J. Am. Chem. Soc.* **1980,** *102,* 7747–7753. doi:10.1021/ja00546a018
29. Saltiel, J.; Curtis, H. C.; Metts, L.; Miley, J. W.; Winterle, J.; Wrighton, M. *J. Am. Chem. Soc.* **1970,** *92,* 410–411. doi:10.1021/ja00705a617
30. Closs, G. L.; Sitzmann, E. V. *J. Am. Chem. Soc.* **1981,** *103,* 3217–3219. doi:10.1021/ja00401a052
31. Goez, M.; Mok, K. H.; Hore, P. J. *J. Magn. Reson.* **2005,** *177,* 236–246. doi:10.1016/j.jmr.2005.06.015
32. von Raumer, M.; Suppan, P.; Haselbach, E. *Chem. Phys. Lett.* **1996,** *252,* 263–266. doi:10.1016/0009-2614(96)00138-8
33. Goez, M. *Chem. Phys. Lett.* **1990,** *165,* 11–14. doi:10.1016/0009-2614(90)87003-A
34. Goez, M. *Chem. Phys.* **1990,** *147,* 143–154. doi:10.1016/0301-0104(90)85030-Z
35. Goez, M.; Eckert, G. *Z. Phys. Chem. (Muenchen, Ger.)* **1993,** *182,* 131–142. doi:10.1524/zpch.1993.182.Part_1_2.131
36. Kaptein, R. *J. Chem. Soc., Chem. Commun.* **1971,** 732–733. doi:10.1039/C29710000732
37. Muto, Y.; Nakato, Y.; Tsubomura, H. *Chem. Phys. Lett.* **1971,** *9,* 597–599. doi:10.1016/0009-2614(71)85137-0
38. Kaise, M.; Someno, K. *Chem. Lett.* **1987,** *16,* 1295–1298. doi:10.1246/cl.1987.1295
39. Aarons, L. J.; Adam, F. C. *Can. J. Chem.* **1972,** *50,* 1390–1400. doi:10.1139/v72-217
40. Sieiro, C.; Sanchez, A.; Crouigneau, P. *Spectrochim. Acta, Part A* **1984,** *40,* 453–456. doi:10.1016/0584-8539(84)80077-X
41. Sharpless, N. E.; Bradley, R. B.; Ferretti, J. A. *Org. Magn. Reson.* **1974,** *6,* 115–120. doi:10.1002/mrc.1270060213
42. Wilson, R. *J. Chem. Soc. B* **1968,** 1581–1588. doi:10.1039/J29680001581
43. Castro, E. A.; Aliaga, M.; Campodonico, P. R.; Leis, J. R.; García-Río, L.; Santos, J. G. *J. Phys. Org. Chem.* **2008,** *21,* 102–107. doi:10.1002/poc.1286
44. Nelsen, S. F.; Weaver, M. N.; Luo, Y.; Pladziewicz, J. R.; Ausman, L. K.; Jentzsch, T. L.; O'Konek, J. J. *J. Phys. Chem. A* **2006,** *110,* 11665–11676. doi:10.1021/jp064406v
45. Kavarnos, G. J.; Turro, N. J. *Chem. Rev.* **1986,** *86,* 401–449. doi:10.1021/cr00072a005
46. de Meijere, A.; Chaplinski, V.; Gerson, F.; Merstetter, P.; Haselbach, E. *J. Org. Chem.* **1999,** *64,* 6951–6959. doi:10.1021/jo990458n

47. Kuffner, F.; Koechlin, W. *Monatsh. Chem.* **1962,** *93,* 476–482. doi:10.1007/BF00903145
48. Ghorai, P. K.; Matyushov, D. V. *J. Phys. Chem. A* **2006,** *110,* 8857-8863. doi:10.1021/jp056261i
49. Marcus, R. A. *Annu. Rev. Phys. Chem.* **1964,** *15,* 155–196. doi:10.1146/annurev.pc.15.100164.001103
50. Jensen, B. S.; Ronlán, A.; Parker, V. D. *Acta Chem. Scand., Ser. B* **1975,** *29,* 394–396. doi:10.3891/acta.chem.scand.29b-0394
51. Bondi, A. *J. Phys. Chem.* **1964,** *68,* 441–451. doi:10.1021/j100785a001
52. Rowland, R. S.; Taylor, R. *J. Phys. Chem.* **1996,** *100,* 7384–7391. doi:10.1021/jp953141+
53. Goez, M. *J. Magn. Reson.* **1998,** *135,* 14–16. doi:10.1006/jmre.1998.1504

License and Terms

Beilstein Journal of Organic Chemistry

A new intermediate in the Prins reaction

Shinichi Yamabe*[1], Takeshi Fukuda[2] and Shoko Yamazaki[2]

Full Research Paper

Open Access

Address:
[1]Fukui Institute for Fundamental Chemistry, Kyoto University Takano-Nishihiraki-cho 34-4, Sakyou-ku, Kyoto 606-8103, Japan and [2]Department of Chemistry, Nara University of Education, Takabatake-cho, Nara 630-8528, Japan

Email:
Shinichi Yamabe* - yamabes@fukui.kyoto-u.ac.jp

* Corresponding author

Keywords:
DFT calculations; hemiacetal intermediate; hydrogen bond; Prins reaction; transition state

Beilstein J. Org. Chem. **2013,** *9,* 476–485.
doi:10.3762/bjoc.9.51

Received: 14 November 2012
Accepted: 31 January 2013
Published: 05 March 2013

This article is part of the Thematic Series "New reactive intermediates in organic chemistry".

Guest Editor: G. Bucher

Abstract

Two Prins reactions were investigated by the use of DFT calculations. A model composed of R–CH=CH_2 + $H_3O^+(H_2O)_{13}$ + $(H_2C{=}O)_2$, R = Me and Ph, was adopted to trace reaction paths. For both alkenes, the concerted path forming 1,3-diols was obtained as the rate determining step (TS1). TS stands for a transition state. From the 1,3-diol, a bimolecular elimination (TS2) leads to the allylic alcohol as the first channel. In the second channel, the 1,3-diol was converted via TS3 into an unprecedented hemiacetal intermediate, HO–CH_2–O–CH(R)–CH_2–CH_2–OH. This intermediate undergoes ring closure (TS4), affording the 1,3-dioxane product. The intermediate is of almost the same stability as the product, and two species were suggested to be in a state of equilibrium. While the geometry of TS1 appears to be forwarded to that of a carbocation intermediate, the cation disappeared through the enlargement of the water cluster. Dynamical calculations of a classical trajectory using the atom-centered density matrix propagation molecular dynamics model on the four TSs were carried out, and results of IRC calculations were confirmed by them.

Introduction

The Prins reaction is the acid-catalyzed addition of aldehydes to alkenes and gives different products depending on the reaction conditions. The first work on the condensation of alkenes with aldehydes was made by Kriewitz in 1899 [1]. He found that unsaturated alcohols were produced when pinene (a bicyclic monoterpene) was heated with paraformaldehyde. However, Prins performed the first rather comprehensive study of the reactions between formaldehyde and hydrocarbons with C=C double bonds [2,3]. These were styrene, pinene, camphene and anethole. As a catalyst, sulfuric acid was used, and water or glacial acetic acid was the solvent. A general Prins reaction is shown in Scheme 1.

A typical Prins reaction is exhibited in Scheme 2 [4]. Here, the six-membered ring compound, 4,4-dimethyl-1,3-dioxane, is the major product along with 3-methyl-1,3-butane-diol. The 1,3-dioxane is hydrolyzed to form the 1,3-diol by stirring the former in a 2% (or lower) sulfuric acid solution under reflux [4].

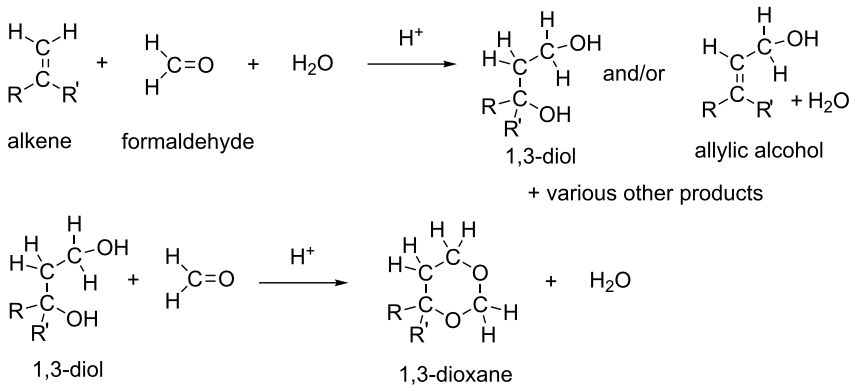

Scheme 1: A general scheme of the Prins reaction.

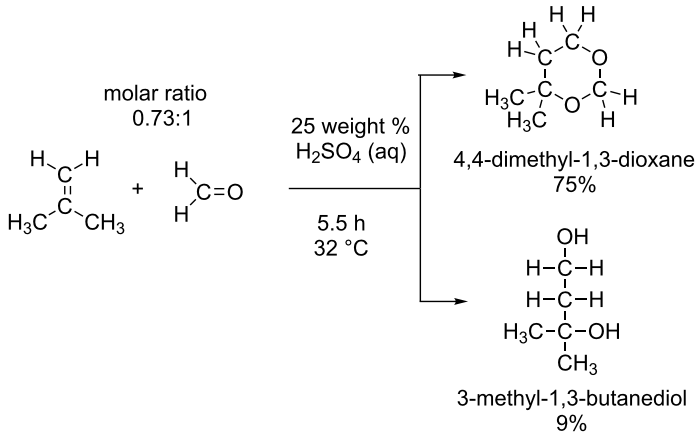

Scheme 2: An example of the Prins reaction [4]. The product yields (%) are based on formaldehyde.

However, the hydrolysis yield on the dioxane charged is only 8–17% depending on the alkene reactants. The result was interpreted in terms of a reversible reaction shown in Scheme 3.

On the other hand, a reaction of longifolene with formaldehyde in acetic acid yielded the acetate of an allylic alcohol (ω-acetoxymethyl longifolene) as a major product under high-temperature conditions (Scheme 4, 140 °C, 24 h) [5].

A scheme was proposed as to the mechanism of the Prins reactions [6-18] to afford 1,3-dioxane, 1,3-diol and allylic alcohol, where the carbocation intermediate (X) is included (Scheme 5).

In the second step, X is formed. From X, two routes, (i) and (ii), are possible. In the route (i), a water molecule is linked with the cation center, which leads to formation of the 1,3-diol and the subsequent allylic alcohol. In (ii), the second $H_2C{=}O$ is bound

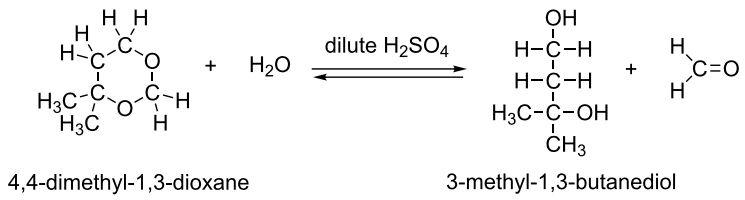

Scheme 3: An equilibrium in the hydrolysis of the product, 1,3-dioxane.

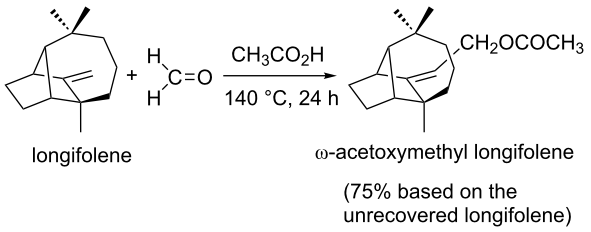

Scheme 4: Formation of the acetate of an allylic alcohol by Prins reaction [5].

to the cation center, leading to formation of the 1,3-dioxane. While tertiary carbocations might intervene, the presence or absence of secondary ones would be critical in the aqueous media. This is because the water cluster has high nucleophilic strength and tends to make C–O bonds to form alcohols , overcoming the intervention of carbocations. In this respect, the mechanism depicted in Scheme 5 needs to be examined by the use of some alkenes theoretically.

A variety of protic acids and Lewis acids are employed to catalyze the reaction, and Prins-type reactions have found numerous synthetic applications [6,19-25]. In spite of the extensive experimental studies, there have been no computational studies of the classic Prins reaction. The reaction is also important, because the constituent atoms are only C, H and O in the original system, and it is a fundamental organic reaction. In this work, as the first attempt, reactions paths were traced by DFT calculations under Prins' original conditions (styrene and formaldehyde in the acidic aqueous media). As an alkene, propene was also employed for comparison. From styrene, 4-phenyl-1,3-dioxane was obtained in 86% yield, and from propene 4-methyl-1,3-dioxane in 65% yield (based on $H_2C{=}O$) [4]. The target of this work is to check whether the seemingly established mechanism shown in Scheme 5 holds for the two alkenes and the expected steps in Scheme 5 are obtained by DFT calculations.

Method of calculations

The reacting systems were investigated by density functional theory calculations. The B3LYP method [26,27] was used for geometry optimizations. In order to check the reliability of B3LYP, M06-2X [28] and a dispersion correction method (ωB97XD [29]) were applied to the rate-determining step of the propene reaction TS1(Me). The basis sets employed were 6-31G(d) and 6-311+G(d,p). Transition states (TSs) were sought first by partial optimizations at bond interchange regions. Second, by the use of Hessian matrices TS geometries were optimized. They were characterized by vibrational analysis, which checked whether the obtained geometries have single imaginary frequencies ($\nu^{\ddagger}$s). From the TSs, reaction paths were traced by the intrinsic reaction coordinate (IRC) method [30,31] to obtain the energy-minimum geometries. Relative energies ΔE were obtained by single-point calculations of

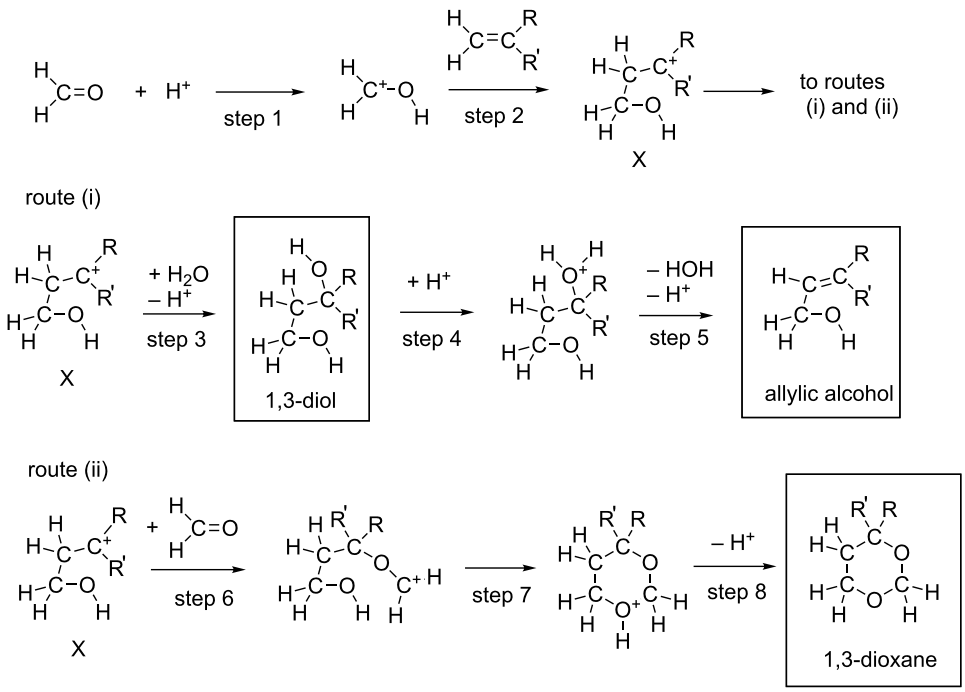

Scheme 5: A reaction mechanism involving the carbonium-ion intermediate X.

RB3LYP/6-311+G(d,p) [self-consistent reaction field (SCRF) = PCM [32-34], solvent = water] on the RB3LYP/6-31G(d) and 6-311+G(d,p) geometries and their ZPE ones. Here, ZPE denotes the zero-point vibrational energy.

In order to confirm the obtained TS characters, dynamical calculations of a classical trajectory calculation using the atom-centered density matrix propagation molecular dynamics (ADMP) model [35-37] on TSs were carried out. Geometries of the TSs at 2000 steps of 0.1 femtoseconds (10^{-15} seconds) were determined.

All the calculations were carried out by using the GAUSSIAN 09 [38] program package. The computations were performed at the Research Center for Computational Science, Okazaki, Japan.

As for the model, alkene, two H_2C=O and H_3O^+ molecules are needed to simulate the paths depicted in Scheme 5. In addition to them, 13 H_2O molecules are included as shown in Scheme 6. In the model, H_2C=O catalyzed by H_3O^+ (a) works as an electrophile to add to the alkene. The addition follows Markownikoff's rule [39]. H_2O (f) is the nucleophile to the left-hand carbon of the alkene. One proton of H_2O (f) moves to H_2O (h) upon the addition, and this becomes a hydronium ion. Around the newly formed ion, six H_2O molecules (i, j, k, l, m, and n) are located. At the same time, toward the carbonyl oxygen of the central H_2C=O, a proton is moved from H_3O^+ (a). To this ion, H_2O (c) and H_2O (d) are attached. H_2O (b) and H_2O (e) are coordinated to the second sp^2 lone-pair orbitals of two H_2C=O molecules.

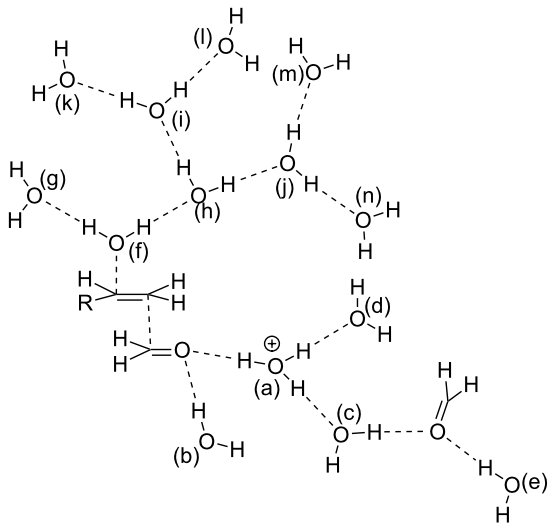

Scheme 6: A reaction model composed of RHC=CH_2, $(H_2C=O)_2$ and $H_3O^+(H_2O)_{13}$ to obtain the path of step 2 (Scheme 5). H_3O^+ and H_2O are labeled with (a), (b), (c) … (n) to explain their positions.

Results and Discussion

The propene reaction

Figure 1 shows precursor and TS geometries in a Prins reaction of propene. In precursor (Me), while two H_2C=O molecules are linked with water ones via hydrogen bonds, hydrophobic propene is outside them. When it is put into the water cluster, the first transition state [TS1(Me)] is brought about. Worthy of note is that various concomitant bond interchanges are involved in TS1(Me). The reaction center is at the C(1)···C(5) bond, and simultaneously the incipient C(6)···O(14) bond is formed. After TS1(Me), not the carbonium ion but rather the butane-1,3-diol, diol(Me), is afforded. This result demonstrates that steps 1, 2 and 3 in Scheme 5 occur at the same time without intervention of the carbocation X. From diol(Me), two TSs were obtained. One is TS2(Me) leading to the allylic alcohol, 2-buten-1-ol, here called ene-ol(Me). The other is TS3(Me) leading to an intermediate, not included in Scheme 5. This species, 3-(hydroxymethoxy)-1-butanol, called here ether(Me), has an ether moiety and is a hemiacetal. Generally, these are formed by the formal addition of an alcohol to the carbonyl group. In this case, 1,3-diol(Me) is the alcohol, and the second formaldehyde is of the C=O group. Closure of the six-membered ring from the ether(Me) [TS4(Me)] gives the product 4-methyl-1,3-dioxane, dioxane(Me). Thus, the obtained route (ii), precursor (Me) → diol(Me) → ether(Me) → dioxane(Me), is different from that in Scheme 5. The first difference is the absence of the carbocation X in the former route. The second one is a new hemiacetal intermediate, ether(Me).

Geometries in Figure S1 (Supporting Information File 1) were obtained by IRC calculations starting from TS ones in Figure 1. In order to confirm the route depicted in Figure 1, ADMP dynamical calculations from TSs were also performed. Geometries after 200 femtosecond from TS1(Me), TS2(Me), TS3(Me) and TS4(Me) are shown as ADMP1(Me), ADMP2(Me), ADMP3(Me) and ADMP4(Me), respectively, in Figure S2 (Supporting Information File 1). These were found to be similar to diol(Me), ene-ol(Me), ether(Me) and dioxane(Me) in Figure S1, respectively. Thus, those TSs were confirmed to be in the reaction channel.

Figure 2 exhibits geometry-dependent energy changes for the transition states depicted in Figure 1 and Figure S1. TS1(Me) was found to be the rate-determining step. The butane-1,3-diol, diol(Me), is the first stable intermediate ($\Delta(E_T + ZPE)$ = −18.77 kcal/mol). From diol(Me), two TSs, TS2(Me) and TS3(Me), were obtained. TS3(Me) leading to the hemiacetal intermediate, ether(Me), is much more likely than TS2(Me) leading to the allylic alcohol, ene-ol(Me). In fact, the latter is not formed under the reaction conditions in Scheme 2. The hemiacetal intermediate, ether(Me), is remarkably stable

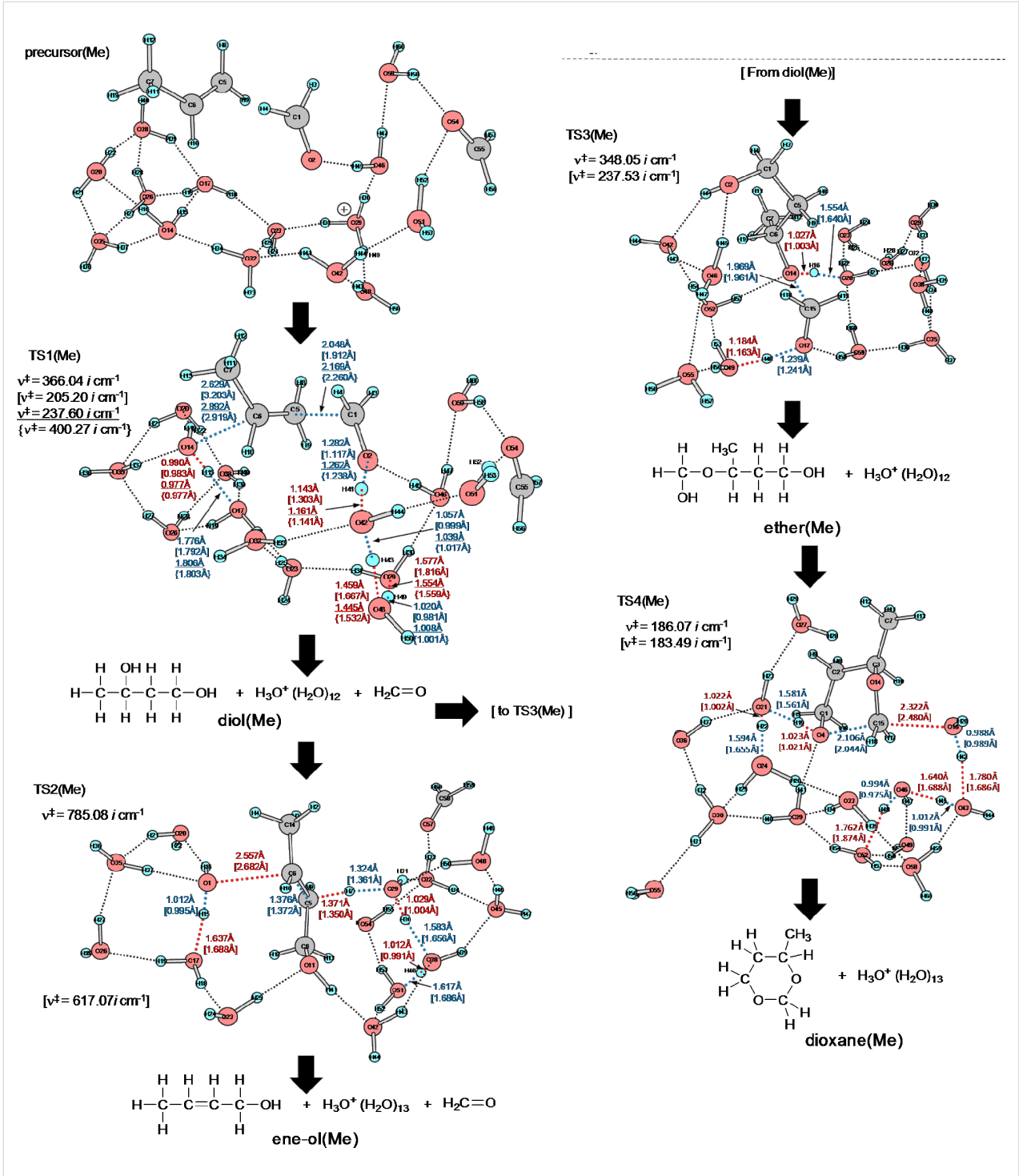

Figure 1: Geometries of the precursor and the transition states (TSs) of the Prins reaction of propene with $(formaldehyde)_2$ and $H_3O^+(H_2O)_{13}$ according to the model of Scheme 6. Sole imaginary frequencies, $\nu^{\ddagger}$s, verifying that the obtained geometries are at saddle points, are also shown. Those of intermediates and products are exhibited in Figure S1 of Supporting Information File 1. "(Me)" denotes the propene (R–HC=CH_2, R = Me) reaction. Distances and imaginary frequencies by B3LYP/6-31G(d) and B3LYP/6-311+G(d,p) (in square brackets) are shown. Underlined numbers are by M06-2X and those in braces by ωB97XD for TS1(Me).

($\Delta(E_T$ + ZPE) = −30.74 kcal/mol). The stability is almost the same as that of the product, dioxane(Me), ($\Delta(E_T$ + ZPE) = −31.37 kcal/mol). This energetic result suggests that both the ether(Me) and dioxane(Me) are products in the propene Prins reaction, whereas the ether(Me) species has not been reported so far.

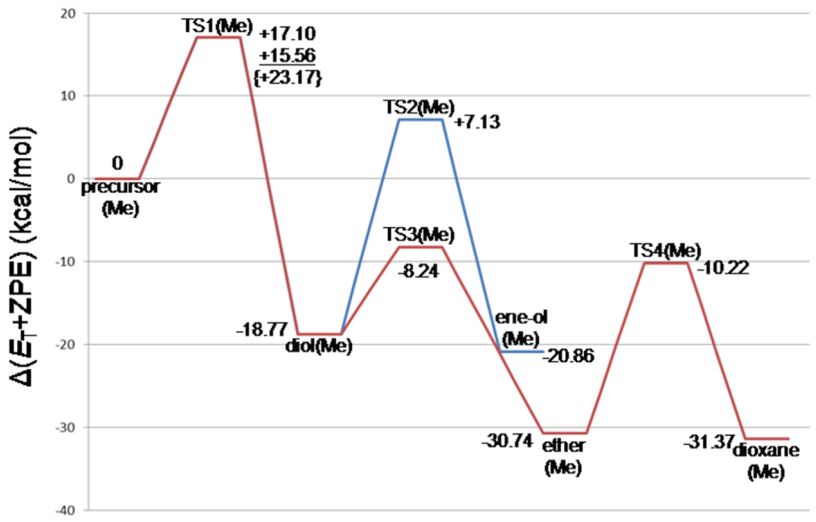

Figure 2: Energy changes (in kcal/mol) of the propene Prins reaction calculated by B3LYP/6-311+G(d,p) SCRF=(PCM, solvent = mwater)// B3LYP/6-31G(d) ZPE. The corresponding geometries are shown in Figure 1 and Figure S1. E_T stands for the total energy. At TS1(Me), while B3LYP/6-311+G(d,p) SCRF=PCM and M06-2X/6-311+G(d,p) SCRF=PCM energies are similar, the {ωB97XD/6-311+G(d,p) SCRF=PCM} energy seems to be overestimated in spite of the similarity of the three geometries in Figure 1.

The styrene reaction

Figure 3 shows geometries of four TSs, and Figure S3 shows those of precursor(Ph), diol(Ph), ene-ol(Ph), ether(Ph) and dioxane(Ph). Geometric changes similar to those of the propene Prins reaction were obtained, i.e., precursor(Ph) → TS1(Ph) → diol(Ph) [→ TS2(Ph) → ene-ol(Ph)] → TS3(Ph) → ether(Ph) → TS4(Ph) → dioxane(Ph). Different from the reaction pattern shown in Scheme 5, the cation center is at H_3O^+ in the intermediates and product. At TS1(Ph), the incipient C(6)···O(14) bond distance (= 3.138 Å) is extraordinarily larger than the standard one (ca. 1.85 Å) for the C···O-forming TS. For instance, it was calculated to be 1.833 {1.879} Å in the first TS of the acid-catalyzed hydrolysis of ethyl acetate by B3LYP/6-31G(d) {M062X/6-311G(d,p)} in our recent work [40]. Through the B3LYP/6-311+G(d,p) geometry optimization, TS1'(Ph) was obtained as the carbocation (X) formation TS shown in Figure S4. Here, the C(6)···O(14) formation is not involved and the concerted diol(Ph)-formation TS could not be obtained. The character of TS1(Ph) needs to be investigated in more detail and will be discussed in the next subsection.

Figure 4 shows the energy changes of the styrene Prins reaction. They are compared with those of the propene Prins reaction (Figure 2). The rate determining step is again TS1(Ph). A noticeable difference is found in the contrast of the stability order, ene-ol(Ph) > ether(Ph) versus ene-ol(Me) < ether(Me). The 3-phenyl-2-propenol (cinnamyl alcohol) is an allylic alcohol with the π conjugation of the phenyl ring and is thought to be the source of the stability of ene-ol(Ph). However, TS2(Ph) has a large activation energy, +18.04 kcal/mol. Thus, while ene-ol(Ph) is thermodynamically favorable, it is unfavorable kinetically. The energy of ether(Ph), −12.40 kcal/mol, is again similar to that of dioxane(Ph), −11.12 kcal/mol. Both ether(Ph) and dioxane(Ph) may be regarded as products of the styrene Prins reaction. In this respect, the equilibrium depicted in Scheme 3 is not for the (dioxane–diol) pair but for the (dioxane–ether) pair. The product 1,3-dioxane may be obtained with aid of the hygroscopy of the 45−55% sulfuric acid. The water is taken off by H_2SO_4, and according to Le Chatelier's principle the equilibrium is shifted toward the dioxane side. Formation of the 1,3-diol in Scheme 3 would arise not from the equilibration with the dioxane but from the high-temperature reflux conditions for the endothermic step, i.e., ether → 1,3-diol.

The carbocation intermediate (X)

In the Prins reaction of styrene, it is critical whether the first transition state leads to diol(Ph) or to the carbocation X(Ph). The intervention of X(Ph) was examined by an extended model shown in Figure S5. In the model, the initial geometry for the optimization was made of that of X(Ph) in Figure S4 and seven additional water molecules (atom numbers, from 68 to 88). Through the optimization by B3LYP/6-31G(d) and B3LYP/6-311+G(d,p), the initial carbocation was found to be converted to the 1,3-diol as shown in the lower side of Figure S5. Thus, the carbocation would intervene when the size of the water cluster surrounding the reactants (alkene and formaldehyde) is small. While this condition corresponds to the reaction in a binary solvent such as acetone–water, the reaction in aqueous media would not involve the carbocation X.

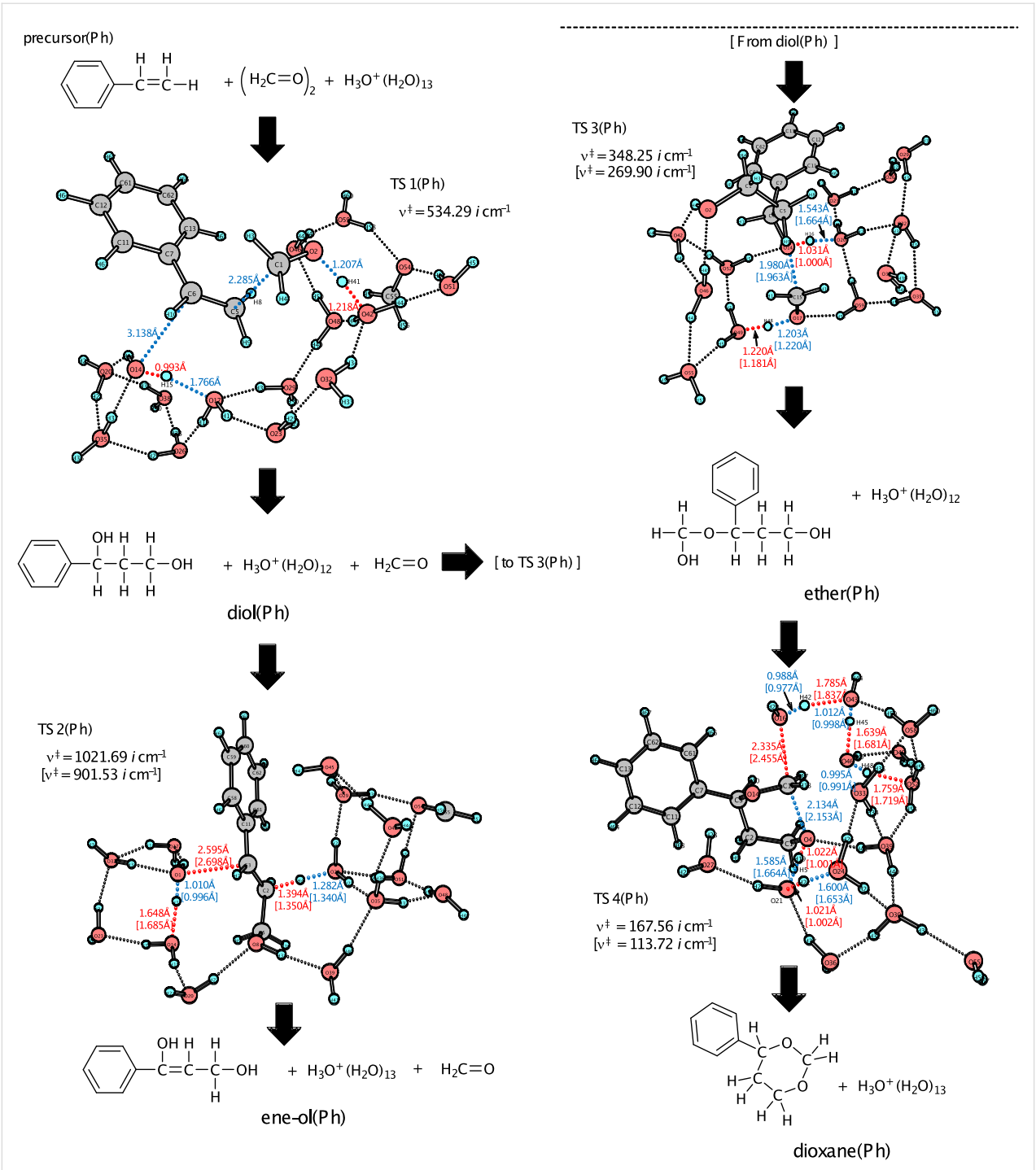

Figure 3: Geometries of the transition states (TSs) of the Prins reaction of styrene + (formaldehyde)$_2$ + $H_3O^+(H_2O)_{13}$. Those of intermediates and products are exhibited in Figure S3 of Supporting Information File 1. "(Ph)" denotes the styrene (R–HC=CH_2, R = phenyl) reaction. The geometry of TS1(Ph) by B3LYP/6-311+G(d,p) is shown in Figure S4 as TS1'(Ph).

Dependence of the number of water molecules on the geometries of TS1(Ph) was investigated by the use of two extended models, styrene + $H_3O^+(H_2O)_n$ + $(H_2C=O)_2$ (n = 20 and 30). The n = 13 TS1(Ph) is shown in Figure 3. The n = 20 and 30 TS1(Ph) geometries are shown in Figure 5.

While the central part of the n = 20 geometry is similar to that of the n = 13 one, the incipient O(14)···C(6) bond in the n = 30 TS1(Ph) is shorter (2.692 Å) than those of the n = 13 and n = 20 TSs. This result indicates that the extended model of the n = 30 TS1(Ph) expresses clearly the 1,3-diol formation.

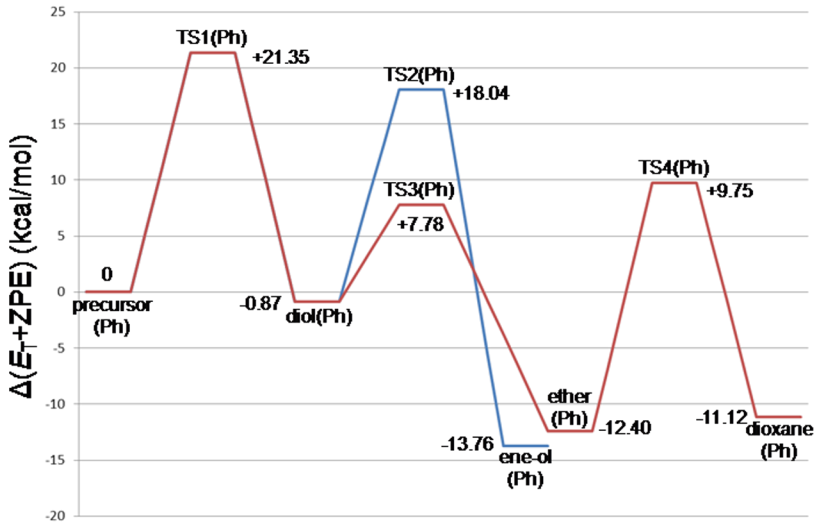

Figure 4: Energy changes (in kcal/mol) of the styrene Prins reaction calculated by B3LYP/6-311+G(d,p) SCRF = (PCM, solvent = water)// B3LYP/6-31G(d) ZPE. The corresponding geometries are shown in Figure 3 and Figure S3.

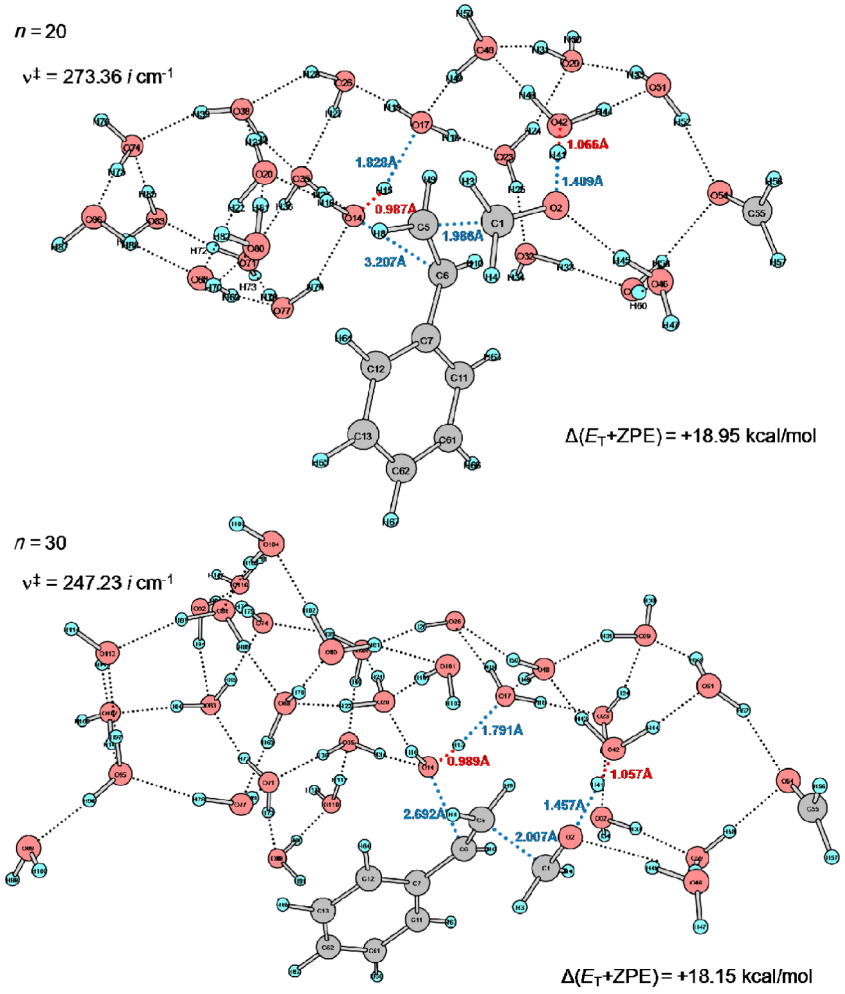

Figure 5: TS1(Ph) geometries of n = 20 and n = 30 in the reacting system of styrene + $H_3O^+(H_2O)_n$ + $(H_2C{=}O)_2$ calculated by B3LYP/6-31G(d).

Conclusion

In this work, two Prins reactions were investigated by the use of B3LYP calculations. A model composed of R–CH=CH_2 + $H_3O^+(H_2O)_{13}$ + $(H_2C=O)_2$, R = Me and Ph, was employed to trace reaction paths. The result is summarized in Scheme 7.

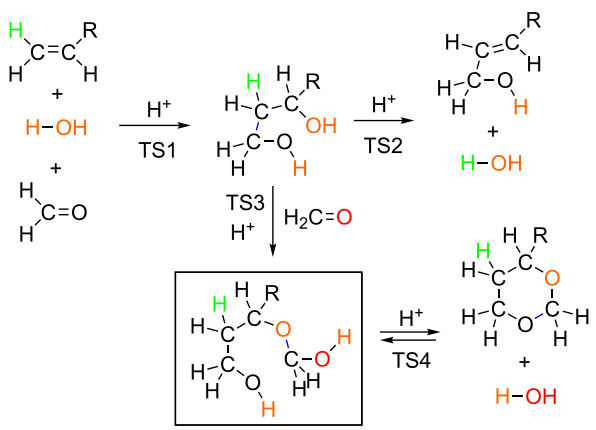

Scheme 7: Summary of the present calculated results. The ether in the box is the new intermediate found in this work. The blue line stands for the newly formed covalent bond at each step.

The 1,3-diol is formed concertedly in the rate-determining step, TS1. From the diol, the ene-ol is afforded in the E2 (bimolecular elimination, TS2) pathway. Most likely, the addition (TS3) of the second formaldehyde to the 1,3-diol leads to the new intermediate (ether or hemiacetal). Ring closure from the ether gives the product, 1,3-dioxane. The 1,3-dioxane is in equilibrium with the ether.

It is critical whether TS1 goes to the 1,3-diol or to the carbocation X. While the intervention is suggested to depend on the concentration of water, in aqueous media the cation is unlikely owing to the high nucleophilicity of the large water cluster.

Supporting Information

Supporting Information File 1

Geometries of the precursor, intermediates and products, and other related geometries.
[http://www.beilstein-journals.org/bjoc/content/supplementary/1860-5397-9-51-S1.pdf]

References

1. Kriewitz, O. *Ber. Dtsch. Chem. Ges.* **1899,** *32,* 57. doi:10.1002/cber.18990320111
2. Prins, H. J. *Chem. Weekbl.* **1919,** *16,* 1072.
3. Prins, H. J. *Chem. Weekbl.* **1919,** *16,* 1510.
4. Arundale, E.; Mikeska, L. A. *Chem. Rev.* **1952,** *51,* 505. doi:10.1021/cr60160a004
5. Nayak, U. R.; Santhanakrishnan, T. S.; Dev, S. *Tetrahedron* **1963,** *19,* 2281. doi:10.1016/0040-4020(63)85044-9
6. Adams, D. R.; Bhatnagar, S. P. *Synthesis* **1977,** 661. doi:10.1055/s-1977-24523
7. Baker, J. W. *J. Chem. Soc.* **1944,** 296. doi:10.1039/JR9440000296
8. John, W. B. *Nature* **1948,** *161,* 171. doi:10.1038/161171a0
9. Portoghese, P. S.; Smissman, E. E. *J. Org. Chem.* **1962,** *27,* 719. doi:10.1021/jo01050a003
10. Bernardi, L.; Leone, A. *Tetrahedron Lett.* **1964,** *5,* 499. doi:10.1016/S0040-4039(00)73262-X
11. Smissman, E. E.; Schnettler, R. A.; Portoghese, P. S. *J. Org. Chem.* **1965,** *30,* 797. doi:10.1021/jo01014a034
12. Dolby, L. J.; Wilkins, C.; Frey, T. G. *J. Org. Chem.* **1966,** *31,* 1110. doi:10.1021/jo01342a029
13. Smissman, E. E.; Witiak, D. *J. Org. Chem.* **1960,** *25,* 471. doi:10.1021/jo01073a617
14. LeBel, N. A.; Liesemer, R. N.; Mehmedbasich, E. *J. Org. Chem.* **1963,** *28,* 615. doi:10.1021/jo01038a003
15. Schowen, K. B.; Smissman, E. E.; Schowen, R. L. *J. Org. Chem.* **1968,** *33,* 1873. doi:10.1021/jo01269a037
16. Blomquist, A. T.; Wolinsky, J. *J. Am. Chem. Soc.* **1957,** *79,* 6025. doi:10.1021/ja01579a048
17. Dolby, L. J.; Lieske, C. N.; Rosencrantz, D. R.; Schwarz, M. J. *J. Am. Chem. Soc.* **1963,** *85,* 47. doi:10.1021/ja00884a009
18. Dolby, L. J.; Wilkins, C. L.; Rodia, R. M. *J. Org. Chem.* **1968,** *33,* 4155. doi:10.1021/jo01275a031
19. Snider, B. B. The Prins and Carbonyl Ene Reactions. In *Comprehensive Organic Synthesis;* Trost, B. M.; Fleming, I.; Heathcock, C. H., Eds.; Pergamon Press: Oxford, U.K., 1991; Vol. 2, pp 527 ff. doi:10.1016/B978-0-08-052349-1.00040-8
20. Olier, C.; Kaafarani, M.; Gastaldi, S.; Bertrand, M. P. *Tetrahedron* **2010,** *66,* 413. doi:10.1016/j.tet.2009.10.069
21. Miles, R. B.; Davis, C. E.; Coates, R. M. *J. Org. Chem.* **2006,** *71,* 1493. doi:10.1021/jo052142n
22. Miranda, P. O.; Carballo, R. M.; Martin, V. S.; Padron, J. I. *Org. Lett.* **2009,** *11,* 357. doi:10.1021/ol802593u
23. Chavre, S. N.; Choo, H.; Lee, J. K.; Pae, A. N.; Kim, Y.; Cho, Y. S. *J. Org. Chem.* **2008,** *73,* 7467. doi:10.1021/jo800967p
24. Jacolot, M.; Jean, M.; Levoin, N.; van de Weghe, P. *Org. Lett.* **2012,** *14,* 58. doi:10.1021/ol202829u
25. Overman, L. E.; Velthuisen, E. J. *J. Org. Chem.* **2006,** *71,* 1581. doi:10.1021/jo0522862
26. Becke, A. D. *J. Chem. Phys.* **1993,** *98,* 5648. doi:10.1063/1.464913
27. Lee, C.; Yang, W.; Parr, R. G. *Phys. Rev. B* **1988,** *37,* 785. doi:10.1103/PhysRevB.37.785
28. Zhao, Y.; Truhlar, D. G. *Theor. Chem. Acc.* **2008,** *120,* 215. doi:10.1007/s00214-007-0310-x
29. Chai, J.-D.; Head-Gordon, M. *Phys. Chem. Chem. Phys.* **2008,** *10,* 6615. doi:10.1039/b810189b
30. Fukui, K. *J. Phys. Chem.* **1970,** *74,* 4161. doi:10.1021/j100717a029
31. Gonzalez, C.; Schlegel, H. B. *J. Chem. Phys.* **1989,** *90,* 2154. doi:10.1063/1.456010
32. Cancés, E.; Mennucci, B.; Tomasi, J. *J. Chem. Phys.* **1997,** *107,* 3032. doi:10.1063/1.474659
33. Cossi, M.; Barone, V.; Mennucci, B.; Tomasi, J. J. *Chem. Phys. Lett.* **1998,** *286,* 253. doi:10.1016/S0009-2614(98)00106-7
34. Mennucci, B.; Tomasi, J. *J. Chem. Phys.* **1997,** *106,* 5151. doi:10.1063/1.473558

35. Iyengar, S. S.; Schlegel, H. B.; Millam, J. M.; Voth, G. A.; Scuseria, G. E.; Frisch, M. J. *J. Chem. Phys.* **2001,** *115,* 10291. doi:10.1063/1.1416876
36. Schlegel, H. B.; Millam, J. M.; Iyengar, S. S.; Voth, G. A.; Daniels, A. D.; Scuseria, G. E.; Frisch, M. J. *J. Chem. Phys.* **2001,** *114,* 9758. doi:10.1063/1.1372182
37. Schlegel, H. B.; Iyengar, S. S.; Li, X.; Millam, J. M.; Voth, G. A.; Scuseria, G. E.; Frisch, M. J. *J. Chem. Phys.* **2002,** *117,* 8694. doi:10.1063/1.1514582
38. *Gaussian 09,* Revision B.01; Gaussian, Inc.: Wallingford, CT, 2009.
39. Markownikoff, W. *Justus Liebigs Ann. Chem.* **1870,** *153,* 228. doi:10.1002/jlac.18701530204
40. Yamabe, S.; Fukuda, T.; Ishii, M. *Theor. Chem. Acc.* **2011,** *130,* 429. doi:10.1007/s00214-011-1019-4

License and Terms

Beilstein Journal of Organic Chemistry

A computational study of base-catalyzed reactions of cyclic 1,2-diones: cyclobutane-1,2-dione

Nargis Sultana[1,2] and Walter M. F. Fabian[*2]

Full Research Paper

Open Access

Address:
[1]Department of Chemistry, University of Sargodha, Sargodha, Pakistan and [2]Institut für Chemie, Karl Franzens Universität Graz, Heinrichstr. 28, A-8010 Graz, Austria

Email:
Walter M. F. Fabian[*] - walter.fabian@uni-graz.at

* Corresponding author

Keywords:
ab initio; density functional; reactive intermediate; rearrangement; ring opening

Beilstein J. Org. Chem. **2013,** *9,* 594–601.
doi:10.3762/bjoc.9.64

Received: 21 December 2012
Accepted: 25 February 2013
Published: 21 March 2013

This article is part of the Thematic Series "New reactive intermediates in organic chemistry".

Guest Editor: G. Bucher

Abstract

The reaction of cyclobutane-1,2-dione with hydroxide was studied by a variety of ab initio (MP2, SCS-MP2, CCSD(T), CEPA/1) and density functional (M06-2X) methods. Three possible reaction paths of the initially formed tetrahedral adduct leading to either 1-hydroxycyclopropane-1-carboxylate (benzilic acid type rearrangement, path A), α-oxobutanoate (path B) or γ-oxobutanoate (path C) were considered. Although the latter two products show similar or even more negative Gibbs free energies of reaction than calculated for the benzilic acid type rearrangement, the Gibbs free energies of activation are substantially higher. According to the calculations, the only feasible reaction appears to be the formation of 1-hydroxycyclopropane-1-carboxylate, which is corroborated by previous experimental observations.

Introduction

Addition of nucleophiles, e.g., OH^-, to 1,2-dicarbonyl compounds leads to the formation of relatively stable tetrahedral adducts (Scheme 1) [1]. These adducts further react either by (i) fission of the R^2–C bond and migration of R^2 (benzil–benzilic acid rearrangement, path A); (ii) fission of the R^2–C bond without migration of R^2 resulting in α-oxocarboxylic acids (path B); or (iii) fission of the carbonyl-C–sp^3-C with formation of an aldehyde and carboxylic acid (path C). In the case of benzils, depending on the substituents on the aryl rings, all three types of reactions have been observed [2].

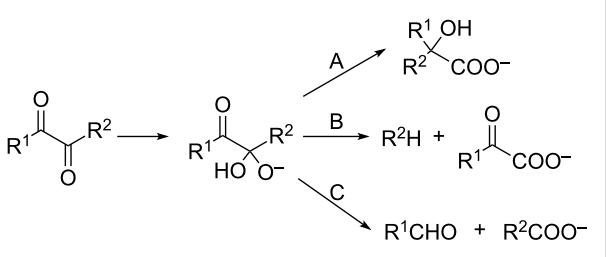

Scheme 1: Reactions of 1,2-dicarbonyl compounds with base.

The benzilic acid rearrangement of cyclic 1,2-diones [3,4] leads to ring contraction, e.g., the rearrangement of cyclobutane-1,2-dione (**1**) to 1-hydroxycyclopropanecarboxylate (**2**) [5-7]. In contrast, cyclobut-3-ene-1,2-diones **3** react to 2-oxobut-3-enoates **4** (at least formally according to path B) [8], whereas benzocyclobutene-1,2-diones **5** lead to 2-formylbenzoates **6** (path C, Scheme 2) [9].

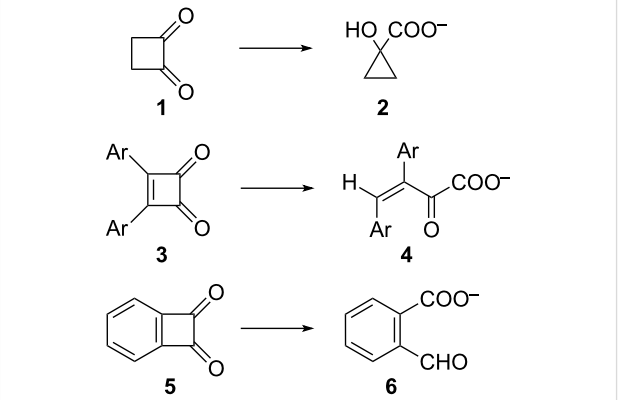

Scheme 2: Reactions of cyclic 1,2-diones with base.

In view of the importance of the benzil–benzilic acid rearrangement in organic chemistry, several computational studies concerning this rearrangement [10,11] or related reactions (Favorskii rearrangement [12-14], halolactonisation [15]) have been published. To the best of our knowledge no attempt has been made so far to consider the additional pathways B and C in these reactions. Here we present a detailed computational study (DFT and ab initio) of the base-catalyzed reactions of cyclobutane-1,2-dione (**1**) taking into account all three possible pathways.

Results and Discussion

The various transition states, intermediates and products initially considered for the three reaction paths A, B, and C are depicted in Scheme 3. It turned out that not all of the structures shown in Scheme 3 could actually be located as stationary points on the potential-energy surface. On the other hand, some other stable as well as highly reactive intermediates and/or transition states were obtained (see below). Generally, in nucleophilic addition reactions to carbonyl compounds in aqueous solution, water not only acts as a solvent but frequently actively participates in the reaction, such as in water-assisted hydrolysis [16-20] or also in the benzil–benzilic acid rearrangement [11]. Therefore, cyclobutane-1,2-dione (**1**) hydrated by two water molecules, and hydroxide ion hydrated by four, i.e., **1**·$(H_2O)_2$ and $[OH(H_2O)_4]^-$, were used as reactants. Hence for all transition states, intermediates and products shown in Scheme 3, hydration by six water molecules is implied.

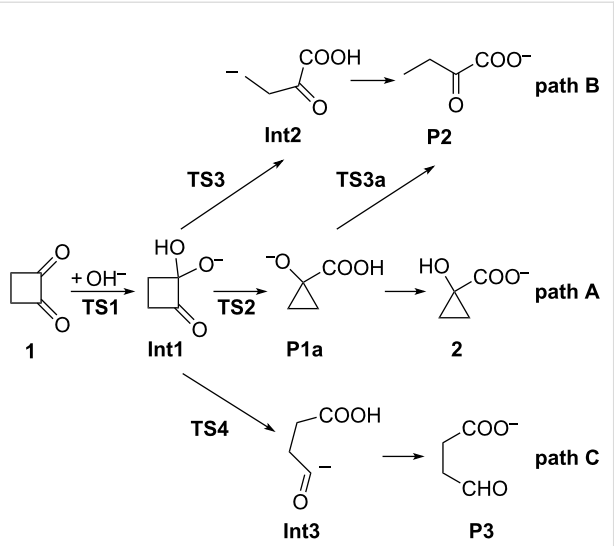

Scheme 3: Possible intermediates, transition structures, and products considered for the reaction of cyclobutane-1,2-dione with hydroxide anion.

Relative Gibbs free energies with respect to the separated reactants **1**·$(H_2O)_2$ + $[OH(H_2O)_4]^-$ including bulk aqueous solvation energies (SMD solvation model [21]) obtained by various computational procedures are collected in Table 1. More detailed results are provided in Supporting Information File 1. Before discussing the individual reaction paths in detail, a comparison of the computational procedures used (M06-2X [22], MP2 [23] and SCS-MP2 [24], the composite energy scheme $E_C = E$(MP2/6-311+G(2df,2p) + E{[CCSD(T) – MP2]/6-31+G(d)}; and LPNO-CEPA/1 [25-27]) is made.

Comparison of computational procedures

Taking the CEPA/1 results as a reference, inspection of Table 1 reveals that all other computational procedures invariably lead to a greater stabilization of all stationary points considered with respect to the separated reactants. The largest deviation from the CEPA/1 energies is obtained with M06-2X, the smallest with SCS-MP2. The corresponding mean absolute deviations and RMS errors are 5.9, 6.3 (M06-2X); 3.6, 3.9 (MP2); 2.5, 2.9 (SCS-MP2); and 3.9, 4.0 (E_C). However, the predicted trends agree very well with that obtained with CEPA/1 [Supporting Information File 1; the corresponding correlation coefficients R^2 are 0.992 (M06-2X); 0.997 (MP2 and SCS-MP2); and 0.999 (E_C)]. Inclusion of an empirical dispersion correction (DFTD3 [28]) in the M06-2X results further lowers the relative energies by ca. 0.8 kcal mol^{-1}.

Figure 1 summarizes the energetic as well as structural aspects of all three possible reaction paths in the reaction of cyclobutane-1,2-dione with hydroxide anions.

Table 1: Relative Gibbs free energies for all stationary points considered[a].

	M06-2X	MP2	SCS-MP2	E_C	CEPA/1
IDC	2.5	4.2	6.7	3.7	7.3
TS1	6.3	6.5	10.0	6.2	11.1
Int1	–6.1	–4.4	–4.1	–5.8	–2.2
TS2	7.7	6.9	9.2	9.4	14.3
P1a	–15.2	–10.3	–11.1	–9.0	–6.2
2	–32.6	–28.6	–29.9	–28.2	–24.4
TS3a	12.8	15.7	17.9	16.6	19.9
P2	–39.8	–37.5	–39.9	–39.4	–36.7
TS4	16.4	17.6	20.2	17.6	22.2
Int4	14.7	17.8	20.7	18.1	22.7
TS5	34.3	38.7	41.0	36.7	42.2
P3a	–29.3	–23.7	–23.1	–23.7	–21.2
Int2a	–25.5	–19.9	–20.9	–22.1	–18.4
P2a	–40.4	–37.3	–38.9	–38.6	–35.3

[a]ΔG (1 mol L^{-1} standard state, kcal mol^{-1}) with respect to separated reactants **1**·$(H_2O)_2$ + $[OH(H_2O)_4]^-$. All geometries optimized with M06-2X/6-31+G(d,p). For M06-2X, MP2, and SCS-MP2 single-point calculations the 6-311+G(2df,2p) basis set was used; LPNO-CEPA calculations were done with the def2-QZVPP basis set; $E_C = E$[MP2/6-311+G(2df,2p)] + E{[CCSD(T) – MP2]/6-31+G(d)}; ΔG_{solv} calculated by SMD M06-2X/6-31G(d).

Individual reaction paths

Addition of neutral nucleophiles to carbonyl compounds generally proceeds via formation of a prereaction complex; if Gibbs free energies instead of pure electronic energies or enthalpies are considered, such complexes usually become unstable [29]. In the present case without inclusion of bulk solvation effects (Supporting Information File 1) this prereaction complex (ion–dipole complex **IDC**) is quite stable with ΔG = –14 to –19 kcal mol^{-1} compared to the separated reactants. However, especially the large calculated [SMD-M06-2X/6-31G(d)] solvation energy of $[OH(H_2O)_4]^-$ compared with that of the ion–dipole complex (ΔG_{solv} = –66 versus –54 kcal mol^{-1}) results in an endergonic formation of this complex (ΔG = 2.5–7.3 kcal mol^{-1}, Table 1). After passing transition state **TS1** (ν = 144 i cm^{-1}), formation of the tetrahedral adduct by attack of $[OH(H_2O)_4]^-$ at C1 leads to the first truly stable intermediate **Int1**. This intermediate is common to all further possible pathways. The nucleophile involved in the formation of **Int1** actually is a water molecule, since formation of the C1–O3 bond is accompanied by proton transfer H3 to O4 of the original hydroxide anion (Figure 2). An analogous concerted addition–proton transfer has also been calculated previously for the benzilic acid type rearrangements of biacetyl and benzil [11]. Car–Parrinello molecular dynamics simulations of the hydrolysis of formamide in basic solution indicated that the traditional view of attack by hydroxide anion rather than a first-solvation-shell water molecule is more likely; however, the more powerful electrophile methyl formate should react according to the general-base mechanism [30]. The second carbonyl group in 1,2-diones efficiently enhances the carbonyl reactivity to make attack by water the preferred mode of reaction.

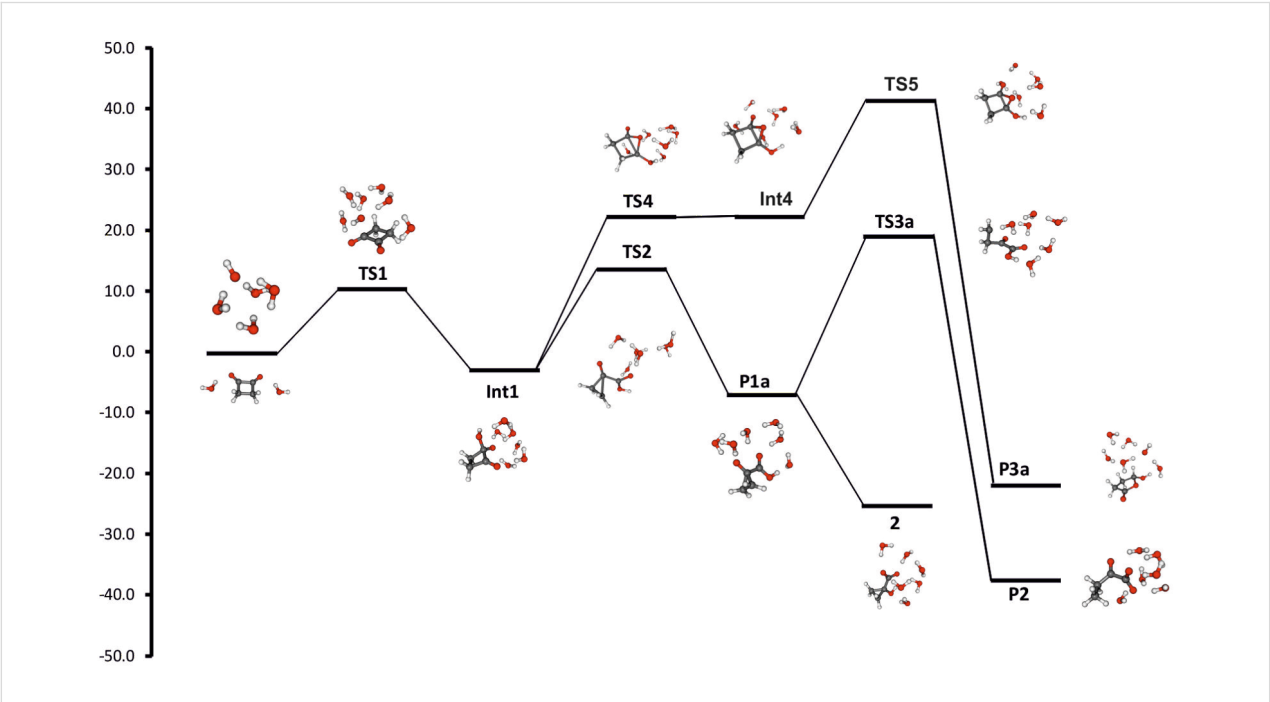

Figure 1: CEPA-1/def2-QZVPP calculated reaction paths for the reaction of **1**·$(H_2O)_2$ + $[OH(H_2O)_4]^-$.

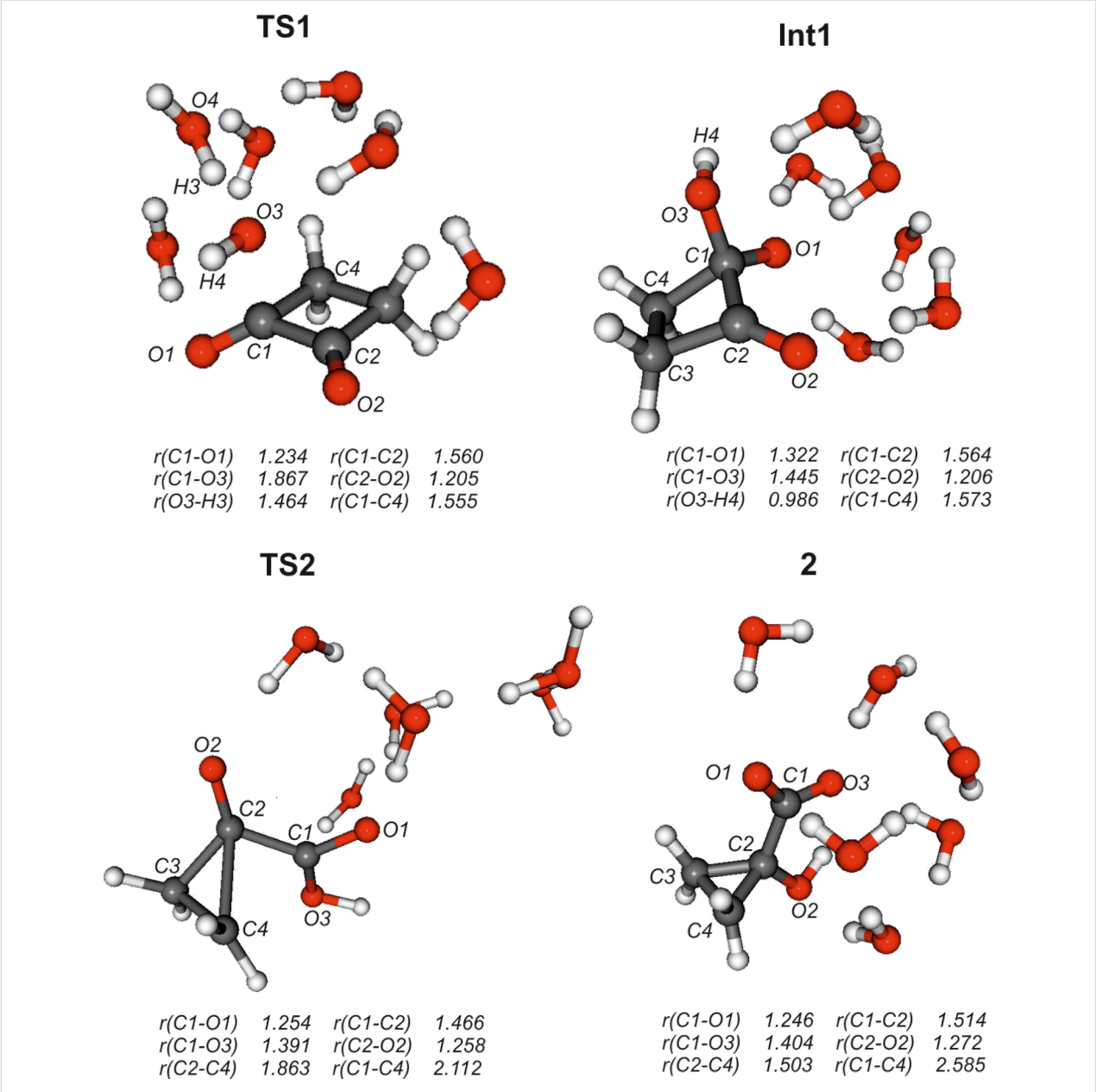

Figure 2: M06-2X/6-31+G(d,p) calculated structures of stationary points along the benzilic acid type rearrangement. Distances are given in angstroms (Å).

Benzil–benzilic acid rearrangement (Path A)

With respect to intermediate **Int1**, the Gibbs free energy of activation of the benzilic acid rearrangement (fission of the C1–C4 and concerted formation of the C2–C4 bond) via **TS2** ($\nu = 246i$ cm^{-1}) is ca. 15 kcal mol^{-1}. The initial product **P1a** (1-carboxycyclopropanolate) is expected to easily convert to the final product 1-hydroxycyclopropanecarboxylate (**2**) by a simple acid–base equilibrium (protonation of the alcoholate, deprotonation of the carboxylic acid, $\Delta pK_a \sim 10$). Overall, path A is not only strongly exergonic [$\Delta G_{react} = -24.4$ (CEPA/1) to –33 kcal mol^{-1}(M06-2X)] but has also a quite low barrier [$\Delta G^{\neq} = 6.9$ (MP2) to 14.3 kcal mol^{-1}(CEPA/1)], Table 1. Thus, this reaction should be quite feasible. Pertinent geometrical data are collected in Table S3 of Supporting Information File 1; M06-2X/6-31+G(d,p) optimized structures of relevant stationary points along path A are depicted in Figure 2.

The breaking C1–C4 bond is stretched from 1.573 Å in **Int1** to 2.112 Å in **TS2** (2.585 Å in **2**), while the newly formed bond C2–C4 is shortened from 2.125 Å in **Int1** to 1.863 Å in **TS2** (1.503 Å in **2**). The Wiberg bond indices resulting from an NBO analysis [31] for the C1–C4 bond are 0.92 (**Int1**) and 0.35

(**TS2**); those for the C2–C4 bond are 0.04 (**Int1**) and 0.40 (**TS2**), indicating nearly equal bond breaking and formation. The feasibility of the carbanion [1,2]-shift in the benzilic acid rearrangement has been attributed to the special shape [11] of the LUMO of 1,2-dicarbonyl compounds.

Path B

Product **P2** should be even more stable than **2**. However, despite several attempts neither **TS3** nor **Int2** could be obtained. Instead, invariably **TS2** or **P1a** were obtained. It is tempting to assume that the relatively close contact between C2 and C4 preferentially results in C2–C4 bond formation rather than addition of a proton to **Int2**. To address this problem, optimization of an extended conformation **Int2'** was attempted. However, such a structure collapsed upon geometry optimization in a concerted proton transfer–nucleophilic addition reaction to intermediate **Int2a**. By a simple acid–base equilibrium (alcoholate–carboxylic acid → alcohol–carboxylate), this intermediate is expected to convert immediately to product **P2a**, i.e., the hydrate of product **P2** (Scheme 4).

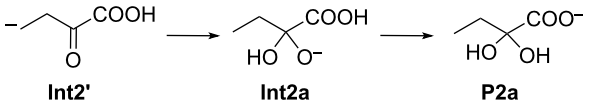

Scheme 4: Reaction sequence calculated for an extended conformation of **Int2**.

While all attempts to locate transition state **TS3** as well as those ones leading to either **Int2'** or **Int2a** were unsuccessful, a path [**TS3a** (ν = 410*i* cm^{-1}, Scheme 3 and Figure 3] directly connecting **P1a** instead of **Int1** with **P2**, could be obtained. Hence, path B actually does not start off from **Int1** but diverges at the initially formed product **P1a** of path A.

Compared with **TS2**, transition state **TS3a** (Figure 3) is characterized by significantly longer C1–C4 and C2–C4 bonds, 2.975 and 2.259 Å in **TS3a** versus 2.112 and 1.863 Å in **TS2**. Similarly, the C2–C3–C4 angle and the C1–C2–C3–C4 dihedral angle are much larger in **TS3a** (96.7° and 76.0°) than those found in **TS2** (76.6° and 54.8°), Table S3 in Supporting Information File 1. The main "movement" in **TS3a** is transfer of a proton from O4 to C4; consequently the imaginary frequency of **TS3a** is larger (ν = 410*i* cm^{-1}) than that of **TS2** (ν = 246*i* cm^{-1}) with C–C bond formation as the associated mode.

Path C

Similar to path B, all attempts to locate the initially proposed intermediate **Int3** were unsuccessful. Instead a more complicated pathway involving a high-energy bicyclic intermediate **Int4** was found (Figure 4).

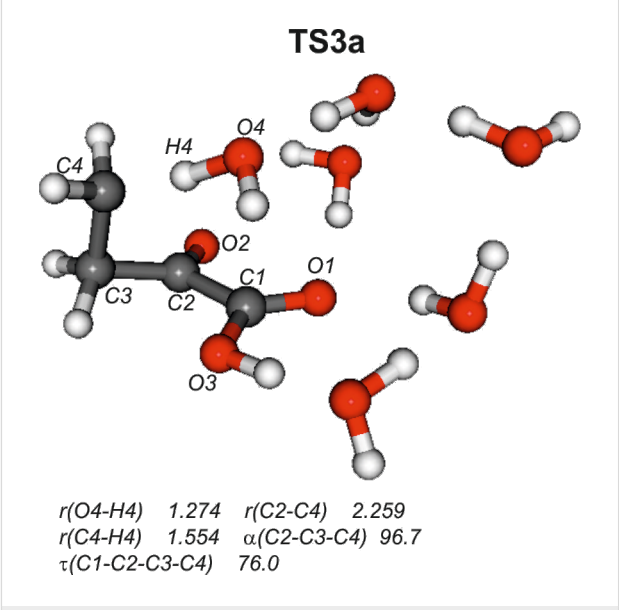

Figure 3: Calculated structure of transition state **TS3a**. Distances are given in angstrom (Å), angles in degrees.

Furthermore, this intermediate did not react to product **P3** but instead through a concerted ring opening and proton transfer to **P3a**. The anticipated product **P3** of path C is a γ-oxocarboxylate. Such γ-oxocarboxylic acids or carboxylates are prone to ring–chain tautomerism [32,33]. Product **P3a** essentially is the ion-dipole complex between the ring tautomer of neutral γ-oxobutanoic acid with $[OH(H_2O)_5]^-$, and hence, its formation is completely reasonable. The actual pathway C obtained by the calculations is indicated in Scheme 5.

In fact, **Int4** is barely stable if Gibbs free energies and bulk aqueous solvation are taken into account (Table 1 and Supporting Information File 1) and should collapse more or less barrierless to the tetrahedral adduct **Int1**. In contrast, rearrangement to **P3a** involves a substantially higher barrier (40–45 kcal mol^{-1} with respect to **Int1**) than path A (ca. 15 kcal mol^{-1} with respect to **Int1**). **TS4**, **Int4** and **TS5** can be considered as bicyclic structures consisting of a 3-membered oxirane and a 4-membered cyclobutane ring. The two rings are inclined to each other as indicated by the angle α measured between the midpoints of the C3–C4 and C1–C2 bonds and the oxygen atom O1 [α = 103° (**TS4**), 106° (**Int4**), and 112° (**TS5**)]. The product **P3a** of path C has a largely planar five-membered ring structure (α = 165°). In both **TS4** and **Int4** the C1–C2 distance (1.48 Å) is in the range of C–C single bonds, while in **TS5** this bond is significantly stretched (r = 1.853 Å; in **P3a** this distance is r = 2.317 Å). In contrast the O1–C2 bond

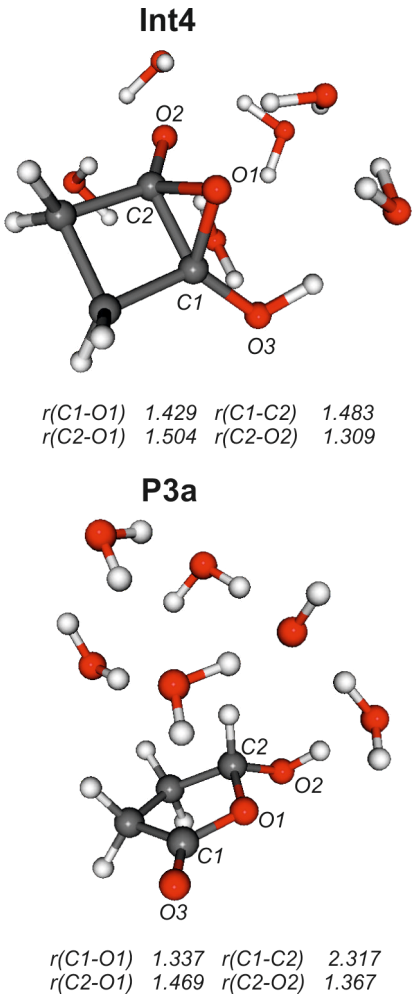

Figure 4: Calculated structures of pertinent stationary points along path C. Distances are given in angstroms (Å).

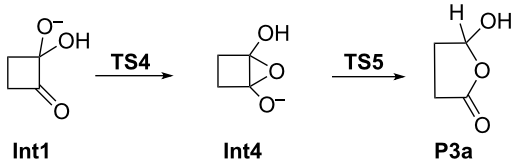

Scheme 5: Actual path C obtained by the calculations (as in Scheme 3, **Int1**, **TS4**, **Int4**, and **TS5** are hydrated by six water molecules; **P3a** is the ion-dipole complex with $[OH(H_2O)_5]^-$).

is shortened, i.e., 1.747 Å (**TS4**), 1.504 Å (**Int4**), and 1.385 Å (**TS5**), with a concomitant lengthening of the C1–O1 bond, i.e., 1.396 Å (**TS4**), 1.429 Å (**Int4**), and 1.531 Å (**TS5**). In the product **P3a** the proton of the O3–H group is transferred by involving the whole water chain to oxygen atom O2. This change in the position of the proton is accompanied by a shortening and lengthening, respectively, of the C1–O3 and C2–O2 distances: in **TS5** *r*(C1–O3) = 1.383 Å and *r*(C2–O2) = 1.233 Å, while in **P3a** *r*(C1–O3) = 1.210 Å and *r*(C2–O2) = 1.367 Å. Finally, it should be noted that intermediates of the type **Int4** have been proposed [9] to be involved in the base-catalyzed reactions of benzocyclobutenediones (reaction **5** → **6** in Scheme 2).

Conclusion

Ab initio (MP2, SCS-MP2, composite energy approach E_C, LPNO-CEPA/1) and density functional methods (M06-2X) were applied to study the reaction of cyclobutane-1,2-dione in basic solution. The reaction system was modeled by using cyclobutane-1,2-dione hydrated with two water molecules and $[OH(H_2O)_4]^-$ as the nucleophilic reagent. Three possible reaction pathways were considered, namely (i) a benzilic acid type rearrangement (path A); (b) ring-opening of the bond between an aliphatic carbon and that bearing the added OH^- group (path B); and (c) fission of the bond between the carbonyl carbon and that bearing the added OH^- group (path C). Attempts to locate path B starting directly from the tetrahedral intermediate **Int1** were unsuccessful. Instead, a reaction sequence diverging from the initially formed product **P1a** of path A was found. Path C involved transformations via high energy bicyclic transition states and/or intermediates. The final products of these latter two paths have comparable (path C) or even substantially more negative reaction energies (path B). However, the corresponding Gibbs free energies of activation are quite large. With respect to **Int1** these are at the CEPA/1 level 22.2 kcal mol^{-1} (path B; with respect to **P1a** $\Delta G^{\neq}$ = 44.3 kcal mol^{-1}) and 44.4 kcal mol^{-1} (path C). In contrast, path A is not only strongly exergonic but also has a significantly lower activation energy, ΔG_{react} = –22.2 kcal mol^{-1} and $\Delta G^{\neq}$ = 16.5 kcal mol^{-1} with respect to **Int1**.

Hence, in agreement with experimental observations [5-7], cyclobutane-1,2-dione is calculated to react via benzilic acid rearrangement to the ring-contracted product, i.e., 1-hydroxycyclopropanecarboxylate (**2**).

Computational details

Geometries were optimized by using the M06-2X density functional [22] and the 6-31+G(d,p) basis set [34,35] and characterized by frequency calculations as minima or transition states. For transition states, IRC calculations [36] were also done. These geometries were then used for M06-2X, MP2 [23] and SCS-MP2 [24] single-point calculations using the 6-311+G(2df,2p) basis set [37]. For coupled cluster CCSD(T) [38] and CEPA-1 [25-27] calculations the 6-31+G(d) and def2-QZVPP [39] basis sets, were used, respectively. Initial coordinates for $[OH(H_2O)_4]^-$ were taken from the WATER27 subset of the GMTKN30 database [40,41] and reoptimized with M06-2X/6-31+G(d,p). $[OH(H_2O)_4]^-$ was then placed about 6 Å

above $\mathbf{1}\cdot(H2O)_2$ and the combined system again optimized, resulting in the ion-dipole complex. An initial structure for **TS1** was obtained from a relaxed (i.e., optimization of all other coordinates) potential energy scan of the OH–carbonyl-carbon distance; this structure was then refined by transition-state optimization and further characterized by IRC calculations along both directions of the normal mode corresponding to the imaginary frequency. The final structures of both IRC calculations were then completely optimized. An analogous procedure, usually considering several possible reaction coordinates, was used for an initial guess of all other transition states. Bulk solvent effects (aqueous solution) were obtained by the SMD solvent model [21] at the M06-2X/6-31G(d) computational procedure. Frequencies obtained at the M06-2X/6-31+G(d,p) level are unscaled. Gibbs free energies are given relative to the separated reactants $\mathbf{1}\cdot(H_2O)_2$ and $[OH(H_2O)_4]^-$ and contain a 1.9 kcal mol^{-1} correction for the standard state conversion 1 atm to 1 mol L^{-1} at T = 298.15 K. Dispersion corrections to the M06-2X results were added by Grimme's DFTD3 procedure [28]. Programs used were ORCA [42], Gaussian 09 [43], GAMESS [44], and DFTD3 [45]; MOLDEN [46] and MOLEKEL [47] were used for structure building and visualization.

Supporting Information

Supporting Information File 1

Detailed computational results and plot of MP2, SCS-MP2 and M06-2X vs. CEPA ΔG_{rel} values, pertinent structural data, and Cartesian coordinates of all stationary structures.
[http://www.beilstein-journals.org/bjoc/content/supplementary/1860-5397-9-64-S1.pdf]

Acknowledgements

Nargis Sultana thanks the Higher Education Commission of Pakistan for the PhD scholarship.

References

1. Bowden, K.; Fabian, W. M. F. *J. Phys. Org. Chem.* **2001,** *14,* 794–796. doi:10.1002/poc.433
2. Bowden, K.; Williams, K. D. *J. Chem. Soc., Perkin Trans. 2* **1994,** 77–81. doi:10.1039/p29940000077
3. Selman, S.; Eastham, J. F. *Q. Rev., Chem. Soc.* **1960,** *14,* 221–235. doi:10.1039/QR9601400221
4. Collins, C. J.; Eastham, J. F. Rearrangements involving the carbonyl group. In *The Carbonyl Group: Volume 1;* Patai, S., Ed.; PATAI'S Chemistry of Functional Groups; John Wiley & Sons: New York, NY, 1966; pp 761–821. doi:10.1002/9780470771051
5. Bloomfield, J. J.; Ireland, J. R. S.; Marchand, A. P. *Tetrahedron Lett.* **1968,** *9,* 5647–5650. doi:10.1016/S0040-4039(00)70742-8
6. Scharf, H.-D.; Droste, W.; Liebig, R. *Angew. Chem., Int. Ed. Engl.* **1968,** *7,* 215–216. doi:10.1002/anie.196802151
7. de Groot, A.; Oudman, D.; Wynberg, H. *Tetrahedron Lett.* **1969,** *10,* 1529–1531. doi:10.1016/S0040-4039(01)87936-3
8. Al-Najjar, A.; Bowden, K.; Horri, M. V. *J. Chem. Soc., Perkin Trans. 2* **1997,** 993–996. doi:10.1039/a606412d
9. Bowden, K.; Horri, M. V. *J. Chem. Soc., Perkin Trans. 2* **1997,** 989–992. doi:10.1039/a606310a
10. Marques, C. S.; Ramalho, J. P. P.; Burke, A. J. *J. Phys. Org. Chem.* **2009,** *22,* 735–739. doi:10.1002/poc.1509
11. Yamabe, S.; Tsuchida, N.; Yamazaki, S. *J. Org. Chem.* **2006,** *71,* 1777–1783. doi:10.1021/jo051862r
12. Castillo, R.; Andrés, J.; Moliner, V. *J. Phys. Chem. B* **2001,** *105,* 2453–2460. doi:10.1021/jp003264g
13. Moliner, V.; Castillo, R.; Safont, V. S.; Oliva, M.; Bohn, S.; Tuñón, I.; Andrés, J. *J. Am. Chem. Soc.* **1997,** *119,* 1941–1947. doi:10.1021/ja962571q
14. Tsuchida, N.; Yamazaki, S.; Yamabe, S. *Org. Biomol. Chem.* **2008,** *6,* 3109–3117. doi:10.1039/b806577b
15. Buchanan, J. G.; Ruggiero, G. D.; Williams, I. H. *Org. Biomol. Chem.* **2008,** *6,* 66–72. doi:10.1039/b714118a
16. Cheshmedzhieva, D.; Ilieva, S.; Hadjieva, B.; Galabov, B. *J. Phys. Org. Chem.* **2009,** *22,* 619–631. doi:10.1002/poc.1492
17. Wolfe, S.; Shi, Z.; Yang, K.; Ro, S.; Weinberg, N.; Kim, C.-K. *Can. J. Chem.* **1998,** *76,* 114–124. doi:10.1139/v97-216
18. Barbosa, L. A. M. M.; van Santen, R. A. *J. Mol. Struct.: THEOCHEM* **2000,** *497,* 173–188. doi:10.1016/S0166-1280(99)00283-3
19. Haeffner, F.; Hu, C.-H.; Brinck, T.; Norin, T. *J. Mol. Struct.: THEOCHEM* **1999,** *459,* 85–93. doi:10.1016/S0166-1280(98)00251-6
20. Xiong, Y.; Zhan, C. *J. Phys. Chem. A* **2006,** *110,* 12644–12652. doi:10.1021/jp063140p
21. Marenich, A. V.; Cramer, C. J.; Truhlar, D. G. *J. Phys. Chem. B* **2009,** *113,* 6378–6396. doi:10.1021/jp810292n
22. Zhao, Y.; Truhlar, D. G. *Acc. Chem. Res.* **2008,** *41,* 157–167. doi:10.1021/ar700111a
23. Møller, C.; Plesset, M. S. *Phys. Rev.* **1934,** *46,* 618–622. doi:10.1103/PhysRev.46.618
24. Grimme, S. *J. Chem. Phys.* **2003,** *118,* 9095–9102. doi:10.1063/1.1569242
25. Liakos, D. G.; Neese, F. *J. Phys. Chem. A* **2012,** *116,* 4801–4816. doi:10.1021/jp302096v
26. Neese, F.; Wennmohs, F.; Hansen, A. *J. Chem. Phys.* **2009,** *130,* 114108. doi:10.1063/1.3086717
27. Neese, F.; Hansen, A.; Wennmohs, F.; Grimme, S. *Acc. Chem. Res.* **2009,** *42,* 641–648. doi:10.1021/ar800241t
28. Grimme, S.; Antony, J.; Ehrlich, S.; Krieg, H. *J. Chem. Phys.* **2010,** *132,* 154104. doi:10.1063/1.3382344
29. Di Valentin, C.; Freccero, M.; Zanaletti, R.; Sarzi-Amadé, M. *J. Am. Chem. Soc.* **2001,** *123,* 8366–8377. doi:10.1021/ja010433h
30. Blumberger, J.; Ensing, B.; Klein, M. L. *Angew. Chem.* **2006,** *118,* 2959–2963. doi:10.1002/ange.200600283
31. Reed, A. E.; Curtiss, L. A.; Weinhold, F. *Chem. Rev.* **1988,** *88,* 899–926. doi:10.1021/cr00088a005
32. Valters, R. E.; Flitsch, W. *Ring-Chain Tautomerism;* Plenum Press: New York, NY, 1985. doi:10.1007/978-1-4684-4883-2
33. Fabian, W. M. F.; Bowden, K. *Eur. J. Org. Chem.* **2001,** 303–309. doi:10.1002/1099-0690(200101)2001:2<303::AID-EJOC303>3.0.CO;2-I
34. Hariharan, P. C.; Pople, J. A. *Theor. Chim. Acta* **1973,** *28,* 213–222. doi:10.1007/BF00533485

35. Clark, T.; Chandrasekhar, J.; Spitznagel, G. W.; von Ragué Schleyer, P. *J. Comput. Chem.* **1983,** *4,* 294–301. doi:10.1002/jcc.540040303
36. Hratchian, H. P.; Schlegel, H. B. Finding minima, transition states, and following reaction pathways on ab initio potential energy surfaces. In *Theory and Applications of Computational Chemistry. The First Forty Years;* Dykstra, C. E.; Frenking, G.; Kim, K. S.; Scuseria, G. E., Eds.; Elsevier: Amsterdam, 2005; pp 195–249.
37. Lynch, B. J.; Zhao, Y.; Truhlar, D. G. *J. Phys. Chem. A* **2003,** *107,* 1384–1388. doi:10.1021/jp021590l
38. Bartlett, R. J. *Wiley Interdiscip. Rev.: Comput. Mol. Sci.* **2012,** *2,* 126–138. doi:10.1002/wcms.76
39. Weigend, F.; Ahlrichs, R. *Phys. Chem. Chem. Phys.* **2005,** *7,* 3297–3305. doi:10.1039/b508541a
40. *GMTKN30;* 2011, http://toc.uni-muenster.de/GMTKN/GMTKN30/GMTKN30main.html.
41. Bryantsev, V. S.; Diallo, M. S.; van Duin, A. C. T.; Goddard, W. A. *J. Chem. Theory Comput.* **2009,** *5,* 1016–1026. doi:10.1021/ct800549f
42. *ORCA;* 2010, http://www.mpibac.mpg.de/bac/logins/neese/description.php.
43. *Gaussian 09,* Revision A.02; Gaussian, Inc.: Wallingford, CT, 2009.
44. Schmidt, M. W.; Baldridge, K. K.; Boatz, J. A.; Elbert, S. T.; Gordon, M. S.; Jensen, J. H.; Koseki, S.; Matsunaga, N.; Nguyen, K. A.; Su, S.; Windus, T. L.; Dupuis, M.; Montgomery, J. A. *J. Comput. Chem.* **1993,** *14,* 1347–1363. doi:10.1002/jcc.540141112
45. *DFT-D3,* Version 3.0 Rev 0; 2012, http://www.thch.uni-bonn.de/tc/index.php?section=downloads&subsection=DFT-D3&lang=english.
46. Schaftenaar, G.; Noordik, J. H. *J. Comput.-Aided Mol. Des.* **2000,** *14,* 123–134. doi:10.1023/A:1008193805436
47. *MOLEKEL,* 5.4.0.8; Swiss National Supercomputing Centre: Lugano, Switzerland, http://molekel.cscs.ch/wiki/pmwiki.php.

License and Terms

Beilstein Journal of Organic Chemistry

Kinetics and mechanism of the anilinolysis of aryl phenyl isothiocyanophosphates in acetonitrile

Hasi Rani Barai and Hai Whang Lee*

Full Research Paper

Open Access

Address:
Department of Chemistry, Inha University, Incheon 402-751, Korea

Email:
Hai Whang Lee* - hwlee@inha.ac.kr

* Corresponding author

Keywords:
anilinolysis; cross-interaction constant; deuterium kinetic isotope effects; phosphoryl transfer reaction; reactive intermediates; Y-aryl phenyl isothiocyanophosphates

Beilstein J. Org. Chem. **2013,** *9,* 615–620.
doi:10.3762/bjoc.9.68

Received: 10 December 2012
Accepted: 06 March 2013
Published: 26 March 2013

This article is part of the Thematic Series "New reactive intermediates in organic chemistry".

Guest Editor: G. Bucher

Abstract

Kinetic studies on the reactions of Y-aryl phenyl isothiocyanophosphates with substituted X-anilines and deuterated X-anilines were carried out in acetonitrile at 55.0 °C. The free-energy relationships with X in the nucleophiles were biphasic concave upwards with a break region between X = H and 4-Cl, giving unusual positive ρ_X and negative β_X values with less basic anilines (X = 4-Cl and 3-Cl). A stepwise mechanism with rate-limiting bond breaking for more basic anilines and with rate-limiting bond formation for less basic anilines is proposed based on the positive and negative ρ_{XY} values, respectively. The deuterium kinetic isotope effects involving deuterated anilines ($XC_6H_4ND_2$) showed primary normal and secondary inverse DKIEs for more basic and less basic anilines, rationalized by frontside attack involving hydrogen-bonded four-center-type TSf and backside attack TSb, respectively. The positive ρ_X values with less basic anilines are substantiated by the tight TS, in which the extent of the bond formation is great and the degree of the bond breaking is considerably small.

Introduction

The nucleophilic substitution reactions of tetracoordinate phosphorus have been studied extensively, experimentally and theoretically, in our lab. Two main types of displacement processes are well known in neutral phosphoryl transfer reactions: a stepwise mechanism involving a trigonal bipyramidal pentacoordinate (TBP-5C) intermediate and a concerted displacement at phosphorus through a single pentacoordinate transition state (TS). To extend the kinetic studies on the phosphoryl transfer reactions, the reactions of Y-aryl phenyl isothiocyanophosphates (**1a**–**e**) with substituted anilines ($XC_6H_4NH_2$) and deuterated anilines ($XC_6H_4ND_2$) have been investigated kinetically in acetonitrile (MeCN) at 55.0 ± 0.1 °C (Scheme 1). The kinetic results of the present work are discussed based on the selectivity parameters and deuterium kinetic isotope effects

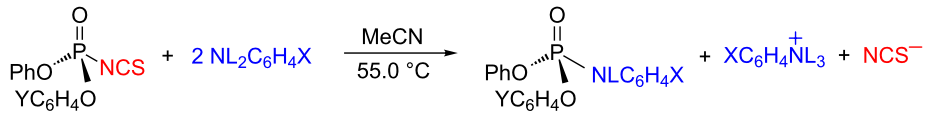

Scheme 1: Reactions of Y-aryl phenyl isothiocyanophosphates (**1a–e**) with $XC_6H_4NH_2(D)_2$ in MeCN at 55.0 °C.

(DKIEs). The aim of this work is to gain further information on the substituent effects, DKIEs and mechanism of the phosphoryl transfer reactions.

Results and Discussion

Table 1 summarizes the second-order rate constants, k_H and k_D, with X-anilines and deuterated X-anilines, respectively. Table 2 and Table 3 summarize the Hammett ($\rho_{X(H \text{ and } D)}$) and Brönsted ($\beta_{X(H \text{ and } D)}$) coefficients with X, and Hammett coefficients ($\rho_{Y(H)}$) with Y, respectively. The second-order rate constants were obtained from the slopes of pseudo-first-order rate constants (k_{obsd}) versus aniline concentration (Equation 1). Base-catalysis or noticeable side reactions could be safely ruled out from the zero intercept, $k_0 \approx 0$, in MeCN.

$$k_{obsd} = k_0 + k_{H(D)}[XC_6H_4NH_2(D)_2] \quad (1)$$

Figure 1 presents the Brönsted plots with X in the nucleophiles. The substituent effects of X on the reaction rates are not

Table 1: Second-order rate constants ($k_{(H \text{ and } D)} \times 10^3/M^{-1}\ s^{-1}$) of the reactions of Y-aryl phenyl isothiocyanophosphates with $XC_6H_4NH_2(D_2)$ in MeCN at 55.0 °C.

X \ Y		4-MeO (**1a**)	4-Me (**1b**)	H (**1c**)	3-MeO (**1d**)	4-Cl (**1e**)
4-MeO	k_H	9.58 ± 0.02[a]	10.2 ± 0.1	12.7 ± 0.1	17.2 ± 0.1	27.5 ± 0.1
	k_D	7.15 ± 0.04	–	8.92 ± 0.01	–	18.7 ± 0.1
4-Me	k_H	2.71 ± 0.01	3.02 ± 0.01	4.38 ± 0.01	6.09 ± 0.03	9.51 ± 0.01
	k_D	2.30 ± 0.01	–	3.44 ± 0.02	–	7.27 ± 0.05
H	k_H	0.400 ± 0.001	0.517 ± 0.005	0.693 ± 0.004	1.04 ± 0.01	1.89 ± 0.01
	k_D	0.384± 0.001	–	0.647 ± 0.001	–	1.67 ± 0.01
4-Cl	k_H	0.206 ± 0.001	0.257 ± 0.001	0.434 ± 0.001	0.787 ± 0.005	1.67 ± 0.01
	k_D	0.244 ± 0.001	–	0.492 ± 0.001	–	1.81 ± 0.02
3-Cl	k_H	0.718 ± 0.002	0.886 ± 0.008	1.48 ± 0.01	2.68 ± 0.01	5.62 ± 0.03
	k_D	0.994± 0.002	–	2.12 ± 0.01	–	8.46 ± 0.04

[a]Standard deviation.

Table 2: Hammett ($\rho_{X(H \text{ and } D)}$)[a] and Brönsted ($\beta_{X(H \text{ and } D)}$)[b] coefficients with X for the reactions of Y-aryl phenyl isothiocyanophosphates with $XC_6H_4NH_2(D_2)$ in MeCN at 55.0 °C.

X \ Y		4-MeO (**1a**)	4-Me (**1b**)	H (**1c**)	3-MeO (**1d**)	4-Cl (**1e**)
4-MeO, 4-Me, H	$\rho_{X(H)}$[c]	−5.09 ± 0.03	−4.76 ± 0.04	−4.68 ± 0.01	−4.51 ± 0.01	−4.29 ± 0.02
	$\rho_{X(D)}$[c]	−4.69 ± 0.02	–	−4.23 ± 0.01	–	−3.87 ± 0.02
	$\beta_{X(H)}$[c]	1.83 ± 0.08	1.72 ± 0.09	1.69 ± 0.04	1.63 ± 0.04	1.55 ± 0.07
	$\beta_{X(D)}$[c]	1.69 ± 0.06	–	1.53 ± 0.04	–	1.40 ± 0.06
4-Cl, 3-Cl	$\rho_{X(H)}$	3.87	3.84	3.81	3.80	3.76
	$\rho_{X(D)}$	4.35	–	4.53	–	4.78
	$\beta_{X(H)}$	−1.18	−1.17	−1.16	−1.16	−1.15
	$\beta_{X(D)}$	−1.33	–	−1.38	–	−1.46

[a]The σ values were taken from [1]. [b]The pK_a values of X-anilines in water were taken from [2]. [c]Correlation coefficients (r) of ρ_X and Brönsted β_X values for X = (4-MeO, 4-Me, H) are better than 0.996.

Table 3: Hammett coefficients ($\rho_{Y(H)}$)[a] with Y for the reactions of Y-aryl phenyl isothiocyanophosphates with $XC_6H_4NH_2$ in MeCN at 55.0 °C.

X	4-MeO	4-Me	H	4-Cl	3-Cl
$\rho_{Y(H)}$[b]	0.88 ± 0.07	1.08 ± 0.05	1.27 ± 0.07	1.77 ± 0.09	1.75 ± 0.09

[a]The σ values were taken from [1]. [b]Correlation coefficients (*r*) of $\rho_{Y(H)}$ values are better than 0.962.

compatible with a typical nucleophilic substitution reaction. The Hammett and Brönsted plots with X are biphasic concave upwards with a break region between X = H and 4-Cl (break point of $\sigma_X \approx 0.13$), giving unusual positive ρ_X and negative β_X values with X = 4-Cl and 3-Cl. Positive ρ_X (and negative β_X) values indicate that the nucleophilic N atom becomes more negative in the TS compared to in the ground state (GS). The substituent effects of Y on the reaction rates are consistent with a typical nucleophilic substitution reaction, and the rate increases with a more electron-withdrawing substituent.

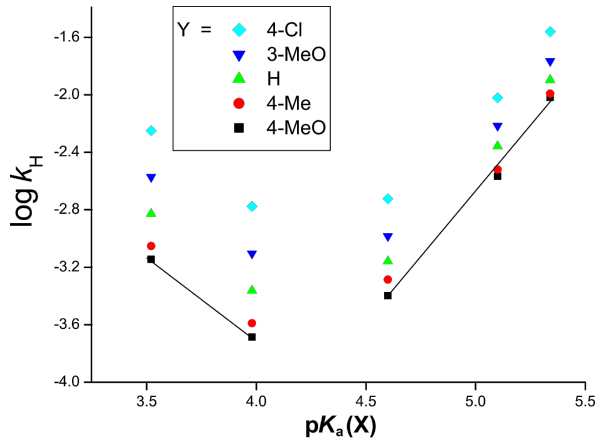

Figure 1: Brönsted plots with X [log k_H versus pK_a(X)] of the reactions of Y-aryl phenyl isothiocyanophosphates with $XC_6H_4NH_2$ in MeCN at 55.0 °C.

The cross-interaction constant (CIC) is defined based on the substituent effects of the nucleophiles, substrates and/or leaving groups on the reaction rates [3-5]. In the present work, the CIC (ρ_{XY}) between substituents X and Y in the nucleophiles and substrates, respectively, is described in Equation 2 and Equation 3.

$$\log\left(k_{XY}/k_{HH}\right) = \rho_X\sigma_X + \rho_Y\sigma_Y + \rho_{XY}\sigma_X\sigma_Y \quad (2)$$

$$\begin{aligned}\rho_{XY} &= \partial^2 \log\left(k_{XY}/k_{HH}\right)/\partial\sigma_X\partial\sigma_Y \\ &= \partial\rho_X/\partial\sigma_Y \\ &= \partial\rho_Y/\partial\sigma_X\end{aligned} \quad (3)$$

The two ρ_{XY} values are obtained because the Hammett plots with X are biphasic. Figure 2 shows the plots of ρ_X versus σ_Y

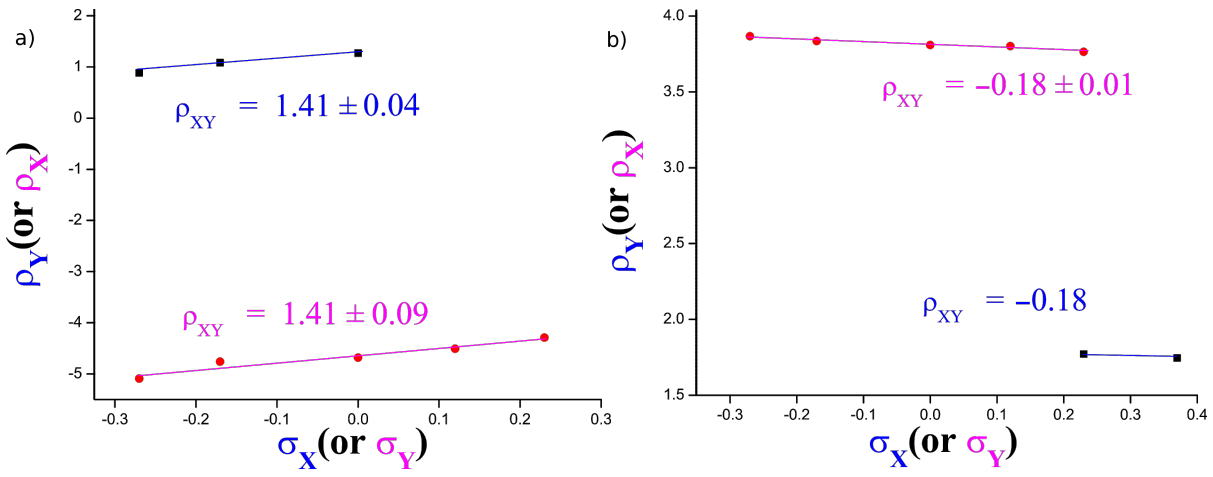

Figure 2: Plots of ρ_X versus σ_Y and ρ_Y versus σ_X of the reactions of Y-aryl phenyl isothiocyanophosphates with $XC_6H_4NH_2$ in MeCN at 55.0 °C. The obtained ρ_{XY} values by multiple regression are as follows: (a) ρ_{XY} = 1.40 ± 0.06 (*r* = 0.992) with more basic anilines and (b) ρ_{XY} = –0.18 ± 0.09 (*r* = 0.975) with less basic anilines.

and ρ_Y versus σ_X to determine the ρ_{XY} values, according to Equation 3. The signs of ρ_{XY} are positive with more basic anilines (X = 4-MeO, 4-Me, H) but negative with less basic anilines (X = 4-Cl, 3-Cl). The number of kinetic data points, 10 k_H values with less basic anilines, to obtain the ρ_{XY} value is not enough to overcome the experimental error. At least, however, the sign of ρ_{XY} is acceptable, and the greater magnitude of ρ_{XY} value with more basic anilines than that with less basic anilines is also acceptable. Accordingly, the authors propose the following reaction mechanism: (i) a stepwise process with rate-limiting leaving-group departure from the intermediate for more basic anilines based on the positive sign of ρ_{XY} (= 1.40), and (ii) a stepwise process with rate-limiting bond formation for less basic anilines based on the negative sign of ρ_{XY} (= −0.18) [3-5]. The greater magnitude of ρ_{XY} value with more basic anilines compared to that with less basic anilines suggests that the interaction between X and Y with more basic anilines is larger than that with less basic anilines in the TS (see below).

The DKIEs are primary normal with more basic anilines (X = 4-MeO, 4-Me, H) while secondary inverse with less basic anilines (X = 4-Cl, 3-Cl) as shown in Table 4. Primary normal DKIEs (k_H/k_D > 1.0) indicate that partial deprotonation of the aniline occurs in a rate-limiting step by hydrogen bonding [6-12]. In contrast, secondary inverse DKIEs (k_H/k_D < 1.0) indicate that the N–H(D) vibrational frequencies invariably increase upon going to the TS because of an increase in the steric congestion in the bond-making process in a stepwise process with a rate-limiting bond formation (or a normal S_N2 reaction) [13-15]. The magnitudes of the k_H/k_D values invariably decrease as the aniline becomes less basic. The magnitudes of the k_H/k_D values invariably increase for X = (4-MeO, 4-Me, H, 4-Cl) while they invariably decrease for X = 3-Cl as the substituent Y changes from electron-donating to electron-withdrawing. The maximum value of k_H/k_D = 1.47 with X = 4-MeO and Y = 4-Cl indicates extensive hydrogen bonding whereas the minimum value of k_H/k_D = 0.66 with X = 3-Cl and Y = 4-Cl indicates severe steric congestion in the TS, suggesting a great extent of bond formation. The secondary inverse and primary normal DKIEs are substantiated by backside nucleophilic attack involving in-line-type TSb and frontside attack involving hydrogen-bonded, four-center-type TSf, respectively (Scheme 2).

The hydrogen-bonded four-center type of TSb-H could be another plausible TS structure, in which hydrogen bonding of an amine hydrogen atom occurs on the P=O oxygen atom (Scheme 3). In the present work, three possible TSs could substantiate the primary normal DKIEs: (i) TSf, (ii) TSb-H or (iii) both TSb-H and TSf. The anilinolyses of tetracoordinate phosphorus with the Cl^- leaving group have been extensively studied in this lab, and the obtained data of primary normal DKIEs involving deuterated anilines are rationalized by TSf-type in which hydrogen bonding of an amine hydrogen atom occurs on the departing chloride [17-23]. The authors also suggested TSf-type, in which hydrogen bonding of an amine hydrogen atom occurs to the departing phenoxy oxygen atom for the anilinolyses of aryl dimethyl, methyl and diphenyl phosphinates [24]. Thus, at this point, the authors are in favor of TSf for the present work.

Table 4: The DKIEs (k_H/k_D) of the reactions of Y-aryl phenyl isothiocyanophosphates with $XC_6H_4NH(D)_2$ in MeCN at 55.0 °C.

X \ Y	4-MeO (**1a**)	H (**1c**)	4-Cl (**1e**)
4-MeO	1.34 ± 0.01[a]	1.42 ± 0.01	1.47 ± 0.01
4-Me	1.18 ± 0.01	1.27 ± 0.01	1.31 ± 0.01
H	1.04 ± 0.01	1.07 ± 0.01	1.13 ± 0.01
4-Cl	0.844 ± 0.005	0.882 ± 0.003	0.922 ± 0.012
3-Cl	0.722 ± 0.002	0.698 ± 0.001	0.664 ± 0.004

[a]Standard error {= $1/k_D[(^{\Delta}k_H)^2 + (k_H/k_D)^2 \times (^{\Delta}k_D)^2]^{1/2}$} from [16].

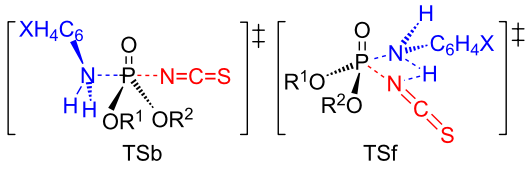

Scheme 2: Backside attack involving in-line-type TSb and frontside attack involving a hydrogen-bonded, four-center-type TSf.

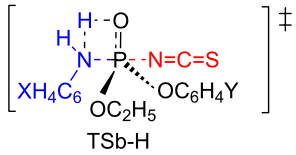

Scheme 3: Backside attack involving a hydrogen-bonded, four-center-type TSb-H.

The focus will now shift to the unusual positive ρ_X and negative β_X values with X = 4-Cl and 3-Cl. These values can be observed because of (i) desolvation of the GS [25,26] or (ii) TS imbalance phenomenon [27-29]. However, in the present work, the positive ρ_X and negative β_X values for less basic anilines are not ascribed to (i) a desolvation step prior to the rate-limiting nucleophilic attack, because the aniline nucleophile is neutral and the MeCN solvent is dipolar aprotic; and to (ii) a TS imbalance phenomenon, because the leaving group of isothiocyanate

is too poor to form an ion-pair type. The unusual positive ρ_X (and negative β_X) values with X = (4-Cl and 3-Cl) indicate that the nucleophilic N atom becomes more negative in the TS compared to in the GS. The authors, thus, propose that the structure of the TS is similar to what would be if the isothiocyante were the nucleophile and aniline were the leaving group, such that the nucleophilic N atom becomes more negative in the TS compared to in the GS. In other words, the TS is very tight and in which the degree of bond formation is very great while the degree of bond breaking is considerably small, resulting in the positive ρ_X. The very small value of k_H/k_D = 0.66 with X = 3-Cl and Y = 4-Cl could be supporting evidence. The relatively small magnitude of ρ_{XY} = −0.18 with less basic anilines could be another piece of supporting evidence, because the normal S_N2 mechanism (or stepwise mechanism with rate-limiting bond formation) gives a magnitude of $\rho_{XY} \approx -0.7$ [3-5]. This would be attributed to the strong interaction between the nucleophile (X) and leaving group over the nucleophile (X) and substrate (Y) (see above).

Finally, the authors propose the following reaction mechanism of the present work: (i) for more basic anilines (X = 4-MeO, 4-Me, H), a stepwise process with rate-limiting leaving-group departure from the intermediate, involving a predominant frontside attack with a hydrogen-bonded four-center-type TSf based on the positive ρ_{XY} and primary normal DKIEs; and (ii) for less basic anilines (X = 4-Cl , 3-Cl), a stepwise process with rate-limiting bond formation, involving a predominant backside attack TSb, and very tight TS, in which the extent of the bond formation is great and the degree of bond breaking is very small based on the negative ρ_{XY}, secondary inverse DKIEs and positive ρ_X.

Activation parameters, enthalpies and entropies of activation, are determined as shown in Table 5. The enthalpies of activation are relatively low and entropies of activation are of relatively large negative value. The relatively low value of activation enthalpy and large negative value of activation entropy are typical for the aminolyses of P=O systems, regardless of the mechanism, whether stepwise with rate-limiting bond formation (or a concerted) or stepwise with rate-limiting bond breaking.

Table 5: Activation parameters for the reactions of Y-aryl phenyl isothiocyanophosphate with aniline ($C_6H_5NH_2$) in MeCN.

Y	*t*/°C	$k_H \times 10^4/M^{-1}\ s^{-1}$	$\Delta H^{\neq}$/kcal mol^{-1}	$-\Delta S^{\neq}$/cal mol^{-1} K^{-1}
4-MeO (**1a**)	45.0	2.91 ± 0.01	5.7 ± 0.1	56 ± 1
	55.0	4.00 ± 0.01		
	65.0	5.29 ± 0.07		
4-Me (**1b**)	45.0	3.72 ± 0.01	6.2 ± 0.1	55 ± 1
	55.0	5.17 ± 0.05		
	65.0	7.08 ± 0.01		
H (**1c**)	45.0	4.96 ± 0.01	6.3 ± 0.1	54 ± 1
	55.0	6.93 ± 0.01		
	65.0	9.51 ± 0.01		
3-MeO (**1d**)	45.0	7.24 ± 0.01	6.2 ± 0.4	54 ± 1
	55.0	10.4 ± 0.1		
	65.0	13.7 ± 0.1		
4-Cl (**1e**)	45.0	13.5 ± 0.1	6.1 ± 0.1	53 ± 1
	55.0	18.9 ± 0.1		
	65.0	25.5 ± 0.2		

Experimental

Materials. HPLC grade acetonitrile (water content is less than 0.005%) was used without further purification. Deuterated anilines were synthesized as previously described [17-24]. Substrates were prepared as described earlier [30].

Kinetics measurement. Rates were measured conductometrically at 55.0 °C as described previously [17-24]. The initial concentrations of substrates and nucleophiles were as follows; [substrate] = 5×10^{-3} M and [X-aniline] = 0.10–0.30 M. The second-order rate constants ($k_{H(D)}$) were determined for at least five concentrations of anilines. The k_{obsd} values were the average of at least three runs.

Product analysis. Diphenyl isothiocyanophosphate was reacted with excess aniline for more than 15 half-lives at 55.0 °C in MeCN. Acetonitrile was evaporated under reduced pressure. The product mixture was treated with ether by a work-up process with dilute HCl and dried over anhydrous $MgSO_4$. The product was isolated through column chromatography (30% ethyl acetate/*n*-hexane) and then dried under reduced pressure. The analytical and spectroscopic data of the product gave the following results (see also Supporting Information File 1):

[$(C_6H_5O)_2P(=O)NHC_6H_5$]. White solid crystal; mp 132–133 °C; ^{1}H NMR (400 MHz, MeCN-d_3) δ 6.66 (br d, J = 8.8 Hz, 1H, aliphatic), 7.01–7.43 (m, 15H, aromatic); ^{13}C NMR (100 MHz, MeCN-d_3) δ 118.59–131.20 (m, 18C; aromatic); ^{31}P NMR (162 MHz, MeCN-d_3) δ 3.62 (d, J = 8.6 Hz, 1P, P=O); GC–MS (EI, m/z): 325 (M^+).

Supporting Information

Supporting Information File 1

Spectra of product.
[http://www.beilstein-journals.org/bjoc/content/supplementary/1860-5397-9-68-S1.pdf]

Acknowledgements

This work was supported by the Inha University Research Fund.

References

1. Hansch, C.; Leo, A.; Taft, R. W. *Chem. Rev.* **1991,** *91,* 165–195. doi:10.1021/cr00002a004
2. Streitwieser, A.; Heathcock, C. H.; Kosower, E. M. *Introduction to Organic Chemistry,* 4th ed.; Macmillan: New York, NY, 1992; p 735.
3. Lee, I. *Chem. Soc. Rev.* **1990,** *19,* 317–333. doi:10.1039/cs9901900317
4. Lee, I. *Adv. Phys. Org. Chem.* **1991,** *27,* 57–117. doi:10.1016/S0065-3160(08)60064-7
5. Lee, I.; Lee, H. W. *Collect. Czech. Chem. Commun.* **1999,** *64,* 1529–1550. doi:10.1135/cccc19991529
6. Lee, I.; Koh, H. J.; Lee, B.-S.; Lee, H. W. *J. Chem. Soc., Chem. Commun.* **1990,** 335–336. doi:10.1039/C39900000335
7. Barnes, J. A.; Williams, I. H. *J. Chem. Soc., Chem. Commun.* **1993,** 1286–1287. doi:10.1039/C39930001286
8. Lee, I. *Chem. Soc. Rev.* **1995,** *24,* 223–229. doi:10.1039/cs9952400223
9. Marlier, J. F. *Acc. Chem. Res.* **2001,** *34,* 283–290. doi:10.1021/ar000054d
10. Westaway, K. C. *Adv. Phys. Org. Chem.* **2006,** *41,* 217–273. doi:10.1016/S0065-3160(06)41004-2
11. Villano, S. M.; Kato, S.; Bierbaum, V. M. *J. Am. Chem. Soc.* **2006,** *128,* 736–737. doi:10.1021/ja057491d
12. Gronert, S.; Fagin, A. E.; Wong, L. *J. Am. Chem. Soc.* **2007,** *129,* 5330–5331. doi:10.1021/ja070093l
13. Poirier, R. A.; Wang, Y.; Westaway, K. C. *J. Am. Chem. Soc.* **1994,** *116,* 2526–2533. doi:10.1021/ja00085a037
14. Yamataka, H.; Ando, T.; Nagase, S.; Hanamura, M.; Morokuma, K. *J. Org. Chem.* **1984,** *49,* 631–635. doi:10.1021/jo00178a010
15. Zhao, X. G.; Tucker, S. C.; Truhlar, D. G. *J. Am. Chem. Soc.* **1991,** *113,* 826–832. doi:10.1021/ja00003a015
16. Crumpler, T. B.; Yoh, J. H. *Chemical Computations and Errors;* John Wiley: New York, NY, 1940; p 178.
17. Hoque, M. E. U.; Dey, S.; Guha, A. K.; Kim, C. K.; Lee, B.-S.; Lee, H. W. *J. Org. Chem.* **2007,** *72,* 5493–5499. doi:10.1021/jo0700934
18. Hoque, M. E. U.; Dey, N. K.; Kim, C. K.; Lee, B.-S.; Lee, H. W. *Org. Biomol. Chem.* **2007,** *5,* 3944–3950. doi:10.1039/b713167d
19. Dey, N. K.; Hoque, M. E. U.; Kim, C. K.; Lee, B.-S.; Lee, H. W. *J. Phys. Org. Chem.* **2008,** *21,* 544–548. doi:10.1002/poc.1314
20. Dey, N. K.; Hoque, M. E. U.; Kim, C. K.; Lee, B.-S.; Lee, H. W. *J. Phys. Org. Chem.* **2009,** *22,* 425–430. doi:10.1002/poc.1478
21. Hoque, M. E. U.; Guha, A. K.; Kim, C. K.; Lee, B.-S.; Lee, H. W. *Org. Biomol. Chem.* **2009,** *7,* 2919–2925. doi:10.1039/b903148k
22. Barai, H. R.; Lee, H.-W. *Bull. Korean Chem. Soc.* **2011,** *32,* 1939–1944. doi:10.5012/bkcs.2011.32.6.1939
23. Hoque, M. E. U.; Lee, H. W. *Bull. Korean Chem. Soc.* **2012,** *33,* 1879–1884. doi:10.5012/bkcs.2012.33.6.1879
24. Dey, N. K.; Kim, C. K.; Lee, H. W. *Org. Biomol. Chem.* **2011,** *9,* 717–724. doi:10.1039/c0ob00517g
25. Jencks, W. P.; Brant, S. R.; Gandler, J. R.; Fendrich, G.; Nakamura, C. *J. Am. Chem. Soc.* **1982,** *104,* 7045–7051. doi:10.1021/ja00389a027
26. Onyido, I.; Swierczek, K.; Purcell, J.; Hengge, A. C. *J. Am. Chem. Soc.* **2005,** *127,* 7703–7711. doi:10.1021/ja0501565
27. Jencks, W. P. *Chem. Rev.* **1985,** *85,* 511–527. doi:10.1021/cr00070a001
28. Bernasconi, C. F. *Acc. Chem. Res.* **1987,** *20,* 301–308. doi:10.1021/ar00140a006
29. Bernasconi, C. F. *Adv. Phys. Org. Chem.* **1992,** *27,* 119–238. doi:10.1016/S0065-3160(08)60065-9
30. Adhikary, K. K.; Lee, H. W.; Lee, I.-C. *Bull. Korean Chem. Soc.* **2003,** *24,* 1135–1140. doi:10.5012/bkcs.2003.24.8.1135

Beilstein Journal of Organic Chemistry

Photoionisation of the tropyl radical

Kathrin H. Fischer[1], Patrick Hemberger[*2], Andras Bodi[2] and Ingo Fischer[*1]

Full Research Paper

Open Access

Address:
[1]Institute of Physical and Theoretical Chemistry, University of Würzburg, Am Hubland Süd, 97074 Würzburg, Germany and [2]Molecular Dynamics Group, Paul Scherrer Institut (PSI), 5232 Villigen, Switzerland

Email:
Patrick Hemberger[*] - patrick.hemberger@psi.ch;
Ingo Fischer[*] - ingo.fischer@uni-wuerzburg.de

* Corresponding author

Keywords:
dissociative photoionisation; gas phase; reactive intermediates; synchrotron radiation; threshold photoelectron spectroscopy

Beilstein J. Org. Chem. **2013,** *9,* 681–688.
doi:10.3762/bjoc.9.77

Received: 23 January 2013
Accepted: 13 March 2013
Published: 09 April 2013

This article is part of the Thematic Series "New reactive intermediates in organic chemistry".

Guest Editor: G. Bucher

Abstract

We present a study on the photoionisation of the cycloheptatrienyl (tropyl) radical, C_7H_7, using tunable vacuum ultraviolet synchrotron radiation. Tropyl is generated by flash pyrolysis from bitropyl. Ions and electrons are detected in coincidence, permitting us to record mass-selected photoelectron spectra. The threshold photoelectron spectrum of tropyl, corresponding to the $X^+\,{}^1A_1' \leftarrow X\,{}^2E_2''$ transition, reveals an ionisation energy of 6.23 ± 0.02 eV, in good agreement with Rydberg extrapolations, but slightly lower than the value derived from earlier photoelectron spectra. Several vibrations can be resolved and are reassigned to the C–C stretch mode ν_{16}^+ and to a combination of ν_{16}^+ with the ring breathing mode ν_2^+. Above 10.55 eV dissociative photoionisation of tropyl is observed, leading to the formation of $C_5H_5^+$ and C_2H_2.

Introduction

Organic radicals are known to be ubiquitous reactive intermediates in chemistry, biology and material science [1]. Studies on isolated radicals conducted in our group [2] yield their intrinsic properties, which are essential for understanding the reactivity of radicals in both the gas and condensed phase. Here we present a detailed study on the photoionisation of the cycloheptatrienyl radical (C_7H_7), commonly called tropyl, using synchrotron radiation.

The tropyl radical **1** and its cation **2** are depicted in Figure 1. They have been at the focus of research since the 1960s [3,4] due to their symmetry properties. The interest originated in the expected stability of the tropyl cation, which is an aromatic molecular ion according to the Hückel rules. The aromaticity was confirmed and the symmetry of the $C_7H_7^+$ established as D_{7h} [5]. The vibrational structure of the cation was examined by IR and Raman spectroscopy [6-8]. There are 36 normal modes with 20 distinct frequencies, owing to degeneracy. Of these twenty vibrations, four are IR- and seven Raman-active [9].

In contrast to the cation, the odd-electron neutral tropyl radical is expected to be Jahn–Teller (JT) distorted. The nature of this distortion and whether the equilibrium structure of tropyl corresponds to a distorted C_{2v} or to D_{7h} symmetry has been

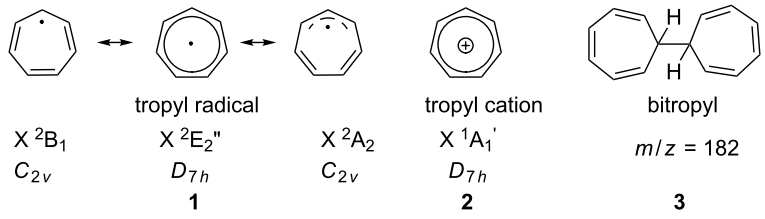

Figure 1: Structure of the tropyl radical **1**, its cation **2** and the precursor bitropyl **3**.

studied experimentally and theoretically. An early electron spin resonance (ESR) experiment found seven equivalent hydrogen atoms and a uniform spin distribution and, therefore, concluded a dynamic D_{7h} structure of the radical [10,11]. Calculations in the 1990s reported C_{2v} symmetry due to Jahn–Teller distortion [9,12]. The most extensive investigation on the vibronic structure of the tropyl radical including the Jahn–Teller distortion was carried out by Miller and co-workers [13,14]. They found that the $^2E_2$" ground state splits into two components of C_{2v} symmetry, an allylic $^2B_1$ and a dienylic $^2A_2$ one (Figure 1). They are stabilized by roughly 1000 cm^{-1} with respect to the undistorted D_{7h} saddle point [14], which corresponds to a conical intersection on the potential-energy surface. In addition to providing chemical insight, the other benefit of identifying the two C_{2v} resonance geometries on the minimum path is that it makes geometry optimisations possible by the symmetry constraint. The IR spectrum of the radical was measured in the gas phase and compared to calculations as well as to that of the benzyl radical [15].

The geometry change upon ionisation and the character of the molecular orbitals triggered interest in the photoelectron spectroscopy of tropyl. The adiabatic ionisation energy of the radical was established by Thrush and Zwolenik (6.24 eV) [3], Elder and Parr (6.236 eV, derived from a photoion yield curve) [4] and Koenig and Chang (6.28 eV) [16]. The latter used helium(I) photoelectron spectroscopy and employed bitropyl **3** as a precursor (Figure 1). This molecule proved to be an efficient source for tropyl radicals generated by pyrolysis. Furthermore, the ground and excited states of the ion have been investigated computationally [9,17]. In the present study we extend the previous work using imaging photoelectron–photoion coincidence (iPEPICO) techniques in combination with VUV synchrotron radiation [18-20]. Coincidence spectroscopy correlates the electron signal with the mass signal and thus permits recording of mass-selected photoelectron spectra. This is particularly advantageous in experiments on reactive intermediates where a clean sample generation cannot always be ensured. An improved resolution is obtained from analysing only the threshold electrons [18,21], i.e., electrons recorded with almost zero initial kinetic energy upon tuning the photon energy. Thus, IR and Raman inactive ionic vibrations can often be observed and assigned in the photoelectron spectrum.

We have shown in the past that these techniques are well suited to study the photoionisation of open-shell species. Ionisation energies have been determined from vibrationally resolved photoelectron spectra for several open-shell species ranging from allyl [22] and propargyl [23] to indenyl (C_9H_7) [24], cyclopropenylidene [25] and fulvenallenyl [26]. In the case of allyl [27,28] and propargyl [29] they are in excellent agreement with high-resolution laser studies. Such data are important for the derivation of bond dissociation energies and heats of formation of radicals, but also aid in the in situ detection of radicals in flames by photoionisation [30]. The goal of the present experimental study was to elucidate the vibrational structure of the tropyl ion ground state with threshold photoelectron spectroscopic (TPES) techniques.

Results and Discussion

The performance of the pyrolysis source can be illustrated by mass spectra at different photon energies with pyrolysis on or off, depicted in Figure 2.

As shown in the top trace of Figure 2 almost no signal is present without pyrolysis at a photon energy of 7.8 eV. At a photon energy of around 8 eV we start to see a signal of the bitropyl precursor **3**. Already at around the same energy a signal at m/z = 91 appears. Since there is no pyrolysis, the signal has to originate from dissociative photoionisation of bitropyl. Hence, in the mass spectrum recorded at 8.7 eV (centre trace of Figure 2) the observed masses are m/z = 91, 92 and 182, which correspond to a tropyl fragment, its ^{13}C isotopologue and the bitropyl precursor. Above a photon energy of 8.9 eV, the m/z = 104 and 167 peaks appear in addition. They are products from higher energy dissociative photoionisation channels and are probably formed through the loss of benzene or a methyl group from the precursor, respectively. When we decrease the photon energy to 7.8 eV again and switch on the pyrolysis, (bottom trace in Figure 2) an intense photoionisation signal is observed at the masses m/z = 91 and 92, which is due to the direct photoionisation of tropyl and its ^{13}C isotopologue. We

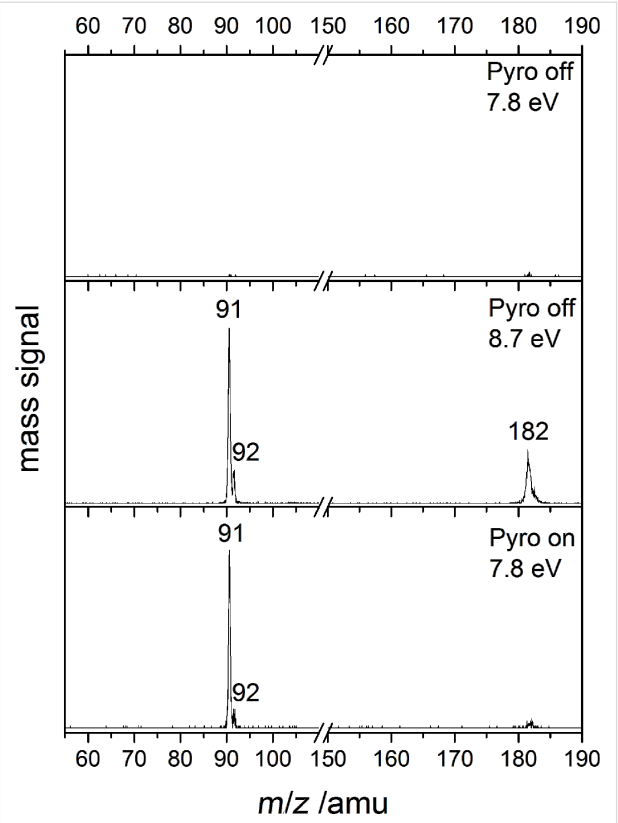

Figure 2: Mass spectra of bitropyl without pyrolysis at 7.8 and 8.7 eV (top and centre trace) and with pyrolysis, recorded at 7.8 eV (bottom trace).

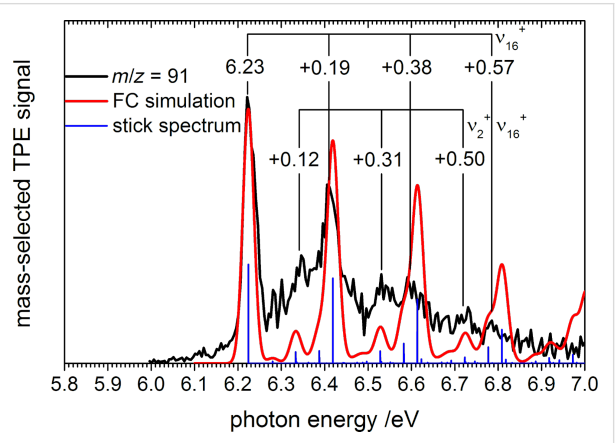

Figure 3: Threshold photoelectron spectrum of tropyl (black line). The Franck–Condon simulation (red line) is based on the computed stick spectrum (blue sticks) convoluted with 30 meV FWHM Gaussians.

note that the small signal at m/z = 182 never disappears completely. This is probably a result of sample contamination by an isomer of bitropyl. Thus, dissociative photoionisation may contribute to the tropyl signal at photon energies above 8 eV. Above 10.5 eV, an m/z = 65 peak appears exclusively in the "pyrolysis on" spectra corresponding to the dissociative photoionisation of the tropyl radical, yielding the cyclopentadienyl cation and acetylene.

Figure 3 shows the region of the ionisation onset of the tropyl radical in high resolution while Figure 4 (see below) exhibits the complete spectrum with the higher energy region in lower resolution. In both mass-selected threshold photoelectron (TPE) spectra the pyrolysis was turned on. The experimental spectrum (Figure 3) shows a sharp onset with a pronounced first maximum at 6.23 eV. It is assigned to the $\tilde{X}^+\ ^1A_1$' (v^+=0) ← $\tilde{X}\ ^2E_2$" (v" = 0) transition and corresponds to the adiabatic ionisation energy of the molecule. As the radical vibrational temperature is typically around 500 K in a continuous beam experiment [31] a contribution from hot and sequence bands cannot be excluded and could be responsible for the signal between 6.1 eV and 6.2 eV. The small peak at around 6.12 eV may correspond to a bending-mode hot band. Our IE value of 6.23 ± 0.02 eV is in excellent agreement with the values obtained from an extrapolation of Rydberg states: a [2 + 1] multiphoton ionisation (MPI) study [32] reported an IE of 50177 ± 46 cm^{-1} (6.221 eV) and the absorption experiment by Thrush and Zwolenik found a value of 6.24 eV. On the other hand, our value is slightly lower than the IE of 6.28 eV reported by conventional photoelectron spectroscopy [16]. It is interesting to note that the ionisation energy of benzyl, the second C_7H_7 isomer, lies at 7.249 eV [33] and is thus almost 1 eV higher.

A number of peaks are apparent that belong to vibrational progressions in the cation. The first progression has a spacing of around 1530 cm^{-1} (0.19 eV). This progression has been observed before. A vibrational spacing of 1528 ± 13 cm^{-1} was reported for high-lying Rydberg states and assigned to the overtone of a C–C–C bending mode of e_3' symmetry with a vibrational frequency of 768 cm^{-1} [32]. A vibrational progression with a spacing of 1424 ± 100 cm^{-1} was also found in conventional PES and attributed to a C–C–C stretching mode of e_1 symmetry with a computed wavenumber of 1470 cm^{-1} [16]. A second pronounced peak is identified +0.12 eV above the origin (970 cm^{-1}). This much weaker progression also appears in combination with members of the +0.19 eV progression, and has also been observed in the previous Rydberg state study [32]. Since it has now been firmly established that the minimum energy geometries are of C_{2v} symmetry [13,14], these earlier assignments have to be reconsidered. Only totally symmetric modes, i.e., a_1' modes in the case of tropyl, appear as fundamentals in a photoelectron spectrum in the absence of vibronic coupling. However, upon photoionisation the symmetry of tropyl changes from C_{2v} to D_{7h}, so transitions have to be discussed in the common subgroup C_{2v}. The irreducible representations e_1', e_2' and e_3' resolve into $a_1 \oplus b_2$ upon going

from D_{7h} to C_{2v}. As this sum contains the totally symmetric representation a_1, these doubly degenerate modes that are symmetric towards σ_h are expected to be symmetry allowed in a $D_{7h} \leftarrow C_{2v}$ transition.

In order to assign the vibrational transitions we performed a Franck–Condon (FC) simulation (Figure 3) with the FCfit program, version 2.8.8 [34] using the $\tilde{X}^+ \, ^2B_1$ allylic resonance structure of the neutral radical. We employed the geometry, frequencies and force constants of the CASSCF calculation from Stakhursky et al. [13] in the simulation. Note that their work accurately describes the Jahn–Teller distortion and thus represents the best available description of the radical potential-energy surface. They chose a (7,7) active space and employed a 6-31G(d) basis set. For the cation the input parameters were calculated by density functional theory (DFT) with the Gaussian 09 suite of programs [35], employing the B3LYP functional and a 6-31G(d) basis set. For a closed-shell molecule without vibronic distortions, a DFT approach provides the same accuracy for the geometries and frequencies as CASSCF. Our geometry and frequencies agree very well with the one reported in the literature [17]. For example a C–C bond length r(C–C) = 1.399 Å was found as compared to r(C–C) = 1.396 Å by Pino et al. [17]. For all vibrational frequencies unscaled values are given below. We note that the computations have been carried out in the Abelian point groups C_s or C_{2v}. The vibrational modes were assigned following the nomenclature of Lee and Wright [9], which has also been used by Pino et al. [17].

In order to compare the FC simulation with the experiment, the stick spectrum was convoluted with a Gaussian with a FWHM (full width at half maximum) of 0.030 eV. As seen in Figure 3, the simulation is in good agreement with the experimental spectrum. The main progression with a spacing of 1530 cm^{-1} (+0.19 eV) can be assigned to the doubly degenerate mode calculated at 1571 cm^{-1} (e_3', ν_{16}^+), which is an in plane C–C stretching vibration. Upon ionisation, the D_{7h} saddle point turns into a true minimum in the absence of Jahn–Teller distortion. As this has to be associated with an adaption of the C–C bond lengths, the corresponding vibrations are expected to be active. In the experimental spectrum and the FC simulation we also observe its first (+0.38 eV, 16_0^2) and second (+0.57 eV, 16_0^3) overtone. However, the simulation overestimates the intensity of the overtones. This is not surprising, considering that the neutral ground state geometry is delocalized and, in a crude approximation, we only use one resonance geometry and its harmonic oscillator functions. Also the second-order Jahn–Teller effect was neglected in the ground-state calculations. Still, no significant changes were observed in the simulated peak intensities when using the other C_{2v} resonance geometry of the neutral, i.e., the dienylic $^2A_2$ component, even though the geometries are somewhat different. The ground state can be described as a superposition of the $^2A_2$ and $^2B_1$ states, and it is reassuring that they both lead to very similar FC simulations. This also explains why the harmonic-oscillator approach works reasonably well in this case.

The first member of the second progression lies +0.12 eV above the origin and can be assigned to the ν_2^+ fundamental of a_1' symmetry in the reference geometry, 2_0^1. A wavenumber of ν_2^+ 881 cm^{-1} was calculated for this ring breathing mode. This ν_2^+ mode has also been observed at +862 cm^{-1} (+0.11 eV) in the previous Rydberg state MPI study [32]. The band is not very pronounced and the maximum is difficult to identify in our spectrum. This probably explains the deviation to the computed value. Two further peaks are assigned to be combination bands with ν_{16}^+, namely $2_0^1 16_0^1$ (+0.31 eV) and $2_0^1 16_0^2$ (+0.50 eV). An additional mode reported in the MPI spectrum at +1284 cm^{-1} is also predicted by the FC-simulations as visible in the stick spectrum in Figure 3. It is buried in the red edge of the +0.19 eV band. We assign it to the ν_{17}^+ C–H in-plane bend of e_3' symmetry, computed at 1320 cm^{-1}.

Figure 4 presents the complete TPES up to 13.0 eV. Note that the photon energy step size changed at 7 eV. A small peak is observed at 7.25 eV. Most likely it corresponds to the adiabatic ionisation energy of the benzyl radical [36], originating either from precursor impurities or from an isomerisation in the pyrolysis. Benzyl is by about 70 kJ mol^{-1} more stable than tropyl [12,37,38], but a high activation barrier can be assumed for the isomerisation reaction in the pyrolysis source. Although we cannot exclude that the signal in the m/z = 91 mass channel might have some contributions from benzyl in the higher photon energy region, the benzyl signal is small compared to the tropyl one in the threshold region. Therefore the amount of the possible benzyl contamination is negligible.

With active pyrolysis an additional m/z = 65 peak appears at around 8.55 eV in the mass spectrum, which can be attributed to $C_5H_5^+$. The mass-selected TPE-signal of m/z = 65 is depicted as a dashed line in Figure 4. Below 10.55 eV the signal is small and has a symmetric peak shape in the mass spectrum, as visible in the upper trace of Figure 5. Due to the small count number it is difficult to determine an accurate onset, but the signal appears around 8.55 eV. The adiabatic IE of the cyclopentadienyl radical was determined to be 8.428 eV by high-resolution photoelectron spectroscopy [39]. Thus, the appearance of $C_5H_5^+$ in this energy range can be interpreted as the direct ionisation of cyclopentadienyl radical produced as a side product in the pyrolysis. Above 10.55 eV, on the other hand, the intensity rises significantly and the time-of-flight peak shape

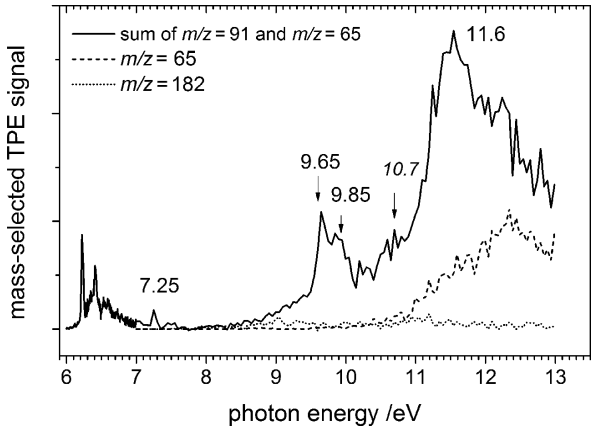

Figure 4: TPE spectrum of tropyl (solid line) and cyclopentadienyl (m/z = 65, dashed line) in the 7–13 eV photon energy range. Since $C_5H_5^+$ is generated by dissociative photoionisation of tropyl at higher energies, the tropyl photoelectron spectrum is displayed as the sum of the two mass channels. The residual signal at the mass of the precursor is given as a dotted line for comparison.

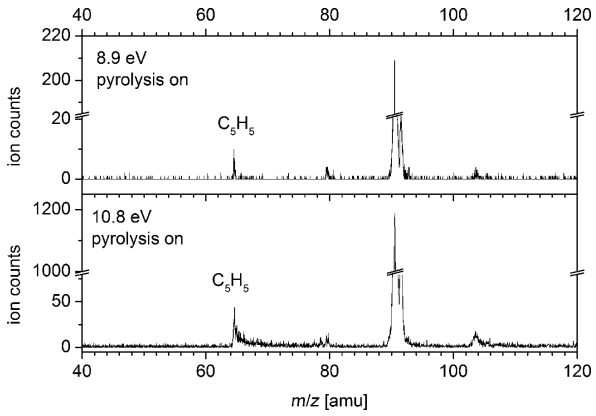

Figure 5: The shape of the $C_5H_5^+$ peak in the mass spectrum changes with photon energy. While the peak is symmetric at 8.9 eV, it shows a pronounced asymmetry at 10.8 eV, indicating the onset of dissociative photoionisation.

becomes asymmetric, as visible in the lower trace of Figure 5. Such an asymmetry indicates that the ion is a dissociation product of a metastable parent ion [40]. Formation of the cyclopentadienyl ion and acetylene upon dissociative photoionisation of tropyl can explain the rise in the mass channel above 10.55 eV and the asymmetric peak shape. Thermochemical calculations reveal that the channel is accessible at 10.52 eV, utilizing the heat of formation at 0 K of $C_7H_7^+$ (896 kJ mol^{-1}) [41], the $\Delta_f H^o$ of cyclopentadienyl radical (276 kJ mol^{-1}) [42], its adiabatic IE (8.428 eV = 813.18 kJ mol^{-1}) [39], and the $\Delta_f H^o$ of acetylene (226.88 kJ mol^{-1}) [43]. This corresponds to around 4.3 eV internal energy in the ion before it dissociates, being in good agreement with our experimentally observed onset value of 10.55 eV. As pyrolysis is not complete, one has to consider dissociative photoionisation of the precursor as a possible source of $C_5H_5^+$. The signal in the m/z = 182 mass channel, corresponding most likely to an isomer of bitropyl, is given as a dotted line in Figure 4. As can be seen, the signal is small throughout the studied energy range.

Between 7 eV and 8.5 eV the spectrum of tropyl has a Franck–Condon gap, and the transition to the first excited electronic state of the ion is visible at 9.65 eV. This peak has a shoulder at 9.85 eV photon energy, i.e., 200 meV higher, which may correspond to either vibrational excitation of the first electronic excited state or to the next electronic state. A noisy feature appears at 10.7 eV, and is followed by the highest intensity peak at 11.6 eV.

The most stable triplet state has been observed before at 9.63 eV [16], and is calculated to lie 3.1 eV above the ground state [9], i.e., at 9.33 eV using the newly determined adiabatic ionisation energy of 6.23 eV. In the same work, Lee and Wright predict the next triplet state at 3.9 eV excitation energy, i.e., at 10.13 eV photon energy. We calculated the EOM-CCSD/cc-pVTZ excitation energies for the triplet states, using QChem 4 [44] at the DFT-optimised ground state tropyl ion geometry, to be 3.82 and 4.00 eV, corresponding to 10.05 and 10.23 eV photon energies. TD-DFT calculations yield 9.70, 10.05 eV (B3LYP/6-311++G(d,p)); 9.86, 10.25 (M06-2X/6-311++G(d,p)) and 9.85, 10.03 eV (BLYP/6-311G(d,p)). Note that both triplet states are of E symmetry. The observed excitation energies are lower than the calculated values, which is due to possible Jahn–Teller distortions in the doubly degenerate triplet states, not considered in calculations of vertical excitation energies. The shoulder at 9.85 eV may thus either be due to the second triplet state, or to a vibrational fundamental of the excited state. For example a C–C stretching mode may be responsible for this peak, 1600 cm^{-1} further to the blue with respect to the first one.

The electronic spectroscopy of mass-selected tropyl cations has recently been investigated in Ne matrix [45]. A progression starting at 275.1 nm (4.51 eV) was assigned to the $^1A_2$" $\leftarrow \tilde{X}^+ \, ^1A_1$' transition of the tropyl cation, corresponding to 10.74 eV in the photoelectron spectrum for the first excited singlet state of the ion. The shoulder at around 10.7 eV in Figure 4 might be tentatively assigned to this state. However, previous calculations predicted the first singlet excited state at photon energies of 11.3 [9] and 11.74 eV [45]. Our EOM-CCSD result at 11.07 and TD-DFT results at 11.09, 11.24 and 10.95 eV with the B3LYP, M06-2X and BLYP functionals, respectively, agree reasonably well with the experimental result of Nagy et al. [45].

Overall the theoretical predictions are less consistent in the range of the maximum TPE signal at 11.6 eV (Figure 4). Lee and Wright reported a further triplet state at 12.4 eV, followed by a 1 eV gap to the next electronic excited state. EOM-CCSD vertical-excitation-energy calculations predict that the next higher lying state is a triplet at 12.48 eV followed by two more triplet states in ca. 100 meV intervals as well as several singlet states around 12.8 eV. TD-DFT calculations, on the other hand, depend greatly on the functional used. B3LYP calculations agree best with the experiment, yielding both a singlet and a triplet state in the 11.8–11.9 eV photon energy range. BLYP yields almost a continuum of states at 11.38 (S), 11.45 (T), 11.54 (S), 11.60 (S) and 11.66 (S) eV, whereas the next singlet state above 11.24 eV is obtained at 12.05 eV with the M06-2X functional. To summarize, wave-function methods, such as CIS, employed by Lee and Wright or EOM-CCSD predict a sparse electronic excitation spectrum with a gap at the experimentally observed main peak at 11.6 eV. Density functional results, on the other hand, are inconsistent in this energy range. Thus an unequivocal assignment of this band is difficult.

Conclusion

We studied the photoionisation of the tropyl radical, generated by pyrolysis of bitropyl, employing the iPEPICO technique. The first band in the mass-resolved threshold photoelectron spectrum at 6.23 eV was assigned to the adiabatic ionisation energy. This value is in very good agreement with a previous extrapolation of Rydberg states. With the help of a Franck–Condon simulation two progressions were assigned. The first includes the vibration ν_{16}^+, an e_3' C–C stretching mode with a spacing of 1530 cm^{-1} (0.19 eV), while the second progression is a combination of the ν_2^+ a_1' ring-breathing mode and ν_{16}^+. The simulations also indicate activity in the ν_{17}^+ C–H in-plane bending mode of e_3' symmetry. Moreover the first triplet and (possibly) singlet excited states of the tropyl ion were observed at 9.65 eV and 10.7 eV, respectively, in agreement with earlier work [5,16]. The second triplet state may also be visible at 9.85 eV. The most intense band appears at 11.6 eV. Computing this part of the spectrum proved challenging, with wave-function methods predicting a gap in this energy range, while DFT results depend greatly on the functional used. At around 10.55 eV (4.3 eV internal energy) the tropyl ion starts to photoionize dissociatively to form the cyclopentadienyl ion. This value is in very good agreement with the appearance energy estimated from a thermochemical cycle.

Experimental

The experiments were carried out at the VUV beamline of the Swiss Light Source at the Paul Scherrer Institut (PSI) in Villigen, Switzerland. The beamline has been described in detail elsewhere [46,47]. The X04DB bending magnet provides synchrotron radiation, which is collimated and sent to a plane grating monochromator with a 600 grooves/mm with a maximum resolving power of 10^4. A mixture of 10% Kr, 30% Ar and 60% Ne at a pressure of 10 mbar was used to suppress radiation at higher harmonics in a differentially pumped gas filter. Below 7 eV a MgF_2 window was used instead of the gas mixture. A photon energy resolution of 5 meV was achieved at 15.764 eV, measured at the 11s resonance of argon.

The iPEPICO (imaging photoelectron photoion coincidence) technique was employed to study the photoionisation of tropyl **1**. This technique allows the mass-selective detection of threshold photoelectrons by detecting them in coincidence with ions. The spectrometer is a combination of a Wiley–McLaren time-of-flight (TOF) mass spectrometer [48] and a velocity map imaging setup [49]. The latter is equipped with a position sensitive detector with a delay line anode (Roentdek DLD40). Only the central part of the electron image, corresponding to an electron energy resolution of around 5 meV, was taken for further analysis. The contribution of hot background electrons was subtracted following the method outlined by Sztáray and Baer [50].

A flange equipped with a molecular beam source and a SiC tube for flash pyrolysis [51] was mounted to the vacuum chamber. Bitropyl **3** was synthesized according to the literature [5], placed in an oven and heated to 90–105 °C to obtain a sufficient vapour pressure. The precursor was seeded in an argon flow of around 70 mbar and expanded through a 0.1 mm pinhole into the pyrolysis tube. The oven was mounted in line with the gas flow. An unskimmed jet was employed. The photon energy was scanned in steps of 5 meV in the region of the ionisation threshold and 10–50 meV in the higher energy regions. Data were averaged for 60 seconds per data point.

Acknowledgements

Financial support by the Deutsche Forschungsgemeinschaft (DFG) within the framework of the research training school GRK 1221 and through contract FI575/7-2 is gratefully acknowledged. This research project has been supported by the European Commission under the 7th Framework Program, Research Infrastructures, grant agreement number 226716. The calculations were performed at the Leibniz-Rechenzentrum der Bayerischen Akademie der Wissenschaften (LRZ Munich). The iPEPICO experiments were carried out at the VUV beamline of the Swiss Light Source, Paul Scherrer Institut. We would like to thank Terry Miller and Gyorgy Tarczay for providing us with details of their computational results. The work was financially supported by the Swiss Federal Office for Energy (BFE Contract Number 101969/152433).

References

1. Chatgilialoglu, C.; Studer, A., Eds. *Encyclopedia of Radicals in Chemistry, Biology and Materials;* John Wiley & Sons: Chichester, 2012. doi:10.1002/9781119953678
2. Alcaraz, C.; Fischer, I.; Schröder, D. Radical Chemistry in the Gas Phase. In *Encyclopedia of Radicals in Chemistry, Biology and Materials;* Chatgilialoglu, C.; Studer, A., Eds.; John Wiley & Sons: Chichester, 2012; Vol. 1, pp 477–502.
3. Thrush, B. A.; Zwolenik, J. J. *Discuss. Faraday Soc.* **1963,** *35,* 196–200. doi:10.1039/df9633500196
4. Elder, F. A.; Parr, A. C. *J. Chem. Phys.* **1969,** *50,* 1027–1028. doi:10.1063/1.1671081
5. Doering, W. V. E.; Knox, L. H. *J. Am. Chem. Soc.* **1957,** *79,* 352–356. doi:10.1021/ja01559a030
6. Fateley, W. G.; Lippincott, E. R. *J. Chem. Phys.* **1957,** *26,* 1471–1481. doi:10.1063/1.1743566
7. Sourisseau, C.; Hervieu, J. *Spectrochim. Acta, Part A* **1978,** *34,* 881–887. doi:10.1016/0584-8539(78)80007-5
8. Howard, J.; Graham, D. *Spectrochim. Acta, Part A* **1985,** *41,* 815–824. doi:10.1016/0584-8539(85)80027-1
9. Lee, E. P. F.; Wright, T. G. *J. Phys. Chem. A* **1998,** *102,* 4007–4013. doi:10.1021/jp980821e
10. Wood, D. E.; McConnell, H. M. *J. Chem. Phys.* **1962,** *37,* 1150–1151. doi:10.1063/1.1733231
11. Silverstone, H. J.; Wood, D. E.; McConnell, H. M. *J. Chem. Phys.* **1964,** *41,* 2311–2323. doi:10.1063/1.1726265
12. Smith, B. J.; Hall, N. E. *Chem. Phys. Lett.* **1997,** *279,* 165–171. doi:10.1016/S0009-2614(97)01016-6
13. Stakhursky, V. L.; Sioutis, I.; Tarczay, G.; Miller, T. A. *J. Chem. Phys.* **2008,** *128,* 084310. doi:10.1063/1.2829437
14. Sioutis, I.; Stakhursky, V. L.; Tarczay, G.; Miller, T. A. *J. Chem. Phys.* **2008,** *128,* 084311. doi:10.1063/1.2829471
15. Satink, R. G.; Meijer, G.; von Helden, G. *J. Am. Chem. Soc.* **2003,** *125,* 15714–15715. doi:10.1021/ja038329i
16. Koenig, T.; Chang, J. C. *J. Am. Chem. Soc.* **1978,** *100,* 2240–2242. doi:10.1021/ja00475a050
17. Pino, T.; Güthe, F.; Ding, H.; Maier, J. P. *J. Phys. Chem. A* **2002,** *106,* 10022–10026. doi:10.1021/jp020910y
18. Baer, T.; Guyon, P.-M. In *High Resolution Laser Photoionisation and Photoelectron Studies;* Powis, I.; Baer, T.; Ng, C. Y., Eds.; John Wiley & Sons: New York, NY, 1995.
19. Baer, T. *Int. J. Mass Spectrom.* **2000,** *200,* 443–457. doi:10.1016/S1387-3806(00)00327-4
20. Baer, T.; Song, Y.; Liu, J.; Chen, W.; Ng, C. Y. *Faraday Discuss.* **2000,** *115,* 137–145. doi:10.1039/a909621c
21. Baer, T.; Sztáray, B.; Kercher, J. P.; Lago, A. F.; Bödi, A.; Skull, C.; Palathinkal, D. *Phys. Chem. Chem. Phys.* **2005,** *7,* 1507–1513. doi:10.1039/b502051d
22. Schüßler, T.; Deyerl, H.-J.; Dümmler, S.; Fischer, I.; Alcaraz, C.; Elhanine, M. *J. Chem. Phys.* **2003,** *118,* 9077–9080. doi:10.1063/1.1576387
23. Schüßler, T.; Roth, W.; Gerber, T.; Fischer, I.; Alcaraz, C. *Phys. Chem. Chem. Phys.* **2005,** *7,* 819–825. doi:10.1039/b414163f
24. Hemberger, P.; Steinbauer, M.; Schneider, M.; Fischer, I.; Johnson, M.; Bodi, A.; Gerber, T. *J. Phys. Chem. A* **2010,** *114,* 4698–4703. doi:10.1021/jp9068569
25. Hemberger, P.; Noller, B.; Steinbauer, M.; Fischer, I.; Alcaraz, C.; Cunha de Miranda, B. K.; Garcia, G. A.; Soldi-Lose, H. *J. Phys. Chem. A* **2010,** *114,* 11269–11276. doi:10.1021/jp104019d
26. Steinbauer, M.; Hemberger, P.; Fischer, I.; Bodi, A. *ChemPhysChem* **2011,** *12,* 1795–1797. doi:10.1002/cphc.201000892
27. Xing, X.; Reed, B.; Lau, K.-C.; Ng, C. Y.; Zhang, X.; Ellison, G. B. *J. Chem. Phys.* **2007,** *126,* 171101. doi:10.1063/1.2737443
28. Gasser, M.; Schulenburg, A. M.; Dietiker, P. M.; Bach, A.; Merkt, F.; Chen, P. *J. Chem. Phys.* **2009,** *131,* 014304. doi:10.1063/1.3157185
29. Gao, H.; Xu, Y.; Yang, L.; Lam, C.-S.; Wang, H.; Zhou, J.; Ng, C. Y. *J. Chem. Phys.* **2011,** *135,* 224304. doi:10.1063/1.3664864
30. Taatjes, C. A.; Hansen, N.; Osborn, D. L.; Kohse-Höinghaus, K.; Cool, T. A.; Westmoreland, P. R. *Phys. Chem. Chem. Phys.* **2008,** *10,* 20–34. doi:10.1039/b713460f
31. Cunha de Miranda, B. K.; Alcaraz, C.; Elhanine, M.; Noller, B.; Hemberger, P.; Fischer, I.; Garcia, G.; Soldi-Lose, H.; Gans, B.; Viera Mendez, L. A.; Boyé-Péronne, S.; Douin, S.; Zabka, J.; Botschwina, P. *J. Phys. Chem. A* **2010,** *114,* 4818–4830. doi:10.1021/jp909422q
32. Johnson, R. D. *J. Chem. Phys.* **1991,** *95,* 7108–7113. doi:10.1063/1.461387
33. Eiden, G. C.; Lu, K.-T.; Badenhoop, J.; Weinhold, F.; Weisshaar, J. C. *J. Chem. Phys.* **1996,** *104,* 8886–8895. doi:10.1063/1.471624
34. Spangenberg, D.; Imhof, P.; Kleinermanns, K. *Phys. Chem. Chem. Phys.* **2003,** *5,* 2505–2514. doi:10.1039/b301228j
35. *Gaussian 09,* Revision B.01; Gaussian, Inc.: Wallingford, CT, 2010.
36. Houle, F. A.; Beauchamp, J. L. *J. Am. Chem. Soc.* **1978,** *100,* 3290–3294. doi:10.1021/ja00479a005
37. Roth, W. R.; Hunold, F.; Neumann, M.; Bauer, F. *Liebigs Ann.* **1996,** 1679–1690. doi:10.1002/jlac.199619961029
38. DeFrees, D. J.; McIver, R. T., Jr.; Hehre, W. J. *J. Am. Chem. Soc.* **1980,** *102,* 3334–3338. doi:10.1021/ja00530a005
39. Wörner, H. J.; Merkt, F. *Angew. Chem., Int. Ed.* **2005,** *45,* 293–296. doi:10.1002/anie.200503032
40. Sztáray, B.; Bodi, A.; Baer, T. *J. Mass Spectrom.* **2010,** *45,* 1233. doi:10.1002/jms.1813
41. Shin, S. K. *Chem. Phys. Lett.* **1997,** *280,* 260–265. doi:10.1016/S0009-2614(97)01145-7
42. Nunes, P. M.; Agapito, F.; Cabral, B. J. C.; dos Santos, R. M. B.; Simões, J. A. M. *J. Phys. Chem. A* **2006,** *110,* 5130–5134. doi:10.1021/jp060325n
43. Stull, D. R.; Prophet, H. *JANAF Thermochemical tables,* 2nd ed.; Midland: Michigan, 1971.
44. Shao, Y.; Molnar, L. F.; Jung, Y.; Kussmann, J.; Ochsenfeld, C.; Brown, S. T.; Gilbert, A. T. B.; Slipchenko, L. V.; Levchenko, S. V.; O'Neill, D. P.; DiStasio, R. A., Jr.; Lochan, R. C.; Wang, T.; Beran, G. J. O.; Besley, N. A.; Herbert, J. M.; Lin, C. Y.; Voorhis, T. V.; Chien, S. H.; Sodt, A.; Steele, R. P.; Rassolov, V. A.; Maslen, P. E.; Korambath, P. P.; Adamson, R. D.; Austin, B.; Baker, J.; Byrd, E. F. C.; Dachsel, H.; Doerksen, R. J.; Dreuw, A.; Dunietz, B. D.; Dutoi, A. D.; Furlani, T. R.; Gwaltney, S. R.; Heyden, A.; Hirata, S.; Hsu, C.-P.; Kedziora, G.; Khalliulin, R. Z.; Klunzinger, P.; Lee, A. M.; Lee, M. S.; Liang, W.; Lotan, I.; Nair, N.; Peters, B.; Proynov, E. I.; Pieniazek, P. A.; Rhee, Y. M.; Ritchie, J.; Rosta, E.; Sherrill, C. D.; Simmonett, A. C.; Subotnik, J. E.; Woodcock, H. L., III; Zhang, W.; Bell, A. T.; Chakraborty, A. K.; Chipman, D. M.; Keil, F. J.; Warshel, A.; Hehre, W. J.; Schaefer, H. F., III; Kong, J.; Krylov, A. I.; Gill, P. M. W.; Head-Gordon, M. *Phys. Chem. Chem. Phys.* **2006,** *8,* 3172–3191. doi:10.1039/b517914a
45. Nagy, A.; Fulara, J.; Garkusha, I.; Maier, J. P. *Angew. Chem., Int. Ed.* **2011,** *50,* 3022–3025. doi:10.1002/anie.201008036
46. Bodi, A.; Johnson, M.; Gerber, T.; Gengeliczki, Z.; Sztáray, B.; Baer, T. *Rev. Sci. Instrum.* **2009,** *80,* 034101. doi:10.1063/1.3082016

47. Johnson, M.; Bodi, A.; Schulz, L.; Gerber, T. *Nucl. Instrum. Methods Phys. Res., Sect. A* **2009,** *610,* 597–603. doi:10.1016/j.nima.2009.08.069
48. Bodi, A.; Sztáray, B.; Baer, T.; Johnson, M.; Gerber, T. *Rev. Sci. Instrum.* **2007,** *78,* 084102. doi:10.1063/1.2776012
49. Whitaker, B. J., Ed. *Imaging in Molecular Dynamics;* Cambridge University Press: Cambridge, 2003. doi:10.1017/CBO9780511535437
50. Sztáray, B.; Baer, T. *Rev. Sci. Instrum.* **2003,** *74,* 3763–3768. doi:10.1063/1.1593788
51. Kohn, D. W.; Clauberg, H.; Chen, P. *Rev. Sci. Instrum.* **1992,** *63,* 4003–4005. doi:10.1063/1.1143254

License and Terms

Beilstein Journal of Organic Chemistry

High-spin intermediates of the photolysis of 2,4,6-triazido-3-chloro-5-fluoropyridine

Sergei V. Chapyshev*[1], Denis V. Korchagin[1], Patrik Neuhaus[2] and Wolfram Sander[2]

Full Research Paper

Open Access

Address:
[1]Institute of Problems of Chemical Physics, Russian Academy of Sciences, 142432 Chernogolovka, Moscow Region, Russian Federation and [2]Lehrstuhl für Organische Chemie II, Ruhr-Universität, D-44780 Bochum, Germany

Email:
Sergei V. Chapyshev* - chapyshevs@mail.ru

* Corresponding author

Keywords:
azides; EPR spectroscopy; high-spin states; matrix isolation; nitrenes; photolysis; reactive intermediates

Beilstein J. Org. Chem. **2013,** *9,* 733–742.
doi:10.3762/bjoc.9.83

Received: 22 January 2013
Accepted: 21 March 2013
Published: 16 April 2013

This article is part of the Thematic Series "New reactive intermediates in organic chemistry".

Guest Editor: G. Bucher

Abstract

In contrast to theoretical expectations, the photolysis of 2,4,6-triazido-3-chloro-5-fluoropyridine in argon at 5 K gives rise to EPR peaks of just two triplet mononitrenes, two quintet dinitrenes, and a septet trinitrene. EPR spectral simulations in combination with DFT calculations show that observable nitrenes can be assigned to triplet 2,4-diazido-3-chloro-5-fluoropyridyl-6-nitrene (D_T = 1.026 cm^{-1}, E_T = 0), triplet 2,6-diazido-3-chloro-5-fluoropyridyl-4-nitrene (D_T = 1.122 cm^{-1}, E_T = 0.0018 cm^{-1}), quintet 4-azido-3-chloro-5-fluoropyridyl-2,6-dinitrene (D_Q = 0.215 cm^{-1}, E_Q = 0.0545 cm^{-1}), quintet 2-azido-3-chloro-5-fluoropyridyl-4,6-dinitrene (D_Q = 0.209 cm^{-1}, E_Q = 0.039 cm^{-1}) and septet 3-chloro-5-fluoropyridyl-2,4,6-trinitrene (D_S = −0.1021 cm^{-1}, E_S = −0.0034 cm^{-1}). Preferential photodissociation of the azido groups located in *ortho*-positions to the fluorine atom of pyridines is associated with strong π-conjugation of these groups with the pyridine ring. On photoexcitation, such azido groups are more efficiently involved in reorganization of the molecular electronic system and more easily adopt geometries of the locally excited predissociation states.

Introduction

High-spin nitrenes are highly reactive intermediates formed during photolysis or thermolysis of aromatic polyazides. Both these processes are widely used in modern science and technology [1-6]. When aromatic polyazides contain nonequivalent azido groups, these groups can undergo selective photolysis, providing important information about the selective cleavage of chemical bonds in organic molecules with light. The direction and selectivity of such processes can be monitored with EPR spectroscopy allowing the reliable identification of isomeric high-spin nitrenes [7-10]. Thus, previous EPR studies have

shown that irradiation of triazide **1a** with light at λ = 313 nm selectively gave quintet dinitrene **4a** as the major intermediate product (Scheme 1) [7,8]. Most recently, a similar selectivity was observed during the photolysis of triazide **1b** where quintet dinitrene **4b** was the major intermediate product (Scheme 1) [9]. By contrast, the photolysis of triazide **7** occurs selectively on the azido group located on the γ-phenyl ring, yielding dinitrene **9** as a single quintet intermediate (Scheme 1) [10]. All these photochemical studies became possible owing to extensive EPR investigations of various high-spin nitrenes in the past two decades [11-31]. Nowadays, the EPR spectral identification of high-spin nitrenes is based on comparison of their zero-field splitting (ZFS) parameters derived from experimental EPR spectra and calculated by quantum chemistry methods. The most accurate theoretical estimations are obtained at the PBE/DZ level of theory, which overestimates the experimental ZFS values of nitrenes by only about 10% [32]. This accuracy of calculations is sufficient for reliable identification of isomeric dinitrenes **4a**–**c** and **5a**–**c** formed during the photolysis of triazides **1a**–**c** (Scheme 1). Although these dinitrenes show nearly the same D_Q values (≈0.21 cm^{-1}), the E_Q values of **4a**–**c** and **5a**–**c** differ significantly (E_{Q4} ≈ 0.055 cm^{-1}, E_{Q5} ≈ 0.040 cm^{-1}), thus allowing one to unambiguously discriminate such isomers [29-31].

A new level of complexity is the EPR identification of high-spin intermediates formed during the photolysis of asymmetric triazides such as **11** (Scheme 2). Theoretically, the photolysis of triazide **11** may give three triplet nitrenes **12**–**14**, three quintet dinitrenes **15**–**17**, and septet trinitrene **18**. So far, no attempt was undertaken to discriminate such structurally alike isomers as quintet dinitrenes **16** and **17**.

In the present work, we report on matrix isolation and EPR studies of high-spin intermediates formed during the photolysis of asymmetric triazide **11**, providing the first information about selective photochemical decomposition of three nonequivalent azido groups in monocyclic aromatic compounds.

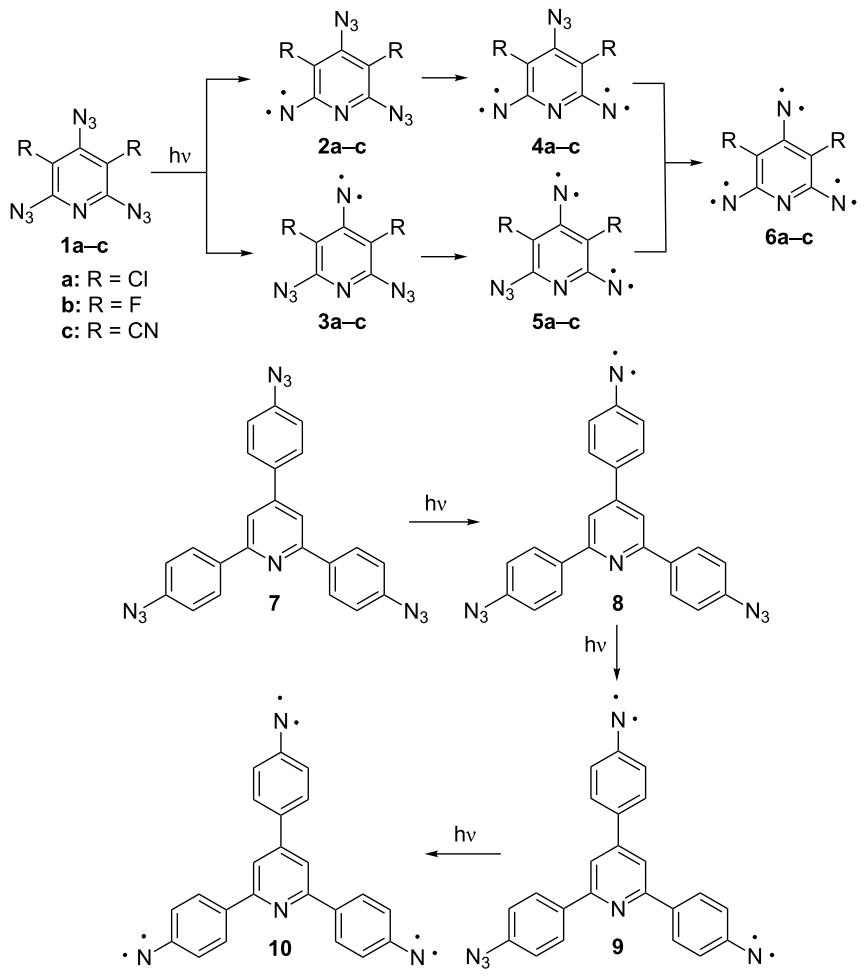

Scheme 1: Examples of selective photolysis of the azido groups.

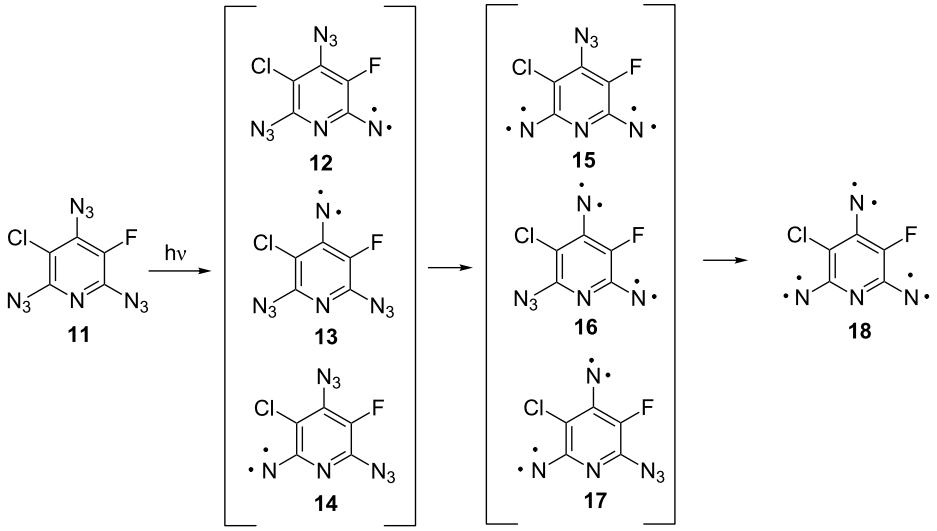

Scheme 2: Possible photoproducts of triazide **11**.

Results and Discussion

Brief UV irradiation (2 min, λ = 260–320 nm) of triazide **11** in the argon matrix leads to the appearance of just two strong EPR signals of triplet nitrenes at 6985 and 7217 G as well as weak Y_2-transitions of quintet dinitrenes at 3077 and 3337 G. Upon more extended irradiation, new signals in the 30–7000 G region appear due to gradual accumulation of high-spin nitrenes. The intensities of these signals reached their maximum values after 45 min of irradiation and then gradually decayed upon further irradiation. The EPR spectrum recorded after 45 min of irradiation is shown in Figure 1b.

The EPR spectral simulations show that the products of the reaction are two triplet nitrenes with D_T = 1.026 cm^{-1}, E_T = 0 cm^{-1} and D_T = 1.122 cm^{-1}, E_T = 0.0018 cm^{-1}, two quintet dinitrenes with D_Q = 0.209 cm^{-1}, E_Q = 0.039 cm^{-1} and D_Q = 0.215 cm^{-1}, E_Q = 0.0545 cm^{-1}, and a septet trinitrene with D_S = −0.1021 cm^{-1}, E_S = −0.0034 cm^{-1} in a 14:12:20:5:1 ratio (Figure 1a). Surprisingly, the ZFS parameters of quintet and septet nitrenes formed in the reaction were very close to the magnetic parameters of previously studied quintet dinitrenes **4c** (D_Q = 0.210 cm^{-1}, E_Q = 0.039 cm^{-1}) and **5c** (D_Q = 0.209 cm^{-1}, E_Q = 0.0542 cm^{-1}) and septet trinitrene **6c** (D_S = −0.1011 cm^{-1}, E_S = −0.0043 cm^{-1}) [31]. The EPR spectra of such nitrenes, including the complete assignment of all transitions, have been reported previously [29-31]. Quintet and septet nitrenes formed during the photolysis of triazide **11** display very similar EPR spectra.

The septet product formed in the reaction can be safely assigned to trinitrene **18** since only this trinitrene has a septet spin state. According to EPR spectral simulations (Figure 1a), this trini-

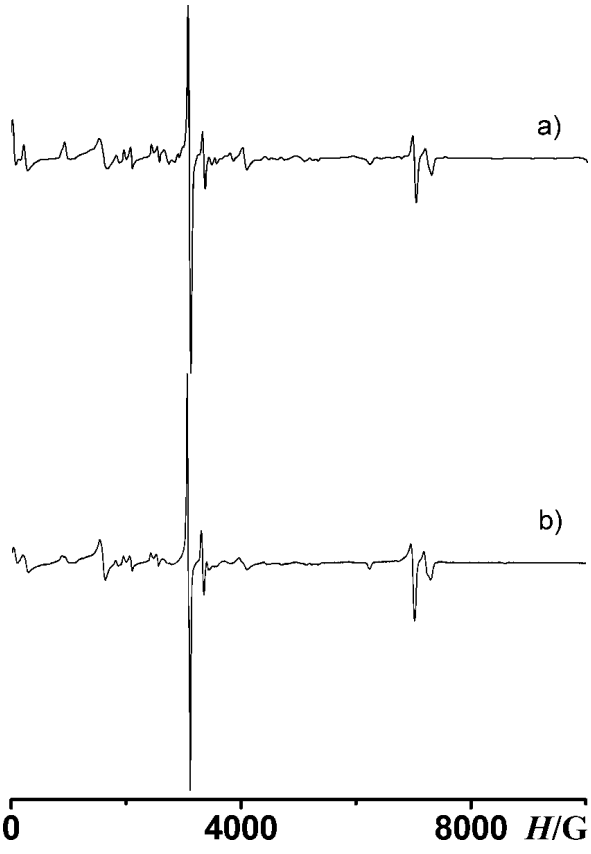

Figure 1: EPR spectra: (a) simulated spectrum for a mixture of five nitrenes with (i) S = 1, g = 2.003, D_T = 1.026 cm^{-1} and E_T = 0; (ii) S = 1, g = 2.003, D_T = 1.122 cm^{-1} and E_T = 0.0018 cm^{-1}; (iii) S = 2, g = 2.003, D_Q = 0.209 cm^{-1}, E_Q = 0.039 cm^{-1}; (iv) S = 2, g = 2.003, D_Q = 0.215 cm^{-1}, E_Q = 0.0545 cm^{-1}; (v) S = 3, g = 2.003, D_S = –0.1021 cm^{-1}, E_S = –0.0034 cm^{-1} in a 14:12:20:5:1 ratio; (b) experimental spectrum after 45 min of UV irradiation of triazide **11**. Microwave frequency ν_0 = 9.605832 GHz.

trene is formed in ca. 2% yield. Due to different substituents in positions 3 and 5 of the pyridine ring, trinitrene **18** has different angles Θ_1, Θ_2, Θ_3 between the nitrene C–N bonds and different Mulliken spin populations on the nitrene units (Table 1). Theoretically, such asymmetric trinitrenes should show rather large E_S values [30]. Nevertheless, the E_S value of trinitrene **18** is even smaller than that of C_{2v} symmetric trinitrene **6c** [31]. DFT calculations show that trinitrene **18**, on comparison with C_{2v} symmetric trinitrenes **6a-c**, has slightly different orientations of the principal magnetic axes due to the presence of only one heavy chlorine atom. Thus, the principal axes $\boldsymbol{D_{XX}}^{\mathbf{SS}}$ and $\boldsymbol{D_{XX}}^{\mathbf{Tot}}$ of C_{2v} symmetric trinitrene **6a** were directed along the line connecting the nitrene units in positions 2 and 6 of the pyridine ring and were parallel to the $\boldsymbol{D_{ZZ}}^{\mathbf{SO}}$ axis of the spin–orbit tensor $\boldsymbol{D}^{\mathbf{SO}}$ connecting two heavy chlorine atoms in positions 3 and 5 of the pyridine ring [30]. In the case of trinitrene **18**, the $\boldsymbol{D_{ZZ}}^{\mathbf{SO}}$ axis of the spin-orbit tensor $\boldsymbol{D}^{\mathbf{SO}}$ almost coincides with the C(3)–Cl bond (Figure 2). As a result, the principal axis $\boldsymbol{D_{XX}}^{\mathbf{Tot}}$ in trinitrene **18** is turned away from the line connecting the α-nitrene units by about 4°.

Previous studies of nitrenes **6a–c** have shown that the most accurate theoretical evaluations of D_S and E_S by the DFT approach were obtained by using the PBE and BLYP functionals in combination with the DZ or EPRII basis sets [32]. Extensive DFT calculations performed in the present work show that the best agreement between the experiment and theory is observed at the BLYP/EPRII level of theory, overestimating the experimental D_S and E_S values of trinitrene **18** by only 6% (Table 2). The breakdown of D_S and E_S into D^{SS}, D^{SO}, E^{SS}, and E^{SO} reveals that the BLYP/EPRII calculations are especially good in estimations of the spin–orbit coupling contributions E^{SO} to the small parameters E_S of septet trinitrenes (Table 3).

By analogy with previous studies of dinitrenes **5a–c** [29-31], the quintet molecule with $D_Q = 0.215$ cm^{-1} and $E_Q = 0.0545$ cm^{-1} can safely be assigned to dinitrene **15** with $\Theta = 115.7°$. Thus, for instance, quintet dinitrene **5a** showed $D_Q = 0.202$ cm^{-1} and $E_Q = 0.0554$ cm^{-1} [30], and its difluoro-derivative **5b** displayed $D_Q = 0.213$ cm^{-1} and $E_Q = 0.0556$ cm^{-1} [29]. The most accurate theoretical estimations of the magnetic parameters in dini-

Table 1: Mulliken spin populations ρ_N on the nitrene units and dipolar angles Θ between the nitrene C–N/C–N bonds in high-spin nitrenes **15**–**18**.

Parameter	Nitrene			
	15	**16**	**17**	**18**
ρ_N	1.63 (2N) 1.62 (6N)	1.55 (4N) 1.53 (6N)	1.53 (2N) 1.55 (4N)	1.62 (2N) 1.54 (4N) 1.63 (6N)
Θ [°]	115.7 (2N/6N)	121.6 (4N/6N)	125.4 (2N/4N)	124.8 (2N/4N) 121.2 (4N/6N) 113.9 (2N/6N)

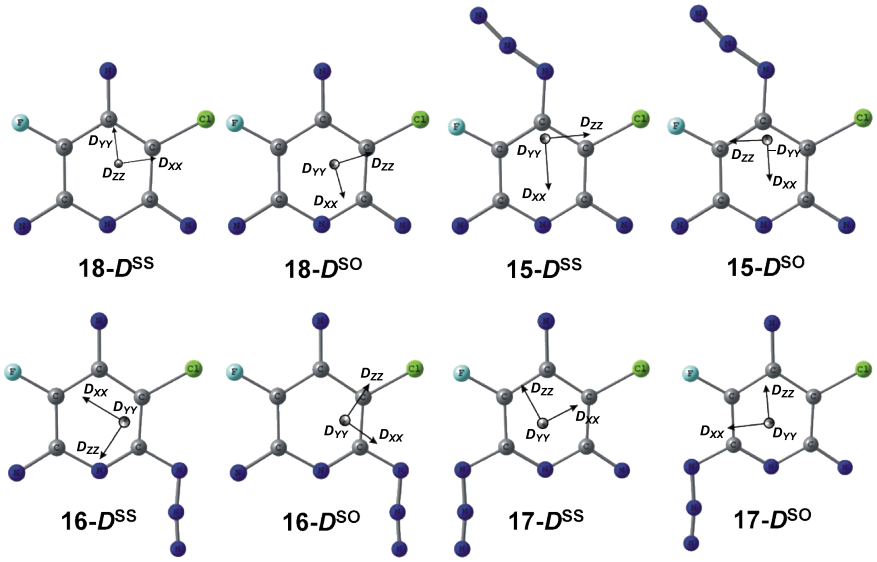

Figure 2: UB3LYP/6-311G*+BLYP/EPRII calculated orientations of the tensors $\boldsymbol{D}^{\mathbf{SS}}$ and $\boldsymbol{D}^{\mathbf{SO}}$ in nitrenes **15**–**18**. The tensors $\boldsymbol{D}^{\mathbf{SS}}$ and $\boldsymbol{D}^{\mathbf{Tot}}$ have the same orientations.

Table 2: DFT calculated and experimental parameters D/E in cm^{-1} of nitrenes **15**–**18**.

Method	D/E of **15**	D/E of **16**	D/E of **17**	D/E of **18**
PBE/TZV	—	—	—	−0.1122/−0.0044
PBE/6-311+G*	—	—	—	−0.1104/−0.0044
BLYP/DZ	0.2249/0.0610	0.2302/0.0398	0.2304/0.0422	−0.1116/−0.0045
PBE/DZ	0.2226/0.0609	0.2279/0.0400	0.2303/0.0416	−0.1108/−0.0046
PBE/EPRII	0.2261/0.0574	0.2265/0.0369	0.2289/0.0387	−0.1089/−0.0042
BLYP/EPRII	0.2259/0.0572	0.2270/0.0366	0.2269/0.0394	−0.1090/−0.0036
Experiment	0.2150/0.0545	0.2090/0.0390	—	−0.1021/−0.0034

Table 3: DFT calculated parameters D^{SS}/E^{SS} and D^{SO}/E^{SO} in cm^{-1} of nitrenes **15**–**18**.

Nitrene	Method	D^{SS}/E^{SS}	D^{SO}/E^{SO}
15	PBE/DZ	0.201/0.059	0.021/0.002
	PBE/EPRII	0.204/0.055	0.022/0.002
	BLYP/EPRII	0.202/0.055	0.024/0.002
16	PBE/DZ	0.212/0.040	0.016/0.001
	PBE/EPRII	0.211/0.036	0.016/0.001
	BLYP/EPRII	0.209/0.035	0.018/0.001
17	PBE/DZ	0.229/0.034	0.002/0.007
	PBE/EPRII	0.227/0.031	0.002/0.007
	BLYP/EPRII	0.226/0.030	0.002/0.007
18	PBE/DZ	−0.1031/−0.0078	−0.008/0.003
	PBE/EPRII	−0.1007/−0.0074	−0.008/0.003
	BLYP/EPRII	−0.0996/−0.0075	−0.009/0.004

trene **5a**–**c** were obtained by using the PBE/DZ calculations [32]. Such calculations are also the most accurate for estimations of D_Q in dinitrene **15** (Table 2). The theoretical value of D_Q = 0.2226 cm^{-1} obtained from the PBE/DZ calculations overestimates the experimental D_Q value in dinitrene **15** by just 3.5%. On the other hand, as in the case with trinitrene **18**, the BLYP/EPRII calculations predict the most realistic value of E_Q = 0.0572 cm^{-1} in dinitrene **15** (Table 2). According to EPR spectral simulations, dinitrene **15** is formed in the photolysis of triazide **11** in only ca. 10% yield.

The major quintet product of the reaction is the dinitrene with D_Q = 0.209 cm^{-1} and E_Q = 0.039 cm^{-1} (38%). This dinitrene can be assigned either to dinitrene **16** or to dinitrene **17**. Previous EPR studies have shown that quintet dinitrenes with Θ = 121 ± 1° displayed E_Q = 0.04 ± 0.001 cm^{-1}, and dinitrenes with Θ = 125 ± 1° showed E_Q = 0.035 ± 0.001 cm^{-1} [21,29-31]. According to DFT calculations, the dipolar angles Θ in dinitrenes **16** and **17** are equal to 121.6° and 125.4°, respectively (Table 1). These data suggest that the dinitrene with E_Q = 0.039 cm^{-1} can safely be assigned to dinitrene **16**. The most realistic theoretical estimation of E_Q in dinitrene **16** is obtained from PBE/DZ calculations of the spin–spin interaction parameter E_Q^{SS} (Table 3). This fact indicates that the contribution of the spin–orbit interactions to the total parameter E_Q of dinitrene **16** is quite small, as is typical for most of quintet dinitrenes [32].

Although we do not observe diagnostic signals of dinitrene **17** in the experimental EPR spectrum, this dinitrene may be a minor product of the photolysis of triazide **11**. Extensive EPR spectral simulations show that five other quintet molecules with E_Q/D_Q = 0.038/0.213, 0.037/0.217, 0.036/0.221, 0.035/0.225 and 0.034/0.229 also display intense Y_2 transitions at 3077 G beside dinitrene **16** with E_Q/D_Q = 0.039/0.209. In EPR spectra of individual molecules, these six quintet species are easily identified owing to different positions of their Z_1, X_1, X_2, Z_2, A_1 and A_2 transitions (See Supporting Information File 1). However, when the mixture of dinitrenes **16** and **17** is formed, isomer **17** becomes detectable in EPR spectra only at relatively high concentrations (>5%). Thus, for instance, in EPR spectra of two quintet molecules with E_Q/D_Q = 0.039/0.209 and 0.038/0.213, the minor component with E_Q/D_Q = 0.038/0.213 becomes visible when its ratio to the major component exceeds

1:6 (14%). Based on these data, we do not exclude that dinitrene **17** with $E_Q/D_Q \approx 0.036/0.221$ may be formed in ca. 5% yield along with dinitrene **16** (≈33%) during the photolysis of triazide **11**.

Theoretically, several triplet mononitrenes can be formed during the photolysis of triazide **11** (Figure 3). As a rule, triplet pyridyl-2-nitrenes show D_T = 1.03 ± 0.02 cm^{-1} and $E_T \approx$ 0 cm^{-1}, while triplet pyridyl-4-nitrenes show D_T = 1.13 ± 0.02 cm^{-1} and $E_T \approx 0$ cm^{-1} [29-31]. When chlorine atoms are set in *ortho*-positions to the nitrene center, such triplet pyridylnitrenes show $E_T > 0.003$ cm^{-1} [30]. Since one of triplet mononitrenes obtained in the present work shows D_T = 1.026 cm^{-1} and $E_T = 0$ cm^{-1}, this nitrene can safely be assigned to **12** (Scheme 2). Another triplet mononitrene shows a D_T = 1.122 cm^{-1} typical for pyridyl-4-nitrenes and a small parameter $E_T = 0.0018$ cm^{-1} that is characteristic for triplet nitrenes with one chlorine atom in an *ortho*-position to the nitrene center. This mononitrene can safely be assigned to **13**. According to EPR spectral simulations, triplet nitrenes **12** and **13** are formed in 27 and 23% yield, respectively. DFT calculations of the parameters D_T^{SS} agree well with the experiment, overestimating the D_T parameters of nitrenes **12** and **13** by just 2 and 3%, respectively (Figure 3). Unfortunately, as in the case of many other triplet mononitrenes [32], such calculations are too crude for estimations of the parameters E_T, predicting E_T = 0.006 ± 0.001 cm^{-1} for all isomers of **12**–**14**.

Recent EPR studies have shown that the best EPR spectral simulations for high-spin nitrenes were obtained only when an additional line-broadening parameter Γ(*E*) was used in the spin-Hamiltonian calculations [24]. The necessity of the use of this parameter in calculations is due to the presence in matrices of numerous conformational isomers of the starting azides. Upon UV irradiation, these conformers decompose to high-spin nitrenes that slightly differ each from other in the angles N–C–C and Θ and the parameters *E*. The formation of such high-spin nitrenes affects significantly the line-width and intensity of some lines in the experimental EPR spectra. Similar effects were also observed in EPR spectra of nitrenes **15**–**18**. In order to adequately reproduce the experimental EPR spectrum from Figure 1b, the line-broadening parameters Γ(*E*) = 75 MHz for dinitrenes **15** and **16** and Γ(*E*) = 40 MHz for trinitrene **18** were used in the spectral simulations. According to these values of Γ(*E*), the variations in the angles Θ for dinitrenes **15**/**16** and trinitrene **18** do not exceed 0.7° and 0.4°, respectively. Despite these very small variations in the angles Θ, all our attempts to theoretically reproduce the experimental EPR spectrum from Figure 1b without the use of the line-broadening parameters Γ(*E*) were unsuccessful. EPR spectra of nitrenes **15**, **16** and **18** simulated for Γ(*E*) = 0, 40 and 75 MHz are presented in Supporting Information File 1.

The results obtained show that almost all triplet and quintet nitrenes detected in the present study arise from the photolysis of the azido groups located in *ortho*-positions to the fluorine atom of pyridines. On comparison with the chlorine, the fluorine is a much more electron-negative and less bulky atom. Both of these factors favor strong π– conjugation of the *ortho*-azido groups with the pyridine ring. On photoexcitation, such azido groups should be more efficiently involved in reorganization of the molecular electronic system and more easily adopt geometries of the locally excited predissociation states [33,34]. DFT calculations show that namely azido groups located in positions 4 and 6 of triazide **11** have high localization of the lowest unoccupied molecular orbital (LUMO) density (see below in Figure 4). Similar localization of the LUMO density has previously been calculated for the azido group set on the γ-phenyl ring of triazide **7**, which underwent selective photolysis to form triplet nitrene **8** (Scheme 1) [10]. All these data indicate that of the three azido groups of triazide **11** the azido groups in *ortho*-positions to the fluorine atom should be the most photoactive.

The photodissociation of the azido groups in triazide **11** can be modeled by computational methods [8,34]. Thus, for instance,

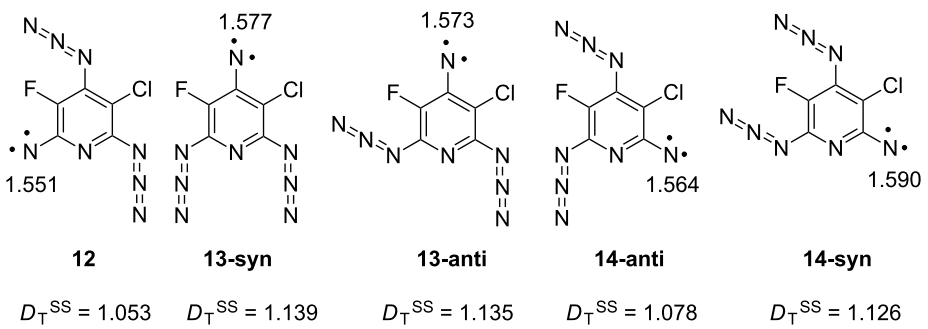

Figure 3: Mulliken spin populations on the nitrene units and parameters D_T^{SS} in cm^{-1} of triplet nitrenes **12**–**14** at the PBE/DZ level of theory.

the geometry optimizations of the most stable rotamers **11a** and **11b** in their lowest singlet excited states by using CIS/PM3 or CIS/6-311+G* calculations yield structures **11a**-S_1* and **11b**-S_1*, in which the azido groups in *ortho*-positions to the fluorine atom are locally excited (Scheme 3). These calculations confirm that the local excitation of such groups requires lower activation energies [8,34]. According to theory [34-36], the local excitation of the azido group during the photoexcitation results in considerable bending of the N=N=N fragment from about 171° to about 117° and appearance of the σ-type antibonding interactions in the N–N_2 bond. Figure 4 illustrates these effects for the structure **11a**-S_1*.

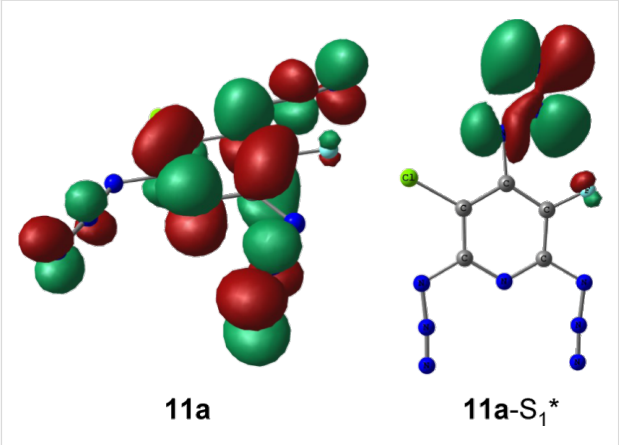

Figure 4: UB3LYP/6-311+G* orbital density in the LUMO of triazide **11** and CIS/6-311+G* orbital density in the highest singly occupied orbital of excited state **11a**-S_1*.

Thus, the first stage of the photolysis of triazide **11** in argon matrices involves the photochemical generation of excited states **11a**-S_1* and **11b**-S_1*, which then undergo dissociation of the locally excited azido groups to form triplet nitrenes **12** and **13** (Scheme 3). On the second stage, triplet nitrenes **12** and **13** are excited to triplet states **12a**-T_1*, **12b**-T_1* and **13a**-T_1* which then dissociate to quintet dinitrenes **15** and **16**. The latter is formed as the major product owing to efficient excitation of the azido groups located in *ortho*-positions to the fluorine atom of nitrenes **12** and **13**. The photoexcitation of the azido group in

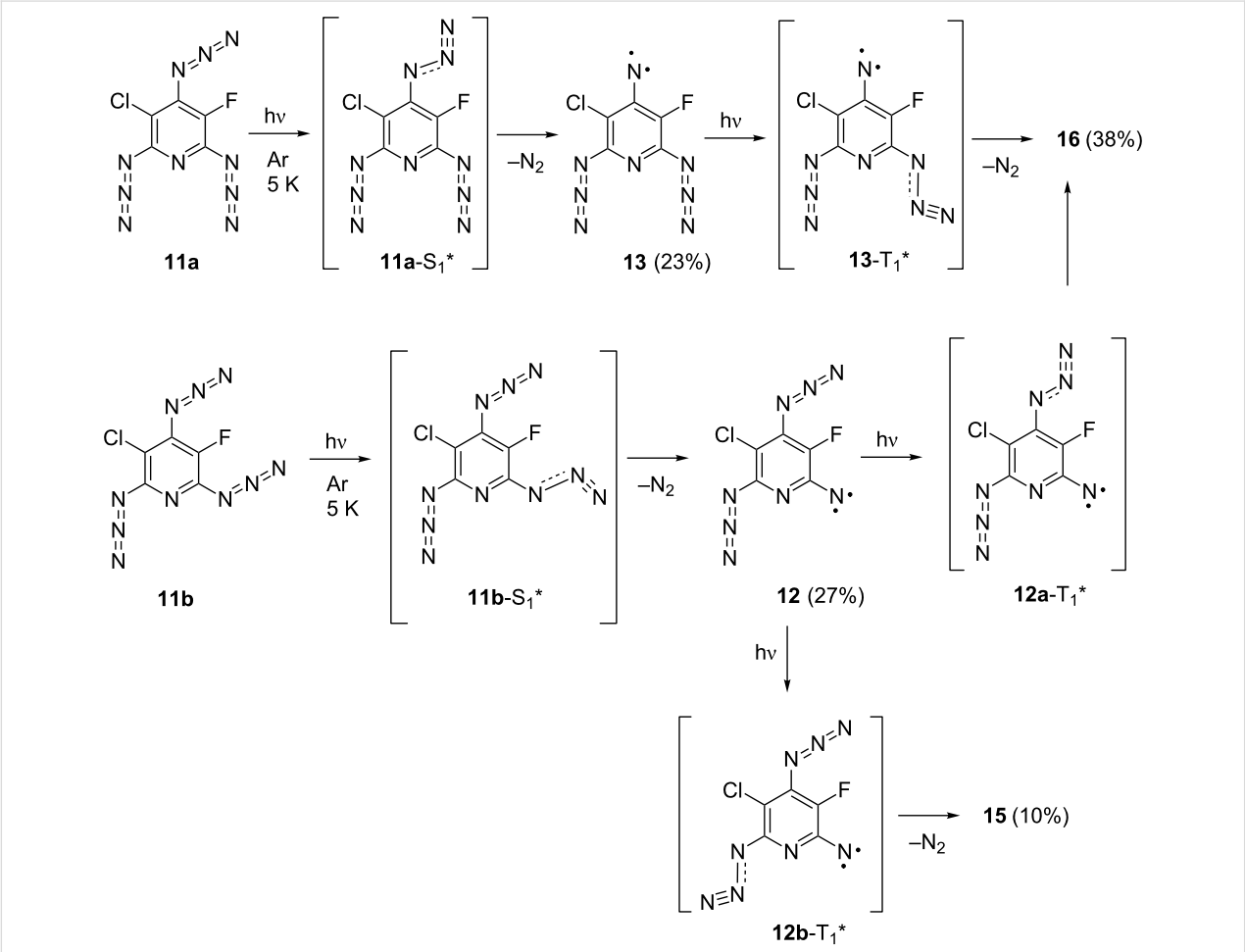

Scheme 3: Initial stages of the photolysis of triazide **11**.

position **2** of nitrene **12** is a less efficient process leading to the formation of dinitrene **15** in just about 10% yield. The photoexcitation of the azido group in position **2** of nitrene **13** is a still much less efficient process. Quintet dinitrene **17** either is not formed at all or its yield is very low (<6%). Finally, the photodecomposition of the remaining azido groups in dinitrenes **15** and **16** gives septet trinitrene **18** in just about 2% yield. The low yield of trinitrene **18** may be associated with low efficiency of the azido group excitation in quintet dinitrene **16**. One also cannot exclude that the photoexcitation of quintet azidonitrenes into predissociation states is a much less efficient process in comparison with the photoexcitation of singlet azides. In contrast to singlet azides, quintet azidonitrenes already have four singly occupied orbitals, and photoexcitation of these species may lead to excited states in which the azido groups are not locally excited.

Conclusion

In contrast to theoretical expectations, photodissociation of triazide **11** with light at λ = 260–320 nm occurs selectively on the azido groups located in positions 4 and 6 of the pyridine ring to give triplet mononitrenes **12** and **13** as the primary photoproducts. On further irradiation, quintet dinitrenes **15** and **16** and septet trinitrene **18** are formed. The maximum yield of the latter is about just 2%. Preferential photodissociation of the azido groups located in *ortho*-positions to the fluorine atom of pyridines is associated with strong π-conjugation of these groups with the pyridine ring. On photoexcitation, such azido groups are more efficiently involved in reorganization of the molecular electronic system and more easily adopt geometries of the locally excited predissociation states. Despite the lack of symmetry, trinitrene **18** shows a small parameter of E_S = −0.0034 cm^{-1} due to a large positive value of the spin-orbit coupling parameter E_S^{SO} (≈0.005 cm^{-1}). In overall, the ZFS parameters of **18** are very close to the ZFS parameters of previously studied C_{2v} symmetric septet pyridyl-2,4,6-trinitrenes. The most accurate theoretical predictions of the ZFS parameters of **18** are obtained at the BLYP/EPRII level of theory. At the same time, modern DFT calculations are still too crude to be used for reliable EPR spectral identification of such structurally alike quintet isomers as dinitrenes **16** and **17**. Such quintet isomers are better discriminated based on analysis of their dipolar angles Θ. Among theoretical approaches, the most accurate estimations of the ZFS parameters of dinitrene **16** are obtained from PBE/DZ calculations of its parameters D_S^{SS} and E_S^{SS}. The study also demonstrates that successful EPR spectral simulations for nitrenes **15**, **16** and **18** are possible only if additional line-broadening parameters Γ(E) of 40–75 MHz along with appropriate values of g, S, D, E and ν_0 are used in the spin-Hamiltonian calculations.

Experimental

Triazide **11** was synthesized according to the literature procedure [37]. X-band EPR spectra were recorded with a Bruker-Elexsys E500 EPR spectrometer with an ER077R magnet (75 mm gap between pole faces), an ER047 XG-T microwave bridge, and an ER4102ST resonator with a TE_{102} cavity. Solid argon matrices doped with triazide **11** were prepared by vacuum co-deposition of two separate molecular beams (Ar and triazide **11** vapor) on the tip of an oxygen-free high-conductivity copper rod (75 mm length, 3 mm diameter) cooled at 5 K. The vapor of **11** was produced by an oven heating the polycrystalline **11** to 60 °C. The matrix-isolated samples were irradiated with a high-pressure mercury lamp, by using a filter passing the light at λ = 260–320 nm, and spectra were recorded at various irradiation times.

The computer simulations of EPR spectra were performed by using the *EasySpin* program package (version 4.0.0) [38]. The simulations were performed by using matrix diagonalization methods for S = 1, 2 or 3 using the parameters ν_0 = 9.605832 GHz and g = 2.0023 and line widths ΔH = 60 G for S = 1, and 30 G for S = 2 and S = 3.

The geometries of the molecules were optimized at the B3LYP/6-311G(d) level of theory with the Gaussian 03 program package [39]. The nature of the stationary points was assessed by means of vibrational frequency analysis. The spin-Hamiltonian parameters (g, D, E) and orientations of the $\boldsymbol{D}$ tensor were obtained from additional single-point calculations with the ORCA program package [40,41]. DFT calculations of the direct spin–spin (SS) coupling D^{SS} and spin–orbit coupling (SO) D^{SO} parts of the $\boldsymbol{D}$ tensors were performed by using the McWeeny–Mizuno and Pederson–Khanna approaches, respectively [42].

Supporting Information

Supporting Information features EPR spectral simulations for quintet dinitrenes **15**–**17** and septet trinitrene **18** as individual species and for the mixtures of quintet molecules with E_Q/D_Q = 0.039/0.209, 0.038/0.213 and 0.036/0.221 at different molar ratios as well as EPR spectral simulations for nitrenes **15**, **16** and **18** at different values of the line-broadening parameter Γ(E).

Supporting Information File 1

EPR spectral simulations.
[http://www.beilstein-journals.org/bjoc/content/supplementary/1860-5397-9-83-S1.pdf]

Acknowledgements

This work was financially supported by the Deutsche Forschungsgemeinschaft, the Russian Foundation for Basic Research (grant RFBR 09-03-91330-DFG), the Russian Academy of Sciences (program OX-1) and the Fonds der Chemischen Industrie.

References

1. Bräse, S.; Banert, K., Eds. *Organic Azides: Synthesis and Applications;* Wiley-VCH: Chichester, U.K., 2010.
2. Scriven, F. F. V., Ed. *Azides and Nitrenes, Reactivity and Utility;* Academic Press: New York, USA, 1984.
3. Bräse, S.; Gil, C.; Knepper, K.; Zimmermann, V. *Angew. Chem., Int. Ed.* **2005,** *44,* 5188–5240. doi:10.1002/anie.200400657
4. Scriven, E. V. F.; Turnbull, K. *Chem. Rev.* **1988,** *88,* 297–368. doi:10.1021/cr00084a001
5. Chapyshev, S. V. *Synlett* **2009,** 1–8. doi:10.1055/s-0028-1087479
6. Chapyshev, S. V. *Russ. Chem. Bull.* **2011,** *60,* 1274–1285. doi:10.1007/s11172-011-0195-7
7. Chapyshev, S. V.; Walton, R.; Sanborn, J. A.; Lahti, P. M. *J. Am. Chem. Soc.* **2000,** *122,* 1580–1588. doi:10.1021/ja993131c
8. Chapyshev, S. V.; Walton, R.; Lahti, P. M. *Mendeleev Commun.* **2000,** *10,* 187–188. doi:10.1070/MC2000v010n05ABEH001308
9. Finke, C.; Grote, D.; Seidel, R. W.; Chapyshev, S. V.; Sander, W. *J. Phys. Org. Chem.* **2012,** *25,* 486–492. doi:10.1002/poc.1943
10. Chapyshev, S. V.; Korchagin, D. V.; Budyka, M. F.; Gavrishova, T. N.; Neuhaus, P.; Sander, W. *ChemPhysChem* **2012,** *13,* 2721–2728. doi:10.1002/cphc.201200200
11. Nimura, S.; Yabe, A. In *Magnetic Properties of Organic Materials;* Lahti, P. M., Ed.; Marcel Dekker: New York, 1999; pp 127–145.
12. Fukuzawa, T. A.; Sato, K.; Ichimura, A. S.; Kinoshita, T.; Takui, T.; Itoh, K.; Lahti, P. M. *Mol. Cryst. Liq. Cryst.* **1996,** *278,* 253–260. doi:10.1080/10587259608033683
13. Kalgutkar, R. S.; Lahti, P. M. *J. Am. Chem. Soc.* **1997,** *119,* 4771–4772. doi:10.1021/ja963723k
14. Chapyshev, S. V.; Walton, R.; Lahti, P. M. *Mendeleev Commun.* **2000,** *10,* 114–115. doi:10.1070/MC2000v010n03ABEH001281
15. Miura, Y.; Oka, H.; Teki, Y. *Bull. Chem. Soc. Jpn.* **2001,** *74,* 385–386. doi:10.1246/bcsj.74.385
16. Kalgutkar, R. S.; Lahti, P. M. *Tetrahedron Lett.* **2003,** *44,* 2625–2628. doi:10.1016/S0040-4039(03)00385-X
17. Chapyshev, S. V.; Tomioka, H. *Bull. Chem. Soc. Jpn.* **2003,** *76,* 2075–2089. doi:10.1246/bcsj.76.2075
18. Sato, T.; Narazaki, A.; Kawaguchi, Y.; Niino, H.; Bucher, G.; Grote, D.; Wolff, J. J.; Wenk, H. H.; Sander, W. *J. Am. Chem. Soc.* **2004,** *126,* 7846–7852. doi:10.1021/ja031794v
19. Chapyshev, S. V.; Walton, R.; Serwinski, P. R.; Lahti, P. M. *J. Phys. Chem. A* **2004,** *108,* 6643–6649. doi:10.1021/jp048764e
20. Chapyshev, S. V.; Lahti, P. M. *J. Phys. Org. Chem.* **2006,** *19,* 637–641. doi:10.1002/poc.1106
21. Chapyshev, S. V. *Russ. Chem. Bull.* **2006,** *55,* 1126–1131. doi:10.1007/s11172-006-0388-7
22. Chapyshev, S. V. *Russ. Chem. Bull.* **2006,** *55,* 1593–1597. doi:10.1007/s11172-006-0459-9
23. Misochko, E. Ya.; Akimov, A. V.; Chapyshev, S. V. *J. Chem. Phys.* **2008,** *128,* No. 124504. doi:10.1063/1.2840351
24. Koto, T.; Sato, K.; Shiomi, D.; Toyota, K.; Itoh, K.; Wasserman, E.; Takui, T. *J. Phys. Chem. A* **2009,** *113,* 9521–9526. doi:10.1021/jp9042717
25. Chapyshev, S. V.; Misochko, E. Ya.; Akimov, A. V.; Dorokhov, V. G.; Neuhaus, P.; Grote, D.; Sander, W. *J. Org. Chem.* **2009,** *74,* 7238–7244. doi:10.1021/jo9010848
26. Chapyshev, S. V. *Russ. J. Phys. Chem. A* **2009,** *83,* 254–259. doi:10.1134/S0036024409020186
27. Chapyshev, S. V.; Korchagin, D. V.; Budyka, M. F.; Gavrishova, T. N.; Neuhaus, P.; Sander, W. *J. Phys. Chem. A* **2011,** *115,* 8419–8425. doi:10.1021/jp203038k
28. Misochko, E. Ya.; Akimov, A. V.; Masitov, A. A.; Korchagin, D. V.; Yakushchenko, I. K.; Chapyshev, S. V. *J. Chem. Phys.* **2012,** *137,* No. 064308. doi:10.1063/1.4742342
29. Chapyshev, S. V.; Grote, D.; Finke, C.; Sander, W. *J. Org. Chem.* **2008,** *73,* 7045–7051. doi:10.1021/jo800425k
30. Misochko, E. Ya.; Akimov, A. V.; Chapyshev, S. V. *J. Chem. Phys.* **2008,** *129,* No. 174510. doi:10.1063/1.3005378
31. Chapyshev, S. V.; Neuhaus, P.; Grote, D.; Sander, W. *J. Phys. Org. Chem.* **2010,** *23,* 340–346. doi:10.1002/poc.1622
32. Misochko, E. Ya.; Korchagin, D. V.; Bozhenko, K. V.; Chapyshev, S. V.; Aldoshin, S. M. *J. Chem. Phys.* **2010,** *133,* No. 064101. doi:10.1063/1.3474574
33. Reiser, A.; Marley, R. *Trans. Faraday Soc.* **1968,** *64,* 1806–1815. doi:10.1039/TF9686401806
34. Korchagin, D. V.; Bozhenko, K. V.; Chapyshev, S. V.; Aldoshin, S. M. *High Energy Chem.* **2009,** *43,* 289–293. doi:10.1134/S0018143909040080
35. Budyka, M. F.; Zyubina, T. S. *J. Mol. Struct.* **1997,** *419,* 191–199. doi:10.1016/S0166-1280(97)00244-3
36. Budyka, M. F. *Russ. Chem. Rev.* **2008,** *77,* 709–723. doi:10.1070/RC2008v077n08ABEH003793
37. Chapyshev, S. V. *J. Fluorine Chem.* **2011,** *132,* 991–994. doi:10.1016/j.jfluchem.2011.07.012
38. Stoll, S.; Schweiger, A. *J. Magn. Reson.* **2006,** *178,* 42–55. doi:10.1016/j.jmr.2005.08.013
39. *Gaussian 03,* Revision D.01; Gaussian, Inc.: Wallingford, CT, 2004.
40. *ORCA, an ab initio, density functional and semiempirical program package,* Version 2.8.0.2; University of Bonn: Germany, 2011. The program was downloaded from http://cec.mpg.de/forum/
41. Neese, F. *Wiley Interdiscip. Rev.: Comput. Mol. Sci.* **2012,** *2,* 73–78. doi:10.1002/wcms.81
42. Neese, F. *J. Chem. Phys.* **2007,** *127,* No. 164112. doi:10.1063/1.2772857

Beilstein Journal of Organic Chemistry

3-Pyridylnitrene, 2- and 4-pyrimidinylcarbenes, 3-quinolylnitrenes, and 4-quinazolinylcarbenes. Interconversion, ring expansion to diazacycloheptatetraenes, ring opening to nitrile ylides, and ring contraction to cyanopyrroles and cyanoindoles

Curt Wentrup*[1], Nguyen Mong Lan[2], Adelheid Lukosch[3], Pawel Bednarek[1] and David Kvaskoff[1]

Full Research Paper

Open Access

Address:
[1]School of Chemistry and Molecular Biosciences, The University of Queensland, Brisbane, Qld 4072, Australia, [2]Institut de Chimie Organique, Université de Lausanne, CH-1009 Lausanne, Switzerland and [3]Fachbereich Chemie der Universität Marburg, D-3550 Marburg, Germany

Email:
Curt Wentrup* - wentrup@uq.edu.au

* Corresponding author

Keywords:
carbene-nitrene interconversion; diazepines; flash vacuum thermolysis; matrix photochemistry; nitrile ylides; reactive intermediates

Beilstein J. Org. Chem. **2013,** *9,* 743–753.
doi:10.3762/bjoc.9.84

Received: 31 January 2013
Accepted: 21 March 2013
Published: 17 April 2013

This article is part of the Thematic Series "New reactive intermediates in organic chemistry".

Guest Editor: G. Bucher

Abstract

Precursors of 3-pyridylnitrene and 2- and 4-pyrimidinylcarbenes all afford mixtures of 2- and 3-cyanopyrroles on flash vacuum thermolysis, but 3-cyanopyrroles are the first-formed products. 3-Quinolylnitrenes and 4-quinazolinylcarbenes similarly afford 3-cyanoindoles. 2-Pyrimidinylcarbenes rearrange to 3-pyridylnitrenes, but 4-pyrimidinylcarbenes and 4-quinazolinylcarbenes do not necessarily rearrange to the corresponding 3-pyridylnitrenes or 3-quinolylnitrenes. The ring contraction reactions are interpreted in terms of ring opening of either the nitrenes or the diazacycloheptatetraenes to nitrile ylides.

Introduction

A multitude of rearrangements of heterocyclic nitrenes have been described in a recent review [1] and in several books [2-5]. This is illustrated by the ring expansion of 4-pyridylnitrene (**1**) and 2-pyrazinylcarbene (**3**) to 1,5-diazacyclohepta-1,2,4,6-tetraene (**2**, Scheme 1) [6]. Similarly, 2-pyridylnitrene (**4**) interconverts with 1,3-diazacyclohepta-1,2,4,6-tetraene (**5**) under conditions of photolysis in solution or in matrices as well as under flash vacuum thermolysis (FVT) (Scheme 2) [1,7-10].

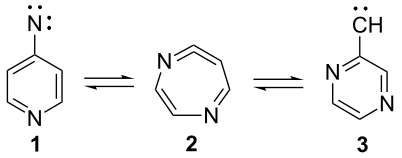

Scheme 1: 4-Pyridylnitrene–2-pyrazinylcarbene interconversion.

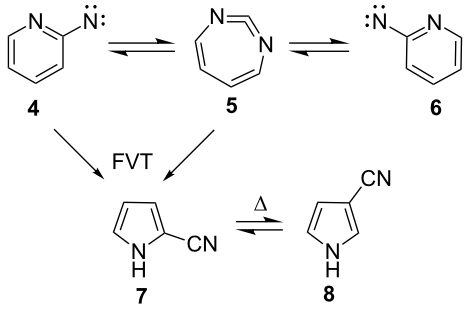

Scheme 2: Ring expansion and ring contraction in 2-pyridylnitrene (**4**).

The end products under FVT conditions are the 2- and 3-cyanopyrroles **7** and **8** [10,11]. A competing ring-opening of 2-pyridylnitrenes to cyanobutadienylnitrenes can lead to the formation of glutacononitriles in low yields [12].

In contrast, 3-pyridylnitrene (**10**) undergoes a different type of ring opening to the observable nitrile ylide **11** and subsequently the ketenimine **12** (Scheme 3) [13]. Nitrile imines [14] and nitrile ylides [15,16] may have either allenic or propargylic structures, and for this reason their cumulene-type IR absorptions can occur over a wide frequency range, 1900–2300 cm^{-1}, depending on substituents. The IR absorption of **11** was observed at 1961 cm^{-1}, indicating an allenic structure. Nitrene **10** can also undergo ring expansion to two diazacycloheptatetraenes **15** and **16** via the azirenes **13** and **14** (Scheme 3) [13]. The diazacycloheptatetraenes were not observed directly in this study, but aza- and diazacycloheptatetraenes have been observed in several other cases [1,17,18] and the ring-expansion reactions have been the subject of detailed theoretical investigation [19].

Results and Discussion

3-Pyridylnitrene

Flash vacuum thermolysis (FVT) of 3-azidopyridine (**9**) yields predominantly 3-cyanopyrrole (**8**, Scheme 4). Under the mildest conditions, FVT of **9** at 370 °C/10^{-3} mbar generates **8** and **7** in a 3:1 ratio. A temperature increase to 500 °C causes the ratio to drop to 1.2:1 due to the thermal interconversion of **7** and **8** [10,20]. The reaction mechanism was probed by calculations at

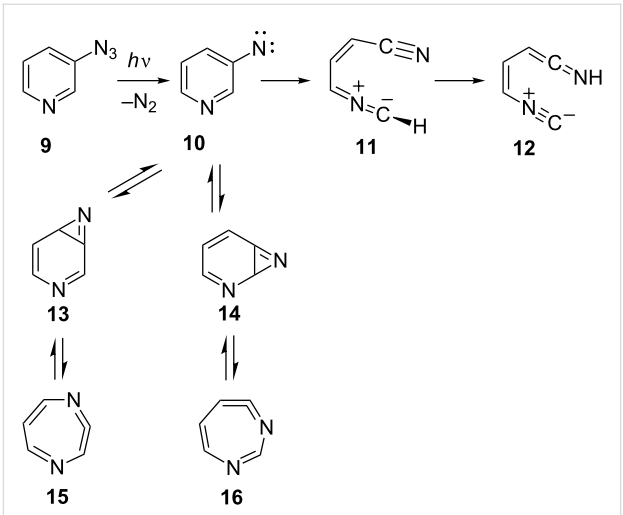

Scheme 3: Ring opening and ring expansion in 3-pyridylnitrene (**10**).

the B3LYP/6-31G* level, which has been found to be adequate for other, similar reactions [11,13,17,21]. The transition state for the ring opening of the cyclic ketenimine **16** to the (s,*Z*)-nitrile ylide **11** lies 5 kcal/mol above the open shell singlet nitrene S_1 **10**, i.e., the barrier is only 11 kcal/mol above the cyclic ketenimine **16**. This is lower than the barrier for direct ring opening of the nitrene **10** itself (16 kcal/mol) (Scheme 4 and Figure 1) [13]. Thus, while both the nitrene **10** and the ketenimine **16** may undergo ring opening with rather low activation barriers, the ring opening of the ketenimine has the lowest barrier. Both of these reactions can take place with ease under conditions of FVT.

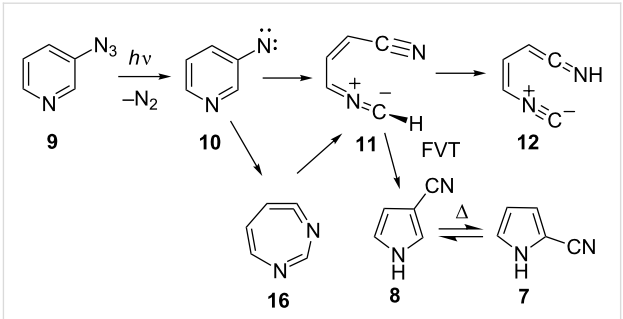

Scheme 4: Ring opening and ring contraction in 3-pyridylnitrene (**10**) and diazacycloheptatetraene **16**.

With a low barrier for ring opening, recyclization of the nitrile ylide **11** now becomes the energetically most favourable mechanism of formation of 3-cyanopyrrole (**8**) via the 3*H* tautomer **18** with a barrier of only 10 kcal/mol above the S_1 nitrene or 16 kcal/mol above the nitrile ylide (Scheme 4 and Figure 1). This explains why 3-cyanopyrrole (**8**) is the predominant isomer, in contrast to the reaction of 2-pyridylnitrene, where 2-cyano-

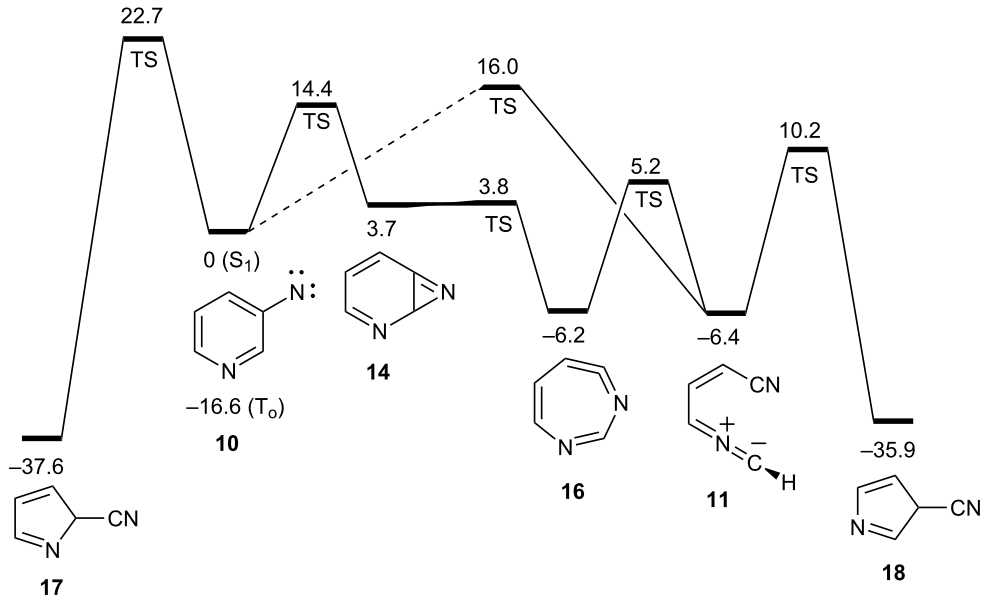

Figure 1: Energy profile for the ring opening and ring contraction in 3-pyridylnitrene **10** and 1,6-diazacyclohepta-1,2,4,6-tetraene (**16**, energies in kcal/mol at the B3LYP/6-31G* level).

pyrrole is formed preferentially [11]. In the analogous case of 3-quinolylnitrene, 3-cyanoindole is formed exclusively under mild FVT conditions [21]. A direct, concerted ring contraction in 3-pyridylnitrene would be possible (via **17** and **18**, Scheme 5), but such reactions have considerably higher activation barriers, ca. 30 kcal/mol in the case of phenylnitrene [22]. A transition state for the concerted ring contraction of 3-pyridylnitrene (**10**) to 3*H*-3-cyanopyrrole (**18**) was not found, but we calculate a barrier of 23 kcal/mol for the concerted ring contraction to 2-cyano-2*H*-pyrrole (**17**, Figure 1). Furthermore, a higher proportion of 2-cyanopyrrole would be expected if Scheme 5 was operating. Concerted ring contraction in the 7-membered ring ketenimine **16** is also possible [22], but this type of reaction has an even higher activation energy. The lowest-energy path for (di)azacycloheptatetraenes to undergo ring contraction is by ring opening.

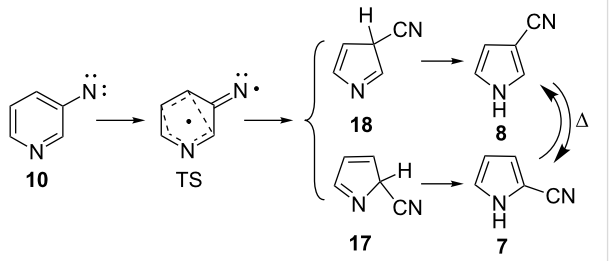

Scheme 5: Potential direct ring contraction in 3-pyridylnitrene (**10**).

The nitrile ylide **11** is not directly observable under FVT conditions, because the barriers for its reactions are very low. The calculated barrier for cyclization to 3-cyano-3*H*-pyrrole (**18**) is 16 kcal/mol (Scheme 6 and Figure 1).

2- and 4-pyrimidinylcarbenes

FVT of tetrazolylpyrimidines of type **19** causes elimination of N_2 to generate 4- and 2-diazomethylpyrimidines **20**, which can ring-close to the corresponding 1,2,3-triazolopyrimidines **21** (Scheme 7) [23]. Endothermic ring-chain valence isomerization of the type **21** → **20**, with free energies of activation of 18–22 kcal/mol in solution, has been demonstrated for 1,2,3-triazolo[1,5-*a*]pyrimidines [24] but not for 1,2,3-triazolo[1,5-*c*]pyrimidines [25,26]. However, 7-benzyl-3-ethoxycarbonyl-

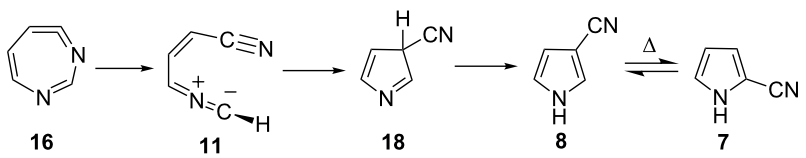

Scheme 6: Ring contraction by ring opening to nitrile ylide **11**.

1,2,3-triazolo[1,5-*c*]pyrimidin-5-ol and its diazo valence tautomer, 6-(2-diazoethoxycarbonylmethylene)-2-(α-hydroxybenzyl)pyrimidin-4-(2*H*)-one, have been reported [27].

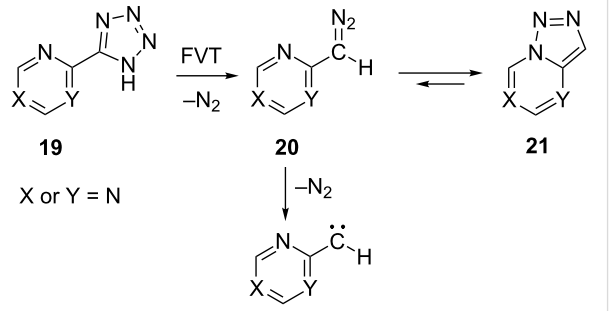

Scheme 7: Generation of pyrimidinyldiazomethanes and pyrimidinylcarbenes.

We find that FVT of the 4- and 2-(5-tetrazolyl)pyrimidines **22**–**24** also affords cyanopyrroles (Scheme 8). FVT of 2-(5-tetrazolyl)pyrimidine (**22**) affords a ca. 1:1 ratio of 2- and 3-cyanopyrroles (Scheme 8). The results of FVT of tetrazoles **23** and **24** are collected in Table 1. The formation of different mixtures of the three cyanodimethylpyrroles **25**–**27** depending on the conditions can be explained in terms of chemical activation. The formation of (hetero)arylcarbenes and their rearrangement to (hetero)arylnitrenes and cyanopyrroles are strongly exothermic reactions. Consequently, when the reaction is performed in the low-pressure gas phase, the reaction products carry excess thermal (rovibrational) energy, which facilitates the sigmatropic shifts of H, CN, and CH_3, which will cause interconversion of the cyanopyrroles [28]. In many cases, this cannot be completely avoided, even by using the mildest possible FVT temperatures, but an increase in pressure (1 hPa N_2) will help to remove excess thermal energy and so preserve the initial reaction products. Therefore, as seen in Table 1, it can be concluded that the dimethylcyanopyrrole **25** is the primary reaction product of **23**, and **27** is the predominant product from **24**. That chemical activation is the cause is seen in the fact that FVT of the individual dimethylcyanopyrroles **25** and **27** afford mixtures very similar to those obtained from **23** and **24**, respectively, but a temperature of 800 °C is required for this, whereas 400 °C suffices in the FVT of the tetrazoles (Table 1).

Following the analysis of the ring contraction in 3-pyridylnitrene (**10**) by ring expansion and ring opening to a nitrile ylide (Scheme 4 and Figure 1), we can interpret the reactions in terms of ring expansion of the pyrimidinylcarbenes **28** and **33** to diazacycloheptatetraenes **29** and **34**, ring contraction to 3-pyridylnitrenes **30** and **35** and/or ring opening to nitrile ylides **31** and **37**, and ring closure to cyanopyrroles (Scheme 9).

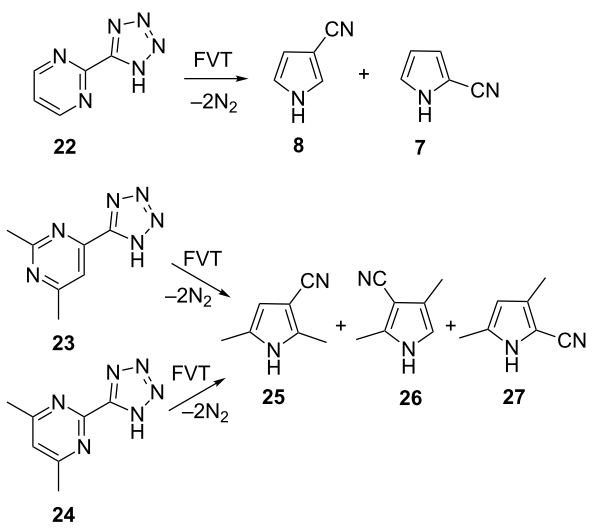

Scheme 8: Formation of cyanopyrroles by FVT of tetrazolylpyrimidines.

Table 1: Dimethylcyanopyrroles from tetrazolylpyrimidines.

Starting material	Conditions	Products, rel. yields (%)		
	T (°C)/*p* (hPa)	**25**	**26**	**27**
23	400/10^{-3}	63	29	7
	400/1 N_2	98	2	<0.5
	600/10^{-1}	79	19	2
24	400/10^{-3}	34	23	43
	400/1 N_2	21	10	69
	600/10^{-1}	25	23	44[a]
25	800/10^{-3}	49	32	14[a]
27	800/10^{-3}	22	22	50[a]

[a]6–8% yields of other, isomeric dimethylcyanopyrroles were also formed.

In the case of the 4-pyrimidinylcarbene **28** a direct ring opening of the diazacycloheptatetraene **29** to the nitrile ylide **31** is possible. However, in the case of the 2-pyrimidinylcarbene **33**, the first-formed diazacycloheptatetraene **34** cannot open directly to a nitrile ylide but must first rearrange to the 3-pyridylnitrene **35**. Either the 3-pyridylnitrene **35** or the second diazacycloheptatetraene **36** may then undergo ring opening to the nitrile ylide **37**. Sigmatropic shifts of H, CN, or CH_3 in the 3*H*-pyrroles **32** and **38** lead to the final products.

We have previously reported strong evidence for the ring expansion of a 2-pyrimidinylcarbene **39** to a diazacycloheptatetraene **40** and subsequent ring contraction to a 3-pyridylnitrene **41**, which undergoes cyclization to afford the pyridoindole (4-azacarbazole) **42** (Scheme 10) [29].

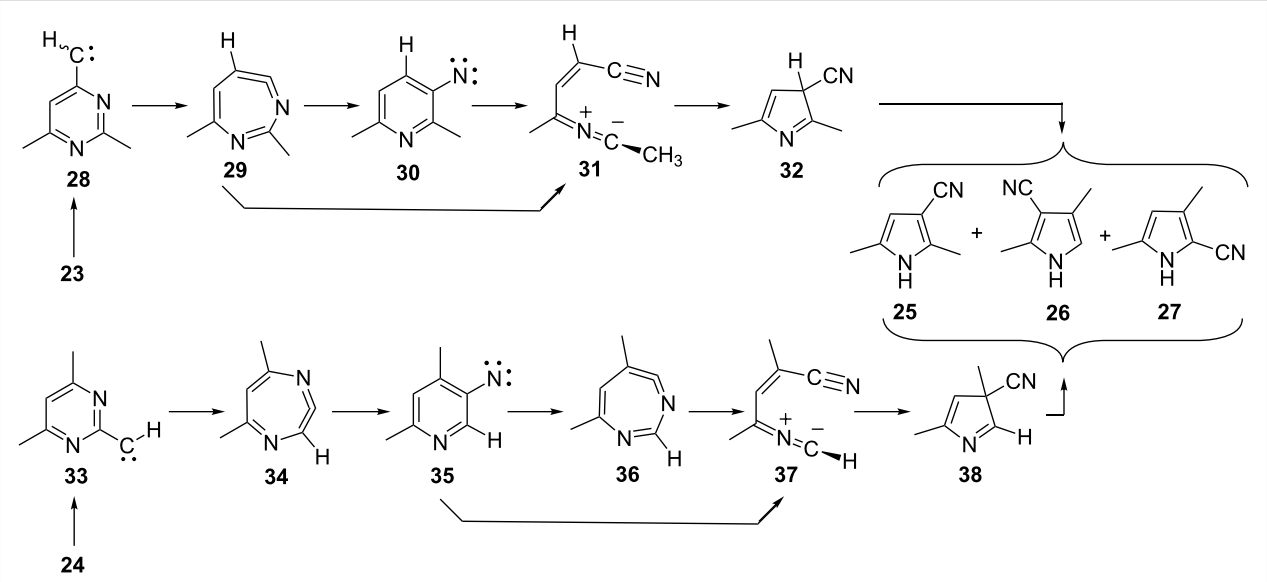

Scheme 9: Rearrangements of pyrimidinylcarbenes to cyanopyrroles via nitrile ylides **31** and **37**.

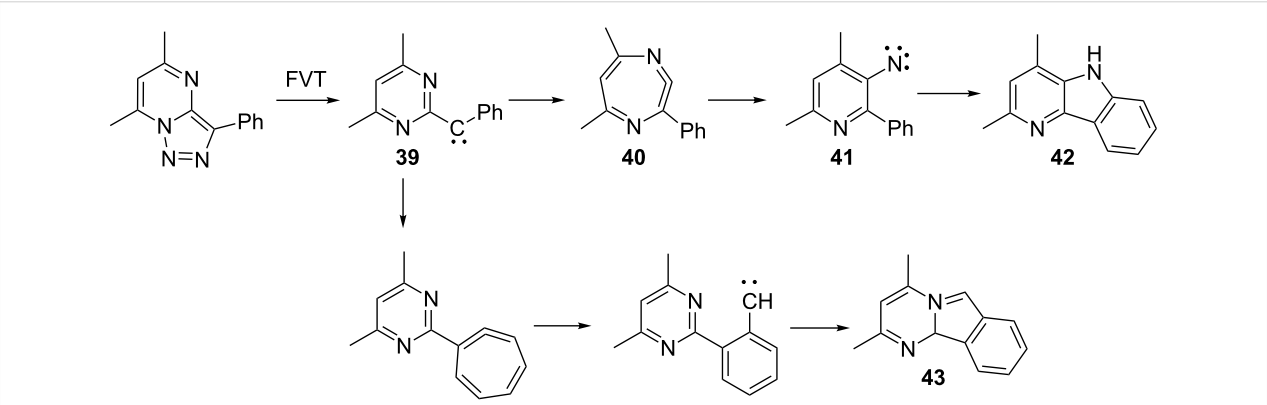

Scheme 10: Rearrangements of phenyl(dimethylpyrimidinyl)carbene.

The alternative ring expansion/ring contraction/recyclization to the pyrimidoisoindole **43** also takes place [29]. The formation of **42** is important, as it demonstrates that 2-pyrimidinylcarbenes can rearrange to 3-pyridylnitrenes, whereas 4-pyrimidinylcarbenes do not necessarily rearrange to 3-pyridylnitrenes (see **55** below).

2-Phenyl-3-quinolylnitrene

Matrix photolysis of 3-azido-2-phenylquinoline (**44**) at λ = 308 nm or 310–390 nm affords a blue nitrile ylide **47** (observed IR 2220, 2154 cm^{-1}; calcd (B3LYL/6-31G*) 2233, 2171 cm^{-1}; UV–vis λ_{max} 400 and 680 nm) (Scheme 11, Figure 2 and Figure 3).

It could be converted to the seven-membered ring ketenimine **46** (IR: 1920; calcd: 1921 cm^{-1}) on photolysis above 550 nm. The ketenimine **46** was again converted to ylide **47** on photolysis at 310–390 nm. We assume the nitrene **45** is formed initially, but it is converted to **46** and **47** at the same wavelength. As in the examples described above, the ring opening to the ylide **47** may take place either from the nitrene or from the cyclic ketenimine, although we only observed the latter reaction directly. It was possible to cycle many times between these two intermediates (Figure 2 and Figure 3), but eventually signal intensity was lost, probably because another reaction, the cyclization to the isocarbazole **49**, took place. This reaction is analogous to the photocyclization of *o*-biphenylylnitrene to isocarbazole [30]. As shown below, the indoloquinoline **50** is indeed a major product under FVT conditions. It is possible that **49** could contribute to the observed visible spectrum, but it obviously cannot explain the IR spectrum. The same visible spectrum was obtained by photolysis of **44** embedded in

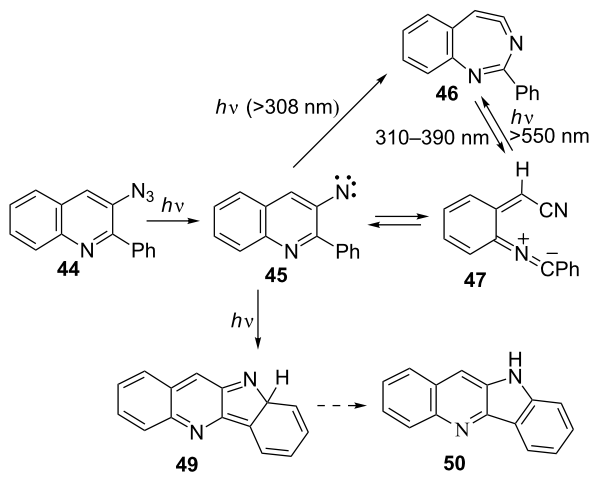

Scheme 11: Photolysis of 3-azido-2-phenylquinoline.

a PVC film at 11 K, and the carrier of the spectrum was stable up to 90 K, as can be expected of a highly reactive nitrile ylide **47**. The calculated IR and UV–vis spectra of **45**, **46**, **47** and **49** are listed in Supporting Information File 1.

Preparative FVT of azide **44** at 400–800 °C affords the indoloquinoline **50** in 52–60% yield (Scheme 12). Importantly, smaller amounts of amine **51** and the ring-contraction product 2-phenyl-3-cyanoindole (**48**, 21–15%) were also isolated.

Formation of amines is diagnostic for triplet nitrenes, even in low-pressure gas-phase reactions [10,22]. The 3-cyanoindole **48** is expected to be formed by cyclization of the nitrile ylide **47** in the same way that the 3-cyanoindole is obtained from the unsubstituted 3-quinolylnitrene [21]. The three products, **48**, **50** and **51** were formed even on thermolysis of **44** in solution.

4-Quinazolinylcarbenes

The tetrazolylquinazoline **52** and the triazoloquinazoline **53** undergo pyrolysis via the diazomethylquinazoline **54** (Scheme 13) [23]. Both afforded the 3-cyanoindole **48** in nearly quantitative yield (up to 98%) on FVT at 400–600 °C, but no traces of either indoloquinoline **50** or the 3-aminoquinoline **51** were detectable. The same was true when the thermolysis was performed in solution. In other words, nitrene **45** was not formed (Scheme 13).

This is in agreement with the conclusion reached for 4-quinazolinylcarbene itself [21], namely that ring contraction takes place via the pathway 2-phenyl-4-quinazolinylcarbene (**55**) → cyclic ketenimine **46** → nitrile ylide **47** → nitrile **48**. The data demonstrate that carbene **55** does not convert thermally to nitrene **45**. In other words, although carbene–nitrene

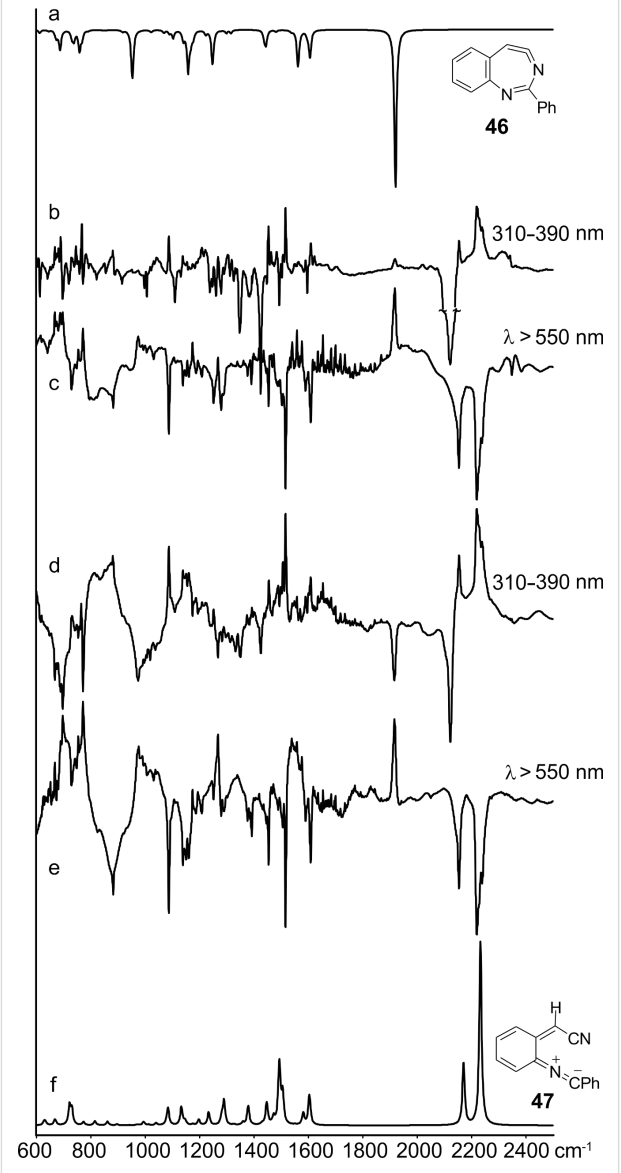

Figure 2: IR difference spectra from the photolysis of 3-azido-2-phenylquinoline (**44**) in Ar matrix. (a) Calculated spectrum of **46**. (b) Initial difference spectrum after 240 s; the negative peaks are due to the azide. (c)–(e) Further irradiation as indicated for 900, 400 and 600 s, respectively. (f) Calculated spectrum of **47**. Ordinate in arbitrary absorbance units. See also Figures S1–S3 in Supporting Information File 1.

rearrangements are known to occur [1,19] (see, e.g., Scheme 1 and Scheme 10 above), they may be bypassed when ring opening to nitrile ylides becomes more favourable.

Conclusion

The rearrangement of 2- and 4-pyrimidinylcarbenes **28** and **33** to mixtures of 2- and 3-cyanopyrroles on FVT implies prior isomerization to 3-pyridylnitrenes and/or diazacycloheptatetraenes and nitrile ylides. 3-Quinolylnitrenes and 4-quinazolinylcarbenes afford 3-cyanoindoles **48** on FVT. In addition, 2-phe-

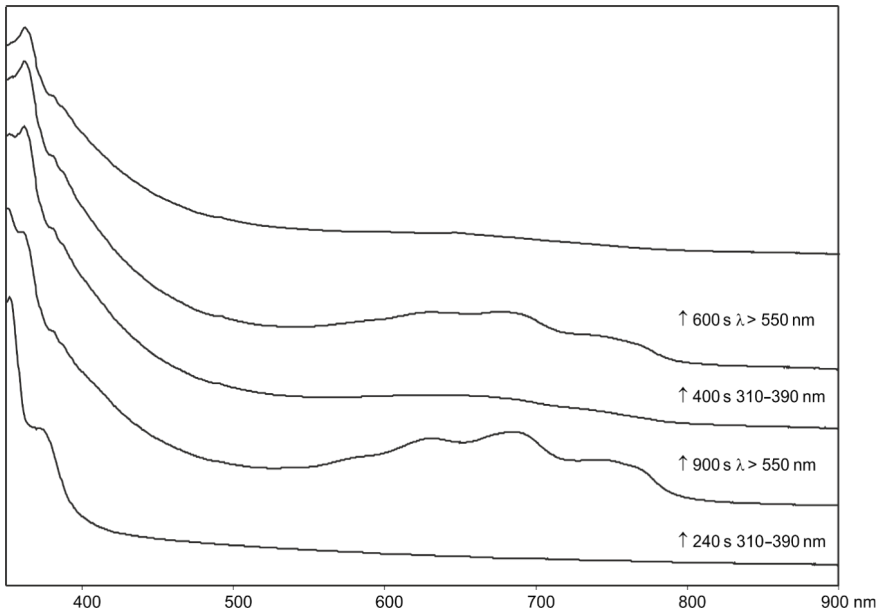

Figure 3: UV–vis spectra from the sequential photolysis of 3-azido-2-phenylquinoline (**44**) in Ar matrix at 310–390 nm and 550 nm. Abscissa in nanometres and ordinate in arbitrary absorbance units. These spectra correspond to the IR spectra in Figure 2. See Supporting Information File 1 for the calculated electronic transitions.

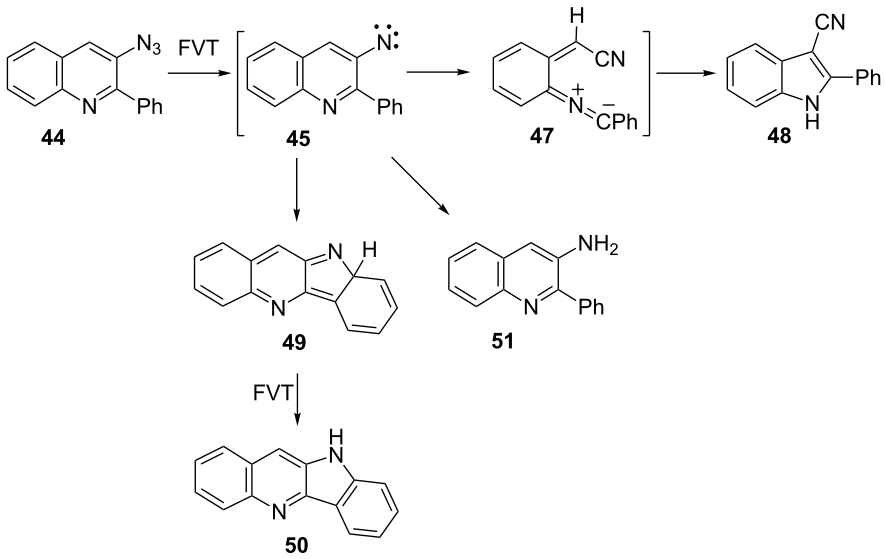

Scheme 12: Preparative FVT of 3-azido-2-phenylquinoline.

nyl-3-quinolylnitrene (**45**) cyclizes to indoloquinoline **50**, but this compound is not formed at all from the isomeric 2-phenyl-4-quinazolinylcarbene (**55**). This demonstrates that carbene **55** does not isomerize to nitrene **45**. Instead, the ring contraction to **48** takes place via the nitrile ylide **47**. Matrix photolysis of 2-phenyl-3-azidoquinoline (**44**) revealed a reversible photochemical interconversion of the benzodiazacycloheptatetraene **46** and the nitrile ylide **47**.

Experimental

General

The apparatus and procedures for preparative FVT [31] and for Ar matrix isolation [11,32,33] were as previously described. KBr and CsI windows were used for IR spectroscopy. FVT products were isolated in liquid nitrogen (77 K) in the preparative thermolysis, and at 22–25 K in Ar matrices for IR experiments. IR spectra of the Ar matrices were measured at 7–10 K

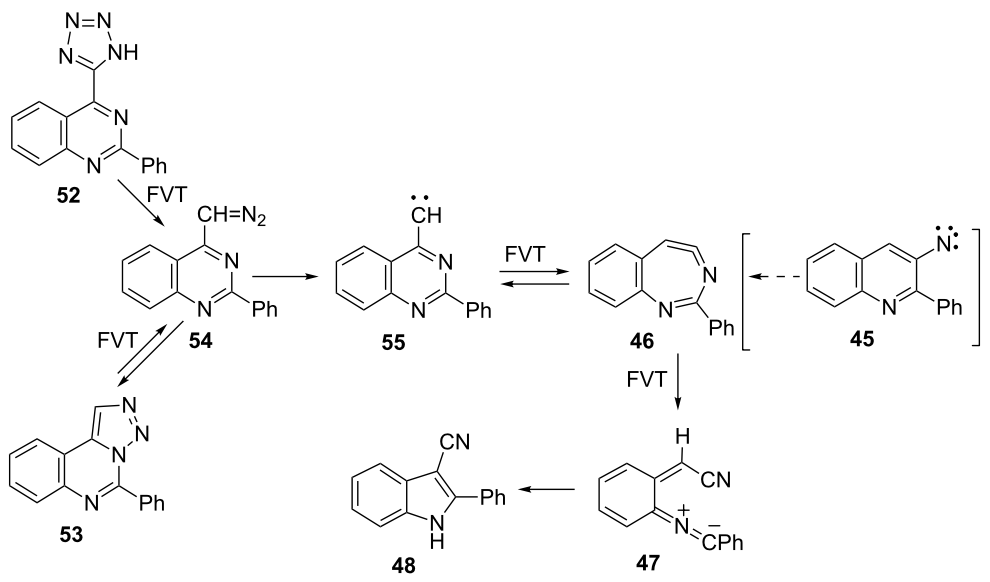

Scheme 13: FVT of 2-phenyl-4-quinazolinylcarbene precursors.

with a resolution of 1 cm^{-1}. Photolyses were done through quartz by using a 75 W low pressure Hg lamp (254 nm) or a 1000 W high pressure Hg/Xe lamp equipped with a monochromator and appropriate filters. A water filter was used to remove infrared radiation, and a 7.5% $NiSO_4$ or a $NiSO_4/CuSO_4$ solution (7.5 and 2.5%, respectively) to remove visible light where required. Analytical gas chromatography used a 10% OV 17 column programmed at 120–180 °C at 2°/min with N_2 as carrier gas at 0.6 bar. Preparative gas chromatography used a 20% Carbowax column at 200 °C with H_2 as carrier gas at 60 mL/min.

Materials

3-Azidopyridine (**9**) [34,35], 2-(5-tetrazolyl)pyrimidine (**22**) [36,37], 2-phenyl-4-(5-tetrazolyl)quinazoline (**52**) [23], and 5-phenyl-1,2,3-triazolo[1,5-*a*]quinazoline (**53**) [23] were prepared according to literature procedures. 4,6-Dimethyl-2-(5-tetrazolyl)pyrimidine (**24**) and 2,4-dimethyl-6-(5-tetrazolyl-pyrimidine) (**23**) were prepared from the dimethylpyrimidine-carbonitriles [38,39] by adaptation of the literature method [36,37].

4,6-Dimethyl-2-(5-tetrazolyl)pyrimidine (24): From 3.0 g (22.5 mmol) of 4.6-dimethylpyrimidine-2-carbonitrile was obtained 2.8 g (71%); mp 209–210 °C (dec); ^{1}H NMR ($CDCl_3$) 12.0 (very broad), 7.37 (s, 1H), 2.50 (s, 6H); MS *m/z*: 176 (M^+, 21), 148 (33), 134 (46), 120 (100), 119 (71), 107 (36), 105 (12), 93 (13), 92 (16), 80 (15), 67 (76), 66 (56), 53 (26); anal. calcd for $C_7H_8N_6$: C, 47.72; H. 4.58; N, 47.70; found: C, 47.89; H, 4.40; N, 47.52.

2,4-Dimethyl-6-(5-tetrazolyl)pyrimidine (23): Prepared as the preceding entry in 41% yield; mp 208–209 °C (dec); ^{1}H NMR ($CDCl_3$) 7.43 (s, 1H), 2.66 (s, 3H), 2.56 (s, 3H); MS *m/z*: 176 (M^+, 49), 148 (12), 135 (10), 134 (100), 120 (19), 119 (65), 107 (42), 93 (17), 97 (15), 78 (17), 66 (66), 52 (54); anal. calcd for $C_7H_8N_6$: C, 47.72; H. 4.58; N, 47.70; found: C, 47.90; H, 4.80; N, 47.75.

3-Azido-2-phenylquinoline (44): This compound was prepared according to a standard literature procedure [40]. A sample of 2.54 g (11.5 mmol) of 3-amino-2-phenylquinoline [41] was dissolved in a mixture of 2 mL of conc. sulfuric acid (d = 1.84) and 13 mL water at 40 °C and then cooled to 0 °C. A solution of 900 mg (13 mmol) of $NaNO_2$ in 8 mL water was added dropwise at 0 °C, causing the formation of a yellow, crystalline diazonium sulfate, which was not isolated. After 30 min at 0 °C a solution of 11 g (16.9 mmol) of NaN_3 in 7 mL water was added. An amorphous, yellow precipitate formed immediately with simultaneous evolution of N_2. After stirring for 3 h at rt, the yellow solid was filtered and recrystallized from petroleum ether, yielding 2.33 g (82%) of the azide, mp 93–94 °C; ^{1}H NMR (DMSO-d_6) 8.41 (s, 1H), 8.05–8.01 (m, 2H), 7.87–7.83 (m, 2H), 7.73 (dd, J = 8.2 Hz, J = 1.2 Hz, 1H), 7.64 (dd, J = 8.2 Hz, J = 1.2 Hz, 1H), 7.53–7.47 (m, 3H); ^{13}C NMR (DMSO-d_6) 151.4, 144.0, 137.3, 132.2, 129.6, 129.1, 128.9, 128.7, 127.9, 127.5, 127.4, 126.7, 124.9; IR (KBr): 3030 (w), 2100 (s), 1590 (w), 1485 (m), 1415 (s), 1340 (s), 1288 (m), 1270 (s), 1255 (m), 1245 (m), 1230 (m), 955 (m), 895 (s), 860 (m), 770 (s), 750 (s), 710 (s), 695 (s) cm^{-1}; UV (CH_3CN) λ_{max}: 257, 260, 337 nm; MS *m/z*: 246 (M^+, 5), 220 (9), 219 (26), 218

(100), 190 (8), 115 (20), 88 (9), 78 (3); anal. calcd for $C_{15}H_{10}N_4$: C, 73.16; H, 4.09; N, 22.75; found: C, 73.10; H, 4.18; N, 22.68.

FVT of 3-azidopyridine (9): The azide (0.50 g) was distilled into the FVT apparatus from a sample flask held at −30 °C and thermolysed at 370–500 °C/10^{-3}–10^{-4} mbar in the course of 2 h. The pyrolysate was examined by GC/MS and ^{1}H NMR spectroscopy. The 2- and 3-cyanopyrroles **7** and **8** were separated by flash chromatography on silica gel 60, eluted with hexane/ethyl acetate 3:7 and identified by comparison with authentic materials reported previously [10,20]. Yields were determined by GC as previously described [10]. The following ratios of 3- to 2-cyanopyrroles at different temperatures were obtained: 370 °C: 2.29:1 (81% 3-azidopyridine remained unreacted); 400 °C: 1.63:1 (36% 3-azidopyridine remained unreacted); 500 °C: 1.48:1 (6% 3-azidopyridine remained unreacted). GC/MS retention times and molecular masses: 2-cyanopyrrole 3.60 min (*m/z* 92); 3-cyanpyrrole 5.45 min (*m/z* 92); 3-azidopyridine 2.19 min (*m/z* 120); ^{1}H NMR ($CDCl_3$) 2-cyanopyrrole: 9.01 (br, 1H), 6.98 (m, 1H), 6.88 (m, 1H), 6.28 (m, 1H); 3-cyanopyrrole: 8.80 (br, 1H), 7.36 (m, 1H), 6.84 (m, 1H), 6.53 (m, 1H); IR (Ar, 20 K): 2-cyanopyrrole: 2236 cm^{-1}; 3-cyanopyrrole: 2234 and 2247 cm^{-1}.

FVT of 2-(5-tetrazolyl)pyrimidine (22): A portion of **22** (300 mg) was sublimed into the pyrolysis tube at 170 °C and pyrolysed at 600 °C/10^{-3} mbar in the course of 12 h. The resulting pyrolysate (120 mg) was identified as a 1:1 mixture of 2- and 3-cyanopyrroles **7** and **8** by comparison of the ^{1}H NMR, IR and mass spectra with those of authentic materials. Yields were determined by GC as above [10].

FVT of 2,4-dimethyl-6-(5-tetrazolyl)pyrimidine (23) and 4,6-dimethyl-2-(5-tetrazolyl)pyrimidine (24): A portion of **23** or **24** (500 mg) was sublimed at 150 °C and pyrolysed at 10^{-3} mbar in the course of 12–18 h. The pyrolyzates were extracted with diethyl ether, and the products were analysed and separated by GC on the Carbowax column. The yields of 2,6-dimethyl-3-cyanopyrrole (**25**), 2,4-dimethyl-3-cyanopyrrole (**26**) and 3,5-dimethyl-2-cyanopyrrole (**27**) at various temperatures are collected in Table 1. Yields were determined by GC, and the pyrroles were characterized as follows:

2,6-Dimethyl-3-cyanopyrrole (25): Retention time 63 min. ^{1}H NMR ($CDCl_3$) 8.4 (br, 1H), 5.95 (m, 1H), 2.38 (s, 3H), 2.20 (s, 3H); IR (KBr): 3470 (br), 2210 (s), 1600 (w), 1430 (w), 1050 (m), 780 (m); UV (EtOH) λ_{max}: 245 nm; MS *m/z*: 120 (M^+, 67), 119 (100), 106 (28), 105 (71), 78 (10), 65 (3). The spectra data were in agreement with literature values [42].

2,4-Dimethyl-3-cyanopyrrole (26): Retention time 57 min; ^{1}H NMR ($CDCl_3$) 8.60 (br, 1H), 6.38 (m, 1H), 2.38 (s 3H), 2.12 (s, 3H); IR (KBr): 3460 (br), 2210 (s), 1580 (w), 1400 (m), 1110 (m), 800 (m); MS *m/z*: 120 (M^+, 55), 119 (100), 106 (25), 105 (60), 78 (12), 65 (3); UV (EtOH) λ_{max}: 240 nm. The spectra data were in agreement with literature values [42].

3,5-Dimethyl-2-cyanopyrrole (27): Residence time 31 min; ^{1}H NMR ($CDCl_3$) 9.0 (br, 1H), 5.76 (m, 1H), 2.23 (s, 3H), 2.17 (s, 3H); IR (KBr): 3460 (br), 2210 (s), 1580 (w), 1460 (w), 1390 (w), 1300 (w), 1270 (m), 800 (m); MS *m/z*: 120 (M^+, 73), 119 (100), 106 (48), 105 (86), 92 (8), 78 (14), 65 (10); UV (EtOH) λ_{max}: 257, 234 nm. The spectra data were in agreement with literature values [42]. Anal. calcd for $C_7H_8N_2$: C, 69.97; H, 6.71; N, 23.31; found: C, 69.61; H, 6.31; N, 23.21

Matrix photolysis of 3-azido-2-phenyl-3-quinoline (44): The azide was sublimed at 80 °C and deposited with Ar at 22 K to form a matrix. Principal absorptions of the azide at 11 K: 2100, 1590, 1420, 1340, 1270, 1100 cm^{-1}. Irradiation of the azide **44** at 308 nm or at 310–390 nm for 30 s afforded the nitrile ylide **47** together with a smaller amount of the cyclic ketenimine **46** (2220, 2154, 1920, 1610, 1516, 1500, 1450, 1390, 1088 cm^{-1}). Further photolysis for 210 s caused additional formation of the ylide **47** (IR, Ar, 10 K: 2220, 2154, 1609, 1516, 1453, 1088, 740 cm^{-1} (Figure 2); UV–vis λ_{max} ca. 350 and 585, 635, 700, 775 nm (Figure 3)). Subsequent irradiation at $\lambda > 550$ nm bleached the long-wavelength band in the visible spectrum and the IR bands at 2154 and 2220 cm^{-1} in the IR. The intensity of the band at 1918 cm^{-1} due to **46** increased substantially at the same time (Figure 2). Renewed irradiation at 310–390 nm caused diminution of the IR bands ascribed to **46** and reformation of the IR and UV–vis bands ascribed to the nitrile ylide **47**. It was possible to cycle several times between these two species by using $\lambda > 550$ nm and λ = 310–390 nm, respectively (Figure 2 and Figure 3).

FVT of 3-azido-2-phenyl-3-quinoline (44): (a) A sample of the azide (0.2 g, 0.8 mmol) was sublimed at 60–80 °C and pyrolysed at 500 °C/10^{-4} mbar in the course of 3 h. The products were separated by flash chromatography on silica gel, eluting with chloroform. Indolo[3,2-*b*]quinoline (**50**) was obtained in 56–65% yield in different experiments: mp 250–251 °C (lit. [43] 248 °C; lit. [44] 251–252 °C); ^{1}H NMR (DMSO-d_6) 11.40 (s, 1H), 8.35 (d, J = 8.3 Hz, 1H), 8.27 (s, 1H), 8.18 (d, J = 8.3 Hz, 1H), 8.09 (d, J = 8.3 Hz, 1H), 7.66–7.52 (m, 4H), 7.28 (dd, J = 7.4 Hz, J = 1.0 Hz, 1H); ^{13}C NMR 145.6, 144.0, 143.3, 132.4, 129.6, 128.5, 127.4, 126.6, 125.9, 124.7, 121.3, 120.9, 119.2, 113.0, 111.4; IR (KBr): 3300–3000 (br), 1610 (s), 1490 (s), 1460 (m), 1400 (s), 1340 (s), 1220 (s), 1120 (m), 750 (m), 730 (s) cm^{-1}; UV (EtOH) λ_{max}: 347, 276 nm; MS *m/z*: 219

(M^+ + 1, 16), 218 (M^+, 100), 217 (16), 190 (15), 109 (M^{++}, 11), 108 (10), 96 (17), 95 (10), 89 (20), 77 (10). 3-Cyano-2-phenylindole (**48**) was obtained in 18–20% yield in different experiments: mp 241–243 °C (lit. [45] 246–248 °C, lit. [46] 240 °C); ^{1}H NMR ($CDCl_3$) 8.91 (br s, 1H), 7.89–7.96 (m, 2H), 7.76 (dd, *J* = 7.2 Hz, *J* = 0.6 Hz, 1H), 7.56–7.42 (m, 4H), 7.35–7.27 (m, 2H); ^{13}C NMR ($CDCl_3$) 144.7, 135.5, 129.9, 129.4, 129.2, 128.3, 126.9, 123.8, 122.0, 118.3, 117.0, 112.6, 81.4; IR (KBr): 3240–3180 (br s), 2220 (s), 1490 (m), 1450 (s), 1420 (m), 1370 (w), 1320 (br w), 1240 (m), 770 (m), 730 (s), 710 (w), 680 (m); MS *m/z*: 219 (M^+ + 1, 17), 218 (M^+, 100), 190 (9), 115 (5), 109 (8), 96 (6). (b) In analogous experiments at 450–700 °C the products of FVT were condensed on a KBr window at 77 K for IR spectroscopy. In each case the product was a mixture of 3-cyano-2-phenylindole and indolo[3,2-*b*]quinoline according to IR spectroscopy of the crude and TLC of the isolated material.

Thermolysis of 3-azido-2-phenylquinoline (44) in solution: A solution of 200 mg (0.81 mmol) of the azide in xylene was heated under reflux for 3 days. After distillation of the solvent, the residue was chromatographed on silica, eluting with petroleum ether/chloroform to yield 3-cyano-2-phenylindole (**48**, 3 mg; 2%), 3-amino-2-phenylquinoline (**51**, 80 mg; 45%), and indolo[3,2-*b*]quinoline (52 mg; 29%).

FVT of 2-phenyl-4-(5-tetrazolyl)quinazoline (52): (a) A sample of 300 mg (1.10 mmol) was sublimed at 150 °C and pyrolysed at 600 °C/10^{-3}–10^{-4} mbar in the course of 12 h. Chromatography yielded 178 mg (75%) of 3-cyano-2-phenylindole (**48**). (b) In similar experiments with FVT at 600–800 °C the product was isolated on a KBr window at 77 K for IR spectroscopy. In each case 3-cyano-2-phenylindole (**48**) was the exclusive product.

Thermolysis of 2-phenyl-4-(5-tetrazolyl)quinazoline (52) in solution: (a) A solution of 250 mg (0.91 mmol) in 50 mL of xylene was heated under reflux for 6 d. Chromatography after distillation of the solvent yielded 166 mg (74%) 2-phenyl-1,2,3-triazolo[1,5-*c*]quinazoline **53**, mp 192–193 °C (dec) (lit. [23] 192–193 °C (dec)). (b) A solution of 50 mg (0.18 mmol) in 10 mL of diphenylmethane was heated at 180 °C for 1 h. After distilling the solvent vacuum and chromatography of the residue, 6 mg (15%) of 3-cyano-2-phenylindole (**48**) was obtained.

FVT of 2-phenyl-1,2,3-triazolo[1,5-*c*]quinazoline (53): (a) A sample of 50 mg (0.20 mmol) was sublimed at a temperature increasing gradually to 190 °C and pyrolysed at 660 °C/10^{-3} mbar. The product (43 mg; 98%) consisted exclusively of 3-cyano-2-phenylindole (**48**). (b) In similar experiments with FVT at 300–600 °C the product was isolated on a KBr window at 77 K for IR spectroscopy. No reaction was observable below 400 °C. The 4-diazomethyl-2-phenylquinazoline (**54**) was detectable by absorption at 2095 cm^{-1} in the 400 °C experiment. In each case, at FVT temperatures of 400–600 °C, 3-cyano-2-phenylindole (**48**) was the only other identified product, characterized by its absorption at 2220 cm^{-1}.

Thermolysis of 2-phenyl-1,2,3-triazolo[1,5-*c*]quinazoline (53) in solution: A solution of 20 mg (0.08 mmol) in 5 mL of diphenylmethane was heated at 180 °C for 1 h. Chromatography of the resulting mixture yielded 2 mg (10%) of 3-cyano-2-phenylindole (**48**).

Supporting Information

Supporting Information File 1

Computational details, calculated and experimental IR spectra, and calculated electronic transitions.
[http://www.beilstein-journals.org/bjoc/content/supplementary/1860-5397-9-84-S1.pdf]

Acknowledgements

This work was aided by the National Computing Merit Allocation Scheme, project g01, supported by the Australian Government.

References

1. Wentrup, C. *Acc. Chem. Res.* **2011,** *44,* 393. doi:10.1021/ar700198z
2. Lwowski, W. *Nitrenes;* Wiley-VCH: New York, NY, USA, 1970.
3. Scriven, E. F. V., Ed. *Azides and Nitrenes;* Academic Press: Orlando, FL, USA, 1984.
4. Bräse, S.; Banert, K. *Organic Azides – Synthesis and Applications;* Wiley-VCH: Chichester, UK, 2010.
5. Falvey, D. E.; Gudmundsdottir, A. D., Eds. *Nitrenes and Nitrenium Ions;* Wiley-VCH: Hoboken, NJ, USA, 2013.
6. Wentrup, C.; Reisinger, A.; Kvaskoff, D. *Beilstein J. Org. Chem.* **2013,** *9,* 754–760. doi:10.3762/bjoc.9.85
7. Reisinger, A.; Bernhardt, P. V.; Wentrup, C. *Org. Biomol. Chem.* **2004,** *2,* 246. doi:10.1039/b311247k
8. Reisinger, A.; Koch, R.; Bernhardt, P. V.; Wentrup, C. *Org. Biomol. Chem.* **2004,** *2,* 1227. doi:10.1039/b317099c
9. Addicott, C.; Wentrup, C. *Aust. J. Chem.* **2008,** *61,* 592. doi:10.1071/CH08252
10. McCluskey, A.; Wentrup, C. *J. Org. Chem.* **2008,** *73,* 6265. doi:10.1021/jo800899t
11. Kvaskoff, D.; Bednarek, P.; Wentrup, C. *J. Org. Chem.* **2010,** *75,* 1600. doi:10.1021/jo902570d
12. Wentrup, C.; Kvaskoff, D. *Aust. J. Chem.* **2013,** *66,* 286–296. doi:10.1071/CH12502.
13. Bednarek, P.; Wentrup, C. *J. Am. Chem. Soc.* **2003,** *125,* 9083. doi:10.1021/ja035632a

14. Bégué, D.; Qiao, G. G.; Wentrup, C. *J. Am. Chem. Soc.* **2012,** *134,* 5339. doi:10.1021/ja2118442
15. Orton, E.; Collins, S. T.; Pimentel, G. C. *J. Phys. Chem.* **1986,** *90,* 6139. doi:10.1021/j100281a018
16. Rajam, S.; Murthy, R. S.; Jadhav, A. V.; Li, Q.; Keller, C.; Carra, C.; Pace, T. C. S.; Bohne, C.; Ault, B. S.; Gudmundsdottir, A. D. *J. Org. Chem.* **2011,** *76,* 9934. doi:10.1021/jo200877k
17. Kvaskoff, D.; Vosswinkel, M.; Wentrup, C. *J. Am. Chem. Soc.* **2011,** *133,* 5413. doi:10.1021/ja111155r
18. Crabtree, K. N.; Hostetler, K. J.; Munsch, T. E.; Neuhaus, P.; Lahti, P. M.; Sander, W.; Poole, J. S. *J. Org. Chem.* **2008,** *73,* 3441. doi:10.1021/jo8001936
19. Karney, W. L.; Borden, W. T. Differences between Phenylcarbene and Phenylnitrene and the Ring Expansion Reactions they Undergo. In *Advances in Carbene Chemistry;* Brinker, U. H., Ed.; Elsevier: Amsterdam, 2001; Vol. 3, p 205.
20. Wentrup, C.; Crow, W. D. *Tetrahedron* **1970,** *26,* 3965. doi:10.1016/S0040-4020(01)93037-6
21. Kvaskoff, D.; Mitschke, U.; Addicott, C.; Finnerty, J.; Bednarek, P.; Wentrup, C. *Aust. J. Chem.* **2009,** *62,* 275. doi:10.1071/CH08523
22. Kvaskoff, D.; Bednarek, P.; George, L.; Pankajakshan, S.; Wentrup, C. *J. Org. Chem.* **2005,** *70,* 7947. doi:10.1021/jo050898g
23. Wentrup, C. *Helv. Chim. Acta* **1978,** *61,* 1755. doi:10.1002/hlca.19780610522
24. Tennant, G.; Vevers, R. J. S. *J. Chem. Soc., Chem. Commun.* **1974,** 671. doi:10.1039/C3974000671B
25. Maury, G.; Paugam, J.-P.; Pougam, R. *J. Heterocycl. Chem.* **1978,** *15,* 1041. doi:10.1002/jhet.5570150627
26. Abarca, B.; Ballesteros, R.; Chadlaoui, M.; Miralles, J.; Murillo, J. V.; Colonna, D. *Tetrahedron* **2001,** *57,* 10111. doi:10.1016/S0040-4020(01)01053-5
27. Ezema, B. E.; Akpanisi, L. E. S.; Ezema, C. G.; Onoabedje, A. E. *Chem. Mater. Res.* **2012,** *2,* 12.
28. Wentrup, C. *Tetrahedron* **1974,** *30,* 1301. doi:10.1016/S0040-4020(01)97303-X
29. Mayor, C.; Wentrup, C. *J. Am. Chem. Soc.* **1975,** *97,* 7467. doi:10.1021/ja00859a014
30. Tsao, M.-L.; Gritsan, N.; James, T. R.; Platz, M. S.; Hrovat, D. A.; Borden, W. T. *J. Am. Chem. Soc.* **2003,** *125,* 9343. doi:10.1021/ja0351591
31. Wentrup, C.; Blanch, R.; Briehl, H.; Gross, G. *J. Am. Chem. Soc.* **1988,** *110,* 1874. doi:10.1021/ja00214a034
32. Kuhn, A.; Plüg, C.; Wentrup, C. *J. Am. Chem. Soc.* **2000,** *122,* 1945. doi:10.1021/ja993859t
33. Kappe, C. O.; Wong, M. W.; Wentrup, C. *J. Org. Chem.* **1995,** *60,* 1686. doi:10.1021/jo00111a029
34. Dyall, L. K.; Moloney, D. W. J.; Harvey, J. J.; Fulloon, B. E. *Aust. J. Chem.* **1996,** *49,* 761. doi:10.1071/CH9960761
35. Dyall, L. K.; Wong, M. W. *Aust. J. Chem.* **1985,** *38,* 1045. doi:10.1071/CH9851045
36. Robba, M. *Ann. Chim. (Cachan, Fr.)* **1960,** *5,* 351.
37. Holland, G. F.; Pereira, J. N. *J. Med. Chem.* **1967,** *10,* 149. doi:10.1021/jm00314a004
38. Klötzer, W. *Monatsh. Chem.* **1956,** *87,* 131. doi:10.1007/BF00903597
39. Klötzer, W. *Monatsh. Chem.* **1956,** *87,* 526. doi:10.1007/BF00917846
40. Smith, P. A. S.; Brown, B. B. *J. Am. Chem. Soc.* **1951,** *73,* 2438. doi:10.1021/ja01150a009
41. Baumgarten, H. E.; Saylor, J. L. *J. Am. Chem. Soc.* **1957,** *79,* 1502. doi:10.1021/ja01563a063
42. Elsom, L. F.; Jones, R. A. *J. Chem. Soc. B* **1970,** 79. doi:10.1039/j29700000079
43. Long, L. M.; Troutman, H. D. *J. Am. Chem. Soc.* **1949,** *71,* 2469. doi:10.1021/ja01175a067
44. Clemo, G. R.; Felton, D. G. I. *J. Chem. Soc.* **1952,** 1658. doi:10.1039/jr9520001658
45. Tamura, Y.; Adachi, M.; Kawasaki, T.; Yasuda, H.; Kita, Y. *J. Chem. Soc., Perkin Trans. 1* **1980,** 1132. doi:10.1039/P19800001132
46. Mehta, G. *Synthesis* **1978,** 374. doi:10.1055/s-1978-24751

License and Terms

Beilstein Journal of Organic Chemistry

4-Pyridylnitrene and 2-pyrazinylcarbene

Curt Wentrup*, Ales Reisinger and David Kvaskoff

Full Research Paper

Open Access

Address:
School of Chemistry and Molecular Biosciences, The University of Queensland, Brisbane, Qld 4072, Australia

Email:
Curt Wentrup* - wentrup@uq.edu.au

* Corresponding author

Keywords:
carbene–nitrene interconversion; diazepines; flash vacuum thermolysis; matrix photochemistry; nitrile ylides; reactive intermediates

Beilstein J. Org. Chem. **2013,** *9,* 754–760.
doi:10.3762/bjoc.9.85

Received: 29 January 2013
Accepted: 22 March 2013
Published: 17 April 2013

This article is part of the Thematic Series "New reactive intermediates in organic chemistry".

Guest Editor: G. Bucher

Abstract

Both flash vacuum thermolysis (FVT) and matrix photolysis generate 2-diazomethylpyrazine (**22**) from 1,2,3-triazolo[1,5-*a*]pyrazine (**24**). FVT of 4-azidopyridine (**18**) as well as of **24** or 2-(5-tetrazolyl)pyrazine (**23**) affords the products expected from the nitrene, i.e., 4,4'-azopyridine and 2- and 3-cyanopyrroles. Matrix photolyses of both **18** and **24** result in ring expansion of 4-pyridylnitrene/2-pyrazinylcarbene to 1,5-diazacyclohepta-1,2,4,6-tetraene (**20**). Further photolysis causes ring opening to the ketenimine **27**.

Introduction

The carbene–nitrene interconversion exemplified with phenylnitrene (**1**) and 2-pyridylcarbene (**3**) has been described in considerable detail [1-3]. The three species **1**–**3** have all been observed directly by IR or ESR spectroscopy in low-temperature matrices. The normal reaction products of phenylnitrene are azobenzene (**4**) and aniline (**5**), but under forcing flash vacuum thermolysis (FVT) conditions cyanocyclopentadiene **6** is formed (Scheme 1). Several other carbene–nitrene rearrangements have been reported [3-5].

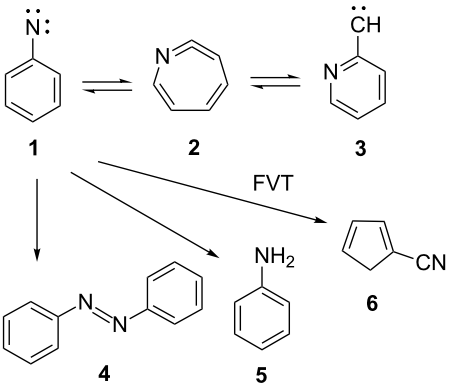

Scheme 1: Phenylnitrene–2-pyridylcarbene rearrangement.

In addition to the ring expansion (**1**–**2**–**3**), two ring opening reactions have been investigated in recent years. Type I ring opening takes place in nitrenes possessing a 1,3-relationship between a nitrene centre and a ring nitrogen atom and leads to nitrile ylides, such as **9** in the case of 3-pyridylnitrene (**7**),

whereby the actual ring opening may take place in either the nitrene itself or the ring-expanded ketenimine **8** (Scheme 2) [6-8]. A 1,7-H shift finally converts the nitrile ylide **9** to the open-chain ketenimine **10** (Scheme 2). 3-Pyridylcarbene undergoes analogous Type I ylidic ring opening to an ethynylvinylnitrile imine [6]. Type II ring opening is diradicaloid and proceeds via an open-chain vinylnitrene or biradical **13** in nitrenes such as 2-pyridylnitrene (**11**). This leads to minor amounts of ketenimines **14** or glutacononitriles **15** beside the main product, the cyclic carbodiimide **12**, which is formed in a degenerate rearrangement (**11**≡**11**). The major end products of FVT are the cyanopyrroles **16** and **17** (Scheme 2) [3,9-11].

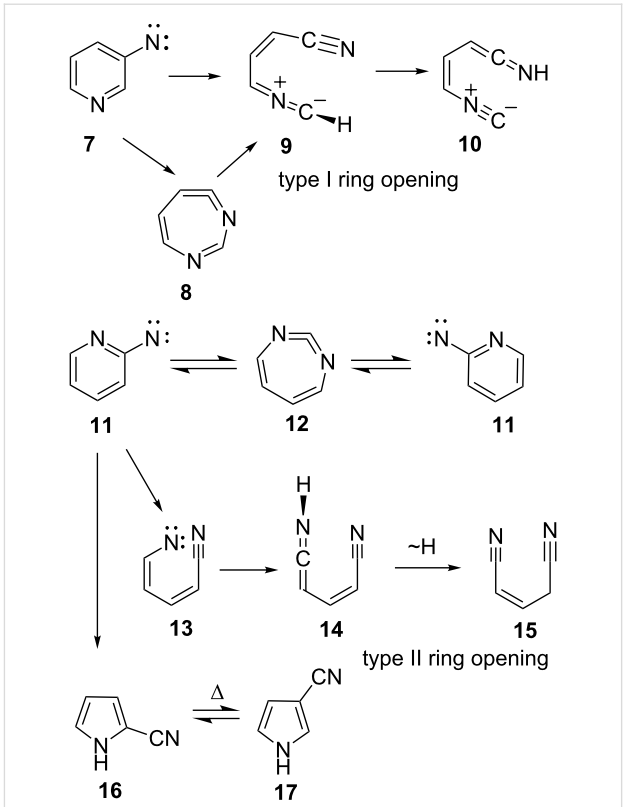

Scheme 2: Type I and type II ring opening and ring expansion in 3- and 2-pyridylnitrenes, respectively.

Results and Discussion

Here, we report details of the FVT as well as matrix photolysis reactions of 4-azidopyridine (**18**) and the isomeric triazolo[1,5-*a*]pyrazine (**24**) and its precursor, 2-(5-tetrazolyl)pyrazine (**23**). Furthermore, we report evidence for ring expansion as well as ring opening of 4-pyridylnitrene (**19**) and 2-pyrazinylcarbene (**21**) (Scheme 3). Mild FVT of **18** at 400 °C, even in high vacuum, affords 4,4'-azopyridine (**25**) in 54% yield [12]. This kind of reaction is typically ascribed to the dimerization of triplet nitrenes. Most importantly, FVT of the pyrazinylcarbene precursor **23** also affords a small amount of 4,4'-azopyridine (**25**), thus implying a rearrangement of carbene **21** to nitrene **19** (Scheme 3). Presumably, this takes place via the diazacycloheptatetraene, **20**, which was not directly observed under the FVT conditions. It was, however, readily observed under photolysis conditions, as described below. Since nitrenes are intrinsically more stable than the isomeric carbenes [3,12,13], a rearrangement of **21** to **19** is perfectly reasonable.

In the case of phenylazide, mild FVT results in the formation of azobenzene (**4**) (Scheme 1), but violent FVT, where the pressure is allowed to rise to ca. 1 mbar due to a shock wave induced by rapid distillation of the azide into the furnace under high vacuum, results in ring contraction to cyanocyclopentadiene **6** [12]. Similar pyrolysis of 4-azidopyridine results in ring contraction to a mixture of 2- and 3-cyanopyrroles **16** and **17**. Because the ring contraction is highly exothermic, the product will be chemically activated [14], and therefore interconversion of the two cyanopyrroles cannot be avoided. Only a minute trace of 4,4'-azopyridine is formed under these conditions. The total yield of the cyanopyrroles is low because of heavy charring inside the pyrolysis tube. The exact mechanisms of ring contraction in arylnitrenes are under investigation, but in the case of 2-pyridylnitrene (Scheme 2) three routes to the cyano-

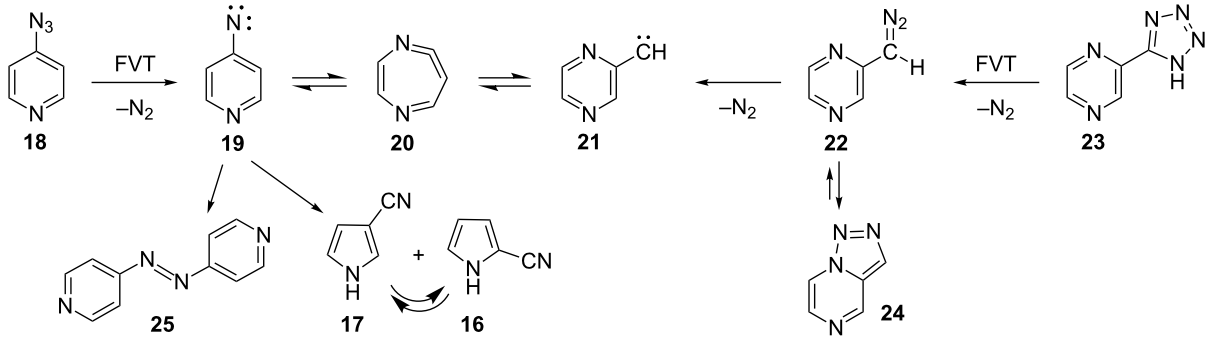

Scheme 3: FVT reactions of 4-azidopyridine (**18**), 2-(5-tetrazolyl)pyrazine (**23**) and triazolo[1,5-*a*]pyrazine (**24**).

pyrroles have been described [10], as has their thermal interconversion [9,10]. The analogous, concerted ring contraction of phenylnitrene to 5-cyanocyclopentadiene has a calculated barrier of ca. 30 kcal/mol [15].

FVT of the tetrazole **23** at 400 °C/10^{-4} mbar causes loss of N_2 and formation of 2-diazomethylpyrazine (**22**), which is easily observed directly by its strong absorption at 2080 cm^{-1} when the pyrolysate is isolated neat in liquid N_2 at −196 °C, or at 2092 cm^{-1} upon isolation in an Ar matrix at 10 K. The diazo compound is also formed on matrix photolysis of the triazole (Figure 1). Compound **22** can exist as s-*Z* and s-*E* conformers. One conformer dominates, absorbing strongly at 2092 cm^{-1}; the other, minor absorption is at 2076 cm^{-1} (Figure 1). Warming the neat diazo compound to ca. −30 °C causes ring closure to triazole **24**. Compound **24** can be isolated in up to 20% yield in preparative pyrolysis of **23** [16]. Further FVT of either **23** or **24** at ≥450 °C/10^{-3} mbar results in the formation of approximately equal amounts of the cyanopyrroles **16** and **17** and azo compound **25**, but the overall yield is again poor, ca. 30%, due to heavy charring in the pyrolysis tube. It is worth noting that ethynylimidazoles, which could be thought of as ring-contraction products of carbene **21**, were not detectable.

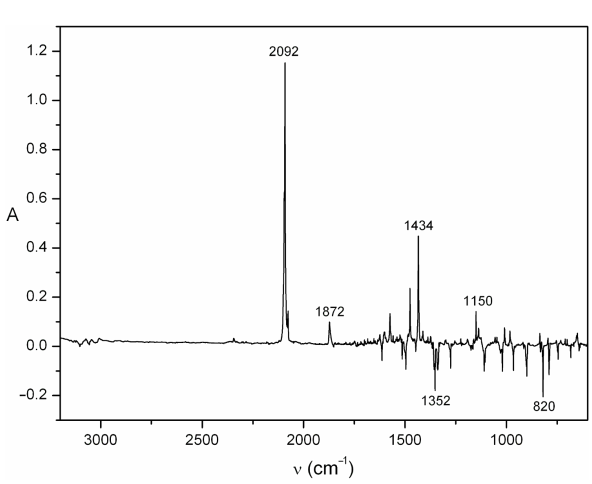

Figure 1: Difference-IR spectrum of 2-diazomethylpyrazine (**22**) (positive peaks) in Ar matrix at 7 K, obtained by photolysis of triazolopyrazine **24** at 290 nm for 10 min (negative peaks). Spectrum assigned to **22**: 795, 835, 918, 1009, 1056, 1150, 1299, 1434, 1476, 1574, 2076 and 2092 cm^{-1}; the latter two absorptions are assigned to the two s-*E* and s-*Z* conformations of the diazo group. The peak at 1872 cm^{-1} is due to the formation of a small amount of the photoproduct **20**. See the Supporting Information File 1, Figure S1 for a full spectrum of **24** with peak listing.

Photolysis of either 4-azidopyridine (**18**) or triazole **24** in an Ar matrix at 7–10 K causes efficient ring expansion to the cyclic seven-membered ring ketenimine **20** as observed by IR spectroscopy (Figure 2). In the case of triazole **24**, efficient ring opening to the diazo compound **22** happens first (Figure 1), so

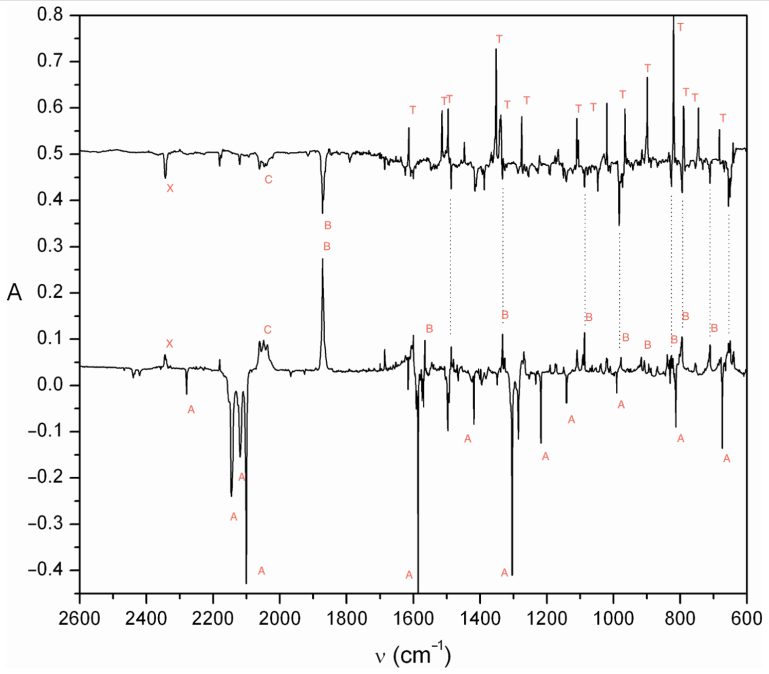

Figure 2: Ar matrix IR-difference spectra showing the products of broadband UV photolysis of 4-azidopyridine (**18**) (bottom, bands labelled A) and 1,2,3-triazolo[1,5-*a*]pyrazine (**24**) (top, bands labelled T). In the photolysis of **18** the negative peaks (A) are due to the subtracted spectrum of azide **18**; the positive peaks are due to the products **20** (B) and **27** (C). In the photolysis of **24** the negative peaks are the products **20** and **27**; the positive peaks are due to the subtracted spectrum of the triazole **24** (T). A small peak labelled X at 2340 cm^{-1} is due to CO_2. Ordinate in arbitrary absorbance units. See Figure S1–S3 in Supporting Information File 1 for full spectra of **18**, **20** and **24** with peak listings.

the latter is the immediate precursor of **20**. The IR spectrum of the triazole **24** is shown in Figure S1, Supporting Information File 1.

It is clearly seen in Figure 2 that the two starting materials **18** and **24** afford nearly identical product mixtures, and the absorptions of ketenimine **20** account for the majority of the spectrum, including the very strong cumulenic absorption at 1872 cm^{-1}. This cumulene **20** is obtained nearly pure after short photolysis times (Figure 3).

Further photolysis, especially at higher energy (254 nm), causes formation of a second product with prominent signals in the IR spectrum at 2028, 2038, 2049, 2060 and 2120 cm^{-1} (Figure 4 and Supporting Information File 1, Figure S4 and Figure S5). The group of bands at 2028–2060 cm^{-1} is ascribed to the ketenimine moiety (N=C=C), and the band at 2120 cm^{-1} to the isocyanide (NC) function in the ring-opened *N*-(isocyanovinyl)ketenimine (**27**) (Scheme 4). The latter band is not seen in the the pyridyl azide photolysis in Figure 2 because of masking by the strong, negative azide bands. However, the 2120 cm^{-1} band is clearly seen later in the photolysis when most of the azide has been consumed (see Figure 4 and Supporting Information File 1, Figure S5). The temporal evolution of the azide photolysis reveals that the cyclic ketenimine **20** is formed first, followed by the open chain ketenimine **27** (Figure S3, Supporting Information File 1). It should be noted that ketenimine **27** can exist as four different s-*E* and s-*Z* conformers, with slightly different IR absorptions (the calculated spectra are shown in Figure 4 and Figure S6 and Figure S7, Supporting Information File 1). The experimental spectra indicate that all four conformers of **27** are formed, giving rise to bands at 2028–2060 cm^{-1}, i.e., there is enough energy available to effect *E*–*Z* and s-*E*–s-*Z* isomerization in the matrix. Also the isocyanide band at 2120 cm^{-1} shows splitting, but this is less well resolved (Figure 4). All this makes it difficult to assign other, much weaker, peaks in the IR spectra to compound **27**. However, the following bands, which are not ascribed to the cyclic ketenimine **20**, can be assigned to **27**: Observed wavenumbers and, in parentheses, the calculated harmonic frequencies of the conformers of **27** at the B3LYP/6-31G* level, scaled by 0.9613: 711 (691–703), 1300 (1256–1290), 1380 (1373–1377), 1608–1624 (1612–1634), 2028, 2038, 2049, 2061 (2038–2063), 2119–2124 (2112–2117) cm^{-1} (see Supporting Information File 1 for computational details).

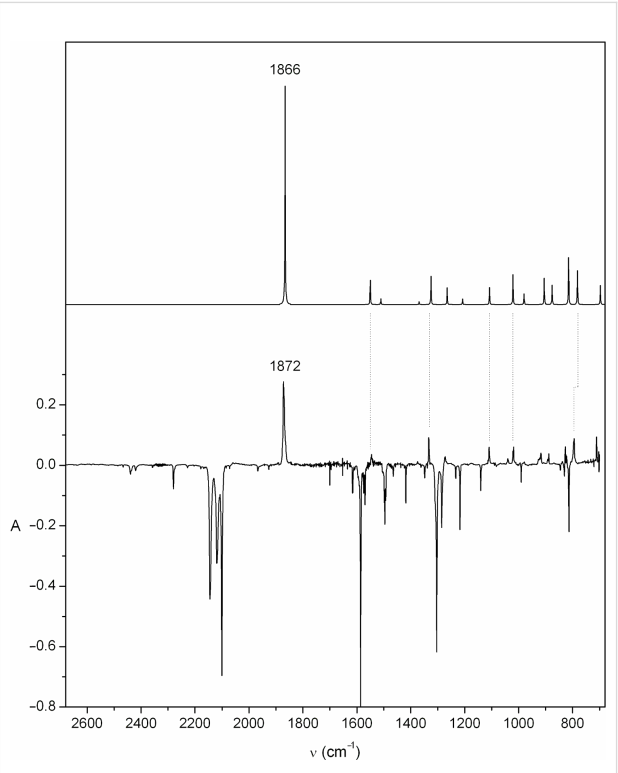

Figure 3: Top: calculated IR spectrum of **20** at the B3LYP/6-31G* level (wavenumbers scaled by 0.9613): ν' (relative intensity) 697 (9), 782 (16), 815 (22), 876 (9), 905 (12), 980 (5), 1021 (14), 1108 (8), 1208 (3), 1265 (8), 1325 (13), 1511 (3), 1550 (11), 1866 (100) cm^{-1}. Ordinate in arbitrary absorbance units. Bottom: Ar matrix IR-difference spectrum of diazacycloheptatetraene **20** (ν' 710, 794, 826, 887, 1028, 1109, 1272, 1332, 1545, 1872 cm^{-1}), formed by photolysis of 4-azidopyridine (**18**) (3 min broadband UV; positive bands due to **20**; negative bands due to **18**). See Figures S2 and S3 in Supporting Information File 1 for full spectra of **18** and **20** with peak listings.

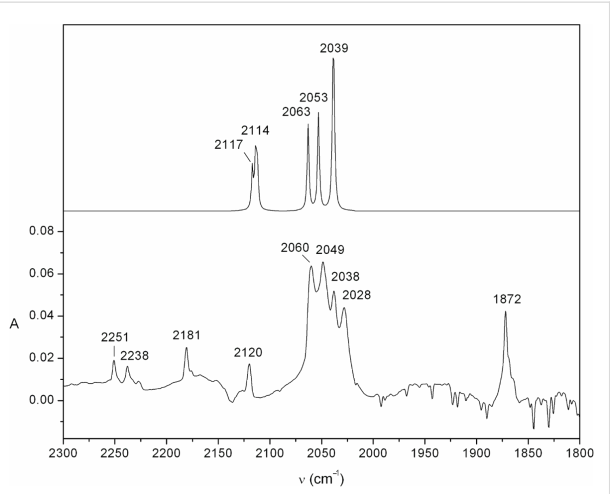

Figure 4: Bottom: IR spectrum from the matrix photolysis of azide **18** after the azide has been depleted completely (10 min broadband UV, followed by 30 min low pressure Hg lamp at 254 nm). Top: the calculated absorptions of the four isomers of the open chain ketenimine **27** (1:1:1:1 ratio of the s-*E*,*E*; s-*E*,*Z*; s-*Z*,*E*; and s-*Z*,*Z* isomers). The calculated peak at 2039 cm^{-1} is due to the overlapping peaks of two isomers at 2039 and 2040 cm^{-1}. See Figure S6 and Figure S7 in Supporting Information File 1 for structures and spectra of the individual isomers. Calculated spectra are at the B3LYP/6-31G* level (wavenumbers scaled by 0.9613). The 254 nm photolysis causes a faster rearrangement of **20** to **27**; broadband UV photolysis achieves a similar change in ca. 60 min.

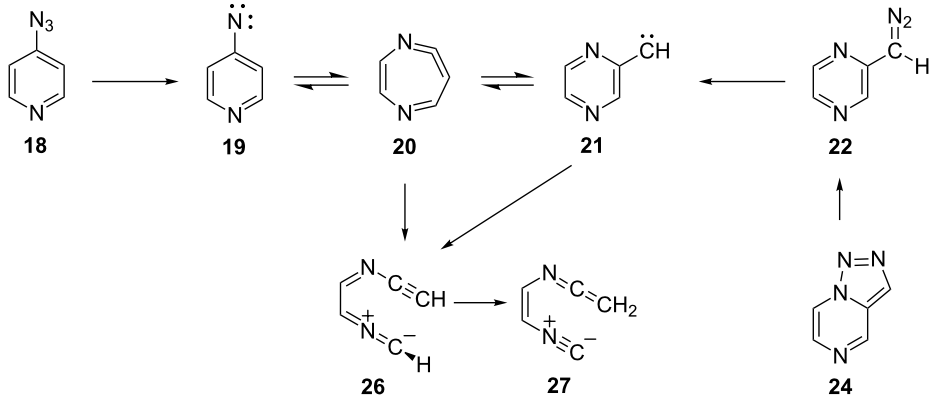

Scheme 4: Photolysis reactions of azide **18** and triazole **24** in Ar matrix.

We postulate that the rearrangement to **27** occurs via the unobserved nitrile ylide intermediate **26** (Scheme 4). The calculated IR spectra of the four s-*E* and s-*Z* conformers of **26** are shown in Figure S8 and Figure S9 in Supporting Information File 1. Related nitrile ylides are known to undergo very facile 1,7-H shifts (see, e.g., Scheme 2) [3,6]. Both the nitrile ylide and the ring-expanded ketenimine were observed in the corresponding benzannelated systems, viz 4-azidoquinoline and 2-diazomethylquinoxaline [17], and the ylidic ring opening is very facile in 3-pyridylcarbene [6]. Thus, there is good precedence for transformations of the type **26**→**27** (Scheme 4).

Conclusion

2-Pyrazinylcarbene (**21**) rearranges to 4-pyridylnitrene (**19**) on FVT as evidenced by the isolation of 4,4'-azopyridine (**25**). Both **19** and **21** undergo ring expansion to the diazacycloheptatetraene **20** on UV photolysis. Compound **20** is clearly identified by its matrix IR spectrum, particularly the strong cumulenic stretch at 1872 cm^{-1}. Further photolysis causes the gradual depletion of **20** and formation of the ring opened ketenimine **27**. The latter reaction indicates ring opening of either cumulene **20** or carbene **21** to the nitrile ylide **26** followed by a rapid 1,7-H shift to **27**.

In summary, 4-pyridylnitrene **19** behaves much like phenylnitrene **1**. The thermal chemistry of both the nitrene **19** and the carbene **21** is dominated by nitrene reactions (giving azopyridine and cyanopyrroles), because the carbene rearranges to the lower energy nitrene. However, the 2-pyrazinylcarbene **21** possesses a 1,3-relationship between the carbene centre and a ring nitrogen atom like in 3-pyridylcarbene [6] and therefore undergoes ylidic ring opening. Thanks to the reversible carbene–nitrene rearrangement (**19** ⇄ **20** ⇄ **21**) formation of the ylide **26** and hence the ketenimine **27** becomes the dominant reaction under the conditions of matrix photolysis.

Experimental

General

The apparatus and procedures for preparative FVT [18] and for Ar matrix isolation [11,19,20] were as previously described. KBr and CsI windows were used for IR spectroscopy. FVT products were isolated in liquid nitrogen (77 K) in the preparative thermolyses, and at 22–25 K in Ar matrices for IR experiments. IR spectra of the Ar matrices were measured at 7–10 K with a resolution of 1 cm^{-1}. Photolyses were done through quartz by using a 75 W low-pressure Hg lamp (254 nm) or a 1000 W high pressure Hg/Xe lamp equipped with a monochromator and appropriate filters. A water filter was used to remove infrared radiation.

Materials

4-Azidopyridine (**18**) was prepared from 4-bromopyridine and NaN_3 in 10% ethanol under reflux for 8 h by adaptation of a literature method [21]. 1,2,3-Triazolo[1,5-*a*]pyrazine (**24**) was prepared according to a literature procedure [16].

FVT of 4-azidopyridine (**18**)

The azide (0.50 g) was distilled into the FVT apparatus from a sample flask held at 35 °C and thermolysed at 400 °C/10^{-2}–10^{-3} mbar in the course of 1 h. 4,4'-Azopyridine (**25**) (54% yield; red solid, mp 107–108 °C) was identified by comparison with a sample prepared according to den Hertog et al. (mp 107.5 °C) [22]. Traces of unreacted azide **18** and 2- and 3-cyanopyrroles **16** and **17**were detected by GC–MS and IR spectroscopy.

"Violent pyrolysis" was achieved by holding the sample flask at 100 °C. The rapid distillation causes a shock wave and a pressure increase to 1 mbar under continuous pumping with a two-stage oil pump capable of a base vacuum of 10^{-4} mbar. The whole reaction is finished in a matter of seconds. The 2- and

3-cyanopyrroles **16** and **17** were isolated in a ratio of ca. 1:1 in a total yield of 10% as analysed by GC. Only a trace of 4,4'-azopyridine (**25**) was formed under these conditions. There was heavy charring inside the pyrolysis tube.

Photolysis of 4-azidopyridine (**18**)

The azide (5–10 mg) was evaporated from a reservoir at −30 to −40 °C and codeposited with Ar at 25 K. After cooling to 7 K, the spectrum was recorded (Figure S2, Supporting Information File 1): IR (Ar, 7 K) 813, 1271, 1303, 1586, 2100, 2119, 2145, 2280 cm^{-1}.

The azide matrix was irradiated with broadband UV light from the high-pressure Xe/Hg lamp, at 290 nm using the monochromator, or at 254 nm using the low-pressure Hg lamp. The resulting product-difference IR spectra are shown in Figure 2, Figure 3 and Figure 4. The temporal evolution of the spectrum under continuous broadband photolysis at 7 K is shown in Figure S3, Figure S4 and Figure S5, Supporting Information File 1.

FVT of 2-(5-tetrazolyl)pyrazine (**23**)

The preparation of triazolopyrazine **24** by FVT of **23** at 400 °C has been described previously [19]. FVT of **23** at 450 °C/ 10^{-3} mbar caused formation of triazole **24**, 4,4'-azopyridine (**25**) and the 2- and 3-cyanopyrroles **16** and **17** in a ca. 2:1:2:2 ratio and a total yield of ca. 30%. There was heavy charring inside the pyrolysis tube. The cyanopyrroles were isolated by distillation and separated by GC [9]. Compounds **24** and **25** were separated by chromatography on alumina, eluting with $CHCl_3$. The products were identified by comparison of IR, NMR and mass spectra with those of authentic materials [9,22]. Careful searches for ethynylimidazoles were negative.

Photolysis of 1,2,3-triazolo[1,5-*a*]pyrazine (**24**)

The triazole was purified by recrystallization from hexane/ethyl acetate and then sublimed from a sample tube held at 50–60 °C and codeposited with Ar at 25 K. After cooling to 7 K, the spectrum was recorded (Supporting Information File 1, Figure S1): IR (Ar, 7 K) 642, 683, 745, 790, 820, 899, 966, 1020, 1105, 1110, 1165, 1275, 1338, 1352, 1447, 1496, 1514, 1613, 3057 cm^{-1}. Irradiation at 290 nm for 10 min afforded 2-diazomethylpyrazine with principal absorptions at 2092 cm^{-1} (major conformer) and 2076 cm^{-1} (minor conformer) (Figure 1): IR (Ar, 7 K) 795, 835, 918, 1009, 1056, 1150, 1299, 1434, 1476, 1574, 2076, 2092 cm^{-1}. A small amount of the photoproduct **20** also appeared (1872 cm^{-1}; Figure 1). Further photolysis afforded the product spectrum shown in Figure 2 and in Supporting Information File 1, Figure S3, Figure S4 and Figure S5.

Supporting Information

Supporting Information File 1

Additional matrix IR spectra of **18**, **24**, and their photolysis products, calculated IR spectra of **20**, **26** and **27**, and computational details.
[http://www.beilstein-journals.org/bjoc/content/supplementary/1860-5397-9-85-S1.pdf]

Acknowledgements

This work was aided by the National Computing Merit Allocation Scheme, project g01, supported by the Australian Government.

References

1. Crow, W. D.; Wentrup, C. *Tetrahedron Lett.* **1968,** 6149. doi:10.1016/S0040-4039(00)70816-1
2. Chapman, O. L.; Sheridan, R. S.; LeRoux, J. P. *J. Am. Chem. Soc.* **1978,** *100,* 6245. doi:10.1021/ja00487a054
3. Wentrup, C. *Acc. Chem. Res.* **2011,** *44,* 393. doi:10.1021/ar700198z
4. Bräse, S.; Banert, K., Eds. *Organic Azides: Syntheses and Applications;* Wiley-VCH: Chichester, UK, 2010.
5. Falvey, D. E.; Gudmundsdottir, A. D., Eds. *Nitrenes and Nitrenium Ions;* Wiley-VCH: Hoboken, NJ, USA, 2013.
6. Bednarek, P.; Wentrup, C. *J. Am. Chem. Soc.* **2003,** *125,* 9083. doi:10.1021/ja035632a
7. Kvaskoff, D.; Mitschke, U.; Addicott, C.; Finnerty, J.; Bednarek, P.; Wentrup, C. *Aust. J. Chem.* **2009,** *62,* 275. doi:10.1071/CH08523
8. Kvaskoff, D.; Vosswinkel, M.; Wentrup, C. *J. Am. Chem. Soc.* **2011,** *133,* 5413. doi:10.1021/ja111155r
9. McCluskey, A.; Wentrup, C. *J. Org. Chem.* **2008,** *73,* 6265. doi:10.1021/jo800899t
10. Kvaskoff, D.; Bednarek, P.; Wentrup, C. *J. Org. Chem.* **2010,** *75,* 1600. doi:10.1021/jo902570d
11. Wentrup, C.; Kvaskoff, D. *Aust. J. Chem.* **2013,** *66,* 286. doi:10.1071/CH12502
12. Minisci, F.; Hendrickson, J. B.; Wentrup, C. Rearrangements and interconversions of carbenes and nitrenes. Topics in Current Chemistry, Vol. 62; 1976; pp 173–251. doi:10.1007/BFb0046048
13. Kemnitz, C. R.; Karney, W. L.; Borden, W. T. *J. Am. Chem. Soc.* **1998,** *120,* 3499. doi:10.1021/ja973935x
14. Wentrup, C. *Tetrahedron* **1974,** *30,* 1301. doi:10.1016/S0040-4020(01)97303-X
15. Kvaskoff, D.; Bednarek, P.; George, L.; Pankarakshan, S.; Wentrup, C. *J. Org. Chem.* **2005,** *70,* 7947. doi:10.1021/jo050898g
16. Wentrup, C. *Helv. Chim. Acta* **1978,** *61,* 1755. doi:10.1002/hlca.19780610522
17. Addicott, C.; Lüerssen, H.; Kuzaj, M.; Kvaskoff, D.; Wentrup, C. *J. Phys. Org. Chem.* **2011,** *24,* 999. doi:10.1002/poc.1904
18. Wentrup, C.; Blanch, R.; Briehl, H.; Gross, G. *J. Am. Chem. Soc.* **1988,** *110,* 1874. doi:10.1021/ja00214a034
19. Kuhn, A.; Plüg, C.; Wentrup, C. *J. Am. Chem. Soc.* **2000,** *122,* 1945. doi:10.1021/ja993859t
20. Kappe, C. O.; Wong, M. W.; Wentrup, C. *J. Org. Chem.* **1995,** *60,* 1686. doi:10.1021/jo00111a029

21. Tanno, M.; Kamiya, S. *Chem. Pharm. Bull.* **1979,** *27,* 1824. doi:10.1248/cpb.27.1824
22. den Hertog, H. J.; Combé, W. P. *Recl. Trav. Chim. Pays-Bas* **1951,** *70,* 581. doi:10.1002/recl.19510700704

License and Terms

Beilstein Journal of Organic Chemistry

Ring opening of 2-aza-3-borabicyclo[2.2.0]hex-5-ene, the Dewar form of 1,2-dihydro-1,2-azaborine: stepwise versus concerted mechanisms

Holger F. Bettinger* and Otto Hauler

Full Research Paper

Open Access

Address:
Institut für Organische Chemie, Universität Tübingen, Auf der Morgenstelle 18, 72072 Tübingen, Germany

Email:
Holger F. Bettinger* - holger.bettinger@uni-tuebingen.de

* Corresponding author

Keywords:
ab initio; azaborine; BN aromatics; Dewar isomer; reaction mechanism

Beilstein J. Org. Chem. **2013,** *9,* 761–766.
doi:10.3762/bjoc.9.86

Received: 12 February 2013
Accepted: 21 March 2013
Published: 18 April 2013

This article is part of the Thematic Series "New reactive intermediates in organic chemistry".

Guest Editor: G. Bucher

Abstract

The ring opening of the Dewar form of 1,2-dihydro-1,2-azaborine, 2-aza-3-borabicyclo[2.2.0]hex-5-ene (**3**) is investigated by theoretical methods by using multiconfiguration SCF (CASSCF) and coupled cluster theory [CCSD(T)] with basis sets up to polarised quadruple-zeta quality. The title compound was previously reported to form photochemically in cryogenic noble gas matrices from 1,2-dihydro-1,2-azaborine (**4**). Four reaction paths for the thermal ring opening of **3** to **4** could be identified. These are the conventional disrotatory and conrotatory electrocyclic ring-opening pathways where the BN unit is only a bystander. Two more favourable paths are stepwise and involve 1,3-boron–carbon interactions. The lowest energy barrier for the isomerisation reaction, 22 kcal mol^{-1}, should be high enough for an experimental observation in solution. However, in solution the dimerisation of **3** is computed to have a very low barrier (3 kcal mol^{-1}), and thus **3** is expected to be a short-lived reactive intermediate.

Introduction

The barrier for ring opening of Dewar benzene (**1**) to yield benzene (**2**) is high enough to give this benzene valence isomer a half life of about two days [1] at room temperature despite the significant exothermicity (60–70 kcal mol^{-1}) of the isomerisation reaction (Scheme 1) [2-6]. The relatively high barrier ($\Delta H^{\ddagger}$ = 25.1 ± 2 kcal mol^{-1}) [7,8] is due to the fact that the formation of benzene from **1** would require a disrotatory ring opening that is orbital-symmetry-forbidden according to the Woodward–Hoffmann rules [9-11]. The allowed conrotatory electrocyclic opening of one of the cyclobutene moieties of **1**, on the other hand, would result in a highly strained *cis*,*cis*,*trans*-cyclohexa-1,3,5-triene (*trans*-benzene) isomer [10,11].

Computational investigations of the isomerisation have been performed to reveal mechanistic details [12-14]. The most sophisticated investigation [14] (multireference configuration interaction, energies based on complete active space self-consistent field geometries, MRCI//CASSCF) confirmed an earlier conclu-

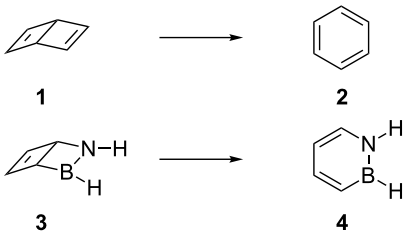

Scheme 1: Isomerisation of bicyclo[2.2.0]hexa-1,3-diene, Dewar benzene (**1**), to benzene (**2**) and of 2-aza-3-borabicyclo[2.2.0]hex-5-ene (**3**) to 1,2-dihydro-1,2-azaborine (**4**).

sion [13] that the conrotatory motion is the lowest energy pathway. It was also demonstrated that the conrotatory transition structure connects **1** and benzene directly, i.e., without the involvement of *trans*-benzene [14]. The barrier computed (32.6 kcal mol^{-1}) is lower than that for the disrotatory pathway by 6.6 kcal mol^{-1} [14].

We have recently reported that the irradiation (λ = 254 nm) of 1,2-dihydro-1,2-azaborine (**4**), a boron-nitrogen heterocycle that is isoelectronic and isosteric with benzene [15], results in its Dewar isomer 2-aza-3-borabicyclo[2.2.0]hex-5-ene (**3**) under the conditions of cryogenic noble gas matrix isolation [16]. Under these experimental conditions (T < 35 K), the isomerisation back to **4** is not observed [16]. Can **3** exist outside of cryogenic matrices? To answer this question, we report here a computational investigation of important intramolecular and intermolecular decomposition pathways of **3**.

Results and Discussion

Ring opening of 3

Conrotatory and disrotatory ring opening

We have performed explorative computations using the CASSCF(6,6)/6-31G* method and could locate transition states for the conrotatory (**TS1**; n_{imag} = 1, i556 cm^{-1}) and disrotatory (**TS2**; n_{imag} = 1, i628 cm^{-1}) ring opening of **3**. Computation of the intrinsic reaction coordinates confirms that both **TS1** and **TS2** connect the Dewar form **3** to 1,2-dihydro-1,2-azaborine. These transition states are similar in geometry to those described earlier for the all-carbon system (see Figure 1 and Figure 2) [14]. The C1–C4 distance is shorter in **TS1** (2.247 Å) than it is in **TS2** (2.313 Å). The BN unit is a bystander in these two mechanisms as it is not involved in the ring-opening process.

The energies of these transition states were refined with multireference perturbation theory (MRMP2). In agreement with the results obtained for the all-carbon system [14], the barrier for the orbital-symmetry-allowed conrotatory ring opening is lower (26.5 kcal mol^{-1}) than it is for the forbidden

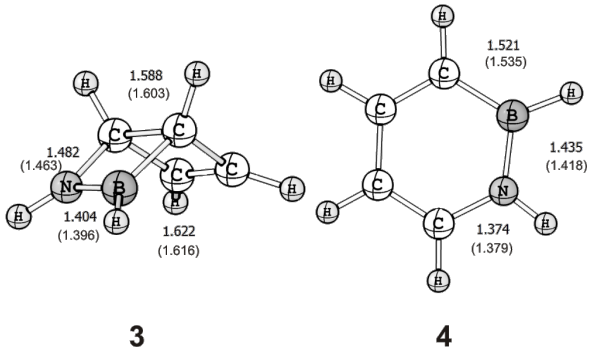

Figure 1: Geometries of **3** and **4** computed at the CCSD(T)/TZ2P and CASSCF(6,6)/6-31G* (in parentheses) levels of theory. Bond lengths are given in angstroms (Å).

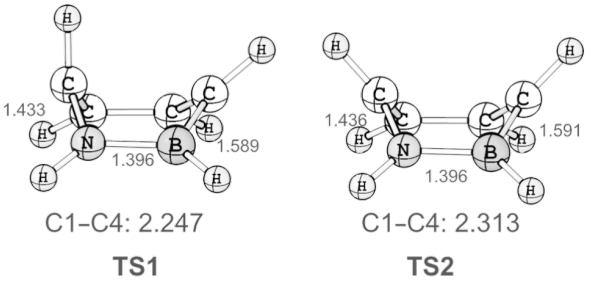

Figure 2: Geometries of **TS1** and **TS2** computed at the CASSCF(6,6)/6-31G* level of theory. C1–N, N–B, C4–B, and C1–C4 distances are given in angstroms (Å).

disrotatory reaction (30.1 kcal mol^{-1}) (Table 1). The energy difference of about 4 kcal mol^{-1} is slightly smaller than that reported for the all-carbon system (7 kcal mol^{-1}) [14]. Due to the use of different levels of theory (MRMP2 in the present work, MRCI by Havenith et al. [14]), the energy barriers for conrotatory ring opening of **1** and **3** cannot be directly compared. We have made no attempt to increase the level of theory for **TS1** and **TS2** beyond MRMP2, because we found two additional reaction paths that are significantly more favourable.

Stepwise ring opening

Two additional pathways, both of them stepwise, for the ring opening of **3** could be identified. As the energies for the two reactions paths are very similar, we used coupled-cluster theory to obtain highly accurate structures (see Figure 3) and energies of the stationary points involved in ring opening. The CCSD(T) geometry optimizations arrive at a minimum on the potential-energy surface (**MIN1**). Characteristic of this intermediate **MIN1** is a short B–C1 distance of 1.858 Å, while the C1–C4 distance is increased to 2.318 Å. The nitrogen atom is strongly pyramidalised resulting in an H–N–C1–H dihedral angle of 175.2°. A second minimum **MIN2** between **3** and 1,2-dihydro-

Table 1: Relative energies (E_{rel}, in kcal mol^{-1} including zero-point vibrational energies, ZPVE) of 1,2-dihydro-1,2-azaborine (**4**), its Dewar valence isomer **3**, high energy minima, and the transition states for ring opening of **3** as computed at the MRMP2 and CCSD(T) levels of theory.

Compounds	E_{rel}(MRMP2)[a]	E_{rel}(CCSD(T))[b]
3	0	0
4		−59.3
TS1 (conrotatory)	26.5	31.0[c]
TS2 (disrotatory)	30.1	–
MIN1	–	20.3
TS3	–	21.7
TS4	–	25.8
MIN2	---	17.8
TS5	–	19.1
TS6	–	22.2

[a]MRMP2-CASSCF(6,6)/6-31G*//CASSCF(6,6)/6-31G*, ZPVE were obtained at CASSCF(6,6)/6-31G*; [b]CCSD(T)/cc-pVQZ//CCSD(T)/TZ2P, ZPVE were obtained at CCSD(T)/DZP; [c] CCSD(T)/cc-pVQZ based on CASSCF(6,6)/6-31G*+ZPVE data for **TS1** and **3**.

1,2-azaborine could also be located with the CCSD(T) method. The structure of **MIN2** is characterised by an almost ecliptic orientation of the N–H and C1–H bonds as the dihedral angle is only 7.8°. The B–C1 distance of 1.827 Å is slightly shorter, while the C1–C4 distance of 2.336 Å is slightly longer than in **MIN1**. Hence **MIN1** and **MIN2** mainly differ by the relative orientation of the N–H bond. The strong pyramidalisation of the nitrogen atom and the short B–C1 distance show that in these two reaction pathways the BN unit is no longer just a bystander. The mode of rotation that results in **MIN1** and **MIN2** may be considered conrotatory, but the C4H group has moved significantly more than the C1H group. The electron pair of the breaking C1–C4 bond is utilized for interaction with the boron centre. As a consequence, the nitrogen lone pair is more localised resulting in a pyramidalisation of the nitrogen centre.

At our highest level of theory, CCSD(T)/cc-pVQZ, **MIN2** is more stable than **MIN1** by 2.5 kcal mol^{-1}. **MIN2** is 17.8 kcal mol^{-1} higher in energy than the Dewar form. Both **MIN1** and **MIN2** correspond to shallow minima on the potential energy surface. The barrier for collapse of **MIN1** to the Dewar form **3** through transition state **TS3** is only 1.4 kcal mol^{-1}, while formation of 1,2-dihydro-1,2-azaborine from **MIN1** through **TS4** has a barrier of 5.5 kcal mol^{-1}. Likewise, collapse of **MIN2** to the Dewar form **3** via **TS5** has a barrier of only 1.3 kcal mol^{-1}, and formation of 1,2-dihydro-1,2-azaborine through **TS6** has a barrier of 4.4 kcal mol^{-1}.

For most of the stationary points the T_1 diagnostic [17], a measure of the reliability of single-reference based CCSD(T) theory, is below the critical value of 0.02 indicating that the

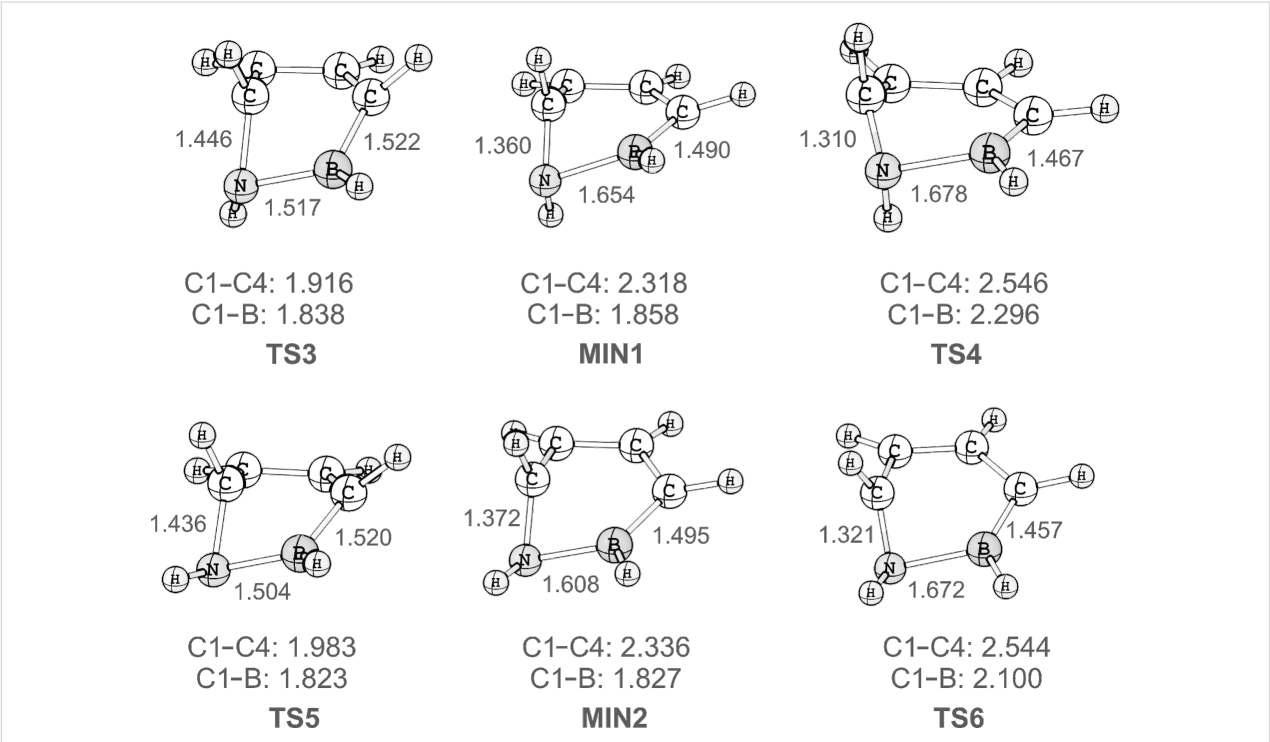

Figure 3: Geometries of **MIN1**, **TS3**, **TS4** and **MIN2**, **TS5**, **TS6** computed at the CCSD(T)/TZ2P level of theory. C1–N, N–B, C4–B, C1–C4, and C1–B distances are given in angstroms (Å).

CCSD(T) treatment should produce highly reliable results. Only for **TS4** and **TS6** are the T_1 diagnostics 0.024 and 0.023, respectively. To confirm that the single reference CCSD(T) treatment produces satisfactory results also for these stationary points, we have computed the completely renormalised CR-CCSD(T)L energies for all species, as CR-CCSD(T)L has been shown to dramatically improve CCSD(T) results of multireference cases. The CR-CCSD(T)L energies are within 0.2 kcal mol^{-1} of the CCSD(T) values for all these species, including those (**TS4** and **TS6**) with slightly elevated T_1 diagnostics.

Comparison of the energies of the stationary points along the stepwise pathways with **TS1** and **TS2** is hampered by problems associated with locating the latter at the CCSD(T) level. We have thus computed the barrier for conrotatory ring opening at the CCSD(T) and CR-CCSD(T) levels using the CASSCF(6,6) geometries. This shows that the stepwise mechanism is more favourable than the conrotatory opening by 9 kcal mol^{-1}.

In summary, the energetically most favourable pathway for the ring opening of **3** to 1,2-dihydro-1,2-azaborine involves **MIN2** as a shallow intermediate and has a highest energy barrier of 22 kcal mol^{-1}. This is roughly 10 kcal mol^{-1} lower than the lowest energy pathway for ring opening of Dewar benzene. Therefore, the lifetime of the Dewar form **3** is expected to be significantly lower than that of Dewar benzene. Nonetheless, with a barrier for isomerisation of about 22 kcal mol^{-1}, **3** should be observable in solution.

Dimerisation of 3

Alternative pathways for disappearance of **3** may be provided by intermolecular reactions that are in principle feasible in solution. Such pathways are of particular importance, as the BN unit in **3** is an aminoborane (RHB=NHR) derivative. Aminoboranes with small substituents are unstable with respect to dimerisation or oligomerisation. In 1,2-dihydro-1,2-azaborine, such a dimerisation is not observed, probably due to the aromatic character of the six-membered ring. In **3**, however, this aromatic stabilisation is no longer available.

For the sake of simplicity, we only considered dimers of **3** (see Figure 4 and Supporting Information File 1 for structures). All three diastereomeric dimers of **3** are thermodynamically more stable than two noninteracting monomers. Formation of the most stable dimer, **DIM1**, is favourable by 37 kcal mol^{-1}. The barrier for its formation at the SCS-RIMP2/def2-TZVP level of theory is only 3.4 kcal mol^{-1} with respect to infinitely separated monomers, and 5.6 kcal mol^{-1} with respect to the energy of a van-der-Waals complex of two monomers.

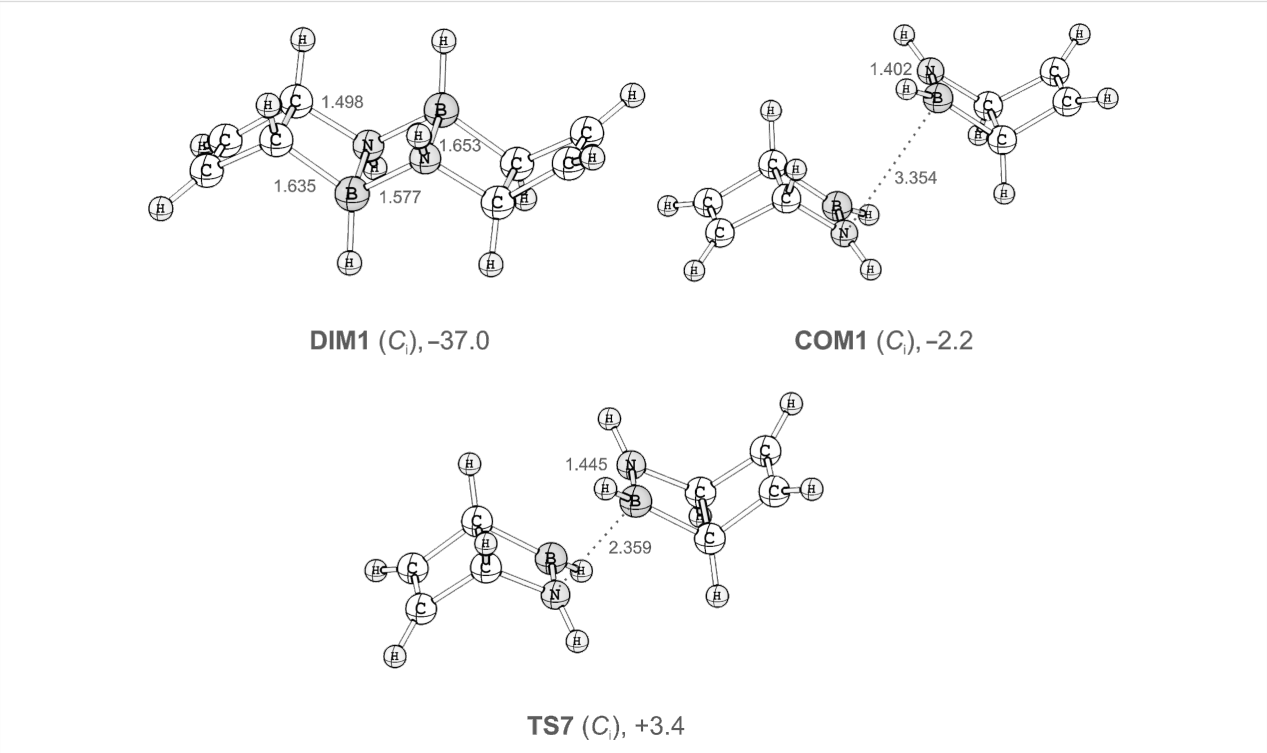

Figure 4: Geometries of **DIM1**, **COM1**, and **TS7** computed at the SCS-RIMP2/def2-TZVP level of theory. Distances are given in angstroms (Å). Energies (in kcal mol^{-1}) relative to two separated molecules of **3** were obtained at the same level of theory and include ZPVE corrections obtained with the smaller def-SV(P) basis set.

Conclusion

The following conclusions can be drawn from the computational investigation.

1. The "classical" conrotatory and disrotatory ring-opening reactions provide pathways for the isomerisation of **3** to 1,2-dihydro-1,2-azaborine. Similar to previous investigations of the ring opening of Dewar benzene (**1**), we find that the conrotatory pathway is lower in energy than the orbital-symmetry-forbidden disrotatory pathway. Both pathways are concerted.

2. In addition, two step-wise pathways that involve conformational isomeric minima were identified. Both of the minima have in common short 1,3-transannular C–B distances. The two pathways have very similar energy barriers (within 4 kcal mol^{-1}). The more favourable one is lower in energy than the conrotatory ring opening by 9 kcal mol^{-1}.

3. The lowest energy pathway for ring opening of **3** has a barrier of 22 kcal mol^{-1}.

4. The lifetime of **3** in solution will not be limited by the ring opening to **4**, but rather by dimerisation. This is a strongly exothermic process that has a low barrier of 3 kcal mol^{-1} with respect to separated monomers. Thus, **3** is expected to be a highly reactive compound that will rapidly undergo dimerisation (or oligomerisation) reactions.

Experimental

The active space in the CASSCF(6,6) computations included the π and π* orbitals for the 1,2-dihydro-1,2-azaborine system, while the four π and π* orbitals along with the C3–C6 σ/σ* orbitals were used for the Dewar form **3** and transition states **TS1** and **TS2**. Geometries were fully optimised and the nature of stationary points was confirmed by analytic computation of second derivatives. Intrinsic reaction coordinates were computed starting from the transition states by using the Schlegel–Gonzalez algorithm [18,19]. The same (6,6) active space was employed for the subsequent multireference second-order perturbation theory (MRMP2) [20] single-point-energy computations. All multireference computations employed the 6-31G* [21] basis set and were performed with the Gamess-US software [22].

The coupled-cluster method with single, double, and a perturbative estimate of triple excitations [CCSD(T)] [23] was employed for geometry optimisation by using analytic gradients [24] in conjunction with Dunning's [25,26] DZP and TZ2P basis sets. Harmonic vibrational frequencies were computed by analytic second derivatives [27] using the DZP basis set to confirm the nature of stationary points and to obtain zero-point vibrational energies (ZPVE). The CCSD(T) gradient and Hessian computations were performed with CFOUR [28]. The CCSD(T)/TZ2P geometries were used for further energy refinement with Dunning's [29] correlation consistent basis sets, cc-pVDZ, cc-pVTZ, and cc-pVQZ. These single point calculations were performed with the Turbomole program [30]. Its implementation of CCSD(T) uses integral-direct techniques and the resolution-of-the-identity approximation [31]. Therefore, the appropriate fitting basis set was chosen [32]. In addition, the so-called rigorously size-extensive completely renormalised coupled-cluster theory [CR-CC(2,3) or CR-CCSD(T)L] [33,34] was used in conjunction with the cc-pVDZ basis set using Gamess-US. The dimerisation of **3** was investigated by using Grimme's spin-component-scaled MP2 method (SCS-MP2) [35], with the resolution-of-identity (RI) approximation for fast computations of two-electron integrals within the second-order Møller–Plesset perturbation theory (MP2) [36,37]. SCS-MP2 was shown recently to yield improved interaction energies compared to conventional MP2 [38-41]. The def-SV(P) [B/C/N: 3s2p1d; H: 2s] [42] and def2-TVZP [B/C/N: 5s3p2d1f; H: 4s2p1d] [37] basis sets in conjunction with the corresponding fitting bases were employed [37]. Harmonic vibrational frequencies were determined by using the def-SV(P) basis set by finite differences of analytic gradients and provided the zero-point vibrational energies (ZVPE).

Supporting Information

Supporting Information File 1

Additional data.
[http://www.beilstein-journals.org/bjoc/content/supplementary/1860-5397-9-86-S1.pdf]

Acknowledgements

This work was supported by the Deutsche Forschungsgemeinschaft and Fonds der chemischen Industrie.

References

1. van Tamelen, E. E.; Pappas, S. P. *J. Am. Chem. Soc.* **1963,** *85,* 3297–3298. doi:10.1021/ja00903a056
2. Volger, H. C.; Hogeveen, H. *Recl. Trav. Chim. Pays-Bas* **1967,** *86,* 830–832. doi:10.1002/recl.19670860806
3. Oth, J. F. M. *Recl. Trav. Chim. Pays-Bas* **1968,** *87,* 1185–1195. doi:10.1002/recl.19680871012
4. Schäfer, W. *Angew. Chem., Int. Ed. Engl.* **1966,** *5,* 669. doi:10.1002/anie.196606691
5. Adam, W.; Chang, J. C. *Int. J. Chem. Kinet.* **1969,** *1,* 487–492. doi:10.1002/kin.550010509
6. Oth, J. F. M. *Angew. Chem., Int. Ed. Engl.* **1968,** *7,* 646.
7. Breslow, R.; Napierski, J.; Schmidt, A. H. *J. Am. Chem. Soc.* **1972,** *94,* 5906–5907. doi:10.1021/ja00771a068

8. Lechkten, P.; Breslow, R.; Schmidt, A. H.; Turro, N. J. *J. Am. Chem. Soc.* **1973,** *95,* 3025–3027. doi:10.1021/ja00790a054
9. Woodward, R. B.; Hoffmann, R. *Angew. Chem.* **1969,** *81,* 797–869. doi:10.1002/ange.19690812102
10. van Tamelen, E. E. *Angew. Chem., Int. Ed. Engl.* **1965,** *4,* 738–745. doi:10.1002/anie.196507381
11. van Tamelen, E. E. *Acc. Chem. Res.* **1972,** *5,* 186–192. doi:10.1021/ar50053a004
12. Dewar, M. J. S.; Ford, G. P.; Rzepa, H. S. *J. Chem. Soc., Chem. Commun.* **1977,** 728–730. doi:10.1039/C39770000728
13. Johnson, R. P.; Daoust, K. J. *J. Am. Chem. Soc.* **1996,** *118,* 7381–7385. doi:10.1021/ja961066q
14. Havenith, R. W. A.; Jenneskens, L. W.; van Lenthe, J. H. *J. Mol. Struct.: THEOCHEM* **1999,** *492,* 217–224. doi:10.1016/S0166-1280(99)00166-9
15. Marwitz, A. J. V.; Matus, M. H.; Zakharov, L. N.; Dixon, D. A.; Liu, S.-Y. *Angew. Chem., Int. Ed.* **2009,** *48,* 973–977. doi:10.1002/anie.200805554
16. Brough, S. A.; Lamm, A. N.; Liu, S.-Y.; Bettinger, H. F. *Angew. Chem., Int. Ed.* **2012,** *51,* 10880–10883. doi:10.1002/anie.201203546
17. Lee, T. J.; Taylor, P. R. *Int. J. Quantum Chem., Quantum Chem. Symp.* **1989,** *36* (Suppl. S23), 199–207. doi:10.1002/qua.560360824
18. Gonzalez, C.; Schlegel, H. B. *J. Chem. Phys.* **1989,** *90,* 2154–2161. doi:10.1063/1.456010
19. Gonzalez, C.; Schlegel, H. B. *J. Phys. Chem.* **1990,** *94,* 5523–5527. doi:10.1021/j100377a021
20. Hirao, K. *Chem. Phys. Lett.* **1993,** *201,* 59–66. doi:10.1016/0009-2614(93)85034-L
21. Hariharan, P. C.; Pople, J. A. *Theor. Chim. Acta* **1973,** *28,* 213–222. doi:10.1007/BF00533485
22. Schmidt, M. W.; Baldridge, K. K.; Boatz, J. A.; Elbert, S. T.; Gordon, M. S.; Jensen, J. H.; Koseki, S.; Matsunaga, N.; Nguyen, K. A.; Su, S.; Windus, T. L.; Dupuis, M.; Montgomery, J. A., Jr. *J. Comput. Chem.* **1993,** *14,* 1347–1363. doi:10.1002/jcc.540141112
23. Raghavachari, K.; Trucks, G. W.; Pople, J. A.; Head-Gordon, M. *Chem. Phys. Lett.* **1989,** *157,* 479–483. doi:10.1016/S0009-2614(89)87395-6
24. Scuseria, G. E. *J. Chem. Phys.* **1991,** *94,* 442–447. doi:10.1063/1.460359
25. Dunning, T. H. *J. Chem. Phys.* **1970,** *53,* 2823–2833. doi:10.1063/1.1674408
26. Dunning, T. H. *J. Chem. Phys.* **1971,** *55,* 716–723. doi:10.1063/1.1676139
27. Gauss, J.; Stanton, J. F. *Chem. Phys. Lett.* **1997,** *276,* 70–77. doi:10.1016/S0009-2614(97)88036-0
28. Stanton, J. F.; Gauss, J.; Harding, M. E.; Szalay, P. G. CFOUR, Coupled-Cluster techniques for Computational Chemistry, For the current version, see http://www.cfour.de
29. Dunning, T. H. *J. Chem. Phys.* **1989,** *90,* 1007–1023. doi:10.1063/1.456153
30. TURBOMOLE ,V6.4 2012, University of Karlsruhe and Forschungszentrum Karlsruhe GmbH, 1989-2007, TURBOMOLE GmbH, since 2007; available from http://www.turbomole.com
31. Hättig, C.; Weigend, F. *J. Chem. Phys.* **2000,** *113,* 5154–5161. doi:10.1063/1.1290013
32. Weigend, F.; Köhn, A.; Hättig, C. *J. Chem. Phys.* **2002,** *116,* 3175–3183. doi:10.1063/1.1445115
33. Piecuch, P.; Kucharski, S. A.; Kowalski, K.; Musial, M. *Comput. Phys. Commun.* **2002,** *149,* 71–96. doi:10.1016/S0010-4655(02)00598-2
34. Piecuch, P.; Wloch, M. *J. Chem. Phys.* **2005,** *123,* 224105. doi:10.1063/1.2137318
35. Grimme, S. *J. Chem. Phys.* **2003,** *118,* 9095–9102. doi:10.1063/1.1569242
36. Weigend, F.; Häser, M. *Theor. Chem. Acc.* **1997,** *97,* 331–340. doi:10.1007/s002140050269
37. Weigend, F.; Häser, M.; Patzelt, H.; Ahlrichs, R. *Chem. Phys. Lett.* **1998,** *294,* 143–152. doi:10.1016/S0009-2614(98)00862-8
38. Hill, J. G.; Platts, J. A.; Werner, H.-J. *Phys. Chem. Chem. Phys.* **2006,** *8,* 4072–4078. doi:10.1039/b608623c
39. Antony, J.; Grimme, S. *J. Phys. Chem. A* **2007,** *111,* 4862–4868. doi:10.1021/jp070589p
40. Takatani, T.; Sherrill, C. D. *Phys. Chem. Chem. Phys.* **2007,** *9,* 6106–6114. doi:10.1039/b709669k
41. Bachorz, R. A.; Bischoff, F. A.; Höfener, S.; Klopper, W.; Ottiger, P.; Leist, R.; Frey, J. A.; Leutwyler, S. *Phys. Chem. Chem. Phys.* **2008,** *10,* 2758–2766. doi:10.1039/b718494h
42. Schäfer, A.; Horn, H.; Ahlrichs, R. *J. Chem. Phys.* **1992,** *97,* 2571–2577. doi:10.1063/1.463096

License and Terms

Beilstein Journal of Organic Chemistry

Utilizing the σ-complex stability for quantifying reactivity in nucleophilic substitution of aromatic fluorides

Magnus Liljenberg[*1], Tore Brinck[*2], Tobias Rein[1] and Mats Svensson[1]

Full Research Paper

Open Access

Address:
[1]AstraZeneca, S-151 85 Södertälje, Sweden and [2]Applied Physical Chemistry, KTH Royal Institute of Technology, S-100 44 Stockholm, Sweden, Fax: +46 8 790 8207, Tel: +46 8 790 8210

Email:
Magnus Liljenberg[*] - magnus.liljenberg@astrazeneca.com;
Tore Brinck[*] - tore@physchem.kth.se

* Corresponding author

Keywords:
computational; DFT; nucleophilic aromatic substitution; reactivity; substrate selectivity; reactive intermediates

Beilstein J. Org. Chem. **2013,** *9,* 791–799.
doi:10.3762/bjoc.9.90

Received: 04 February 2013
Accepted: 26 March 2013
Published: 23 April 2013

This article is part of the Thematic Series "New reactive intermediates in organic chemistry".

Guest Editor: G. Bucher

Abstract

A computational approach using density functional theory to compute the energies of the possible σ-complex reaction intermediates, the "σ-complex approach", has been shown to be very useful in predicting regioselectivity, in electrophilic as well as nucleophilic aromatic substitution. In this article we give a short overview of the background for these investigations and the general requirements for predictive reactivity models for the pharmaceutical industry. We also present new results regarding the reaction rates and regioselectivities in nucleophilic substitution of fluorinated aromatics. They were rationalized by investigating linear correlations between experimental rate constants (k) from the literature with a theoretical quantity, which we call the sigma stability (*SS*). The *SS* is the energy change associated with formation of the intermediate σ-complex by attachment of the nucleophile to the aromatic ring. The correlations, which include both neutral (NH_3) and anionic (MeO^-) nucleophiles are quite satisfactory ($r = 0.93$ to $r = 0.99$), and *SS* is thus useful for quantifying both global (substrate) and local (positional) reactivity in S_NAr reactions of fluorinated aromatic substrates. A mechanistic analysis shows that the geometric structure of the σ-complex resembles the rate-limiting transition state and that this provides a rationale for the observed correlations between the *SS* and the reaction rate.

Introduction

Background

Computational chemistry has become an indispensible tool for medicinal chemists, biologists and pharmacologists throughout all stages of the pharmaceutical research process. One application is in the selection or virtual screening of the, in many cases, numerous possible alternative synthetic routes to a target molecule, e.g., a candidate drug. To this end, efficient models that enable the prediction of product selectivity and relative reaction rates in a quantitative or semiquantitative way would be highly valuable. As a complement to experimental work, the use of such tools can help to minimize "trial and error" experimenta-

tion. However, one condition for such a tool to be of practical value is that there is a balance between accuracy and throughput: the ideal model should give a sufficiently high accuracy over as large a synthetic space as possible while at the same time allowing a high throughput and robustness. The main interest, and also the original reason for this work, was to investigate whether it is possible to develop a predictive reactivity model that could combine high throughput with a quantitative or semiquantitative accuracy.

Predictive reactivity models

In pharmaceutical research there is a need to run large substance libraries through the virtual screening procedures, and this has set a number of boundary conditions or guiding principles for the predictive reactivity models:

1. Generality. The ideal method should be applicable to as large a reactant space as possible. It should at least not depend on previously determined experimental results for the specific, narrow subset of reactants presently under study.

2. Accuracy. The predictive models developed would have to have an accuracy that is high enough for the medicinal chemist to be able to judge a reaction as suitable or not for further investigations. From a regioselectivity perspective, for example, this means that it is not sufficient to simply be able to predict the probable main site for electrophilic or nucleophilic attack: it would also be very advantageous to be able to sort out any reaction that is likely to give a (hard to separate) mixture of isomers for the coming process.

3. Throughput. On the other hand, elaborate and time-consuming modeling of reactions that closely reproduce the experimental results would be too costly. It is of little value to know whether a regioisomeric mixture of two isomers for a reaction is likely to be a 70:30 or a 60:40 mixture; on the other hand, it is of key importance to predict whether a reaction will give a 70:30 or a 99:1 mixture.

4. Robustness. It would be a great advantage if the procedures suggested could be scripted and the computations could be performed automatically as "black box" calculations, with the input being large substance libraries. To this end it, would be advantageous if one could chose relevant structures on the potential energy surface (PES) that have large convergence radii for default starting structures, that is, where the geometry optimization is fairly insensitive to the exact starting geometry. It would also be an advantage if the procedure did not require a highly trained expert to perform the calculations, but was instead within the reach of, e.g., a synthetic chemist.

There are two main types of theoretical assessment of reactivity: property- or descriptor-based and direct modeling of the PES, especially of the rate-determining TS. The first type is generally termed QSAR (quantitative structure–activity relationships), where experimentally known or calculated properties are fitted to observed reactivities. These models frequently utilize descriptors derived from the reactants and they also require access to experimental data from substances of roughly the same type as those that are to be predicted [1]. Many of the property- or descriptor-based methods are fast and robust, but inherent is a poorer accuracy since they do not take the relevant TS or solvation into account.

Quantum chemistry methods exploring the PES on the other hand can, with sufficient modeling and appropriate level of theory, yield very accurate results and do not rely on predetermined experimental data. However, this procedure is slow, computationally costly and in many cases difficult to automate, and it also requires manual input from an expert in computational chemistry. In summary the property- or descriptor-based methods typically fulfill the requirements 3 and 4 above but fail 1 and 2, while the TS methods typically fulfill the requirements 1 and 2 but fail 3 and 4.

There are approaches reported where successful attempts have been made to strike a compromise between generality/accuracy and throughput/robustness. One example is the so-called Q2MM method, which is designed to apply molecular mechanics calculations to transition states in chemical reactions, especially for predictive catalysis. It is particularly suitable for stereoselectivity calculations where there is a need to virtually screen large ligand libraries [1]. Another example are the so-called QM/MM methods [2], where part of the structure is treated with QM methods and other parts with MM methods, for example, in enzymes where the active site can be modeled with QM and the remaining structure with MM methods.

Predictive models for the S_NAr reaction

This paper is a continuation of our work on the predictive computational modeling of the synthetically and industrially important S_NAr and S_EAr reactions (nucleophilic and electrophilic aromatic substitution, respectively) [3-5]. The putative mechanism for the S_NAr reaction involves attack of a nucleophile and the formation of an intermediate σ-complex (also called the Meisenheimer complex) followed by elimination of the leaving group [6]. In the case of attack of anionic nucleophiles (such as MeO^-) on fluorinated aromatics, the intermediate σ-complex is anionic and the leaving group is F^-, whereas in the case of neutral nucleophiles (such as NH_3) the intermediate σ-complex is zwitterionic and the leaving group is

HF. The departure of H and F can proceed along different mechanisms [7-9].

Several methods for predicting local reactivity, or regioselectivity, in S_NAr reactions have been reported. Among the earlier ones is the I_π-repulsion theory based on calculating the fractional charge with Hückel theory [10,11], and an approach based on the frontier molecular orbital method [12]. More recent attempts include calculation based on Fukui indices [13], local softness and hardness reactivity descriptors [14], dual descriptors for both electrophilicity and nucleophilicity [15], and calculation of the thermodynamic stability of the σ-complex [4,5,16,17]. A number of theoretical studies have also been carried out that concern global or substrate reactivity in S_NAr reactions. In one paper the reactivity of two systems was computed, in order to elucidate the energy barriers in different mechanistic steps for these systems [18]. In another, a simple numerical method based on a few reactivity parameters was used to predict the relative reactivities in the reaction between methoxide anion and a series of chlorofluorobenzene derivatives [19]. In two other articles, the authors studied the effect of different substituents on the reactivity of one model substance. The first dealt with the Newman–Kwart rearrangement of an aromatic thionocarbamate by intramolecular nucleophilic aromatic substitution [20], the second applied semiempirical methods to study the reaction between methoxide anion and a number of 4-substituted 1-chloro-2-nitrobenzenes [21].

There are also many studies dealing with the formulation of empirical rules concerning reactivity in the nucleophilic substitution of fluorinated aromatics [22-25]. The nature of the empirical rules that typically emerge can be exemplified by the following (concerning perfluoroaromatic systems): "trifluoromethyl, like ring nitrogen, activates both ortho- and para-positions to a similar degree" [22]. Such rule-based mnemonics can be useful as qualitative tools, but tend to be highly case-specific and not quantitatively accurate. Should there, in this specific example, be a deactivating substituent on the system beside trifluoromethyl, or should the substituent be fluoromethyl instead of trifluoromethyl, then another empirical rule would have to be developed.

To the best of our knowledge, a more general reactivity treatment is still lacking: a treatment that can be of use on at least a semiquantitative basis with respect to both global and local reactivity, that is, substrate as well as positional selectivity, for a wider range of substrates and nucleophiles. In this study we have included both different carbocyclic and heterocyclic substrates as well as neutral and anionic nucleophiles.

The σ-complex intermediate in S_NAr reactions has been considered to be the crucial intermediate governing both reactivity and regioselectivity [26]. Our method is based on calculation of the relative stabilities of the σ-complex intermediates using density functional theory, and is intended for kinetically controlled reactions. We assume that their properties, rather than those of the initial aromatic reactants, are crucial in determining reactivity. We have successfully applied the σ-complex approach to predict regioselectivity in reactions of carbocyclic as well as heterocyclic fluorinated substrates [4,5]. Anionic nucleophiles (anions of methanol, benzyl alcohol and hydrogen sulfide) were investigated, as well as neutral nucleophiles (amines). The accuracy was well within 1 kcal/mol and the predictions can be used in a quantitative way. It was necessary to include polarizable continuum model (PCM) solvent calculations, either as an a posteriori single point calculation or by optimizing the structures directly in solvent, to obtain the accuracy at this level. Muir and Baker [16,17] have investigated the case of nucleophilic attack of anionic nucleophiles to aromatic fluorides for a great many examples. They found that an approach using F^- as model nucleophile without solvent calculations was sufficient to give a good qualitative prediction of the main site of nucleophilic attack. The σ-complex approach failed when the leaving group was Cl^-/HCl or Br^-/HBr both for anionic and neutral nucleopiles, because of difficulties in finding relevant σ-complex structures. Instead an approach where we assumed a concerted substitution step and used such transition-state structures gave quantitatively useful results [5]. Recent results by Fernandez et al [26] show that σ-complex structures can be found if the leaving group is bound to the ring through an element in the second row of the periodic table (i.e., –F, $–NH_2$, –OH), but not (unless the structure is highly stabilized, e.g., by several nitro groups) if the element is from the third or fourth row (i.e., –Cl, –Br, sulfur groups).

In this study we introduce a concept that we call the Sigma Stability, *SS*, to also encompass global reactivity, that is, investigations dealing with the relative reactivity between different systems. This is the energy required for the formation of the σ-complex, $SS = E_{\sigma\text{-complex}} - (E_{\text{aromate}} + E_{\text{nucleophile}})$. The purpose of the present study is to evaluate the scope and reliability of this widened application and to find the minimum level of theory and basis set necessary to strike a reasonable balance between the requirements 1–4 above. The success of this approach is based on a number of assumptions, which we have described in our previous work on S_NAr reactions [4,5].

The approach has an attractive feature in that it represents a distinct simplification compared to finding TS structures (as it mean optimizations to local minima), while preserving an accu-

racy that in many cases is sufficient for an, at least semiquantitative, prediction of reactivity.

Results

The performance of the *SS* concept was examined on the basis of correlations with experimentally determined reaction rate constants (k) of three series of reactions (series A, B and C). The first series (series A) deals with the amination of nine different fluorinated heterocyclic substrates run at 25 °C. The second series (series B) with the amination of seven different carbocyclic substrates run at 80 °C. Except for the temperature, reaction series A and B were run under identical conditions, i.e., reaction of the substrate and ammonia in dioxane/water (60:40 v/v). The third series (series C) deals with the methoxylation of a series of 10 different polychlorofluorobenzenes run under identical conditions, i.e., reaction of the substrate and sodium methoxide in methanol at 50 °C. The experimental reaction rates span more than six orders of magnitude, both for the aminations and for the methoxylations.

For the series of aminations (series A and B) the investigated structures and the numbering of positions are shown in Figure 1.The calculated *SS* values as well as experimental rate constants for series A and B are shown in Table 1 and Table 2, respectively. The correlation between *SS* values in water and experimental –log k values are shown in Figure 2. The *SS* values for the structures where experimental kinetic data are given for more than one positional isomer (Table 1, reactant **7**, entries 7 and 8; reactant **8**, entries 9 and 11) lie well on the correlation line in Figure 2 (these data points are indicated in the figure). The correlation coefficient is 0.99 for series A and 0.93 for series B. This corresponds to a mean average deviation of 0.5 kcal/mol and 1.4 kcal/mol, respectively. *SS* values based on in vacuo energies (obtained from the structures optimized in solvent) correlate poorly with the experimental –log k values [27]. In order to make a true kinetic prediction of an isomer in reaction series A that has not been experimentally observed in the literature, we calculated the *SS* value for position 3 in reactant **1**. This data is presented as entry 12 in Table 1 and it has, as might be expected, a very low predicted reaction rate constant. Experimental kinetic data were given at both 25 °C and 80 °C [28] for reactant **4** in Figure 1, and we tried to include this 80 °C data point in reaction series B, even though reactant **4** is a heterocyclic substrate (entry 8 in Table 2), but this made the correlation much poorer.

For the series of methoxylations (series C) the investigated structures and the numbering of positions are shown in Figure 3. The calculated *SS* values as well as experimental rate constants are shown in Table 3. The correlation between *SS*

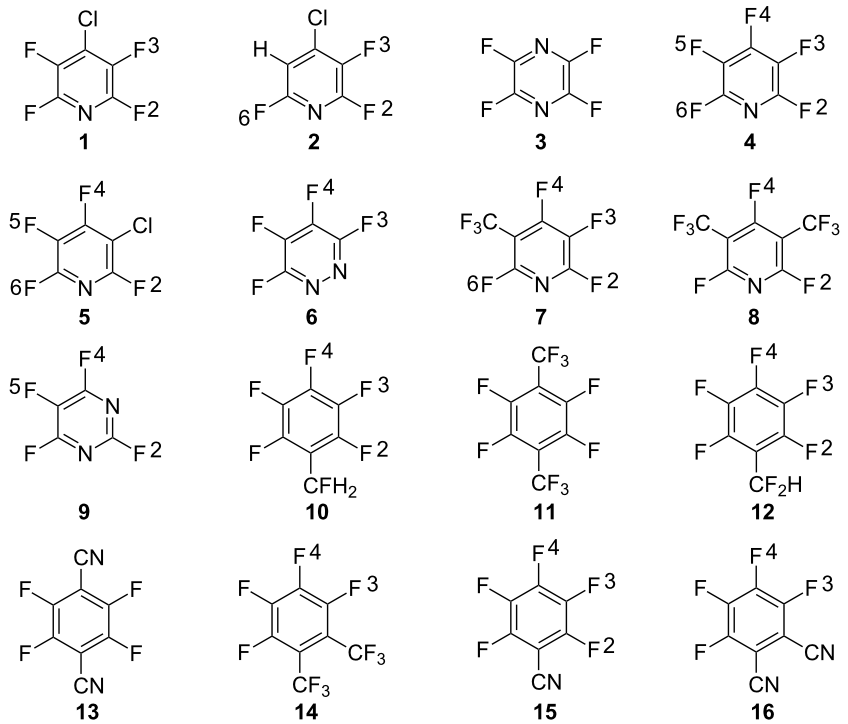

Figure 1: The structures investigated in the amination of heterocyclic and carbocyclic derivatives (series A and B, respectively) and the numbering of their positions.

Table 1: Series A. Sigma stability (*SS*), experimental rate constants [28,29] and negative logarithms for experimental rate constants (−log *k*) for the aminations (with NH_3) of different reactants in dioxane/water (60:40 v/v) at 25 °C. The structures of the reactants are shown in Figure 1.

Entry	Reactant (Figure 1)	Position of amination	*SS* (kcal mol^{-1}) water	Reaction rate, *k* (l mol^{-1} s^{-1})[a]	−log *k*
1	**1**	2	14.00	1.55×10^{-6}	5.81
2	**2**	2	12.47	5.92×10^{-6}	5.23
3	**3**	Equal	10.70	5.07×10^{-5}	4.29
4	**4**	4	9.26	6.80×10^{-4}	3.17
5	**5**	4	8.37	1.92×10^{-3}	2.72
6	**6**	4	4.67	2.52×10^{-2}	1.60
7	**7**	2	6.66	2.66×10^{-2}	1.58
8	**7**	4	4.63	5.31×10^{-2}	1.27
9	**8**	2	2.46	1.31	−0.12
10	**9**	4	1.23	1.35	−0.13
11	**8**	4	1.15	3.39	−0.53
12	**1**	3	20.85	9.1×10^{-10} [b]	9.04[b]

[a]All rate constants are corrected for statistical factors (=degenerate positions). [b]Value predicted from the regression line in Figure 2.

Table 2: Series B. Sigma stability (*SS*), experimental rate constants [22,28] and negative logarithms for experimental rate constants (−log *k*) for the amination (with NH_3) of different reactants in dioxane/water (60:40 v/v) at 80 °C. The structures of the reactants are shown in Figure 1.

Entry	Reactant (Figure 1)	Position of amination	*SS* (kcal mol^{-1}) water	Reaction rate, *k* (l mol^{-1} s^{-1})[a]	−log *k*
1	**10**	4	18.30	1.1×10^{-5}	4.96
2	**11**	equal	16.02	1.23×10^{-5}	4.91
3	**12**	4	16.26	5.0×10^{-5}	4.30
4	**13**	equal	11.09	7.54×10^{-5}	4.12
5	**14**	4	13.21	1.19×10^{-4}	3.92
6	**15**	4	9.16	2.5×10^{-4}	3.60
7	**16**	4	6.85	1.35×10^{-3}	2.87
8[b]	**4**	4	9.26	2.8×10^{-2}	1.55

[a]All rate constants are corrected for statistical factors (=degenerate positions). [b]This entry is not part of the correlation of reaction series B, as it is a heterocyclic substrate.

values in methanol and experimental –log *k* values are shown in Figure 4. The overall picture for this data set is quite analogous to the previous two and the *SS* values for the structures where experimental kinetic data are given for more than one positional isomer (Table 3, reactant **20**, entries 4 and 7; reactant **21**, entries 5, 8 and 9) falls well onto the correlation line in Figure 4 (these data points are indicated in the figure). The correlation coefficient is 0.96 for this data series, which corresponds to a mean average deviation of 1.1 kcal/mol. As for series A and B the *SS* values based on in vacuo energies show poor correlation coefficients with the experimental −log *k* values [27].

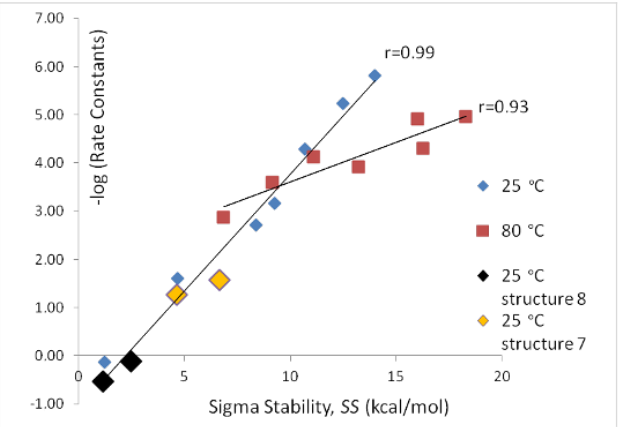

Figure 2: –log *k* as a function of *SS* in water for series A and B.

It would seem that the *SS* values for the methoxylation reactions are significantly lower than the true absolute energy values for forming the σ-complex and also that they are underestimated in a systematic fashion. The probable reason is that the solvation model used [30] systematically overestimates the solvation energy for the anionic σ-complexes. Experimental solvation energy values for σ-complexes are scarce, but Dillow and Kebarle [31] give the value −58 kcal/mol for the σ-complex resulting from the reaction between F^- and C_6F_6 in

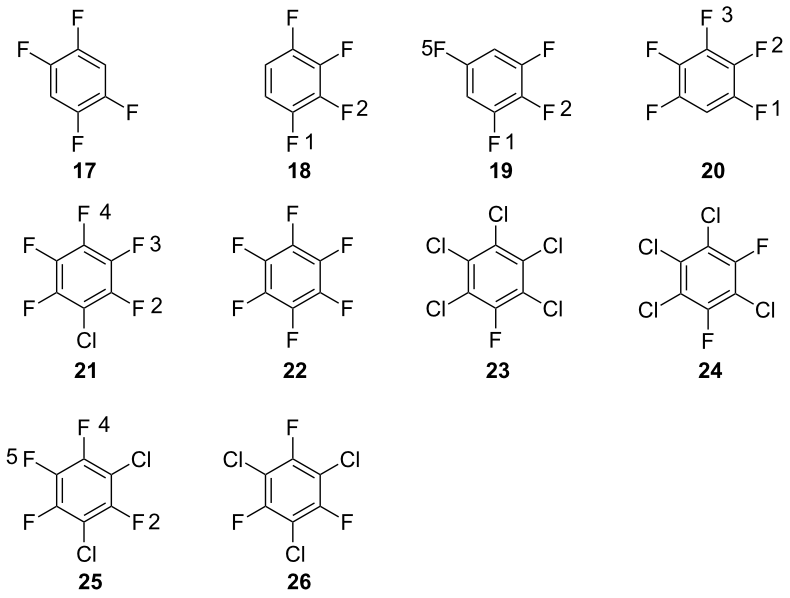

Figure 3: The structures investigated in the methoxylation of polychlorofluorobenzene derivatives (series C) and the numbering of their positions.

Table 3: Series C. Sigma stability (*SS*), experimental rate constants [19] and negative logarithms for experimental rate constants (−log *k*) for the reaction between sodium methoxide with different chlorofluorobenzene reactants in methanol at 50 °C. The structures of the reactants are shown in Figure 3.

Entry	Reactant (Figure 3)	Position of methoxylation	*SS* (kcal mol^{-1}) methanol	Reaction rate, *k* (l mol^{-1} s^{-1})[a]	−log *k*
1	**17**	equal	−3.17	2.5×10^{-9}	8.60
2	**18**	2	−6.71	4.0×10^{-7}	6.40
3	**19**	1	−7.41	1.2×10^{-6}	5.92
4	**20**	1	−7.63	2×10^{-6} [b]	5.70
5	**21**	3	−11.49	5.3×10^{-5}	4.28
6	**22**	equal	−10.85	7.56×10^{-5}	4.12
7	**20**	3	−10.96	1.01×10^{-4}	4.00
8	**21**	2	−13.46	1.5×10^{-4}	3.82
9	**21**	4	−15.24	2.52×10^{-3}	2.60
10	**23**	One position	−19.39	3.3×10^{-3}	2.48
11	**24**	equal	−18.82	4.8×10^{-3}	2.32
12	**25**	4	−17.62	5.3×10^{-3}	2.28
13	**26**	equal	−18.49	6.8×10^{-3}	2.17

[a]All rate constants are corrected for statistical factors (=degenerate positions). [b]Approximate value.

DMSO. The solvation energy obtained from our calculations of entry 6 in Table 3 (which is also from C_6F_6 but with MeO^- instead of F^- as nucleophile and with MeOH instead of DMSO as solvent) was −73 kcal/mol, and all of the σ-complexes in Table 3 that do not contain chlorine substituents (entries 1–4 and 6–7 in Table 3) have a calculated solvation energy in the range −73 to −78 kcal/mol. The problem with continuum models that gravely overestimate the solvation energy for anionic species is well known [32]: one reason is probably the scarcity of relevant solvation-energy data for organic ions in organic solvents, used in the parametrization work. This systematic underestimation is, however, without practical importance if the purpose is only semiquantitative ranking of substrate and positional reactivity.

Discussion

Our results show that the substrate and positional reactivity can be predicted from the computed energy of the σ-complex. Performing single-point calculations at the optimized geometries using larger basis sets, by adding diffuse functions, does

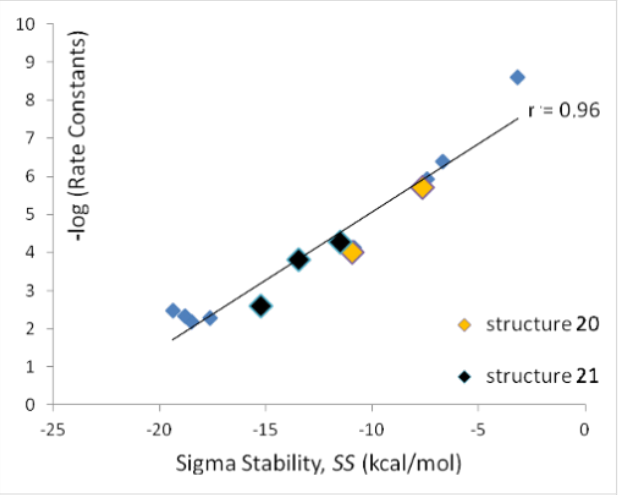

Figure 4: −log *k* as a function of *SS* in methanol for series C.

not in an appreciable way improve the correlation. Thermodynamic corrections taken from frequency calculations (harmonic approximations) of key intermediates also have minor effects on the correlation. The comparatively moderate levels of theory and basis set used by us in this study yielded an accuracy of the *SS* values of around 1 kcal/mol, measured as mean average deviation. Thus, it seems that the level of theory employed, B3LYP/6-31G(d,p), is sufficient for the present purpose, which is to make semiquantitative rankings of substrate and positional reactivity between species that are run under the same reaction conditions. It is important to note that the *SS* values do not give an explicit indication of absolute energy barriers, and the approach is thus limited to reactivity comparisons where species are run under the same reaction conditions. It is also worth noting that the correlation became poor in the one case where we tried to mix carbocyclic and heterocyclic substrates in one reaction series (Table 2). Any reactivity comparisons between series must be done with the utmost caution.

In order to deduce the mechanistic basis behind the very good correlations between SS values and reaction rates, we computed the stationary points on the potential energy surface for the amination of **4.** We found that this characterization had to be performed using a larger basis set with diffuse functions to obtain accurate geometries and energy differences. The B3LYP/6-31+G(d,p) optimized geometries of TS1, the σ-complex and TS2 with PCM water solvation are depicted in Figure 5. All three structures are very similar, and the main difference between the σ-complex and TS2 is a slight elongation of less than 0.1 Å of the breaking C–F bond in TS2. An IRC-calculation showed that F leaves as F^- without the assistance of explicit hydrogen bonds from the NH_2-group, and that the proton transfer to form HF takes place late in the concerted reaction step going from the σ-complex via TS2 to the products. An analysis of the energy differences between the three stationary points shows that the potential energy surface is extremely flat in the vicinity of the σ-complex. TS1 is only 2.2 kcal/mol higher in energy than the σ-complex, and TS2 has an almost identical energy to that of the σ-complex. The energy ordering of the two latter is even inversed after incorporation of zero-point vibrational energies. As we have already indicated, diffuse functions are important for obtaining an accurate potential energy surface for this reaction. This is not surprising, since during the process of going from TS1 via the σ-complex to TS2 the localization of negative charge at the fluorine atom is continuously increasing. Consequently, after removal of the diffuse functions the energy of TS1 relative to the σ-complex is decreased to 0.13 kcal/mol and the energy of TS2 is increased to 6.5 kcal/mol. Consistent with the picture that diffuse functions are needed to describe the negative charge formed at the fluorine, the C–F bond is much longer (1.83 Å) in the TS2 structure optimized without diffuse functions.

The fact that the σ-complex is very close both in energy and geometry to the rate-limiting transition state (TS1) provides a rationale for the very good correlations between *SS* values and reaction rates. However, a recent study has shown that the B3LYP functional predicts a concerted reaction in some cases, including an intramolecular S_NAr reaction, where the M06-2X functional and high level ab initio theory show that the reaction is stepwise [33]. In light of these observations, we investigated the potential energy surface also at the M06-2X/6-31+G(d,p) level of theory. The computed stationary points and their energies are depicted in Figure 5. The geometries are very similar to those obtained with the B3LYP functional. The largest difference is found for TS2, where the breaking C–F is extended from 1.64 to 1.85 Å with M06-2X. Observing the relative energies, we see much larger differences. TS2 is rate-determining with the M06-2X functional, and lies 4.6 kcal/mol higher in energy than the σ-complex. Also the relative energy of TS1 is raised, but only by 1.2 kcal/mol compared to B3LYP. Removing the diffuse functions from the basis set has a similar effect on the relative energies as in the B3LYP calculations; TS2 lies 12.8 kcal/mol above the σ-complex at the M06-2X/6-31G(d,p) level of theory.

On the basis of the current study, we cannot make any conclusive statement regarding whether TS1 or TS2 is rate-determing for S_NAr reactions with F as leaving group. In fact it may differ depending upon the nucleophile and the substrate. However, our analyses using both the B3LYP functional and the M06-2X functional strongly indicate that the structure of σ-complex is similar to the structure of the rate-limiting transition state, and that changes in the molecular structure that affect the relative energy of the transition state will affect the energy of the

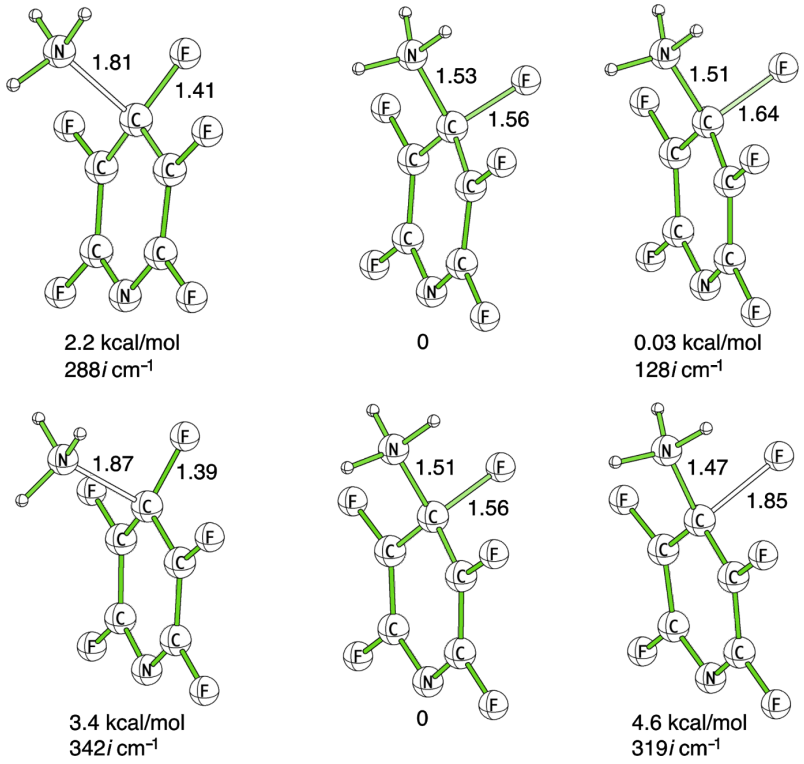

Figure 5: Optimized geometries, relative energies, and imaginary frequencies for the transition states and the σ-complex (middle structure) formed in the reaction between ammonia and **4**. The top and bottom rows show the results from optimizations at the B3LYP/6-31+G(d,p) and M06-2X/6-31+G(d,p) levels of theory, respectively.

σ-complex to a similar extent. In light of these observations the good correlations between *SS* values and reaction rates are not surprising.

A distinct advantage with the σ-complex as model for the rate-limiting TS (apart from the more practical advantage that it is normally easier and faster to find computationally than the transition-state structure) is that there is no ambiguity in the structure of this stationary point on the potential-energy surface. Furthermore, our mechanistic analysis shows that a basis set with diffuse functions is necessary to describe the energy and structure of the rate-limiting transition state, and this increases the computational cost of a transition-state approach even further. It is tempting to investigate the generality of the *SS* concept further, by adding different nucleophiles, temperatures and reaction conditions, but this is at present unfortunately limited by the scarcity of experimental kinetic data.

Conclusion

We have shown for several series of fluorinated aromatics that there exist good correlations between the relative σ-complex stabilization and experimental rate constants for S_NAr reactions involving both neutral and anionic nucleophiles. Thus, in combination with our previous studies, the present study demonstrates that the *SS* concept provides a methodology for the quantitative prediction of both regioselectivity and relative reactivity of S_NAr reactions of fluorinated substrates. Due to the low computational requirements and the potential for automatization, this method may find use in virtual reactivity screening in pharmaceutical research and development. We have further shown that the method has a solid mechanistic foundation, as the structure of the σ-complex is similar to the structure of the rate-determining transtion state of the reaction.

Theoretical method

SS values were computed using DFT with the B3LYP hybrid functional and a 6-31G(d,p) basis set with effective core potentials on heavy atoms by using the Jaguar program [30]. Preliminary calculations showed that the zwitterionic σ-complex does not exist as a stationary point on the potential energy surface in vacuo. Therefore, all structures were optimized within the Poisson–Boltzmann finite-element solvation model (PBF) incorporated in the Jaguar software [30], using water as solvent for the amination reactions and methanol for the methoxylation reactions.

A more detailed analysis of the potential energy surface for the amination of one substrate was performed by geometry opti-

mizations using the 6-31+G(d,p) basis set and the two functionals B3LYP and M06-2X. In these computations solvent effects were included by means of the polarizable continuum model as implemented in the Gaussian 09 suite of software [34]. All stationary points were characterized by means of frequency and IRC calculations.

Supporting Information

Supporting Information File 1

Coordinates of all optimized structures, electronic energies, *SS* values calculated with larger basis set, and zero-point energies.
[http://www.beilstein-journals.org/bjoc/content/supplementary/1860-5397-9-90-S1.pdf]

References

1. Nilsson Lill, S. O.; Forbes, A.; Donoghue, P.; Verdolino, V.; Wiest, O.; Rydberg, P.; Norrby, P.-O. *Curr. Org. Chem.* **2010,** *14,* 1629–1645. doi:10.2174/138527210793563224
2. Svensson, M.; Humbel, S.; Froese, R. D. J.; Matsubara, T.; Sieber, S.; Morokuma, K. *J. Phys. Chem.* **1996,** *100,* 19357–19363. doi:10.1021/jp962071j
3. Liljenberg, M.; Brinck, T.; Herschend, B.; Rein, T.; Rockwell, G.; Svensson, M. *J. Org. Chem.* **2010,** *75,* 4696–4705. doi:10.1021/jo100310v
4. Liljenberg, M.; Brinck, T.; Herschend, B.; Rein, T.; Rockwell, G.; Svensson, M. *Tetrahedron Lett.* **2011,** *52,* 3150–3153. doi:10.1016/j.tetlet.2011.04.032
5. Liljenberg, M.; Brinck, T.; Herschend, B.; Rein, T.; Tomasi, S.; Svensson, M. *J. Org. Chem.* **2012,** *77,* 3262–3269. doi:10.1021/jo202569n
6. March, J. *Advanced Organic Chemistry,* 2nd ed.; McGraw-Hill: New York, NY, USA, 1984.
7. Um, I.-K.; Min, S.-W.; Dust, J. M. *J. Org. Chem.* **2007,** *72,* 8797–8803. doi:10.1021/jo701549h
8. Mancini, P. M.; Fortunato, G. G.; Vottero, L. R. *J. Phys. Org. Chem.* **2005,** *18,* 336–346. doi:10.1002/poc.869
9. Schroeder, G.; Eitner, K.; Gierczyk, B.; Rózalski, B.; Brzezinski, B. *J. Mol. Struct.* **1999,** *478,* 243–253. doi:10.1016/S0022-2860(98)00758-3
10. Burdon, J. *Tetrahedron* **1965,** *21,* 3373–3380. doi:10.1016/S0040-4020(01)96958-3
11. Burdon, J.; Parsons, I. W. *J. Am. Chem. Soc.* **1977,** *99,* 7445–7447. doi:10.1021/ja00465a007
12. Epiotis, N. J.; Cherry, W. *J. Am. Chem. Soc.* **1976,** *98,* 5432–5435. doi:10.1021/ja00434a003
13. Bulat, F. A.; Chamorro, E.; Fuentealba, P.; Toro-Labbe, A. *J. Phys. Chem. A* **2004,** *108,* 342–349. doi:10.1021/jp036416r
14. Roy, R. K.; Krishnamurti, S.; Geerlings, P.; Pal, S. *J. Phys. Chem. A* **1998,** *102,* 3746–3755. doi:10.1021/jp973450v
15. Morell, C.; Grand, A.; Toro-Labbe, A. *J. Phys. Chem. A* **2005,** *109,* 205–212. doi:10.1021/jp046577a
16. Muir, M.; Baker, J. *J. Fluorine Chem.* **2005,** *126,* 727–738. doi:10.1016/j.jfluchem.2005.02.018
17. Baker, J.; Muir, M. *Can. J. Chem.* **2010,** *88,* 588–597. doi:10.1139/V10-047
18. Nova, A.; Mas-Ballesté, R.; Ujaque, G.; González-Duarte, P.; Lledós, A. *Dalton Trans.* **2009,** 5980–5988. doi:10.1039/b901697j
19. Bolton, R.; Sandall, J. P. B. *J. Chem. Soc., Perkin Trans. 2* **1976,** 1541–1545. doi:10.1039/p29760001541
20. Clabo, D. A. In *Abstract, 61st Southeast Regional Meeting of the American Chemical Society,* San Juan, Puerto Rico, Oct 21–24, 2009; 2009.
21. Pankratov, A. N. *Afinidad* **2001,** *58,* 137–140.
22. Chambers, R. D.; Martin, P. A.; Sandford, G.; Williams, D. L. H. *J. Fluorine Chem.* **2008,** *129,* 998–1002. doi:10.1016/j.jfluchem.2008.04.009
23. Chambers, R. D.; Seabury, M. J.; Williams, D. L. H.; Hughes, N. *J. Chem. Soc., Perkin Trans. 1* **1988,** 255–257. doi:10.1039/P19880000255
24. Chambers, R. D. *Dyes Pigm.* **1982,** *3,* 183–190. doi:10.1016/0143-7208(82)80021-1
25. Chambers, R. D.; Waterhouse, J. S.; Williams, D. L. H. *J. Chem. Soc., Perkin Trans. 2* **1977,** 585–588. doi:10.1039/p29770000585
26. Fernández, I.; Frenking, G.; Uggerud, E. *J. Org. Chem.* **2010,** *75,* 2971–2980. doi:10.1021/jo100195w
27. The in vacuo correlation coefficients were 0.62 and 0.51 for reaction series A and B respectively; and 0.25 for reaction series C.
28. Chambers, R. D.; Martin, P. A.; Waterhouse, J. S.; Williams, D. L. H. *J. Fluorine Chem.* **1982,** *20,* 507–514. doi:10.1016/S0022-1139(00)82276-9
29. Chambers, R. D.; Close, D.; Musgrave, W. K. R.; Waterhouse, J. S.; Williams, D. L. H. *J. Chem. Soc., Perkin Trans. 2* **1977,** 1774–1778. doi:10.1039/p29770001774
30. *Jaguar,* version 7.8; Schrödinger, LLC: New York, NY, USA, 2007.
31. Dillow, G. W.; Kebarle, P. *J. Am. Chem. Soc.* **1988,** *110,* 4877–4882. doi:10.1021/ja00223a001
32. Pliego, J. R., Jr.; Riveros, J. M. *Chem. Phys. Lett.* **2002,** *355,* 543–546. doi:10.1016/S0009-2614(02)00377-9
33. Chéron, N.; Jacquemin, D.; Fleurat-Lessard, P. *Phys. Chem. Chem. Phys.* **2012,** *14,* 7170–7175. doi:10.1039/C2CP40438A
34. *Gaussian 09,* Revision B.01; Gaussian, Inc.: Wallingford, CT, 2009.

License and Terms

Beilstein Journal of Organic Chemistry

Spectroscopic characterization of photoaccumulated radical anions: a litmus test to evaluate the efficiency of photoinduced electron transfer (PET) processes

Maurizio Fagnoni, Stefano Protti, Davide Ravelli and Angelo Albini*

Full Research Paper

Open Access

Address:
PhotoGreen Lab, Department of Chemistry, University of Pavia, V. Le Taramelli 12, 27100 Pavia, Italy

Email:
Angelo Albini* - angelo.albini@unipv.it

* Corresponding author

Keywords:
aromatic nitriles; persistent radical anion; photochemical activation; photoinduced electron transfer (PET); photooxidant; reactive intermediates

Beilstein J. Org. Chem. **2013,** *9,* 800–808.
doi:10.3762/bjoc.9.91

Received: 13 February 2013
Accepted: 03 April 2013
Published: 24 April 2013

This article is part of the Thematic Series "New reactive intermediates in organic chemistry".

Guest Editor: G. Bucher

Abstract

Steady-state irradiation in neat acetonitrile of some aromatic nitriles, imides and esters (10^{-5}–10^{-3} M solution) in the presence of tertiary amines allowed the accumulation of the corresponding radical anions, up to quantitative yield for polysubstituted benzenes and partially with naphthalene and anthracene derivatives. The condition for such an accumulation was that the donor radical cation underwent further evolution that precluded back electron transfer and any chemical reaction with the radical anion. In fact, no accumulation occurred with 1,4-diazabicyclo[2.2.2]octane (DABCO), for which this condition is not possible. The radical anions were produced from benzene polyesters too, but decomposition began early. Ipso substitution was one of the paths with secondary amines and the only reaction with tetrabutylstannane. The results fully support the previously proposed mechanism for electron transfer (ET) mediated photochemical alkylation of aromatic acceptors via radical ions and radical intermediates.

Introduction

Redox reactions between organic molecules have a limited scope because of the rarely matched redox potential. On the other hand, the very structure of electronically excited states makes them both easily oxidized (by donating the electron promoted to an empty orbital) and reduced (an electron is transferred to the low-lying semi-occupied orbital). As a result, redox reactions are quite common in photochemistry and occur under mild conditions, avoiding the use of aggressive inorganic reagents otherwise required. Photoinduced electron transfer indeed offers an advantageous access to radical ions as well as

the possibility to control the ensuing chemistry, in a way hardly attained through electrochemical or chemical methods [1-6]. A radical ion formed at a cathode/anode finds itself in an environment where electrons/holes are abundant. Likewise, reducing/oxidizing chemicals must be used at a sufficiently high concentration to be active, and again the radical ions are formed in an environment where a subsequent electron-transfer step in the same direction is likely. In contrast, photoinduced electron transfer generates a radical-ion pair. Electron transfer in the reverse direction (back electron transfer, BET) is thus likely and leads again to the starting molecules [7], unless one or both of the radical ions undergoes a sufficiently fast reaction (Scheme 1). In the simplest case, one of the radical ions reacts, while the other one persists. At some point in the mechanism, BET occurs, such that the final product has undergone no net change of the oxidation level, or an equimolecular mixture of a reduced and an oxidized product is formed.

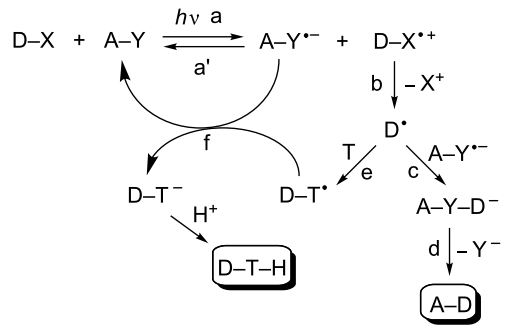

Scheme 1: Photoinduced electron transfer as an access to radical chemistry.

As an example, the largely positive reduction potential of aromatic nitriles [5,8,9] and cyanophthalimides [10] in the singlet excited state or of aromatic esters in the triplet state [5,11] makes PET a common occurrence upon irradiation of such substrates in the presence of a variety of donors (D–X, step a). In all of the above cases, the generated radical anion ($A–Y^{\bullet-}$) is a persistent species easily detected by laser flash photolysis. This approach applies to a variety of donors, including amines [12,13], carboxylic acids or their derivatives [14,15], aliphatic acetals and ketals [16], ethers [17], organostannanes [18,19], organosilanes [20-22], aromatics [10,23,24], and even alkanes [25-27]. BET (path a') could ensue, thus leading to no chemical change. However, when the $D–X^{\bullet+}$ intermediate contained a good electrofugal group (such as a silyl, stannyl, *t*-Bu group or a hydrogen [12-27]), unimolecular fragmentation was possible and gave neutral alkyl radicals ($D^{\bullet}$) with a reasonable (0.1 or higher) quantum yield (Scheme 1, step b) [5]. Addition to the aromatic radical anion and re-aromatization gave an alkylated aromatic (A–D, path c → d), while trapping of the radical by an electron-withdrawing substituted alkene T (step e) [28,29] followed by BET from the radical anion (step f) of the acceptor (that was thus recovered) led to photocatalyzed alkylation of the alkene [5,30,31]. Both processes have found some application in synthesis for the mild and selective activation of aliphatic derivatives, in particular of a C–H bond [32].

The role of the acceptor radical anion in the above processes is thus decisive, and we report below a steady-state investigation of such species arising from aromatic compounds known to participate in photosubstitution or photocatalytic alkylation reactions. It was proposed to ascertain whether these may accumulate, as often observed in electrochemistry [33,34] and by pulse radiolysis [35], but rarely in photochemistry.

Results

The acceptors chosen for this study were nitriles, viz. 1,2,4,5-tetracyanobenzene (TCB), 1,3,5-tricyanobenzene (1,3,5-TrCB), 1,2,4-tricyanobenzene (1,2,4-TrCB), 1,4-dicyanonaphthalene (DCN), 9,10-dicyanoanthracene (DCA); imides, viz. 4,5-dicyanophthalimide (DCP), and its *N*-methylated derivative (DCP-Me); and esters (methyl pyromellitate, PME, and methyl mellitate, ME). Radical anions of this type have been previously observed in glasses (e.g., from the irradiation of TCB and α-methylstyrene in isoamyl alcohol glass at 113 K) [36] and in a few cases in fluid solution (from dicyanoanthracene in the presence of methoxide [37] and from 2,6,9,10-tetracyanoanthracene with amines [38]). As for the donors, these were chosen on the basis of their oxidation potential (see Table 1 and Figure 1), to allow for an overall exergonic electron transfer from the donor to the excited acceptor in all of the cases considered below [39]. The relevant redox parameters for the ground states of acceptors and donors are gathered in Figure 1, along with the reduction potentials for the excited states of the aromatics.

In the experiments, a MeCN solution of the acceptor in the presence of the chosen donor was deaerated by freeze–pump–thaw technique and irradiated at 313 nm. Thus, irradiation of a 2×10^{-4} M solution of TCB in the presence of Bu_4Sn (10^{-2} M) caused a stepwise blue shift of the near UV band of TCB and a weak absorption in the visible (see Figure 2a), along with a fluorescence peak centered at 510 nm. The conversion was complete after a few minutes, and readmitting air caused little change in the spectrum. Chromatographic examination confirmed the complete consumption of TCB and the formation of a single product, identified as 5-butyl-1,2,4-tricyanobenzene by comparison with an authentic sample [18]. The measured quantum yield of TCB consumption was 0.40. The examination was then extended to a series of nitrogen-based

Table 1: Spectroscopic properties of the examined radical anions.

acceptor/ donor	$A^{\bullet-}$ (main band) λ_{max} (nm)	ε (× 10^{-3}) L mol^{-1} cm^{-1}	$A^{\bullet-}$ (further maxima) λ_{max} (nm)	$\Phi_A{}^{\bullet-}$
TCB/OXA		10.3		0.15
TCB/TEA		9.6		0.15
TCB/iPr_3N	462	9.8	436, 414, 375, 354	0.08
TCB/Et_2NH[a]		6.7		0.15
TCB/MAE[a]		2.9		0.05
TCB (literature)[b,c]	462	4.9,[b] 14.6–15.4[c]	–	–
1,2,4-TrCN/OXA	351	2.3	433, 397	–
DCN/OXA	389, 512	5.4, 1.0	621, 500, 481	–
DCN (literature)[d]	512	3.6[d]	–	–
DCA/OXA	705, 640	0.6, 0.4	520	–
DCA (literature)[e]	640	5.6[e]	–	–
DCP/OXA	577	25.6	536, 382	–
DCP-Me/OXA	578	26.3	537, 390	–
ME/OXA[a]	527	0.80	368	–
PME/OXA[a]	533	1.4	371	–

[a]An irreversible reaction occurred. [b]Measured by pulse radiolysis in 2-methyltetrahydrofuran, at 77 K; from [35]. [c]Measured by laser flash photolysis at room temperature of a MeCN solution of 1,2,4-trimethylbenzene or *o*-xylene as donors, see [24]. [d]Measured by laser flash photolysis at room temperature of a DMF solution of alkyltriphenyl borate anions as donors; from [40]. [e]Measured by electrolysis in DMF at room temperature; from [34].

donors. In the presence of 2,2,3-trimethyloxazolidine (OXA), a yellow color developed and a spectrum with maxima at 462, 375 and 354 nm was registered (see Figure 2b) along with shoulders at 436 and 414 nm. The final absorption was qualitatively and quantitatively close to that reported in the literature for the TCB radical anion (see Table 1). Thus, conversion was deemed to be complete, with a 0.15 quantum yield of formation of $TCB^{\bullet-}$. Readmitting air in this case caused the disappearance of the color and the full regeneration of the starting nitrile, as confirmed by chromatographic analysis.

Exactly the same behavior was observed by using triethylamine (TEA) as the donor. It is noteworthy from the practical point of view that with OXA the $TCB^{\bullet-}$ was formed at about the same rate also in a nitrogen- or argon-flushed solution, whereas with TEA and the other donors discussed below a more rigorous deaeration such as the freeze–pump–thaw method was required. Again similar was the behavior of triisopropylamine, which showed a somewhat lower quantum yield (0.08), however, in the formation of $TCB^{\bullet-}$. The use of diethylamine (Et_2NH) led initially to the accumulation of the $TCB^{\bullet-}$ absorption up to ca. 2/3rd of the maximum value with TEA, but then a different evolution began to manifest. In this case, oxygen quenching eliminated the radical anion but left some absorption (with maxima at 390 and 290 nm). With *N*-(methylamino)ethanol (MAE) a lesser amount of $TCB^{\bullet-}$ was formed and the new absorption at 290 nm, as above, was apparent already during the irradiation (not shown). On the other hand, the $TCB^{\bullet-}$ spectrum did not develop in the presence of DABCO. In this case, TCB was only sluggishly consumed, and a new absorption band with a maximum at 380 nm grew, which was unaffected when air was readmitted.

The investigation was then extended to further acceptors by using TEA and OXA, which had demonstrated to be the best donors for the accumulation of the acceptors radical anions. Actually, almost superimposable results were obtained, and in the following, only the results with the latter donor are mentioned.

The irradiation of a 5×10^{-4} M solution of 1,2,4-TrCB in the presence of OXA resulted in the development of a new absorption band, with sharp peaks at 351 and 433 nm and a broad shoulder around 400 nm, fully reversed on readmitting air. The signals were attributed to the 1,2,4-TrCB radical anion, to the best of our knowledge not previously characterized (see Figure 3a), on the basis of the analogy with $TCB^{\bullet-}$. This was not the case for 1,3,5-TrCB, where little if any of the radical anion [35,41,42] was formed and an irreversible modification of the spectrum occurred. Indeed none of the maxima known in the literature for this radical anion (532, 342 and 332 nm) developed [35].

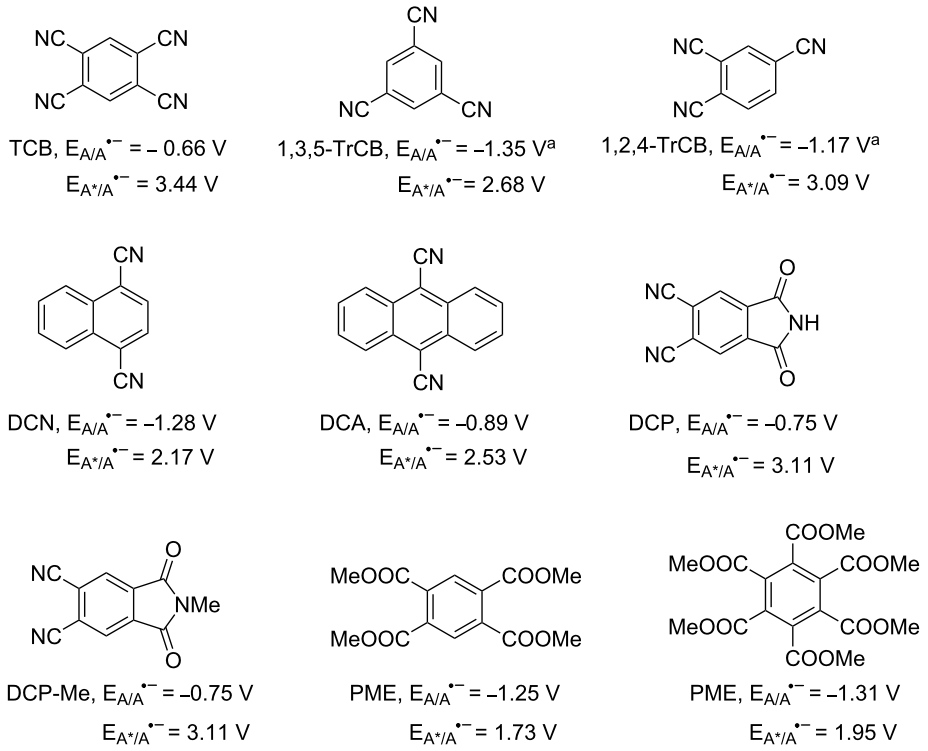

Figure 1: Reduction potential (versus SCE) of the ground and excited state of acceptors and oxidation potential of the ground-state donors examined in this work. [a]Value measured in the present work (see Experimental).

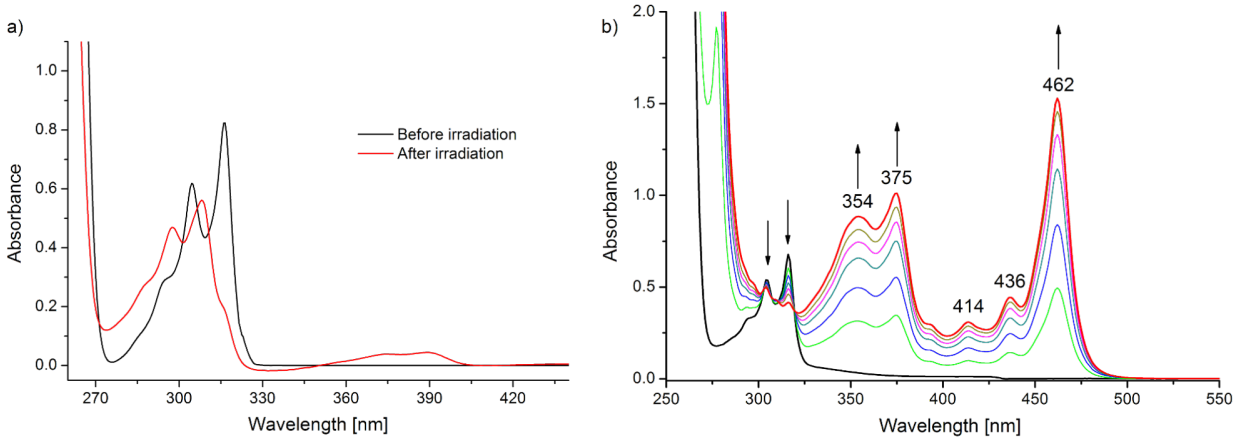

Figure 2: UV-monitoring of: (a) a 2 × 10^{-4} M solution of TCB in the presence of Bu_4Sn (10^{-2} M) and (b) a 1.5 × 10^{-4} M solution of TCB in the presence of OXA (5 × 10^{-2} M) in freeze–pump–thaw deoxygenated MeCN (λ_{IRR} = 313 nm) from 0 (black line) to 15 min (red line).

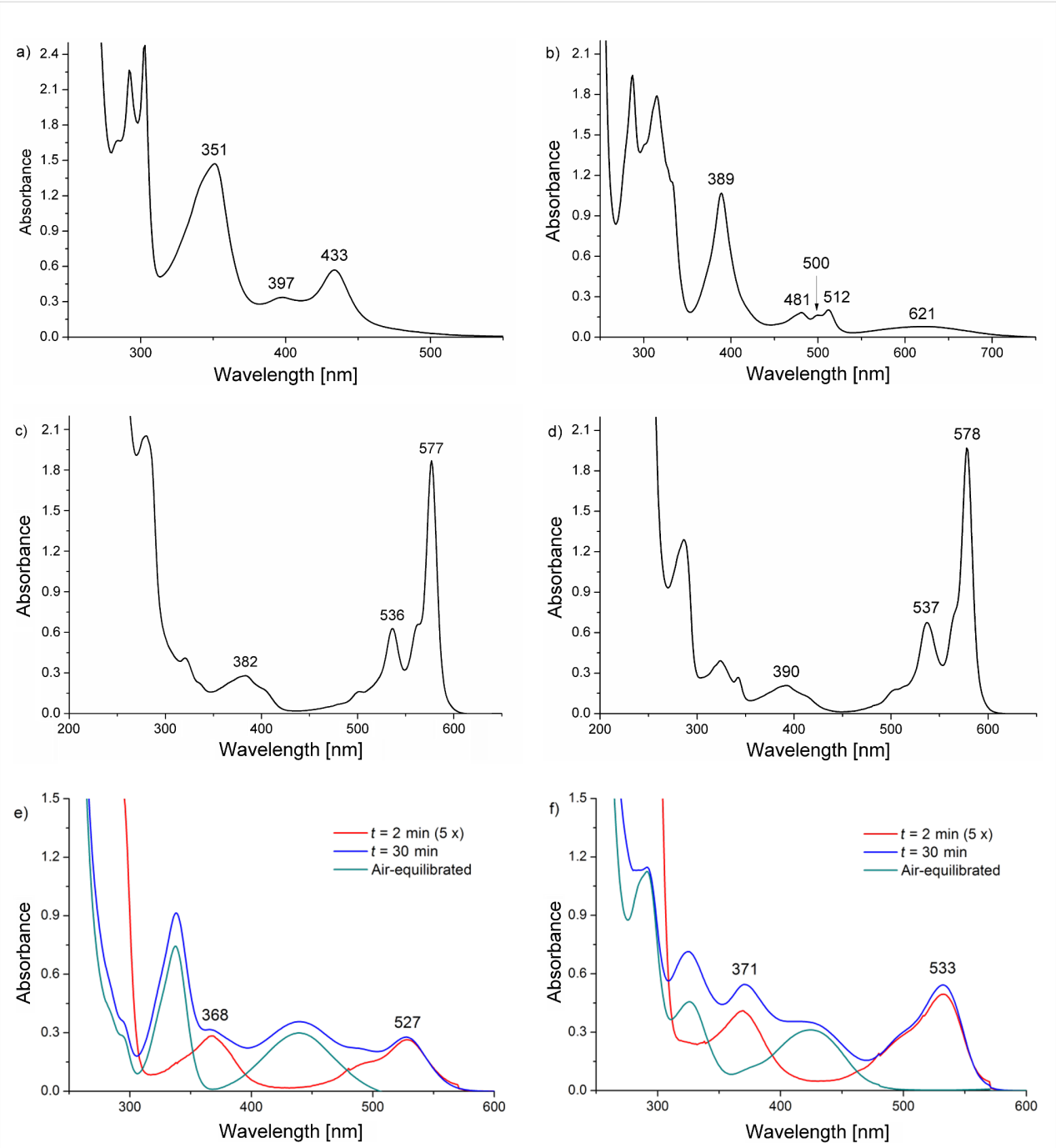

Figure 3: Absorption spectra of a freeze–pump–thaw deoxygenated MeCN solution irradiated at 313 nm of (a) 1,2,4-TrCB (5×10^{-4} M) in the presence of OXA (5.0×10^{-2} M), 20 min irradiation; (b) DCN (2×10^{-4} M) in the presence of OXA (5.0×10^{-2} M) and $Bu_4NH_2PO_4$ (5×10^{-3} M), 60 min irradiation; (c) DCP (7.5×10^{-5} M) and OXA (5.0×10^{-2} M), 3 min irradiation; (d) DCP-Me (7.5×10^{-5} M) and OXA (5.0×10^{-2} M), 3 min irradiation; (e) ME (4×10^{-4} M) in the presence of OXA (5.0×10^{-2} M) after 2 (red) and 30 (blue) min irradiation and after air equilibration of the 30 min photolyzed solution (green); (f) PME (4×10^{-4} M) in the presence of OXA (5.0×10^{-2} M) after 2 (red) and 30 (blue) min irradiation and after air equilibration of the 30 min photolyzed solution (green).

Analogously, in the case of DCN the corresponding radical anion [40] was not detected, while a broad, non-oxygen-sensitive band at ca. 390 nm was observed. On the other hand, when the same irradiation was performed after the addition of $Bu_4NH_2PO_4$ (5×10^{-3} M) the formation of pale green $DCN^{\bullet-}$ occurred with moderate efficiency (30% yield based on the ε of $DCN^{\bullet-}$ reported in the literature, 3578 L mol^{-1} cm^{-1} at 512 nm [40]; see Figure 3b). As for DCA, only a tiny amount of the

radical anion [35] was generated (data not shown). A purple color and conspicuous bands developed in the case of phthalimides DCP and DCP-Me, with sharp peaks at 577–578 and 535–536 nm and a broad band at ca. 400 nm (see Figure 3c and Figure 3d), reversible with air. These were attributed to the corresponding radical anions, not previously characterized, but fitting with a computational prediction of 559 nm for the radical anion of the unsubstituted *N*-methylphthalimide [43]. Finally, with both of the aromatic esters investigated, the bands of the corresponding pink radical anions (ME, 368 and 527 nm [44]; PME, 371 and 533 nm, $Bu_4NH_2PO_4$ added) were initially formed, but prolonged irradiation caused the formation of different absorption bands around 335 and 440 nm (see Figure 3e and Figure 3f). The former signals disappeared after air equilibration, while the latter persisted. Chromatographic analysis showed the formation of a strongly polar product (not identified).

Discussion

Figure 2 and Figure 3 and comparison with the literature allow us to classify the behavior of the acceptors into three groups. Polycyanobenzenes (with the exception of 1,3,5-TrCB) and cyanophthalimides form conspicuously the radical anion. Where known (as in the case of TCB), the spectrum corresponds closely to that reported (with small differences due to the different medium), and the intensity of the signals observed suggests that the conversion is almost complete. The accumulation of such species up to quantitative yield is demonstrated in neat MeCN. This can be related to extensive localization of the charge at the electronegative atoms, which makes these radical anions nonbasic and not nucleophilic [19,23,38]. In the second group, DCN gives a much less than unitary amount (ca. 30%) of the radical anion, and DCA barely a trace. This is reasonably related to the lower charge delocalization on the nitrogen atoms with respect to the above benzonitriles. In accordance with this idea, the DCN radical anion has been shown to accumulate to a larger degree in the presence of salts that afford a better stabilization. Finally, the esters accumulate to a certain extent (ca. 30%), but at this level, within the time of the steady-state experiments, they begin to undergo some decomposition. These radical anions have been reported to undergo loss of the alkyl group [45], and this reasonably explains the observed irreversible decomposition. The notes above define the requirement for accumulation of radical anions: no chemical reaction (and this excludes esters) and sufficient stabilization by both aromatic substituent and medium.

On the other hand, the choice of the donor is equally decisive, because of the different reactivity of the corresponding radical cations. These may be classed again in three groups: those that undergo exclusively BET (Scheme 2, path a'), those that undergo an irreversible reaction not involving the radical anion (path b'), and those that react with it (path c').

Thus, tertiary amines are known to undergo deprotonation from the α-position to produce a radical that is in turn easily oxidized

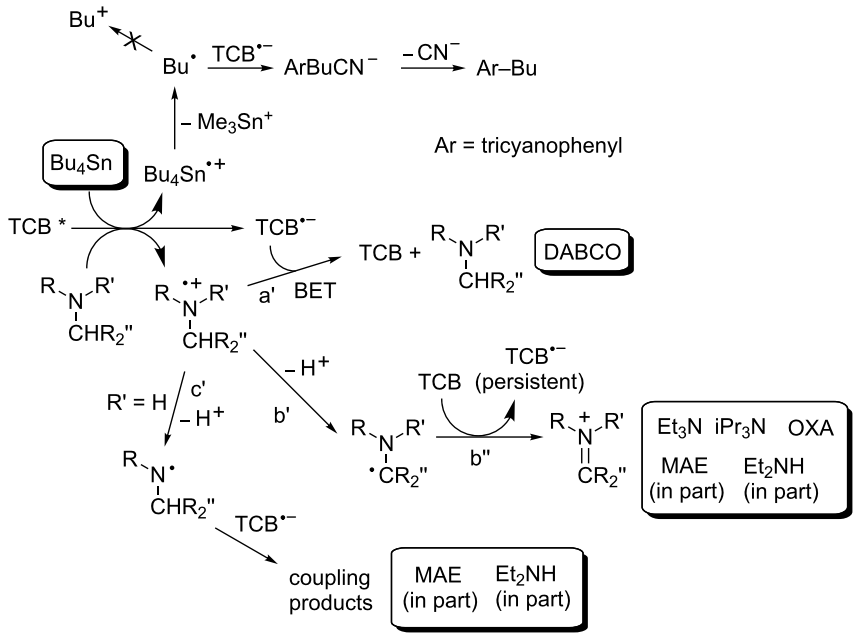

Scheme 2: Mechanistic scheme.

to the iminium cation. In the present examples, such radicals are oxidized by the ground-state sensitizer (E = −1.12 V versus SCE for the α-aminoradical resulting from TEA, see path β in Figure 4 [46] and path b'' in Scheme 2). In this way, radical cations are destroyed, and a second equivalent of $TCB^{\bullet-}$ is generated and accumulated. The quantum yield is $2k_{b'}/(k_{a'} + k_{b'})$, although the measured value (0.15) is probably lower than the ideal value because of side processes in solution. Notice that, although TEA and OXA form $TCB^{\bullet-}$ at the same rate in rigorously deaerated solutions, only the latter donor allows accumulation in solutions that have been merely nitrogen flushed and capped. Separation of radical ions appears to be faster in OXA due to conformational factors, in particular the steric bulk of the methyl groups. The more efficiently formed radicals scoop away traces of oxygen still present under these conditions.

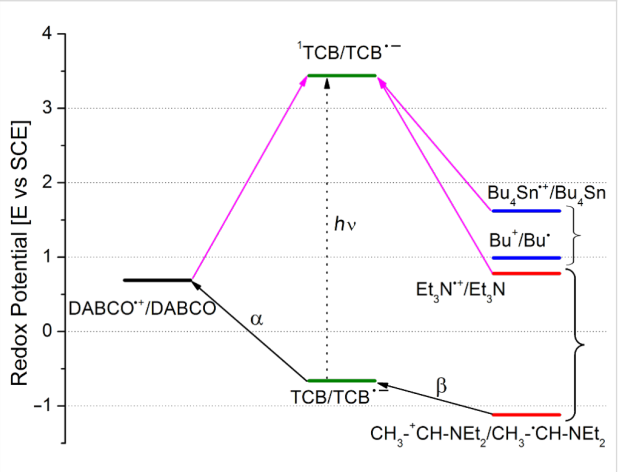

Figure 4: Thermodynamics of the redox processes discussed (solid arrows represent exergonic electron donation in the sense indicated). Thus, Et_3N, Bu_4Sn and DABCO all are oxidized by ^{1}TCB (ET; purple arrows). Likewise BET from $TCB^{\bullet-}$ is always viable and is the only possibility for DABCO (path α). $Et_3N^{\bullet+}$ cleaves and the radical generated is oxidized by TCB (path β), whereas this is not possible for the $Bu^\bullet$ radical formed by cleavage of the stannane (the potential of the $Bu^+/Bu^\bullet$ couple is approximated here by that of the ethyl cation/ethyl radical couple [47]).

Likewise, in accordance with the role of amine radical cation deprotonation, is the fact that, of the two further tertiary amines, iPr_3N causes a somewhat slower accumulation (the conformation of the radical cation is known to be less favorable for deprotonation) [48-50], and DABCO (for which deprotonation is impossible [51,52]) causes no detectable formation of $TCB^{\bullet-}$. Indeed, previous laser flash photolysis experiments had shown that DABCO formed the TCB radical anion on the nanosecond time scale just as the other tertiary amines [53]. However, no reaction able to eliminate radical cations was viable in this case, and thus BET predominated (path a' in Scheme 2 and path α in Figure 4).

Irreversible decomposition of TCB takes place to a small extent with DABCO, but it is much more conspicuous with secondary amines and the only path with the stannane. Radical cations of secondary amines are rather acidic (pK_a = 5.3 for $Et_2NH^{\bullet+}$ [54]) and undergo both α-C–H and N–H deprotonation, the latter process being also kinetically favored. Furthermore, the aminyl radical has been reported to couple with cyanoaromatics in a nonreversible process as reported by Correa et al. [55]. This justifies the formation of a stable photoproduct non-reoxidized by oxygen (path c' in Scheme 2). As for the stannane, cleavage of the radical cation to give Bu_3Sn^+ and $Bu^\bullet$ is favored. The C-centered radical is not oxidized by $TCB^{\bullet-}$ (see Figure 4) but couples with it, resulting in efficient ipso-substitution of the nitrile (Φ 0.40) [18]. Thus, only path b' alone leads to the accumulation of the radical anion.

Conclusion

The above experiments evidence the possibilities and the requirements for accumulating radical anions of electron-withdrawing substituted aromatics in neat organic solution. Apart from the spectroscopic interest, these data have a bearing on the mechanism of ET reactions such as those in Scheme 1 and Scheme 2. Aliphatic radical cations absorb poorly and are difficult to detect, but the conspicuous absorbance of the accompanying aromatic radical anions (the spectroscopic properties of which have been gathered in Table 1) gives most of the required information about the kinetic viability of the processes competing, offering through their bright colour a sort of litmus test for their evolution.

Experimental

The photochemical acceptors TCB, DCA, as well as the donors triethylamine (Et_3N), triisopropylamine (iPr_3N), 1,4-diazabicyclo[2.2.2]octane (DABCO), diethylamine (Et_2NH) and 2-(*N*-methylamino)ethanol (MAE) were commercially available. 1,3,5-TrCB [56], 1,2,4-TrCB [56], DCN [57], DCP [10], DCP-Me [10], ME [58], PME [11] and OXA [59] were obtained by known procedures. Since oxygen could interact with the photogenerated radical anions, resulting in a back oxidation [6], all of the experiments were carried out in freeze–pump–thaw deoxygenated solutions, except where otherwise noted. The examined solutions were irradiated on an optical bench equipped with a 150 W high-pressure mercury lamp, (λ_{IRR} = 313 nm). The electrochemical properties of TCB [8,9], DCN [8,9], DCA [8,9], DCP [10], DCP-ME [10], ME [45], PME [28], Et_3N [60], iPr_3N [61], DABCO [61] and Bu_4Sn [62] were available in the literature. Electrochemical measurements (cyclic voltammetry) on the other compounds (Et_2NH, MAE, OXA, 1,3,5-TrCB and 1,2,4-TrCB) were performed on 5 × 10^{-2} M solutions of the analyte in a three-electrode cell (volume 10 mL; *n*-Bu_4NClO_4 0.1 M as the supporting electrolyte) with glassy carbon (dia-

meter 2 mm) as the working electrode, Pt wire as the auxiliary electrode, and Ag/AgCl (3 M NaCl) as the reference electrode. Scan speed was 50 mV s^{-1}. The potential range investigated was 0/+2.5 V for oxidation and 0/−2.5V for reduction processes. The electrochemical measurements were carried out by a BASi computer-controlled electrochemical analyzer. The potentials measured were then referred to SCE, applying the equation E (versus SCE) = E (versus Ag/AgCl; 3 M NaCl) − 35 mV. The redox potential of the excited state of compounds TCB [8,9], DCN [8,9], DCA [8,9], DCP [10] and DCP-ME [10] were taken from the literature, whereas the redox potentials of the excited state of 1,3,5-TrCB [21], 1,2,4-TrCB [21], ME [58] and PME [28] were determined by the Rehm–Weller equation [63].

Acknowledgements

We thank Dr. Daniele Merli for the electrochemical measurements. S.P. acknowledges MIUR, Rome (FIRB-Futuro in Ricerca 2008 project RBFR08J78Q) for financial support.

References

1. Hoffmann, N. *J. Photochem. Photobiol., C: Photochem. Rev.* **2008,** *9,* 43–60. doi:10.1016/j.jphotochemrev.2008.04.002
2. Ischay, M. A.; Yoon, T. P. *Eur. J. Org. Chem.* **2012,** 3359–3372. doi:10.1002/ejoc.201101071
3. Albini, A.; Fagnoni, M.; Mella, M. Photoinduced electron transfer: perspectives in organic synthesis. In *Chemistry at the Beginning of the Third Millennium: Molecular Design, Supramolecules, Nanotechnology and Beyond,* Proceedings of the German–Italian Meeting of Coimbra Group Universities, Pavia, Oct 7–10, 1999; Fabbrizzi, L.; Poggi, A., Eds.; Springer: Berlin, 2000; pp 83–101. doi:10.1007/978-3-662-04154-3_5
4. Griesbeck, A. G.; Hoffmann, N.; Warzecha, K.-D. *Acc. Chem. Res.* **2007,** *40,* 128–140. doi:10.1021/ar068148w
5. Mella, M.; Fagnoni, M.; Freccero, M.; Fasani, E.; Albini, A. *Chem. Soc. Rev.* **1998,** *27,* 81–89. doi:10.1039/A827081Z
6. Marin, M. L.; Santos-Juanes, L.; Arques, A.; Amat, A. M.; Miranda, M. A. *Chem. Rev.* **2012,** *112,* 1710–1750. doi:10.1021/cr2000543
7. Fox, M. A. Photoinduced Electron Transfer in Organic Systems: Control of Back Electron Transfer. In *Advances in Photochemistry;* Volman, D. H.; Hammond, G. S.; Gollnick, K., Eds.; John Wiley & Sons, Inc.: Hoboken, NJ, USA, 1986; Vol. 13, p 237. doi:10.1002/9780470133439.ch4
8. Fox, M. A. *Photoinduced Electron Transfer part A. Conceptual Basis*; Chanon, M., Ed.; Elsevier: Amsterdam, 1988.
9. Schmittel, M.; Ghorai, M. K. Reactivity patterns in radical ions – A unifying picture of radical-anion and radical-cation transformations. In *Electron Transfer in Chemistry;* Balzani, V., Ed.; Wiley-VCH: Weinheim, Germany, 2001; pp 5–54. doi:10.1002/9783527618248.ch15
10. Freccero, M.; Fasani, E.; Albini, A. *J. Org. Chem.* **1998,** *58,* 1740–1745. doi:10.1021/jo00059a023
11. Fagnoni, M.; Mella, M.; Albini, A. *J. Phys. Org. Chem.* **1997,** *10,* 777–780. doi:10.1002/(SICI)1099-1395(199710)10:10<777::AID-POC940>3.0.CO;2-V
12. Yamada, S.; Nakawaga, Y.; Watabiki, O.; Suzuki, S.-i.; Ohashi, M. *Chem. Lett.* **1986,** 361–364. doi:10.1246/cl.1986.361
13. Ohashi, M.; Kudo, H.; Yamada, S. *J. Am. Chem. Soc.* **1979,** *101,* 2201–2202. doi:10.1021/ja00502a045
14. Koshima, H.; Ding, K.; Chisaka, Y.; Matsuura, T.; Ohashi, Y.; Mukasa, M. *J. Org. Chem.* **1996,** *61,* 2352–2357. doi:10.1021/jo951642l
15. Fasani, E.; Peverali, D.; Albini, A. *Tetrahedron Lett.* **1994,** *35,* 9275–9278. doi:10.1016/0040-4039(94)88486-2
16. Mella, M.; Fasani, E.; Albini, A. *J. Org. Chem.* **1992,** *57,* 3051–3057. doi:10.1021/jo00037a020
17. Hasegawa, E.; Brumfield, M. A.; Mariano, P. S.; Yoon, U. C. *J. Org. Chem.* **1988,** *53,* 5435–5442. doi:10.1021/jo00258a007
18. Kyushin, S.; Masuda, Y.; Matsushita, M.; Nakadaira, Y.; Ohashi, M. *Tetrahedron Lett.* **1990,** *31,* 6395–6398. doi:10.1016/S0040-4039(00)97074-6
19. Fagnoni, M.; Mella, M.; Albini, A. *Tetrahedron* **1994,** *50,* 6401–6410. doi:10.1016/S0040-4020(01)80656-6
20. Mizuno, K.; Ikeda, M.; Otsuji, Y. *Tetrahedron Lett.* **1985,** *26,* 461–464. doi:10.1016/S0040-4039(00)61911-1
21. Mella, M.; d'Alessandro, N.; Freccero, M.; Albini, A. *J. Chem. Soc., Perkin Trans. 2* **1993,** 515–519. doi:10.1039/P29930000515
22. Mella, M.; Fasani, E.; Albini, A. *J. Org. Chem.* **1992,** *57,* 6210–6216. doi:10.1021/jo00049a031
23. Bardi, L.; Fasani, E.; Albini, A. *J. Chem. Soc., Perkin Trans. 1* **1994,** 545–549. doi:10.1039/P19940000545
24. Shukla, D.; Young, R. H.; Farid, S. *J. Phys. Chem. A* **2004,** *108,* 10386–10394. doi:10.1021/jp0466340
25. Mella, M.; Freccero, M.; Albini, A. *J. Chem. Soc., Chem. Commun.* **1995,** 41–42. doi:10.1039/C39950000041
26. Schreiner, P. R.; Wittkopp, A.; Gunchenko, P. A.; Yaroshinsky, A. I.; Peleshanko, S. A.; Fokin, A. A. *Chem.–Eur. J.* **2001,** *7,* 2739–2744. doi:10.1002/1521-3765(20010702)7:13<2739::AID-CHEM2739>3.0.CO;2-R
27. Mella, M.; Freccero, M.; Albini, A. *Tetrahedron* **1996,** *52,* 5549–5562. doi:10.1016/0040-4020(96)00195-0
28. Fagnoni, M.; Mella, M.; Albini, A. *J. Am. Chem. Soc.* **1995,** *117,* 7877–7881. doi:10.1021/ja00135a004
29. Fagnoni, M.; Mella, M.; Albini, A. *J. Org. Chem.* **1998,** *63,* 4026–4033. doi:10.1021/jo980093r
30. Fagnoni, M.; Dondi, D.; Ravelli, D.; Albini, A. *Chem. Rev.* **2007,** *107,* 2725–2756. doi:10.1021/cr068352x
31. Ravelli, D.; Fagnoni, M.; Albini, A. *Chem. Soc. Rev.* **2013,** *42,* 97–113. doi:10.1039/C2CS35250H
32. Albini, A.; Fagnoni, M.; Mella, M. *Pure Appl. Chem.* **2000,** *72,* 1321–1326. doi:10.1351/pac200072071321
33. Wagner-Czauderna, E.; Kalinowski, M. K. *Collect. Czech. Chem. Commun.* **2000,** *65,* 1573–1579. doi:10.1135/cccc20001573
34. Pedersen, S. U.; Christensen, T. B.; Thomasen, T.; Daasbjerg, K. *J. Electroanal. Chem.* **1998,** *454,* 123–143. doi:10.1016/S0022-0728(98)00195-8
35. Shida, T. Electronic Absorption Spectra of Radical Ions. In *Physical Sciences Data 34;* Elsevier: Amsterdam, 1988.
36. Masahiro Irie, M.; Tomimoto, S.; Hayashi, K. *J. Phys. Chem.* **1972,** *76,* 1419–1424. doi:10.1021/j100654a008
37. Freccero, M.; Mella, M.; Albini, A. *Tetrahedron* **1994,** *7,* 2115–2130. doi:10.1016/S0040-4020(01)85074-2

38. Kellett, M. A.; Whitten, D. G.; Gould, I. R.; Bergmark, W. R. *J. Am. Chem. Soc.* **1991,** *113,* 358–359. doi:10.1021/ja00001a052
39. Δ*G* is always negative in the processes considered; in particular, the electron transfer is expected to be exoergonic by ca. 63 and 12 kcal mol^{-1} in the most and least favorable case, respectively.
40. Lund, T.; Christensen, R.; Wilbrandt, R. *Org. Biomol. Chem.* **2003,** *1,* 1020–1025. doi:10.1039/B209594G
41. Tsukuda, T.; Kondow, T.; Dessent, C. E. H.; Bailey, C. G.; Johnson, M. A.; Hendricks, J. H.; Lyapustina, S. A.; Bowen, K. H. *Chem. Phys. Lett.* **1997,** *269,* 17–21. doi:10.1016/S0009-2614(97)00255-8
42. Del Sesto, R. E.; Arif, A. M.; Novoa, J. J.; Anusiewicz, I.; Skurski, P.; Simons, J.; Dunn, B. C.; Eyring, E. M.; Miller, J. S. *J. Org. Chem.* **2003,** *68,* 3367–3379. doi:10.1021/jo025833h
43. Gosztola, D.; Niemczyk, M. P.; Svec, W.; Lukas, A. S.; Wasielewski, M. R. *J. Phys. Chem. A* **2000,** *104,* 6545–6551. doi:10.1021/jp000706f
44. Webster, R. D.; Bond, A. M.; Coomber, D. C. *J. Electroanal. Chem.* **1998,** *442,* 217–227. doi:10.1016/S0022-0728(97)00465-8
45. Webster, R. D.; Bond, A. M.; Compton, R. G. *J. Phys. Chem.* **1996,** *100,* 10288–10297. doi:10.1021/jp9601173
46. Wayner, D. D. M.; McPhee, D. J.; Griller, D. *J. Am. Chem. Soc.* **1988,** *110,* 132–137. doi:10.1021/ja00209a021
47. Wayner, D. D. M.; Houman, A. *Acta Chem. Scand.* **1998,** *52,* 377–384. doi:10.3891/acta.chem.scand.52-0377
48. von Raumer, M.; Suppan, P.; Haselbach, E. *Chem. Phys. Lett.* **1996,** *252,* 263–266. doi:10.1016/0009-2614(96)00138-8
49. Lalevée, J.; Allonas, X.; Fouassier, J. P. *J. Am. Chem. Soc.* **2002,** *124,* 9613–9621. doi:10.1021/ja0204168
50. Markus von Raumer, M.; Suppan, P.; Haselbach, E. *Helv. Chim. Acta* **1997,** *80,* 719–724. doi:10.1002/hlca.19970800309
51. Inbar, S.; Linschitz, H.; Cohen, S. G. *J. Am. Chem. Soc.* **1981,** *103,* 1048–1054. doi:10.1021/ja00395a009
52. Bhattacharyya, K.; Das, P. K. *J. Phys. Chem.* **1986,** *90,* 3987–3993. doi:10.1021/j100408a032
53. Protti, S.; Fagnoni, M.; Monti, S.; Réhault, J.; Poizat, O.; Albini, A. *RSC Adv.* **2012,** *2,* 1897–1904. doi:10.1039/C2RA01054B
54. Jonsson, M.; Wayner, D. D. M.; Lusztyk, J. *J. Phys. Chem.* **1996,** *100,* 17539–17543. doi:10.1021/jp961286q
55. Lewis, F. D.; Zebrowski, B. E.; Correa, P. E. *J. Am. Chem. Soc.* **1984,** *106,* 187–193. doi:10.1021/ja00313a038
56. Lawton, E. A.; McRichtie, D. A. *J. Org. Chem.* **1959,** *24,* 26–28. doi:10.1021/jo01083a008
57. Çakmak, O.; Kahveci, I.; Demirtaş, I.; Hökelek, T.; Smith, K. *Collect. Czech. Chem. Commun.* **2000,** *65,* 1791–1804. doi:10.1135/cccc20001791
58. Yamasaki, N.; Inoue, Y.; Yokoyama, T.; Tai, A.; Ishida, A.; Takamuku, S. *J. Am. Chem. Soc.* **1991,** *113,* 1933–1941. doi:10.1021/ja00006a011
59. Leonard, N. J.; Paukstelis, J. V.; Brady, L. E. *J. Org. Chem.* **1964,** *29,* 3383–3386. doi:10.1021/jo01034a062
60. Hub, W.; Schneider, S.; Dorr, F.; Oxman, J. D.; Lewis, F. D. *J. Am. Chem. Soc.* **1984,** *106,* 701–708. doi:10.1021/ja00315a040
61. Pischel, U.; Zhang, X.; Hellrung, B.; Haselbach, E.; Muller, P.-M.; Nau, W. M. *J. Am. Chem. Soc.* **2000,** *122,* 2027–2034. doi:10.1021/ja992508b
62. Yoshida, J.-i.; Izawa, M. *J. Am. Chem. Soc.* **1997,** *119,* 9361–9365. doi:10.1021/ja970899t
63. Rehm, D.; Weller, A. *Isr. J. Chem.* **1970,** *8,* 259–271.

License and Terms

Beilstein Journal of Organic Chemistry

Substituent effect on the energy barrier for σ-bond formation from π-single-bonded species, singlet 2,2-dialkoxycyclopentane-1,3-diyls

Jianhuai Ye[1], Yoshihisa Fujiwara[2] and Manabu Abe[*1,3]

Full Research Paper

Open Access

Address:
[1]Department of Chemistry, Graduate School of Science, Hiroshima University, Japan, [2]Department of Mathematical and Life Sciences, Graduate School of Science, Hiroshima University, Japan, and [3]Institute for Molecular Science (IMS), Okazaki, Aichi 444-8787, Japan

Email:
Manabu Abe[*] - mabe@hiroshima-u.ac.jp

* Corresponding author

Keywords:
laser flash photolysis; lifetime; singlet diradicals (biradicals); substituent effect; π-single bond

Beilstein J. Org. Chem. **2013,** *9,* 925–933.
doi:10.3762/bjoc.9.106

Received: 14 March 2013
Accepted: 22 April 2013
Published: 14 May 2013

This article is part of the Thematic Series "New reactive intermediates in organic chemistry".

Guest Editor: G. Bucher

Abstract

Background: Localized singlet diradicals are in general quite short-lived intermediates in processes involving homolytic bond-cleavage and formation reactions. In the past decade, long-lived singlet diradicals have been reported in cyclic systems such as cyclobutane-1,3-diyls and cyclopentane-1,3-diyls. Experimental investigation of the chemistry of singlet diradicals has become possible. The present study explores the substituents and the effect of their substitution pattern at the C(1)–C(3) positions on the lifetime of singlet octahydropentalene-1,3-diyls to understand the role of the substituents on the reactivity of the localized singlet diradicals.

Results: A series of singlet 2,2-dialkoxy-1,3-diaryloctahydropentalene-1,3-diyls **DR** were generated in the photochemical denitrogenation of the corresponding azoalkanes **AZ**. The ring-closed products **CP**, i.e., 3,3-dialkoxy-2,4-diphenyltricyclo[3.3.0.0^{2,4}]octanes, were quantitatively obtained in the denitrogenation reaction. The first-order decay process ($k = 1/\tau$) was observed for the fate of the singlet diradicals **DR** ($\lambda_{max} \approx 580$–$590$ nm). The activation parameters, $\Delta H^{\ddagger}$ and $\Delta S^{\ddagger}$, for the ring-closing reaction (σ-bond formation process) were determined by the temperature-dependent change of the lifetime. The energy barrier was found to be largely dependent upon the substituents Ar and Ar'. The singlet diradical **DRf** (Ar = 3,5-dimethoxyphenyl, OCH_2Ar' = OCH_2(3,5-dimethoxyphenyl)) was the longest-lived, $\tau_{293} = 5394 \pm 59$ ns, among the diradicals studied here. The lifetime of the parent diradical **DR** (Ar = Ph, OCH_2Ar' = OCH_3) was 299 ± 2 ns at 293 K.

Conclusion: The lifetimes of the singlet 1,3-diyls are found to be largely dependent on the substituent pattern of Ar and Ar' at the C(1)–C(3) positions. Both the enthalpy and entropy effect were found to play crucial roles in increasing the lifetime.

Introduction

Localized singlet diradicals are key intermediates in processes involving the homolytic bond-cleavage and formation reactions (Figure 1) [1,2]. The singlet diradicals are, in general, quite short-lived species due to the very fast radical–radical coupling reaction [3]. However, in the past decade, the singlet diradicals have been observed or even isolated in cyclic systems such as cyclobutane-1,3-diyls [4-20] and cyclopentane-1,3-diyls [17,21-26]. Detailed experimental study of singlet diradical chemistry is thus now possible using the long-lived localized singlet diradicals.

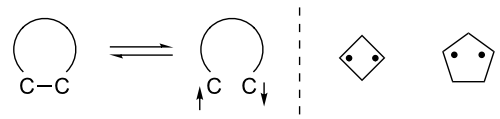

Figure 1: Localized singlet diradicals.

So far, we have studied singlet diradical chemistry using long-lived 2,2-dialkoxy-1,3-diphenyloctahydropentalene-1,3-diyls **DR** with a singlet ground state, which can be cleanly generated by the photochemical denitrogenation of the corresponding azoalkanes **AZ** (Scheme 1). The 2,2-electron-withdrawing-group-substituted singlet 1,3-diradicals are categorized as Type-1 diradicals [1,27], which possess a π-single-bonding character (–π–, closed-shell character) between the two radical sites. The role of the alkoxy group (OR) on the lifetime ($k = 1/\tau$) was investigated by combined studies of experiments and quantum chemical calculations [26,28]. The steric repulsion between the alkoxy group and the phenyl ring, which is indicated in the transition-state structure for the ring-closing reaction (Scheme 1), was found to play an important role in determining the energy barrier of the ring-closing process, τ_{293} = 292 ns (**DRa**: OR = OCH_3, λ_{max} = 574 nm) and 2146 ns (**DRb**: OR = $OC_{10}H_{21}$, λ_{max} = 572 nm) [26]. The study prompted us to further investigate the kinetic stabilization of the singlet diradical species.

In the present study, the effect of the bulky 3,5-dimethoxyphenyl group substituent was investigated on the lifetime of the localized singlet diradicals. Thus, the aryl substituent was introduced at C(1), C(2), or/and C(3) positions of the diradicals **DRd**–**g**, and the substituent effects on the lifetime of the singlet diradicals were compared with the lifetime of a phenyl-group-substituted diradical **DRc** and the parent diradical **DRa**. The laser flash photolysis technique was used for the generation of **DRc**–**g** from the corresponding azoalkanes **AZc**–**g** (Scheme 2).

Results and Discussion

Synthesis of AZc–g and their steady-state photolyses. The precursor azoalkanes **AZc**–**g** were prepared in an analogous method to the synthesis of **AZa,b** [28] (Scheme 3). Pyrazoles **3c**–**f** were synthesized in the reaction of tetrazines **1** (Ar = Ph or 3,5-dimethoxyphenyl) with 2,2-dialkoxy-5,5-dimethyl-Δ^3-1,3,4-oxadiazolines **2** [29], which are the precursor of the dialkoxycarbene (Scheme 3a). Azoalkanes **AZc–f** ($\lambda_{max} \approx$ 360 nm with $\varepsilon \approx 100$) were obtained by a cycloaddition reaction with cyclopentadienes, and followed by a hydrogenation reaction [30,31]. The synthesis of **AZg** (Ar = 3,5-dimethoxyphenyl, Ar' = H) was performed from the corresponding 1,3-diketone **4** (Scheme 3b). 2,2-Dimethoxy-1,3-diarylpropane-1,3-dione **5g** was prepared from 1,3-dione **4** (R = 3,5-dimethoxybenzene) according to the method of Tiecco [32]. Pyrazole **3g** was then synthesized by the reaction with hydrazine hydrate. **AZg** was obtained by the Diels–Alder [4 + 2]-cycloaddition with cyclopentadiene and hydrogenation using PtO_2 as a cata-

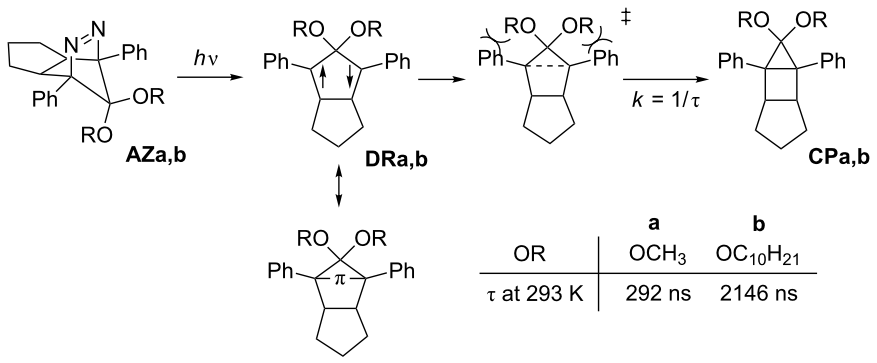

Scheme 1: Alkoxy group effect on the lifetime of π-single-bonded species **DR**.

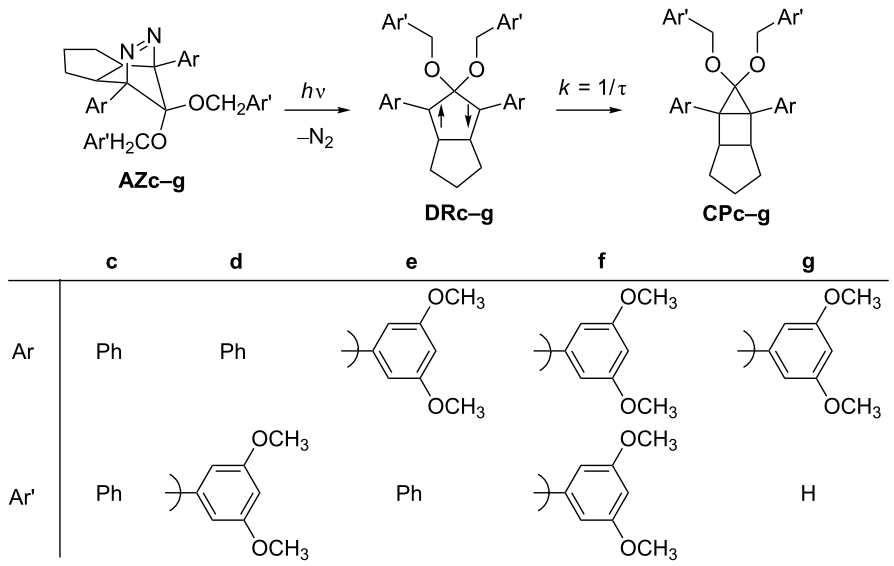

Scheme 2: Generation of singlet diradicals **DRc–g** and their reactivity in the photochemical denitrogenation of **AZc–g**.

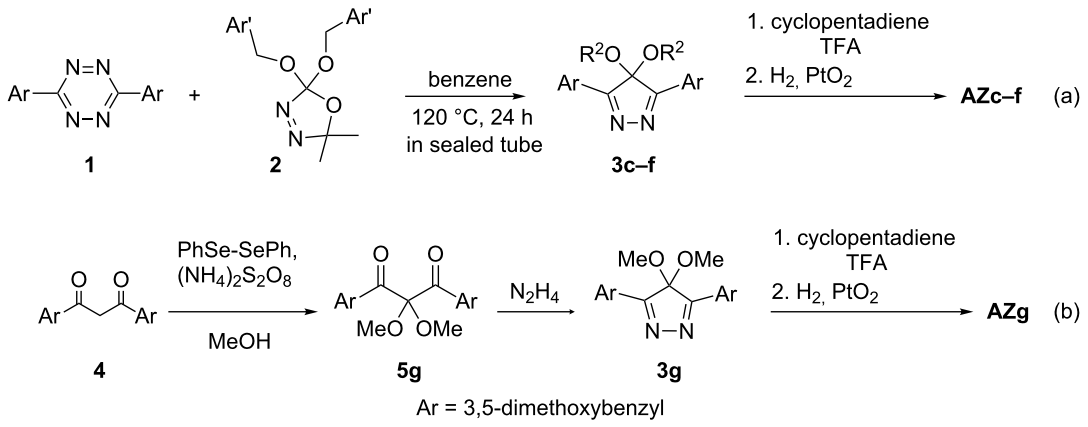

Scheme 3: Synthesis of azoalkanes **AZc–f** and **AZg**.

lyst. The endo-configured structure of azoalkanes **AZc–g** was determined by X-ray crystallographic analysis as well as by NOE measurements.

The steady-state photolyses of **AZc–g** in benzene solution were performed with a Xenon lamp (500 W) through a Pyrex filter ($h\nu$ > 300 nm). The ring-closed compounds **CPc–g** were quantitatively obtained in the denitrogenation reaction (Scheme 2). The quantum yields of the denitrogenation of **AZc–g** were determined to be ≈0.90 by comparison with those reported for similar azoalkanes [33]. The quantitative formation of **CPc–g** and the high quantum yield of the denitrogenation process suggest the clean generation of **DRc–g** in the photoirradiation reaction of **AZc–g**.

Detection of singlet diradicals DRc–g. The detection of singlet diradicals **DRc–g** was examined by the photochemical denitrogenation of azoalkanes **AZc–g** in a glassy matrix of 2-methyltetrahydrofurane (MTHF) at 80 K, [**AZ**] ≈ 4×10^{-3} mol/L, and by the laser flash photolysis experiments of **AZc–g** at room temperature in benzene solution. First of all, the MTHF matrix solution of **AZ** was irradiated with a 500 W Xenon lamp through a monochromator (λ_{irr} = 360 ± 10 nm). A strong absorption band, which corresponds to **DRc–g**, was observed in the visible region at 80 K (570–590 nm, Table 1), as exemplified for the photoirradiation of **AZe** in Figure 2a. The strong absorption bands are quite similar to those of singlet diradicals **DRa,b** with λ_{max} = 574 nm and 572 nm [1,28], respectively. The assignment of the strong band to the singlet diradical is

further supported by the following facts: (a) The absorptions obtained on photolysis in a MTHF glass were thermally persistent at 80 K and resembled that of the transient absorption spectra in solution (for example, **DRe**, λ_{max} = 590 nm, Figure 2b); (b) the species were ESR-silent in the MTHF-matrix at 80 K; (c) the lifetime of the transient was insensitive to the presence of molecular oxygen (decay trace at 580 nm, Figure 2c); and (d) the activation parameters (Table 1) are similar to those for the decay process of **DRa**, in particular, the high (ca. 10^{12} s^{-1}) pre-exponential Arrhenius factors (log*A*) are indicative of a spin-allowed reaction to the ring-closed products **CPc–g** [34].

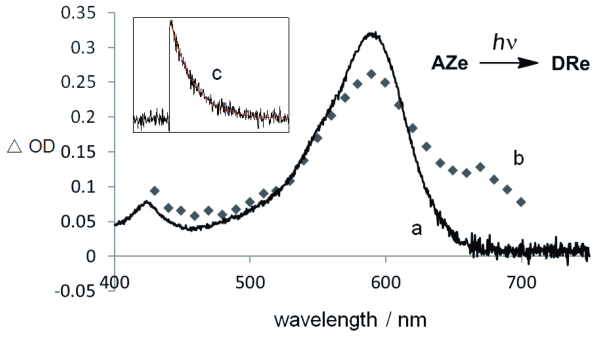

Figure 2: (a) Absorption spectrum of the singlet diradical **DRe** in a MTHF matrix at 80 K; (b) transient absorption spectrum of **AZe** measured immediately after the laser pulse (λ_{exc} = 355 nm); (c) transient decay trace at 580 nm and 20 °C.

Lifetime of singlet diradicals DRc–g and activation parameters for the ring-closing reaction. The decay traces of the intermediary singlet diradicals **DRc–g** at 293–333 K were measured in a benzene solution by the laser flash photolysis technique (λ_{exc} = 355 nm). The lifetime ($\tau = 1/k$) was determined by the first-order decay rate constants (*k*) of **DRc–g** at 580 nm, e.g., Figure 2c for **DRe**. As shown in Table 1, the lifetime of the singlet diradical was largely dependent on the substituents Ar and Ar'. The activation parameters, $\Delta H^{\ddagger}$, $\Delta S^{\ddagger}$, E_a, log*A*, were determined from the Eyring plots and Arrhenius plots, which were obtained from the temperature-dependent change of the lifetime (Table 1). For comparison, the lifetime of diradical **DRa** (Table 1, entry 1) was also measured under similar conditions, and determined to be 299 ns at 293 K. The obtained lifetime was nearly the same as that obtained previously by us (292 ns) [28].

The lifetime of **DRc** (Ar = Ar' = Ph) was found to be 1305 ns at 293 K (Table 1, entry 2), which was ca. 4.5 times longer than the parent **DRa**. On introduction of a 3,5-dimethoxyphenyl ring at C(2) position of the 1,3-diradical, i.e., **DRd** (Ar = Ph, Ar' = 3,5-dimethoxyphenyl), a further increase of the lifetime at 293 K was observed to be 1933 ns (Table 1, entry 3). The result clearly indicates that the steric bulkiness plays an important role in increasing the energy barrier for the ring-closing reaction. Indeed, the activation enthalpy ($\Delta H^{\ddagger}$ = 36.6 kJ mol^{-1}, Table 1, entry 3) for **DRd** was found to be higher than that for **DRa** ($\Delta H^{\ddagger}$ = 32.7 kJ mol^{-1}, Table 1, entry 1). Interestingly, the effect of an aryl group substituent at C(1) and C(3) positions on the lifetime was found to be larger than that at C(2); compare the lifetime of **DRe** (4001 ns, Ar = 3,5-dimethoxyphenyl, Ar' = Ph, Table 1, entry 4) with that of **DRd** (1933 ns, Table 1, entry 3). When the 3,5-dimethoxyphenyl group was introduced at all of the C(1), C(2), and C(3) positions, the lifetime of the diradical **DRf** ($\Delta G^{\ddagger}$ = 42.2 kJ mol^{-1}, Table 1, entry 5) was dramatically increased to 5394 ns at 293 K. The activation entropy ($\Delta S^{\ddagger}$ = −27.8 and −19.4 J mol^{-1}, Table 1, entries 4 and 5) also plays an important role in increasing the lifetime of the singlet species. A much shorter lifetime was found for the diradical **DRg** (Ar = 3,5-dimethoxyphenyl, Ar' = H). Thus, the introduction of the bulky substituents is needed at all positions C(1)–C(3) of the

Table 1: Lifetimes and activation parameters of singlet diradicals **DR**.

entry	DR	τ_{293K} /ns[a]	λ_{max} /nm[b] (at 80 K)	$\Delta G^{\ddagger}_{293K}$[c] /kJ mol^{-1}	$\Delta H^{\ddagger}$[c] /kJ mol^{-1}	$\Delta S^{\ddagger}$[c] /J mol^{-1} K^{-1}	E_a[c] /kJ mol^{-1}	log A[c]
1	**DRa**	299	573	35.1 ± 0.7	32.7 ± 0.2	–8.1 ± 1.2	35.3 ± 0.2	12.8 ± 0.1
2	**DRc**	1305	583	39.1 ± 0.9	33.5 ± 0.6	–17.9 ± 1.7	36.2 ± 0.6	12.3 ± 0.1
3	**DRd**	1933	584	39.6 ± 0.6	36.6 ± 0.1	–10.1 ± 1.1	39.2 ± 0.1	12.7 ± 0.1
4	**DRe**	4001	592	40.9 ± 0.8	33.3 ± 0.4	–27.8 ± 1.3	35.9 ± 0.4	11.8 ± 0.1
5	**DRf**	5394	593	42.2 ± 0.7	36.5 ± 0.3	–19.4 ± 1.0	39.1 ± 0.3	12.2 ± 0.1
6	**DRg**	580	583	36.7 ± 0.4	33.0 ± 0.2	–12.9 ± 1.0	35.6 ± 0.2	12.2 ± 0.1

[a]Experimental errors are ca. 5%.
[b]In MTHF at 80 K.
[c]Activation parameters were determined by measurements of the lifetime of the singlet diradicals at five different temperatures in a temperature range from 293 to 333 K.

1,3-diradicals to increase the lifetime. The repulsive steric interactions of the Ar group with the Ar' group are suggested to play important roles in increasing the energy barrier of the reaction from the diradicals to the ring-closed compounds **CP**. The results clearly indicate that the substituent effect using the sterically bulky group is effective to prolong the lifetime of the singlet diradicals.

Conclusion

We have succeeded in generating long-lived singlet diradical species **DRc–g**, τ_{293} = 580–5394 ns, which were much longer-lived species than **DRa** (τ_{293} = 299 ns). It was found that the lifetimes are largely dependent on the substituent pattern of Ar and Ar' at the C(1)–C(3) positions of the 1,3-diyls. Thus, both the enthalpy and entropy effect were found to play crucial roles in increasing the lifetime.

Experimental

All reagents were purchased from commercial sources and were used without additional purification, unless otherwise mentioned. Azoalkanes **AZc–g** were prepared according to the methods described previously (Scheme 3) and were isolated by silica gel column chromatography and GPC column chromatography. ^{1}H and ^{13}C NMR spectra were reported in parts per million (δ) by using $CDCl_3$ or C_6D_6 as internal standards. Assignments of ^{13}C NMR were carried out by DEPT measurements. IR spectra were recorded with a FTIR spectrometer. UV–vis spectra were taken by a JASCO V-630 spectrophotometer. Mass-spectrometric data were measured by a Mass Spectrometric Thermo Fisher Scientific LTQ Orbitrap XL, performed by the Natural Science Center for Basic Research and Development (NBARD), Hiroshima University.

Preparation of diazenes **AZc–g**

3,6-Diaryl-1,2,4,5-tetrazine 1. 3,6-Diphenyl-1,2,4,5-tetrazine was purchased and directly used. The preparation of 3,6-(3,5-dimethoxyphenyl)-1,2,4,5-tetrazine (Ar = 3,5-dimethoxyphenyl) is as follows: In a 50 mL round-bottom flask, benzonitrile (3.7 g, 22.7 mmol) was dissolved in 10 mL of absolute ethanol. Hydrazine (3.6 mL, 90 mmol) and sulfur (0.43 g, 13.5 mmol) were quickly added, and the solution was stirred at room temperature for 1 h and then heated under reflux for 3 h. The remaining orange cake was solidified further in an ice bath. The solid was vacuum filtered, and washed with cold ethanol (3 × 10 mL) giving the crude dihydrotetrazine. The crude orange solid was then placed in a 50 mL beaker and dissolved in 20% acetic acid (15 mL) and 10 mL ether at room temperature with stirring. An aqueous solution of 10% $NaNO_2$ (20 mL) was added to the solution in an ice bath. The immediate purple cloudiness signifies the completion of the reaction, as well as the evolution of brown nitric oxide gas. Vacuum filtration and washing with hot methanol (3 × 10 mL) gave the tetrazine as a red solid (3.07 g, 81%). mp: 248–250 °C; IR (neat, cm^{-1}): 3022, 2981, 2947, 1611, 1462, 1393, 1221, 1067, 944, 843, 683; ^{1}H NMR (400 MHz, $CDCl_3$) δ 3.88 (s, 6H), 6.60 (t, J = 2.23 Hz, 1H), 7.17 (d, J = 2.23 Hz, 2H); ^{13}C NMR (125 MHz, $CDCl_3$) δ 55.68 (q, OCH_3), 105.48 (d, CH), 105.90 (d, CH), 133.44 (s, C), 161.54 (s, $COCH_3$); ESIMS (m/z): $[M + Na]^+$ calcd for $C_{18}H_{20}O_4N_4$, 379.13768; found, 379.13776.

5,5-Dimethyl-2,2-bis(3,5-dimethoxybenzyl)-Δ^3-1,3,4-oxadiazoline (2f). A solution of (3,5-dimethoxybenzyloxy-carbonyl)hydrazone of acetone (1.30 g, 4.87 mmol) in CH_2Cl_2 (5 mL) was added dropwise to a stirred solution of $Pb(OAc)_4$ (2.59 g, 5.84 mmol) under nitrogen. The reaction mixture was stirred in an ice bath for 2 h, and then at room temperature for 24 h. After the stirring, the solid was filtered over Celite and the organic layer was washed with 10% aq $NaHCO_3$. The mixture was filtered again until no precipitate was deposited. The organic phase was concentrated under reduced pressure. The corresponding 3,5-dimethoxybenzyl alcohol (2.46 g, 14.6 mmol) and TFA (0.04 mL, 0.49 mmol) were then added to the organic mixture. The solution was heated to 40 °C and stirred for 24 h before KOH pellets were added, and stirring was continued for another 3 h. After extracting with CH_2Cl_2, washing with brine, and drying by $MgSO_4$, the organic layer was concentrated under reduced pressure. The product was purified by column chromatography (eluent: EtOAc/hexane = 30/70, R_f = 0.17) to give the product as a yellow liquid (0.48 g, 23%). IR (neat, cm^{-1}): 3006, 2959, 2843, 1750, 1622, 1480, 1386, 1236, 1076, 925, 846, 687; ^{1}H NMR (500 MHz, $CDCl_3$) δ 1.49 (s, 6H), 3.67 (s, 12H), 4.66 (q, J = 11.8 Hz, 36.78 Hz, 4H), 6.29 (t, J = 2.21 Hz, 2H), 6.41 (d, J = 2.21 Hz, 4H); ^{13}C NMR (125 MHz, $CDCl_3$) δ 24.12 (q, CH_3), 55.29 (q, OCH_3), 66.72 (t, CH_2), 99.94 (d, CH, Ar ring), 105.50 (d, CH, Ar ring), 119.63 (s, $C(CH_3)_2$), 136.71 (s, C), 138.97 (s, $C(OCH_2Ar)_2$), 160.83 (s, $COCH_3$); ESIMS (m/z): $[M + Na]^+$ calcd for $C_{22}H_{28}O_7N_2Na$, 455.17887; found, 455.17899.

1,3-Bis(3,5-dimethoxyphenyl)propane-1,3-dione (4). 3,5-dimethoxyacetophenone (2.1 g, 11.7 mmol), 3,5-dimethoxybenzoic acid (2.75 g, 14.04 mmol), and NaH (0.94 g, 23.4 mmol) was dissolved in THF (20 mL) under N_2 atmosphere in a 50 mL flask. The mixture was heated under reflux (75 °C) for 14 h under a N_2 atmosphere, then cooled down to room temperature. The mixture was slowly added to cold HCl. The organic layer was extracted with ether, washed with brine, and dried with anhydrous $MgSO_4$. The solvent was removed by vacuum evaporator. The dry solid was then recrystallized in methanol to give the compound as a yellow crystal (2.77 g, 69%). mp: 132 °C; IR (neat, cm^{-1}): 3140, 3000, 2943, 1562, 1466, 1351, 1298, 1158, 1053, 842, 668; ^{1}H NMR (500 MHz,

$CDCl_3$) δ 3.78 (s, 12H), 6.56 (t, J = 2.28 Hz, 2H), 6.65 (d, J = 2.28 Hz, 4H); ^{13}C NMR (125 MHz, $CDCl_3$) δ 55.56 (q, OCH_3), 93.56 (t, CH_2), 104.62 (d, CH), 105.05 (d, CH), 137.52 (s, C), 160.92 (s, $COCH_3$), 185.47 (s, OC=O); ESIMS (m/z): $[M + Na]^+$ calcd for $C_{19}H_{20}O_6Na$, 367.11521; found, 367.11456.

1,3-Bis(3,5-dimethoxyphenyl)-2,2-dimethoxypropane-1,3-dione (5). 1,3-Dione **4** (2.76 g, 8 mmol) and diphenyl diselenide (1.25 g, 4 mmol) were dissolved in methanol (50 mL), and ammonium persulfate (3.65 g, 16 mmol) was added to the mixture. The solution was heated under reflux for 4 h with stirring under nitrogen. Then the mixture was cooled to room temperature, and slowly added to ice water. The organic compound was extracted by chloroform and purified by silica-gel column chromatography (eluent: EtOAc/hexane = 30/70, R_f = 0.30) to give the product as a yellow liquid (2.9 g, 90%). ^{1}H NMR (500 MHz, $CDCl_3$) δ 3.41 (s, 6H), 3.77 (s, 12H), 6.59 (t, J = 2.44 Hz, 2H), 7.29 (d, J = 2.44 Hz, 4H); ^{13}C NMR (125 MHz, $CDCl_3$) δ 50.97 (q, $C(OCH_3)_2$), 55.53 (q, OCH_3), 103.89 (s, C), 107.22 (d, CH), 107.34 (d, CH), 135.50 (s, C), 160.66 (s, $COCH_3$), 192.47 (s, C=O); IR (neat, cm^{-1}): 3027, 2965, 2845, 1691, 1605, 1466, 1429, 1321, 1162, 1070, 1036, 863, 671; ESIMS (m/z): $[M + Na]^+$ calcd for $C_{21}H_{24}O_8Na$, 427.13634; found, 427.13602.

4,4-diaryloxy-3,5-diarylpyrazole (**3c–f**)

General Procedure. Oxadiazoline (1 mmol) was dissolved in benzene (2 mL) in a sealed tube. The mixture was stirred with tetrazine (1.10 mmol) in a sealed tube for 24 h at 120 °C under nitrogen. After filtration, the crude was purified by column chromatograph (in ca. 40% yield).

4,4-Dibenzyloxy-3,5-diphenylpyrazole (3c). Yellow powder (from MeOH), mp: 150–151 °C; IR (neat, cm^{-1}): 3070, 3066, 2948, 2881, 1585, 1557, 1498, 1447, 1391, 1382, 1111, 970, 916, 856, 694; ^{1}H NMR (500 MHz, $CDCl_3$) δ 4.21 (s, 4H), 7.04–7.06 (m, 4H), 7.19–7.20 (m, 6H), 7.50–7.57 (m, 6H), 8.38–8.39 (m, 4 H); ^{13}C NMR (125 MHz, $CDCl_3$) δ 66.73 (t, CH_2), 115.96 (s, C), 127.74 (d, CH, benzyloxy), 127.95 (d, CH, benzyloxy), 128.13 (d, CH, phenyl), 128.18 (d, CH, benzyloxy), 128.26 (d, CH, phenyl), 129.03 (d, CH, phenyl), 132.47 (s, C, phenyl), 135.45 (s, C, benzyloxy), 167.09 (s, C); HRMS–EI calcd for $C_{29}H_{24}N_2O_2$, 432.1838; found, 432.1842; R_f = 0.40 (EtOAc/hexane = 30/70).

4,4-Bis(3,5-dimethoxybenzyloxy)-3,5-diphenylpyrazole (3d). Yellow powder (from MeOH), mp: 140–141 °C; IR (neat, cm^{-1}): 3024, 2951, 2845, 1603, 1475, 1456, 1388, 1160, 1118, 1102, 851; ^{1}H NMR (500 MHz, C_6D_6) δ 3.19 (s, 12H), 4.21 (s, 4H), 6.28 (d, J = 2.36 Hz, 4H), 6.42 (t, J = 2.36 Hz, 2H), 7.07 (d, J = 8.15 Hz, 6H, phenyl), 8.68 (m, 4H, phenyl); ^{13}C NMR (125 MHz, C_6D_6) δ 55.76 (q, OCH_3), 67.11 (t, CH_2), 100.99 (d, CH, aryl), 106.15 (d, CH, aryl), 116.69 (s, C), 128.35 (d, CH, phenyl), 128.77 (s, C), 129.24 (d, CH, phenyl), 132.30 (d, CH, phenyl), 138.40 (s, C), 161.30 (s, C), 167.29 (s, C); ESIMS (m/z): $[M + Na]^+$ calcd for $C_{33}H_{32}O_6N_2Na$, 575.21526; found, 575.21387; R_f = 0.27 (EtOAc/hexane = 30/70).

4,4-Dibenzyloxy-3,5-bis(3,5-dimethoxyphenyl)pyrazole (3e). Yellow powder (from MeOH), mp: 183–184 °C; IR (neat, cm^{-1}): 3025, 2952, 2847, 1605, 1551, 1456, 1426, 1371, 1160, 1117, 849, 670; ^{1}H NMR (500 MHz, C_6D_6) δ 3.33 (s, 12H), 4.31 (s, 2H), 6.78 (t, J = 2.28 Hz, 2H), 6.93–7.01 (m, 10H), 8.02 (t, J = 2.28 Hz, 4H); ^{13}C NMR (125 MHz, C_6D_6) δ 55.06 (q, OCH_3), 67.02 (t, CH_2), 105.54 (d, CH, aryl), 106.52 (d, CH, aryl), 116.22 (s, C), 128.59 (d, CH, phenyl), 128.45 (d, CH, phenyl), 128.19 (d, CH, phenyl), 130.47 (s, C, aryl), 136.24 (s, C, phenyl), 161.81 (s, $COCH_3$), 167.53 (s, C); ESIMS (m/z): $[M + H]^+$ calcd for $C_{33}H_{33}N_6O_2$, 553.23331; found, 553.23267; R_f = 0.13 (EtOAc/hexane = 20/80).

4,4-Bis(3,5-dimethoxybenzyloxy)-3,5-bis(3,5-dimethoxyphenyl)pyrazole (3f). IR (neat, cm^{-1}): 3010, 2942, 1605, 1552, 1441, 1371, 1140, 1120, 849; ^{1}H NMR (500 MHz, $CDCl_3$) δ 3.24 (s, 12H), 3.34 (s, 12H), 4.36 (s, 6H), 6.38 (d, J = 2.36 Hz, 4H), 6.43 (t, J = 2.36 Hz, 2H), 6.70 (t, J = 2.28 Hz, 2H), 8.04 (d, J = 2.28 Hz, 4H); ^{13}C NMR (125 MHz, C_6D_6) δ 54.74 (q, OCH_3), 55.03 (q, OCH_3), 67.19 (t, CH_2), 101.16 (d, CH), 105.71 (d, CH), 106.08 (d, CH), 106.28 (d, CH), 116.36 (s, C), 130.46 (s, C), 138.47 (s, C), 161.33 (s, $COCH_3$), 161.77 (s, $COCH_3$), 167.58 (s, C); ESIMS (m/z): $[M + Na]^+$ calcd for $C_{37}H_{40}O_{10}N_2Na$, 695.25752; found, 695.25775; R_f = 0.17 (EtOAc/hexane = 30/70).

4,4-Dimethoxy-3,5-bis(3,5-dimethoxyphenyl)pyrazole (3g). To a solution of 1,3-bis(3,5-dimethoxyphenyl)-2,2-dimethoxypropane-1,3-dione (2.8 g, 6.92 mmol) in chloroform (10 mL) was added dropwise $NH_2NH_2{\cdot}H_2O$ (0.40 mL, 8.30 mmol). The mixture was heated under reflux and kept under stirring for 6 h. The reaction was quenched with HCl. A solution of 10% $NaHCO_3$ was added to the mixture. After extraction with chloroform, the organic phase was washed with brine, dried with Na_2SO_4, concentrated and then purified by column chromatography to give **3g** in 89.6% yield. mp: 179–180 °C; ^{1}H NMR (500 MHz, $CDCl_3$) δ 3.04 (s, 6H), 3.83 (s, 12H), 6.62 (t, J = 2.28 Hz, 2H), 7.40 (d, J = 2.28 Hz, 4H); ^{13}C NMR (125 MHz, $CDCl_3$) δ 51.93 (q, CH_3), 55.52 (q, OCH_3), 105.21 (d, CH,), 105.27 (d, CH), 116.91 (s, C), 129.23 (s, C), 161.00 (s, $COCH_3$), 166.84 (s, C); IR (neat, cm^{-1}): 3012, 2951, 1597, 1548, 1427, 1375, 1158, 1125, 1062, 980, 844; ESIMS (m/z): calcd for $C_{21}H_{25}N_6O_2$, 401.17071; found, 401.17041; R_f = 0.10 (EtOAc/hexane = 20/80).

endo-2,3-Diazo-10,10-diaryloxy-1,4-diaryltricyclo[5.2.1.$0^{5,9}$]dec-2-ene (**AZc–g**)

General procedure. To a solution of cyclopentadiene (1 mL) and pyrazole (2 mmol) in CH_2Cl_2 (2 mL) was added dropwise trifluoroacetic acid (1 mmol) in an ice bath under nitrogen. The reaction was traced by TLC analysis. After stirring for about 15 min, the reaction was quenched with 10% aq $NaHCO_3$ until the pH of the solution reached 8. After washing with water and brine, the organic phase was dried with $MgSO_4$, then filtered and concentrated. The [4 + 2] cycloadduct was dissolved in benzene (2 mL), and 5 mg of PtO_2 was added as a catalyst. The mixture was stirred under a hydrogen atmosphere for 24 h at room temperature. After stirring, the catalyst was removed by filtration over Celite, and the solvent was evaporated under reduced pressure. The product was purified by column chromatograph to give the product as colorless liquid (ca. 60%). The endo configuration was determined by NOE measurements.

***endo*-2,3-Diazo-10,10-dibenzyloxy-1,4-diphenyltricyclo[5.2.1.$0^{5,9}$]dec-2-ene (AZc).** IR (neat, cm^{-1}): 3037, 2968, 2886, 1739, 1607, 1498, 1456, 1387, 1139, 1085, 1029, 702; UV (MTHF) λ_{max} 365 (ε 106.7); ^{1}H NMR (500 MHz, C_6D_6) δ 1.20–1.75 (m, 6H), 3.69 (t, J = 5.13 Hz, 2H), 4.15 (s, 2H), 4.29 (s, 2H), 6.90–8.19 (m, 20H, overlapping with C_6H_6); ^{13}C NMR (125 MHz, C_6D_6) δ 25.96 (t, CH_2, cyclopentane), 28.16 (t, CH_2, cyclopentane), 49.27 (d, CH, cyclopentane), 66.16 (t, $COCH_2$), 66.34 (t, OCH_2), 94.83 (s, C), 119.57 (s, C), 126.66 (d, CH), 126.87 (d, CH), 127.33 (d, CH), 128.61 (d, CH), 128.71 (d, CH), 129.01 (d, CH), 137.22 (s, C), 138.13 (s, C), 138.19 (s, C); HRMS–EI (*m*/*z*): calcd for $C_{34}H_{32}O_2N_2$, 500.6301; found, 500.2462. R_f = 0.57 (EtOAc/hexane = 20/80).

***endo*-2,3-Diazo-10,10-bis(3,5-dimethoxybenzyloxy)-1,4-diphenyltricyclo[5.2.1.$0^{5,9}$]dec-2-ene (AZd).** IR (neat, cm^{-1}): 3022, 2966, 2844, 1751, 1603, 1473, 1326, 1162, 1072, 930, 844, 703; UV (MTHF) λ_{max} 364 (ε 175.1); ^{1}H NMR (500 MHz, $CDCl_3$) δ 1.25–1.66 (m, 6H), 3.68 (s, 6H), 3.70 (t, J = 5.33 Hz, 2H), 3.75 (s, 6H), 3.89 (s, 2H), 4.12 (s, 2H), 6.07 (d, J = 2.36 Hz, 2H), 6.24 (t, J = 2.36 Hz, 1H), 6.30 (d, J = 2.36 Hz, 2H), 6.36 (t, J = 2.36 Hz, 1H), 7.40–8.03 (m, 10H); ^{13}C NMR (125 MHz, C_6D_6) δ 26.21 (t, CH_2, cyclopentane), 28.34 (t, CH_2, cyclopentane), 49.42 (d, CH, cyclopentane), 55.69 (q, OCH_3), 55.74 (q, OCH_3), 66.17 (t, $COCH_2$), 95.15 (s, C), 99.80 (d, CH), 100.00 (d, CH), 104.26 (d, CH), 105.04 (d, CH), 119.54 (s, C), 128.55 (d, CH), 128.92 (d, CH), 128.96 (d, CH), 136.67 (s, C), 140.41 (s, C), 140.67 (s, C), 161.00 (s, C) , 161.28 (s, C); ESIMS (*m*/*z*): $[M + H]^+$ calcd for $C_{38}H_{41}O_6N_2$, 621.29591; found, 621.29449; R_f = 0.27 (EtOAc/hexane = 20/80).

***endo*-2,3-diazo-1,4-bis(3',5'-dimethoxybenzyloxy)-10,10-dibenzyloxytricyclo[5.2.1.$0^{5,9}$]dec-2-ene (AZe).** IR (neat, cm^{-1}): 3014, 2972, 1600, 1461, 1450, 1357, 1157, 1069, 973, 856; UV (MTHF) λ_{max} 365 (ε 184.2); ^{1}H NMR (500 MHz, C_6D_6) δ 1.20–1.83 (m, 6H), 3.41 (s, 12H), 3.57 (t, J = 4.47 Hz, 2H), 4.31 (s, 2H), 4.46 (s, 2H), 6.68 (t, J = 2.28 Hz, 2H), 6.95 (d, J = 2.28 Hz, 4H), 7.02–7.57 (m, 10H, overlapping with C_6D_6); ^{13}C NMR (125 MHz, C_6D_6) δ 26.13 (t, CH_2, cyclopentane), 28.19 (t, CH_2, cyclopentane), 49.50 (d, CH, cyclopentane), 54.91 (q, OCH_3), 66.04 (t, $COCH_2$), 66.32 (t, $COCH_2$), 94.96 (s, C), 101.03 (d, CH), 107.11 (d, CH), 119.74 (s, C), 127.00 (d, CH), 127.16 (d, CH), 127.38 (d, CH), 127.72 (d, CH), 128.54 (d, CH), 128.60 (d, CH), 138.19 (s, C), 138.24 (s, C), 139.58 (s, C), 161.62 (s, C); ESIMS (*m*/*z*): $[M + Na]^+$ calcd for $C_{38}H_{40}O_6N_2Na$, 643.27786; found, 643.27802.

***endo*-2,3-Diazo-1,4-bis(3,5-dimethoxybenzyloxy)-10,10-bis(3,5-dimethoxyphenoxy)tricyclo[5.2.1.$0^{5,9}$]dec-2-ene (AZf).** IR (neat, cm^{-1}): 3009, 2965, 2842, 1606, 1467, 1430, 1352, 1160, 1070, 1057, 943, 840; UV (MTHF) λ_{max} 365 (ε 249.6); ^{1}H NMR (500 MHz, C_6D_6) δ 1.20–1.80 (m, 6H), 3.23 (s, 6H), 3.32 (s, 6H), 3.44 (s, 12H), 3.60 (t, J = 5.37 Hz, 2H), 4.38 (s, 2H), 4.56 (s, 2H), 6.33 (d, J = 2.29 Hz, 2H), 6.40 (t, J = 2.29 Hz, 1H), 6.46 (t, J = 2.29 Hz, 1H) 6.54 (d, J = 2.29 Hz, 2H), 6.64 (t, J = 2.28 Hz, 2H), 7.62 (d, J = 2.28 Hz, 4H); ^{13}C NMR (125 MHz, C_6D_6) δ 26.11 (t, CH_2, cyclopentane), 28.16 (t, CH_2, cyclopentane), 49.52 (d, CH, cyclopentane), 54.69 (q, OCH_3), 54.81 (q, OCH_3), 54.91 (2×q, OCH_3), 65.93 (t, $COCH_2$), 66.32 (t, $COCH_2$), 95.11 (s, C), 100.08 (d, CH), 100.32 (d, CH), 100.92 (2×d, CH), 104.62 (s, C), 104.70 (s, C), 107.23 (2×s, C), 119.91 (s, C), 139.46 (2×s, C), 140.66 (s, C), 140.77 (s, C), 161.33 (2×s, C), 161.58 (s, C), 161.62 (s, C); ESIMS (*m*/*z*): $[M + Na]^+$ calcd for $C_{42}H_{48}O_{10}N_2Na$, 763.32012; found,763.32043.

***endo*-2,3-Diazo-1,4-bis(3,5-dimethoxybenzyloxy)-10,10-dimethoxytricyclo[5.2.1.$0^{5,9}$]dec-2-ene (AZg).** IR (neat, cm^{-1}): 2973, 2846, 1602, 1464, 1359, 1158, 1088, 1022, 942, 848; UV (MTHF) λ_{max} 364 (ε 169.9); ^{1}H NMR (500 MHz, C_6D_6) δ 0.9–1.75 (m, 6H), 2.69 (s, 3H), 2.80 (s, 3H), 3.36 (t, J = 5.49 Hz, 2H), 3.42 (s, 12H), 6.64 (t, J = 2.28 Hz, 2H), 7.48 (d, J = 2.28 Hz, 4H); ^{13}C NMR (125 MHz, C_6D_6) δ 26.08 (t, CH_2, cyclopentane), 28.16 (t, CH_2, cyclopentane), 49.29 (d, CH, cyclopentane), 51.46 (q, OCH_3), 51.75 (q, OCH_3), 51.92 (2×q, OCH_3), 94.65 (s, C), 100.30 (d, CH), 107.33 (d, CH), 119.76 (s, C), 139.86 (s, C), 161.52 (s, C); ESIMS (*m*/*z*): $[M + Na]^+$ calcd for $C_{26}H_{32}O_6N_2Na$, 491.21526; found, 491.21466.

General procedure for photolysis. A sample (30.0 mg) of the diazenes **AZ** was dissolved in 1.0 mL of C_6D_6. The photolysis was performed with a 500 W Xenon-lamp through a Pyrex filter ($h\nu$ > 300 nm) at room temperature (ca. 20 °C). The photolysate was directly analyzed by NMR spectroscopy (^{1}H: 500 MHz,

^{13}C: 125 MHz), which indicated the quantitative formation of the housanes **CP**. The housanes **CPc–g** were isolated by using silica-gel column chromatography. The spectroscopic data are as follows:

3,3-Dibenzyloxy-2,4-diphenyltricyclo[3.3.0.0^{2,4}]octane (CPc). ^{1}H NMR (500 MHz, C_6D_6) δ 1.41–1.93 (m, 6H), 3.19 (d, *J* = 6.34 Hz, 2H), 4.31 (s, 2H), 4.92 (s, 2H), 6.96–7.45 (m, 20H, overlapping with C_6D_6); ^{13}C NMR (125 MHz, C_6D_6) δ 25.28 (t, CH_2, cyclopentane), 28.38 (t, CH_2, cyclopentane), 41.73 (d, CH, cyclopentane), 48.05 (s, C), 67.16 (t, $COCH_2$), 69.66 (t, OCH_2), 98.43 (s, C), 126.57 (d, CH), 127.26 (d, CH), 127.40 (d, CH), 127.92 (d, CH), 128.12 (d, CH), 128.35 (d, CH), 128.46 (d, CH), 128.68 (d, CH), 130.54 (d, CH), 135.25 (s, C, phenyl), 138.59 (s, C, benzyloxy), 138.90 (s, C, benzyloxy); HRMS–EI (*m*/*z*): calcd for $C_{34}H_{32}O_2$, 472.2402; found, 472.2424.

3,3-Bis(3,5-dimethoxybenzyloxy)-2,4-diphenyltricyclo[3.3.0.0^{2,4}]octane (CPd). ^{1}H NMR (500 MHz, $CDCl_3$) δ 1.40–1.92 (m, 6H), 3.12 (d, *J* = 6.29 Hz, 2H), 3.22 (s, 6H), 3.37 (s, 6H), 4.35 (s, 2H), 4.99 (s, 2H), 6.31 (d, *J* = 2.36 Hz, 2H), 6.41 (t, *J* = 2.36 Hz, 1H), 6.56 (d, *J* = 2.36 Hz, 1H), 6.81 (d, *J* = 2.36 Hz, 2H), 7.02–7.46 (m, 10H, overlapping with C_6D_6); ^{13}C NMR (125 MHz, C_6D_6) δ 25.22 (t, CH_2, cyclopentane), 28.34 (t, CH_2, cyclopentane), 41.68 (d, CH, cyclopentane), 48.18 (s, C), 54.68 (q, OCH_3), 54.89 (q, OCH_3), 67.07 (t, $COCH_2$), 69.78 (t, $COCH_2$), 98.46 (s, C), 100.04 (d, CH), 100.06 (d, CH), 104.91 (d, CH), 105.94 (d, CH), 126.48 (2×d, CH, phenyl), 128.04 (2×d, CH, phenyl), 130.51 (2×d, CH, phenyl), 135.22 (2×s, C, phenyl), 140.90 (s, C), 141.30 (s, C), 161.19 (s, $COCH_3$), 161.64 (s, COCH); ESIMS (*m*/*z*): $[M + Na]^+$ calcd for $C_{38}H_{41}O_6Na$, 615.27171; found, 615.27130.

3,3-Bisbenzyloxy-2,4-bis(3,5-dimethoxyphenyl)tricyclo[3.3.0.0^{2,4}]octane (CPe). ^{1}H NMR (500 MHz, C_6D_6) δ 1.40–2.02 (m, 6H), 3.05 (d, *J* = 6.40 Hz, 2H), 3.29 (s, 12H), 4.41 (s, 2H), 4.90 (s, 2H), 6.43 (t, *J* = 2.28 Hz, 2H), 6.80 (d, *J* = 2.28 Hz, 4H), 6.86–7.34 (m, 10H, overlapping with C_6D_6); ^{13}C NMR (125 MHz, C_6D_6) δ 25.44 (t, CH_2, cyclopentane), 28.43 (t, CH_2, cyclopentane), 41.82 (d, CH, cyclopentane), 48.47 (s, C), 54.78 (q, OCH_3), 67.44 (t, $COCH_2$), 69.51 (t, $COCH_2$), 98.39 (s, C), 99.22 (d, CH), 108.88 (d, CH), 127.19 (d, CH), 127.54 (d, CH), 127.80 (d, CH), 128.06 (d, CH), 128.18 (d, CH), 128.59 (d, CH), 137.30 (s, C), 138.50 (s, C, phenyl), 138.81 (s, C, phenyl), 160.97 (s, C); ESIMS (*m*/*z*): $[M + Na]^+$ calcd for $C_{38}H_{40}O_6Na$, 615.27171; found, 615.27167.

3,3-Bis(3,5-dimethoxybenzyloxy)-2,4-bis(3,5-dimethoxyphenyl)tricyclo[3.3.0.0^{2,4}]octane (CPf). ^{1}H NMR (500 MHz, C_6D_6) δ 1.43–2.08 (m, 6H), 3.15 (d, *J* = 6.17 Hz, 2H), 3.30 (s, 6H), 3.35 (s, 12H), 3.38 (s, 6H), 4.51 (s, 2H), 5.01 (s, 2H), 6.34 (d, *J* = 2.36 Hz, 2H), 6.41 (t, *J* = 2.36 Hz, 1H), 6.47 (t, *J* = 2.28 Hz, 2H), 6.54 (t, *J* = 2.36 Hz, 1H), 6.80 (d, *J* = 2.36 Hz, 2H), 6.87 (d, *J* = 2.28 Hz, 4H); ^{13}C NMR (125 MHz, C_6D_6) δ 25.46 (t, CH_2, cyclopentane), 28.44 (t, CH_2, cyclopentane), 41.80 (d, CH, cyclopentane), 48.64 (s, C), 54.67 (q, OCH_3), 54.78 (q, OCH_3), 54.89 (2×q, OCH_3), 67.29 (t, $COCH_2$), 69.76 (t, $COCH_2$), 98.41 (s, C), 99.18 (2×d, CH), 100.12 (d, CH), 100.32 (d, CH), 104.93 (d, CH), 105.96 (d, CH), 108.89 (2×d, CH), 137.30 (2×s, C), 140.88 (s, C), 141.26 (s, C), 160.96 (2×s, $COCH_3$), 161.187 (s, $COCH_3$), 161.59 (s, $COCH_3$); ESIMS (*m*/*z*): $[M + Na]^+$ calcd for $C_{42}H_{48}O_{10}Na$, 735.31397; found,735.31415.

3,3-Dimethoxy-2,4-bis(3',5'-dimethoxyphenyl)tricyclo[3.3.0.0^{2,4}]octane (CPg). ^{1}H NMR (500 MHz, C_6D_6) δ 1.43–2.03 (m, 6H), 2.94 (s, 3H), 2.96 (d, *J* = 6.47 Hz, 2H), 3.37 (s, 12H), 3.48 (s, 3H), 6.51 (t, *J* = 2.28 Hz, 2H), 6.79 (d, *J* = 2.28 Hz, 4H); ^{13}C NMR (125 MHz, C_6D_6) δ 25.49 (t, CH_2, cyclopentane), 28.45 (t, CH_2, cyclopentane), 41.83 (d, CH, cyclopentane), 48.13 (s, C), 52.37 (q, OCH_3), 54.01 (q, OCH_3), 54.85 (2×q, OCH_3), 98.61 (s, C), 99.05 (d, CH), 108.88 (d, CH), 137.59 (s, $COCH_3$), 161.07 (s, C); ESIMS (*m*/*z*): $[M + Na]^+$ calcd for $C_{26}H_{32}O_6Na$, 463.20911; found, 463.20844.

Supporting Information

Supporting Information File 1

NMR spectra of compounds **1**–**5**, **AZc**–**g**, and **CPc**–**g**.
[http://www.beilstein-journals.org/bjoc/content/supplementary/1860-5397-9-106-S1.pdf]

Acknowledgements

NMR and MS measurements were performed at N-BARD, Hiroshima University. This work was supported by a Grant-in-Aid for Science Research on Innovative Areas "Stimuli-responsive Chemical Species" (No. 24109008), "pi-Space" (No. 21108516), and No. 19350021 from the Ministry of Education, Culture, Sports, Science and Technology, Japan, and by the Tokuyama Science Foundation.

References

1. Abe, M.; Ye, J.; Mishima, M. *Chem. Soc. Rev.* **2012,** *41,* 3808–3820. doi:10.1039/c2cs00005a
2. Abe, M. *Chem. Rev.* **2013,** in press.
3. De Feyter, S.; Diau, E. W.-G.; Zewail, A. H. *Angew. Chem., Int. Ed.* **2000,** *39,* 260–263. doi:10.1002/(SICI)1521-3773(20000103)39:1<260::AID-ANIE260>3.0.CO;2-R

4. Niecke, E.; Fuchs, A.; Baumeister, F.; Nieger, M.; Schoeller, W. W. *Angew. Chem., Int. Ed. Engl.* **1995,** *34,* 555–557. doi:10.1002/anie.199505551
5. Schoeller, W. W.; Niecke, E. *Phys. Chem. Chem. Phys.* **2012,** *14,* 2015–2023. doi:10.1039/c1cp23016f
6. Scheschkewitz, D.; Amii, H.; Gornitzka, H.; Schoeller, W. W.; Bourissou, D.; Bertrand, G. *Science* **2002,** *295,* 1880–1881. doi:10.1126/science.1068167
7. Cui, C.; Brynda, M.; Olmstead, M. M.; Power, P. P. *J. Am. Chem. Soc.* **2004,** *126,* 6510–6511. doi:10.1021/ja0492182
8. Wang, X.; Peng, Y.; Olmstead, M. M.; Fettinger, J. C.; Power, P. P. *J. Am. Chem. Soc.* **2009,** *131,* 14164–14165. doi:10.1021/ja906053y
9. Cox, H.; Hitchcock, P. B.; Lappert, M. F.; Pierssens, L. J.-M. *Angew. Chem., Int. Ed.* **2004,** *43,* 4500–4504. doi:10.1002/anie.200460039
10. Beweries, T.; Kuzora, R.; Rosenthal, U.; Schulz, A.; Villinger, A. *Angew. Chem., Int. Ed.* **2011,** *50,* 8974–8978. doi:10.1002/anie.201103742
11. Takeuchi, K.; Ichinohe, M.; Sekiguchi, A. *J. Am. Chem. Soc.* **2011,** *133,* 12478–12481. doi:10.1021/ja2059846
12. Sugiyama, H.; Ito, S.; Yoshifuji, M. *Angew. Chem., Int. Ed.* **2003,** *42,* 3802–3804. doi:10.1002/anie.200351727
13. Yoshifuji, M.; Hirano, Y.; Schnakenburg, G.; Streubel, R.; Niecke, E.; Ito, S. *Helv. Chim. Acta* **2012,** *95,* 1723–1729. doi:10.1002/hlca.201200442
14. Henke, P.; Pankewitz, T.; Klopper, W.; Breher, F.; Schnöckel, H. *Angew. Chem., Int. Ed.* **2009,** *48,* 8141–8145. doi:10.1002/anie.200901754
15. Ma, J.; Ding, Y.; Hattori, K.; Inagaki, S. *J. Org. Chem.* **2004,** *69,* 4245–4255. doi:10.1021/jo035687v
16. Abe, M.; Ishihara, C.; Takegami, A. *J. Org. Chem.* **2004,** *69,* 7250–7255. doi:10.1021/jo0490447
17. Abe, M.; Kubo, E.; Nozaki, K.; Matsuo, T.; Hayashi, T. *Angew. Chem., Int. Ed.* **2006,** *45,* 7828–7831. doi:10.1002/anie.200603287
18. Nakamura, T.; Gagliardi, L.; Abe, M. *J. Phys. Org. Chem.* **2010,** *23,* 300–307. doi:10.1002/poc.1643
19. Nakamura, T.; Takegami, A.; Abe, M. *J. Org. Chem.* **2010,** *75,* 1956–1960. doi:10.1021/jo902714c
20. Mondal, K. C.; Roesky, H. W.; Schwarzer, M. C.; Frenking, G.; Tkach, I.; Wolf, H.; Kratzert, D.; Herbst-Irmer, R.; Niepötter, B.; Stalke, D. *Angew. Chem., Int. Ed.* **2013,** *52,* 1801–1805. doi:10.1002/anie.201204487
21. Xu, J. D.; Hrovat, D. A.; Borden, W. T. *J. Am. Chem. Soc.* **1994,** *116,* 5425–5427. doi:10.1021/ja00091a054
22. Adam, W.; Borden, W. T.; Burda, C.; Foster, H.; Heidenfelder, T.; Heubes, M.; Hrovat, D. A.; Kita, F.; Lewis, S. B.; Scheutzow, D.; Wirz, J. *J. Am. Chem. Soc.* **1998,** *120,* 593–594. doi:10.1021/ja972977i
23. Abe, M.; Adam, W.; Heidenfelder, T.; Nau, W. M.; Zhang, X. *J. Am. Chem. Soc.* **2000,** *122,* 2019–2026. doi:10.1021/ja992507j
24. Abe, M.; Kubo, E.; Nozaki, K.; Matsuo, T.; Hayashi, T. *Angew. Chem., Int. Ed.* **2012,** *51,* 11924.
25. Abe, M.; Furunaga, H.; Ma, D.; Gagliardi, L.; Bodwell, G. J. *J. Org. Chem.* **2012,** *77,* 7612–7619. doi:10.1021/jo3016105
26. Nakagaki, T.; Sakai, T.; Mizuta, T.; Fujiwara, Y.; Abe, M. *Chem.–Eur. J.* **2013,** in press. doi:10.1002/chem.201300038
27. Schoeller, W. W.; Rozhenko, A.; Bourissou, D.; Bertrand, G. *Chem.–Eur. J.* **2003,** *9,* 3611–3617. doi:10.1002/chem.200204508
28. Abe, M.; Adam, W.; Hara, M.; Hattori, M.; Majima, T.; Nojima, M.; Tachibana, K.; Tojo, S. *J. Am. Chem. Soc.* **2002,** *124,* 6540–6541. doi:10.1021/ja026301l
29. Lu, X.; Reid, D. L.; Warkentin, J. *Can. J. Chem.* **2001,** *79,* 319–327.
30. Beck, K.; Hünig, S. *Chem. Ber.* **1987,** *120,* 477–483. doi:10.1002/cber.19871200406
31. Adam, W.; Heidenfelder, T.; Sahin, C. *Synthesis* **1995,** 1163–1170. doi:10.1055/s-1995-4072
32. Tiecco, M.; Testaferri, L.; Tingoli, M.; Bartoli, D.; Marini, F. *J. Org. Chem.* **1991,** *56,* 5207–5210. doi:10.1021/jo00017a039
33. Clark, W. D. K.; Steel, C. *J. Am. Chem. Soc.* **1971,** *93,* 6347–6355. doi:10.1021/ja00753a001
34. Johnston, L. J.; Scaiano, J. C. *Chem. Rev.* **1989,** *89,* 521–547. doi:10.1021/cr00093a004

License and Terms

Beilstein Journal of Organic Chemistry

An aniline dication-like transition state in the Bamberger rearrangement

Shinichi Yamabe*, Guixiang Zeng, Wei Guan and Shigeyoshi Sakaki

Full Research Paper

Open Access

Address:
Fukui Institute for Fundamental Chemistry, Kyoto University, Takano-Nishihiraki-cho 34-4, Sakyo-ku, Kyoto 606-8103, JAPAN.
Phone: +81-075-711-7907

Email:
Shinichi Yamabe* - yamabes@fukui.kyoto-u.ac.jp.

* Corresponding author

Keywords:
Bamberger rearrangement; DFT calculations; *N*-phenylhydroxylamine; proton transfer; reactive intermediates; transition states

Beilstein J. Org. Chem. **2013,** *9,* 1073–1082.
doi:10.3762/bjoc.9.119

Received: 11 March 2013
Accepted: 14 May 2013
Published: 03 June 2013

This article is part of the Thematic Series "New reactive intermediates in organic chemistry".

Guest Editor: G. Bucher

Abstract

A Bamberger rearrangement of *N*-phenylhydroxylamine, Ph–N(OH)H, to *p*-aminophenol was investigated by DFT calculations for the first time. The nitrenium ion, C_6H_5–NH^+, suggested and seemingly established as an intermediate was calculated to be absent owing to the high nucleophilicity of the water cluster around it. First, a reaction of the monoprotonated system, Ph–N(OH)H + $H_3O^+(H_2O)_n$ (n = 4 and 14) was examined. However, the rate-determining transition states involving proton transfers were calculated to have much larger activation energies than the experimental one. Second, a reaction of the diprotonated system, Ph–N(OH)H + $(H_3O^+)_2(H_2O)_{13}$, was traced. An activation energy similar to the experimental one was obtained. A new mechanism of the rearrangement including the aniline dication-like transition state was proposed.

Introduction

The fundamental Bamberger rearrangement is defined in Scheme 1 [1,2].

In the aqueous sulfuric acid, 4-aminophenol was afforded exclusively by the rearrangement. On the other hand, the 2- and 4-chloro-amino derivatives were afforded when hydrochloric acid was used. In spite of the classic and well-known reaction, the mechanism of the Bamberger rearrangement is still unclear. Heller et al. suggested that an S_N1 mechanism is more likely, but the S_N2 one cannot be ruled out [3]. The reaction was proven to occur via the intermolecular rearrangement by the ^{18}O exchange in Scheme 2 [4].

The intermolecular nature was also proven by a rearrangement of *N*-ethyl-*N*-phenylhydroxylamine, Et–N(OH)–Ph **3**, in methanol leading to *p*-(ethylamino)anisole **4** (Scheme 3) [5].

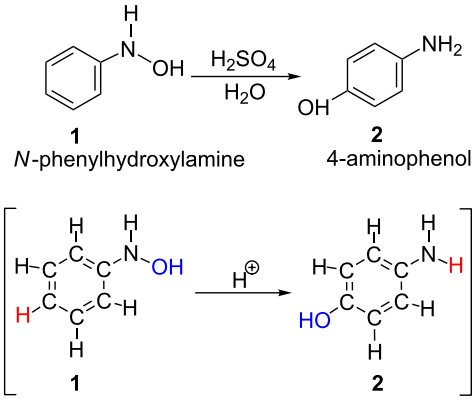

Scheme 1: The Bamberger rearrangement. In the square bracket, the apparent exchange of H and OH is shown.

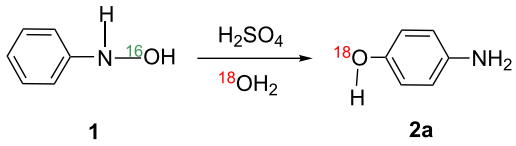

Scheme 2: The reaction occurs through the intermolecular rearrangement, on the basis that treatment of **1** in $H_2[^{18}O]H_2SO_4$ provides an [^{18}O]-incorporated *p*-aminophenol, **2a**.

Through the kinetic measurement, the rearrangement was claimed to occur by an S_N1 mechanism [6]. Also, it was reported that the elimination of water from Ar–N^+H_2OH is rate determining and a diprotonated species, Ar–$N^+H_2OH_2^+$, contributes significantly to the observed reaction rate at the acid-catalyst concentration [H_2SO_4] > 0.50 mol/L. The activation energy of the rearrangement in Scheme 1 was measured to be 24.8 kcal/mol. The S_N1 mechanism suggested by Heller et al. [3] involves a nitrenium ion **7** as shown in Scheme 4.

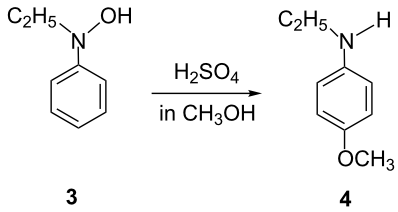

Scheme 3: A reaction of *N*-ethyl-*N*-phenylhydroxylamine, which demonstrates that the Bamberger rearrangement does not take the route of the direct [1,5]-OH shift.

In Scheme 4, a water molecule is taken off from the O-protonated form **6**, which leads to the nitrenium ion **7**. To the para position of the ion H_2O is added, and the subsequent proton removal and attack give the product **2**H^+. While the N-protonated species **5** appears to be more favorable than the O-protonated one **6**, the former has been regarded as not being an intermediate for the reaction progress. While the mechanism in Scheme 4 appears to be established, there is a significant question as to "…why in some cases, for example where the nucleophile is water, only the 4-isomer product is formed from phenylhydroxylamine, whereas in other cases, e.g., when chloride ion is present, both 2- and 4-chloro isomers are formed" [7]. This is a natural question in light of the ortho–para orientation onto the cationic phenyl ring.

So far, there have been no theoretical studies of the rearrangement, and in this study DFT calculations were carried out to address the following three unsolved issues:

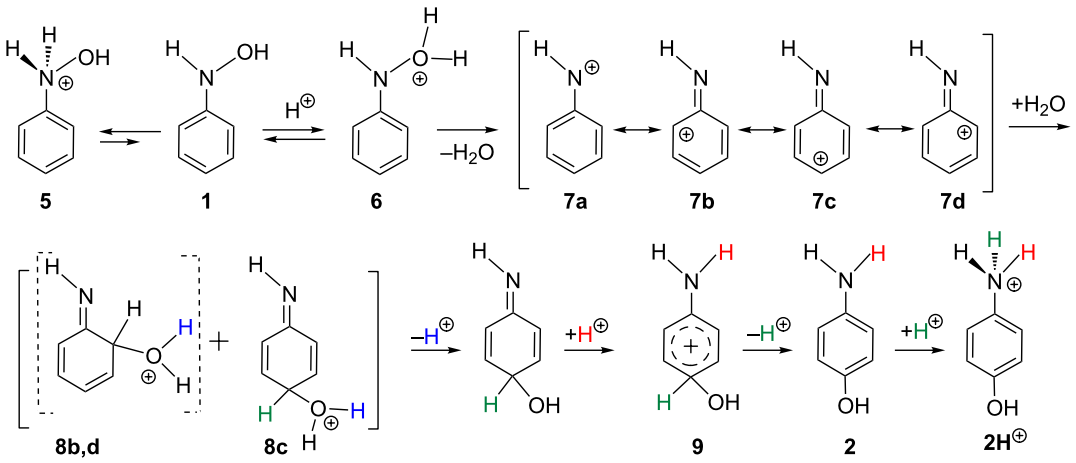

Scheme 4: A mechanism involving the nitrenium-ion intermediate **7**. **8a** is equal to **6**.

(a) Is the nitrenium ion **7** a plausible intermediate?

(b) How does the N-protonated species (**5** in Scheme 4) participate in the rearrangement? The reverse route (**5** → **1** + H^+ needed for the reaction progress) seems to be unlikely.

(c) Why is the para-product afforded exclusively in the H_2SO_4 aqueous media?

It will be shown that the size of the hydrogen-bond network of water clusters in the diprotonated system controls the reactivity of the rearrangement.

Theoretical calculations

The reacting systems were investigated by density functional theory (DFT) calculations. The B3LYP [8,9] method was used to trace the reaction path. The basis sets employed were 6-31G(d) and 6-311+G(d,p), where the latter was adopted for the key (OH transfer) steps. For the Cl-containing model, 6-31(+)G(d) was used where the diffuse sp function is only the chlorine atom.

Transition states (TSs) were sought first by partial optimizations at bond-interchange regions. Second, by the use of Hessian matrices, TS geometries were optimized. They were characterized by vibrational analyses, which checked whether the obtained geometries have single imaginary frequencies ($\nu^{\neq}$s). From TSs, reaction paths were traced by the intrinsic reaction coordinate (IRC) method [10,11] to obtain the energy-minimized geometries.

Relative energies (ΔEs) were obtained by single-point calculations of the B3LYP/6-311+G(d,p) method (SCRF = PCM, solvent = water) [12-14] on the B3LYP/6-31G(d) and B3LYP/6-311+G(d,p) geometries and their zero-point vibrational energies (ZPEs).

All the calculations were carried out by using the Gaussian 09 [15] program package. The computations were performed at the Research Center for Computational Science, Okazaki, Japan.

Results and Discussion

The monoprotonated reacting system

First, the possibility of the nitrenium intermediate **7** was examined by the use of a model of **7** + $(H_2O)_{18}$. Figure S1, Supporting Information File 1 exhibits the assumed initial geometry (a) and B3LYP/6-31G(d) and B3LYP/6-311+G(d,p) optimized ones (b).

By both computational methods, the nitrenium ion disappeared, and the **7** + $(H_2O)_{18}$ model was converted to a geometry of *o*-OH imine and $H_3O^+(H_2O)_{16}$. The nitrenium ion was calculated to be inevitably subject to the nucleophilic attack of OH_2. This attack proceeds energetically downhill without the transition state, and the nitrenium ion was absent. Thus, there should be a mechanism other than that in Scheme 4. Second, a reaction model (Scheme 5) involving proton transfers was investigated.

In the scheme, the N-protonated form Int1 (i.e., **5** in Scheme 4) undergoes the transfer via the water dimer (or trimer) at TS2. The transfer pattern is drawn for the rearrangement to the para position (apparently, a [1,5]-OH shift); that to the ortho one would be a [1,3]-OH shift. Figure S2, Supporting Information File 1 shows the three obtained TS2 geometries. Their presence demonstrates that paths involving [1,5]- and [1,3]-shifts with more water molecules than those in Figure S2 should be examined on an equal footing. Figure S3, Supporting Information

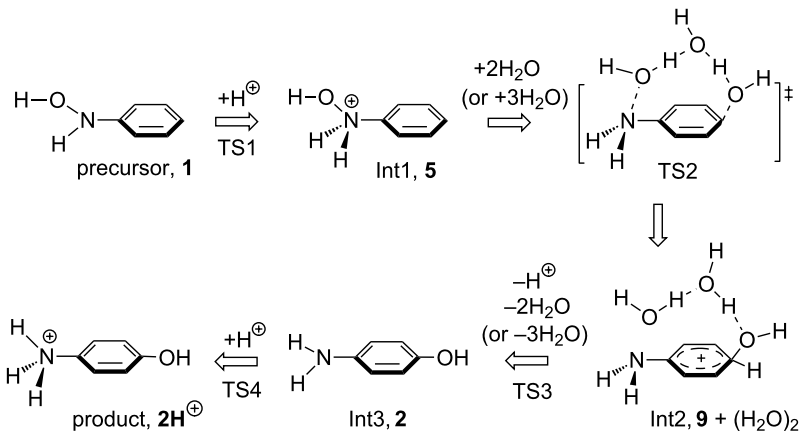

Scheme 5: A reaction scheme of the OH rearrangement containing one proton. Int is an intermediate. Species, **1**, **2**, **5**, $\mathbf{2H}^+$ and **9**, are defined in Scheme 4.

File 1 shows the path calculated by a model, called here model(I), composed of Ph–NH(OH) and $H_3O^+(H_2O)_4$.

The geometric changes expected in Scheme 5 were obtained: Precursor(I) → TS1(I) → Int1(I) → TS2(I, $2H_2O$) → Int2(I), Int2'(I) → TS3(I) → Int3(I) → Product(I). Here, Int2(I) and Int2'(I) are isomers where the positions of water clusters are different. TS4(I) leading to the protonated *p*-aminophenol could not be obtained, probably owing to the limited size of the reaction system. TS2(I, $3H_2O$) and TS2(I, [1,3]-shift) were also obtained and are shown at the end of Figure S3. Here, TS2(I, $2H_2O$), TS2(I, $3H_2O$) and TS2(I, [1,3]-shift) correspond to three TS2s in Figure S2, respectively.

Figure 1 shows the path calculated by a further extended reaction system, Ph–NH(OH) and $H_3O^+(H_2O)_{14}$, called here model(II). This is constructed on the basis of the hydrogen-bond network depicted in Figure 2. Again, the geometric changes

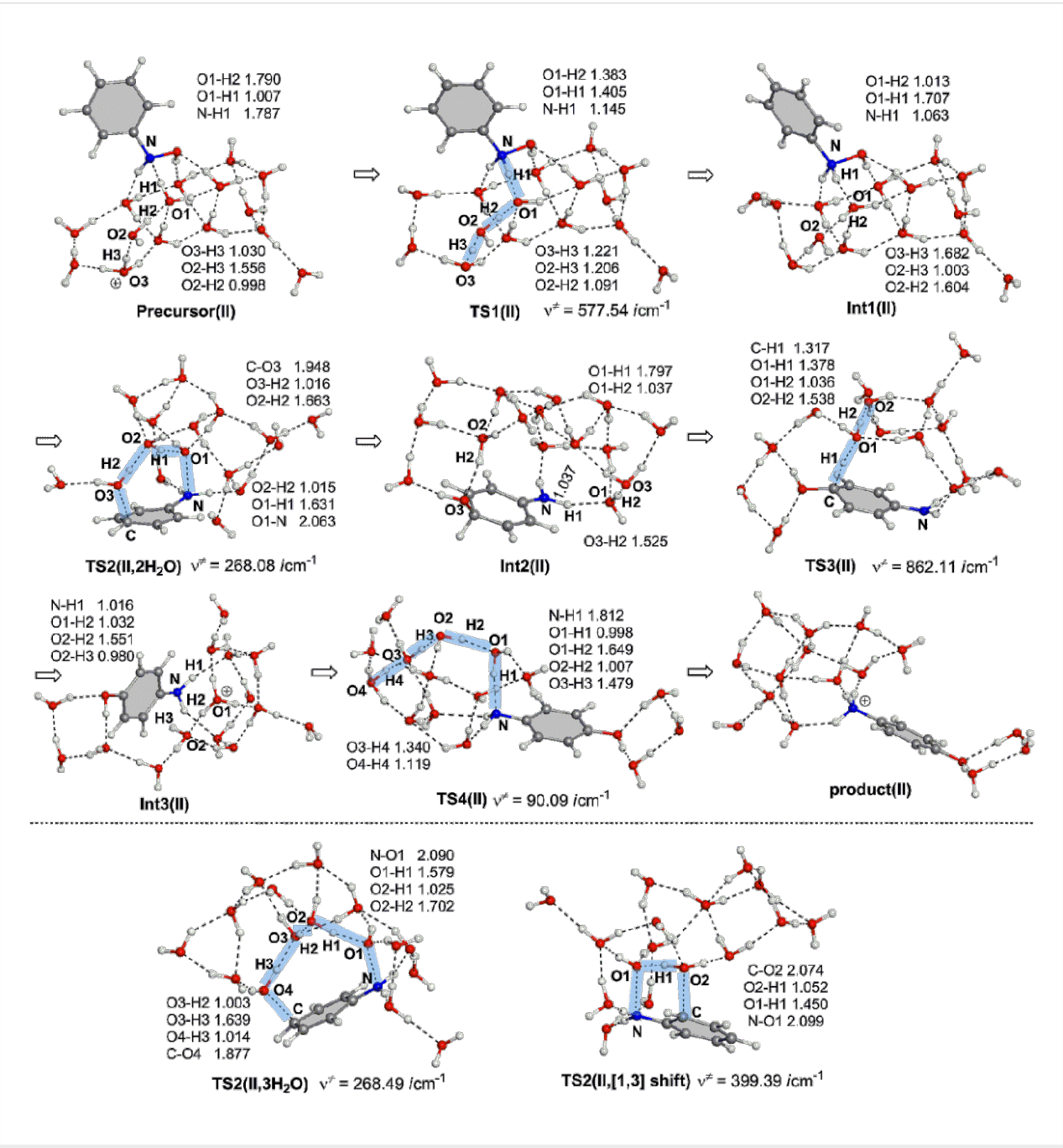

Figure 1: Geometric changes in the reaction of model II, (HO)HN–C_6H_5 + $H_3O^+(H_2O)_{14}$ → H_3N^+–C_6H_4–OH + $(H_2O)_{15}$.

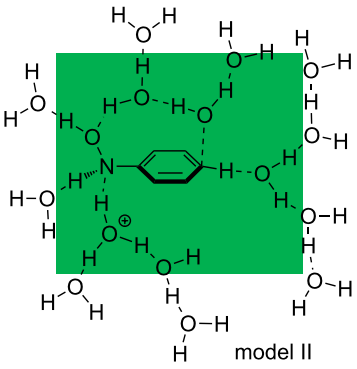

Figure 2: An assumed reaction system composed of Ph–NHOH and $H_3O^+(H_2O)_{14}$. The green area represents the reaction region of TS2. To protons of H_3O^+ and H_2O in the area, catalytic water molecules are linked in the O–H•••OH_2 hydrogen-bond pattern.

expected in Scheme 5 were obtained: Precursor(II) → TS1(II) → Int1(II) → TS2(II, $2H_2O$) → Int2(II) → TS3(II) → Int3(II) → TS4(II) → Product(II) along with TS(II, $3H_2O$) and TS2(II, [1,3]-shift). Thus, the reaction pattern predicted in Scheme 5 holds for the system Ph–NH(OH) and $H_3O^+(H_2O)_n$ (n = 4 and 14).

Figure 3 shows the energy change of the reaction in Figure 1. The reaction was calculated to be very exothermic (= −40.70 kcal/mol at Product(II)). However, the activation energies of the three TS2s, +38.59, +37.48 and +43.13 kcal/mol, of the high-energy steps are much larger than the experimental one, +24.8 kcal/mol [6]. Also, the three activation energies of model I in the broken box are large, +34.14, +35.83 and 37.09 kcal/mol. Thus, although reasonable geometric changes were obtained in Figure 1, these large energies demonstrate that the monoprotonated reaction is unlikely.

Diprotonated reacting systems

The large activation energies of TS2s in the monoprotonated systems would arise from the poor proton-donating strength to the oxygen of the N–O bond in the model of Scheme 5. In order to enhance the donation, a dication system was constructed at the left of Scheme 6. However, the bond-interchange transition state could not be obtained in spite of many attempts. Attempts including more water molecules also failed. An alternative model was considered and is shown in Scheme 7. This model was constructed in light of the results of preliminary calculations shown in Figure S4 and Figure S5, Supporting Information File 1.

Figure S4a shows that a TS geometry was successfully obtained in a model in which one H_2O molecule is subtracted from that in Scheme 7. However, when the size of the water cluster is

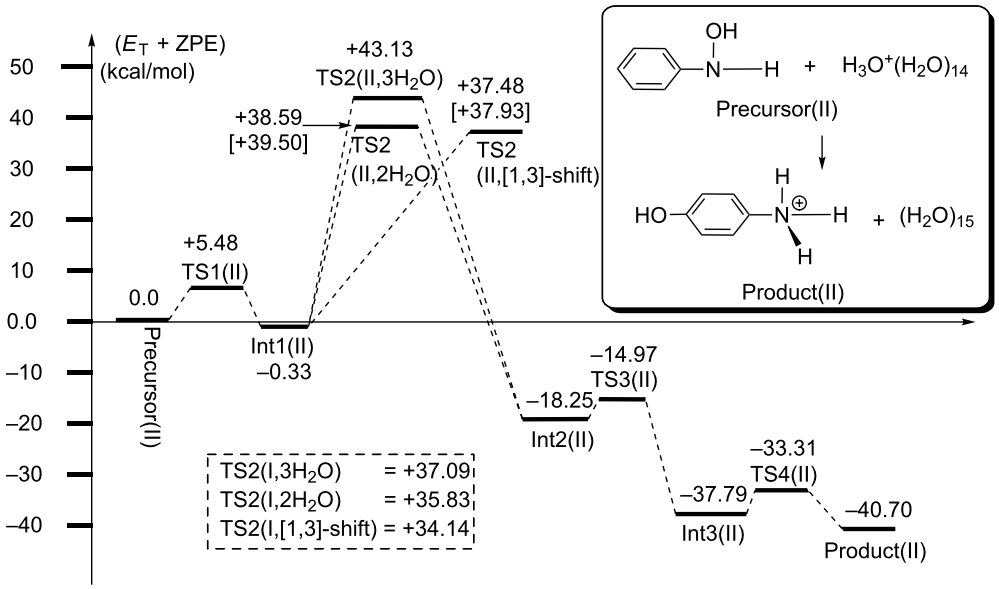

Figure 3: Energy changes (in kcal/mol) of Δ(E+ZPE) by B3LYP/6-311+G(d,p) SCRF = PCM//B3LYP/6-31G(d) and by [B3LYP/6-311+G(d,p) SCRF = PCM//B3LYP/6-311+G(d,p) at TS2] of model II. The corresponding geometries are shown in Figure 1. In the broken box, three activation energies of TS2(I, $2H_2O$), TS2(I, $3H_2O$) and TS2(I, [1,3]-shift) of Figure S3 are exhibited.

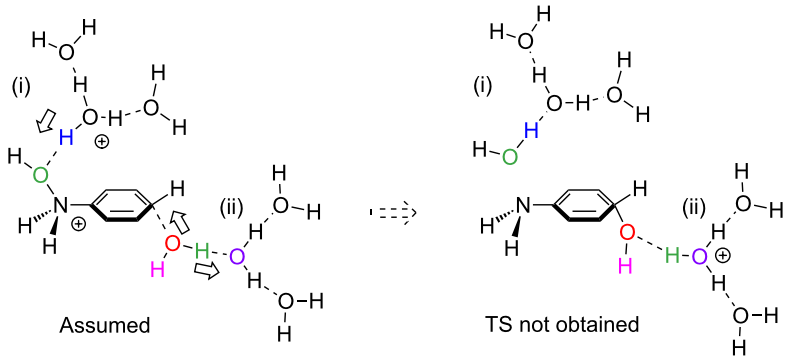

Scheme 6: A trans-type bond interchange was assumed. But, the reaction path could not be obtained. The group (i) works as a proton donor and the group (ii) acts as an acceptor.

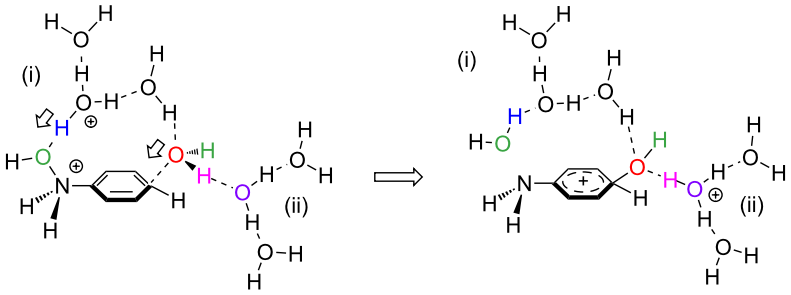

Scheme 7: An alternative model for the OH [1,5]-rearrangement in the dication system.

enlarged, the TS structure cannot be obtained, as shown in Figure S4b. On the other hand, a TS geometry following Scheme 7 could be obtained as shown in Figure S5, Supporting Information File 1. These results demonstrate that not $H_3O^+(H_2O)$ (in Figure S4) but $H_3O^+(H_2O)_2$ (in Figure S5) should participate in the reaction center.

On the basis of the result in Figure S5, paths in a reaction of $(HO)HN–C_6H_5 + (H_3O^+)_2(H_2O)_{13} \rightarrow H_3N^+–C_6H_4–OH + (H_3O^+)(H_2O)_{14}$ were investigated and are shown in Figure 4. This system is called here model III and is isoelectronic with that in Figure 1.

Geometric changes similar to those in Figure 1 were obtained: Precursor(III) → TS1(III) → Int1(III), Int1'(III) → TS2(III) → Int2(III), Int2'(III) → TS3(III) → Int3(III) → TS4(III) → Product(III) along with TS2(III, [1,3]-shift). Geometries of TS2(III) and TS2(III, [1,3]-shift) are like those of the aniline dication and $(H_2O)_{16}$.

Figure 5 shows the energy change of the reaction in Figure 4. The rate-determining step is TS2, and TS2(III,[1,3]-shift) = +32.20 kcal/mol is much larger than TS2(III) = +26.25 kcal/mol. The latter value is close to the experimental one, +24.8 kcal/mol [6], and the superiority of the [1,5]-OH shift over the [1,3]-OH one is clearly indicated. Thus, the dication system may be subject to the Bamberger rearrangement in the para-orientation, which is in line with the experimental suggestion [6].

The reaction pattern exhibited in Scheme 7 was examined further by a large system composed of $Ph–NH(OH) + (H_3O^+)_2(H_2O)_{24}$ with the molecular formula of the system, $C_6H_{61}NO_{27}^{2+}$. This is called here model IV. Geometries of TS2(IV) and TS2(IV, [1,3]-shift) are shown in Figure 6. They are similar to those of TS2(III) and TS2(III, [1,3]-shift) in Figure 4, respectively. Again, the aniline dication-like structures were obtained. The proton-transfer pattern depicted in Scheme 7 was confirmed. As for the activation energies of

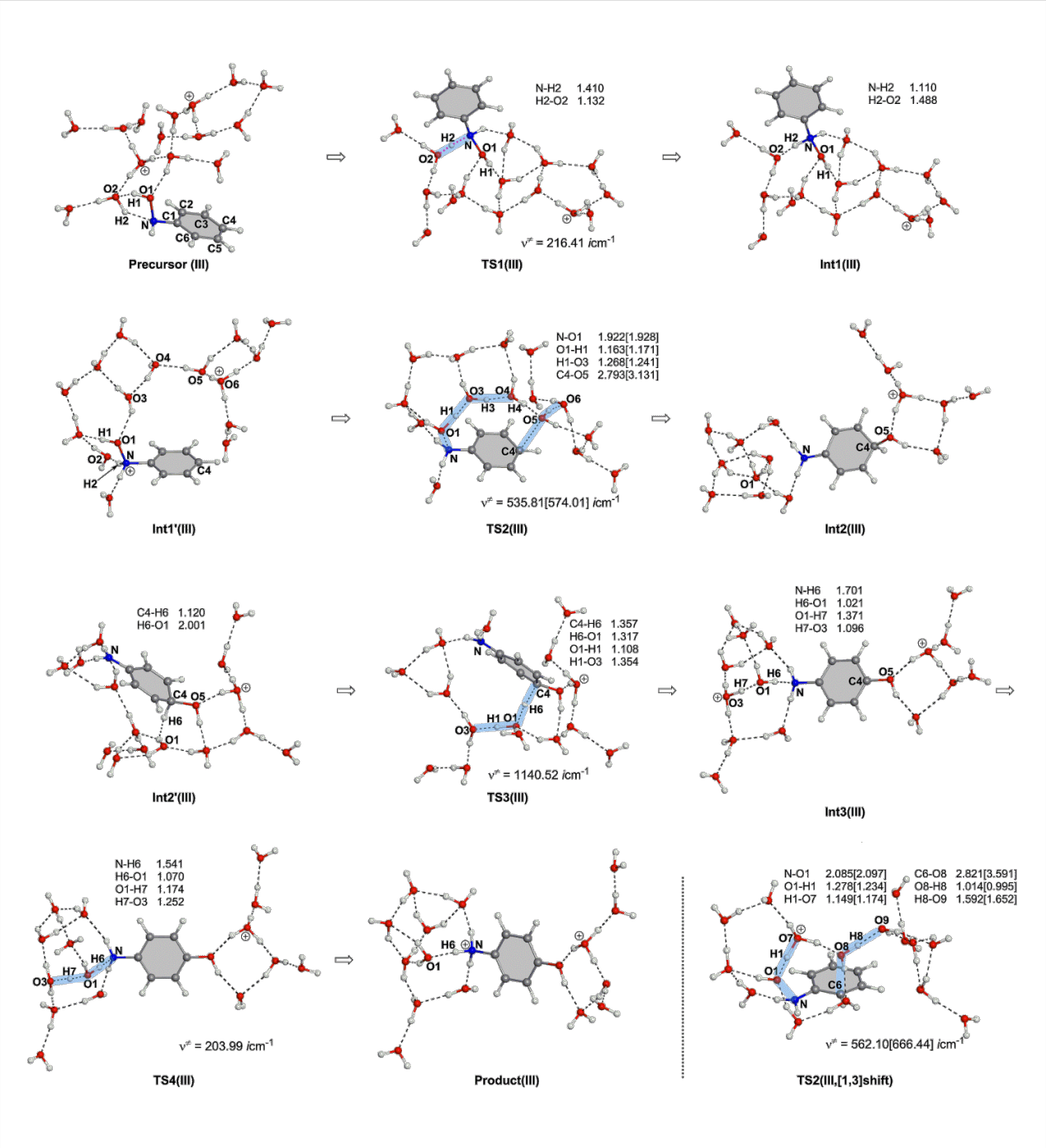

Figure 4: Geometric changes in the reaction of model III, (HO)HN–C_6H_5 + $(H_3O^+)_2(H_2O)_{13}$ → H_3N^+–C_6H_4–OH + $(H_3O^+)(H_2O)_{14}$.

TS2(IV), $\Delta(E_T + ZPE)$ = +27.58 kcal/mol by B3LYP/6-311+G(d,p) SCRF = PCM//B3LYP/6-31G(d) and {+26.04 by B3LYP/6-311+G(d,p) SCRF = PCM//B3LYP/6-311+G(d,p)} are close to the experimental one (+24.8). These are much smaller than +36.25 kcal/mol and {+35.28} of TS2(IV, [1,3]-shift), respectively. Thus, the calculated results showed that the para-orientation of the rearrangement is superior to the ortho one.

The monoprotonated reacting system with Cl^-

In the Introduction, the experimental result that the rearrangement gave the 2- and 4-chloro-amino derivatives in hydrochloric acid was cited [1]. The nucleophile Cl^- would be free from the hydrogen-bond constraint depicted in Scheme 7. Then, such less sterically congested trans substitution as that shown in Scheme 6 becomes feasible. By the use of a model

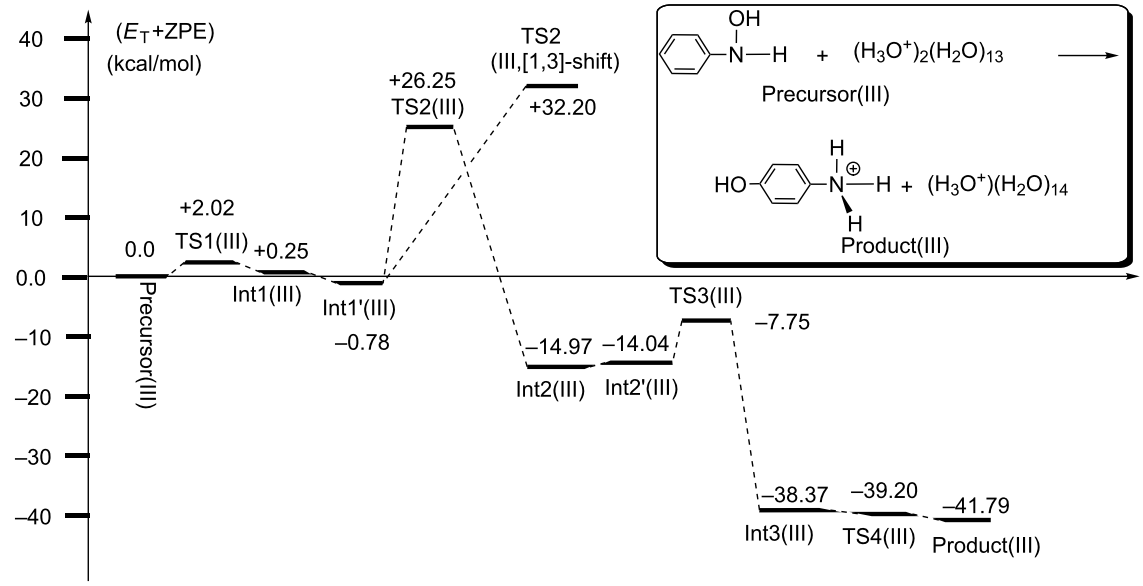

Figure 5: Energy changes (in kcal/mol) of model III. The corresponding geometries are shown in Figure 4. The apparent small reversal of energies of Int3(III) and TS4(III) comes from the splicing method, B3LYP/6-311+G(d,p) SCRF = PCM//B3LYP/6-31G(d), Et(B3LYP/6-31G(d)) of Int3(III) = −1509.9900126 Hartree and Et(B3LYP/6-31G(d)) of TS4(III) = −1509.9895045 Hartree.

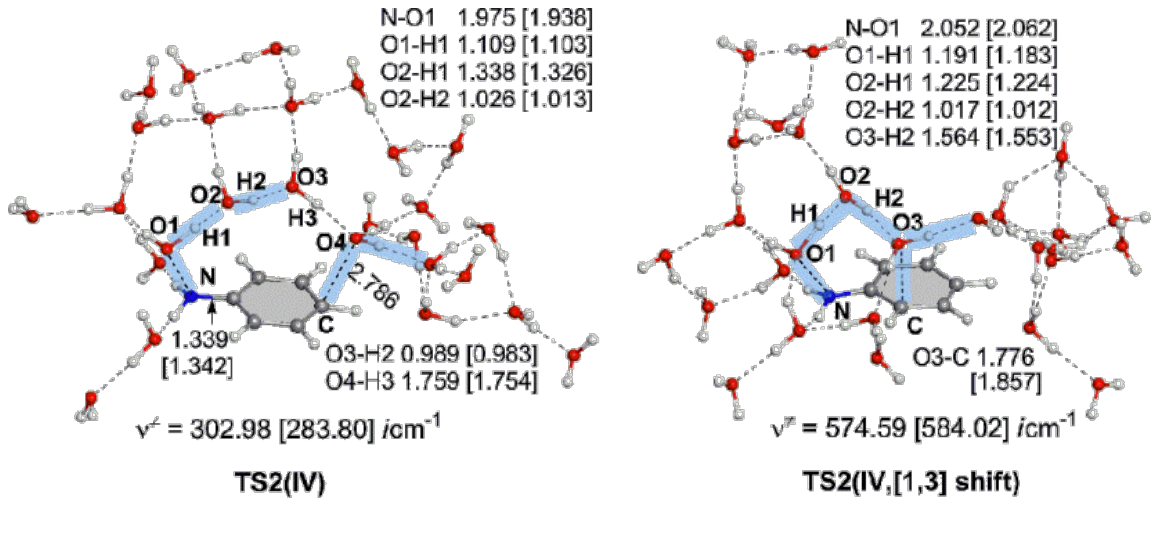

Figure 6: TS2(IV) and TS2(IV, [1,3]-shift) in the reaction (model IV), Ph–NH(OH) + $(H_3O^+)_2(H_2O)_{24}$ → HO–C_6H_4–NH_3^+ + $H_3O^+(H_2O)_{25}$.

(called here model V) of Ph–NH(OH) + $(H_3O^+)_2(H_2O)_{13}$ + Cl^-, the trans-type substitution paths were traced. In fact, TS2(V) and TS2(V, [1,3]-shift) geometries were obtained and are shown in Figure 7. Their activation energies were calculated to be +28.52 kca/mol and +29.57 kcal/mol relative to the energy of Int1(V), respectively. These similar values indicate that both 2- and 4-Cl-substituted anilines may be formed almost equally according to the normal ortho- and para-orientation.

Conclusion

In this work, the Bamberger rearrangement was studied by means of DFT calculations. In the Introduction, three questions (a), (b), and (c) were raised:

1. The nitrenium ion **7** was calculated to be absent. It cannot intervene owing to the high nucleophilicity of the water cluster.

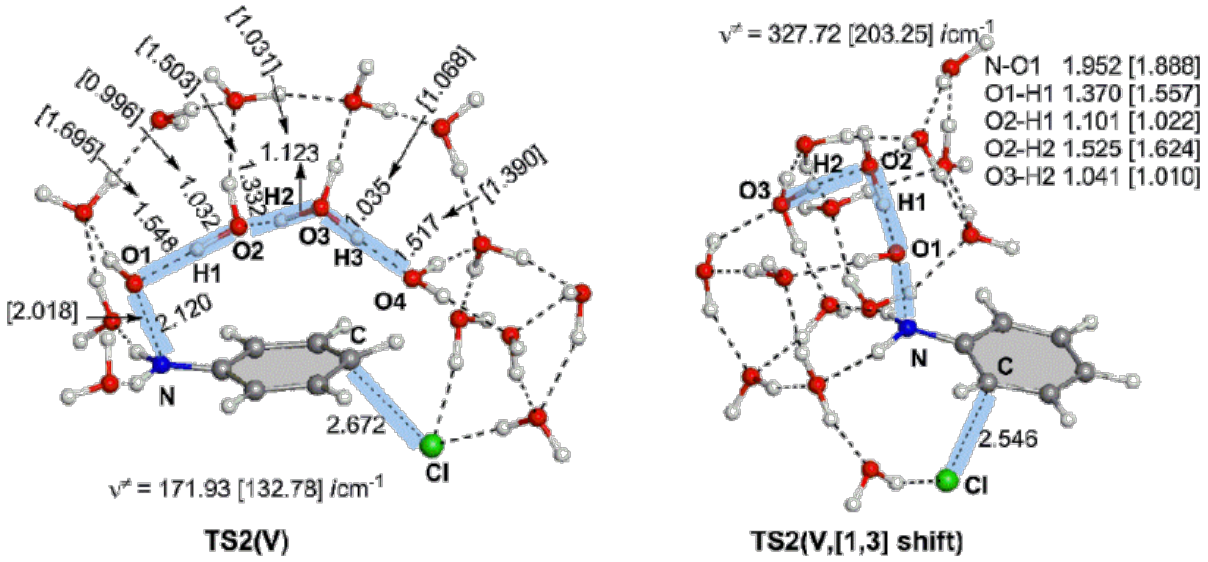

Figure 7: TS2(V) and TS2(V, [1,3]-shift) in the reaction (model V), Ph–NH(OH) + $(H_3O^+)_2(H_2O)_{13}$ + Cl^- → *o*- and *p*-Cl–C_6H_4–NH_3^+ + $(H_2O)_{16}$.

2. The N-protonated substrate (**5** in Scheme 4) is in the reaction route. By the protonation, the N–O bond becomes directed to the π space of the phenyl ring. The direction is fit for the subsequent bond interchange of TS2 in the diprotonated system.
3. Without good nucleophiles such as Cl^-, a constrained hydrogen-bond network shown in Scheme 7 may give the OH shift via bond interchanges. The ortho-position is too close to the N–O bond and is not fit for the constrained network.

On the basis of the calculated results, Scheme 4 may be revised to Scheme 8.

Supporting Information

Supporting Information File 1

Figures S1–S5, Cartesian coordinates of TS geometries.
[http://www.beilstein-journals.org/bjoc/content/supplementary/1860-5397-9-119-S1.pdf]

Acknowledgements

This work is financially supported by Grants-in-Aid from the Ministry of Education, Culture, Science, Sport, and Technology through Grants-in-Aid of Specially Promoted Science and Technology (No. 22000009) and Grand Challenge Project

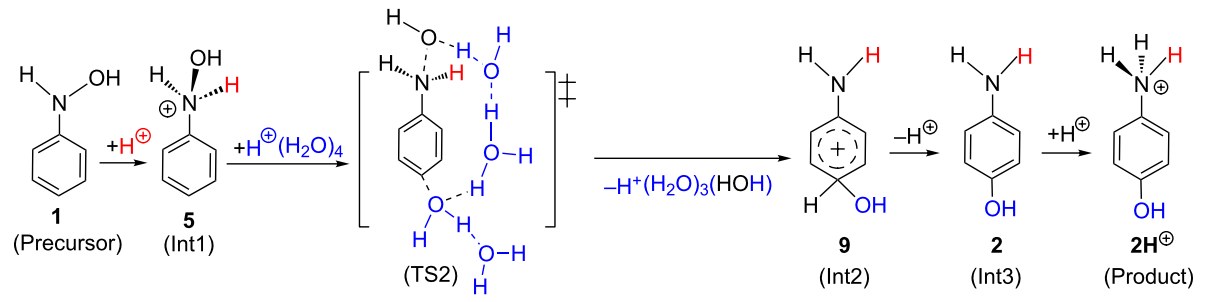

Scheme 8: A mechanism of the Bamberger rearrangement based on the present results. **1**, **2**, $\mathbf{2H^+}$, **5** and **9** are defined in Scheme 4. In parentheses, our notations such as (Precursor) and (Int1) are shown. TS2 is regarded as the complex of the aniline di-cation and $(H_2O)_5$ cluster.

(IMS, Okazaki, Japan). We are also thankful to the computational facility at the Institute of Molecular Science, Okazaki, Japan.

References

1. Bamberger, E. *Chem. Ber.* **1894,** *27,* 1548–1557. doi:10.1002/cber.18940270276
2. Bamberger, E. *Chem. Ber.* **1894,** *27,* 1347–1350. doi:10.1002/cber.18940270229
3. Heller, H. E.; Hughes, E. D.; Ingold, C. K. *Nature* **1951,** *168,* 909–910. doi:10.1038/168909a0
4. Kukhtenko, I. I. Z. *Russ. J. Org. Chem.* **1971,** *7,* 330.
5. Wang, Z. Bamberger Rearrangement. *Comprehensive Organic Name Reactions and Reagents;* Wiley-Interscience, 2010; pp 191–194.
6. Sone, T.; Tokuda, Y.; Sakai, T.; Shinkai, S.; Manabe, O. *J. Chem. Soc., Perkin Trans. 2* **1981,** 298–302. doi:10.1039/p29810000298
7. Kohnstam, G.; Petch, W. A.; Williams, D. L. H. *J. Chem. Soc., Perkin Trans. 2* **1984,** 423–427. doi:10.1039/p29840000423
8. Becke, A. D. *J. Chem. Phys.* **1993,** *98,* 5648–5652. doi:10.1063/1.464913
9. Lee, C.; Yang, W.; Parr, R. G. *Phys. Rev. B* **1988,** *37,* 785–789. doi:10.1103/PhysRevB.37.785
10. Fukui, K. *J. Phys. Chem.* **1970,** *74,* 4161–4163. doi:10.1021/j100717a029
11. Gonzalez, C.; Schlegel, H. B. *J. Chem. Phys.* **1989,** *90,* 2154–2161. doi:10.1063/1.456010
12. Cancès, E.; Mennucci, B.; Tomasi, J. *J. Chem. Phys.* **1997,** *107,* 3032–3041. doi:10.1063/1.474659
13. Cossi, M.; Barone, V.; Mennucci, B.; Tomasi, J. *Chem. Phys. Lett.* **1998,** *286,* 253–260. doi:10.1016/S0009-2614(98)00106-7
14. Mennucci, B.; Tomasi, J. *J. Chem. Phys.* **1997,** *106,* 5151–5158. doi:10.1063/1.473558
15. *Gaussian 09,* Revision B.01; Gaussian, Inc.: Wallingford, CT, 2010.

License and Terms

Beilstein Journal of Organic Chemistry

True and masked three-coordinate T-shaped platinum(II) intermediates

Manuel A. Ortuño[1], Salvador Conejero*[2] and Agustí Lledós*[1]

Review

Open Access

Address:
[1]Departament de Química, Universitat Autònoma de Barcelona, 08193 Cerdanyola del Vallès, Spain and [2]Instituto de Investigaciones Químicas (IIQ), Departamento de Química Inorgánica, CSIC and Universidad de Sevilla, Avda. Américo Vespucio 49, 41092 Sevilla, Spain

Email:
Salvador Conejero* - sconejero@iiq.csic.es; Agustí Lledós* - agusti@klingon.uab.es

* Corresponding author

Keywords:
C–H bond activation; intermediate; platinum(II); reactive intermediates; three-coordinate; T-shaped

Beilstein J. Org. Chem. **2013,** *9,* 1352–1382.
doi:10.3762/bjoc.9.153

Received: 05 April 2013
Accepted: 10 June 2013
Published: 09 July 2013

This article is part of the Thematic Series "New reactive intermediates in organic chemistry".

Guest Editor: G. Bucher

Abstract

Although four-coordinate square-planar geometries, with a formally 16-electron counting, are absolutely dominant in isolated Pt(II) complexes, three-coordinate, 14-electron Pt(II) complexes are believed to be key intermediates in a number of platinum-mediated organometallic transformations. Although very few authenticated three-coordinate Pt(II) complexes have been characterized, a much larger number of complexes can be described as operationally three-coordinate in a kinetic sense. In these compounds, which we have called masked T-shaped complexes, the fourth position is occupied by a very weak ligand (agostic bond, solvent molecule or counteranion), which can be easily displaced. This review summarizes the structural features of the true and masked T-shaped Pt(II) complexes reported so far and describes synthetic strategies employed for their formation. Moreover, recent experimental and theoretical reports are analyzed, which suggest the involvement of such intermediates in reaction mechanisms, particularly C–H bond-activation processes.

Review

Scope of this review

Reaction intermediates are transient species able to undergo transformations along chemical processes. Electron deficient transition-metal complexes with vacant coordination sites are well-suited to play such a role. Coordinatively and electronically unsaturated species have often been invoked as crucial intermediates in reactions involving late transition-metal complexes. Ligand dissociation, forming intermediates with open coordination sites, has been proposed as the initial step in many reactions involving square-planar d^8 organometallic complexes [1]. Four-coordinate square-planar structures, with a formally 16-electron counting, are absolutely dominant in isolated Pt(II) complexes. However, three-coordinate, 14-elec-

tron Pt(II) complexes are believed to be key intermediates in a number of reactions, e.g., β-hydrogen elimination, thermal decomposition of dialkyls, insertion of olefins into M–H bonds, electrophilic attack at Pt–C bonds, and ligand cycloplatination [2]. Likewise, related Pd(II) complexes [3,4] are relevant in cross-coupling reactions and C–H bond-activation processes. The accessibility of three-coordinate Pd(II) species have been recently discussed [5].

Three-coordinate Pt(II) intermediates are the focus of this review. Despite the kinetic perception of the intermediacy of these coordinatively unsaturated species in important organometallic processes, direct proofs of 14-electron Pt(II) complexes have been difficult to find. The strong readiness to alleviate the unsaturation makes them very reactive species but hampers their isolation. Low-coordinate Pt(II) complexes have been generated in gas-phase experiments [6,7] but have remained elusive in solution. With a few exceptions the fourth coordination site is occupied by a weak ligand, e.g., an agostic interaction, a counteranion or a solvent molecule. However, if this additional interaction is weak and labile enough, the three-coordinate species is very accessible and the complex can be considered as "operationally unsaturated" in a kinetic sense [8]. We will name these compounds "masked" three-coordinate complexes to distinguish them from the true low-coordinate complexes. In this review, we will summarize recent advances in true and masked three-coordinate Pt(II) complexes, highlighting both their structural features and their possible participation as reaction intermediates. Computational studies have become an invaluable tool for the investigation of short-lived elusive intermediates and will be quoted throughout the article. The review is organized as follows. First, a general picture of the electronic and geometrical structure of three-coordinate Pt(II) complexes will be presented. Then, the structural features of the main families of these compounds will be summarized. The next sections will be devoted to the spectroscopic tools for their detection and the synthetic strategies employed to their formation. Afterwards, the rearrangement processes exhibited by the low-coordinate complexes in solution will be discussed. Finally, participation of three-coordinate Pt(II) intermediates in reactions, mainly C–H bond-activation processes and ligand exchanges, will be analyzed. A thorough review on the bonding and stereochemistry of three-coordinate transition-metal compounds was published several years ago [9].

Electronic and geometrical structure

As we will discuss later on, three-coordinate, 14-electron Pt(II) d^8 complexes display a T-shaped structure, i.e., a structure with two ligands mutually *trans* and the third ligand *trans* to the vacant position. A qualitative molecular orbital scheme of the d block of a T-shaped d^8 metal complex can be easily derived from that of a square-planar complex by removing one of the ligands (Figure 1) [10,11]. The three nonbonding orbitals in square-planar complexes (d_{xz}, d_{xy} and d_{yz}) are not affected by the removal of a ligand. The d_z^2 orbital is slightly stabilized due to the disappearance of a small antibonding interaction. However, the most striking difference is observed in the lowest unoccupied $d_{x^2-y^2}$ orbital; its energy strongly decreases by removing an antibonding interaction with one ligand and its shape changes by mixing with the p_y orbital. This hybridization takes place so that the orbital is directed away from the three ligands toward the empty coordination site, making this position suitable for the approach of an incoming ligand. This simple picture has been corroborated by DFT calculations on T-shaped $[Pt(alkyl)(PMe_3)_2]^+$ complexes [2].

The splitting of the d-block orbitals favors a singlet ground state for T-shaped d^8 complexes and these species usually exhibit a low-spin reactivity. Recent DFT calculations on the 14-electron $[Pt(^{F}PNP)]^+$ complex (^{F}PNP = (4-F-2-(iPr_2P)C_6H_3)$_2$N) predict a relatively small (10–12 kcal mol^{-1}) separation between the singlet and the triplet states of this intermediate [12]. It is worth pointing out that a d^8 C_{2v} ML_3 fragment is isolobal with CH_2, although the ordering of the two valence orbitals a_1 and b_2 differs. For a singlet 14-electron T-shaped ML_3, the two electrons fill the b_2 level (d_{yz}), while for a singlet CH_2 fragment they occupy the a_1 orbital (empty $d_{x^2-y^2}$ in ML_3, Figure 1) [13].

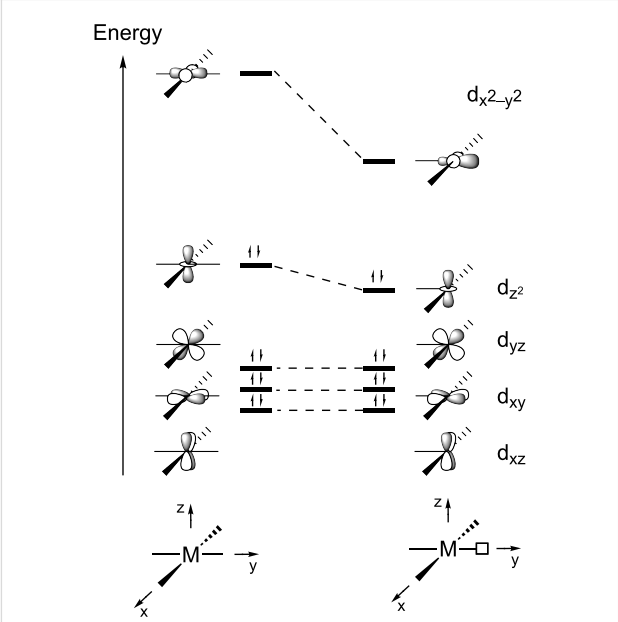

Figure 1: Qualitative orbital diagram for a d^8 metal in ML_4 square-planar and ML_3 T-shaped complexes.

Steric reasons should favor trigonal-planar D_{3h}-like structures for three-coordinate Pt(II) complexes instead of the sterically

unfavorable T-shaped structure. The preference of these Pt(II) compounds (with a low spin d^8 configuration) for T-shaped structures is due to electronic effects and can be understood from the Walsh diagram shown in Figure 2. The Walsh diagram describes the variation of the L–M–L angle from a T-shaped structure through D_{3h} to a Y-shaped structure. A d^8, 14-electron ML_3 complex would have the lowest four levels filled in Figure 2. In a D_{3h} geometry, the degeneracy of e' orbitals will promote a Jahn–Teller distortion towards T or Y geometries [10,14].

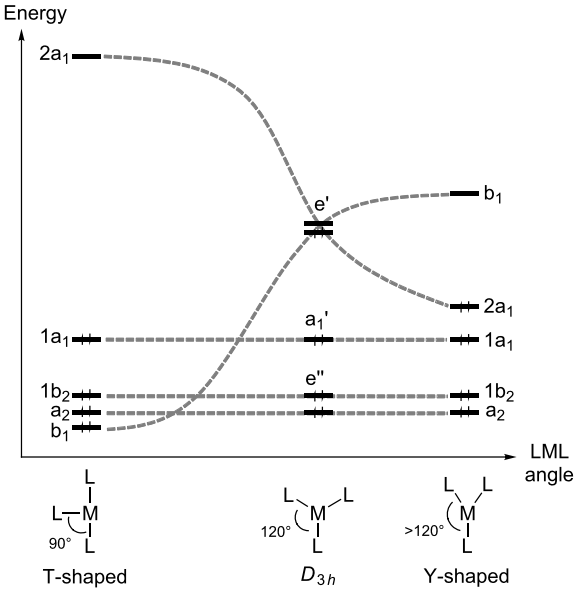

Figure 2: Walsh diagram for the d-block of a d^8 ML_3 complex upon bending of one L–M–L angle.

DFT calculations on asymmetric *cis*-$[Pt(alkyl)(PMe_3)_2]^+$ show that, in spite of the reduced symmetry, the bending energy profile maintains the same basic features: the T-shaped configurations of the 14-electron species are energy minima, and their *cis*-like to *trans*-like interconversion occurs via transition states with Y-shaped configurations [2].

The X-ray structure of the recently reported three-coordinate platinum complex $[Pt(SiMe_2Ph)_2(IPr)]$ (IPr = 1,3-bis(2,6-diisopropylphenyl)imidazol-2-ylidene) shows a unique Y-shaped geometry in which the Si–Pt–Si angle is very acute (80.9°) and far from the ideal values for both trigonal-planar and T-shaped structures (**Y1**, Figure 3) [15]. Computations on non-sterically demanding models $[Pt(R)_2(Im)]$ (R = $SiMe_3$, Me; Im = imidazol-2-ylidene) appealed to the *trans* influence of both NHC and silyl ligands to explain the structure. However, a recent DFT investigation concluded that **Y1** is better described as a Pt(0) σ-disilane complex [16] than as a Pt(II) disilyl species. Thorough geometrical and electronic analyses support a Pt(0)···disilane coordination via donation and back-donation interactions. This suggestion also explains the experimentally observed ^{195}Pt NMR chemical shift, which is closer to the Pt(0) rather than the Pt(II) species.

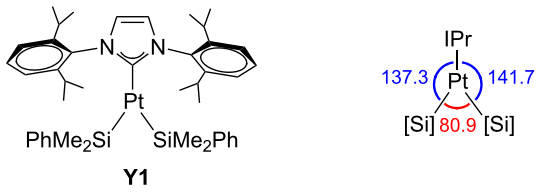

Figure 3: Neutral Y-shaped Pt complex **Y1** [15]. Angles are given in degrees.

The nonequivalence of axial and equatorial positions in ML_3 complexes raises the question of which positions are preferred by the ligands in such compounds. Although in most of the experimentally characterized systems the steric demands dictate the disposition of the ligands, electronic effects are also at work, and they were analyzed for simple model systems with theoretical methods. An early study based on perturbation theory concluded that in T-shaped ML_3 d^8 complexes both axial and equatorial bonds should have similar strength and that the most electronegative atoms will substitute axially [17]. DFT calculations on $[PtXY(PH_3)]$ (X, Y = Cl, CH_3, SiH_3, $Si(OH)_3$) demonstrated the importance of the *trans* influence in governing the stability of T-shaped isomers. In the most stable isomer, the ligand with the smaller *trans* influence is located *trans* to the PH_3 ligand [18].

Structurally characterized compounds

The T-shaped structure is easily recognized by the absence of one ligand in a square-planar disposition. Nevertheless, the number of well-characterized three-coordinate Pt(II) complexes is very low. To achieve a true T-shaped structure, the vacancy at the metal center must be blocked to avoid intra- and intermolecular interactions, such as agostic bonds and counteranion or solvent coordination. These interactions mask the T-shaped structure, but due to their potential labile nature, the three-coordinate species are still accessible.

In this section we will describe the main families of T-shaped Pt(II) complexes, which are structurally characterized (Figure 4). First, true T-shaped structures with no stabilization at the vacant site are compiled. Then, complexes involving agostic, counteranion and solvent interactions will be summarized. From now on, true T-shaped complexes are labeled as **T** complexes, while agostic, counteranion and solvent-stabilized complexes are designated as **A**, **C** and **S** complexes, respectively.

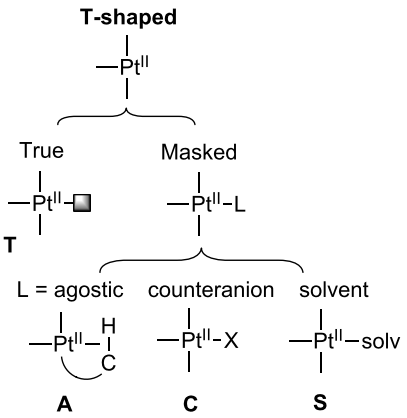

Figure 4: General classification of T-shaped Pt(II) structures according to the fourth coordination site.

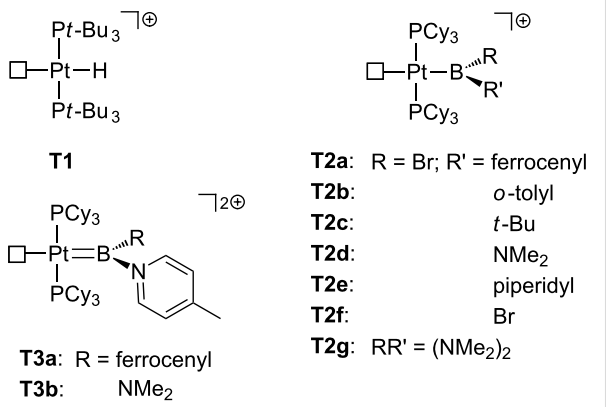

Figure 5: Hydride, boryl and borylene true T-shaped Pt(II) complexes.

True T-shaped

The isolation and characterization of such highly electrophilic species is challenging. Accordingly, the number of well-characterized true T-shaped Pt(II) complexes is scarce. The empty site should be blocked somehow to prevent undesirable contacts, and in most cases, bulky ligands are required to protect the empty coordination site. Strong electron-donor ligands also help stabilizing the formally 14-electron compounds. It is worthy of note that almost all of them are cationic.

The first true T-shaped complexes were prepared by using phosphine ligands (Figure 5). In the 80s, Goel et al. proposed, from nuclear magnetic resonance (NMR) data, a T-shaped structure for the cationic hydride *trans*-$[(t\text{-}Bu_3P)_2Pt(H)]^+$ **T1** containing bulky phosphine ligands [19]. However, it was not until 2005 when Braunschweig et al. successfully characterized a true 14-electron T-shaped Pt(II) boryl complex **T2a** by means of X-ray studies [20]. By halide abstraction, the cationic *trans*-$[Pt(B(Fc)Br)(PCy_3)_2]^+$ **T2a** (Fc = ferrocenyl; Cy = cyclohexyl) could be obtained, in which the boryl ligand is located *trans* to the empty site. No agostic interactions were detected, the shortest Pt–H and Pt–C distances being 2.542 Å and 3.117 Å, respectively. Inspired by this chemical template, the synthesis of Pt–boryl derivatives of the type *trans*-$[Pt(BRR')(PCy_3)_2]^+$ has been extended [21]. Even at extreme electronic conditions in dicationic *trans*-$[Pt(BR(4\text{-picoline}))(PCy_3)_2]^{2+}$ **T3**, the complex remains truly T-shaped, although small Lewis donors such as CO and acetonitrile can coordinate to the open coordination site of **T3** [22]. DFT-based electron localization function (ELF) analyses [20] and geometry optimizations [22] supported the lack of agostic interactions in these complexes. This absence has been attributed to the strong *trans* influence exerted by the ligand in *trans* position with respect to the vacant site [23,24].

Moreover, in the past few years the synthesis of 14-electron Pt(II) complexes was extended by using N-heterocyclic carbene (NHC) ligands (Figure 6), which have been proven to be useful

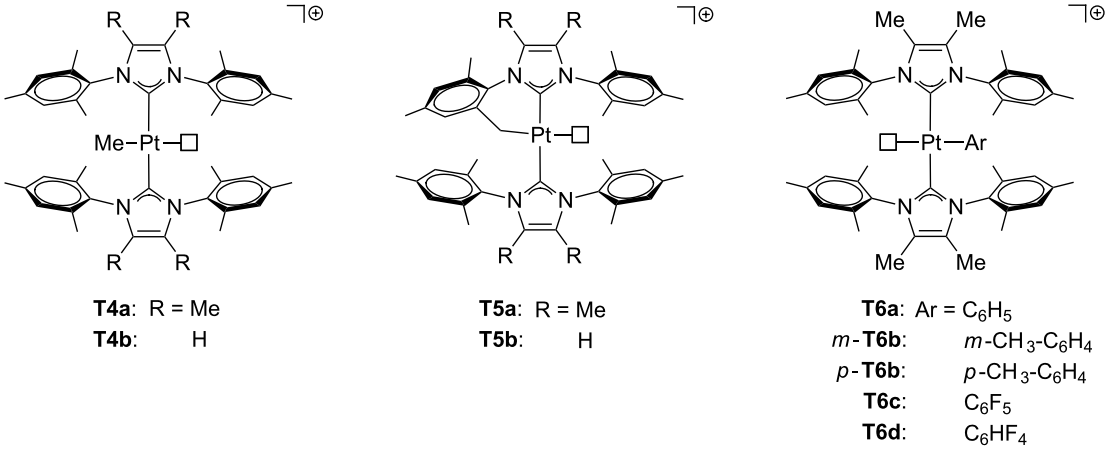

Figure 6: NHC-based true T-shaped Pt(II) complexes.

stabilizing electron-deficient transition-metal species [25-27]. In this regard, recent studies state that the use of IMes* (4,5-dimethyl-1,3-bis(2,4,6-trimethylphenyl)imidazol-2-ylidene) and IMes (1,3-bis(2,4,6-trimethylphenyl)imidazol-2-ylidene) ligands in $[Pt(Me)(NHC)_2]^+$ **T4** and $[Pt(NHC')(NHC)]^+$ **T5** (NHC = IMes*, IMes; NHC' = cyclometalated ligand) provides pure T-shaped species with no agostic stabilization [28]. Additionally, the resulting $[Pt(Ar)(IMes^*)_2]^+$ **T6** formed after C–H bond activation has also proven to be a three-coordinate species with no agostic interactions according to the X-ray structure of the derivative **T6d**, in which the closest Pt–H contact is located at 3.117 Å. The absence of agostic interactions has been attributed to geometrical constraints, the limited flexibility of the mesityl groups in IMes* and IMes hampering the approach of the CH bond to the metal center. Once again, Lewis acids as acetonitrile can access the empty site, which means that a potential reactant molecule can coordinate to the metal for further reactions.

Masked T-shaped via agostic interaction

The agostic interaction [29,30] is usually explained as an intramolecular 3-center-2-electron interaction between a metal M and a C–H bond. This type of contact is a recurrent event in unsaturated transition-metal complexes [31] and it can be characterized by structural and spectroscopic techniques [29,30] together with computational tools [32,33]. The agostic interaction shows different behaviors. It can be a transient species prior to the C–H bond breaking or stabilize low electron count situations. In this section we will focus on the latter aspect. Since this intramolecular interaction is difficult to avoid, even in the presence of bulky ligands, it is the most common motif for the stabilization of three-coordinate complexes.

Early works on T-shaped Pt(II) species are related to complexes stabilized with phosphine ligands (Figure 7). Pioneering studies on alkyl complexes from Orpen's and Spencer's research groups reported the synthesis of cationic $[Pt(norbornyl)(P–P)]^+$ complexes **A1a–e** (P–P = bidentate phosphine ligand) [34,35]. Further studies involved other alkyl ligands such as ethyl (**A2b–c**), 3,3-dimethylbutyl (**A3b–c**) and 2,3,3-trimethylbutyl (**A4**) [36-38]. NMR spectroscopic data and X-ray structures of **A1a** [34] and **A2b** [36] demonstrate that these compounds display a β-agostic interaction filling the fourth coordination site. This interaction is strong enough to cleave the C–H bond, creating a chemical equilibrium with the corresponding hydrido–alkene derivatives. Indeed, the detected ground state of the compounds in brackets (**A2a**, **A2d**, **A2e** and **A3a** in Figure 7) is the hydrido–alkene isomer instead of the agostic–alkyl one. Later, Baratta et al. succeeded in the isolation of 14-electron Pt(II) complexes bearing bulky phosphine

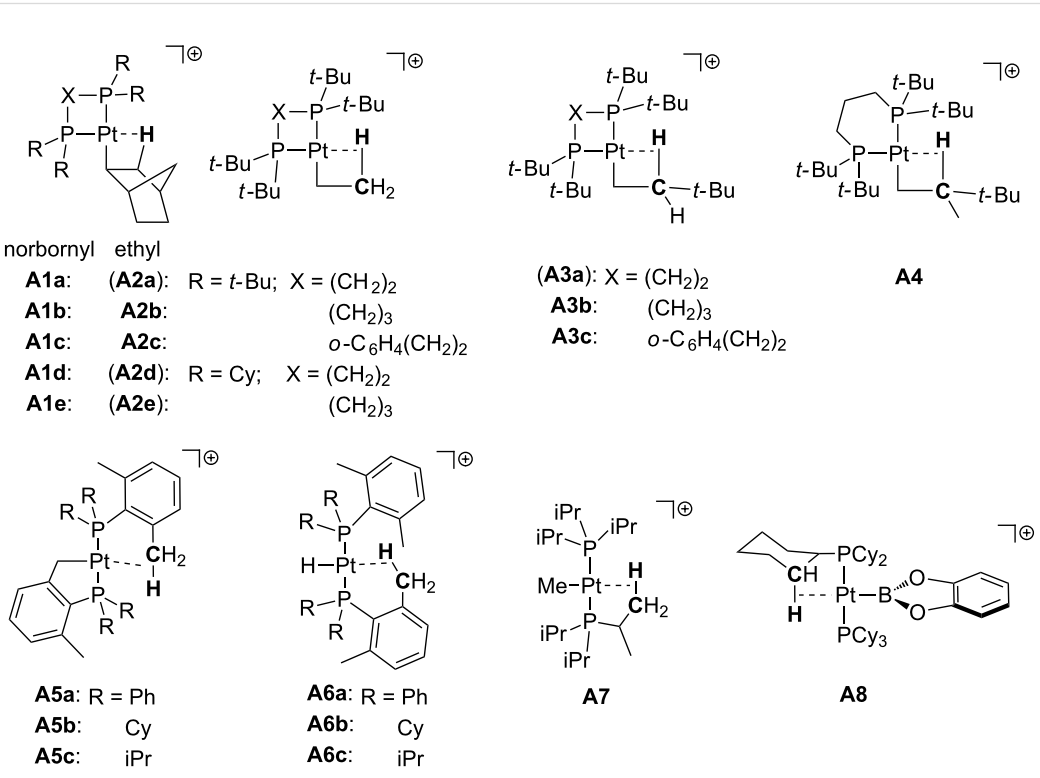

Figure 7: Phosphine-based agostic T-shaped Pt(II) complexes. Compounds in brackets correspond with hydrido–alkene ground states.

ligands [39]. The usage of *trans*-[Pt(Me)Cl(PR_3)$_2$] as a starting material, followed by halide removal and the release of methane by intramolecular C–H bond activation provided the cationic T-shaped cyclometalated complexes **A5a**–**b**. The X-ray structure of **A5b** shows that the platinum atom exhibits a δ-agostic interaction with one hydrogen atom of the methyl group of the non-cyclometalated phosphine ligand. Subsequent hydrogenation generates the corresponding hydride complexes **A6a**–**b**. On the basis of NMR studies ($^1J_{Pt,H}$ values of ca. 2000 Hz, see next section), a weak interaction *trans* to the hydride ligand, typically an agostic contact, is supposed to exist. Carmona and co-workers also prepared quite similar complexes, **A5c** and **A6c**, where R labels represent isopropyl groups [40]. Weller and co-workers reported the formation of complex *trans*-[Pt(Me)($PiPr_3$)$_2$]$^+$ **A7** in which a γ-agostic interaction is located in the fourth coordination site [41]. The addition of tetrahydrofuran (THF) rapidly forms the corresponding adduct. Braunschweig et al. obtained the agostic structure **A8** by employing BCat as a ligand (BCat = catecholatoboryl) in three-coordinate Pt(II) complexes [21]. Unlike the previous pure T-shaped boryl complexes **T2** (Figure 5), the weaker *trans* influence of the BCat ligand allows the formation of an agostic contact. Treatment of **A8** with Lewis bases also removes the agostic interaction, generating the adduct complex.

Natural Bond Orbital (NBO) and Atoms In Molecules (AIM) calculations on complexes **A1**, **A2b**, **A5b** and **A7** classified the Pt···H–C contacts as agostic interactions for all the species with the only exception being **A7**, in which a H-bond character can also be ascribed [42].

Concerning other types of ligands (Figure 8), the phenylpyridyl complex **A9** reported by Rourke and co-workers exhibits a bifurcated δ-agostic interaction that has been determined by X-ray studies [43]. This is one of the rare neutral T-shaped Pt(II) complexes. Referring to NHC ligands, Rivada-Wheelaghan et al. isolated the three-coordinate methyl [Pt(Me)(IPr)$_2$]$^+$ (**A10**) and cyclometalated [Pt(NHC')NHC]$^+$ complexes (NHC = IPr **A11a**, I*t*-Bu (1,3-bis(*tert*-butyl)imidazol-2-ylidene) **A11b**; NHC' = cyclometalated ligand) [44]. In sharp contrast with the analogous **T5** and **T6** (Figure 6) [28], δ- and ζ-agostic interactions at the fourth coordination site were detected by X-ray and NMR studies for complexes containing IPr (**A11a**) and I*t*-Bu (**A11b**), respectively.

Selected Pt···H–C parameters from the X-ray structures of agostic compounds are collected in Table 1. As it can be expected, short Pt–H and Pt–C distances are observed for the

Table 1: Selected geometrical parameters of X-ray characterized agostic T-shaped Pt(II) structures.

Complex	Agostic length	Pt–H distance/Å	Pt–C distance/Å	Pt–H–C angle/degrees	Reference
A1a	β	1.895	2.309	91.2	[34]
A2b	β	—[a]	2.282	—[a]	[37]
A5b	δ	2.057	2.432	102.5	[39]
A7	γ	2.244	2.855	124.2	[41]
A8	γ	2.322	2.923	118.2	[21]
A9	δ	2.151, 2.138[b]	2.472	96.5, 94.6[b]	[42]
A11a	ζ	2.017	2.876	145.1	[44]

[a]Not available. [b]Bifurcated agostic interaction.

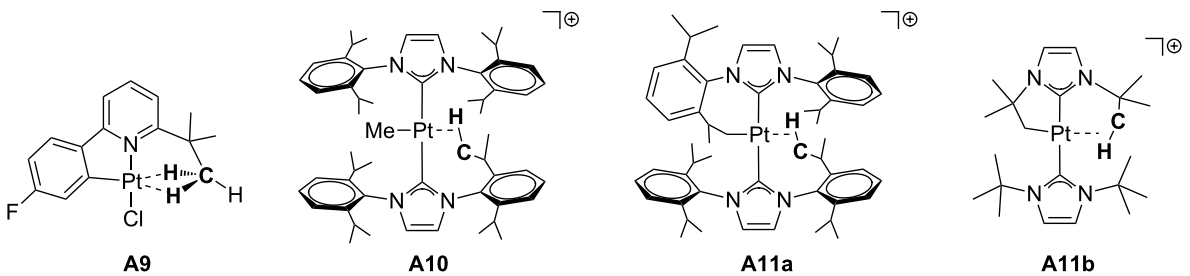

Figure 8: Phenylpyridine and NHC-based agostic T-shaped Pt(II) complexes.

β-agostic interactions in **A1a** and **A2b**. In addition, Pt–H–C angles larger than 100° correlate with large Pt–C distances as shown in **A7**, **A8** and **A11a**. Although a remote contact is described in **A11a**, the largest distances correspond with the γ-agostic **A8**. In other words, the strength of the agostic interaction is not only governed by geometrical constraints and the surroundings of the CH group, but also by the *trans* influence of the ligand in *trans* position with respect to the agostic interaction [23,24]. In this case, the boryl ligand in **A8** exhibits a higher *trans* influence than the alkyl group in **A11a** [45,46], and therefore the agostic interaction in the former is weaker.

Masked T-shaped via counteranion interaction

Most of the T-shaped Pt(II) complexes are cationic. Thus, there is the possibility of stabilizing the unsaturated structure by nonbulky, weakly coordinating counteranions. Triflate (OTf = SO_3CF_3) and tetrafluoroborate are the best candidates to play such a role (Figure 9). All the well-characterized compounds bear a coordinated triflate anion. In the 80s, Whitesides et al. described the synthesis of *trans*-[Pt(Np)(OTf)(PMe_3)$_2$] (Np = neopentyl) **C1a**. This compound reacts with benzene forming *trans*-[Pt(Ph)(OTf)(PMe_3)$_2$] **C1b** through a mechanism that involves *trans*-[Pt(Np)(PMe_3)$_2$]$^+$ as a reactive intermediate [47]. The labile character of the coordinated triflate has been alleged to justify the significant difference between the $^1J_{Pt,P}$ found for [Pt(Me)(OTf)(dmpe)] **C2** (dmpe = 1,2-bis(dimethylphosphino)ethane) in CD_2Cl_2 (4572 Hz) and in acetone (4305 Hz). In the latter media one solvent molecule is proposed to displace the triflate ligand, forming [Pt(Me)(acetone)(dmpe)][OTf] [48]. The complex [Pt(Me)(OTf)(dbbipy)] **C3** (dbbipy = 4,4'-di-*tert*-butyl-2,2'-bipyridine) was prepared by treatment of [PtCl(Me)(dbbipy)] with AgOTf [49]. Regarding tridentate ligands, the X-ray structure of the triflate complex [Pt(3,3'-iPr$_2$-BQA)(OTf)] **C4b** (BQA = bis(8-quinolinyl)amine) shows a coordinated OTf ligand (Pt–O = 2.097 Å) in *trans* position to the amido N-donor of the pincer-like amido ligand. In solution, the labile triflate ligand can be displaced, allowing a reaction with benzene [50]. Milstein and co-workers have reported a series of pincer-type Pt(II) complexes **C5**–**8** containing an XCX ligand core (X = N, P), incorporating the anions OTf^- and BF_4^- [51-53]. The structure of **C5b** was determined by X-ray crystallography [51]. The Pt–O bond distance in this compound, in which the triflate anion is coordinated to platinum in *trans* position with respect to the aromatic ring, is considerably longer than in **C4b** (**C4b**: 2.097 Å [50]; **C5b**: 2.249 Å [51]). The weakly coordinating character of triflate accounts for its sensitivity to the *trans* influence.

Masked T-shaped via solvent coordination

In solution, a solvent molecule can occupy the vacant position of a T-shaped three-coordinate Pt(II) compound via σ-interaction. A number of phosphine-based complexes with different solvent molecules coordinated to the T-shaped frame have been characterized (Figure 10). In this regard, Kubas and co-workers prepared a set of hydride *trans*-[PtH($PiPr_3$)$_2$(solv)]$^+$ compounds where "solv" stands for η^1-$ClCH_2Cl$ (**S1a**), OEt_2 (**S1b**) and THF (**S1c**) solvent molecules [54]. Interestingly, the closely related species **T1** (Figure 5) does not include any solvent molecule filling the vacancy [19]. Moreover, the structures of **S1a** and **S1c** were fully confirmed by X-ray studies. The similar dichloromethane adduct **S1d** was later detected by NMR spectroscopy [55]. This work was extended to methyl complexes

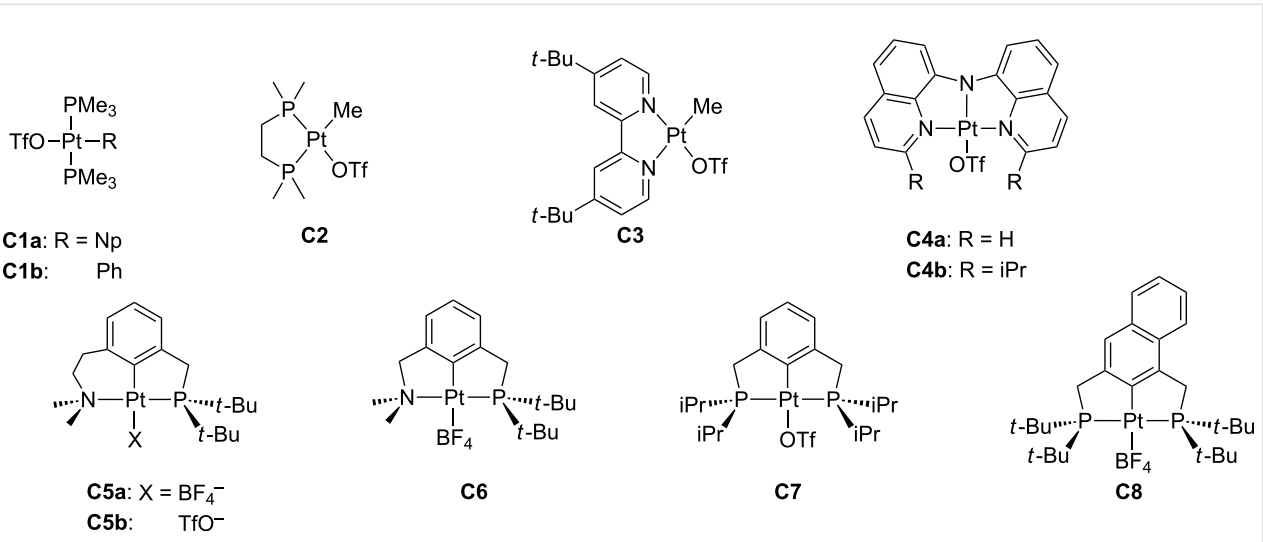

Figure 9: Counteranion coordination in T-shaped Pt(II) complexes.

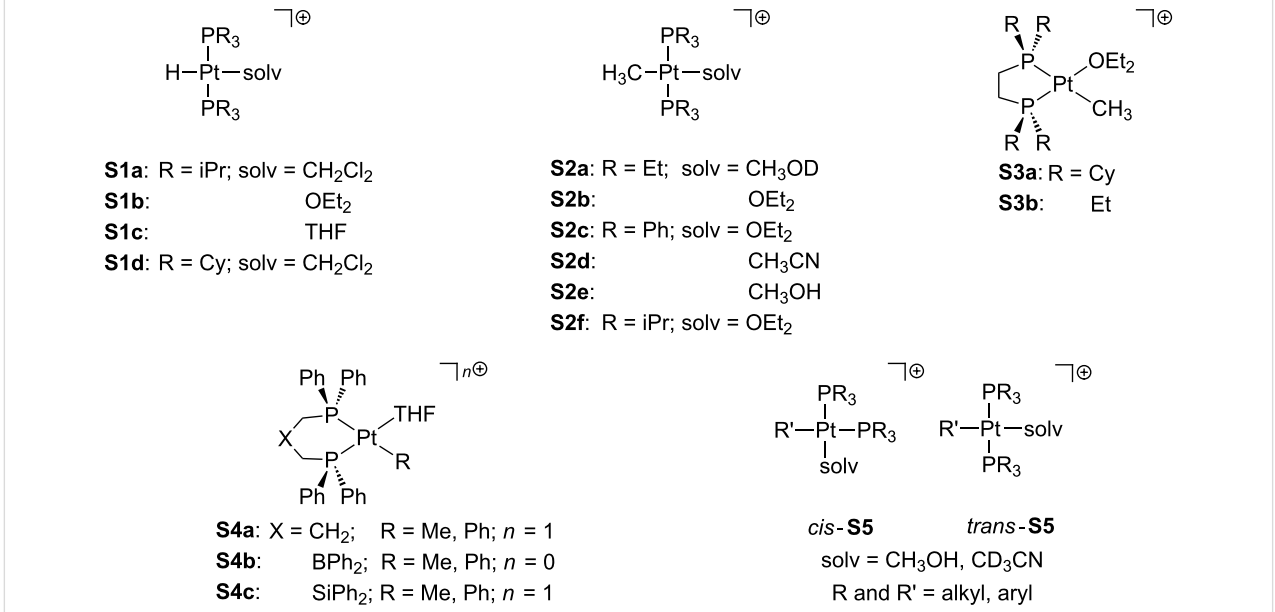

Figure 10: Phosphine-based solvento Pt(II) complexes.

with the formula *trans*-[Pt(Me)$(PR_3)_2$(solv)] (**S2**) [56,57]. Similar structures have been obtained by the use of chelating phosphine ligands in diethylether (**S3**) [58]. In this line, Peters and co-workers developed several bidentate phosphine ligands to yield complexes **S4** in which one THF molecule is coordinated to the metal center [59,60]. Romeo's group was actively working on solvento Pt(II) complexes **S5**. For instance, they employed an extended series of phosphine ligands to obtain *cis* and *trans*-solvento complexes containing methanol [61]. The formation of acetonitrile-d_3 adducts with triethylphosphine ligands was also reported [2,62].

Several examples involving chelating nitrogen-based ligands have also been reported (Figure 11). Bercaw and co-workers developed cationic solvento Pt(II) complexes **S6** bearing tetramethylethylenediamine (tmeda) [63]. X-ray crystallography of **S6a**·BAr^F and **S6c**·BAr^F verified the solvent coordination [64]. Diimine analogues, valuable in C–H bond-activation processes, have been extensively reported elsewhere (**S7**) [65-72]. Later, Tilset's group prepared and characterized a set of solvento tolyl complexes of the type [Pt(Tol)(N–N)(CH_3CN)] **S8** by means of ^1H and ^{19}F NMR [73]. The formation of *p*-xylene derivates **S9** containing a molecule of the weakly coordinating 2,2,2-trifluoroethanol (TFE) has also been reported [69,74]. Unsaturated bipyridyl compounds **S10** have been isolated in which the presence of solvent molecules has been detected [75,76]. The stabilizing role of the solvent molecule is quite relevant. For instance, the removal of the THF molecule in **S10b** provokes the decomposition of the complex [75]. The facile displacement of the solvent ligand allows the use of these

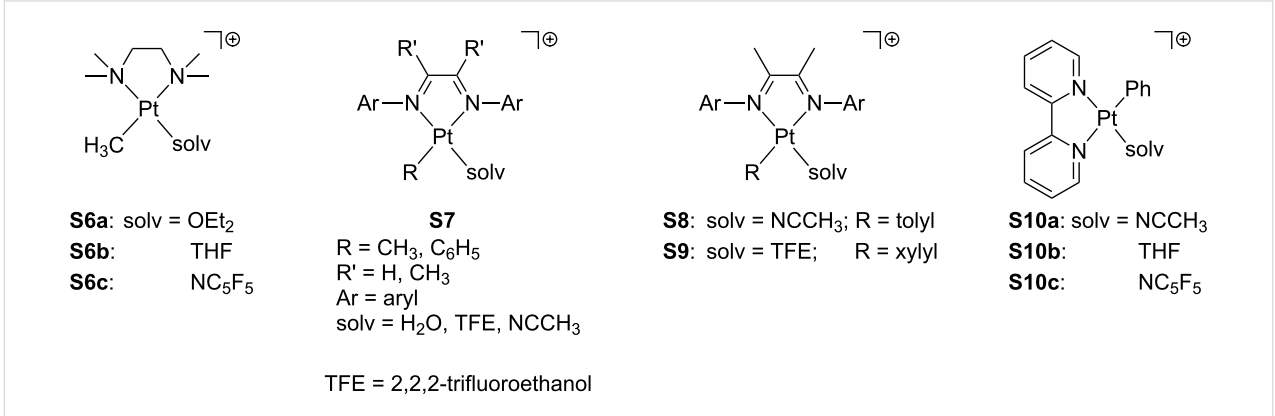

Figure 11: Nitrogen-based solvento Pt(II) complexes.

compounds as catalysts in hydrophenylation reactions [76]. Other related complexes have been prepared elsewhere [77-81].

Pincer ligands [82,83] naturally define a three-coordinate environment and, in this way, they are well-suited as ligands in T-shaped compounds. Accordingly, a number of T-shaped Pt(II) pincer complexes with an additional solvent molecule as a fourth ligand have been reported (**S11**–**19**, Figure 12). Van Eldik and co-workers studied the aquo complexes **S11** by using several tridentate nitrogen-based ligands (NNN) [84]. Peters and co-workers isolated [Pt(OTf)(NNN)] species, though NMR data were collected in acetonitrile-d_3 solution, in which the solvento adduct **S12** is favored [50]. Extensive work carried out by van Koten and co-workers [85,86] concerned NCN aquo compounds such as **S13**. Unsaturated complexes bearing NCP ligands were characterized by Milstein and co-workers, including water (**S14a**) [51] and acetone (**S14b**) [87] solvent molecules. Isolation of compound **S15** in acetone/pyridine solution provided suitable crystals for X-ray studies, which showed that a pyridine molecule has been added [87]. Other investigations have been devoted to complexes with PCP ligands. For instance, Bullock and co-workers prepared a dihydrogen adduct of the type $[PtH_2(PCP)]^+$ in dichloromethane, but NMR data suggest a mixture of the former compound and the corresponding solvento complex **S16a** [88]. Milstein et al. proposed that the closely related complex **S16b** exists in THF solution, since an interaction with the BF_4^- counteranion is not observed, although the elemental analysis evidences the lack of the THF molecule in the solid state [89]. Contrarily, the naphthyl derivative **S17** was found together with the BF_4^- adduct **C8** (Figure 9) [53]. For silicon-related ligands, Turculet and co-workers successfully crystallized **S18** in a diethylether solution at low temperature, showing one diethylether molecule directly coordinated to the platinum center [90]. A set of dicationic complexes based on carbene groups have been developed by Limbach and co-workers, forming pyridine **S19a** and acetonitrile **S19b**,**c** adducts [91].

The relevance of solvent-stabilized T-shaped Pt(II) complexes extends beyond the organometallic field. Their presence in cisplatin–protein adducts has also been proposed concerning the bovine Cu, Zn superoxide dismutase [92] and the hen egg white lysozyme [93]. The corresponding crystallographic structures show the platinum coordinated to a histidine residue of the protein and two ligands (Cl^- [92] or NH_3 [93]). However, in both situations the fourth ligand was not fully detectable, so that the authors suggested the participation of a coordinating water molecule. Indeed, quantum mechanics/molecular mechanics (QM/MM) calculations on the cisplatin–hen egg white lysozyme adduct confirmed the facile inclusion of a solvent water molecule in the first coordination shell of the platinum complex (Figure 13) [94].

NMR coupling constants to ^{195}Pt as sensitive probes for coordinatively unsaturated Pt(II) complexes

NMR spectroscopy has provided additional evidence for the existence of low electron-count Pt(II) complexes not only

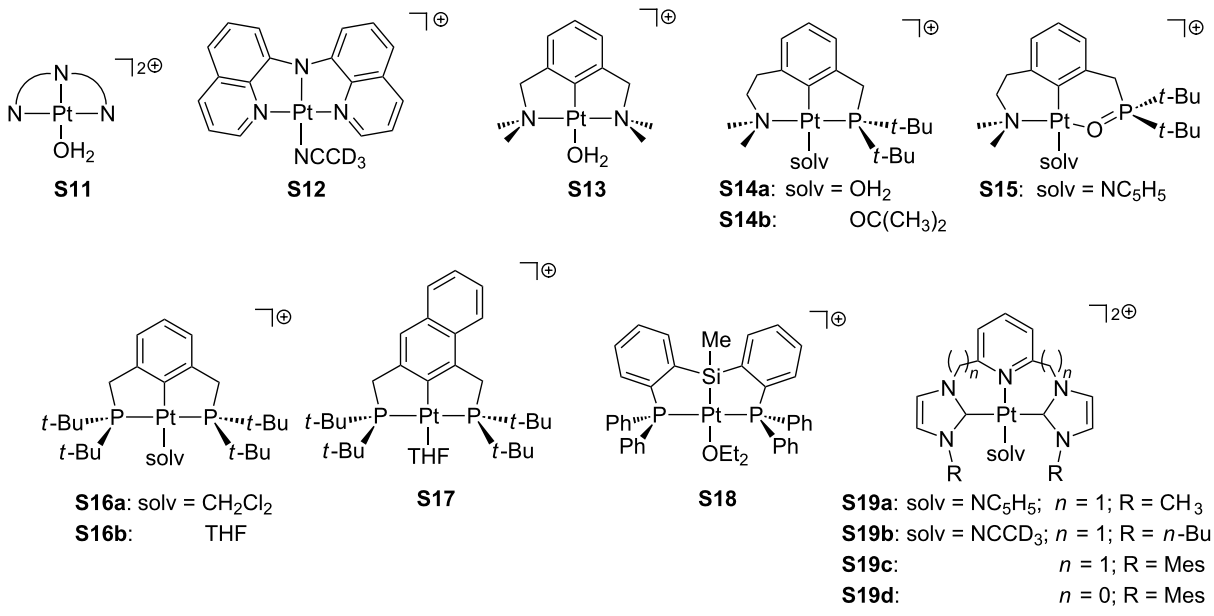

Figure 12: Pincer-based solvento Pt(II) complexes.

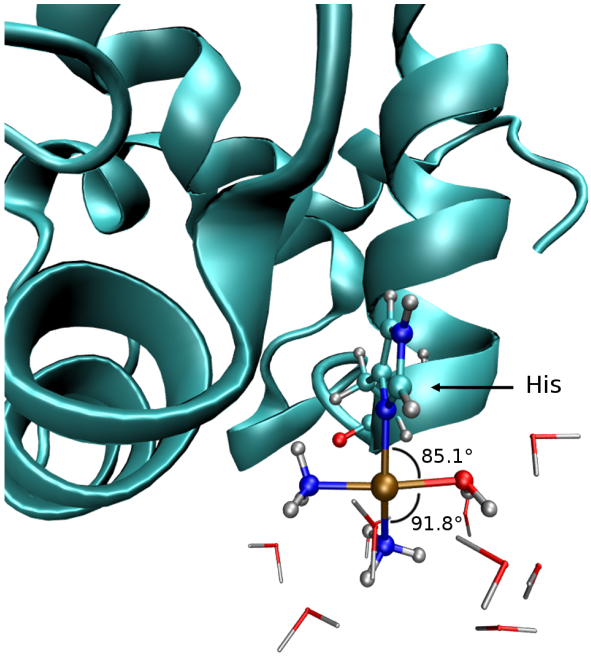

Figure 13: Structure of the QM/MM optimized cisplatin–protein adduct [94].

through the observation (in some cases) of NMR signals for the C–H bonds involved in agostic interactions, but also by the magnitude of the coupling constant of some of the ligands around the metal center with the NMR active ^{195}Pt nuclei (33.7% natural abundance). This is actually not the case with ^{31}P NMR, for which the $J_{Pt,P}$ values seem to be virtually insensitive to the nature of the complex. As an example, in the boryl derivatives reported by Braunschweig et al. [21] the $J_{Pt,P}$ coupling constant is almost the same both in the starting material, [Pt(BR$_2$)Br(PCy$_3$)$_2$], and in the three-coordinate Pt(II) species, [Pt(BR$_2$)(PCy$_3$)$_2$][BAr^F] **T2**. On the other hand, the coupling constants of the proton and carbon atoms of alkyl and hydride ligands with ^{195}Pt are very sensitive to the presence of coordinating ligands *trans* to them (Figure 14).

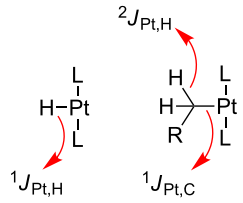

Figure 14: NMR coupling constants used for the characterization of three-coordinate Pt(II) species.

A nice example is illustrated in the hydride, T-shaped Pt(II) complex *trans*-[PtH(P*t*-Bu$_3$)$_2$][X] **T1** (X = PF$_6$, BF$_4$, ClO$_4$, SO$_3$CF$_3$) reported by Goel and Srivastava [19]. The magnitude of the $^1J_{Pt,H}$ coupling constant of the hydride ligand in its precursor *trans*-[PtHCl(P*t*-Bu$_3$)$_2$] is 1070 Hz, but in the 14-electron derivative *trans*-[PtH(P*t*-Bu$_3$)$_2$][X] **T1** it increases to ca. 2600 Hz, the largest $^1J_{Pt,H}$ reported in the literature. A decrease of this coupling constant to 2050–2070 Hz was observed in the related hydride Pt(II) complexes *trans*-[PtH(PR$_2$(2,6-Me$_2$C$_6$H$_3$))$_2$]$^+$ (Figure 7, R = Ph **A6a**, Cy **A6b**, iPr **A6c**), which are stabilized by agostic interactions involving the methyl groups of the aryl fragments. In the same vein, weakly coordinating ligands such as the solvent stabilized Pt(II) derivatives *trans*-[PtH(ClCH$_2$Cl)(PR$_3$)$_2$][BAr^F] (Figure 10, R = iPr **S1a**, Cy **S1d**) exhibit a smaller $J_{Pt,H}$ of 1480 (R = Cy) or 1852 Hz (R = iPr) in agreement with the presence of a ligand *trans* to the hydride. With regard to Pt–H two-bond and Pt–C one-bond coupling constants in Pt–C$_{alkyl}$ complexes (Figure 15 and Table 2), Weller et al. reported that the methyl group in the complex *trans*-[Pt(Me)(PiPr$_3$)$_2$]$^+$ **A7** exhibits a $^2J_{Pt,H}$ value of 106 Hz. This value is almost identical to those reported for the NHC derivatives *trans*-[Pt(Me)(NHC)$_2$]$^+$ (NHC = IMes* **T4a**, IMes **T4b**; 110 and 103 Hz, respectively). The $^1J_{Pt,C}$ is also very large for these methyl derivatives, ranging from 755 to 780 Hz (Table 2). Cyclometalated phosphine [39,40] and NHC [28,44] Pt(II) compounds were also shown to have very large $^2J_{Pt,H}$ coupling constants (slightly larger than those for the non-cyclometalated versions) spanning from 107 Hz to ca. 135 Hz (average) and $^1J_{Pt,C}$ values between 805 and 975 Hz.

Table 2: NMR coupling constants of selected three-coordinate Pt(II) complexes.

Complex	$^2J_{Pt,H}$/Hz	$^1J_{Pt,C}$/Hz	Reference
A7	106	755	[41]
T4a	103	—[a]	[28]
T4b	110	—[a]	[28]
A10	—[a]	780	[44]
A5a	109	840	[39]
A5b	107	806	[39]
A5c	107	—[a]	[40]
T5a	132 (av.)	—[a]	[28]
T5b	135	—[a]	[28]
A11a	113 (av.)	860	[44]
A11b	120	975	[44]

[a]Not available.

In those cases where solvent molecules (THF, acetonitrile) have been reported to coordinate to some of the complexes shown in Figure 15, smaller values of both the $^2J_{Pt,H}$ and the $^1J_{Pt,C}$ coupling constant are observed. For example, the $^2J_{Pt,H}$ of the methyl ligand decreases to 98 Hz in the THF adduct of derivative **A7**, whereas the acetonitrile adduct of complex **A11b**

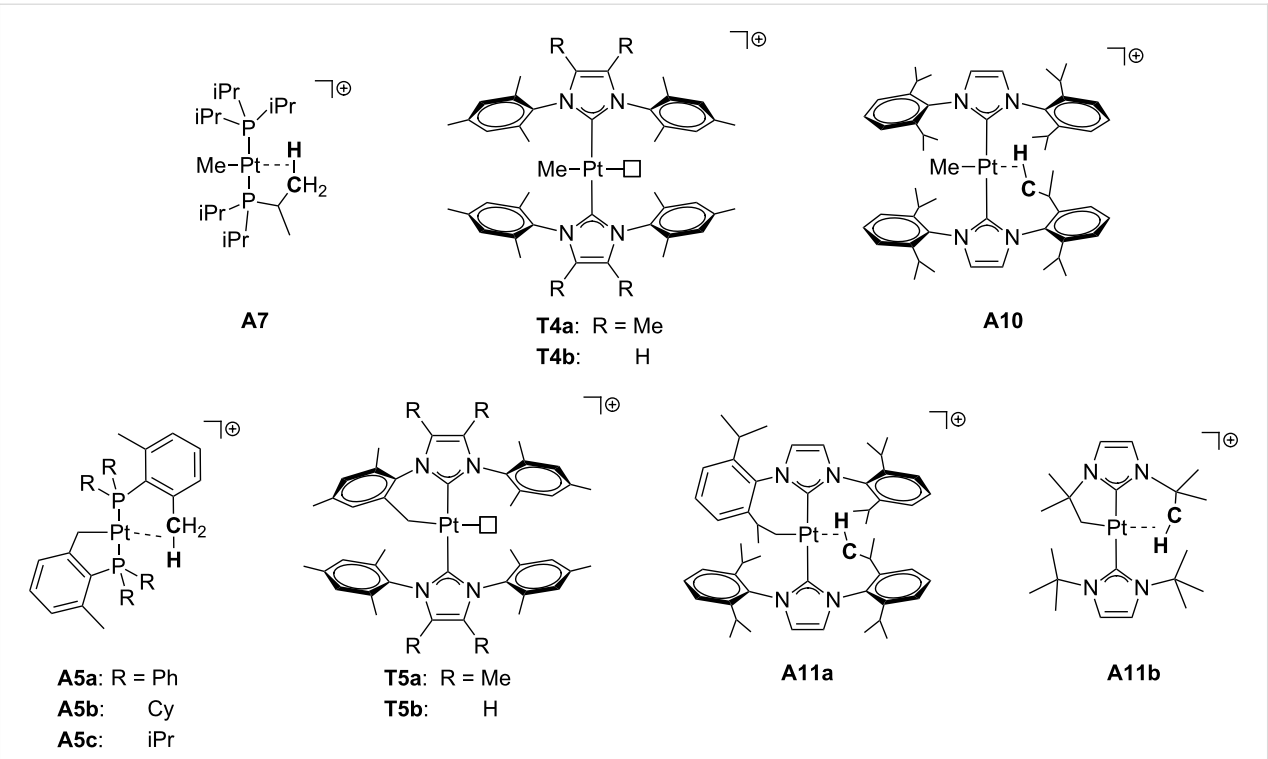

Figure 15: The chemical formula of the complexes discussed in Table 2.

(**A11b**·NCMe) shows resonances for the Pt–CH_2 fragment with $^2J_{Pt,H}$ and $^1J_{Pt,C}$ values of 87 and 798 Hz, respectively [28].

Synthetic routes to stable, solvent-stabilized and transient 14-electron Pt(II) species

True and agostic T-shaped Pt(II) complexes

Several methods have been described to prepare coordinatively unsaturated Pt(II) complexes with a T-shaped geometry. Although the number of species that have been authenticated by crystallographic or spectroscopic methods is still very limited, the best and most general method for obtaining them is by removing a halogen ligand (Cl, Br, I) from the platinum coordination center in **1** by using a halogen abstractor with a poor coordinating anion, such as tetrakis[3,5-(trifluoromethyl)phenyl]borate or hexafluoroantimonate (Scheme 1) [19-21,28,39,44].

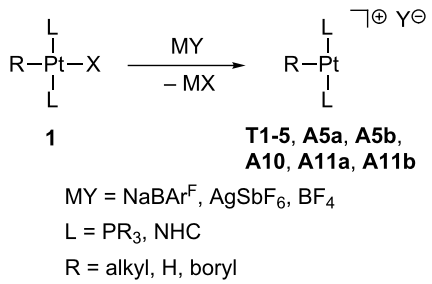

Scheme 1: Halogen abstraction from **1**.

This procedure has been successfully employed for the generation of complexes stabilized by two phosphine PR_3 or two NHC ligands, in which the third coordination site is occupied by alkyl, hydride or boryl ligands. Therefore, high *trans*-influence ligands are present in all these cases, favoring the dissociation of the Pt–X bond. The generality of this method is so powerful that it has provided access to an intriguing dicationic borylene Pt(II) complex **T3** which is not stabilized by agostic interactions (Scheme 2) [22].

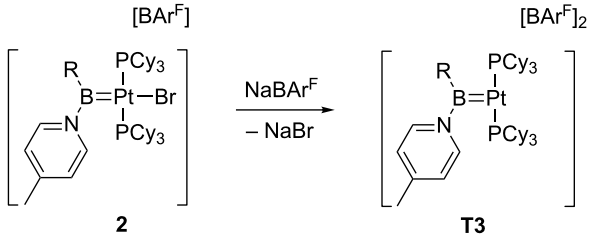

Scheme 2: Halogen abstraction from **2** forming the dicationic complex **T3** [22].

A stable T-shaped structure *trans*-$[Pt(Me)(PiPr_3)_2]^+$ (**A7**) has also been generated [41] by methide abstraction from the neutral derivative *cis*-$[Pt(Me)_2(PiPr_3)_2]$ by using highly electrophilic Lewis acids such as $B(C_6F_5)_3$ or $[CPh_3][1\text{-H-}closo\text{-}CB_{11}Me_{11}]$ (with the concomitant formation of $MeB(C_6F_5)_3^-$ or $MeCPh_3$, respectively). This synthetic route uses the same procedure described by Goldberg et al. for the generation of a transient, neutral Pt(II) derivative $[Pt(Me)(\kappa^2\text{-}Tp^{Me2})]$ from the anionic Pt(II) complex $K[Pt(Me)_2(\kappa^2\text{-}Tp^{Me2})]$ [95]. Alternatively, the cationic compound $[Pt(Me)(PiPr_3)_2]^+$ was synthesized by homolytic cleavage of the Pt–Me bond by using the neutral radical $[1\text{-H-}closo\text{-}CB_{11}Me_{11}]^\bullet$ as a reagent.

H_2 addition across Pt–C_{alkyl} bonds can also lead to electron-deficient Pt(II) species stabilized by agostic interactions. Baratta and co-workers studied the addition of H_2 to preformed T-shaped Pt(II) complexes **A5a**,**b** to prepare Pt(II) hydrides **A6a**,**b** (Scheme 3) [39].

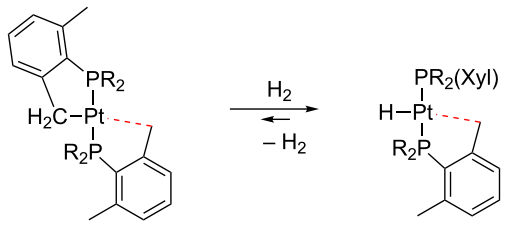

Scheme 3: Hydrogenation of complexes **A5a** and **A5b** [39].

Alternatively, Carmona and co-workers have recently described that the hydrogenation of the 16-electron Pt(II) carbene **3** bearing a cyclometalated phosphine ligand (Scheme 4) resulted in the formation of the cyclometalated complex **A5c**, which can be further hydrogenated to give the Pt(II) hydride **A6c** [40], similar to those reported by Baratta [39].

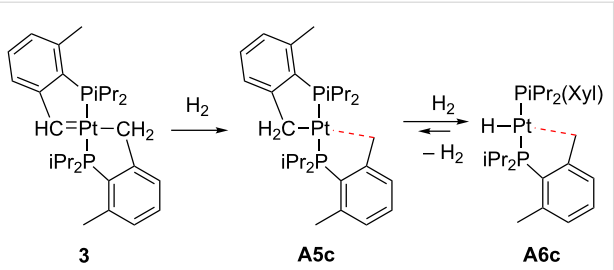

Scheme 4: Hydrogenation of complexes **3** and **A5c** [40].

Low electron-count species can also be prepared by C–H bond-activation reactions from coordinatively unsaturated compounds in a way similar to the addition of H_2 to Pt–C_{alkyl} bonds mentioned above. The cyclometalated complex **T5a** shown in Scheme 5 reacts with aromatic compounds to yield the corresponding aryl complexes while keeping the unsaturated nature at the platinum atom. The complexes thus synthesized are not stabilized by agostic interactions according to spectroscopic (NMR), crystallographic and theoretical methods [28].

Spencer et al. reported that the formation of stable electron-deficient Pt(II) complexes stabilized by strong β-agostic interactions can be accessible by protonation of electron-rich alkene Pt(0) compounds **4** (Scheme 6) [35,36].

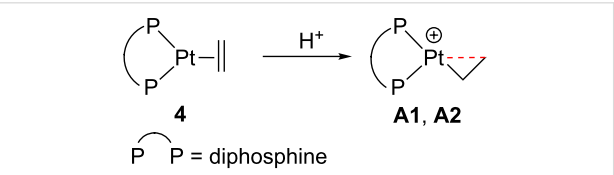

Scheme 6: Protonation of complexes **4** [35,36].

Finally, Rourke et al. isolated a neutral Pt(II) derivative **A9** by a direct and simple approach that involves a cyclometalation process of the 2-substituted bulky pyridine **5** when it is reacted with the platinum salt K_2PtCl_4 (Scheme 7) [43].

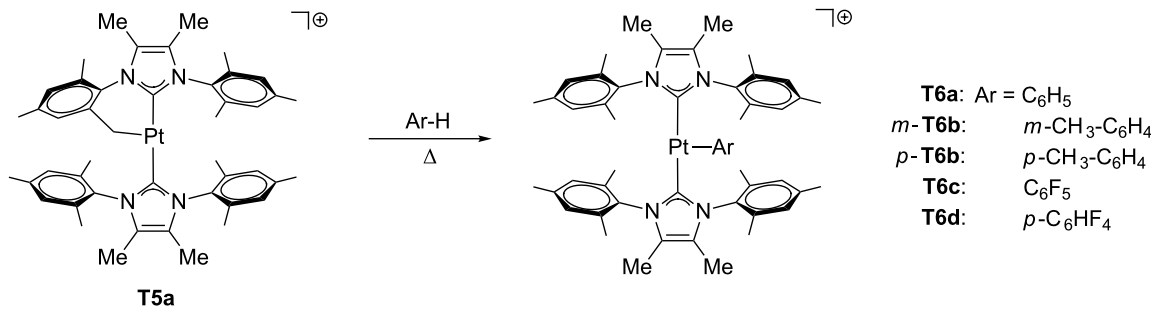

Scheme 5: Intermolecular C–H bond activation from **T5a** [28].

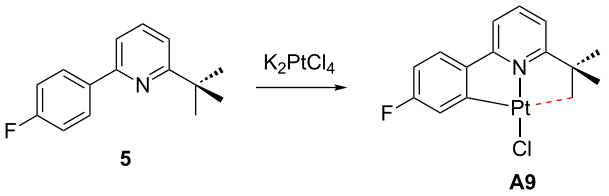

Scheme 7: Cyclometalation of **5** [43].

Pt(II) complexes stabilized by solvent molecules

Although some of these compounds have been prepared by halogen [58] or methide [74] abstraction as described above, the vast majority of the Pt(II) derivatives stabilized by solvent molecules have been obtained by protonation of neutral alkyl, aryl or hydride Pt(II), as shown in Scheme 8 (see for example: [55,59,60,63,67,69,72,77-81]), or Pt(IV) complexes [96-98]. Nonetheless, this method has not yet been exploited for the preparation of true 14-electron species or agostic stabilized derivatives.

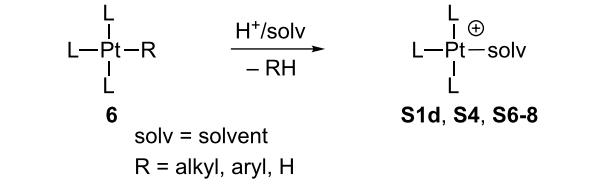

Scheme 8: Protonation of **6**.

Transient electron-deficient Pt(II) complexes from six- and five-coordinate Pt(IV) derivatives

In some cases, transient, highly reactive 14-electron Pt(II) compounds have been generated by thermal decomposition of trimethyl, five-coordinate Pt(IV) complexes **7**. These latter compounds are in some cases sufficiently stable to be isolated and characterized by X-ray diffraction studies, but thermally unstable at moderate to high temperatures releasing ethane and a three-coordinate Pt(II) intermediate $[Pt(Me)L_2]^+$ (Scheme 9). The coordinatively unsaturated complexes $[Pt(Me)L_2]^+$ thus generated undergo subsequent reactivity with appropriate reagents [99-102].

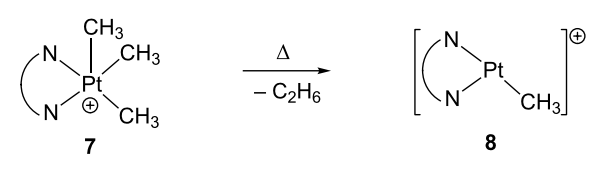

Scheme 9: Reductive elimination of ethane from **7**.

Similarly, methane reductive elimination from Pt(IV) complexes $[PtH(Me)(R)(\eta^3\text{-}N_3)]^{n+}$ **9** (R = Me, H; N_3 = tris-pyridine[2.1.1]-(2,6)-pyridinophane or tris(pyrazolyl)borate; *n* = 0, 1) produces a transient three-coordinate Pt(II) complex $[Pt(R)(\eta^2\text{-}N_3)]^{n+}$ **10** (Scheme 10), which is able to activate C–H bonds of hydrocarbons or form solvent adducts [103-105].

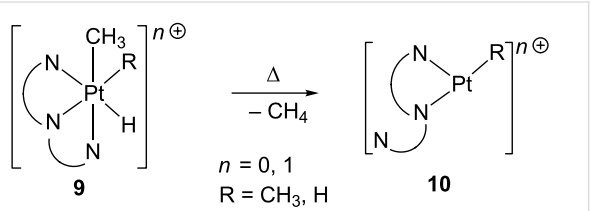

Scheme 10: Reductive elimination of methane from six-coordinate Pt(IV) complexes.

Solution behavior

In masked three-coordinate d^8 complexes, the fourth coordination site is occupied by a weakly bound ligand, which can be easily displaced. In this way, in solution the ligands of these compounds are opened to conformational events that will be discussed in this section. The empty site can also be available for incoming substrates, allowing the participation of these complexes as reaction intermediates. This aspect will be discussed in the next section.

Most of the reports of fluxional processes correspond to agostic bonded complexes. The equivalence of ^1H and ^{13}C chemical shifts observed in solution for the γ-, δ- and remote-agostic contacts is a common feature of the complexes collected in Figure 15 and arises from the rapid intramolecular exchange of the C–H bond involved in the agostic interaction. In several cases, such as **A11a** [44], the overlapping of the proton signals and signal averaging of the ligands avoid drawing a conclusion about the nature of the agostic interaction at work in solution. Recently, ab initio molecular dynamics (AIMD) simulations of some representative T-shaped Pt(II) complexes (**T5b**, **A2b** and **A11a**), performed in explicit dichloromethane solvent, have provided a detailed description of the mechanism by which the equivalence of signals takes place [106]. Simulations showed that the dynamics of the agostic interaction in solution strongly depends on the complex. Contingent upon the strength of the agostic interaction and the flexibility of the ligand, several events related with the occupation of the fourth coordination site by an agostic bond could happen: (i) the same C–H bond maintains the agostic interaction with the platinum atom for the entire simulation (**A2b**); (ii) an agostic interaction is present throughout the simulation, though the C–H bond changes by a rotation of alkyl groups (**A11b**); (iii) the agostic interaction moves on and off (**A11a**) [106].

There are indirect evidences that agostic bonds, solvent and weakly coordinating counteranions could easily exchange their role of stabilizing the unsaturated complex by placement at the vacant site. Although no kinetic studies on exchanges of these kinds of ligands have been reported, the detection of the agostic and solvent complexes for the same system and, for pincer complexes, of the counteranion and solvent forms, suggests that the exchange can take place. For instance, in *trans*-$[Pt(Me)(PiPr_3)_2]^+$ (**A7**) a γ-agostic interaction can be displaced by addition of THF, forming the corresponding adduct [41]. NMR data in CD_3CN of the triflate complex [Pt(BQA)(OTf)] (**C4a**) leads to its formulation as $[Pt(BQA)(NCCD_3)][OTf]$ (**S12**) [50]. Similar behavior has been observed for other pincer complexes. The naphthyl-based PCP–Pt(II) complex was found in THF as a 1:2 mixture of the counteranion (BF_4^-, **C8**) and solvent (**S17**) forms [53].

Energetically accessible T-shaped species can also be intermediates in the site exchange of bidentate ligands of square-planar complexes. Fluxional motions of the 2,9-dimethyl-1,10-phenanthroline ligand (dmphen) have been observed in cationic complexes as $[Pt(Me)(NN)(L)]^+$ (NN = dmphen; L = SOR(R'), PR_3) [107-111]. The driving force of these flipping processes is the distortion of the dmphen ligand with respect to the coordination plane, which is caused by the methyl groups. Indeed, the fluxional motion is not detected when the unhindered 1,10-phenanthroline ligand is used. Interestingly, the mechanism can be switchable between associative and dissociative [107-109]. For the latter scenario, 14-electron T-shaped species involving phosphine ligands can be envisaged as feasible intermediates. The dissociative pathway fully prevails when overcrowded PR_3 ligands are employed, where R stands for *o*-methoxyphenyl **11** [110] and *o*-tolyl **12** [111]. The detailed mechanism (Scheme 11) is described as follows: (i) dissociative nitrogen decomplexation, (ii) isomerization between two nonequivalent exchanging sites, and (iii) nitrogen coordination recovering the initial chelating situation. The fluxional motion of dmphen is not affected by the counteranion, solvent, or the presence of weak nucleophiles deliberately added. In addition, for **11a** and **12a** both flipping of dmphen and phosphine rotation motions are synchronized, behaving as molecular gears. The calculated activation barriers are ca. 13.3 and 16.4 kcal mol^{-1} for the motions involving **11** and **12**, respectively.

Concerning 14-electron intermediates **b** and **b'**, the assistance of methoxy groups in **11b**,**b'** [110] as well as the presence of agostic interactions in **12b**,**b'** [111] can be postulated (Figure 16). Indeed, **12a** easily undergoes a cyclometalation process, probably assisted by an agostic contact via intermediate **12b**.

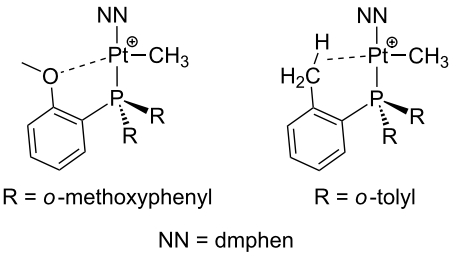

Figure 16: Feasible interactions for unsaturated intermediates **11b** (left) and **12b** (right) during fluxional motions [110,111].

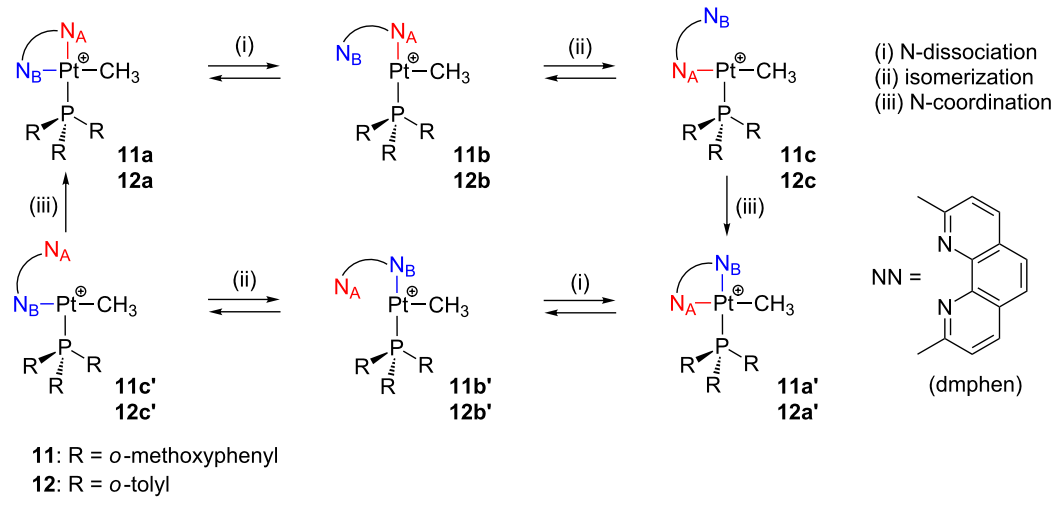

Scheme 11: Proposed dissociative mechanism for the fluxional motion of dmphen in $[Pt(Me)(dmphen)(PR_3)]^+$ complexes.

Three-coordinate Pt(II) species as reaction intermediates

Coordinatively unsaturated Pt(II) species are considered as intermediates in many organometallic processes. Early studies by Whitesides and co-workers dealing with the thermal decomposition of $[Pt(R)_2L_2]$ complexes demonstrated that the dissociation of a phosphine ligand is a preliminary requisite for the reaction to occur [112]. Since then, T-shaped three-coordinate 14-electron intermediates have been proposed in a large number of reaction mechanisms. A review concerning dissociative pathways in Pt(II) complexes was published in 1990 [113].

Due to both the low electron count and the presence of a vacant site in the coordination sphere, T-shaped Pt(II) species are suitable intermediates in ligand-exchange and bond-breaking processes of unreactive bonds, such as C–H bond activations. A selection of results from the past few years regarding these two issues are collected in this section to illustrate the growing importance of three-coordinate Pt(II) species as reaction intermediates.

Intramolecular C–H bond activation

Intramolecular C–H bond activation is a common reaction of unsaturated Pt(II) complexes. Cyclometalation processes, sometimes involving agostic situations [114], have been thoroughly reviewed recently [115].

According to Baratta and co-workers, the abstraction of Cl from **13a**,**b** with $Na[BAr^F]$ directly generates the cyclometalated products **A5a**,**b** and methane (Scheme 12) [39]. Unsaturated intermediates such as $[Pt(Me)(PR_3)_2]^+$, probably stabilized by agostic contacts, might be considered.

Weller et al. reported some reactivity features of complex **A7** [41]. Although it shows an agostic interaction, no cyclometalation via C–H bond activation is observed in CD_2Cl_2 (40 °C, 7 days). However, the addition of THF rapidly traps the T-shaped complex forming the adduct **14** (Scheme 13). This species does undergo cyclometalation in the presence of trace amounts of acids to yield **16** [116]. The unsaturated agostic species **15** has been proposed as a reaction intermediate.

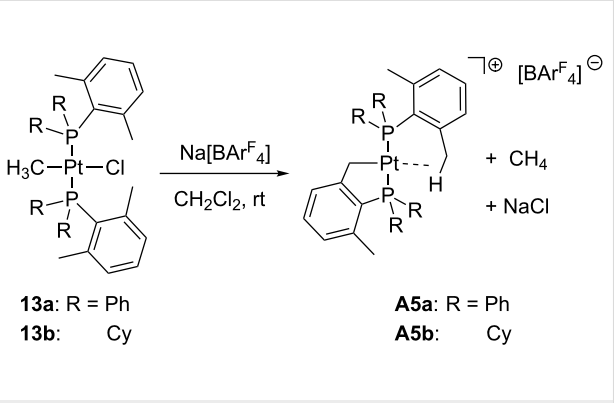

Scheme 12: Halogen abstraction from **13a**,**b** and subsequent cyclometalation to yield complexes **A5a**,**b** [39].

Goldberg and co-workers put forward the participation of T-shaped Pt(II) species in processes, implying the five-coordinate Pt(IV) complex **7a** (Scheme 14) [102]. This compound undergoes reductive elimination in benzene-d_6 solvent with the concomitant formation of ethane. The resulting three-coordinate **8a** is supposed to be stabilized by an agostic interaction or solvent coordination. Indeed, two possible scenarios related to these interactions are envisaged. Firstly, **8a** evolves to **17** through a cyclometalation process ((i) in Scheme 14) which involves one *t*-Bu group of the bidentate ligand. On the other hand, **8a** can also activate the C–D bonds of benzene-d_6 molecules forming **18** ((ii) in Scheme 14). Since both **17** and **18** exhibit potential empty coordination sites, benzene activation from **17** and cyclometalation from **18** are plausible scenarios. Nevertheless, the three-coordinate intermediate **17** is not isolable and reacts further with a molecule of the starting material **7a** leading to the dinuclear species **19**. The inclusion of deuterium atoms in the *t*-Bu groups of **19** suggests that both intra- and intermolecular C–H bond activations are competitive pathways. The transient formation of derivative **17** was confirmed by trapping experiments with ethylene.

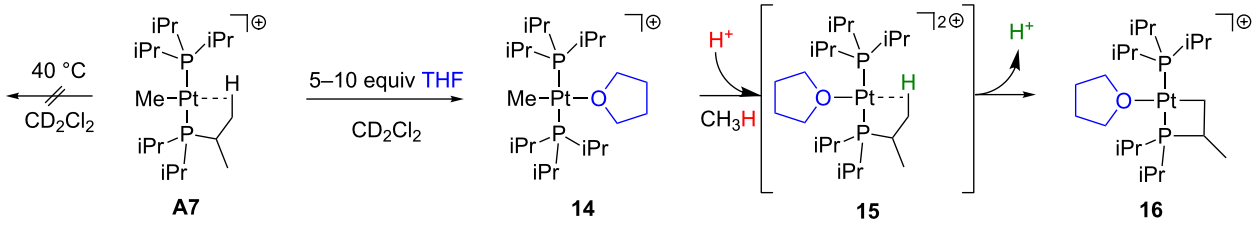

Scheme 13: Proposed mechanism for the acid-catalyzed cyclometalation of **14** via intermediate **15** [41].

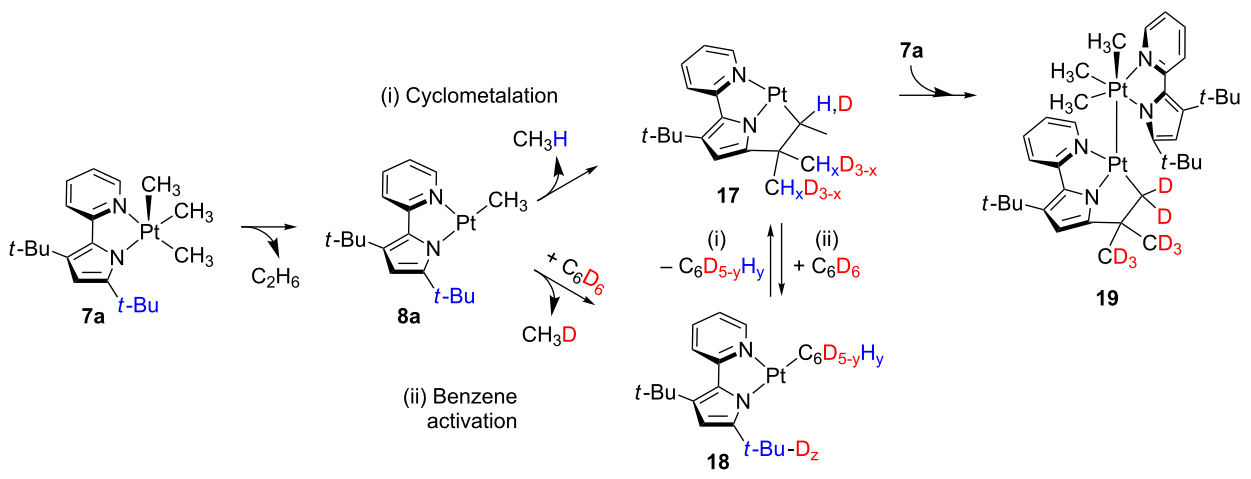

Scheme 14: Proposed mechanism for the formation of **19** [102].

Examples of cyclometalation processes preceded by ligand dissociation have been described by Romeo and co-workers [111,117,118]. For instance, $[Pt_2(Hbph)_4(\mu\text{-}SEt_2)_2]$ **20** (Hbph = η^1-biphenyl monoanion) undergoes cyclometalation to form $[Pt_2(bph)_2(\mu\text{-}SEt_2)_2]$ **22** and biphenyl H_2bph (Scheme 15) [117]. Intramolecular C–H bond activation seems to be driven by thioether dissociation via **21**, a process previously reported for the complex $[Pt_2(Me)_4(\mu\text{-}SMe_2)_2]$ [119].

Marrone et al. computed the cyclometalation process of $[Pt(Me)_2(PR_3)(DMSO)]$ **23** to yield $[Pt(Me)(PR_2R')(DMSO)]$ **28** (R = *o*-tolyl, R' = cyclometalated group; DMSO = dimethylsulfoxide) [120] as experimentally reported in [118]. They demonstrated that the reaction involves coordinatively unsaturated 14-electron T-shaped complexes through (i) DMSO dissociation, (ii) C–H bond activation, (iii) methane release, and (iv) DMSO association (Figure 17). Starting from **23**, initial ligand dissociation generates the T-shaped intermediate **24**, in which one *o*-tolyl group of the phosphine ligand establishes an agostic interaction with the platinum center. This agostic interaction weakens the C–H bond inducing an oxidative-addition (OA) process. The resulting five-coordinate Pt(IV) hydride complex **25**, located at 26.0 kcal mol^{-1} above reactants, quickly undergoes reductive elimination (RE) providing the methane adduct **26**. After methane releasing, the cyclometalated T-shaped structure **27** is obtained, once again stabilized by an agostic interaction. The corresponding transition states for OA and RE processes are isoenergetic with respect to **25**. Finally, the agostic coordination mode in **27** is displaced by a DMSO molecule forming the cyclometalated product **28**. Moreover, they showed that the reaction mechanism starting from the four-coordinate 16-electron complex **23** does not provide low-energy paths for OA, demonstrating the kinetic inertness of these types of compounds.

Three-coordinate species have been invoked by Nolan and co-workers to account for the reaction of *cis*-$[Pt(NO_3)_2L_2]$ **29** with tetramethylthiourea (tmtu) (Scheme 16) [121]. The sulfur atom of tmtu displaces one nitrate ligand of **29** forming **30**, which eventually evolves to the cyclometalated product **33** via C–H bond activation. The increase of nitrate concentration as well as the addition of coordinating agents, such as triethylamine and triphenylphosphine, clearly retard the process. Therefore, a dissociative mechanism has been proposed to

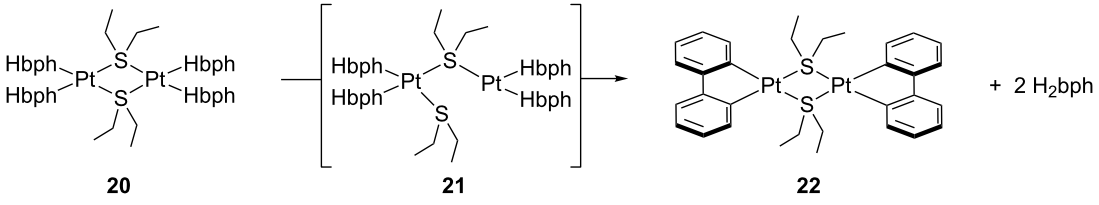

Scheme 15: Cyclometalation of **20** via thioether dissociation [117].

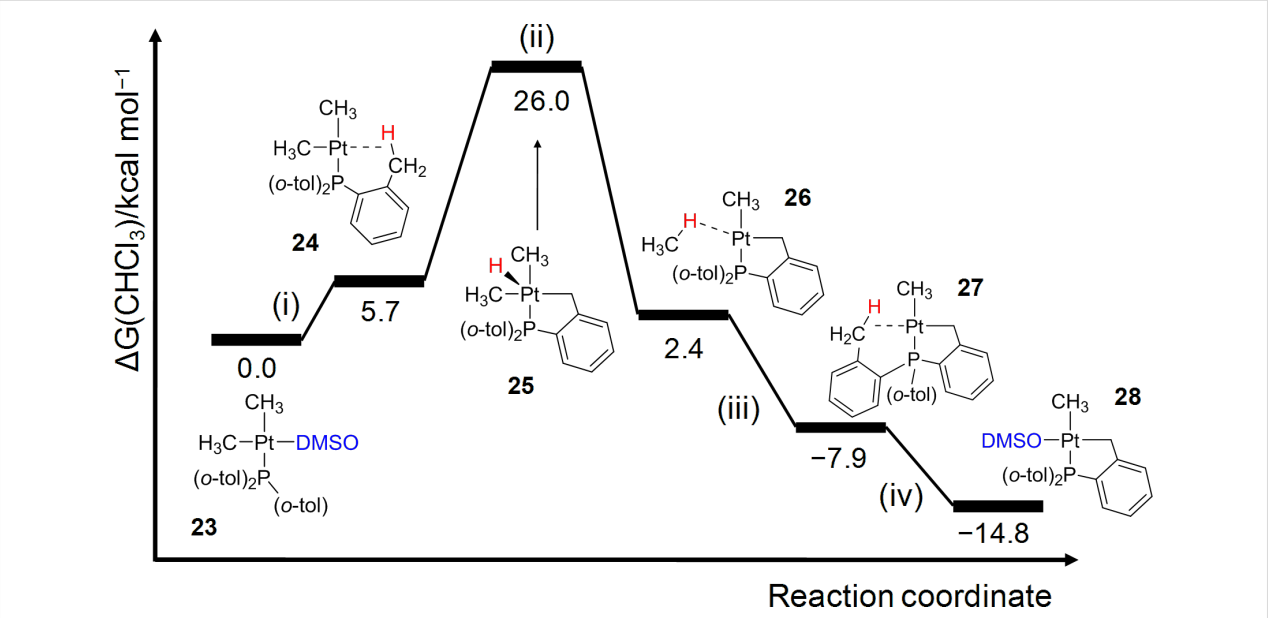

Figure 17: Gibbs energy profile (in chloroform solvent) for the cyclometalation of **23** [120].

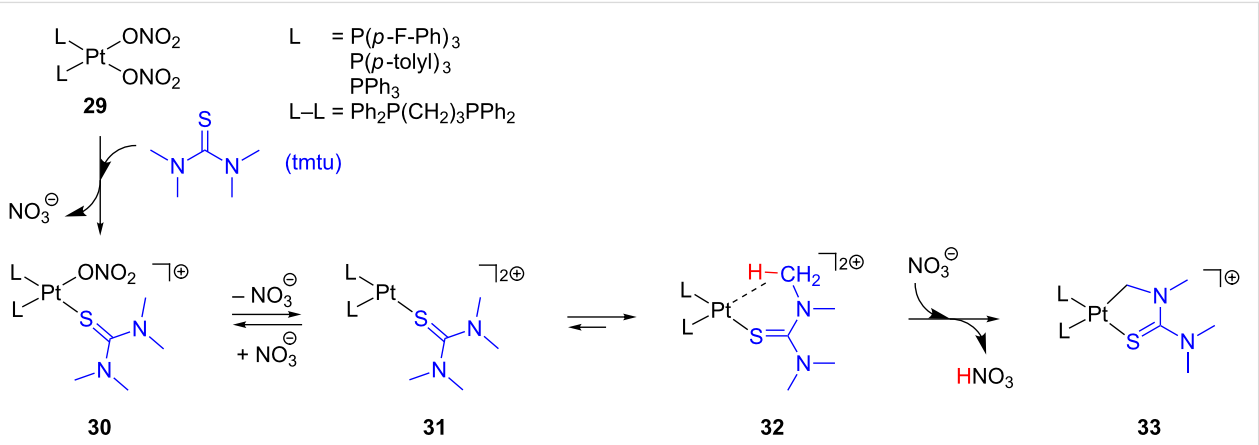

Scheme 16: Coordination of tmtu to **29** and subsequent C–H bond activation via three-coordinate species **31** and **32** [121].

generate the unsaturated species **31**. Then, one methyl group of the coordinated tmtu can stabilize the open coordination site via agostic interaction, **32**, inducing an intramolecular C–H bond activation process to yield **33**. It was also observed that less σ-donor phosphine ligands increase the reaction rate. Less-electron-donating ligands may not stabilize **31**, favoring an agostic contact in **32**, which, consequently, accelerates the cyclometalation reaction. Indeed, the presence of stronger σ-donors such as ICy ligand (1,3-biscyclohexylimidazol-2-ylidene) inhibits the process.

T-shaped Pt(II) complexes bearing NHC ligands can be prepared starting from the pertinent iodo-precursors by halide removal (Scheme 17) [44]. For IPr [44], IMes* and IMes

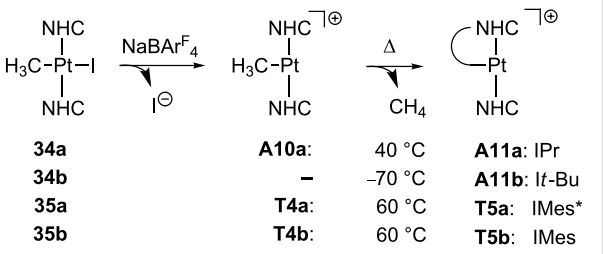

Scheme 17: Cyclometalation process of NHC-based Pt(II) complexes [28,44].

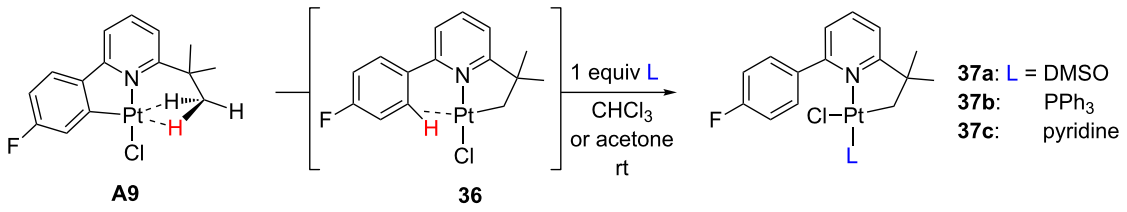

Scheme 18: Cyclometalation process of complex **A9** [43].

ligands [28], the corresponding methyl complexes **A10a** and **T4a**,**b** can be isolated. Interestingly, cyclometalation involving a methyl group of the carbene arm was observed upon heating these methyl derivatives. It is noteworthy that the process barely depends on the nature of the fourth coordination site, either agostic **A10a** or pure empty site **T4a**,**b**. In the case of I*t*-Bu ligand [44], a similar cyclometalation reaction is observed even at low temperatures (−70 °C), but the putative methyl intermediate could not be detected.

The agostic complex **A9** can exchange the site of cyclometalation by C(sp^3)–H bond activation (Scheme 18) [43]. The addition of one equivalent of L (L = DMSO, PPh_3 or pyridine) to **A9** in chloroform or acetone at room temperature yields the products **37**, in which one methyl group (previously agostic) has been cyclometalated, and L has entered into the coordination sphere of the platinum atom. The authors reasonably propose a σ-bond metathesis (σ-CAM) mechanism via intermediate **36** invoking the well-known capacity of agostic interactions to facilitate the C–H bond cleavage.

The "rollover" process is a class of cyclometalation, in which a heteroaryl ligand undergoes decoordination and bond-rotation processes prior to C–H bond activation. A recent review on this topic collects the most important features of this reaction [122]. Early work by Young and co-workers [123] proposes the formation of coordinately unsaturated species **39** and **39'** as intermediates in the "rollover" reactions of **38**, leading to polymeric species (Scheme 19).

Zucca and co-workers reported the synthesis of several cyclometalated compounds **44** by means of substitution and "rollover" processes (Scheme 20) [124]. Starting from derivative **41**, DMSO displacement by 6-substituted 2,2'-bipyridines

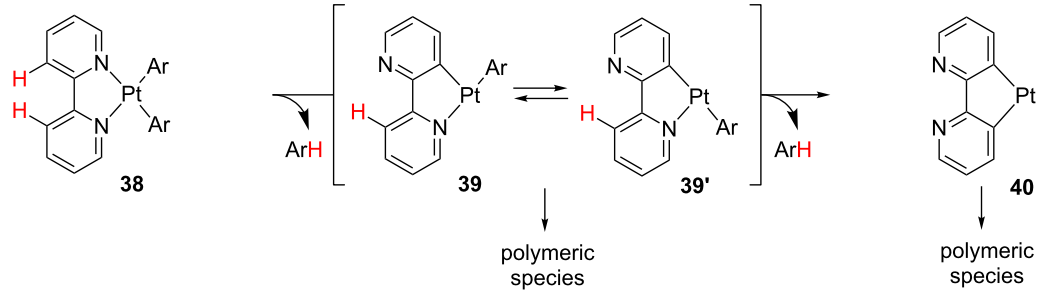

Scheme 19: "Rollover" reaction of **38** and subsequent oligomerization [123].

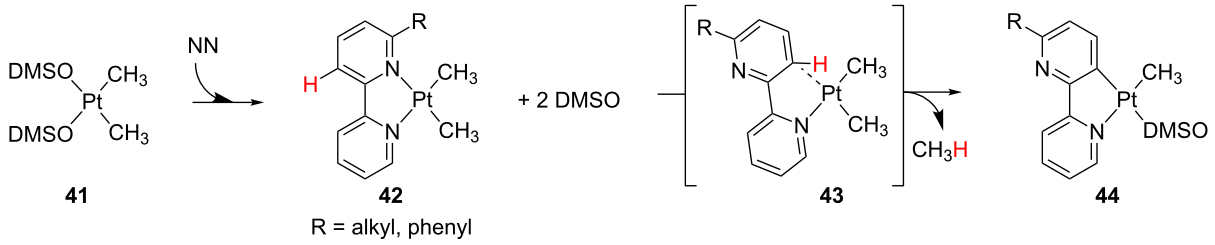

Scheme 20: Proposed mechanism for the formation of cyclometalated species **44** [124].

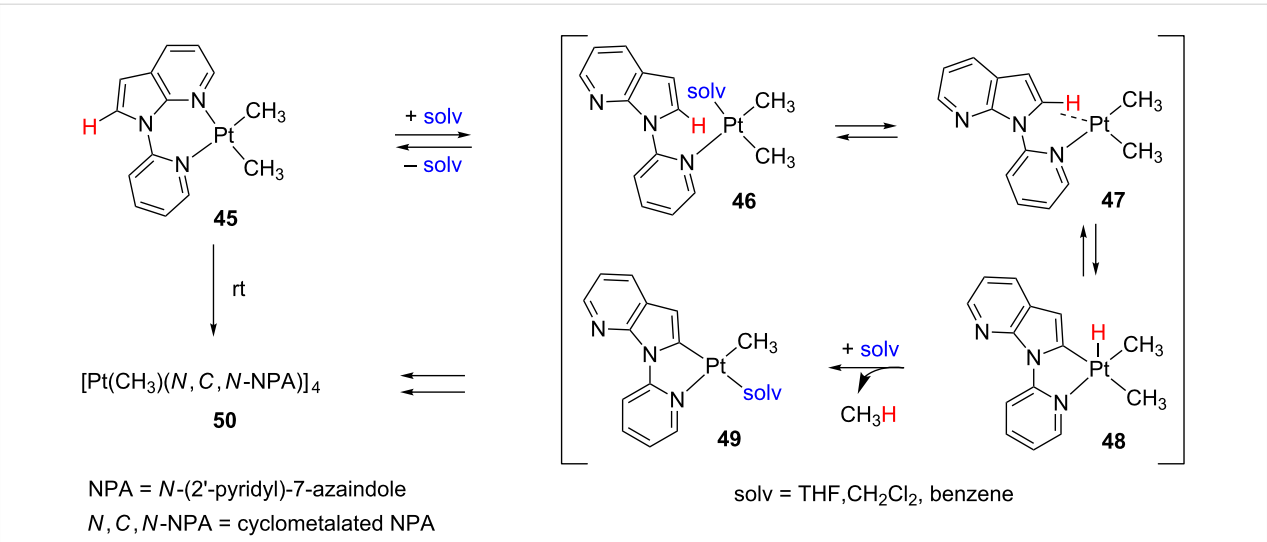

Scheme 21: Self-assembling process of **45** by "rollover" reaction [126].

(NN ligands) yields the corresponding bidentate derivatives **42**. Due to the steric congestion between the R group of the bipyridine and the methyl ligand **42** becomes unstable promoting the decoordination of the nitrogen atom. Subsequent C–H bond activation is proposed to take place through an agostic intermediate **43** generated by rotation around the 2,2'-C–C bond of the bipyridine ligand. After the release of methane, the vacant site is easily occupied by one DMSO ligand yielding **44**. Interestingly, from **44** (R = *t*-Bu, Ph) the corresponding hydride compounds can be prepared [125]. It is worth pointing out that, depending on the ligand present in solution, both 16-electron and 14-electron species are obtained, though the latter are not stable, and only oligomers with bridging hydrides can be detected [125].

Wang and co-workers disclosed the spontaneous self-assembling of [Pt(Me)$_2$(NPA)] **45** by a "rollover" cyclometalation process (Scheme 21) [126]. The suggested mechanism begins with a C–N bond rotation by chelating ligand dissociation forming species **46**, which is stabilized by solvent coordination. Eventually, an agostic interaction in **47** prior to the rate-determining C–H bond cleavage should displace the solvent molecule. An oxidative addition and reductive elimination (OA/RE) scenario via hydride Pt(IV) **48** and subsequent methane release yield the corresponding solvent adduct **49**, from which self-association generates the cyclic tetramer **50**. Indeed, when good coordinating agents such as acetonitrile are added, the reaction slows down.

A "rollover" process has been observed for the already cyclometalated compound **A9** in DMSO providing two zwitterionic products, *cis*- and *trans*-**51** (Scheme 22) [127]. On the other hand, by switching the DMSO solvent to the less polar chloroform the expected cyclometalated product **37a** (Scheme 18) is obtained. DFT calculations correctly explain the relative stabilities

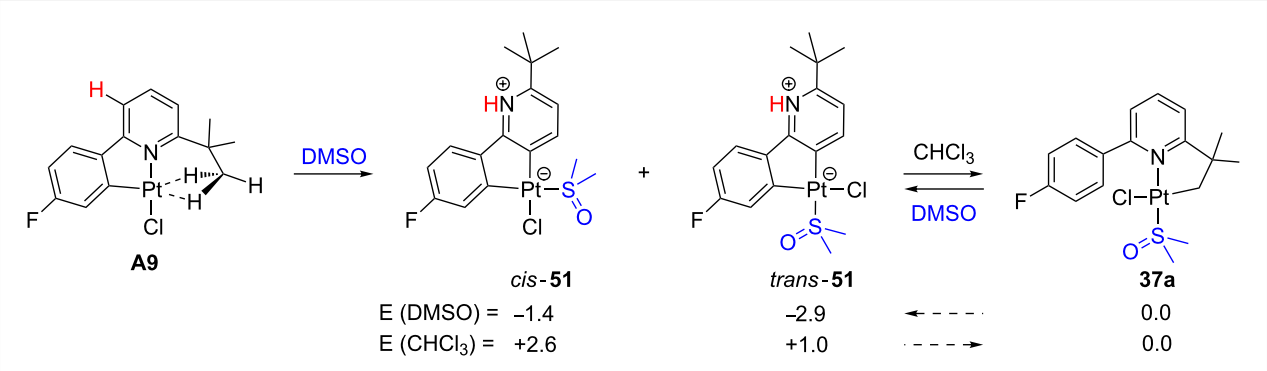

Scheme 22: "Rollover" reaction of **A9**. Energies (solvent) in kcal mol^{-1} [127].

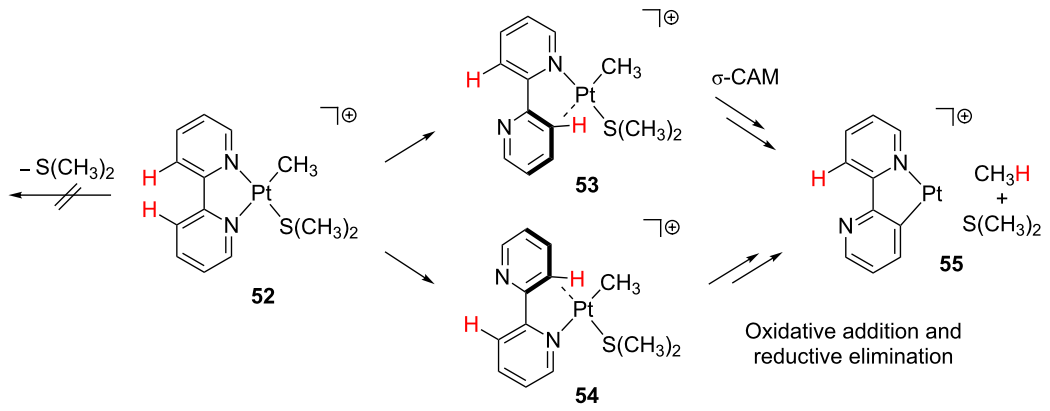

Scheme 23: Proposed mechanisms for the "rollover" cyclometalation of **52** in gas-phase ion-molecule reactions [128].

of **51** with respect to **37a** depending on the polarity of the solvent [127].

This kind of reactivity has also attracted attention in gas-phase conditions [122]. The gas-phase behavior of cationic species **52** has been analyzed by means of combined experimental and computational studies (Scheme 23) [128]. DFT calculations discourage the initial loss of dimethylsulfide. Instead, decomplexation and C–C bond rotation processes starting from the four-coordinate complex **52** are favored. The resulting isomeric compounds exhibit an empty coordination site that is filled by an agostic interaction prior to the C–H bond activation. Intermediate **53** evolves through a σ-CAM process, whereas intermediate **54** undergoes oxidative addition and reductive elimination processes. The release of methane and dimethylsulfide yields **55**. Further studies including labeling experiments support the reversibility of these "rollover" reactions. The highly unsaturated species **55** is still reactive and can coordinate and decompose XMe_2 molecules (X = S [128] and O [129]) and dehydrogenate alkanes [130]. Finally, other cyclometalation processes including "rollover" reactions have also been observed for the complex [Pt(Me)L(SMe_2)] bearing a diimine ligand instead of the ubiquitous bipyridyl backbone [131].

β-H elimination

As previously noted, the agostic complexes **A1**–**4** (Figure 7) are in equilibrium with the hydrido–alkene isomers [34-38]. Experimental evidence points out that substituted alkyls and large chelate ring-size diphosphine ligands favor the β-agostic isomer. As a representative example, Scheme 24 shows the β-H elimination for **A1d** together with the reverse 1,2-insertion for **56**. Interestingly, upon crystallization in dichloromethane solvent, **A1d** eliminates norbornene from **56** and generates the dinuclear complex **57** [35]. The presence of chloride as a bridging ligand suggests that solvent molecules are involved in the reaction. Therefore, the participation of T-shaped intermediates, probably stabilized as solvento adducts, might be relevant in the overall process.

Although β-elimination should be easily accomplished, Goldberg and co-workers realized that other reactions can compete. The thermolysis of five-coordinate Pt(IV) complexes **7** containing nacnac ([{(*o*-$iPr_2C_6H_3$)NC(CH_3)}$_2$CH]$^-$, **7b**) [99,101] and AnIM ([*o*-C_6H_4-{N($C_6H_3iPr_2$)}(CH=N$C_6H_3iPr_2$)]$^-$, **7c**) [101] ligands produces D-**59** in benzene-d_6 (Scheme 25). The first step in this reaction seems to be the direct reductive elimination of **7** liberating ethane. The resulting intermediate **8** undergoes cyclometalation

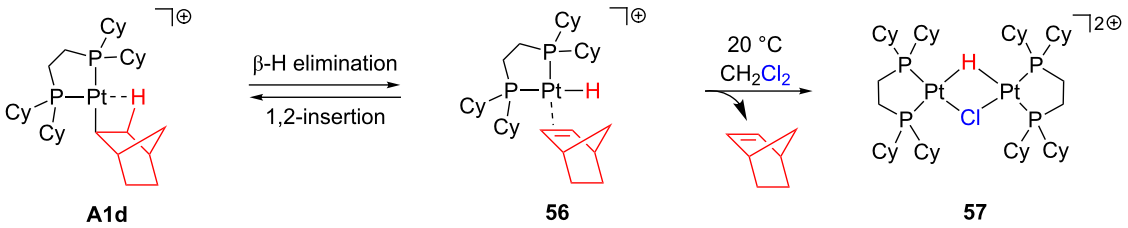

Scheme 24: β-H elimination and 1,2-insertion equilibrium involving **A1d** and the subsequent generation of **57** [35].

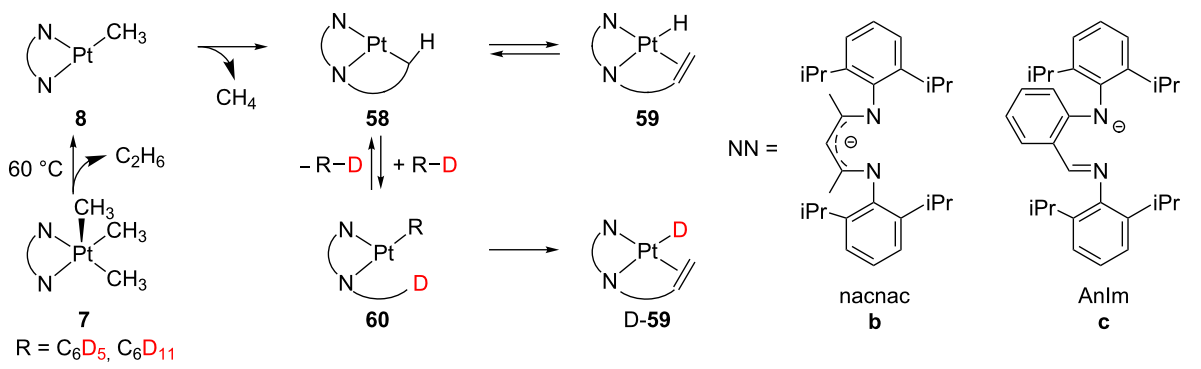

Scheme 25: Proposed mechanism for thermolysis of **7b** and **7c** in benzene-d_6 and cyclohexane-d_{12} solvents [101].

to give the complex **58**. The subsequent β-H elimination process shall provide the expected hydride complex **59**. However, solvent molecules come into play, so that the unsaturated intermediate **58** activates the C–D bond of benzene-d_6 forming **60**. Cyclometalation and subsequent β-H elimination processes generate D-**59**, which has fully incorporated the corresponding deuterium atoms. This latter evidence suggests that the intermolecular C–D bond activation of benzene-d_6 is indeed faster than the β-elimination. On the other hand, when the reaction is conducted in a cyclohexane-d_{12} solution, D-**59** is hardly obtained and **59** prevails. It means that, in sharp contrast to the arene solvent, the intermolecular C–D bond activation of alkanes becomes slower than the β-elimination.

This type of reaction has also been observed for the agostic complex **A11a** [28], although the CH group of the agostic contact is not involved. Upon heating or under UV irradiation (Scheme 26), one hydrogen of the cyclometalated isopropyl group in **A11a** undergoes a β-H elimination process yielding **61**, in which the alkene and the hydride ligands are located mutually *trans*.

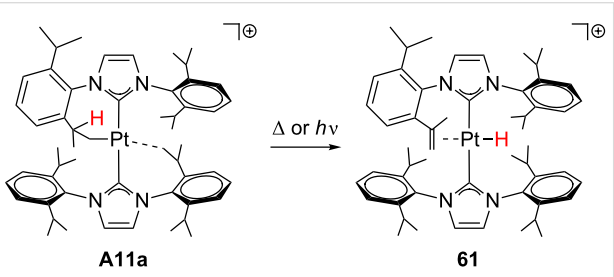

Scheme 26: β-H elimination process of **A11a** [28].

Intermolecular C–H bond activation

Three-coordinate T-shaped Pt(II) complexes have been postulated in hydrocarbon C–H bond activations, particularly in the Shilov system for the functionalization of methane. A number of excellent reviews about C–H bond activation have been published [132-137].

Labile ligands in masked T-shaped compounds allow further reactivity. Although some solvent complexes exhibit associative pathways eluding 14-electron species [73,138], the participation of such coordinatively unsaturated intermediates should be taken into account for other systems [135,136]. A good example is the investigation reported by Wick and Goldberg (Scheme 27) [95]. From the anionic species $[Pt(Me)_2Tp']^-$ **62**, they attempted to generate the unsaturated species **63** through the abstraction of one methyl ligand. Indeed, the treatment of **62** with $B(C_6F_5)_3$ in benzene, cyclohexane and *n*-pentane provides

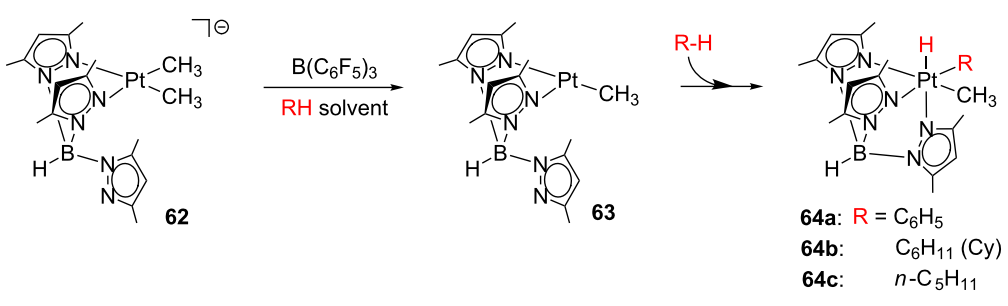

Scheme 27: Intermolecular C–H bond activation from **62** [95].

the products **64** arising from the C–H bond activation of solvent molecules. Interestingly, the activation of pentane molecules only occurs at the primary carbon atom.

A similar situation has been observed for the reductive elimination of methane in the complex **65** (Scheme 28) [105]. Experimental evidence is consistent with a dissociative methane loss from **66** as the rate-determining step. Therefore, as shown in Scheme 27, the unsaturated intermediate **63** is supposed to operate again. When the reaction is carried out in CD_3CN/C_6F_6 mixtures, acetonitrile binds the transient **63** forming the corresponding adduct **67**. On the other hand, when benzene-d_6 and toluene-d_8 are used as solvents, intermolecular C–D bond activations occur with the formation of **68**. In cyclohexane-d_{12} solution, the observation of deuterated methane isotopomers indicates C–D bond-activation processes, though the corresponding alkyl Pt(IV) product could not be characterized.

Nevertheless, the participation of one arm of the Tp' ligand stabilizing the open coordination site in **63** should be considered. As pointed out by Keinan and co-workers [139], the intermediate [Pt(Me)Tp] can adopt two different structures; the bidentate κ^2 coordination mode (**69**) provides a T-shaped structure (Figure 18 left) whereas the κ^3-complex (**69'**) exhibits a see-saw geometry (Figure 18 right). The former is slightly favored by only 1.8 kcal mol^{-1}.

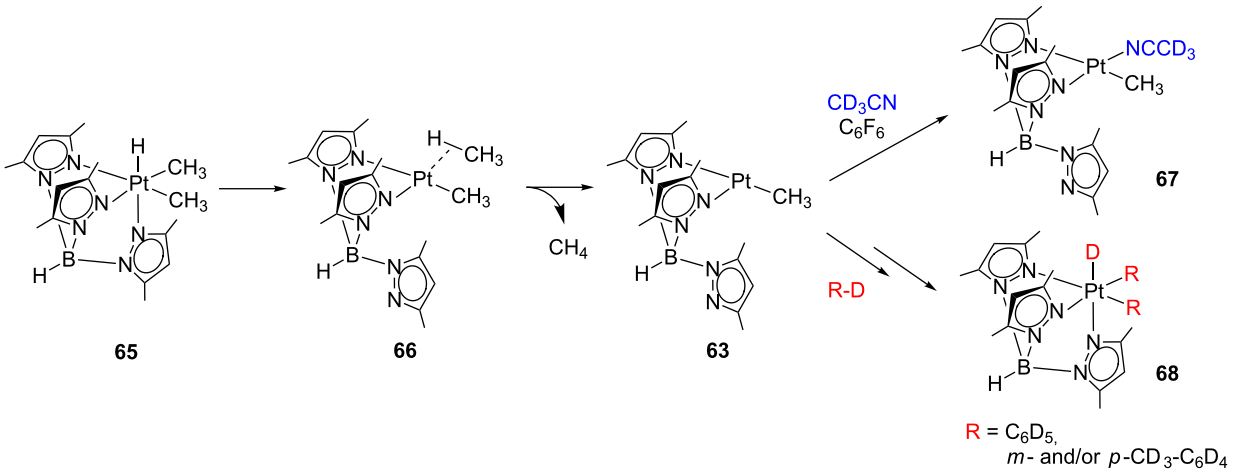

Scheme 28: Reductive elimination of methane from **65** followed by CD_3CN coordination or C–D bond-activation processes [105].

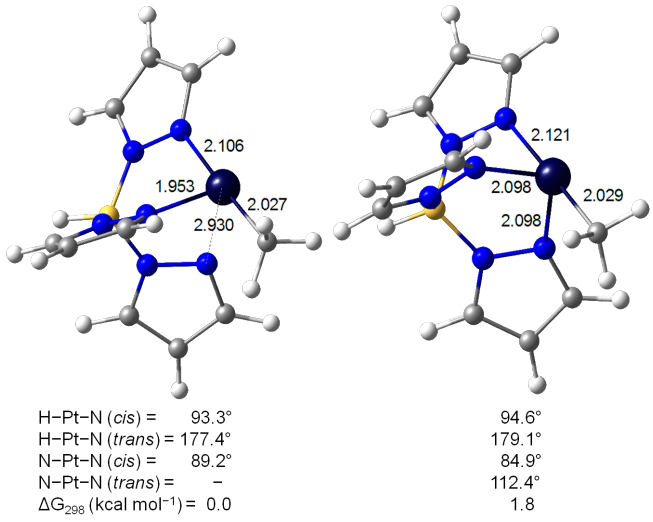

Figure 18: DFT-optimized structures describing the κ^2 (**69**, left) and κ^3 (**69'**, right) coordination modes of [Pt(Me)Tp] [139]. Bond distances in angstroms, angles in degrees and Gibbs energies in kcal mol^{-1}.

Recently, arene activation has been reported regarding true T-shaped species with NHC ligands [28]. The cyclometalated complexes **A11a**, **A11b**, **T5a** and **T5b** were tested toward C–H bond-activation processes by using benzene as a solvent (Scheme 29). No reaction was observed for **A11a** and **A11b** even under drastic conditions (high temperatures and long reaction times). On the other hand, **T5a** yields the phenyl product **T6a**, whereas **T5b** barely reacts.

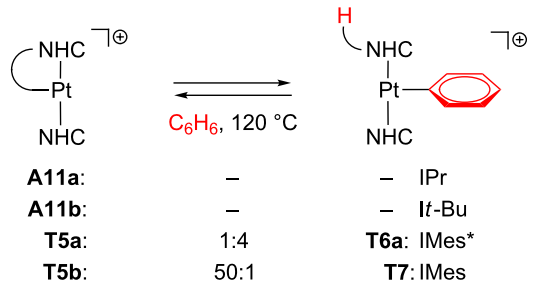

Scheme 29: Intermolecular arene C–H bond activation from NHC-based complexes [28].

DFT calculations suggest an oxidative addition and reductive elimination scenario via Pt(IV) hydride intermediates **70** (Figure 19). The steric environment of the agostic complexes **A11a** and **A11b** complicates the reaction, which is reflected in the high energy barriers (more than 40 kcal mol^{-1}, red line). In sharp contrast, the true T-shaped species **T5a** and **T5b**, with no agostic bonds, show lower energy profiles (ca. 30 kcal mol^{-1}, blue line) and the reaction thermodynamics (ΔE_r values, Figure 19) accounts for the observation of **T6a** and the poor detection of **T7**.

Other arenes can also be activated by the use of **T5a** to afford **T6** (Figure 6). In toluene solvent, only the two products *m*-**T6b** and *p*-**T6b** corresponding to *meta*- and *para*-site activations are observed in a 5:1 molar ratio. Neither *ortho*- nor benzylic C–H bond activations are detected. Once again, DFT calculations provide reasonable $\Delta E^{\ddagger}$ for both *meta* and *para*-routes (ca. 30 kcal mol^{-1}), and the thermodynamic effects, i.e., that only *m*-**T6b** and *p*-**T6b** are slightly more stable than **T5a**, explain the experimental evidence.

Some pincer complexes can indeed activate the C–H bonds of benzene, though the mechanism is not fully understood [50,140]. In this line, Ozerov and co-workers have attempted to access unsaturated species by means of abstraction of triflate ligand from **71** (Scheme 30) [12]. The presumable generation of the low electron-count intermediate **72**, results in the intermolecular C–H bond activation of several arene solvents. Phenyl **73a** and phenyl-d_5 **73b** together with *o*-fluoro **73c** and *o*-chlorophenyl **73d** are obtained. The toluene solvent also reacts forming a mixture of *o*-, *m*- and *p*-tolyl complexes (8% *o*-**73e** and 92% *m*-**73e** and *p*-**73e**). Additional experiments proved that the reverse processes are not kinetically accessible.

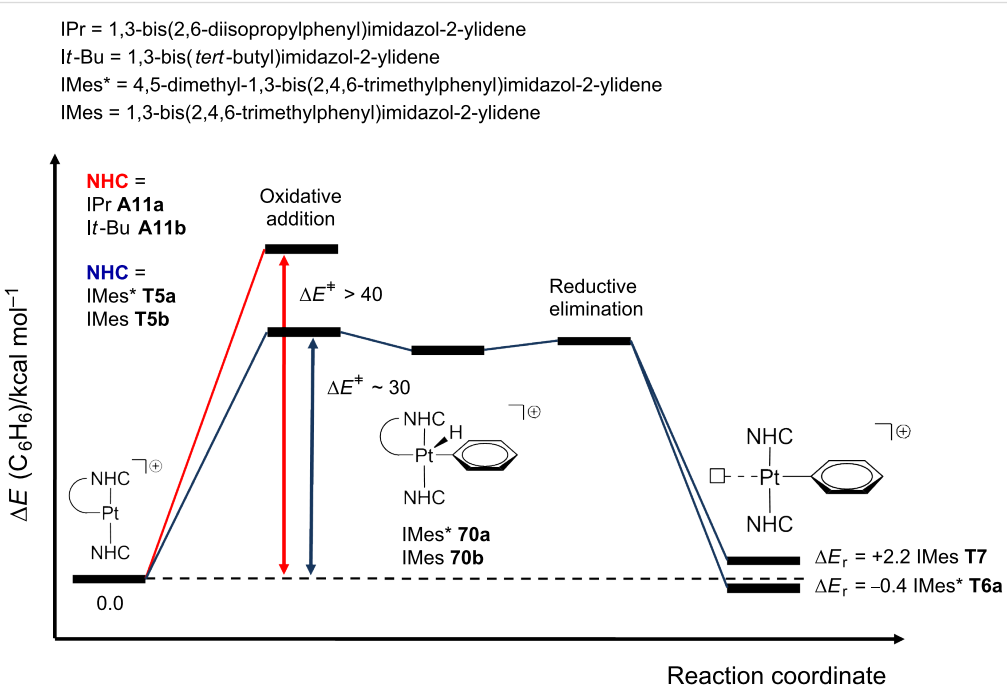

Figure 19: Energy profiles (in benzene solvent) for the benzene C–H bond activation from **A11a**, **A11b**, **T5a** and **T5b** [28].

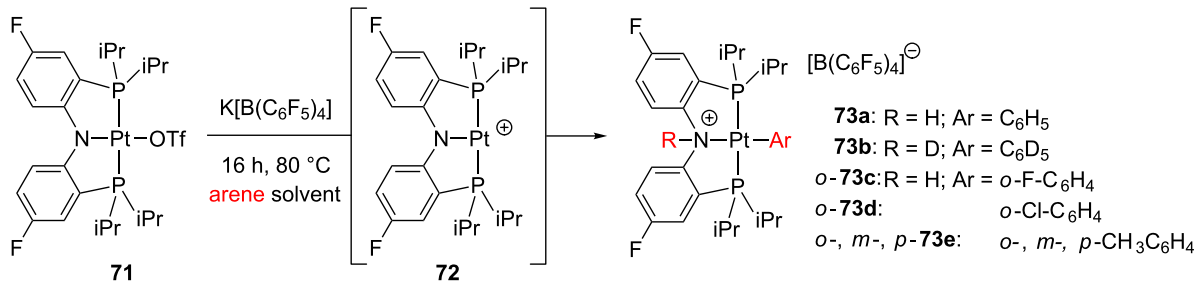

Scheme 30: Intermolecular arene C–H bond activation from PNP-based complex **71** [12].

In some cases, C–X bond-activation processes involving PhBr and CH_2Cl_2 molecules have also been registered.

Complexes of the type $[Pt(Me)(NN)]^+$ **74** (Scheme 31) have shown reactivity toward the C–H bond activation of benzene in gas-phase ion-molecule reactions [7]. Suitable labeling experiments disclose the reversibility of the C–H bond activation. Interestingly, the relative rate constants reveal that **74d** reacts slower than **74a**–**c**. In the absence of solvent, both reactants **74a**–**c** and phenyl products **76a**–**c** are believed to exhibit true T-shaped structures. On the other hand, the lower reactivity of **74d** has been attributed to an interaction of the empty site of the platinum with one *ortho*-chlorine atom of the (*o*,*o*'-$Cl_2C_6H_3$)N=C(CH_3)–C(CH_3)=N(*o*,*o*'-$Cl_2C_6H_3$) ($^{Me}DAB^{DCP}$) ligand [141], which blocks the approach of a benzene molecule. Oxidative addition and reductive elimination (OA/RE) as well as σ-CAM scenarios have been evaluated for **74b**, but unfortunately the results are functional-dependent. B3LYP cannot reproduce the experimental evidences, mPW1K and mPW1PW91 favor the σ-CAM mechanism, and M05-2X considers both of them [7]. The bipyridyl complex **74b** can also activate toluene and methane molecules forming **74bb** and **74bc**, respectively [142]. Concerning the toluene activation, *meta*-, *para*- and benzylic positions can be activated forming *m*-**76bb**, *p*-**76bb** and Bn-**76bb**, respectively. BP86 calculations suggest that OA/RE and σ-CAM are competitive pathways.

H_2 activation

Some agostic complexes previously reported can activate small molecules such as H_2 (Scheme 32). For instance, the complexes **A5a** and **A5b** react with dihydrogen (1 atm H_2, 20 °C) in dichloromethane solution to yield the corresponding agostic hydride products **A6a** and **A6b** [39]. Both species were found in equilibrium, exhibiting **A5**/**A6** ratios of 4:1 and 1:2 for species **a** and **b**, respectively. A similar behavior is observed for the

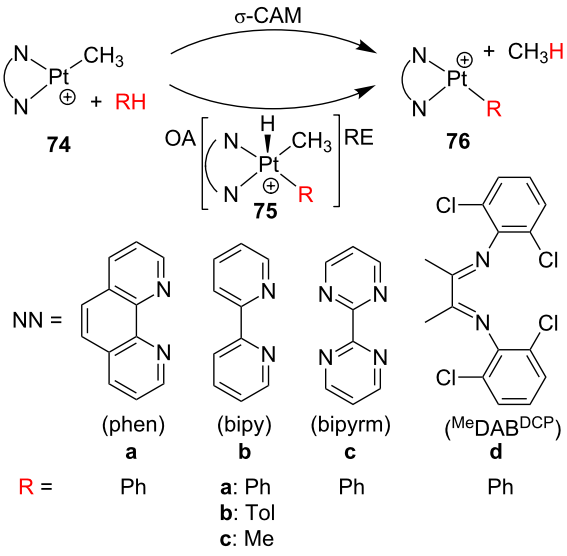

Scheme 31: Intermolecular C–H bond-activation by gas-phase ion-molecule reactions of **74** [7,142].

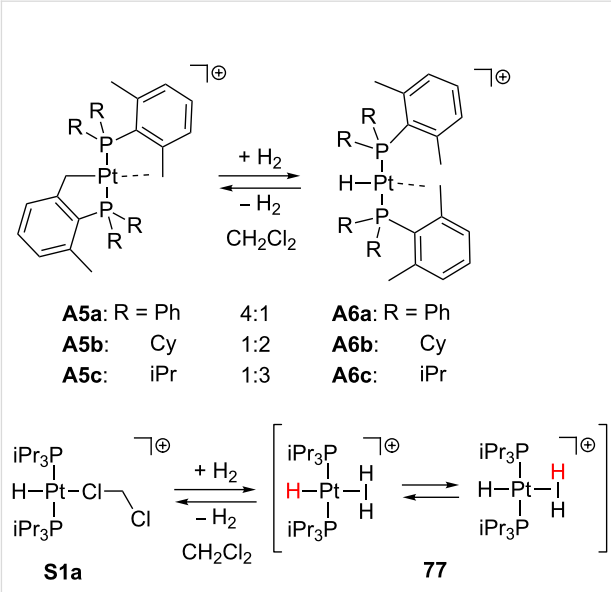

Scheme 32: Dihydrogen activation through complexes **A5a**, **A5b** [39], **A5c** [40] and **S1a** [54].

analogous reaction of **A5c** (1 bar H_2, −30 °C to room temperature), in which **A6c** is obtained in a 1:3 ratio [40]. These results suggest that hydride species seem to be favored according to the basicity of the phosphine ligand. In previous works, the dichloromethane molecule in the solvento complex **S1a** was labile enough to allow H_2 activation but, unlike **A6**, the corresponding dihydrogen adduct **77** was observed (Scheme 32) [54]. The latter undergoes a fluxional process which can be slowed down by cooling at −60 °C.

Weller and co-workers reported an alternative procedure to obtain **77** from **A7** by addition of dihydrogen in CD_2Cl_2 solution (Scheme 33) [41]. The agostic interaction in **A7** is supposed to be displaced by one dihydrogen molecule forming the putative intermediate **78**. The concomitant release of methane may be the driving force of the reaction, thus the entropic factors together with the nature of the phosphine ligands should be taken into account. Additionally, the related compound **16** (Scheme 13) can also activate dihydrogen molecules; the cyclometalated ring is opened and the corresponding hydride complex **S1c** is obtained [54].

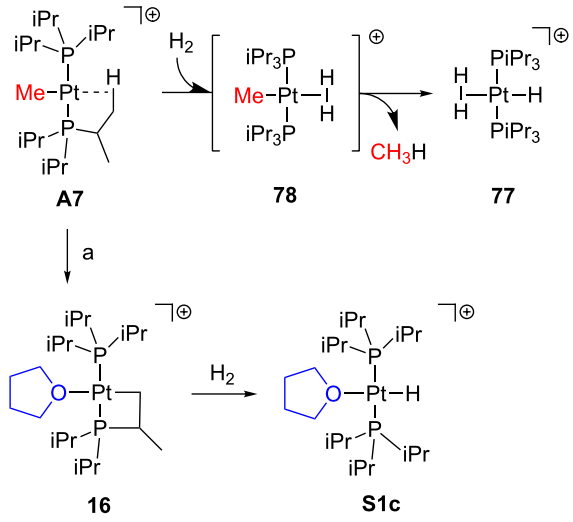

Scheme 33: Dihydrogen activation through complexes **A7** and **16** [41]. For a: see Scheme 13.

X_2 activation

The cyclometalated compounds **A11a** and **T5a** can activate X_2 molecules (X = Br, I) in dichloromethane solution affording **79** and **80** in which one C(sp^3)–X bond is constructed (Scheme 34) [143]. It is noteworthy that the reaction occurs in the presence (**A11a**) or the absence (**T5a**) of agostic interactions in the starting materials.

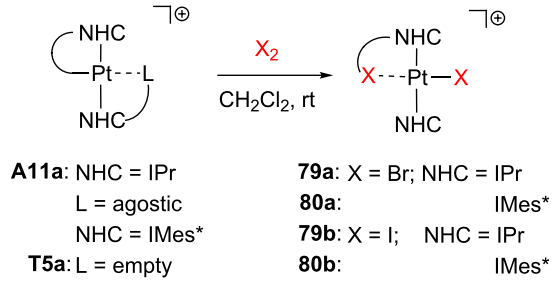

Scheme 34: Br_2 and I_2 bond activations through complexes **A11a** and **T5a** [143].

Interestingly, during the reaction of **A11a** with Br_2 at low temperature (−78 °C) a paramagnetic, see-saw Pt(III) alkyl intermediate **81a** could be isolated and characterized (Scheme 35), although the iodo-analogue **81b** could not. DFT calculations correctly predicted the feasibility of **81a** (−9.5 kcal mol^{-1} below reactants) and explained the nondetection of **81b** (+4.5 kcal mol^{-1} above reactants) in terms of higher relative energies.

A related Cl_2 activation process involving unsaturated species has been recently reported by Rourke and co-workers (Scheme 36) [144]. Under certain conditions, the reaction of **82** with PhI·Cl_2 yields **83**. Although suitable crystals of **83** could not be obtained, the structure was elucidated by NMR studies showing the formation of one C(sp^3)–Cl bond. Similarly to the

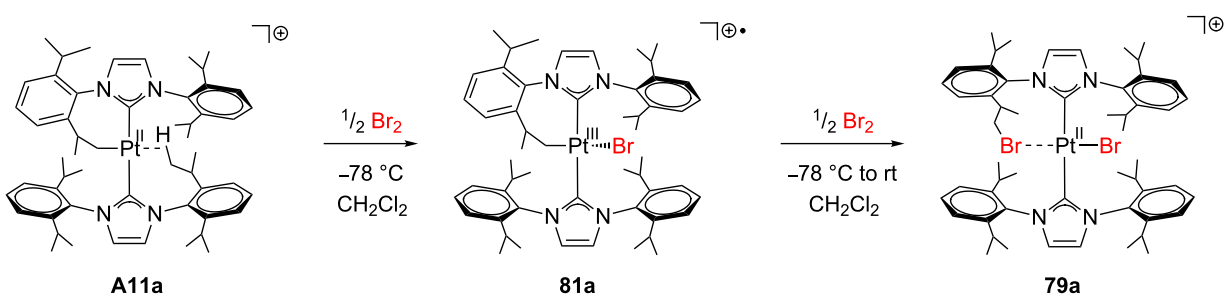

Scheme 35: Detection and isolation of the Pt(III) complex **81a** [143].

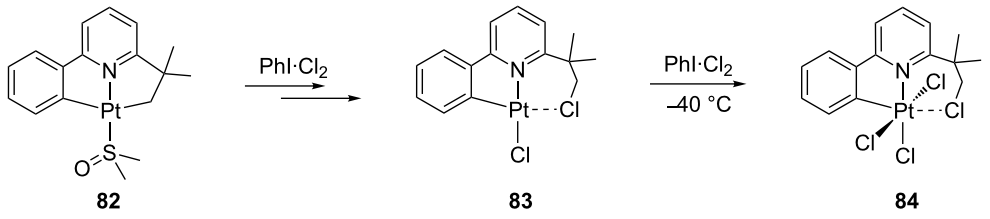

Scheme 36: Cl_2 bond activation through complexes **82** and **83** [144].

agostic species **A9**, the resulting CH_2Cl group is interacting with the open coordination site. Further reaction of **83** with $PhI{\cdot}Cl_2$ forms the oxidation product **84**.

cis–trans Isomerization

The *cis–trans* isomerization of several solvento species **S5** has been studied and the formation of low electron-count Pt(II) complexes **85** through dissociative pathways accounts for the experimental observations [2,61]. The general mechanism is depicted as follows: (i) rate-determining dissociation step of a solvent molecule, (ii) isomerization process, and (iii) fast association of a solvent molecule (Scheme 37).

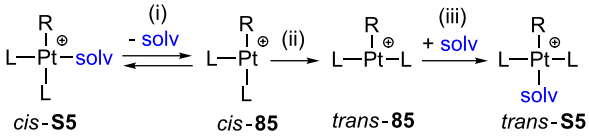

Scheme 37: *cis–trans* Isomerization mechanism of the solvento Pt(II) complexes **S5** [2,61].

As shown in Scheme 37, the 14-electron structures **85** are involved in the process. Due to their high tendency to fulfill the empty coordination site, these species strongly favor intramolecular contacts. Indeed, it has been experimentally observed that the complexes **S5** bearing R = Et, *n*-Pr and *n*-Bu groups react much faster than other derivatives with R groups without β-hydrogen atoms [61]. This phenomenon has been called the β-hydrogen kinetic effect [2]. It is defined by an incipient β-agostic interaction that can stabilize transient T-shaped intermediates and transition states, and therefore, an increase of the reaction rate would be expected. Further computational studies were performed on complexes $[Pt(R)(PMe_3)_2(solv)]^+$ **85** describing the isomerization process in different solvents [2]. The β-hydrogen kinetic effect can be detected during the first steps of the isomerization energy profiles (Figure 20) for both the methyl (**85a**, red line) and the ethyl (**85b**, blue line)

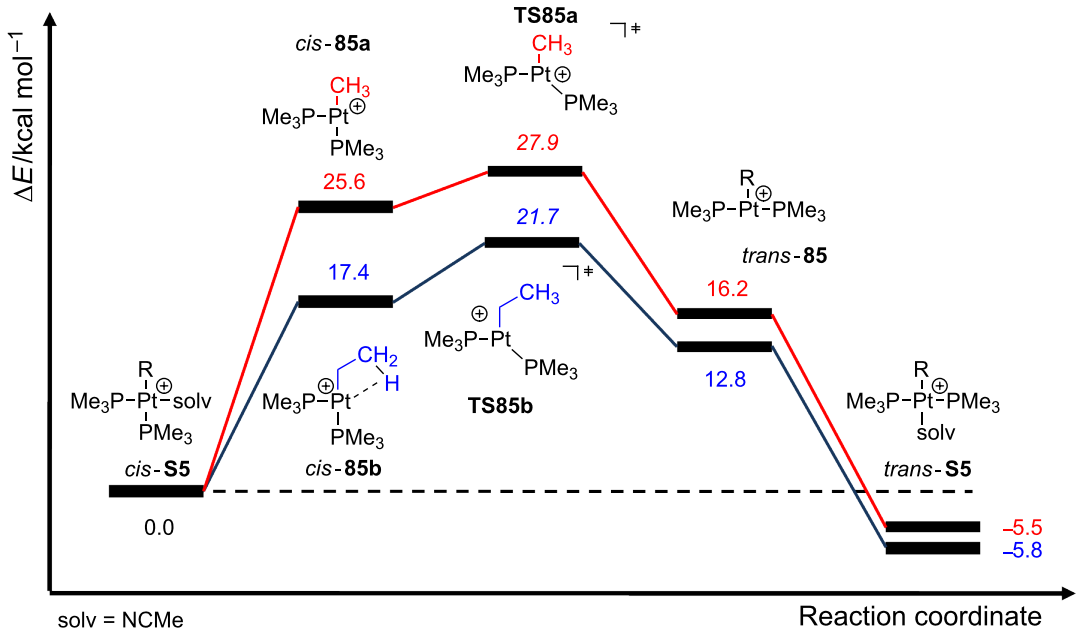

Figure 20: Energy profiles for the isomerization of complexes $[Pt(R)(PMe_3)_2(NCMe)]^+$ where R means Me (**85a**, red line) and Et (**85b**, blue line) [2].

complexes in acetonitrile. Note that the agostic contact in *cis*-**85b** decreases the overall energy requirement with respect to *cis*-**85a**, but at the same time, it increases the relative energy barrier to reach the Y-shaped transition state **TS85**, i.e., 4.3 kcal mol^{-1} for the ethyl (**TS85b**) and 2.3 kcal mol^{-1} for the methyl (**TS85a**) derivatives. By removal of the agostic interaction in *cis*-**85b** (through a rotation of the C–C bond of the ethyl ligand), this energy stabilization was estimated to be 5.9 kcal mol^{-1}. Other solvents such as methanol, dimethylsulfoxide and benzene were also considered. The donor ability strongly affects the dissociation step, although it has a little impact on the strength of the agostic interaction.

In the presence of benzyl ligands, a similar *cis*–*trans* isomerization via the unsaturated species $[Pt(R)(PEt_3)_2]^+$ (Scheme 37) has been claimed [62]. DFT calculations on the model derivative $[Pt(Bn)(PMe_3)_2]^+$ predict a Pt···η^2-benzyl coordination mode in **86** involving the ipso-carbon of the benzyl ligand (Figure 21). This stabilization accounts for 7.6 kcal mol^{-1}, i.e., 1.7 kcal mol^{-1} stronger than the above-mentioned agostic contact for the same family of compounds (5.9 kcal mol^{-1}, [2]). The interaction is favored by electron-donating groups on the phenyl ring and, as a consequence, the reaction rate is enhanced.

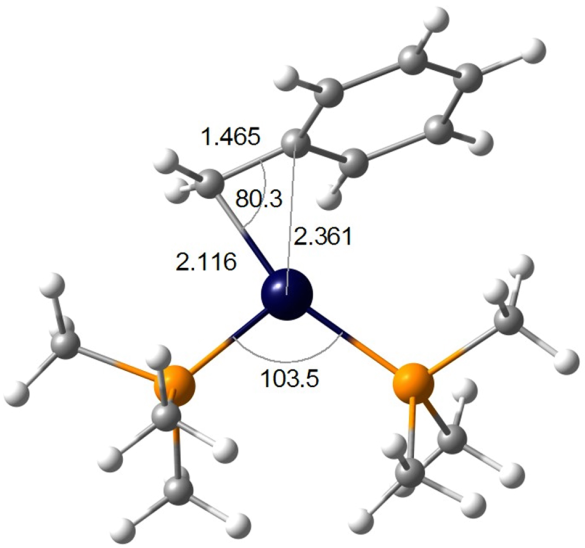

Figure 21: DFT-optimized structure of intermediate **86** [62]. Bond distances in angstrom and angles in degrees.

Dissociative ligand substitution

Experimental evidences obtained in poorly coordinating solvents strongly support that neutral complexes of the type *cis*-$[Pt(R)_2S_2]$ (**87**) undergo ligand substitutions through dissociative pathways as depicted in Scheme 38: (i) sulfur ligand dissociation/reassociation via transient 14-electron structures (**88**), (ii) subsequent ligand addition (**89**), and (iii) displacement of the sulfur ligand (**90**) [117,119]. The electron-rich metal, the Pt–S bond weakening due to the *trans*-influence of the R groups, and the stabilization of T-shaped intermediates favor this dissociative pathway. Interestingly, for the complex *cis*-$[Pt(Ph)_2(CO)(SMe_2)]$, in which one thioether ligand has been replaced by CO, the operating mechanism becomes associative [145]. Steric and β-hydrogen kinetic effects [2] have been invoked to explain the fast reaction of $[Pt(Hbph)_2(DMSO)_2]$ (Hbph = η^1-biphenyl monoanion) compared to species containing other R groups [117].

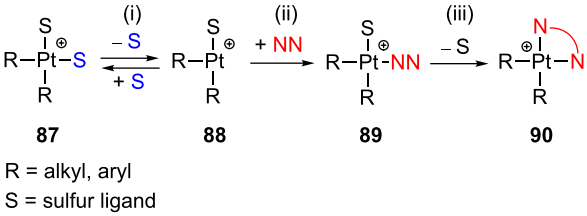

Scheme 38: Proposed dissociative ligand-substitution mechanism of *cis*-$[Pt(R)_2S_2]$ complexes (**87**) [117].

Puddephatt and co-workers have demonstrated that, depending on the nature of the R group, dissociative mechanisms can also facilitate the substitution of dimethylsulfide by phthalazine in the dinuclear species **91** (Scheme 39) [146]. When alkyl derivatives are employed, kinetic evidence mainly points to an associative mechanism via **92**, although a minor part of the reaction has been related to a dissociative pathway. The inclusion of phenyl and *p*-tolyl ligands in **91** completely changes the mechanism. A first-order reaction is observed and large negative entropies of activation are collected. The proposed mechanism involves the dissociation of dimethylsulfide generating the puta-

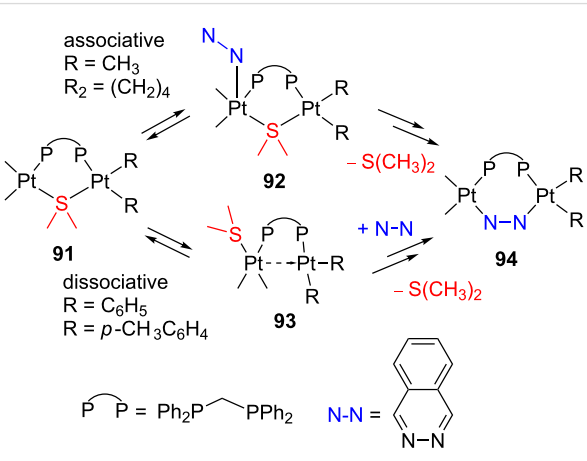

Scheme 39: Proposed mechanisms for the ligand substitution of the dinuclear species **91** [146].

tive unsaturated intermediate **93**. This species is supposed to be stabilized by a donor–aceptor Pt–Pt bond, i.e., the electron-rich four-coordinate platinum atom interacts with the electron-deficient three-coordinate counterpart. Consequently, the electron density of the former platinum atom decreases, thereby favoring the subsequent attack of the N–N ligand to yield **94**.

Conclusion

There are only a very few authenticated three-coordinate Pt(II) complexes. Yet, T-shaped intermediates play an important role in a number of organometallic transformations. Given the electronic and coordinative unsaturated nature of such compounds, they can only be isolated when the vacant coordination site is blocked to avoid intra- and intermolecular interactions. Steric effects are important in preventing the coordination of a fourth external ligand. The use of bulky species, which hamper the entry of ligands into the platinum coordination sphere, is a good strategy toward this goal. The presence of shorter or less flexible alkyl chains in bulky ligands could avoid agostic interactions. Electronic effects, as well as the involvement of strong electron-donating ligands, also have a stabilizing impact. Overall, the number of true T-shaped complexes that are well-characterized is still very low. Nevertheless, a much larger number of Pt(II) complexes can be described as operationally three-coordinate in a kinetic sense. This happens when the fourth position in a square-planar complex is occupied by a very weak ligand, which can be easily displaced. We have named these compounds masked T-shaped complexes. An intramolecular agostic interaction, a weakly coordinated solvent molecule or a counteranion can play such a role. Whether or not the interaction of the platinum atom with the fourth ligand is very weak, the three-coordinate complex should be very close in energy to the square-planar ground state. Consequently, in practice the masked T-shaped complexes can be devised as a resting state of the three-coordinate species.

The accessibility of three-coordinate complexes makes them suitable intermediates in Pt(II) chemistry. In spite of the difficulty in detecting these intermediates, this review gathers a number of recent experimental and theoretical reports, which claim the involvement of T-shaped Pt(II) intermediates in reaction mechanisms. In the near future, the acquired knowledge on the synthetic routes and structural features, as well as the advances in the detection techniques and computational methods, should lead to an improved design of such compounds and to a wider recognition of the role they play in chemical transformations.

Acknowledgements

Financial support from the Spanish Ministerio de Economia y Competitividad (DGICYT, Projects CTQ2010-17476, CTQ2011-23336 and ORFEO Consolider-Ingenio 2010 CSD2007-00006) and the Junta de Andalucía (project No. FQM-3151) is acknowledged. M. A. O thanks the Spanish MECD for a research grant.

References

1. Hartwig, J. F. *Organotransition metal chemistry: from bonding to catalysis;* University Science: Sausalito, CA, USA, 2010.
2. Romeo, R.; D'Amico, G.; Sicilia, E.; Russo, N.; Rizzato, S. *J. Am. Chem. Soc.* **2007,** *129,* 5744–5755. doi:10.1021/ja0702162
3. Yamashita, M.; Hartwig, J. F. *J. Am. Chem. Soc.* **2004,** *126,* 5344–5345. doi:10.1021/ja0315107
4. Walter, M. D.; White, P. S.; Brookhart, M. *New J. Chem.* **2013,** *37,* 1128–1133. doi:10.1039/c3nj41145a
5. Moncho, S.; Ujaque, G.; Lledós, A.; Espinet, P. *Chem.–Eur. J.* **2008,** *14,* 8986–8994. doi:10.1002/chem.200800423
6. Gerdes, G.; Chen, P. *Organometallics* **2003,** *22,* 2217–2225. doi:10.1021/om0209982
7. Butschke, B.; Schröder, D.; Schwarz, H. *Organometallics* **2009,** *28,* 4340–43496. doi:10.1021/om900388k
8. Ozerov, O. V.; Watson, L. A.; Pink, M.; Caulton, K. G. *J. Am. Chem. Soc.* **2007,** *129,* 6003–6016. doi:10.1021/ja062327r
9. Alvarez, S. *Coord. Chem. Rev.* **1999,** *193–195,* 13–41. doi:10.1016/S0010-8545(99)00085-5
10. Albright, T. A.; Burdett, J. K.; Whango, M. H. *Orbital interactions in chemistry;* Wiley: New York, 1985.
11. Jean, Y. *Molecular orbitals of transition metal complexes;* Oxford University Press: New York, 2005.
12. DeMott, J. C.; Bhuvanesh, N.; Ozerov, O. V. *Chem. Sci.* **2013,** *4,* 642–649. doi:10.1039/c2sc21385k
13. Su, M.-D.; Chu, S.-Y. *J. Phys. Chem. A* **1998,** *102,* 10159–10166. doi:10.1021/jp982861o
14. Komiya, S.; Albright, T. A.; Hoffmann, R.; Kochi, J. K. *J. Am. Chem. Soc.* **1976,** *98,* 7255–7265. doi:10.1021/ja00439a024
15. Berthon-Gelloz, G.; de Bruin, B.; Tinant, B.; Markó, I. E. *Angew. Chem.* **2009,** *121,* 3207–3210. doi:10.1002/ange.200900435 *Angew. Chem. Int. Ed.* **2009,** *48,* 3161–3164. doi:10.1002/anie.200900435
16. Takagi, N.; Sakaki, S. *J. Am. Chem. Soc.* **2012,** *134,* 11749–11759. doi:10.1021/ja304110h
17. Su, M.-D. *Mol. Phys.* **1993,** *80,* 1223–1251. doi:10.1080/00268979300102991
18. Sturmayr, D.; Schubert, U. *Monatsh. Chem.* **2003,** *134,* 791–795. doi:10.1007/s00706-002-0568-6
19. Goel, R. G.; Srivastava, R. C. *Can. J. Chem.* **1983,** *61,* 1352–1359. doi:10.1139/v83-238
20. Braunschweig, H.; Radacki, K.; Rais, D.; Scheschkewitz, D. *Angew. Chem.* **2005,** *117,* 5796–5799. doi:10.1002/ange.200501588 *Angew. Chem. Int. Ed.* **2005,** *44,* 5651–5654. doi:10.1002/anie.200501588
21. Braunschweig, H.; Radacki, K.; Uttinger, K. *Chem.–Eur. J.* **2008,** *14,* 7858–7866. doi:10.1002/chem.200800879
22. Braunschweig, H.; Brenner, P.; Dewhurst, R. D.; Jimenez-Halla, J. O. C.; Kupfer, T.; Rais, D.; Uttinger, K. *Angew. Chem., Int. Ed.* **2013,** *125,* 3055–3058. doi:10.1002/anie.201209717
23. Lam, W. H.; Lam, K. C.; Lin, Z.; Shimada, S.; Perutz, R. N.; Marder, T. B. *Dalton Trans.* **2004,** 1556–1562. doi:10.1039/b402632b

24. Toner, A.; Matthes, J.; Gründemann, S.; Limbach, H.-H.; Chaudret, B.; Clot, E.; Sabo-Etienne, S. *Proc. Natl. Acad. Sci. U. S. A.* **2007,** *104,* 6945–6950. doi:10.1073/pnas.0608979104
25. Dorta, R.; Stevens, E. D.; Hoff, C. D.; Nolan, S. P. *J. Am. Chem. Soc.* **2003,** *125,* 10490–10491. doi:10.1021/ja0362151
26. Lavallo, V.; Canac, Y.; De Hope, A.; Donnadieu, B.; Bertrand, G. *Angew. Chem.* **2005,** *117,* 7402–7405. doi:10.1002/ange.200502566 *Angew. Chem., Int. Ed.* **2005,** *44,* 7236–7239 doi:10.1002/anie.200502566
27. Clavier, H.; Nolan, S. P. *Chem. Commun.* **2010,** *46,* 841–861. doi:10.1039/b922984a
28. Rivada-Wheelaghan, O.; Ortuño, M. A.; Díez, J.; Lledós, A.; Conejero, S. *Angew. Chem.* **2012,** *124,* 4002–4005. doi:10.1002/ange.201200070 *Angew. Chem., Int. Ed.* **2012**, *51*, 3936–3939. doi:10.1002/anie.201200070
29. Brookhart, M.; Green, M. L. H. *J. Organomet. Chem.* **1983,** *250,* 395–408. doi:10.1016/0022-328X(83)85065-7
30. Brookhart, M.; Green, M. L. H.; Wong, L. L. Carbon-Hydrogen-Transition Metal Bonds. In *Progress in Inorganic Chemistry;* Lippard, S. J., Ed.; John Wiley & Sons, Inc.: Hoboken, NJ, USA, 1988; Vol. 36, pp 1–124. doi:10.1002/9780470166376.ch1
31. Brookhart, M.; Green, M. L. H.; Parkin, G. *Proc. Natl. Acad. Sci. U. S. A.* **2007,** *104,* 6908–6914. doi:10.1073/pnas.0610747104
32. Clot, E.; Eisenstein, O. *Struct. Bond.* **2004,** *113,* 1–36. doi:10.1007/b97940
33. Lein, M. *Coord. Chem. Rev.* **2009,** *253,* 625–634. doi:10.1016/j.ccr.2008.07.007
34. Carr, N.; Dunne, B. J.; Orpen, A. G.; Spencer, J. L. *J. Chem. Soc., Chem. Commun.* **1988,** 926–928. doi:10.1039/C39880000926
35. Carr, N.; Dunne, B. J.; Mole, L.; Orpen, A. G.; Spencer, J. L. *J. Chem. Soc., Dalton Trans.* **1991,** 863–871. doi:10.1039/DT9910000863
36. Mole, L.; Spencer, J. L.; Carr, N.; Orpen, A. G. *Organometallics* **1991,** *10,* 49–52. doi:10.1021/om00047a026
37. Carr, N.; Mole, L.; Orpen, A. G.; Spencer, J. L. *J. Chem. Soc., Dalton Trans.* **1992,** 2653–2662. doi:10.1039/DT9920002653
38. Spencer, J. L.; Mhinzi, G. S. *J. Chem. Soc., Dalton Trans.* **1995,** 3819–3824. doi:10.1039/DT9950003819
39. Baratta, W.; Stoccoro, S.; Doppiu, A.; Herdtweck, E.; Zucca, A.; Rigo, P. *Angew. Chem.* **2003,** *115,* 109–113. doi:10.1002/ange.200390003 *Angew. Chem. Int. Ed.* **2003,** *42,* 105–108. doi:10.1002/anie.200390035
40. Campos, J.; Peloso, R.; Carmona, E. *Angew. Chem.* **2012,** *124,* 8380–8383. doi:10.1002/ange.201202655 *Angew. Chem. Int. Ed.* **2012,** *51,* 8255–8258. doi:10.1002/anie.201202655
41. Ingleson, M.; Mahon, M. F.; Weller, A. S. *Chem. Commun.* **2004,** 2398–2399. doi:10.1039/b410846a
42. Thakur, T. S.; Desiraju, G. R. *J. Mol. Struct.: THEOCHEM* **2007,** *810,* 143–154. doi:10.1016/j.theochem.2007.02.012
43. Crosby, S. H.; Clarkson, G. J.; Rourke, J. P. *J. Am. Chem. Soc.* **2009,** *131,* 14142–14143. doi:10.1021/ja905046n
44. Rivada-Wheelaghan, O.; Donnadieu, B.; Maya, C.; Conejero, S. *Chem.–Eur. J.* **2010,** *16,* 10323–10326. doi:10.1002/chem.201000955
45. Zhu, J.; Lin, Z. *Inorg. Chem.* **2005,** *44,* 9384–9390. doi:10.1021/ic0513641
46. Braunschweig, H.; Brenner, P.; Müller, A.; Radacki, K.; Rais, D.; Uttinger, K. *Chem.–Eur. J.* **2007,** *13,* 7171–7176. doi:10.1002/chem.200700539
47. Brainard, R. L.; Nutt, W. R.; Lee, T. R.; Whitesides, G. M. *Organometallics* **1988,** *7,* 2379–2386. doi:10.1021/om00101a019
48. Peters, R. G.; White, S.; Roddick, D. M. *Organometallics* **1998,** *17,* 4493–4499. doi:10.1021/om980334l
49. Hill, G. S.; Rendina, L. M.; Puddephatt, R. J. *J. Chem. Soc., Dalton Trans.* **1996,** 1809–1813. doi:10.1039/DT9960001809
50. Harkins, S. B.; Peters, J. C. *Organometallics* **2002,** *21,* 1753–1755. doi:10.1021/om011044z
51. Poverenov, E.; Gandelman, M.; Shimon, L. J. W.; Rozenberg, H.; Ben-David, Y.; Milstein, D. *Organometallics* **2005,** *24,* 1082–1090. doi:10.1021/om049182m
52. Poverenov, E.; Leitus, G.; Shimon, L. J. W.; Milstein, D. *Organometallics* **2005,** *24,* 5937–5944. doi:10.1021/om050637x
53. Schwartsburd, L.; Poverenov, E.; Shimon, L. J. W.; Milstein, D. *Organometallics* **2007,** *26,* 2931–2936. doi:10.1021/om0700720
54. Butts, M. D.; Scott, B. L.; Kubas, G. K. *J. Am. Chem. Soc.* **1996,** *118,* 11831–11843. doi:10.1021/ja961836y
55. Stahl, S. S.; Labinger, J. A.; Bercaw, J. E. *Inorg. Chem.* **1998,** *37,* 2422–2431. doi:10.1021/ic970944y
56. Holtcamp, M. W.; Labinger, J. A.; Bercaw, J. E. *Inorg. Chim. Acta* **1997,** *265,* 117–125. doi:10.1016/S0020-1693(97)05675-2
57. Konze, W. V.; Scott, B. L.; Kubas, G. J. *Chem. Commun.* **1999,** 1807–1808. doi:10.1039/a902274k
58. Konze, W. V.; Scott, B. L.; Kubas, G. J. *J. Am. Chem. Soc.* **2002,** *124,* 12550–12556. doi:10.1021/ja020798h
59. Thomas, J. C.; Peters, J. C. *J. Am. Chem. Soc.* **2001,** *123,* 5100–5101. doi:10.1021/ja0058987
60. Thomas, J. C.; Peters, J. C. *J. Am. Chem. Soc.* **2003,** *125,* 8870–8888. doi:10.1021/ja0296071
61. Romeo, R.; Alibrandi, G. *Inorg. Chem.* **1997,** *36,* 4822–4830. doi:10.1021/ic970210l
62. Guido, E.; D'Amico, G.; Russo, N.; Sicilia, E.; Rizzato, S.; Albinati, A.; Romeo, A.; Plutino, M. R.; Romeo, R. *Inorg. Chem.* **2011,** *50,* 2224–2239. doi:10.1021/ic101879s
63. Holtcamp, M. W.; Labinger, J. A.; Bercaw, J. E. *J. Am. Chem. Soc.* **1997,** *119,* 848–849. doi:10.1021/ja9620595
64. Holtcamp, M. W.; Henling, L. M.; Day, M. W.; Labinger, J. A.; Bercaw, J. E. *Inorg. Chim. Acta* **1998,** *270,* 467–478. doi:10.1016/S0020-1693(97)06102-1
65. Johansson, L.; Ryan, O. B.; Rømming, C.; Tilset, M. *Organometallics* **1998,** *17,* 3957–3966. doi:10.1021/om9801498
66. Johansson, L.; Ryan, O. B.; Tilset, M. *J. Am. Chem. Soc.* **1999,** *121,* 1974–1975. doi:10.1021/ja984028a
67. Johansson, L.; Tilset, M.; Labinger, J. A.; Bercaw, J. E. *J. Am. Chem. Soc.* **2000,** *122,* 10846–10855. doi:10.1021/ja0017460
68. Procelewska, J.; Zahl, A.; van Eldik, R.; Zhong, H. A.; Labinger, J. A.; Bercaw, J. E. *Inorg. Chem.* **2002,** *41,* 2808–2810. doi:10.1021/ic0201710
69. Zhong, H. A.; Labinger, J. A.; Bercaw, J. E. *J. Am. Chem. Soc.* **2002,** *124,* 1378–1399. doi:10.1021/ja011189x
70. Heyduk, A. F.; Labinger, J. A.; Bercaw, J. E. *J. Am. Chem. Soc.* **2003,** *125,* 6366–6367. doi:10.1021/ja029099v
71. Owen, J. S.; Labinger, J. A.; Bercaw, J. E. *J. Am. Chem. Soc.* **2006,** *128,* 2005–2016. doi:10.1021/ja056387t

72. Chen, G. S.; Labinger, J. A.; Bercaw, J. E. *Proc. Natl. Acad. Sci. U. S. A.* **2007,** *104,* 6915–6920. doi:10.1073/pnas.0610981104
73. Johansson, L.; Ryan, O. B.; Rømming, C.; Tilset, M. *J. Am. Chem. Soc.* **2001,** *123,* 6579–6590. doi:10.1021/ja010277e
74. Heyduk, A. F.; Driver, T. G.; Labinger, J. A.; Bercaw, J. E. *J. Am. Chem. Soc.* **2004,** *126,* 15034–15035. doi:10.1021/ja045078k
75. McKeown, B. A.; Foley, N. A.; Lee, J. P.; Gunnoe, T. B. *Organometallics* **2008,** *27,* 4031–4033. doi:10.1021/om8006008
76. McKeown, B. A.; Gonzalez, H. E.; Friedfeld, M. R.; Gunnoe, T. B.; Cundari, T. R.; Sabat, M. *J. Am. Chem. Soc.* **2011,** *133,* 19131–19152. doi:10.1021/ja206064v
77. Thomas, C. M.; Peters, J. C. *Organometallics* **2005,** *24,* 5858–5867. doi:10.1021/om050538j
78. Zhang, F.; Prokopchuk, E. M.; Broczkowski, M. E.; Jennings, M. C.; Puddepthatt, R. J. *Organometallics* **2006,** *25,* 1583–1591. doi:10.1021/om050982m
79. Karshtedt, D.; McBee, J. L.; Bell, A. T.; Tilley, T. D. *Organometallics* **2006,** *25,* 1801–1811. doi:10.1021/om0600902
80. Britovsek, G. J. P.; Taylor, R. A.; Sunley, G. J.; Law, D. J.; White, A. J. P. *Organometallics* **2006,** *25,* 2074–2079. doi:10.1021/om060036l
81. Zhao, S.-B.; Wu, G.; Wang, S. *Organometallics* **2006,** *25,* 5979–5989. doi:10.1021/om0608861
82. Albrecht, M.; van Koten, G. *Angew. Chem.* **2001,** *113,* 3866–3898. doi:10.1002/1521-3773(20011015)113:20<3866::AID-ANGE3866>3.0.CO;2-Y
Angew. Chem., Int. Ed. **2001,** *40,* 3750–3781 doi:10.1002/1521-3773(20011015)40:20<3750::AID-ANIE3750>3.3.CO;2-Y
83. van der Boom, M. E.; Milstein, D. *Chem. Rev.* **2003,** *103,* 1759–1792. doi:10.1021/cr960118r
84. Hofmann, A.; Jaganyi, D.; Munro, O. Q.; Liehr, G.; van Eldik, R. *Inorg. Chem.* **2003,** *42,* 1688–1700. doi:10.1021/ic020605r
85. Grove, D. M.; van Koten, G.; Louwen, J. N.; Noltes, J. G.; Spek, A. L.; Ubbels, H. J. C. *J. Am. Chem. Soc.* **1982,** *104,* 6609–6616. doi:10.1021/ja00388a022
86. Terheijden, J.; van Koten, G.; Vinke, I. C.; Spek, A. L. *J. Am. Chem. Soc.* **1985,** *107,* 2891–2898. doi:10.1021/ja00296a010
87. Poverenov, E.; Efremenko, I.; Frenkel, A. I.; Ben-David, Y.; Shimon, L. J. W.; Leitus, G.; Konstantinovski, L.; Martin, J. M. L.; Milstein, D. *Nature* **2008,** *455,* 1093–1096. doi:10.1038/nature07356
88. Kimmich, B. F. M.; Bullock, R. M. *Organometallics* **2002,** *21,* 1504–1507. doi:10.1021/om0108651
89. Vuzman, D.; Poverenov, E.; Diskin-Posner, Y.; Leitus, G.; Shimon, L. J. W.; Milstein, D. *Dalton Trans.* **2007,** 5692–5700. doi:10.1039/B711444C
90. Mitton, S. J.; McDonald, R.; Turculet, L. *Organometallics* **2009,** *28,* 5122–5136. doi:10.1021/om9003863
91. Serra, D.; Cao, P.; Cabrera, J.; Padilla, R.; Rominger, F.; Limbach, M. *Organometallics* **2011,** *30,* 1885–1895. doi:10.1021/om101128f
92. Calderone, V.; Casini, A.; Mangani, S.; Messori, L.; Orioli, P. L. *Angew. Chem.* **2006,** *118,* 1289–1291. doi:10.1002/ange.200502599
Angew. Chem., Int. Ed. **2006,** *45,* 1267–1269 doi:10.1002/anie.200502599
93. Casini, A.; Mastrobuoni, G.; Temperini, C.; Gabbiani, C.; Francese, S.; Moneti, G.; Supuran, C. T.; Scozzafava, A.; Messori, L. *Chem. Commun.* **2007,** 156–158. doi:10.1039/b611122j
94. Ortega-Carrasco, E.; Cossío, F. P.; Lledós, A.; Maréchal, J.-D. *J. Inorg. Biochem.* **2012,** *117,* 230–236. doi:10.1016/j.jinorgbio.2012.09.020
95. Wick, D. D.; Goldberg, K. I. *J. Am. Chem. Soc.* **1997,** *119,* 10235–10236. doi:10.1021/ja971952g
96. Reinartz, S.; White, P. S.; Brookhart, M.; Templeton, J. L. *Organometallics* **2000,** *19,* 3854–3866. doi:10.1021/om000440z
97. Reinartz, S.; White, P. S.; Brookhart, M.; Templeton, J. L. *J. Am. Chem. Soc.* **2001,** *123,* 6425–6426. doi:10.1021/ja0104047
98. Reinartz, S.; Baik, M.-H.; White, P. S.; Brookhart, M.; Templeton, J. L. *Inorg. Chem.* **2001,** *40,* 4726–4732. doi:10.1021/ic010099q
99. Fekl, U.; Goldberg, K. I. *J. Am. Chem. Soc.* **2002,** *124,* 6804–6805. doi:10.1021/ja0258677
100. Fekl, U.; Kaminsky, W.; Goldberg, K. I. *J. Am. Chem. Soc.* **2003,** *125,* 15286–15287. doi:10.1021/ja037781z
101. Kloek, S. M.; Goldberg, K. I. *J. Am. Chem. Soc.* **2007,** *129,* 3460–3461. doi:10.1021/ja0669629
102. Luedtke, A. T.; Goldberg, K. I. *Inorg. Chem.* **2007,** *46,* 8496–8498. doi:10.1021/ic701504z
103. Vedernikov, A. N.; Caulton, K. G. *Angew. Chem.* **2002,** *114,* 4276–4278. doi:10.1002/1521-3757(20021104)114:21<4276::AID-ANGE4276>3.0.CO;2-8
Angew. Chem. Int. Ed. **2002,** *41,* 4102–4104. doi:10.1002/1521-3773(20021104)41:21<4102::AID-ANIE4102>3.0.CO;2-#
104. Vedernikov, A. N.; Huffman, J. C.; Caulton, K. G. *New J. Chem.* **2003,** *27,* 665–667. doi:10.1039/b302055j
105. Jensen, M. P.; Wick, D. D.; Reinartz, S.; White, P. S.; Templeton, J. L.; Goldberg, K. I. *J. Am. Chem. Soc.* **2003,** *125,* 8614–8624. doi:10.1021/ja028477t
106. Lledós, A.; Ortuño, M. A.; Vidossich, P.; Ujaque, G.; Conejero, S. *Dalton Trans.* **2013**. doi:10.1039/c3dt50761k
107. Romeo, R.; Fenech, L.; Scolaro, L. M.; Albinati, A.; Macchioni, A.; Zuccaccia, C. *Inorg. Chem.* **2001,** *40,* 3293–3302. doi:10.1021/ic0014080
108. Romeo, R.; Fenech, L.; Carnabuci, S.; Plutino, M. R.; Romeo, A. *Inorg. Chem.* **2002,** *41,* 2839–2847. doi:10.1021/ic011206j
109. Romeo, R.; Carnabuci, S.; Plutino, M. R.; Romeo, A.; Rizzato, S.; Albinati, A. *Inorg. Chem.* **2005,** *44,* 1248–1262. doi:10.1021/ic0485920
110. Romeo, R.; Carnabuci, S.; Fenech, L.; Plutino, M. R.; Albinati, A. *Angew. Chem.* **2006,** *118,* 4606–4610. doi:10.1002/ange.200600827
Angew. Chem., Int. Ed. **2006,** *45,* 4494–4498. doi:10.1002/anie.200600827
111. Romeo, R.; D'Amico, G.; Guido, E.; Albinati, A.; Rizzato, S. *Inorg. Chem.* **2007,** *46,* 10681–10692. doi:10.1021/ic701396j
112. Foley, P.; DiCosimo, R.; Whitesides, G. M. *J. Am. Chem. Soc.* **1980,** *102,* 6713–6725. doi:10.1021/ja00542a009
113. Romeo, R. *Comments Inorg. Chem.* **1990,** *11,* 21–57. doi:10.1080/02603599008035817
114. Omae, I. *J. Organomet. Chem.* **2011,** *696,* 1128–1145. doi:10.1016/j.jorganchem.2010.11.023
115. Albrecht, M. *Chem. Rev.* **2010,** *110,* 576–623. doi:10.1021/cr900279a
116. Thorn, D. L. *Organometallics* **1998,** *17,* 348–352. doi:10.1021/om970759s
117. Plutino, M. R.; Scolaro, L. M.; Albinati, A.; Romeo, R. *J. Am. Chem. Soc.* **2004,** *126,* 6470–6484. doi:10.1021/ja030486u
118. Romeo, R.; Plutino, M. R.; Romeo, A. *Helv. Chim. Acta* **2005,** *88,* 507–522. doi:10.1002/hlca.200590035

119. Scott, J. D.; Puddephatt, R. J. *Organometallics* **1983,** *2,* 1643–1648. doi:10.1021/om50005a028
120. Marrone, A.; Re, N.; Romeo, R. *Organometallics* **2008,** *27,* 2215–2222. doi:10.1021/om701070f
121. Fantasia, S.; Pasini, A.; Nolan, S. P. *Dalton Trans.* **2009,** 8107–8110. doi:10.1039/b911164f
122. Butschke, B.; Schwarz, H. *Chem. Sci.* **2012,** *3,* 308–326. doi:10.1039/c1sc00651g
123. Skapski, A. C.; Sutcliffe, V. F.; Young, G. B. *J. Chem. Soc., Chem. Commun.* **1985,** 609–611. doi:10.1039/C39850000609
124. Minghetti, G.; Stoccoro, S.; Cinellu, M. A.; Soro, B.; Zucca, A. *Organometallics* **2003,** *22,* 4770–4777. doi:10.1021/om0301583
125. Minghetti, G.; Stoccoro, S.; Cinellu, M. A.; Petretto, G. L.; Zucca, A. *Organometallics* **2008,** *27,* 3415–3421. doi:10.1021/om800027g
126. Zhao, S.-B.; Wang, R.-Y.; Wang, S. *J. Am. Chem. Soc.* **2007,** *129,* 3092–3093. doi:10.1021/ja0702770
127. Crosby, S. H.; Clarkson, G. J.; Rourke, J. P. *Organometallics* **2011,** *30,* 3603–3609. doi:10.1021/om200293e
128. Butschke, B.; Schlangen, M.; Schröder, D.; Schwarz, H. *Chem.–Eur. J.* **2008,** *14,* 11050–11060. doi:10.1002/chem.200801658
129. Butschke, B.; Tabrizi, S. G.; Schwarz, H. *Chem.–Eur. J.* **2010,** *16,* 3962–3969. doi:10.1002/chem.200902742
130. Butschke, B.; Schwarz, H. *Chem.–Eur. J.* **2012,** *18,* 14055–14062. doi:10.1002/chem.201201652
131. Butschke, B.; Schlangen, M.; Schröder, D.; Schwarz, H. *Helv. Chim. Acta* **2008,** *91,* 1902–1915. doi:10.1002/hlca.200890204
132. Shilov, A. E.; Shul'pin, G. B. *Chem. Rev.* **1997,** *97,* 2879–2932. doi:10.1021/cr9411886
133. Periana, R. A.; Taube, D. J.; Gamble, S.; Taube, H.; Satoh, T.; Fujii, H. *Science* **1998,** *280,* 560–564. doi:10.1126/science.280.5363.560
134. Labinger, J. A.; Bercaw, J. E. *Nature* **2002,** *417,* 507–514. doi:10.1038/417507a
135. Fekl, U.; Goldberg, K. I. *Adv. Inorg. Chem.* **2003,** *54,* 259–320. doi:10.1016/S0898-8838(03)54005-3
136. Lersch, M.; Tilset, M. *Chem. Rev.* **2005,** *105,* 2471–2526. doi:10.1021/cr030710y
137. Balcells, D.; Clot, E.; Eisenstein, O. *Chem. Rev.* **2010,** *110,* 749–823. doi:10.1021/cr900315k
138. Johansson, L.; Tilset, M. *J. Am. Chem. Soc.* **2001,** *123,* 739–740. doi:10.1021/ja002505v
139. Iron, M. A.; Lo, H. C.; Martin, J. M. L.; Keinan, E. *J. Am. Chem. Soc.* **2002,** *124,* 7041–7054. doi:10.1021/ja025667v
140. Liang, L.-C.; Lin, J.-M.; Lee, W.-Y. *Chem. Commun.* **2005,** 2462–2464. doi:10.1039/b501520k
141. Moret, M.-E.; Chen, P. *Organometallics* **2007,** *26,* 1523–1530. doi:10.1021/om0610039
142. Butschke, B.; Schwarz, H. *Organometallics* **2011,** *30,* 1588–1598. doi:10.1021/om101138d
143. Rivada-Wheelaghan, O.; Ortuño, M. A.; Díez, J.; García-Garrido, S. E.; Maya, C.; Lledós, A.; Conejero, S. *J. Am. Chem. Soc.* **2012,** *134,* 15261–15264. doi:10.1021/ja307139p
144. Crosby, S. H.; Thomas, H. R.; Clarkson, G. J.; Rourke, J. P. *Chem. Commun.* **2012,** *48,* 5775–5777. doi:10.1039/c2cc31572f
145. Romeo, R.; Grassi, A.; Scolaro, L. M. *Inorg. Chem.* **1992,** *31,* 4383–4390. doi:10.1021/ic00047a028
146. Rashidi, M.; Nabavizadeh, S. M.; Zare, A.; Jamali, S.; Puddephatt, R. J. *Inorg. Chem.* **2010,** *49,* 8435–8443. doi:10.1021/ic1010067

License and Terms

Beilstein Journal of Organic Chemistry

Electron self-exchange activation parameters of diethyl sulfide and tetrahydrothiophene

Martin Goez*[1] and Martin Vogtherr[2]

Full Research Paper

Open Access

Address:
[1]Institut für Chemie, Martin–Luther-Universität Halle–Wittenberg, Kurt–Mothes-Str. 2, 06120 Halle/Saale, Germany and [2]Merck KGaA, NMR Spectroscopy, Frankfurter Straße 250, 64293 Darmstadt, Germany

Email:
Martin Goez* - martin.goez@chemie.uni-halle.de

* Corresponding author

Keywords:
CIDNP; electron transfer; free radicals; kinetics; photochemistry; pyrylium salts; self-exchange; sulfides

Beilstein J. Org. Chem. **2013,** *9,* 1448–1454.
doi:10.3762/bjoc.9.164

Received: 01 May 2013
Accepted: 27 June 2013
Published: 19 July 2013

This article is part of the Thematic Series "New reactive intermediates in organic chemistry".

Guest Editor: G. Bucher

Abstract

Electron transfer between the title compounds and their radical cations, which were generated by photoinduced electron transfer from the sulfides to excited 2,4,6-triphenylpyrylium cations, was investigated by time-resolved measurements of chemically induced dynamic nuclear polarization (CIDNP) in acetonitrile. The strongly negative activation entropies provide evidence for an associative–dissociative electron exchange involving dimeric radical cations. Despite this mechanistic complication, the free energies of activation were found to be well reproduced by the Marcus theory of electron transfer, with the activation barrier still dominated by solvent reorganization.

Introduction

Single-electron transfer is probably the simplest chemical process of an organic molecule, because usually no full bonds are broken or formed. For this reaction type, the relationship between its thermodynamic driving force and its rate is well understood [1,2]; it only depends on a single parameter for each reagent involved, namely, the activation barrier $\Delta G_0^{\ddagger}$ of its self-exchange, e.g.,

$$\mathbf{D} + \mathbf{D}^{\bullet+} \overset{\Delta G_0^{\ddagger}}{\rightleftharpoons} \mathbf{D}^{\bullet+} + \mathbf{D} \qquad (1)$$

Observing these key reactions is complicated by the fact that they involve no change of the sample composition. To make the two sides of the reaction equation distinguishable, it is mandatory to label the reagents; then one can measure the transfer rate of the labels to the other species. For fast reactions, nuclear or electron spins are the only labels that can be applied without disturbing the energetics and kinetics. NMR exchange spectroscopy [3] or EPR line broadening experiments [4] employ radiofrequency pulse schemes to generate a suitable magnetization or coherence for this purpose; however, as all such self-

exchanges by necessity involve radical species, an "automatic" labeling with nonequilibrium magnetizations is also feasible by utilizing the CIDNP [5-10] effect (chemically induced dynamic nuclear polarization).

CIDNP arises through a complex interplay of nuclear-spin-selective intersystem crossing and electron-spin-selective reactivity. Its key intermediates are radical pairs $\overline{\mathbf{R}_1^{\bullet}\mathbf{R}_2^{\bullet}}$, i.e., two radicals possessing a correlation of their electron spins, which originates from the electron spin multiplicity of their precursor. The two radicals of each spin-correlated pair undergo diffusive separations and may reencounter at a later time. During their excursions, the differential precession of their electron spins causes intersystem crossing with a rate that depends on the spin states of their nuclei through the hyperfine interactions; upon reencounter, a chemical reaction serves to distinguish between singlet and triplet pairs (usually, a geminate reaction, i.e., a reaction of the two radicals with each other, is only feasible in the singlet state, whereas the radicals of the triplet pairs escape and ultimately react with other molecules in the sample, i.e., individually). In conjunction, these two processes sort the nuclear spins within the life of the pairs (typically, less than 1 ns) such that polarizations, i.e., nonequilibrium magnetizations, of exactly equal magnitudes but opposite signs are generated in the products from the singlet and triplet exit channels. These experiments are normally carried out in the magnet of an NMR spectrometer, so the polarizations in the diamagnetic products can be directly sampled by a radiofrequency pulse and manifest themselves as anomalous line intensities in the NMR spectrum.

Given an appropriate acceptor/donor combination **A**/**D**, photoinduced electron transfer [11] is an expedient route to radical pairs $\overline{\mathbf{A}^{\bullet-}\mathbf{D}^{\bullet+}}$ by laser flash photolysis. Without further action on the part of the experimenter, the radical pair mechanism then creates opposite polarizations in the geminate products, i.e., in the starting materials **A** and **D** regenerated by reverse electron transfer, and in the escaping free radicals $\mathbf{A}^{\bullet-}$ and $\mathbf{D}^{\bullet+}$, in other words, labels all four species with their respective polarizations, e.g., $\mathbf{D}_{\uparrow}$ and $\mathbf{D}_{\downarrow}^{\bullet+}$. As was first recognized by Closs [12], the self-exchange leads to a gradual cancelation of the opposite polarizations in each substrate and its corresponding radical ion, e.g.,

$$\mathbf{D}_{\uparrow} + \mathbf{D}_{\downarrow}^{\bullet+} \rightarrow \mathbf{D}^{\bullet+} + \mathbf{D} \qquad (2)$$

on a timescale of 1...100 microseconds for suitably chosen substrate concentrations. A radiofrequency pulse (typical duration: microseconds for protons) applied at a certain point of time after the laser flash converts the polarizations present in **D** at that precise moment into observable coherences and isolates them from the further cancelation, which only operates for magnetizations. Hence, a series of such time-resolved CIDNP experiments [13-16] with different delays between laser flash and observation pulse provides a direct way of measuring the self-exchange rates [17-20]. Practically all published studies of electron self-exchange – apart from indirect determinations based on the Marcus cross relationship [2] – have been carried out on aromatic or olefinic substrates. All known aliphatic radical cations are heteroatom-centered, which considerably increases the mechanistic intricacies. The main complication arises from fast deprotonation of $\mathbf{D}^{\bullet+}$ at the α carbon to give a neutral radical $\mathbf{D}_{-\mathbf{H}}^{\bullet}$, which can occur at the radical-pair stage in a direct reaction (base, $\mathbf{A}^{\bullet-}$) or even at any stage of the reaction by a relayed proton transfer (relay base, **D**) [21-23] and turns the gross reaction $\mathbf{D} \xrightarrow{-e^-} \mathbf{D}^{\bullet+} \xrightarrow{-H^+} \mathbf{D}_{-\mathbf{H}}^{\bullet}$ into a hydrogen abstraction. In a previous report on two aliphatic amines [20], we have used time-resolved CIDNP experiments to distinguish between the ensuing electron and hydrogen self-exchanges of $\mathbf{D}^{\bullet+}$ and $\mathbf{D}_{-\mathbf{H}}^{\bullet}$. In the present work, we investigate two structurally similar aliphatic sulfides, diethyl sulfide **DES** and tetrahydrothiophene **THTP**, for which we have barred the direct deprotonation at C_α by the choice of a suitable sensitizer; for these substrates, a relayed deprotonation is also impossible because they are not sufficiently basic; however, $\mathbf{D}^{\bullet+}$ can stabilize by dimer formation with surplus **D** to give $(\mathbf{D} \therefore \mathbf{D})^+$ [24]. Except for an order-of-magnitude estimate of the exchange rate from EPR line broadening [25] and a brief remark in an earlier communication by us [26], this is the first report on direct measurements of the electron self-exchange of such sulfur-centered aliphatic radical cations. As we will show, the activation parameters provide evidence that the observed exchange indeed takes place between dimeric radical cations and **D**.

Results and Discussion

On the AM1 level, the heats of formation of **D** and $\mathbf{D}_{-\mathbf{H}}^{\bullet}$ are −92 kJ/mol and −14 kJ/mol for diethyl sulfide **DES** as opposed to −69 kJ/mol and +85 kJ/mol for triethylamine, the quencher used in our earlier work [21-23], so for any sensitizer the radical pair containing $\mathbf{D}_{-\mathbf{H}}^{\bullet}$ lies about 75 kJ/mol higher above the reactants in the case of the amine. From the oxidation potentials in the literature (**DES**, 1.65 V [27]; triethylamine, 0.96 V [21]; both in acetonitrile versus SCE) the opposite order, even with a numerically similar difference, is calculated for the radical pair with $\mathbf{D}^{\bullet+}$, although observations [28,29] that for bifunctional donors comprising both an amine and a sulfide moiety photoinduced electron transfer occurs exclusively from **S**, not **N**, cast some doubt on whether these reported potentials are the true equilibrium potentials for these irreversible redox systems. In any case, a sensitizer that is a potent electron

acceptor but has no hydrogen-abstracting power is mandatory to shift the energetics so as to stop the photoreaction after the stage of the electron transfer.

Two other demands on the sensitizer are imposed by the necessity of maximizing the CIDNP effects, because intrinsically low enhancement factors are expected in consequence [6] of the very high *g* values of sulfur-centered radical cations. First, to suppress instant electron return and thereby maximize the number of radical pairs available for generating polarizations, a triplet sensitizer should be used [11]; the long life of a triplet excited state is also the only way to meet the conflicting requirements of bringing the self-exchange rates into the observable kinetic range by correspondingly low donor concentrations while still retaining a sufficient amount of quenching. Second, that sensitizer should be positively charged, because this removes the Coulombic attraction between the radicals of the pair, so they can easily separate to a distance where spin mixing becomes effective [30].

All these conditions are fulfilled by the 2,4,6-triphenylpyrylium cation **TTP**$^+$. Compared to typical carbonyl sensitizers such as benzophenone or xanthone, its reduction potential (−0.29 V in acetonitrile versus SCE [31]) is more favorable by more than 2 V, yet its triplet energy (222 kJ/mol [32]) is only lower by less than 90 kJ/mol. Its first excited singlet state has a lifetime of 2.9 ns [32], so reacts only marginally with the millimolar sulfide concentrations used in our experiments, but its triplet state (intrinsic intersystem-crossing efficiency, 0.48 [32], with evidence for a noticeable increase in the presence of **DES** by an intermolecular heavy-atom effect [33]) is quenched [34] quantitatively (lifetime, 10 µs [32]; diffusion-controlled electron transfer from **DES** [35]) under our experimental conditions. Protonation of the pyranyl radical **TPP**$^\bullet$ is unknown.

The CIDNP effects observed in the photoreaction of **DES** sensitized by **TPP**$^+$ in acetonitrile are typical [12] for a self-exchange: Only the starting materials exhibit CIDNP, i.e., no other spin-polarized products are formed; hence, the radicals must ultimately stabilize by reverse electron transfer. In spectra with continuous illumination, the polarizations are only weak whereas time-resolved experiments (Figure 1) reveal that they are much stronger initially but quickly decay to a low residual level; this cancelation is clear evidence for an exchange between the sulfide-derived radical and its parent compound.

Which sulfide-derived intermediate is the source of CIDNP can be concluded from the the polarization pattern, i.e., from the relative polarization intensities of the different protons; ethyl groups are very convenient for this type of analysis [36]. In an

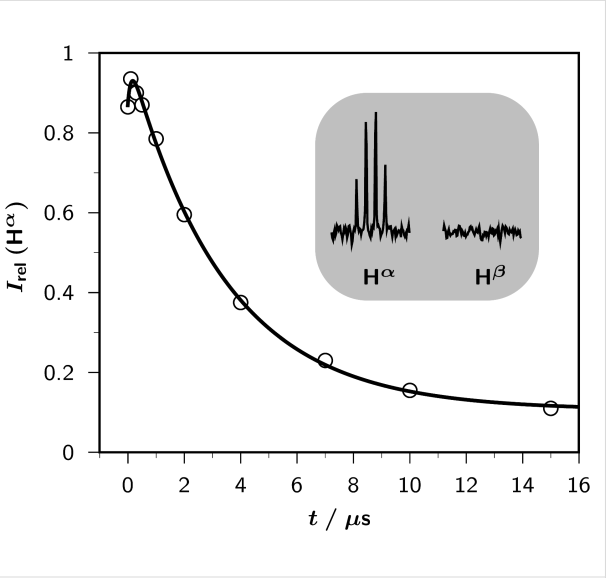

Figure 1: Time-resolved CIDNP measurements on a sample of 5×10^{-3} M **DES** in acetonitrile-d_3 sensitized by 2×10^{-4} M **TPP**$^+$; temperature, 278 K.The main plot shows the relative CIDNP intensities (integrals) $I_{rel}(\mathbf{H}^\alpha)$ of the α protons of the starting sulfide as functions of the delay *t* between the laser flash (wavelength, 308 nm) and the NMR observation pulse (width, 1 µs; tip angle, 22.5°).The fit function is given by Equation 4, in conjunction with Equation 5 and Equation 6. Best-fit kinetic parameters: k_0, 8.80×10^6 s^{-1}, corresponding to a quenching rate constant of 1.8×10^9 M^{-1} s^{-1}; k_{ex}, 5.37×10^7 M^{-1} s^{-1}; T_1, 36.5 µs.The inset displays the actual CIDNP signals of the α and β protons of **DES** ($\mathbf{H}^\alpha$, 2.51 ppm; $\mathbf{H}^\beta$, 1.20 ppm) at a delay of 0 µs. Further explanation, see text.

ethyl-substituted heteroatom-centered radical cation, such as **DES**$^{\bullet+}$, only the α protons experience an appreciable hyperfine coupling, so only these protons can acquire polarizations. In contrast, for an α (heteroatom) substituted ethyl radical, e.g., $\mathbf{DES}^\bullet_{-\mathbf{H}}$, both the α and the β protons possess large hyperfine coupling constants, which are negative and positive, respectively. This would translate into a very different polarization pattern, namely, CIDNP signals of similar magnitude but opposite sign for those two types of protons. As the inset of Figure 1 reveals, only the α protons are polarized in our system, which is thus incontrovertible evidence for the intermediacy of a radical pair containing **DES**$^{\bullet+}$.

A more complete analysis can be given with Kaptein's rule [37] for the polarization phase Γ_i of nucleus *i* in a reaction product ($\Gamma_i = +1$, absorption; $\Gamma_i = -1$, emission),

$$\Gamma_i = \mu \times \varepsilon \times \mathrm{sign}(\Delta g) \times \mathrm{sign}(a_i) \quad (3)$$

In Equation 3, the parameters μ and ε characterize the reaction pathway (μ, precursor multiplicity leading to the radical pair: $\mu = +1$, triplet, $\mu = -1$, singlet; ε, radical-pair multiplicity from

which the product is formed: ε = +1, singlet, ε = −1, triplet), and Δg and a_i are the pertinent magnetic properties of the radical pair (Δg, g-value difference of the two radicals, with the one containing nucleus i taken first; a_i, hyperfine coupling constant of that nucleus in the radical). Together with the fact that the absolute CIDNP intensity of nucleus i is approximately proportional to a_i [7], this sign rule forms the basis for identifying a paramagnetic intermediate through the resulting polarization pattern.

The g value of **DES**$^{\bullet+}$, regardless of whether it is present as a monomeric radical cation (g = 2.017 [38]) or in its dimeric form (g = 2.011 [25]), is much larger than that of the pyranyl radical **TPP**$^{\bullet}$ (g = 2.0031 [39]), so Δg must be positive for the sulfide protons; as stated above, the hyperfine coupling constant of $\mathbf{H}^{\alpha}$ is also positive. For the radical pair, reverse electron transfer is only possible in its singlet state (ε = +1), because the triplet state of **DES** (281 kJ/mol [40]) lies even higher in energy than the initial excited singlet state of **TPP**$^{+}$ (272 kJ/mol [32]). The absorptive polarization for $\mathbf{H}^{\alpha}$ thus confirms the precursor multiplicity expected on the basis of the thermodynamic and photophysical data, i.e., triplet (μ = +1).

The absence of polarizations in the sensitizer is easily rationalized by the low hyperfine coupling constants in its radical **TPP**$^{\bullet}$ (between 2.5 G and 0.4 G [39], as opposed to 18–20 G for $\mathbf{H}^{\alpha}$ in the monomeric [38] and 6.8 G in the dimeric [25] radical cation of the sulfide) in conjunction with its complicated spectral habit, which causes the polarizations to be distributed among many resonances, with concomitant decrease in intensity of the individual peaks.

For tetrahydrothiophene **THTP**, the same polarization pattern (polarizations for $\mathbf{H}^{\alpha}$ only, i.e., CIDNP originating from radical pairs $\overline{\mathbf{THTP}^{\bullet+}\ \mathbf{TTP}^{\bullet}}$) and kinetic behavior of the polarizations was found, which is not surprising given the very similar thermodynamics (ionization potentials of **DES** and **THTP**, 8.42 eV and 8.62 eV, respectively [41]) and magnetic parameters (monomeric **THTP**$^{\bullet+}$ [38], g = 2.014, $a_{\mathbf{H}}\alpha$ = 20...40 G; dimeric radical cation [25], g = 2.010, $a_{\mathbf{H}}\alpha$ = 9.5 G). The main difference between **DES** and **THTP** is a faster decay of the polarizations by the self-exchange in the case of the cyclic sulfide.

For the general reaction mechanism of electron-transfer-induced radical pair formation followed by exchange cancelation, the integrated rate law for the polarization I_{rel} of the regenerated donor as a function of the time t after the laser flash is biexponential [17,19],

$$I_{rel} = A\left[\left(1-1/(\kappa T_1)\right)\exp(-\kappa t)-\left(1-1/(k_0 T_1)\right)\exp(-k_0 t)+(k_0-\kappa)/(k_0\kappa T_1)\right] \quad (4)$$

The fast component k_0 in Equation 4 is the decay rate of the excited state whereas the slow component κ,

$$\kappa = k_{ex} D_0 + 1/T_1 \quad (5)$$

comprises the effects of self-exchange (rate constant, k_{ex}; donor concentration, D_0) and nuclear spin relaxation in the free radicals (relaxation time, T_1). The latter spoils a perfect cancelation of geminate and escape polarizations, so is responsible for the residual magnetization at long times after the flash. Bimolecular recombination of the free radicals, which would lead to an additional term in Equation 5 [17], usually is of marginal importance only [19], and was neglected in our analysis because no dependence of κ on the laser intensity, and hence on the radical concentration, was observed.

Owing to technical reasons, NMR pulses often cannot be made infinitely short on the timescale of the polarization changes, and sampling time-dependent CIDNP with such "long" pulses (duration, τ) then results in a convolution of pulse action and kinetics [42]. Under our experimental conditions, this convolution is tantamount to simply multiplying each exponential term exp(−kt) in Equation 4, where k is k_0 or κ, with a constant factor,

$$\exp(-kt) \rightarrow \frac{1-\exp(-k\tau)}{k\tau}\exp(-kt) \quad (6)$$

The changing of the weights of the two exponentials in Equation 4 by Equation 6 is the reason why the polarizations seen in Figure 1 do not start from zero at time zero after the laser flash.

Eyring plots of the exchange rate constants so obtained for **DES** and **THTP** can be found in Figure 2, and Table 1 lists the activation parameters resulting from these plots. With **DES**, experiments at different concentrations gave slight systematic displacements of the regression lines, corresponding to about 20% lower apparent values of k_{ex} when the amount of sulfide was halved. We tentatively ascribe this to the dimerization of the radical cations discussed below; because of our high radical concentrations, the apparent depletion of **DES** by this complexation is higher for smaller substrate concentrations. On these grounds, we regard the intercept in Figure 2, and thus the activation entropy in Table 1, as a lower limit in the case of **DES**.

The activation enthalpies are unusually small, but much more striking are the strongly negative activation entropies because it

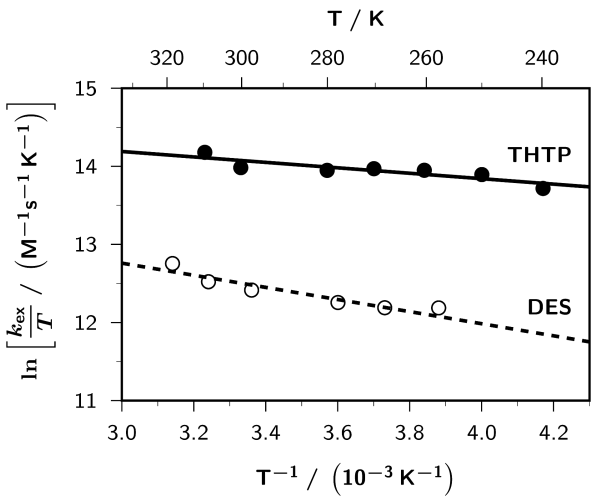

Figure 2: Eyring plots of the self-exchange rate constants k_{ex} for **DES** (open circles and broken line; linear regression, 15.08 – 775/*T*, r^2 = 0.94) and **THTP** (filled circles and solid line; linear regression, 15.24 – 349/*T*, r^2 = 0.88) in acetonitrile-d_3; sensitizer **TTP**$^+$. For all other experimental parameters and further explanation, see Figure 1 and text.

Table 1: Activation parameters (enthalpy $\Delta H_0^{\ddagger}$, entropy $\Delta S_0^{\ddagger}$, and free energy at room temperature $\Delta G_0^{\ddagger}$ (298K)) for the self-exchange reactions of diethyl sulfide **DES** and tetrahydrothiophene **THTP** with their respective radical cations in acetonitrile.

Sulfide	$\Delta H_0^{\ddagger}$ (kJ/mol)	$\Delta S_0^{\ddagger}$ (J K^{-1} mol^{-1})	$\Delta G_0^{\ddagger}$ (298 K) (kJ/mol)
DES	6.4	−72.1	27.9
THTP	2.9	−70.9	24.0

is well known that outer-sphere electron transfer of organic substrates in polar solvents is usually accompanied by small positive activation entropies [43] (e.g., our recent study on triisopropylamine [20] gave an activation entropy of +7.6 JK^{-1} mol^{-1}). Our experimental values indicate transitions states that are much more ordered than usual, which is strong evidence that in these systems the self-exchange does not involve the monomeric radical cations $\mathbf{D}^{\bullet+}$ but the dimeric ones $(\mathbf{D}\therefore\mathbf{D})^{+}$, for which the formation of the new two–center three–electron bond greatly restricts the number of possible orientations of the reacting molecules.

Because of the considerable thermodynamic driving force [24], the initial formation of the dimeric cations must be much faster than the self-exchange, so cannot be captured by our time-resolved CIDNP experiments. It might even occur during the spin-correlated life of the radical pairs without being detectable by the polarization pattern because neither the *g*-value difference nor the distribution of unpaired spin density between the α and β protons changes in it, as discussed above.

Despite the obvious deviation of such an associative–dissociative process from a simple outer-sphere electron transfer, its experimental free energy of activation $\Delta G_0^{\ddagger}$ seems to be well reproduced by the Marcus theory in our case. That theory [1,2] predicts $\Delta G_0^{\ddagger}$ to be one quarter of the reorganization energy λ, which is the hypothetical energy needed for all the geometrical changes occurring in the reaction, but without actually transferring the electron. This includes converting the geometry of the nonradical species into that of the radical species, and vice versa (inner reorganization energy λ_i), as well as rearranging the solvent shell to accommodate the charge distribution of the respective other side of the reaction equation (outer reorganization energy λ_0).

In the majority of cases, λ_i, which is usually calculated from the force constants and geometry differences of the reactants [1,2], constitutes but a small correction to the total reorganization energy, on the order of 10% [44]. At first glance, one would expect the situation to differ for our associative–dissociative electron transfers. For **DES**, however, all bond lengths and angles in the radical cation, regardless of monomeric or dimeric (except, of course, for the bond between the two sulfur atoms, which is only present in the dimer), and in the parent compound are extremely similar, with the maximum changes during the reaction lying well below 0.01 Å [45]; using the known valence force field for **DES** [46], one thus arrives at utterly negligible effects on λ_i from all these bonds. As regards the sulfur–sulfur bond, from the shape of its associated optical absorption band its potential energy curve was concluded [24] to be quite broad and shallow, so it seems reasonable to identify its contribution to λ_i with the free energy of the monomer–dimer equilibrium, which can in turn be estimated from the reported equilibrium constants [24] to lie around 20 kJ/mol. Because that is only about a fifth of the experimental total reorganization energy, the uncertainties of the approximation cannot play an important role; on the other hand, λ_0 obviously also remains the dominant term by far, also for this reaction type.

The solvent dependence of $\Delta G_0^{\ddagger}$ would allow a separation of λ_i and λ_0, as only the latter is polarity dependent. Unfortunately, however, a variation of the solvent proved infeasible. In very nonpolar media, **TPP**$^+$ is not adequately soluble; in protic or nucleophilic solvents, the samples developed a brownish color after only a few laser shots and the CIDNP intensity decreased drastically, so time-resolved measurements could not be performed; in yet further solvents, such as DMSO, the

residual signal of the solvent interfered with an exact determination of the polarization intensities, which are rather small in these systems owing to the large *g*-value differences.

Modeling the reacting molecules as spheres with diameters a_1 and a_2 and a distance d between them, Marcus [1,2] has derived an expression describing λ_0 for the self-exchange between a neutral molecule and an ion of charge z,

$$\lambda_o = \frac{N_A (ze)^2}{4\pi\varepsilon_0} \times \left(\frac{1}{n^2} - \frac{1}{\varepsilon}\right) \times \left(\frac{1}{a_1} + \frac{1}{a_2} - \frac{1}{d}\right) \qquad (7)$$

with N_A, e, and ε_0 being Avogadro's number, the electron charge, and the vacuum permittivity. The second term of the product in Equation 7, the so-called polarity factor, characterizes the ability of the solvent to follow the charge redistribution during the exchange (n, refractive index; ε, relative permittivity); for acetonitrile, its value is 0.527 at room temperature. Several groups [47,48] including ours [49] have extended Equation 7 to multisphere models to take into account the charge distribution in the molecules.

In the associative–dissociative self-exchange between **D** and $(\mathbf{D}\therefore\mathbf{D})^+$, the charge distribution on one half of the dimer remains unchanged, so effectively z amounts to 1/2 only. Furthermore, there is no delocalization in our aliphatic substrates; hence, it seems natural to assume the exchanged charge to be basically localized on two of the three sulfur atoms. In this limit, the multisphere model again turns into Equation 7, with a_1 and a_2 being identical and representing the diameter of the charge cloud around each sulfur. There exists no clear criterion for deciding the value of $a_{1,2}$, but choosing the length of the sulfur–sulfur bond in the dimer (2.9 Å [45]) as a reasonable approximation of this quantity and using the data of Table 1 as well as λ_i estimated above, one arrives at physically very reasonable distances d of 5.3 Å and 3.7 Å for **DES** and **THTP**. In the latter case, a closer approach is in line with expectation because the restricted geometric freedom and more compact configuration of the aliphatic substituents leave the sulfur atom more accessible; furthermore, the obtained reaction distance is practically equal to twice the van-der-Waals radius of sulfur [50], so is also very plausible.

Conclusion

The present study has shed light on an unusual variant of electron self-exchange, namely, an associative–dissociative mechanism involving dimeric radical cations and monomeric parent compounds. It serves to illustrate the power of CIDNP to isolate certain steps within a complex reaction scheme and investigate their kinetics. Not only does it permit the identification of early, short-lived paramagnetic intermediates by freezing their spin-density distribution as a pattern of nuclear spin polarizations, but those polarizations then provide convenient labels that establish a connection with subsequent species on the reaction coordinate and, specific to this work, make the two sides of a self-exchange reaction distinguishable, as to allow one to measure its rate.

Experimental

All chemicals were commercially available. **DES** was purified by distillation, $\mathbf{TPP}^+$ and **THTP** were used as received, the solvent acetonitrile-d_3 was dried to a water content below 5×10^{-4} M in a dedicated apparatus [51]. Oxygen was removed by bubbling nitrogen through the ice-cooled (to reduce losses of sulfide and solvent) solutions; the samples were then sealed. The final concentration of the sulfide in the samples was determined by NMR spectroscopy. Time-resolved ^{1}H (250 MHz) CIDNP measurements were performed on a Bruker WM 250 NMR spectrometer with a special probe [17] that provided illumination of the samples from the side. All unchanging background magnetization was removed by presaturation pulse sequences [52]. Excitation was done with a Lambda Physik EMG 101 excimer laser (medium, XeCl; wavelength, 308 nm; pulse width, 15 ns) triggered by the computer of the spectrometer. The probe was thermostated to ±0.3 K. Quantum mechanical calculations were carried out with the Gaussian 09 package [53] using the AM1 Hamiltonian.

References

1. Marcus, R. A. *Annu. Rev. Phys. Chem.* **1964,** *15,* 155–196. doi:10.1146/annurev.pc.15.100164.001103
2. Marcus, R. A.; Sutin, N. *Biochim. Biophys. Acta, Rev. Bioenerg.* **1985,** *811,* 265–322. doi:10.1016/0304-4173(85)90014-X
3. Burri, J.; Fischer, H. *Chem. Phys.* **1992,** *161,* 429–435. doi:10.1016/0301-0104(92)80158-R
4. Grampp, G. *Spectrochim. Acta, Part A* **1998,** *54,* 2349–2358. doi:10.1016/S1386-1425(98)00215-7
5. Steiner, U. E.; Ulrich, T. *Chem. Rev.* **1989,** *89,* 51–147. doi:10.1021/cr00091a003
6. Goez, M. *Adv. Photochem.* **1997,** *23,* 63–163. doi:10.1002/9780470133545.ch2
7. Goez, M. *Annu. Rep. NMR Spectrosc.* **2009,** *66,* 77–147. doi:10.1016/S0066-4103(08)00403-1
8. Goez, M. In *Carbon-Centered Free Radicals and Radical Cations: Structure, Reactivity, and Dynamics;* Forbes, M. D., Ed.; Wiley Series on Reactive Intermediates in Chemistry and Biology, Vol. 3; 2010; pp 185–204.
9. Berliner, L. J.; Bagryanskaya, E. In *Multifrequency Electron Paramagnetic Resonance;* Misra, S. K., Ed.; Wiley-VCH: Weinheim, 2011; pp 947–992.
10. Goez, M. Top. Curr. Chem. 2012. doi:10.1007/128_2012_348.
11. Kavarnos, G. J.; Turro, N. J. *Chem. Rev.* **1986,** *86,* 401–449. doi:10.1021/cr00072a005

12. Closs, G. L.; Sitzmann, E. V. *J. Am. Chem. Soc.* **1981,** *103,* 3217–3219. doi:10.1021/ja00401a052
13. Schäublin, S.; Wokaun, A.; Ernst, R. R. *J. Magn. Reson.* **1977,** *27,* 273–302. doi:10.1016/0022-2364(77)90077-4
14. Closs, G. L.; Miller, R. J. *J. Am. Chem. Soc.* **1979,** *101,* 1639–1641. doi:10.1021/ja00500a068
15. Goez, M.; Kuprov, I.; Hore, P. J. *J. Magn. Reson.* **2005,** *177,* 139–145. doi:10.1016/j.jmr.2005.06.017
16. Goez, M.; Kuprov, I.; Mok, K. H.; Hore, P. J. *Mol. Phys.* **2006,** *104,* 1675–1686. doi:10.1080/00268970600634431
17. Goez, M. *Chem. Phys.* **1990,** *147,* 143–154. doi:10.1016/0301-0104(90)85030-Z
18. Goez, M. *Z. Phys. Chem.* **1990,** *169,* 123–132. doi:10.1524/zpch.1990.169.Part_2.123
19. Goez, M.; Eckert, G. *Ber. Bunsen-Ges. Phys. Chem.* **1991,** *95,* 1179–1186. doi:10.1002/bbpc.19910951004
20. Goez, M.; Frisch, I.; Sartorius, I. *Beilstein J. Org. Chem.* **2013,** *9,* 437–446. doi:10.3762/bjoc.9.46
21. Goez, M.; Sartorius, I. *J. Am. Chem. Soc.* **1993,** *115,* 11123–11133. doi:10.1021/ja00077a009
22. Goez, M.; Sartorius, I. *Chem. Ber.* **1994,** *127,* 2273–2276. doi:10.1002/cber.1491271128
23. Goez, M.; Sartorius, I. *J. Phys. Chem. A* **2003,** *107,* 8539–8546. doi:10.1021/jp030244g
24. Asmus, K. D. *Acc. Chem. Res.* **1979,** *12,* 436–442. doi:10.1021/ar50144a003
25. Werst, D. W. *J. Phys. Chem.* **1992,** *96,* 3640–3646. doi:10.1021/j100188a017
26. Vogtherr, M.; Goez, M. *J. Inf. Rec.* **1998,** *24,* 23–27.
27. Ando, W. *Sulfur Rep.* **1981,** *1,* 147–207. doi:10.1080/17415998109408001
28. Mönig, J.; Göbl, M.; Asmus, K.-D. *J. Chem. Soc., Perkin Trans. 2* **1985,** 647–651. doi:10.1039/p29850000647
29. Goez, M.; Rozwadowski, J.; Marciniak, B. *J. Am. Chem. Soc.* **1996,** *118,* 2882–2891. doi:10.1021/ja9536678
30. Aizawa, T.; Sakata, T.; Itoh, S.; Maeda, K.; Azumi, T. *Chem. Phys. Lett.* **1992,** *195,* 16–20. doi:10.1016/0009-2614(92)85903-N
31. Saeva, F. D.; Olin, G. R. *J. Am. Chem. Soc.* **1980,** *102,* 299–303. doi:10.1021/ja00521a047
32. Miranda, M. A.; Garcia, H. *Chem. Rev.* **1994,** *94,* 1063–1089. doi:10.1021/cr00028a009
33. Bonesi, S. M.; Manet, I.; Freccero, M.; Fagnoni, M.; Albini, A. *Chem.–Eur. J.* **2006,** *12,* 4844–4857. doi:10.1002/chem.200501144
34. Bonesi, S. M.; Carbonell, E.; Garcia, H.; Fagnoni, M.; Albini, A. *Appl. Catal., B* **2008,** *79,* 368–375. doi:10.1016/j.apcatb.2007.10.037
35. Banu, I. S.; Ramamurthy, P. *J. Photochem. Photobiol., A* **2009,** *201,* 175–182. doi:10.1016/j.jphotochem.2008.10.019
36. Roth, H. D.; Manion, M. L. *J. Am. Chem. Soc.* **1975,** *97,* 6886–6888. doi:10.1021/ja00856a060
37. Kaptein, R. *J. Chem. Soc. D* **1971,** 732–733. doi:10.1039/C29710000732
38. Rao, D. N. R.; Symons, M. C. R.; Wren, B. W. *J. Chem. Soc., Perkin Trans. 2* **1984,** 1681–1687. doi:10.1039/p29840001681
39. Degani, I.; Lunazzi, L.; Pedulli, G. F. *Mol. Phys.* **1968,** *14,* 217–222. doi:10.1080/00268976800100241
40. Shiraishi, Y.; Koizumi, H.; Hirai, T. *J. Phys. Chem. B* **2005,** *109,* 8580–8586. doi:10.1021/jp045639u
41. NIST Chemistry WebBook; NIST Standard Reference Database Number 69; Linstrom, P., Mallard, W., Eds.; National Institute of Standards and Technology, Gaithersburg MD, 20899. http://webbook.nist.gov (accessed April 22, 2013).
42. Goez, M. *Chem. Phys. Lett.* **1990,** *165,* 11–14. doi:10.1016/0009-2614(90)87003-A
43. Ghorai, P. K.; Matyushov, D. V. *J. Phys. Chem. A* **2006,** *110,* 8857–8863. doi:10.1021/jp056261i
44. Jensen, B. S.; Ronlán, A.; Parker, V. D. *Acta Chem. Scand., Ser. B* **1975,** *29,* 394–397. doi:10.3891/acta.chem.scand.29b-0394
45. Deng, Y.; Illies, A. J.; James, M. A.; McKee, M. L.; Peschke, M. *J. Am. Chem. Soc.* **1995,** *117,* 420–428. doi:10.1021/ja00106a048
46. Scott, D. W.; El-Sabban, M. Z. *J. Mol. Spectrosc.* **1969,** *30,* 317–337. doi:10.1016/0022-2852(69)90267-7
47. Peover, M. E.; Powell, J. S. *J. Electroanal. Chem. Interfacial Electrochem.* **1969,** *20,* 427–433. doi:10.1016/S0022-0728(69)80172-5
48. Grampp, G.; Jaenicke, W. *Ber. Bunsen-Ges. Phys. Chem.* **1984,** *88,* 325–334. doi:10.1002/bbpc.19840880403
49. Goez, M. *Z. Phys. Chem.* **1990,** *169,* 133–145. doi:10.1524/zpch.1990.169.Part_2.133.
50. Bondi, A. *J. Phys. Chem.* **1964,** *68,* 441–451. doi:10.1021/j100785a001
51. Goez, M. *J. Magn. Reson.* **1998,** *135,* 14–16. doi:10.1006/jmre.1998.1504
52. Goez, M.; Mok, K. H.; Hore, P. J. *J. Magn. Reson.* **2005,** *177,* 236–246. doi:10.1016/j.jmr.2005.06.015
53. *Gaussian 09,* Revision A.1; Gaussian, Inc.: Wallingford, CT, 2009.

License and Terms

Beilstein Journal of Organic Chemistry

Isolation and X-ray characterization of palladium–N complexes in the guanylation of aromatic amines. Mechanistic implications

Abdessamad Grirrane[*1], Hermenegildo Garcia[*1] and Eleuterio Álvarez[2]

Full Research Paper

Open Access

Address:
[1]Instituto Universitario de Tecnología Química CSIC-UPV, Universidad Politécnica de Valencia, Av. De los Naranjos s/n, 46022 Valencia, Spain and [2]Instituto de Investigaciones Químicas CSIC-US, Departamento de Química Inorgánica, Av. Américo Vespucio 49, 41092 Sevilla, Spain

Email:
Abdessamad Grirrane[*] - grirrane@itq.upv.es; Hermenegildo Garcia[*] - hgarcia@qim.upv.es

* Corresponding author

Keywords:
coordination chemistry; guanylation reaction; homogeneous catalysis; palladium complexes; reactive intermediates

Beilstein J. Org. Chem. **2013,** *9,* 1455–1462.
doi:10.3762/bjoc.9.165

Received: 03 April 2013
Accepted: 21 June 2013
Published: 22 July 2013

This article is part of the Thematic Series "New reactive intermediates in organic chemistry".

Guest Editor: G. Bucher

Abstract

In the context of palladium-catalyzed guanylation of anilines herein, we have been able to characterize and isolate bis(anilino) and bis(guanidino)Pd(II) complexes using reaction conditions under which stoichiometric amounts of palladium salts are used. Characterization of these palladium complexes strongly supports a mechanistic proposal for the catalytic guanylation of anilines using $PdCl_2(NCCH_3)_2$ as catalyst that involves the intermediacy of these Pd(II) complexes.

Introduction

N-Arylguanidines are important compounds with interesting biological activities [1,2] such as fungicides [3] and also in supramolecular chemistry as complementary partners of carboxylate and nitro groups [4-7]. Some of these guanidines are commercially used as antifouling agents in marine paints and in the formulation of protective surface coatings [8-10]. *N*-Arylguanidines can be obtained by aniline insertion into the corresponding carbodiimide [11-18]. This nucleophilic addition can be efficiently catalyzed by palladium salts [19], such as $PdCl_2$ or $Pd(OAc)_2$ in homogenous phase. Also recently we have reported that palladium nanoparticles supported on magnesia can be a solid catalyst for this process [20]. Working with $PdCl_2(NCCH_3)_2$ in dichloromethane we were able to isolate two types of palladium complexes with iodoaniline and guanidine, respectively, (see Scheme 1) that give some clue about the reaction mechanism of the catalytic process.

Results and Discussion

In order to provide further support to the mechanistic proposal for the C–N insertion promoted by palladium(II) suggested by us [20], in the present report we describe the study of palladium-catalyzed guanylation of three additional anilines (**1a**–**c**)

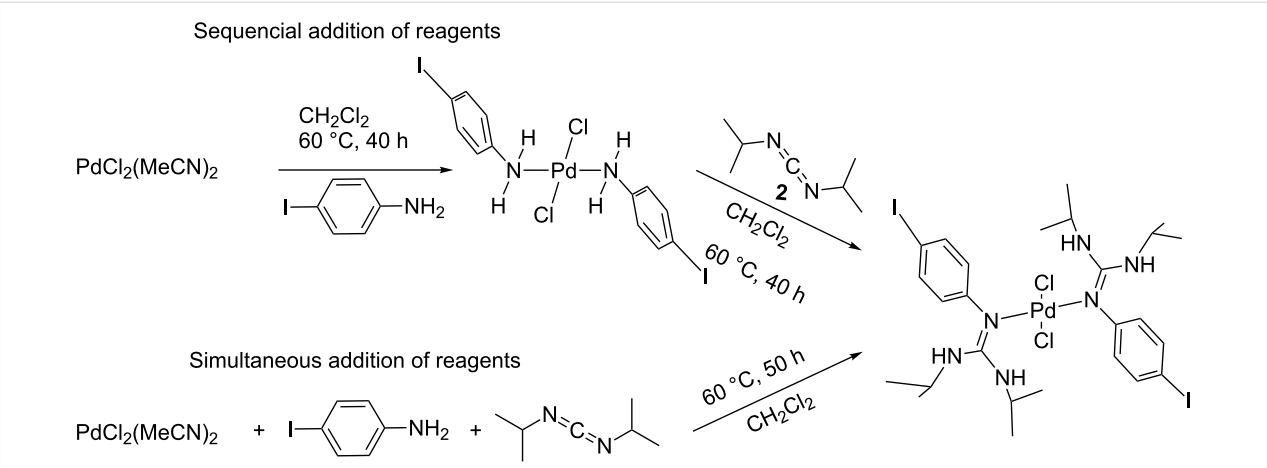

Scheme 1: Isolation of *trans*-dichlorobis(4-iodoanilino-*κN*)palladium(II) and *trans*-dichlorobis[1,3-diisopropyl-2-(4-iodophenyl)guanidino-*κN*(aryl)]palladium(II) complexes formed by reaction of $PdCl_2(MeCN)_2$ with 4-iodoaniline (upper row) or with 4-iodoaniline and *N*,*N*'-diisopropylcarbodiimide (lower reaction).

with *N*,*N*'-diisopropylcarbodiimide (**2**). For these reactions we have been able to characterize three palladium complexes of the type of bis(anilino)Pd(II) (**3a**–**c**) as well as three palladium complexes of the type of bis(guanidino)Pd(II) (**4a**–**c**) (Scheme 2) whose structures have been characterized by single-crystal X-ray structural analysis, as well as to obtain evidence for the intermediacy of these complexes in the catalytic process. Overall the present data reinforce the previous proposal for the mechanism of aniline guanylation.

When a stoichiometric (2:2:1) mixture of anilines **1a**–**c** and carbodiimide **2** with $PdCl_2(MeCN)_2$ is stirred at 60 °C in CH_2Cl_2, evolution at initial reaction times of a solid precipitate is observed (Scheme 2). Filtration of these precipitates and subsequent washing with CH_2Cl_2 renders three solids whose combustion analysis is in accordance with the percentages expected for dichlorobis(anilino-*κN*)palladium(II) (**3a**–**c**) (see Supporting Information File 1, experimental section). IR spectra of complexes **3a**–**c** show the characteristic absorption peaks due to the coordinated anilines **1a**–**c** (see Supporting Information File 1, Figures S1–S3); these are compatible with the proposed structure for these intermediates. Complex **3a** derived from **1a** has been recently characterized by single-crystal X-ray diffraction [21] showing similar coordination to *trans*-dichlorobis(4-

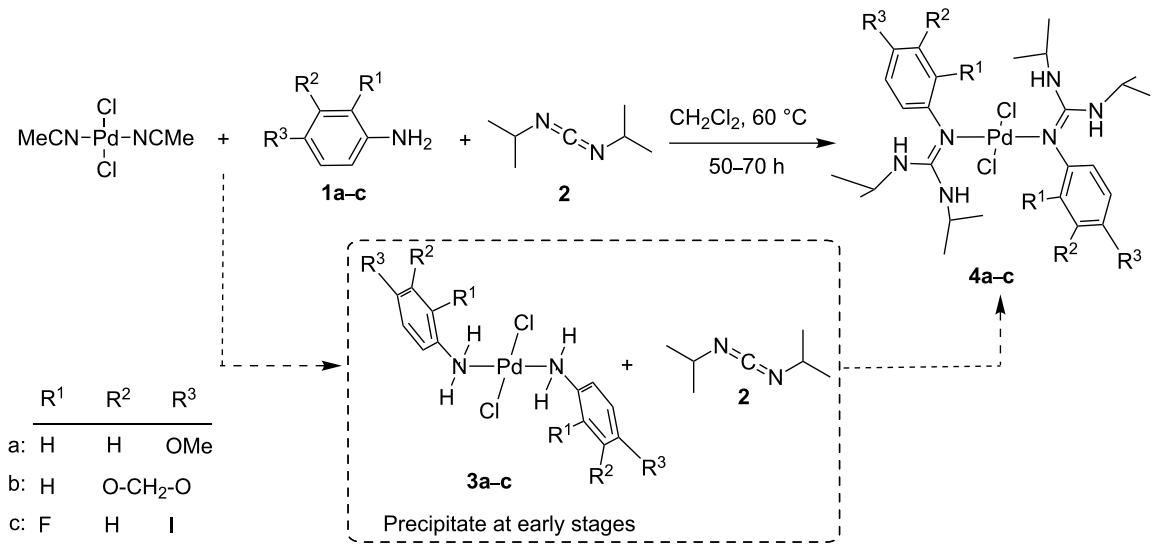

Scheme 2: Isolation of *trans*-dichlorobis[1,3-diisopropyl-2-(aryl)guanidino-*κN*(aryl)]palladium(II) complexes (**4a**–**c**) by reaction of $PdCl_2(MeCN)_2$ with anilines **1a**–**c** and *N*,*N*'-diisopropylcarbodiimide (**2**). Dashed lines indicate the formation of *trans*-dichlorobis(anilino-*κN*)palladium(II) complexes (**3a**–**c**) as primary intermediates during the reaction, and their subsequent reaction with **2** to led **4a**–**c**.

iodoaniline-κN)palladium(II) complex recently published by us [20]. Compounds **3a**–**c** were also characterized by solid state ^{13}C NMR spectroscopy that gave spectra showing carbon peaks compatible with the proposed structure (see Supporting Information File 1, Figures S4–S6).

After prolonging the reaction time, the initially evolved precipitate undergoes dissolution indicating that it has been transformed under the reaction conditions. At this stage, filtering of the transparent orange-red (**4a**,**b**) and red (**4c**) solutions followed by subsequent addition of ethyl ether or toluene and slow solvent evaporation at ambient temperature allows the formation of crystals with suitable quality for a crystallographic diffraction study. The structures of these intermediates solved by X-ray analysis showed that these compounds corresponding to *trans*-dichlorobis[arylguanidino-κN(aryl)]palladium(II). Figure 1, Figure 2 and Figure 3 present ORTEP views of complexes **4a**–**c** as well as selected views along some crystallographic axes (see Tables S1–S3 and also Figures S7, S11 and S15 in Supporting Information File 1, and for full details of the crystallographic data see Supporting Information File 2).

Besides X-ray crystal structure analysis, palladium complexes **4a**–**c** were also characterized by NMR spectroscopy, ESIMS and combustion analysis (see experimental section in Supporting Information File 1). ^{1}H, ^{13}C and ^{19}F NMR spectroscopy of **4a**–**c** in CD_2Cl_2 solution provides evidence showing that under the reaction conditions the starting reagents ($PdCl_2(MeCN)_2$, **1a**–**c** and **2**) including intermediates bis(anilino-κN)palladium(II) (**3a**–**c**) are completely converted into the corresponding bis(guanidino-κN)palladium(II) (**4a**–**c**) (see Supporting Information File 1, Figures S8 and S9 for **4a**, Figures S12 and S13 for **4b** and Figures S16–S18 for **4c**). ESIMS of a solution obtained after dissolving complexes **4a**–**c** in CH_2Cl_2/CH_3CN (1:1) shows single positive MS peaks at 639.3, 667.2 and 867.1 attributable, respectively, to the complexes $[C_{28}H_{46}Cl_2N_6O_2Pd$ (**4a**) $- Cl^-]^+$, $[C_{28}H_{42}Cl_2N_6O_4Pd$ (**4b**) $- Cl^-]^+$ and $[C_{26}H_{38}Cl_2F_2I_2N_6Pd$ (**4c**) $- Cl^-]^+$. Also negative MS shows single peaks at 711.2, 739.1 and 938.9 attributable, respectively, to the complexes $[C_{28}H_{46}Cl_2N_6O_2Pd$ (**4a**) $+ Cl^-]^-$, $[C_{28}H_{42}Cl_2N_6O_4Pd$ (**4b**) $+ Cl^-]^-$ and $[C_{26}H_{38}Cl_2F_2I_2N_6Pd$ (**4c**) $+ Cl^-]^-$ (see Supporting Information File 1, Figures S10, S14 and S19).

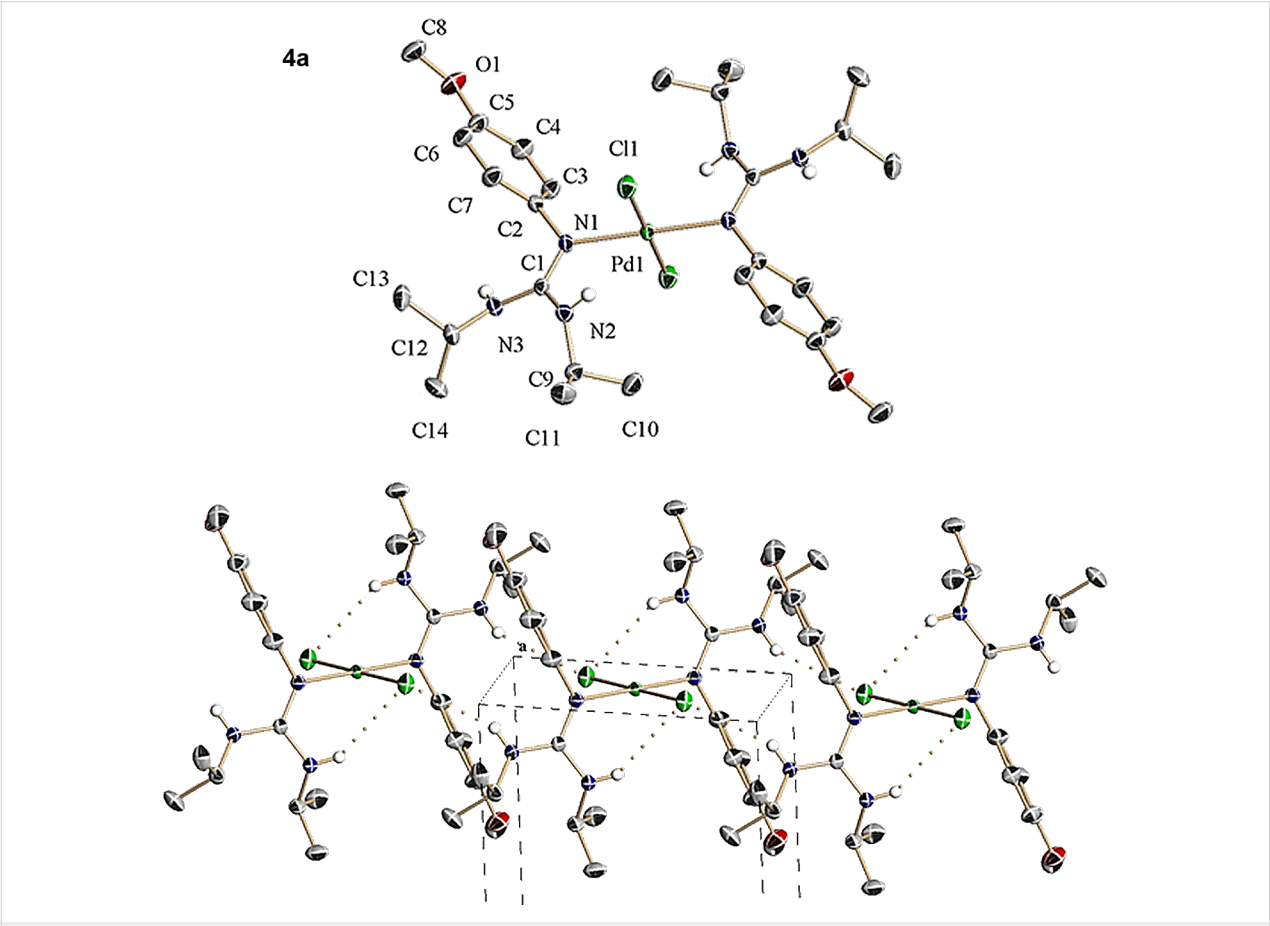

Figure 1: (Top) ORTEP view of the centrosymmetric molecule **4a**. (Bottom) Crystal packing detail of **4a** viewed along the *a*-axis showing the presence of inter- and intramolecular hydrogen bonds between Cl and H (NH groups) atoms.

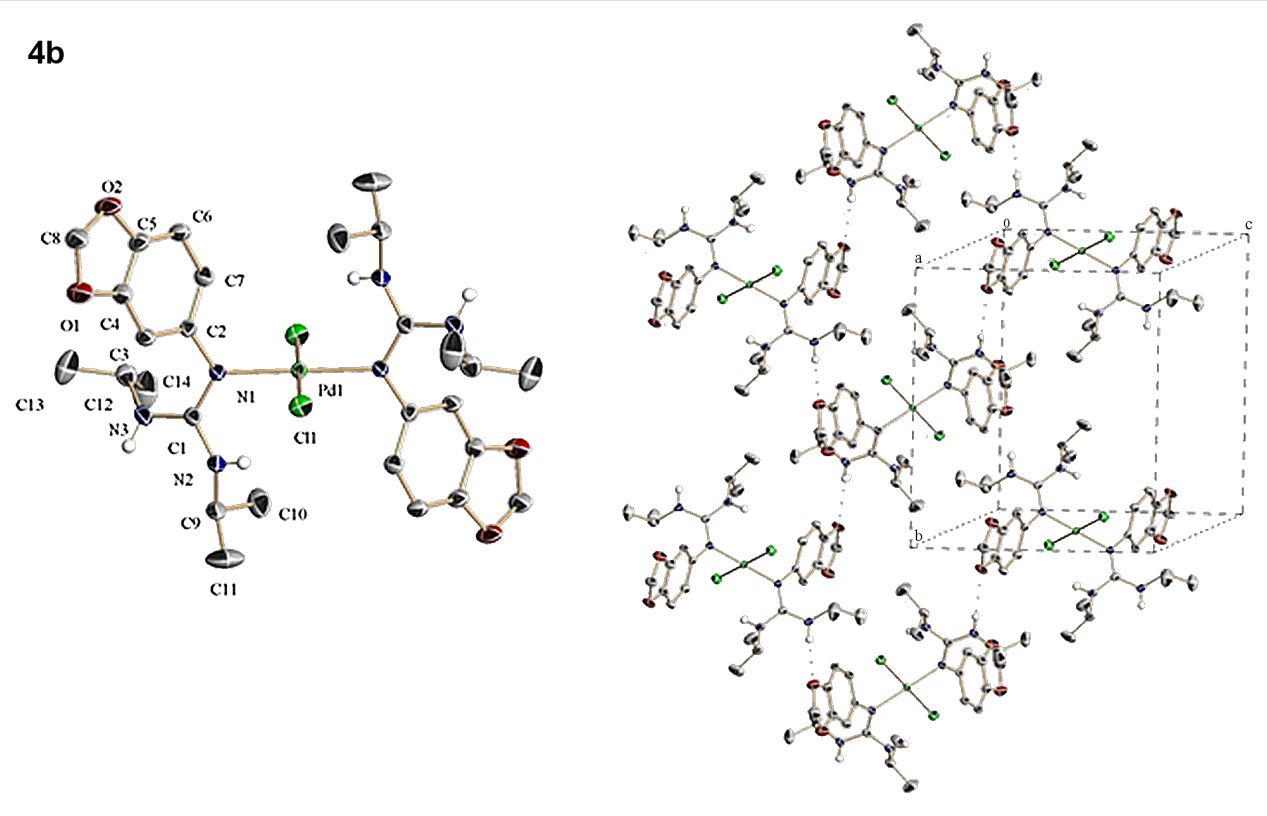

Figure 2: (Left) ORTEP representation of **4b**. (Right) Crystal packing detail of **4b** viewed along the *a*-axis showing the presence of intermolecular hydrogen bonds between O (from the dioxole moieties) and N (NH groups) atoms.

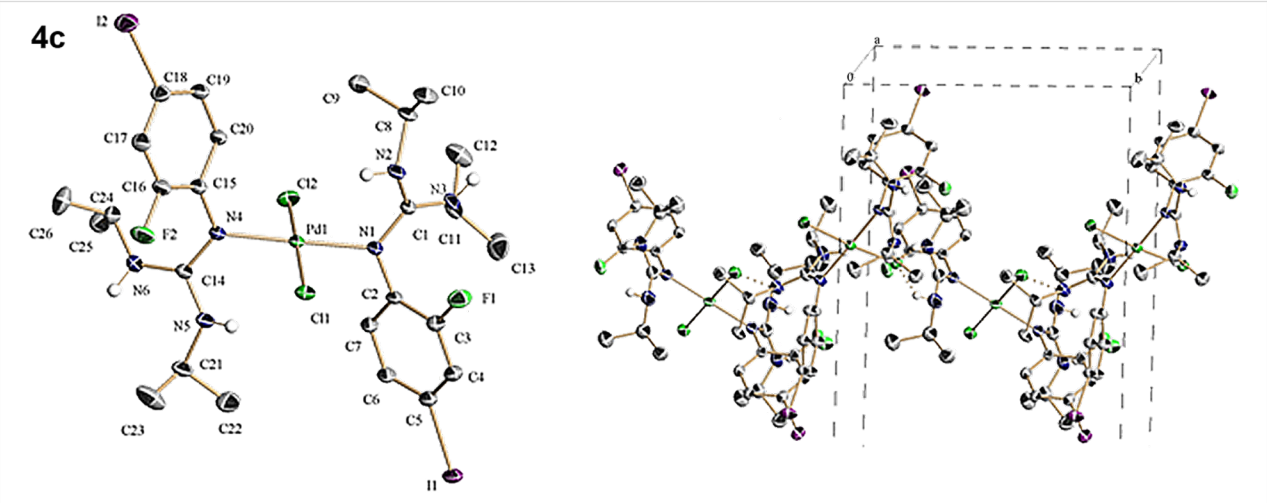

Figure 3: (Left) ORTEP representation of **4c**. (Right) Crystal-packing detail of **4c** viewed along the *a*-axis showing the presence of intermolecular hydrogen bonds between Cl and N (NH groups) atoms.

Similar reactions were carried out mixing anilines **1a**–**c** and *N*,*N*'-diisopropylcarbodiimide (**2**), but in this case in the presence of only a catalytic amount of $PdCl_2(NCCH_3)_2$ (4 mol %) (Scheme 3). Under these conditions no evidence for the formation of palladium complexes (**3a**–**c**) and (**4a**–**c**) could be obtained due to the low amount of palladium and no solid precipitates were observed. In contrast, in the presence of catalytic amounts of palladium, formation of the corresponding *N*-arylguanidines was observed in almost quantitative yield. These guanidines **5a**–**c** formed by nucleophilic attack of anilines **1a**–**c** to *N*,*N*'-diisopropylcarbodiimide (**2**) catalyzed by palladium were fully characterized by analytical and spectro-

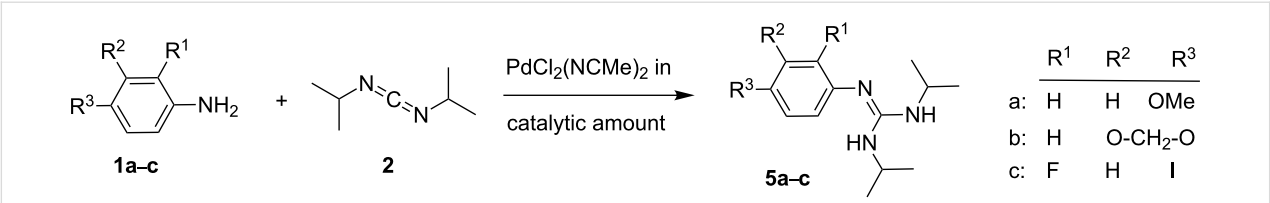

Scheme 3: Guanylation reactions of anilines **1a–c** by *N*,*N*'-diisopropylcarbodiimide (**2**) catalyzed by Pd(II) salt.

scopic data (see Supporting Information File 1, experimental section).

Structure of guanidine **5a** was confirmed by single-crystal X-ray analysis, Figure 4 shows the corresponding ORTEP for compound **5a** as well as some views of the crystal packing (see also Supporting Information File 1, Table S4 and Figure S20 and for full details of crystallographic data see Supporting Information File 2). Beside X-ray crystal analysis of guanidine **5a**, guanidines **5a–c** were also characterized by ^{1}H, ^{13}C and ^{19}F NMR spectroscopy and combustion analysis (see Figures S21 and S22 for **5a**, Figures S24 and S25 for **5b**, our recent published work for **5c** [20] and experimental section in Supporting Information File 1). ESIMS and GC–MS of solutions obtained respectively after dissolving guanidines **5a** and **5b** in CH_2Cl_2/MeOH (1:1) and CH_2Cl_2 shows a single positive MS peak at 250.2 and 263.2 Da attributable, respectively, to the complexes $[C_{14}H_{23}N_3O$ (**5a**) + $H^+]^+$ and $C_{14}H_{21}N_3O_2$ (**5b**) (see Figure S23 and Figure S26 in Supporting Information File 1).

Overall the information obtained from the experiments performed in the presence of a large palladium excess, in which two kinds of palladium complexes have been detected and isolated, with the formation of guanidines under conditions in which a catalytic amount of palladium is present, allows us to make reasonable mechanistic proposals. Thus, upon contacting anilines **1a–c** and $PdCl_2(MeCN)_2$, a rapid formation of dichlorobis(anilino-*κN*)palladium(II) (**3a–c**) complexes should take place. These palladium complexes will interact with the *N*,*N*'-diisopropylcarbodiimide (**2**) giving rise to the dichlorobis(guanidino-*κN*)palladium(II) (**4a–c**) complexes. When Pd is used in catalytic amounts, cleavage of this bis(guanidino-*κN*) complex by aniline will form another dichlorobis(anilino-*κN*)palladium(II) (**3a–c**) completing one cycle and liberating guanidines **5a–c** as free products of this catalytic reaction with high yields and selectivities (see Scheme 4). In this mechanism the rate determining step will be the attack of dichlorobis(anilino-*κN*)palladium(II) (**3a–c**) to the *N*,*N*'-diisopropylcarbodiimide (**2**) (Scheme 4).

In this process, coordination of nitrogen to palladium should strongly reduce the nucleophilicity of the corresponding nitrogen atom and, therefore, the attack at the carbodiimide would be significantly slowed down compared to free uncoordinated aniline. However, this negative effect of palladium coor-

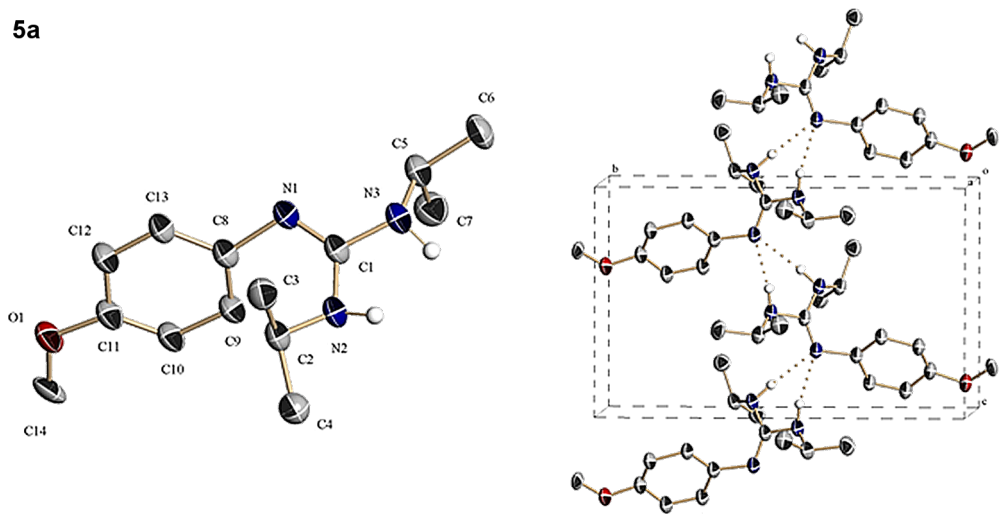

Figure 4: (Left) ORTEP representation of **5a**. (Right) Crystal packing details of **5a** viewed along the *a*-axis showing the presence of intermolecular hydrogen bonds between N atoms.

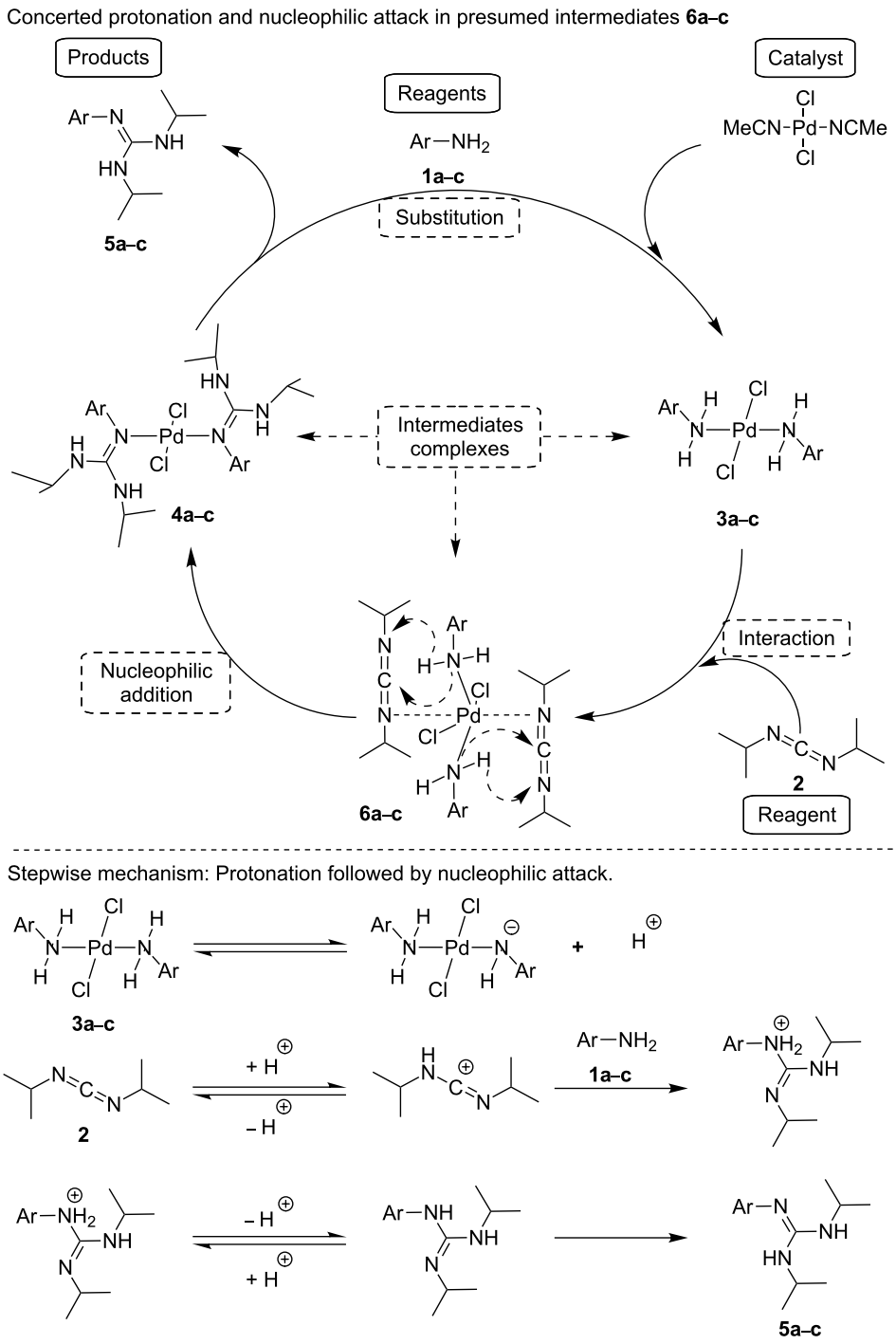

Scheme 4: Possible mechanisms for the C–N coupling catalyzed by $PdCl_2(NCMe)_2$ in homogeneous phase.

dination to aniline should be overcompensated by coordination of carbodiimide to palladium in close proximity to aniline in fixed geometry as indicated in the presumed intermediates **6a**–**c**. There are precedents in the literature [22] showing that palladium(II) can interact weakly with accumulated carbodiimide bonds, but this type of complex is typically very labile and difficult to isolate under the reaction conditions due the presence of an aniline excess, and for this reason we have been unable to isolate labile intermediates **6a**–**c**. This preassociation between complexes **3a**–**c** and carbodiimide **2** to form intermediates **6a**–**c** would make easier the key step of C=N insertion leading to guanidines (Scheme 4).

Alternatively, it can be also envisioned that the acidity of hydrogen atoms bonded to nitrogen in intermediates **3a**–**c** increases sufficiently to protonate the nitrogen atom of the carbodiimide that subsequently would be activated to accept the nucleophilic attack of the resulting anilide anion or aniline (see Scheme 4). This mechanism would be similar to that accepted for peptide-bond formation mediated by carbodiimides [23-26]. It can also be possible that these two steps, i.e., protonation and nucleophilic attack occur in a quasi-concerted manner around the intermediates **6a**–**c**.

Conclusion

In conclusion, we show the possibility to isolate and characterize palladium complexes by performing some reactions using large amounts of palladium salts. The structures of these complexes shed light onto the reaction mechanism of the palladium-catalyzed reaction. In this case, we have applied this methodology to isolate and characterize bis(anilino)- and bis(guanidino)palladium complexes that are proposed to be reaction intermediates, together with the still not isolated aniline–carbodiimide palladium complex **6**, in the mechanism of the guanylation of anilines. Our study opens the way to apply a similar methodology to study the reaction mechanism of other catalytic reactions.

Supporting Information

Supporting Information File 1

Experimental details of preparation, isolation and full characterization of new palladium compounds **3a**–**c**, **4a**–**c** as well as guanidine compounds **5a**,**b**, including IR, NMR, ESIMS and GC–MS spectra for new compounds.
[http://www.beilstein-journals.org/bjoc/content/supplementary/1860-5397-9-165-S1.pdf]

Supporting Information File 2

X-Ray structure analysis data for **4a** (CCDC-931786, **4b** (CCDC-931787), **4c** (CCDC-931788) and **5a** (CCDC-931789) are given. These data can also be obtained free of charge from The Cambridge Crystallographic Data Centre via http://www.ccdc.cam.ac.uk/data_request/cif.
[http://www.beilstein-journals.org/bjoc/content/supplementary/1860-5397-9-165-S2.cif]

Acknowledgements

Financial support by the Spanish Ministry of Economy and competitiveness (Severo Ochoa and CTQ2012-36351) and Generalidad Valenciana (Prometeo 2012-014) is gratefully acknowledged.

References

1. Membrino, A.; Paramasivam, M.; Cogoi, S.; Alzeer, J.; Luedtke, N. W.; Xodo, L. E. *Chem. Commun.* **2010,** *46,* 625–627. doi:10.1039/b918964e
2. Blondeau, P.; Segura, M.; Pérez-Fernández, R.; de Mendoza, J. *Chem. Soc. Rev.* **2007,** *36,* 198–210. doi:10.1039/b603089k
3. Thevissen, K.; Pellens, K.; De Brucker, K.; François, I. E. J. A.; Chow, K. K.; Meert, E. M. K.; Meert, W.; Van Minnebruggen, G.; Borgers, M.; Vroome, V.; Levin, J.; De Vos, D.; Maes, L.; Cos, P.; Cammue, B. P. A. *Bioorg. Med. Chem. Lett.* **2011,** *21,* 3686–3692. doi:10.1016/j.bmcl.2011.04.075
4. Guanidines: Historical, biological, biochemical and clinical aspects of the naturally occurring guanidino compounds. In *Proceedings of the international symposium on guanidino compounds,* Tokyo, Japan, Sept 5–7, 1983; Mori, A.; Cohen, B. D.; Lowenthal, A., Eds.; Plenum Press: New York, NY, USA, 1985.
5. Berlinck, R. G. S.; Burtoloso, A. C. B.; Kossuga, M. H. *Nat. Prod. Rep.* **2008,** *25,* 919–954. doi:10.1039/b507874c
6. Berlinck, R. G. S.; Kossuga, M. H. *Nat. Prod. Rep.* **2005,** *22,* 516–550. doi:10.1039/b209227c
7. Bae, I.; Han, H.; Chang, S. *J. Am. Chem. Soc.* **2005,** *127,* 2038–2039. doi:10.1021/ja0432968
8. Tamura, A.; Tamura, N.; Shibuya, H.; Ouchi, S.; Kuwahara, M. Antifouling agent for underwater noxious attached organism. Japanese Patent 2000128717, May 9, 2000.
9. Denneman, M. A.; Karzijn, W. Process for removing fouling. WO 2010076259, July 8, 2010.
10. Omae, I. *Chem. Rev.* **2003,** *103,* 3431–3448. doi:10.1021/cr030669z
11. Liu, C.; Zhou, S.; Wang, S.; Zhang, L.; Yang, G. *Dalton Trans.* **2010,** *39,* 8994–8999. doi:10.1039/c0dt00246a
12. Ong, T. G.; Yap, G. P. A.; Richeson, D. S. *J. Am. Chem. Soc.* **2003,** *125,* 8100–8101. doi:10.1021/ja035716j
13. Montilla, F.; Pastor, A.; Galindo, A. *J. Organomet. Chem.* **2004,** *689,* 993–996. doi:10.1016/j.jorganchem.2004.01.005
14. Zhang, W.-X.; Li, D.; Wang, Z.; Xi, Z. *Organometallics* **2009,** *28,* 882–887. doi:10.1021/om801035t
15. Rowley, C. N.; Ong, T.-G.; Priem, J.; Richeson, D. S.; Woo, T. K. *Inorg. Chem.* **2008,** *47,* 12024–12031. doi:10.1021/ic801739a
16. Ong, T.-G.; O'Brien, J. S.; Korobkov, I.; Richeson, D. S. *Organometallics* **2006,** *25,* 4728–4730. doi:10.1021/om060539r
17. Zhu, X.; Xu, F.; Shen, Q. *Chin. J. Chem.* **2009,** *27,* 19–22. doi:10.1002/cjoc.200990017
18. Wu, Y.; Wang, S.; Zhang, L.; Yang, G.; Zhu, X.; Liu, C.; Yin, C.; Rong, J. *Inorg. Chim. Acta* **2009,** *362,* 2814–2819. doi:10.1016/j.ica.2008.12.030
19. Li, D.; Guang, J.; Zhang, W.-X.; Wang, Y.; Xi, Z. *Org. Biomol. Chem.* **2010,** *8,* 1816–1820. doi:10.1039/b923249b
20. Grirrane, A.; Garcia, H.; Corma, A.; Alvarez, E. *Chem.–Eur. J.* **2012,** *18,* 14934–14938. doi:10.1002/chem.201202823
21. Bon, V.; Orysyk, S.; Pekhnyo, V. *Acta Crystallogr., Sect. E* **2009,** *65,* M673. doi:10.1107/S1600536809018509
22. Anderson, R. A.; Einstein, F. W. B. *Acta Crystallogr., Sect. B* **1978,** *34,* 271–272. doi:10.1107/S0567740878002770
23. Wendlberger, G. *Houben–Weyl: Methoden der Organischen Chemie;* Georg Thieme Verlag: Stuttgart, Germany, 1974; Vol. 15/2, p 101.
24. Rich, D. H.; Singh, J. In *The Peptides: Analysis, Synthesis, Biology;* Gross, E.; Meienhofer, J., Eds.; Academic Press: New York, NY, USA, 1979; pp 241–261.
25. Jones, J. *The Chemical Synthesis of Peptides;* Oxford University Press: Oxford, U.K., 1991.

26. Bodanszky, M. *Peptide Chemistry. A Practical Textbook,* 2nd ed.; Springer Verlag: Berlin, Germany, 1993. doi:10.1007/978-3-642-78206-0

Beilstein Journal of Organic Chemistry

Thermochemistry and photochemistry of spiroketals derived from indan-2-one: Stepwise processes versus coarctate fragmentations

Götz Bucher[*1,2], Gernot Heitmann[3] and Rainer Herges[*3]

Full Research Paper

Open Access

Address:
[1]Lehrstuhl für Organische Chemie II, Ruhr-Universität Bochum, Universitätsstr. 150, D-44801 Bochum, Germany, [2]WestCHEM, School of Chemistry, University of Glasgow, Joseph-Black-Building, University Avenue, Glasgow G12 8QQ, United Kingdom and [3]Otto-Diels-Institut für Organische Chemie, Universität Kiel, Otto-Hahn-Platz 4, D-24098 Kiel, Germany

Email:
Götz Bucher[*] - goebu@chem.gla.ac.uk;
Rainer Herges[*] - rherges@oc.uni-kiel.de

* Corresponding author

Keywords:
coarctate reaction; fragmentation; matrix isolation; photolysis; pyrolysis; spiroketal

Beilstein J. Org. Chem. **2013,** *9,* 1668–1676.
doi:10.3762/bjoc.9.191

Received: 01 March 2013
Accepted: 22 July 2013
Published: 15 August 2013

This article is part of the Thematic Series "New reactive intermediates in organic chemistry".

Associate Editor: M. S. Sherburn

Abstract

Coarctate reactions are defined as reactions that include atoms at which two bonds are made and two bonds are broken simultaneously. In the pursuit of the discovery of new coarctate reactions we investigate the fragmentation reactions of cyclic ketals. Three ketals with different ring sizes derived from indan-2-one were decomposed by photolysis and pyrolysis. Particularly clean is the photolysis of the indan-2-one ketal **1**, which gives *o*-quinodimethane, carbon dioxide and ethylene. The mechanism formally corresponds to a photochemically allowed coarctate fragmentation. Pyrolysis of the five-ring ketal yields a number of products. This is in agreement with the fact that coarctate fragmentation observed upon irradiation would be thermochemically forbidden, although this exclusion principle does not hold for chelotropic reactions. In contrast, fragmentation of the seven-ring ketal **3** is thermochemically allowed and photochemically forbidden. Upon pyrolysis of **3** several products were isolated that could be explained by a coarctate fragmentation. However, the reaction is less clean and stepwise mechanisms may compete.

Introduction

Pericyclic reactions, according to the original definition, are characterized by a cyclic array of bond making and bond breaking [1-3]. At each atom, involved in the reaction, one bond is made and one bond is broken. However, there are a number of reactions that include a linear system of atoms, or at least one atom, at which *two* bonds are made and *two* bonds broken sim-

ultaneously. Nevertheless, their transition states exhibit a cyclic overlap of basis orbitals. The orbital basis can be derived from the orbital basis of pericyclic transition states by constriction (coarctation, Figure 1). Hence, these reactions have been coined "coarctate" reactions [4,5].

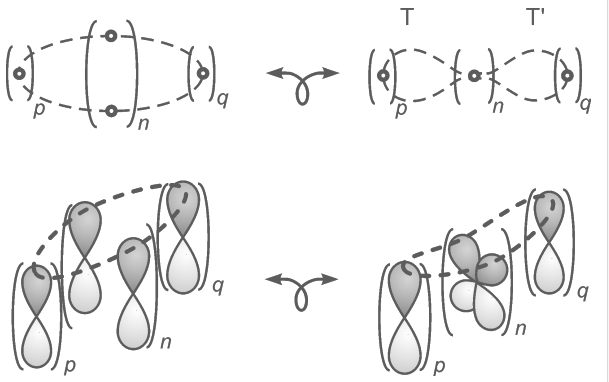

Figure 1: Formal, topological approach to derive coarctate reactions from pericyclic reactions; *p*, *q*: number of atoms or basis orbitals in the terminator groups T and T'; *n*: number of orthogonal pairs of basis orbitals in the transition state of coarctate reactions.

Similar to pericyclic reactions [6], rules were derived to predict their stereochemistry, and whether they would be thermochemically or photochemically allowed. The atom (or the linear system of atoms) at which two bonds are made and broken, each contribute two basis orbitals to the transition state (Figure 1, bottom, right). A cyclic array of orbitals is attained if the linear system of orbital overlap at each end is bound by terminating groups, e.g. a lone pair, or two atoms to form a three-ring, or four atoms to a five-ring, etc. Similar to pericyclic reactions, thermochemical coarctate reactions proceed via Hückel transition states, if the number of delocalized electrons in the transition state is $4n + 2$, and they exhibit Möbius transition states with $4n$ electrons. If in a formal, topological transformation a closed ribbon is transformed into a coarctate band, the two loops T and T' that are formed are coplanar. The analogous transformation of a Möbius ribbon leads to a band whose loops are orthogonal with respect to each other (Figure 2).

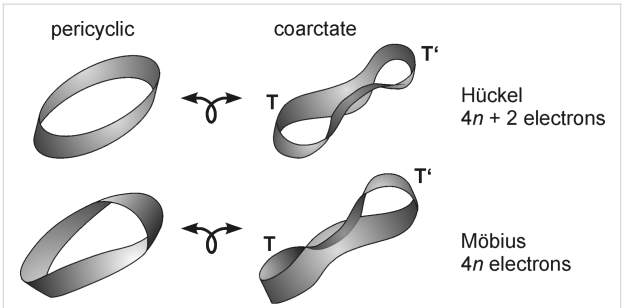

Figure 2: Stereochemistry of coarctate reactions derived from a Hückel (top) and a Möbius band (bottom). The terminator loops T and T' are coplanar in the coarctate Hückel system and orthogonal in the coarctate Möbius transition state.

Following the above principle we developed a number of novel coarctate reactions [7-11], several of which provide synthetic access to a broad range of heterocycles [12-21]. Synthetically probably less useful, but suitable to check the coarctate stereochemical rules, is a peculiar fragmentation reaction that we discovered 15 years ago (Scheme 1) [9,10].

The reaction proceeds spontaneously at temperatures below −80 °C. Quantum chemical calculations of the parent reaction predict an activation barrier of 11.3 kcal/mol and a concerted mechanism. This is in agreement with the stereochemical rule that a coarctate reaction with eight ($4n$) electrons should proceed via a Möbius transition state, with the two terminating groups orthogonal with respect to each other. The orthogonal arrangement is provided by the spiro connection of the three- and the five-membered rings. Following these rules, a Möbius type coarctate fragmentation with two five-ring terminators (10 electrons) should proceed as a photochemical reaction, and a corresponding fragmentation with a seven- and a five-ring (12 electrons) should be thermochemically activated (Scheme 2) [22].

To test the above hypothesis, we now investigate the thermochemistry and the photochemistry of the ketals **1** and **3**, derived from indan-2-one and ethylene glycol, and *cis*-2-butene-1,4-diol (Scheme 3). The ketal **2**, derived from 1,3-propanediol, was chosen as a reference system that cannot undergo a coarctate fragmentation.

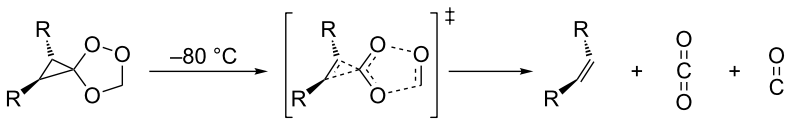

Scheme 1: Coarctate fragmentation of the spiroozonide derived from methylenecyclopropane.

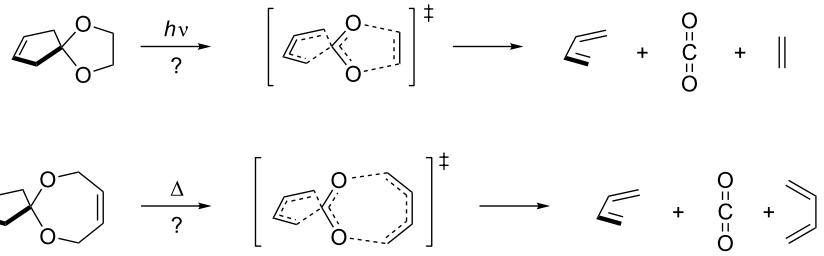

Scheme 2: Photochemically and thermally allowed coarctate fragmentations of spiroketals.

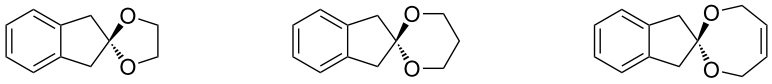

Scheme 3: Precursors used in this study.

Results

Photolysis and pyrolysis of the ketals. Photolysis (λ_{exc} = 254 nm, Hg low-pressure lamp) of indan-2-one ethylene ketal (**1**), matrix-isolated in Ar at 10 K, leads to the formation of CO_2 (vs, ν = 2342.1 cm^{-1}), *o*-xylylene (**XY**, ν = 1550.4, 1470.8, 1467.4, 873.1, 776.2, 738.7 cm^{-1}) [23], ethylene (**ET**, ν = 1438.1, 953.8 cm^{-1}) and indan-2-one (**IN**, ν = 1761.0 cm^{-1}). Some weak product bands could not be assigned. A difference IR spectrum (product bands at a very early stage of the photolysis minus precursor bands) is given in Figure 3.

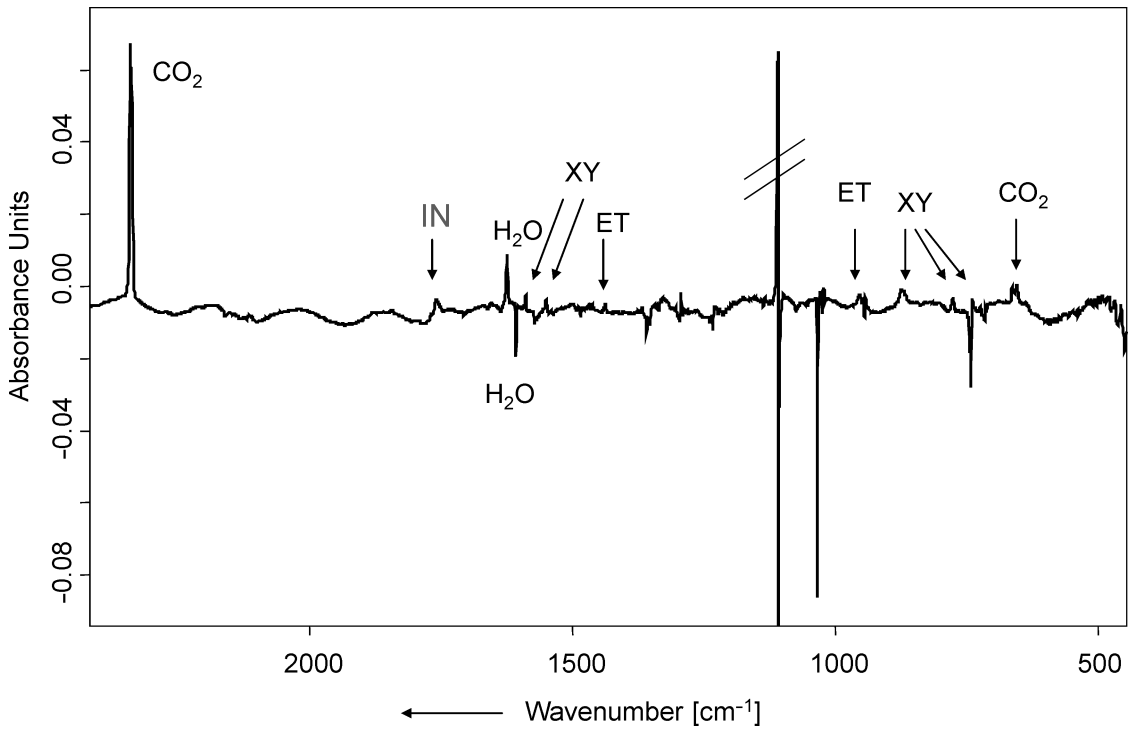

Figure 3: Difference infrared spectrum, showing the changes in the IR spectrum after photolysis (λ_{exc} = 254 nm, 20 min) of **1** in Ar matrix. Except for the water band, all IR bands pointing downwards belong to **1**. Product bands pointing upwards are labelled according to their assignment (**XY** = *o*-xylylene, **ET** = ethylene, **IN** = indan-2-one). The intense band pointing upwards at 1109 cm^{-1} is an artefact due to a subtraction error of a very intense precursor band.

Figure 3 clearly shows that at least at this early stage of photolysis, practically no CO (ν = 2138.4 cm^{-1}) is formed. At a later stage of photolysis (20 h, λ = 254 nm), CO is also detected, and the relative integrals of the CO_2 and CO bands yield an estimated ratio of CO_2 and CO of 2.5:1. It is noted, however, that the formation of CO may well be due to photolysis of CO_2 due to hard UV radiation (λ = 185 nm) also emitted by the Hg low-pressure lamp used [24].

In contrast to the very clean photochemistry of **1**, flash vacuum pyrolysis FVP (T = 870 °C) of **1**, followed by trapping of the reaction products in solid argon, yielded a variety of products whose identity could only partially be elucidated. The ratio of CO_2/CO being formed in the pyrolysis reaction was different from the photochemical decomposition of **1**. Based on the integrals of the CO_2 and CO bands, it can be estimated as 1:27. Figure 4 shows an infrared spectrum of the pyrolysis products.

The organic products include formaldehyde (**FA**), acetaldehyde (**AA**), ethene (**ET**), *o*-xylylene (**XY**), benzocyclobutene (**BC**), styrene (**ST**), and indan-2-one (**IN**). Some peaks could not be assigned. The assignment of the pyrolysis products is based on a comparison with literature data (**XY**) [21], as well as reference spectra of authentic samples (**ET**, **BC**, **IN**, **AA**, **FA**, **ST**). By calibrating IR band integrals to calculated (B3LYP/6-31G(d,p)) IR band intensities of selected bands, a crude measure of product ratios could be obtained. Relative to $[CO_2]$ = 1.0, the concentrations of the other pyrolysis products are as follows: [CO] = 27.2, [**IN**] = 3.8, [**ET**] = 15.9, [**BC**] = 11.4, [**XY**] = 1.3, [**AA**] = 3.9 [25]. Formaldehyde is formed as a minor product only.

The photochemistry of ketals **2** and **3** was investigated as well by matrix isolation spectroscopy. Unfortunately no product could be unambiguously identified. The FVP of **2** yielded the product spectrum shown in Figure 5. Again, both carbon monoxide and carbon dioxide were formed along with the organic products. Carbon monoxide was formed in large excess over carbon dioxide (CO/CO_2 = 13.5:1). Organic products include mostly **FA**, **ET**, and **IN**, as well as **BC** and **XY**, but many peaks have to remain unassigned. Propene was not formed. Compared to the FVP of **1**, the FVP of **2** yields significantly increased amounts of 2-indanone and formaldehyde. Relative to $[CO_2]$ = 1.0, the concentrations of the other pyrolysis products are as follows: [CO] = 13.5, [**IN**] = 9.1, [**ET**] = 15.4, [**BC**] = 19.4, [**XY**] = 1.2, [**FA**] = 12.2.

Flash vacuum pyrolysis of indan-2-one *cis*-*2*-butene-1,4-diol ketal (**3**) again gave rise to a complex mixture of products (Figure 6). Among them, the two conformers of 1,3-butadiene (**tBD** and **cBD**) could be assigned based on a comparison with literature data [26]. Further products include *o*-xylylene (**XY**), benzocyclobutene (**BC**), indan-2-one (**IN**), and formaldehyde (**FA**). Again, a number of IR peaks have to remain unassigned.

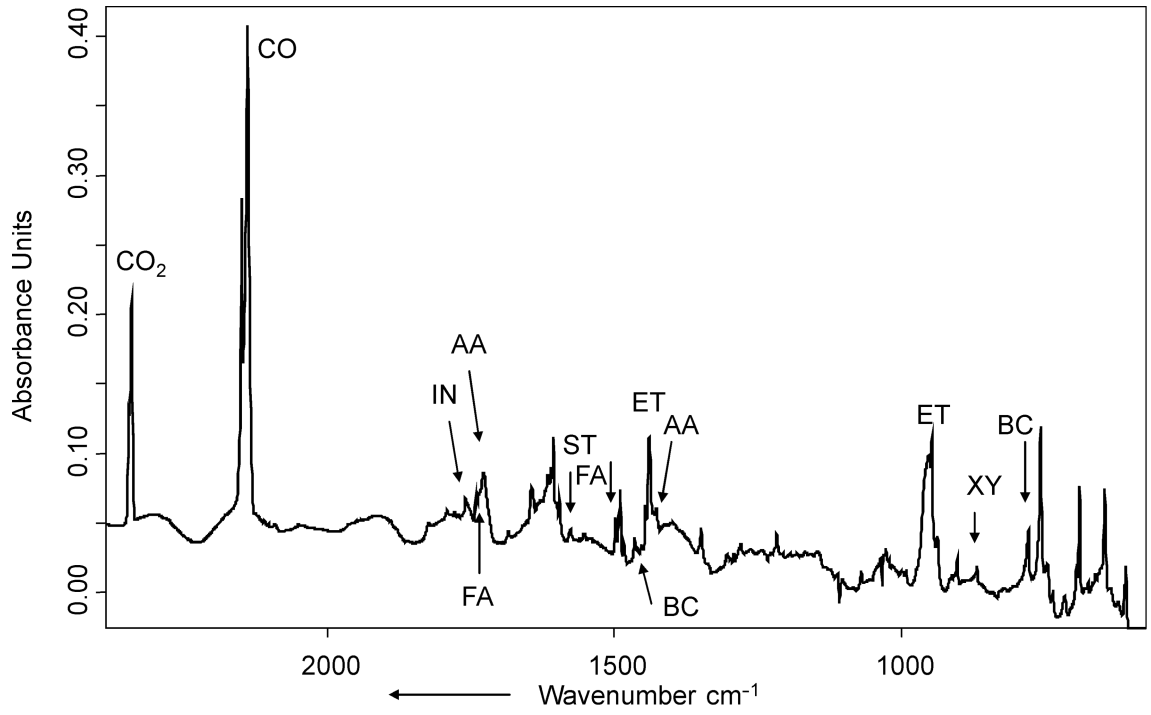

Figure 4: Infrared spectrum obtained upon FVP of **1** at T = 1143 K and trapping the pyrolysate in solid argon at T = 10 K.

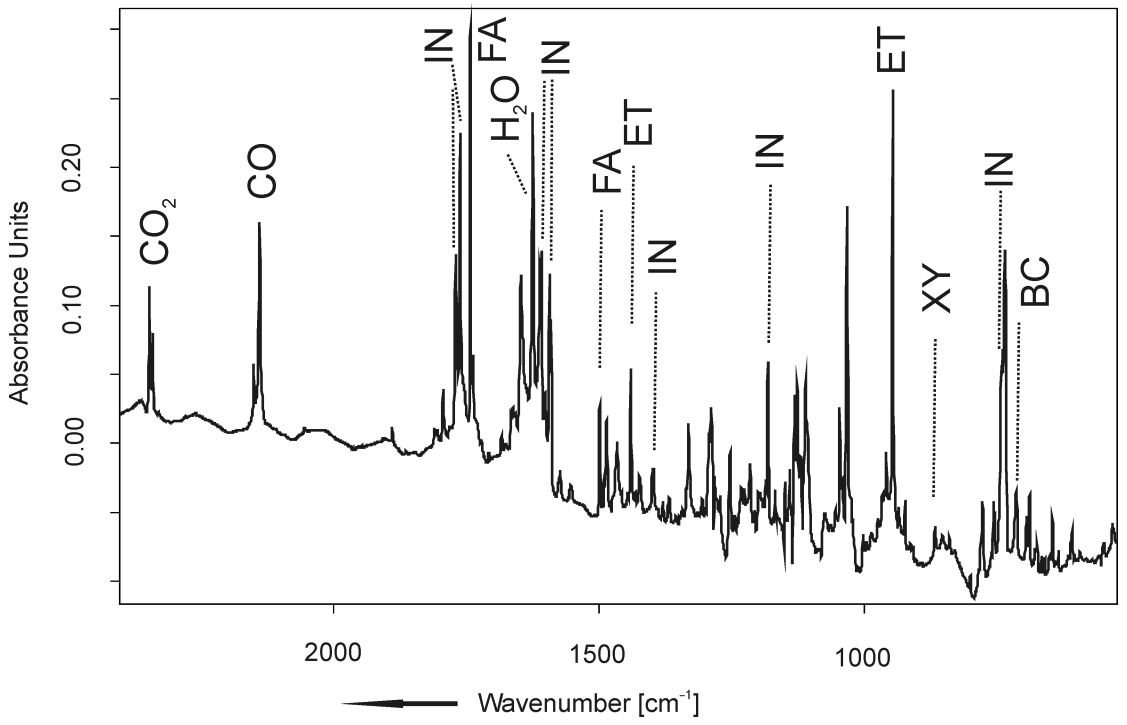

Figure 5: Infrared spectrum obtained upon FVP of **2** at T = 963 K and trapping the pyrolysate in solid argon at T = 10 K.

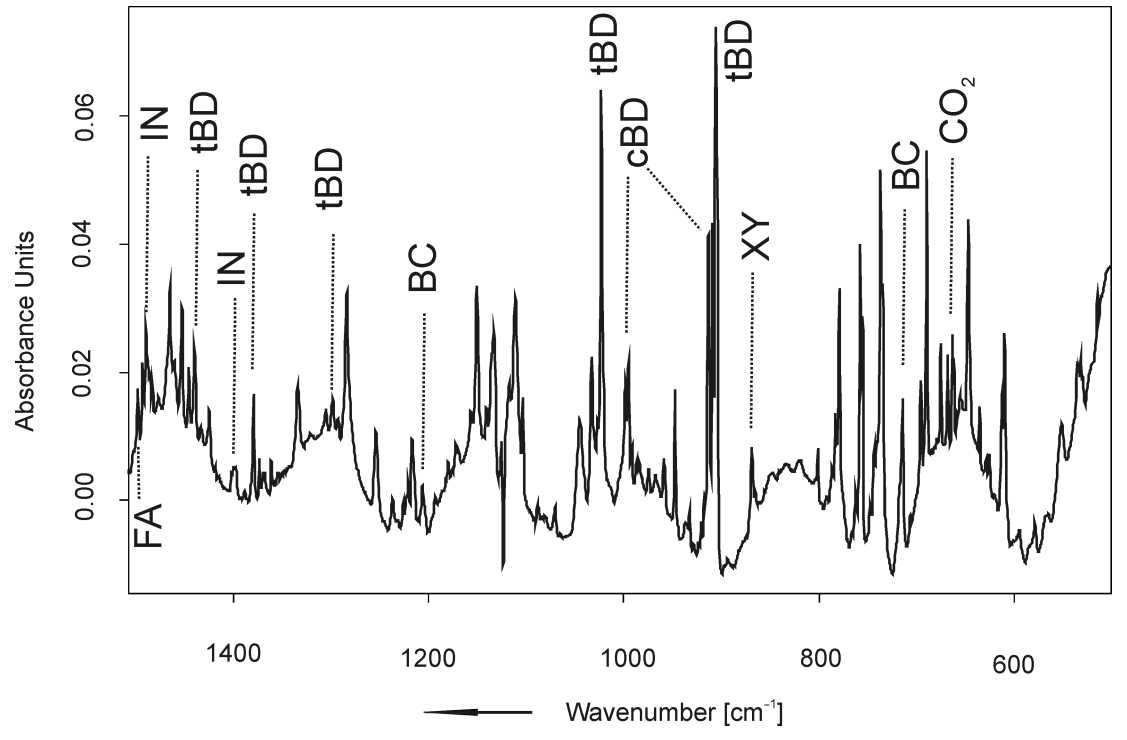

Figure 6: Infrared spectrum obtained upon FVP of **3** at T = 1043 K and trapping the pyrolysate in solid argon at T = 10 K.

CO_2 and CO are formed in a ratio of 1:2.6 in this pyrolysis reaction. Relative to [CO_2] = 1.0, the concentrations of the pyrolysis products are as follows: [CO] = 2.6, [**IN**] = 1.0, [**tBD**] = 7.4, [**cBD**] = 1.5, [**BC**] = 6.3, [**XY**] = 0.4.

Discussion

Flash vacuum pyrolysis of **1** yields a complex mixture, which contains a variety of fragmentation products derived from both sides of the spiroketal linkage. The relative ratio of carbon dioxide and carbon monoxide being formed (CO_2/CO = 1:27) indicates that a coarctate fragmentation of **1** can play a minor role only, if any. The composition of the product mixture is best rationalized by a series of stepwise processes, which starts with either a C–C cleavage (pathway A, more favourable) or a C–O cleavage (pathways B or C, less favourable). In principle, a chelotropic elimination of 1,3-dioxol-2-ylidene is also conceivable (pathway D). Scheme 4 shows a possible mechanistic scenario. While it is questionable whether the biradical intermediates shown in Scheme 4 are in fact true minima or not, we note that they will be exceedingly short-lived at T = 1143 K in any event.

As the C–C bond being broken in mechanism A is significantly weaker than the C–O bonds that need to be cleaved in mechanisms B and C, pathway A is expected to be the most facile decay mechanism for **1**. The primarily formed benzyl-dialkoxymethyl biradical **4** should undergo a very facile ring-opening reaction to yield an ester biradical **7**, which can either cleave into ethylene, carbon dioxide and *o*-xylylene (**XY**), or eliminate acetaldehyde (**AA**) to yield an acyl-benzyl diradical **9** [27]. The latter can then either undergo ring closure to form indan-2-one (**IN**), or decarbonylate to give *o*-xylylene (**XY**). The equilibrium of **XY** and benzocyclobutene (**BC**) is established in the literature [28], as well as the formation of styrene **ST** from **BC** [29]. An alternative mechanism, the chelotropic elimination of 1,3-dioxolan-2-ylidene is not likely. This carbene has been generated from a norbornadiene spiro ketal, and it cleanly fragmented into CO_2 and ethylene [30]. Theoretical calculations support the low barrier for fragmentation [31]. We explain the different reaction behaviour of our spiroketal **1** by the fact that two energetically unfavourable products would have to be formed (a quinodimethane and a carbene), whereas the fragmentation of the norbornadiene ketal gives benzene and a carbene. The mechanism for the thermal decomposition of **2** is likely to be similar. The high yield of formaldehyde in the pyrolysis of **2** is readily explained by the fact that the ester biradical **13** formed can lose one equivalent of ethene and formaldehyde to yield the acyl-benzyl type biradical **15** (Scheme 5).

In the FVP of **1** and **2**, CO is formed in large excess over CO_2. This excess is far less pronounced in the FVP of **3**. This could possibly indicate that a coarctate fragmentation of **3** (which would be a concerted version of pathway C in Scheme 3) could

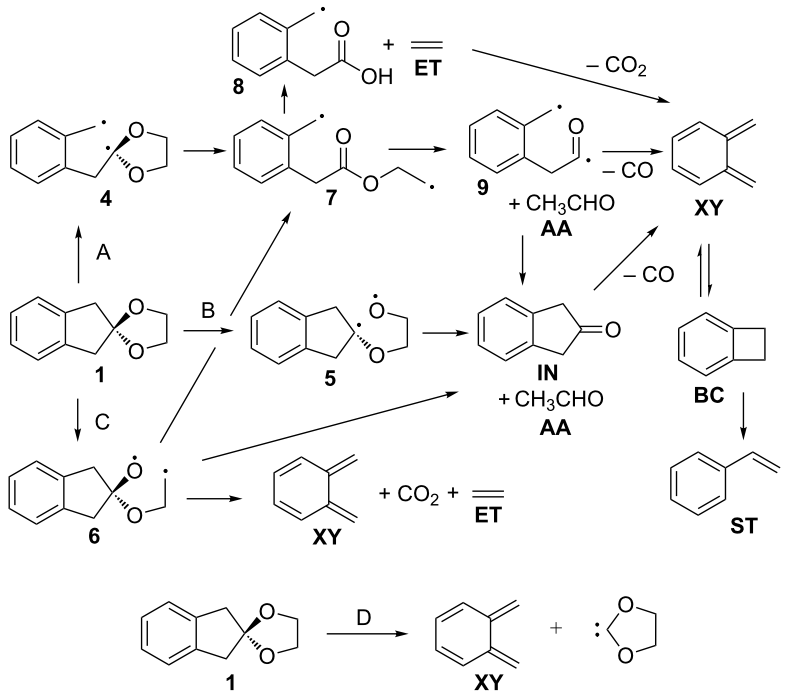

Scheme 4: Possible fragmentation pathways in the FVP of **1**.

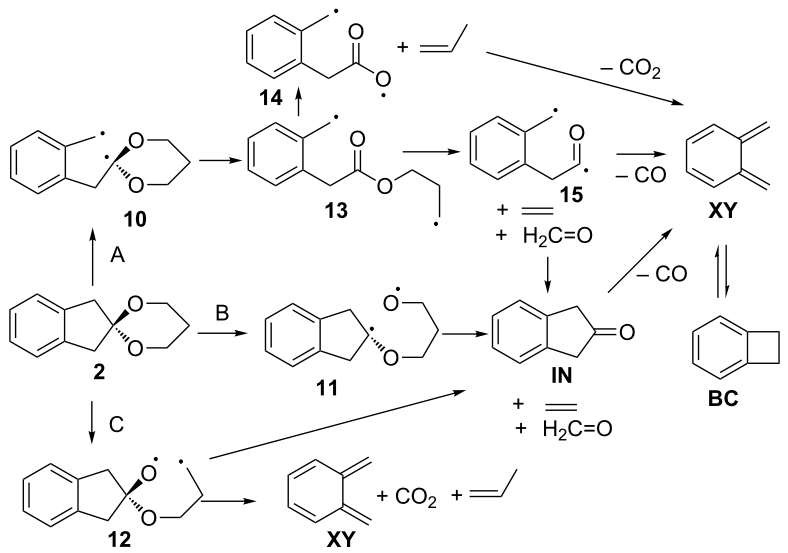

Scheme 5: Possible fragmentation pathways in the FVP of **2**.

possibly also contribute to the product distribution (Scheme 6). A chelotropic reaction forming 4,7-dihydro-1,3-dioxepine-2-ylidene as discussed in the fragmentation of 5-ring spiroketal **1** cannot be excluded. It is known that the sulfur analogue 4,7-dihydro-1,3-dithiepine-2-yldidene cleanly fragments into carbon disulfide and butadiene [32]; however, 4,7-dihydro-1,3-dioxepine-2-ylidene does not give carbon dioxide and butadiene [33].

Conclusion

In agreement with predictions, spiroketals derived from indan-2-one undergo photochemical coarctate fragmentation, if both terminators are 5-membered rings, and thermal coarctate fragmentation, if both a 5-ring and a 7-ring terminator are present. In the latter case, the experimental evidence suggests that the thermal coarctate fragmentation competes with stepwise processes.

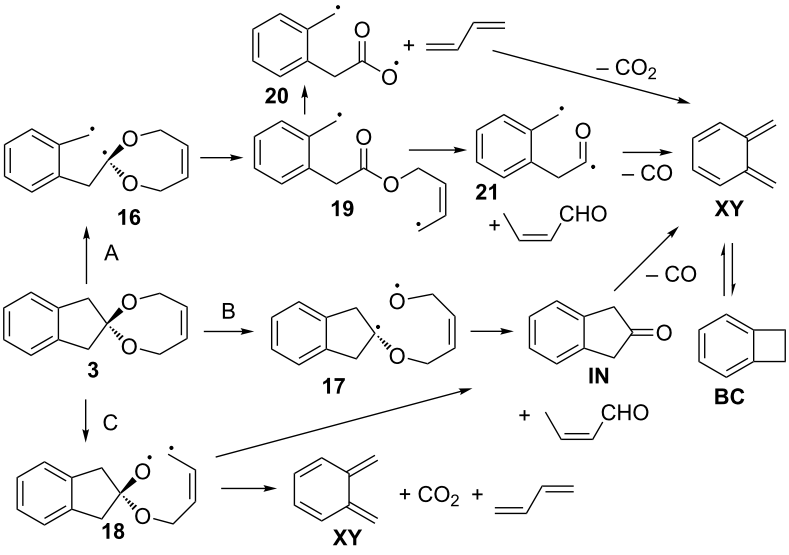

Scheme 6: Possible fragmentation pathways in the FVP of **3**.

Experimental

General: Matrix-isolation experiments were performed using standard matrix-isolation techniques [34]. For sample deposition, the slow-spray-on technique was used. Sample temperatures for deposition were ambient temperature (**1**), ca. 40 °C (**2**), and ca. 60 °C (**3**). The argon used was of 99.999% purity. In pyrolysis experiments, the length of the pyrolysis zone was ca. 5 cm. Reference IR spectra of benzocyclobutene, styrene, indan-2-one, acetaldehyde, formaldehyde, ethene and propene in Ar matrices were independently measured. IR spectra were recorded with a resolution of 0.5 cm^{-1}. The outer matrix window used for photolysis was from Suprasil quartz specified for transmission down to λ = 190 nm.

Ketal **1** was synthesized according to a published procedure [35]. Ketals **2** and **3** were prepared analogously, starting from indan-2-one and propane-1,3-diol and *cis*-2-butene-1,4-diol, respectively.

Indan-2-one ethylene ketal (1): IR (Ar, 10 K) ν: 3109.2 (vw), 3084.4 (vw), 3057.7 (vw), 3034.8 (w), 2993.3 (w), 2989.6 (w), 2962.3 (w), 2928.9 (vw), 2898.5 (w), 2894.8 (w), 2878.1 (w), 2834.1 (vw), 1598.6 (vw), 1485.5 (m), 1472.5 (vw), 1465.1 (vw), 1421.1 (vw), 1342.4 (vw), 1331.9 (m), 1305.9 (vw), 1292.9 (s), 1233.4 (m), 1222.9 (w), 1200.0 (w), 1160.9 (vw), 1136.8 (m), 1110.3 (vs), 1074.2 (w), 1051.9 (vw), 1033.3 (s), 1027.8 (m), 1019.7 (w), 944.4 (w), 867.0 (vw), 785.9 (vw), 741.7 (s), 715.7 (m), 597.7 (vw), 590.5 (vw), 536.8 (vw) cm^{-1}.

Synthesis of 2: Indan-2-one propane-1,3-diol ketal (**2**) was prepared as described for the synthesis of **1**, with the exception of the use of toluene rather than benzene as solvent. Indan-2-one (2.0 g, 0.015 mol) and 1,3-propanediol (1.4 g, 0.018 mol) were heated under reflux in 100 mL toluene together with 20 mg *p*-toluenesulfonic acid. The mixture was heated under reflux for 12 h, during which time the water formed was distilled off as an azeotrope with toluene. The toluenic solution was then washed twice with aq $NaHCO_3$ and once with water. After drying over anhydrous Na_2SO_4, the toluene was removed on a rotary evaporator. Purification of the crude product thus obtained was achieved by distillation in high vacuum. Yield 1.2 g (42%) after distillation. bp 93–97 °C (0.01 mbar); mp 44 °C; ^{1}H NMR ($CDCl_3$, 400 MHz) δ 7.14 (m, 4H), 3.97 (t, *J* = 5.5 Hz, 4H), 3.28 (s, 4H), 1.78 (m, 2H) ppm; ^{13}C NMR ($CDCl_3$, 100 MHz) δ 139.68, 126.65, 124.71, 109.23, 61.52, 42.54, 25.56 ppm; IR (Ar, 10 K) ν: 3111.7 (vw), 3084.8 (vw), 3076.7 (vw), 3060.8 (vw), 3050.1 (w), 3039.8 (w), 3035.7 (w), 2993.7 (w), 2983.8 (m), 2980.1 (m), 2972.7 (m), 2962.7 (m), 2949.8 (m), 2943.1 (m), 2930.7 (m), 2908.2 (w), 2899.4 (w), 2891.9 (w), 2884.6 (m), 2879.0 (m), 2876.1 (m), 2858.9 (m), 2849.9 (w), 2727.6 (vw), 2717.7 (vw), 1620.4 (w), 1612.1 (vw), 1592.5 (vw), 1572.9 (vw), 1488.3 (m), 1477.1 (w), 1464.8 (w), 1433.4 (w), 1425.9 (w), 1381.5 (w), 1369.9 (w), 1333.7 (m), 1305.7 (vw), 1298.5 (w), 1284.5 (vs), 1254.1 (m), 1237.4 (w), 1215.2 (w), 1170.3 (vw), 1150.9 (vs), 1135.6 (vs), 1133.0 (vs), 1117.7 (s), 1111.0 (vs), 1081.2 (w), 1045.9 (s), 1032.9 (s), 1024.0 (m), 966.3 (w), 937.6 (w), 868.8 (w), 734.8 (s), 678.9 (vw), 607.2 (vw), 594.3 (vw), 555.4 (vw) cm^{-1}; EIMS *m*/*z*: M^+ 190 (100), 176, 161, 132 (68), 104 (80), 91, 77, 51; Anal. calcd for $C_{12}H_{14}O_2$: C, 75.8; H, 7.4; found: C, 75.3; H, 7.2.

Indan-2-one cis-2-butene-1,4-diol ketal (**3**) was prepared analogously. Due to the limited thermal stability of **3**, benzene had to be used as solvent, and the product could not be distilled. Instead, a sample of the solid dark brown crude product was purified by sublimation in ultra-high vacuum (10^{-6} mbar), using matrix-isolation equipment. Colourless crystals, mp 78 °C; ^{1}H NMR ($CDCl_3$, 400 MHz) δ 7.16 (m, 4H), 5.73 (t, *J* = 1.5 Hz, 2H), 4.31 (d, *J* = 1.5 Hz, 4H), 3.25 (s, 4H) ppm; ^{13}C NMR ($CDCl_3$, 100 MHz) δ 139.84, 129.53, 126.63, 124.64, 113.31, 62.93, 44.07 ppm; IR (Ar, 10 K) ν: 3078.6 (vw), 3058.5 (vw), 3046.1 (w), 2986.4 (vw), 2966.8 (vw), 2952.9 (w), 2949.1 (w), 2945.8 (w), 2926.2 (w), 2920.9 (w), 2912.3 (w), 2908.0 (w), 2865.0 (w), 2838.8 (vw), 2718.3 (vw), 1622.9 (w), 1612.3 (vw), 1607.9 (vw), 1592.9 (vw), 1589.4 (vw), 1573.0 (vw), 1487.9 (m), 1465.8 (w), 1449.2 (w), 1425.2 (w), 1390.2 (w), 1363.3 (w), 1330.3 (m), 1306.4 (w), 1284.9 (s), 1227.6 (m), 1220.9 (w), 1201.7 (m), 1167.6 (w), 1155.8 (w), 1123.8 (vs), 1115.4 (w), 1102.2 (vw), 1090.2 (s), 1078.3 (m), 1044.6 (s), 1026.9 (m), 1009.9 (m), 951.9 (vw), 946.6 (vw), 920.8 (vw), 879.4 (vw), 872.8 (vw), 817.4 (vw), 732.5 (s), 684.8 (vw), 667.8 (vw), 641.8 (m), 619.4 (m), 617.4 (m), 595.8 (w), 559.1 (vw), 527.5 (vw) cm^{-1}; EIMS *m*/*z*: M^+ 202 (55), 176, 161, 149, 148, 147, 132, 104 (100), 91, 78, 54 (95), 51, 39; Anal. calcd for for $C_{13}H_{14}O_2$: C, 77.2; H, 7.0; found: C, 77.5; H, 7.0; HRMS–ESI (*m*/*z*): $[M]^+$ calcd for $C_{13}H_{14}O_2Na$, 225.0898; found, 225.0891.

Acknowledgements

Financial support by the Deutsche Forschungsgemeinschaft and EPSRC (Glasgow Centre for Physical Organic Chemistry as part of WestCHEM) is gratefully acknowledged. The authors thank W. Sander for access to matrix isolation equipment.

References

1. Woodward, R. B.; Hoffmann, R. *Angew. Chem.* **1969,** *81,* 797–869. doi:10.1002/ange.19690812102
Angew. Chem., Int. Ed. Engl. **1969,** *8,* 781–853. doi:10.1002/anie.196907811
2. Zimmerman, H. E. *Acc. Chem. Res.* **1971,** *4,* 272–280. doi:10.1021/ar50044a002

3. Dewar, M. J. S. *Angew. Chem.* **1971,** *83,* 859–875. doi:10.1002/ange.19710832202
   Angew. Chem., Int. Ed. Engl. **1971,** *10,* 761–776. doi:10.1002/anie.197107611
4. Herges, R. *Angew. Chem.* **1994,** *106,* 261–283. doi:10.1002/ange.19941060304
   Angew. Chem., Int. Ed. Engl. **1994,** *33,* 255–276. doi:10.1002/anie.199402551
5. Herges, R. *J. Chem. Inf. Comput. Sci.* **1994,** *34,* 91–102. doi:10.1021/ci00017a011
6. Unruh, G. R.; Birney, D. M. *J. Am. Chem. Soc.* **2003,** *125,* 8529–8533. doi:10.1021/ja0353661
7. Banert, K.; Grimme, S.; Herges, R.; Heß, K.; Köhler, F.; Mück-Lichtenfeld, C.; Würthwein, E.-U. *Chem.–Eur. J.* **2006,** *12,* 7467–7481. doi:10.1002/chem.200600318
8. Banert, K.; Köhler, F.; Melzer, A.; Scharf, I.; Rheinwald, G.; Rüffer, T.; Lang, H.; Herges, R.; Heß, K.; Ghavtadze, N.; Würthwein, E.-U. *Chem.–Eur. J.* **2011,** *17,* 10071–10080. doi:10.1002/chem.201101220
9. Herges, R.; Geuenich, D.; Bucher, G.; Tönshoff, C. *Chem.–Eur. J.* **2000,** *6,* 1224–1228. doi:10.1002/(SICI)1521-3765(20000403)6:7<1224::AID-CHEM1224>3.3.CO;2-8
10. Berger, C.; Bresler, C.; Dilger, U.; Geuenich, D.; Herges, R.; Röttele, H.; Schröder, G. *Angew. Chem.* **1998,** *110,* 1951–1953. doi:10.1002/(SICI)1521-3757(19980703)110:13/14<1951::AID-ANGE1951>3.0.CO;2-B
    Angew. Chem., Int. Ed. **1998,** *37,* 1850–1853. doi:10.1002/(SICI)1521-3773(19980803)37:13/14<1850::AID-ANIE1850>3.0.CO;2-B
11. Berger, C.; Dieterich, S.; Dilger, U.; Geuenich, D.; Helios, H.; Herges, R.; Kirchmer, P.; Röttele, H.; Schröder, G. *Angew. Chem.* **1998,** *110,* 1954–1957. doi:10.1002/(SICI)1521-3757(19980703)110:13/14<1954::AID-ANGE1954>3.0.CO;2-U
    Angew. Chem., Int. Ed. **1998,** *37,* 1854–1857. doi:10.1002/(SICI)1521-3773(19980803)37:13/14<1854::AID-ANIE1854>3.0.CO;2-O
12. Kimball, D. B.; Herges, R.; Haley, M. M. *J. Am. Chem. Soc.* **2002,** *124,* 1572–1573. doi:10.1021/ja017227u
13. Kimball, D. B.; Weakley, T. J. R.; Herges, R.; Haley, M. M. *J. Am. Chem. Soc.* **2002,** *124,* 13463–13473. doi:10.1021/ja027809r
14. Shirtcliff, L. D.; Weakley, T. J. R.; Haley, M. M.; Köhler, F.; Herges, R. *J. Org. Chem.* **2004,** *69,* 6979–6985. doi:10.1021/jo049011r
15. Shirtcliff, L. D.; Hayes, A. G.; Haley, M. M.; Köhler, F.; Hess, K.; Herges, R. *J. Am. Chem. Soc.* **2006,** *128,* 9711–9721. doi:10.1021/ja054547v
16. Shirtcliff, L. D.; Haley, M. M.; Herges, R. *J. Org. Chem.* **2007,** *72,* 2411–2418. doi:10.1021/jo0622274
17. McClintock, S. P.; Shirtcliff, L. D.; Herges, R.; Haley, M. M. *J. Org. Chem.* **2008,** *73,* 8755–8762. doi:10.1021/jo801390x
18. McClintock, S. P.; Forster, N.; Herges, R.; Haley, M. M. *J. Org. Chem.* **2009,** *74,* 6631–6636. doi:10.1021/jo9011283
19. Young, B. S.; Köhler, F.; Herges, R.; Haley, M. M. *J. Org. Chem.* **2011,** *76,* 8483–8487. doi:10.1021/jo201378t
20. McClintock, S. P.; Zakharov, L. N.; Herges, R.; Haley, M. M. *Chem.–Eur. J.* **2011,** *17,* 6798–6806. doi:10.1002/chem.201002936
21. Young, B. S.; Herges, R.; Haley, M. M. *J. Org. Chem.* **2013,** *78,* 1977–1983. doi:10.1021/jo3020374
22. The rules do not apply to pseudocoarctate reactions. Similar to pseudopericyclic reactions, pseudocoarctate reactions do not exhibit a cyclic overlap of orbitals. In analogy to pseudopericyclic reactions which do not follow the Woodward–Hoffmann rules, pseudocoarctate reactions do not follow the above stereochemical, or thermal/photochemical selection rules.
23. Tseng, K. L.; Michl, J. *J. Am. Chem. Soc.* **1977,** *99,* 4840–4842. doi:10.1021/ja00456a059
24. Mahata, S.; Bhattacharya, S. K. *Chem. Phys. Lett.* **2009,** *477,* 52–56. doi:10.1016/j.cplett.2009.06.086
25. The amount of CO formed is larger than the sum of organic fragments listed. This is due to the fact that not all organic fragments could be assigned.
26. Arnold, B. R.; Balaji, V.; Michl, J. *J. Am. Chem. Soc.* **1990,** *112,* 1808–1812. doi:10.1021/ja00161a025
27. For entropic reasons, ring-closure of biradicals with formation of medium size rings is highly unfavourable at the temperature of pyrolysis.
28. Roth, W. R.; Biermann, M.; Dekker, H.; Jochems, R.; Mosselman, C.; Hermann, H. *Chem. Ber.* **1978,** *111,* 3892–3903. doi:10.1002/cber.19781111215
29. Chapman, O. L.; McMahon, R. J.; West, P. R. *J. Am. Chem. Soc.* **1984,** *106,* 7973–7974. doi:10.1021/ja00337a055
30. Lemal, D. M.; Gosselink, E. P.; McGregor, S. D. *J. Am. Chem. Soc.* **1966,** *88,* 582–600. doi:10.1021/ja00955a035
31. Davis, D.; Vysotskiy, V. P.; Sajeev, Y.; Cederbaum, L. S. *Angew. Chem.* **2012,** *124,* 8127–8131. doi:10.1002/ange.201204162
    Angew. Chem., Int. Ed. **2012,** *51,* 8003–8007. doi:10.1002/anie.201204162
32. Herges, R.; Hoock, C. *Science* **1992,** *255,* 711–713. doi:10.1126/science.255.5045.711
33. Herges, R., Habilitationsschrift, University of Erlangen-Nuremberg, 1990.
34. Dunkin, I. *Matrix Isolation Techniques: A Practical Approach;* Oxford University Press: Oxford, U.K., 1998.
35. Birch, A. J.; Fitton, P.; Smith, D. C. C.; Steere, D. E.; Stelfox, A. R. *J. Chem. Soc.* **1963,** 2209–2216. doi:10.1039/jr9630002209

License and Terms